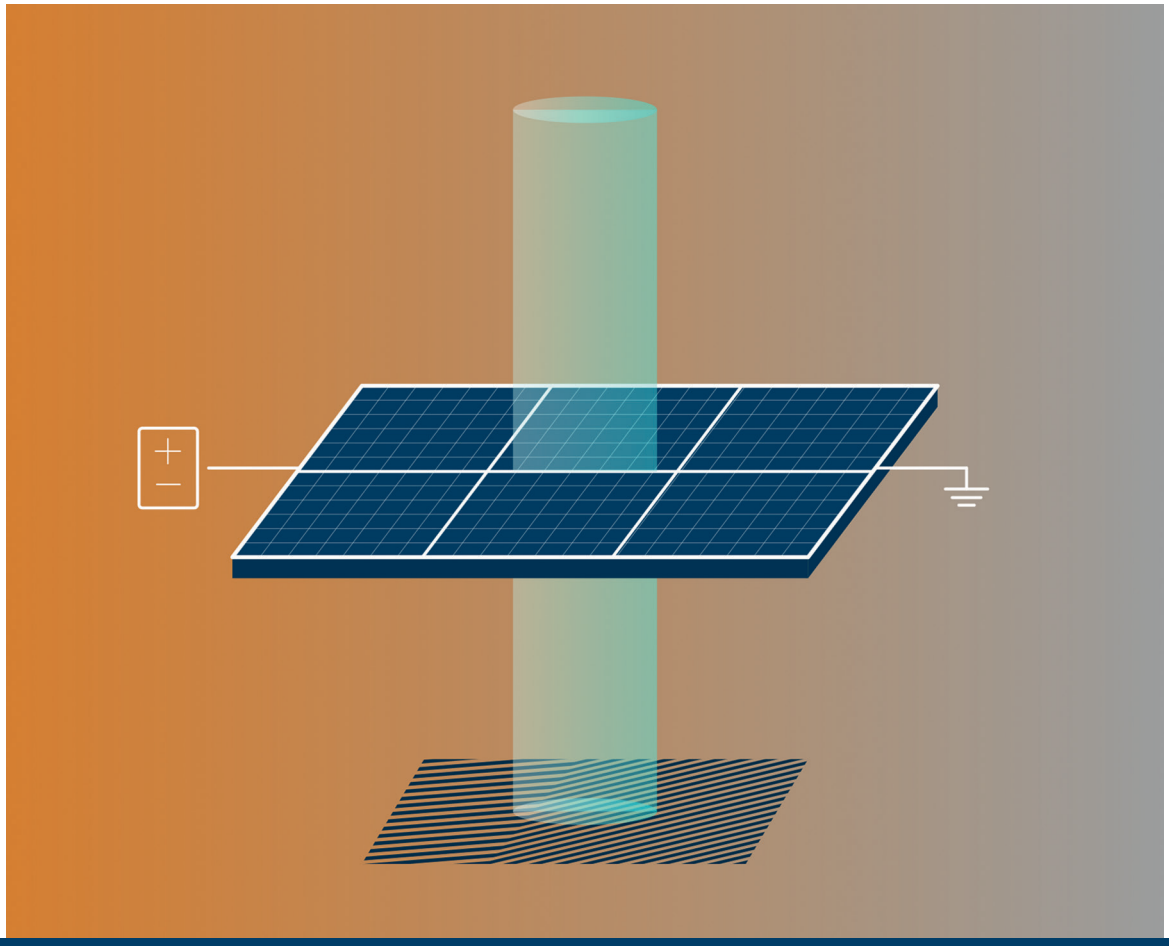

In Situ Biasing Off-Axis Electron Holography and Electron Beam Induced Current Microscopy for the Electrical Investigation of p-n Junctions in High-Efficiency III-V Multi-Junction Solar Cells

Vita Mergner

Schlüsseltechnologien / Key Technologies
Band / Volume 306
ISBN 978-3-95806-925-1

Mitglied der Helmholtz-Gemeinschaft

JÜLICH
Forschungszentrum

Schriften des Forschungszentrums Jülich
Reihe Schlüsseltechnologien / Key Technologies Band / Volume 306

Forschungszentrum Jülich GmbH
Ernst Ruska-Centrum für Mikroskopie und Spektroskopie mit Elektronen (ER-C)
Physik Nanoskaliger Systeme (ER-C-1)

In Situ Biasing Off-Axis Electron Holography and Electron Beam Induced Current Microscopy for the Electrical Investigation of p-n Junctions in High-Efficiency III-V Multi-Junction Solar Cells

Vita Mergner

Schriften des Forschungszentrums Jülich
Reihe Schlüsseltechnologien / Key Technologies Band / Volume 306

ISSN 1866-1807 ISBN 978-3-95806-925-1

Bibliografische Information der Deutschen Nationalbibliothek.
Die Deutsche Nationalbibliothek verzeichnet diese Publikation in der
Deutschen Nationalbibliografie; detaillierte Bibliografische Daten
sind im Internet über http://dnb.d-nb.de abrufbar.

Herausgeber und Vertrieb:	Forschungszentrum Jülich GmbH Zentralbibliothek, Verlag 52425 Jülich Tel.: +49 2461 61-5368 Fax: +49 2461 61-6103 zb-publikation@fz-juelich.de www.fz-juelich.de/zb
Umschlaggestaltung:	Grafische Medien, Forschungszentrum Jülich GmbH
Druck:	Grafische Medien, Forschungszentrum Jülich GmbH
Copyright:	Forschungszentrum Jülich 2026

Schriften des Forschungszentrums Jülich
Reihe Schlüsseltechnologien / Key Technologies, Band / Volume 306

D 82 (Diss. RWTH Aachen University, 2026)

ISSN 1866-1807
ISBN 978-3-95806-924-4 (Print)
ISBN 978-3-95806-925-1 (E-Book)

Vollständig frei verfügbar über das Publikationsportal des Forschungszentrums Jülich (JuSER)
unter www.fz-juelich.de/zb/openaccess.

Acknowledgements

Science is teamwork. Here, I would like to convey my sincere gratitude to the many people who formed the supportive network that accompanied and encouraged me throughout my doctorate. I gratefully acknowledge:

- My supervisor Prof. Dr. Rafal Dunin-Borkowski for providing me with the opportunity to pursue my doctorate and for his continuous support and encouragement. With his non-hierarchical approach to guidance, by asking thoughtful and critical questions, he not only allowed me to find my own path on my PhD journey, but also created a scientific working environment that enables free and outstanding research. I am especially grateful for the opportunity to conduct research stays at CEA Grenoble, and for providing me with access to an international research network.
- Prof. Dr. Joachim Mayer for kindly accepting the role as co-assessor of this dissertation.
- My cooperation partners at Fraunhofer ISE, above all Dr. Frank Dimroth and Dr. David Lackner, for making this collaboration possible, for kindly providing me with interesting samples, and for asking numerous critical questions. I am specifically grateful to Dr. Patrick Schygulla and Malte Klitzke for growing the samples, for the many discussions and the cheerful and enjoyable exchange throughout our collaboration.
- Prof. Dr. Wolfgang Jäger, for being my mentor and providing me with continuous strategic advice throughout this journey. Without his initiative and tireless energy in initiating exciting new research collaborations, this cooperative project would not have come into being.
- Dr. András Kovács, who was my first point of contact for questions of all kinds and who always took the time to reliably support me with both advice and practical help. I thank him for being my first coach training me on the electron microscope and sharing his knowledge, and for inspiring me with his efficient and accurate way of working.
- Dr. David Cooper for kindly welcoming and integrating me into his team at CEA Leti Grenoble, and for supporting and encouraging me in his enthusiastic and energetic manner. I am grateful to him for openly sharing his knowledge and tricks in *in situ* biasing experiments and sample preparation.
- Marie Göcking, Lidia Kibkalo, Maximilian Kruth, Alexander Mueller and René Borowski, for their invaluable support with technical and administrative matters in their unbureaucratic manner and for their efforts in creating a cheerful and pleasant atmosphere in the institute.
- Dr. Ansgar Meise for being my PhD partner in crime from day one.
- My dear fellow students at CEA Grenoble, for their warm welcome into the team, for the motivating peer support, and for all the countless laughs and lunch runs we shared.
- My parents and family for their unconditional support and encouragement, and for being an endless source of strength, optimism, confidence, and good humour.

Abstract

As the world seeks cleaner and more efficient energy solutions, solar power has emerged as a key renewable option. Among the various technologies, III-V multi-junction solar cells absorb an extended range of the solar spectrum and thus achieve the highest conversion efficiencies in photovoltaics today. Further enhancing solar cell performance requires adding more subcells to the III-V layer stack while improving material quality and doping confinement at specific hetero-interfaces, targeting at precise energy band structure design to enhance absorption efficiency and ensure efficient current extraction. Enabling these developments requires a high-resolution probe of crystalline structure and chemical composition, as well as for dopant potential and minority carrier distributions. In this thesis, *in situ* electrical biasing transmission electron microscopy (TEM) is employed to investigate the electronic properties of specific III-V p-n hetero-junctions, as a step towards enabling quantitative functional characterisation of working solar cells with nanometer resolution.

Off-axis electron holography (EH) is employed to measure electrostatic potential distributions in biased GaAs and InP p–n junctions, enabling to develop a methodology for quantifying depletion widths within complex III–V heterostructures at nanometer resolution. To ensure reproducibility across specimens of varying electron-transparent thickness, electrically inactive surface layers from focused ion beam (FIB) preparation are quantified by correlating EH-derived built-in potentials with thickness measured by convergent beam electron diffraction. Electrical contacting is achieved using W and Pt deposition in the FIB. The EH-measured contact characteristics have been found to match the theoretically predicted Schottky barrier heights. Electrostatic potential mapping under *in situ* reverse bias confirmed the electrical functionality of the GaAs p–n junctions via depletion region widening. Complementary electron beam induced current (EBIC) measurements in scanning TEM (STEM) mode are used to map charge carrier generation and collection in electrically biased GaAs p–n junctions. These measurements validated the method's utility for assessing electrical integrity under bias by visualising the increase in junction resistivity and EBIC signal corresponding to enhanced electric field strength during reverse biasing. Low-magnification STEM-EBIC enabled the detection of long-range resistivity variations, while secondary electron-induced surface charging effects in n- and p-doped GaAs are resolved. The results highlight the unique capability of STEM-EBIC to probe electron–specimen interactions at the nanoscale, enabled by the signal's comprehensive electrical sensitivity.

The tunnelling efficiency of p-AlGaAs/n-GaInP hetero-junctions in MJSCs depends on the epitaxial growth direction. To understand this behaviour, comparative *in situ* biasing EH electrostatic potential profiling is used with high spatial-resolution and sensitivity to quantify the depletion widths as a proxy for active dopant distribution and tunnelling performance in operating solar cells. Despite the change in compositional mean inner potential, the p-AlGaAs/n-GaInP depletion width is reproducibly quantified with high accuracy, consistent with electrostatic potential simulations. Finally, *in situ* biasing EH is used to study the p-AlGaAs/n-GaInP tunnel junction within a working III–V tandem cell. Complementary STEM-EBIC mapping has been used to assess the electrical integrity and functional biasing of the device junctions. This work advances *in situ* biasing EH and STEM-EBIC methodologies for III-V hetero-junction analysis, promoting comprehensive, quantitative electrical measurements at high-resolution, which is essential for characterisation and further development of high-efficiency III–V MJSCs.

Table of Content

Acknowledgements **I**

Abstract **III**

List of Acronyms **IX**

List of Figures **XIII**

List of Tables **XXXI**

1 Introduction **1**
1.1 Background and Motivation 1

2 High-Efficiency III-V Multi-Junction Solar Cells **5**
2.1 Introduction to the Concept of III-V MJSCs 5
2.2 Fundamental Properties of Epitaxially-Grown III-V Heterostructures 7
2.2.1 Structural Properties of III-V Semiconductors 8
2.2.2 Elastic Properties 10
2.2.3 Electronic Properties 13
2.3 Motivation for TEM Analysis of MJSCs 17

3 Transmission Electron Microscopy Measurements of III-V Semiconductors **19**
3.1 Fundamental Principles of Transmission Electron Microscopy 19
3.1.1 Electron-Matter Interaction 19
3.1.2 Transmission Electron Microscopy Mode 20
3.1.3 Scanning Transmission Electron Microscopy Mode 22
3.1.4 Spatial Resolution 23
3.2 (S)TEM Techniques for Structural and Chemical Analysis of III-V Semiconductors 24
3.2.1 High-Angle Annular Dark-Field Scanning Transmission Electron Microscopy 25
3.2.2 Energy-Dispersive X-ray Spectroscopy 27

4 (S)TEM Sample Preparation **31**
4.1 Basic Principles of Focused Ion Beam (FIB)-based Specimen Preparation 31
4.1.1 The FIB-SEM System 31
4.1.2 Ion-Matter Interaction 32
4.2 The FIB Preparation Methodology 33
4.2.1 FIB-SEM Devices 33
4.2.2 The Experimental Protocol 34
4.3 Sample Preparation Considerations for Electrical TEM Analysis of III-V Semiconductors 38
4.3.1 Electrical Surface Damage 38
4.3.2 Impurity Implantation 40
4.3.3 Lamella Thickness Uniformity 41
4.3.4 Vacuum Reference Region (Sample Geometry) 42

4.4 TEM Specimen Preparation for *In Situ* Biasing Experiments 42
4.4.1 The Preparation Procedure 43
4.4.2 Electrical Properties of FIB Deposited Metals 46
4.4.3 Specific Considerations 47

5 Off-Axis Electron Holography for Electrostatic Potential Analysis of III-V Devices 49
5.1 Introduction to Off-Axis Electron Holography 49
5.1.1 Fundamental Principles 49
5.1.2 The Experiment and Reconstruction 50
5.2 Experimental Setup and Considerations for Electron Holography 54
5.2.1 Phase Sensitivity 54
5.2.2 Spatial Resolution 57
5.2.3 Information Loss 59
5.2.4 Selecting the Field of View 60
5.2.5 The Influence of Electron Beam Illumination on the Phase Measurement . 62
5.2.6 Limitations and Artefacts 64
5.3 Sample Thickness Assessment for Electron Holography 67
5.3.1 Crystalline Thickness Measurement Using Convergent Beam Electron Diffraction 68
5.3.2 Electrically Inactive Thickness Evaluation 71

6 Electrostatic Potential Analysis of Binary III-V p-n Junctions 73
6.1 The Specimen 73
6.2 The p-n Junction 75
6.3 Simulation of the Electrostatic Potential 78
6.4 Electrostatic Potential Analysis of p-n Homo-Junctions of Binary III-V Compounds 80
6.4.1 GaAs 80
6.4.2 InP 87
6.5 Electrostatic Potential Analysis of *in situ* Electrically Biased III-V P-N Junctions 92
6.5.1 Experimental Description 92
6.5.2 The Built-In Potential of the GaAs p-n Junction Under Applied Bias . . . 94
6.5.3 The Depletion Width of the GaAs p-n Junction Under Applied Bias . . . 96
6.5.4 The Electrical Circuit of the *In Situ* Biasing Specimen 97
6.5.5 The GaAs-Pt and GaAs-W Semiconductor-Metal Contacts 99
6.6 Summary 107

7 STEM-Electron Beam Induced Current Analysis of *In-Situ* Biased III-V Semiconductor Junctions 109
7.1 Fundamental Principles of EBIC Analysis 111
7.1.1 EBIC Signals 111
7.1.2 Signal Generation 112
7.1.3 Approaches to the Qualitative Differentiation of EBIC Signals 114
7.1.4 Factors Influencing the Signal Generation and Yield 116

7.1.5 Experimental Adjustment of the Signal Composition . . . 119
7.2 Experimental Considerations . . . 120
7.2.1 Measurement Geometry . . . 120
7.2.2 Spatial Resolution . . . 120
7.2.3 Acceleration Voltage . . . 121
7.3 STEM-EBIC Methodology . . . 122
7.3.1 The Specimen . . . 122
7.3.2 Experimental Setup and Instrumentation . . . 123
7.3.3 Specimen Connection Geometries and Configurations . . . 123
7.4 Experimental STEM-EBIC: Parameter Adjustment and Signal Optimisation . . . 124
7.4.1 EBIC Maps: Signal Contributions and Qualitative Distribution . . . 124
7.4.2 The Effect of Sample Thickness and Surfaces . . . 128
7.4.3 The Effect of Beam Imaging Conditions: Beam Current and Spotsize . . . 133
7.4.4 The Interrelated Effect of STEM Magnification, Pixel Frame Size and Pixel Dwell Time . . . 136
7.5 STEM-EBIC Analysis of GaAs p-n Junctions . . . 138
7.5.1 Low-Magnification STEM-EBIC Analysis . . . 139
7.5.2 Standard-Magnification STEM-EBIC Analysis . . . 154
7.6 Summary . . . 159
7.7 Towards Quantitative STEM-EBIC: Opportunities and Challenges . . . 161
7.7.1 Work Function Measurements in Electronic Devices . . . 161
7.7.2 Quantitative Field-Related EBIC Measurements at III–V p–n Junctions and the Extraction of Minority Carrier Characteristics . . . 163

8 Investigation of n-GaInP/p-AlGaAs Tunnel Diodes for Multi-Junction Solar Cells 165
8.1 Introduction . . . 165
8.1.1 Tunnel Diodes for Multi-Junction Solar Cells . . . 165
8.1.2 High-bandgap p-AlGaAs/n-GaInP Tunnel Diodes for MJSCs . . . 166
8.1.3 Research Motivation . . . 168
8.2 Bulk Specimen Structures . . . 169
8.3 Structural and Compositional STEM Analysis of p-AlGaAs/n-GaInP Interfaces . . . 170
8.3.1 STEM-HAADF Atomic Structure and Z-Contrast Analysis . . . 171
8.3.2 STEM-EDX Analysis of Major Element Distribution . . . 177
8.3.3 STEM-EELS Verification of P Distribution . . . 180
8.3.4 Measuring HAADF Contrast as a Function of Camera Length . . . 181
8.3.5 Summary of Structural and Compositional Analyses . . . 181
8.4 Electrostatic Potential Analysis of p-AlGaAs/n-GaInP Tunnel Junctions . . . 184
8.4.1 Analysis in Upright and Inverted III-V Tandem Solar Cell Heterostructures 184
8.4.2 Analysis in Upright- and Inverted-Grown Test Structures . . . 194
8.5 *In Situ* Biasing (S)TEM Analysis of Upright-Grown n-GaInP/p-AlGaAs Tunnel Junctions . . . 195
8.5.1 Approach 1 . . . 200
8.5.2 Approach 2 . . . 205

8.6 Investigation of a n-GaInP/ p-AlGaAs Tunnelling Junction in a Working GaInP/GaAs Tandem Solar Cell . . . 210
8.6.1 The Tandem Solar Cell Structure and Bulk Electrical Characteristics . . . 210
8.6.2 Specimen Preparation For *In Situ* Biasing TEM Analysis . . . 214
8.6.3 *In Situ* Biasing Electrostatic Potential Analysis Using Off-Axis Electron Holography . . . 215
8.6.4 STEM-EBIC Current Mapping . . . 224
8.7 Summary . . . 227

9 Summary and Outlook **231**

10 References **235**

List of Publications **259**

List of Acronyms

ADF Annular dark-field

BF Bright field

CBED Convergent beam electron diffraction

CPV Concentrating photovoltaics

DF Dark field

DFT Density functional theory

EBAC Electron beam absorbed current

EBIC Electron beam induced current

EBID Electron-beam induced deposition

EDX Energy-dispersive X-ray spectroscopy

EELS Electron energy loss spectroscopy

EH Off-axis electron holography

EHP Electron-hole pair

fcc Face-centred cubic

FEG Field emission gun

FIB Focused ion beam

FOV Field of view

FT Fourier transform

HAADF High angle annular dark field

IBID Ion-beam induced deposition

ICP Inductively-coupled plasma

LMIS Liquid metal ion source

MED Mean escape depth

MFP Mean free path

MIP Mean inner potential

MJSC Multi-junction solar cell

MOVPE Metalorganic vapor-phase epitaxy

ROI Region of interest

TD Tunnel diode

TEM Transmission electron microscopy

TJ Tunnel junction

SE Secondary electrons

SEY Secondary electron yield

SNR Signal-to-noise ration

STEM Scanning transmission electron microscopy

WPOA Weak phase object approximation

List of Figures

1 (a) Schematic representation of the operating principle of a multi-junction solar cell, exemplified by a GaInP/GaInAs/Ge triple-junction (3-J) cell. Each bandgap material absorbs a specific wavelength range of the solar spectrum (modified after Philipps et al., 2018).[1] (b) Schematic representation of the electrical circuit of a 3-J solar cell. 6

2 Best research-cell efficiency chart (modified after NREL, 2025).[2] The black box highlights the current world record solar cell, a III-V 4-junction solar cell developed at Fraunhofer ISE, achieving an efficiency of 47.6% under concentrated light – the highest reported solar cell efficiency to date.[3] 7

3 Bandgap energy as a function of lattice constant for III-V semiconductor alloys. Direct- and indirect-bandgap semiconductors are represented by solid and dashed lines, respectively. Ternary compounds are represented by lines connecting the constituent binaries. The bandgap combination of a typical $Ga_{0.50}In_{0.50}P$/ $Ga_{0.99}In_{0.01}As$/Ge triple-junction solar cell is highlighted in red, with the red dashed line representing lattice-matched growth (modified after Philipps et al., 2018).[1] 8

4 Schematic unit cell of a zincblende III-V crystal structure. 9

5 Schematic illustration of different types of epitaxial heterostructures. The lattice mismatch between the epitaxial layer (a_e) and the substrate (a_s) determines the nature of the resulting elastic strain deformation. 12

6 Schematic illustration of the primary signals generated by the interaction of a high-energy electron beam with an electron-transparent semiconductor specimen (adapted from Williams & Carter (2008)).[4] 19

7 Schematic illustration of the electron beam trajectory in TEM. Technical details omitted for clarity. 21

8 Schematic representation of the STEM detector setup for BF, DF, and HAADF STEM imaging. Typical detector collection angles are $\theta_1 < 10$ mrad for BF, $\theta_2 \approx 10-50$ mrad for DF, and $\theta_3 > 50$ mrad for HAADF. The choice of convergence semi-angle (α) of the incident beam influences not only the probe size but also the contrast and resolution in different STEM imaging modes. 23

9 High-resolution aberration-corrected STEM-HAADF images of III-V heterointerfaces. 26

10 High-resolution STEM-HAADF images of (a) the micro-core of a twinning dislocation formed under tensile strain in GaAsP buffer layers epitaxially grown on a GaAs substrate. The tensile strain arises from the reduced lattice spacing as the P content in $GaAs_{1-x}P_x$ increases. The width of the micro-twin, defined by the number of atomic columns, varies along the growth direction. (b) and (c) show STEM-HAADF images of the same twin, with the width increasing from 6 to 7 columns and from 7 to 8 columns, respectively, as the wafer surface is approached. Each dislocation step creates a strain field, visible through the bright contrast. The red line marks the additional plane bounded by the dislocation. 26

11 Schematic illustration of EDX signal generation in (S)TEM. Inelastic interactions between the incident electron beam and atomic electron shells produce characteristic X-ray emission. 28

12 Elemental distribution across a GaInP/AlInP/GaAs heterostructure, quantified from STEM-EDX maps using the k-factor method. The inset shows a STEM-HAADF overview image of the analysed sample region. 29

13 a) Schematic representation of a FIB-SEM system. b) Simplified illustration of some ion-matter interaction mechanisms occuring during the FIB-milling of a crystalline specimen. The interaction zone refers to the depth in which ion-induced sample damage occurs, such as amorphisation, vacancies, interstitials and ion implantation. 32

14 Secondary electron SEM images showing the FIB preparation process for conventional TEM samples, acquired at 5 kV and 0.40 nA. (a) Electron-beam induced deposition (EBID) of a first C protective layer at 0°. (b) Ga-ion-beam induced deposition (IBID) of a second C protective layer at 52°. (c) FIB milling of trenches on each side of the protective layer, followed by a cleaning of the side-walls at lower ion-beam energy. (d) The lamella is cut free on one side and at the bottom using an L-cut at 7°. (e) The micro-manipulator is inserted and attached to the lamella with an IBID of C. (f) The last connection of the lamella to the bulk specimen is cut off, allowing the lift-out and (g) the transfer of the lamella to a TEM support grid. (h) The lamella is attached to the grid by a IBID of C and the manipulator is cut off and extracted. (i) Progressive thinning of the lamella to electron-transparent thickness is achieved through iterative milling of the front- and back sides at $52° \pm 2°$, respectively. 35

15 Two (S)TEM sample cut geometries to avoid lamella bending. (a) Side-view and (b) top-view SE SEM images of a flat and short cut STEM-lamella. (c) Side-view and (b) top-view SE SEM images of a ~200 nm thick lamella with an U-shaped electron-transparent window of about 50 nm thickness. 36

16 To attain a U-shape cut, the sample lamella is (a) first milled down to a thickness of 400−500 nm by using the standard procedure described above. Then, (b) in an on-edge tilt position to the FIB, a rectangular cleaning-crosssection pattern is set on the desired window position. Milling parameters of 16 kV and 40 pA are used, and a very small z-depth of 0.1 µm, which can be adapted to the desired depth of the window. To achieve the target thickness, the front window can be iteratively milled with the entire back-side of the lamella, as shown in (c), using small off-tilts of ±0.8° from the edge-on 52°. Image (a) is a SE SEM image, whereas images (b) and (c) are FIB images. 38

17 a) Schematic cross-section of a TEM lamella prepared by FIB milling, including the ion-beam induced damaged surface layers and their influence on the depletion width (in dark grey) of the specimen p-n junction. t_{CBED} refers to the crystalline lamella thickness, which is measured by convergent beam electron diffraction. b) Schematic illustration of the dependency of the surface depletion (or electrically damaged) layer width on the doping concentration. Higher doping results in a smaller surface depletion layer. 40

18 A TEM lamella with steps of different thickness (a) before and (b) after the removal of the protective depositions (ink plus ion-beam induced W deposition) from the top surface. The sequence in (c)-(e) demonstrates the removal of the free-standing W-layer by using the micro-manipulator needle, after the ink-layer was removed by plasma-cleaning. All SE SEM images were acquired at 5 kV and 0.40 nA. 43

19 SE SEM images of the first steps of the *in situ* biasing TEM specimen preparation, acquired at 5 kV and 0.40 nA. (a) Ion-beam induced metal (W or Pt) deposition (IBID) for protection and electrical contacting. (b) By milling side-trenches and performing an L-cut, a free-standing lamella is shaped. (c) The lamella is welded to a manipulator by IBID of W and the last side-connection is cut free to allow the lamella lift-out. 44

20 Preparation of a TEM lamella on a chip for *in situ* biasing TEM analysis. (a) The lamella is transferred to the Si-half MEMS chip, where it will be positioned on the chip trench shown in (b). To allow the manipulator to be cut off, a preliminary metal fixation to the chip is deposited on the back of the lamella at 52° shown in (c). (d) Afterwards, each lamella side is electrically connected to the respective metal tracks by large ion-beam induced metal depositions at 0°. (e) The lamella side-walls are cleaned and damage at the bottom edge is removed by an undercut, and the first isolation is cut for circuit editing. (f) After shaping and thinning the lamella to the desired thickness, the second isolation cut is milled. The preparation is finished off by ion-polishing each side at 2 kV. All SE SEM images were acquired at 5 kV and 0.40 nA. The ion-beam generated image in (c) was taken at 30 kV and 0.46 nA. 44

21 a) Schematic of the Protochips MEMS Si-half chip for *in situ* electrical biasing experiments in a transmission electron microscope. The four large metallized pads are contacted electrically to wires in the sample holder using metal needles. Four metal tracks lead from the pads to a trench, where the specimen is attached for contacting. The dimensions are not on scale. (b)-(c) SE SEM images acquired at 10 kV and 0.54 nA, giving b) an overview of the front-side of a biasing chip and c) a close-up view on the chip trench. 45

22 a) Schematic illustration of the TEM lamella geometry designed for in-situ biasing experiments. b) Schematic representation of the electrical circuit within the TEM lamella. 48

23 Schematic representation of off-axis electron holography in TEM. The FEG provides coherent electron illumination on an electron-transparent specimen and an adjacent vacuum region. An electron biprism is used to interfer the object wave with the vacuum reference wave to form the hologram as an interference pattern on the screen. 50

24 Examples of (a) an object hologram recorded of a III-V multilayer structure and (b) the corresponding reference hologram acquired in vacuum. The zoomed inset in (a) highlights the fringe bending caused by the change in electrostatic potential at the p-n junction, whereas the zoomed inset in (b) shows that the fringes of the unperturbed reference wave exhibit no bending. 51

25 a) Fourier transform of the object hologram shown in Fig. 24, displaying the centerband and sidebands that contain the phase and amplitude information. (b) Reconstructed phase image, and (c) reconstructed amplitude image of the III-V multilayer structure. 53

26 (a)-(d) Electron holograms acquired using the indicated exposure times, with a Gatan K2 direct electron detection camera installed on a FEI Titan HOLO with a biprism voltage of 120 V and a fringe spacing of 2.3 nm. (e) Profiles extracted from the holograms in (a)-(d) perpendicular to the fringes displaying the dependence of the electron counts and the hologram contrast on the exposure time. (f) The phase noise (i.e. the standard deviation in the reconstructed vacuum phase image) and the hologram fringe contrast plotted as a function of the hologram acquisition time. 56

27 Phase distribution in a semiconductor layer structure reconstructed (a) from a single hologram and (b) from a stack of 32 holograms. (c) and (d) The standard deviation of the phase measurement (i.e. the phase noise) improves with an increasing number of averaged phase images (holograms per stack). The standard deviation was measured in the central region of the phase images, reconstructed from hologram stacks acquired in vacuum with an exposure time of 4 s and 8 s per individual frame. The data in (a), (b), and (c) was recorded with a FEI Titan Ultimate using a biprism voltage of 125 V and an interference fringe spacing of 3 nm, while the data represented in (d) was taken with a FEI Titan HOLO using a biprism voltage of 120 V and a fringe spacing of 2.3 nm. 58

28 (a) Schematic illustration of the electron hologram formation by means of an electron biprism. The voltage applied to the biprism controls the distance of the two virtual sources, S_1 and S_2, as well as the deflection angle α, thereby controlling the hologram width and the interference fringe spacing, respectively (modified after Midgley, 2001).[5] (b) The influence of the biprism voltage on the fringe spacing. The holograms were acquired in vacuum at a magnification of 24.5kx using a FEI Titan HOLO microscope equipped with a Gatan K2 camera. 59

29 The dependence of (a) fringe contrast and (b) pixels per fringe sampling on the fringe spacing, controlled by the biprism voltage. The hologram data set was acquired at a constant magnification of 24.5kx using a Gatan K2 camera on a FEI Titan HOLO microscope. 60

30 The diffraction lens excitation can be adjusted to increase the hologram width for analysis requiring a large FOV. (a)–(c) show how the FOV, fringe spacing (fs), and pixels per fringe sampling change for holograms acquired at lens excitations of 12%, 15%, and 20%, which are the common large-FOV lens settings used in this work. The holograms were recorded with a Gatan OneView CCD camera at a FEI Titan Ultimate microscope operated at 200 kV. 62

31 The standard deviation of phase measurements as a function of the number of averaged phase images (images per stack). The hologram stacks were recorded with a magnification of 40.0kx operating a FEI Titan Ultimate at 200 kV. Holograms recorded with a diffraction lens excitation of 89% and a biprism voltage of 200 V correspond to the standard hologram acquisition setting used for higher spatial resolution in this work, yielding a 2.05 nm fringe spacing, with a 8 pixels/fringe sampling and a FOV of 844×844 nm. The lens excitation of 20% combined with a biprism voltage of 80 V is used to record holograms with a large FOV of 5.18×5.18 µm, a fringe spacing of 6.2 nm and a sampling of 4 pixels/fringe. The standard deviation was measured in the central region of the phase images, reconstructed from hologram stacks acquired in vacuum with an exposure time of 4 s and 8 s per individual frame. The phase images were corrected for linear and polynomial distortions. 63

32 (a) Off-axis electron hologram acquired at 200 kV using a FEI Titan Ultimate, a biprism voltage of 200 V and an interference fringe spacing of 2 nm. (b) and (c) show the corresponding phase image reconstructed without and with including a vacuum reference hologram, respectively. 65

33 Schematic illustration of the specimen orientation for EH analysis in this work. (a) The III-V structures are grown in [001] direction and cross-sectional lamellae are cut for viewing along the [110] zone axis. For EH, the specimen are tilted about the [001] axis away from the zone axis. (b) and (c) illustrate the specimen orientation in diffraction space when (b) viewed along the [110] zone axis and (c) tilted about the [001] growth-axis to weakly diffracting conditions for EH. The black dot indicates the changing position of the transmitted electron beam (000) when tilting along the 004 Kikuchi band, indicated by the α-tilt arrow. (b) and (c) are modified after Formanek *et al.* (2006).[6] 68

34 (a) STEM-CBED pattern of GaAs under two-beam conditions, showing characteristic K-M fringe patterns in both diffraction discs. (b) K-A plot method, utilizing the linear relation $y = -\frac{1}{\xi_g^2}x + \frac{1}{t^2}$ to determine the crystalline sample thickness. . 69

35 Schematic illustration of the III-V semiconductor specimen structures, indicating each layer's thickness, III-V compound, as well as doping type and concentration. (a) GaAs p-n homo-junction specimen. (b) InP p-n homo-junction specimen. The dimensions of the epitaxial layers are not to scale. 74

36 Schematic illustration of a p-n junction and its key characteristics in equilibrium conditions (without applied bias). The energy band diagram displays the alignment of the Fermi level, E_F and the resulting bending of the conduction band, E_C, and the valence band, E_V. The built-in potential, V_{bi}, is given by the difference in electrostatic potential, $V(x)$, between the n-type and the p-type layer. The electric field distribution,$E(x)$, is non-zero in the depletion region, which is defined between $x_n - x_p$ with the depletion width W_d. The charge density distribution, $\rho(x)$, is defined as qN_d in the n-side of the SCR and as $-qN_a$ in the p-side. 78

37 Simulation of the a) energy band structure and b) electrostatic potential distribution across the symmetrically 1×10^{18} cm^{-3} doped GaAs p-n junction at equilibrium state (without applied bias). 79

38 Simulated electric field distribution across the symmetrically 10^{18} cm^{-3} doped GaAs p-n junction at different applied reverse biases. 80

39 BF-TEM images of the GaAs specimen α-tilted away from the [110] zone axis around the [001] growth direction. The presence of dark dynamical diffraction contrast varies depending on the tilt orientation. The indicated α-tilt angles are measured relative to the zone-axis orientation at 0°. The green line indicates the approximate position of the GaAs p-n junction. 82

40 (a)-(e) Amplitude images and (f)-(j) phase images reconstructed from electron hologram stacks recorded at the different thickness regions of the GaAs-AuPd specimen. The holograms yielding the images (a)-(d) and (f)-(i) were recorded at +2.35° off-tilt from the zone axis, while those yielding (e) and (j) were taken at −4.26°. 82

41 (a) Phase profiles across the GaAs p-n junction extracted from regions of different crystalline thickness of the GaAs-AuPd lamella shown in Fig. 40. (b) Step in electron phase across the junction as a function of the total crystalline specimen thickness measured by STEM-CBED. The electrically damaged thickness ($t_{inactive}$) is derived from the x-intercept of the linear fit of the experimental phase values. 84

42 (a) Phase profiles across the GaAs p-n junction extracted from regions of different crystalline thickness of the GaAs-W lamella. (b) Step in electron phase across the junction as a function of the total crystalline specimen thickness measured by STEM-CBED. The electrically damaged thickness (t_i) is derived from the x-intercept of the linear fit of the experimental phase values. Accounting for t_i in the simulation, the expected phase shifts for the remaining electrically active specimen thicknesses are shown for comparison. 84

43 Comparison of the electric field distribution across the GaAs p-n junction from experimental data and simulations, both at a specimen thickness of 385 nm. The experimental profile was obtained from the respective phase profile in Fig. 41a using the first differential equation 51. W_d indicates the width of the depletion region derived from the linear extrapolation of the peak flanks to the x-axis. . . . 87

44 Amplitude and phase images reconstructed from electron hologram stacks recorded at thickness regions t1–t5 of the InP specimen using low-magnification (LM) (top and middle rows) and standard (bottom row) EH settings. 89

45 Phase measurements of another InP lamella (InP-2), prepared of the same bulk specimen, are shown here for comparison. (a) Overview BF-TEM image of the specimen highlighting thickness regions labeled r1–r4. (b)–(e) Phase images reconstructed from holograms taken at the positions indicated in (a). (f) Phase distributions measured across the structure at each region. Each phase image was obtained from stacks of 30 holograms recorded with an 8 s acquisition time per hologram, using standard diffraction lens settings, a biprism voltage of 200 V, and a magnification of 28.5kx, resulting in a fringe spacing of 2.3 nm. 90

46 (a) Evaluating the measured step in phase across the InP p-n junction as a function of the total crystalline specimen thickness yielded an inactive thickness of 103 ± 18 nm. (b) Comparison between standard and low-magnification (LM) phase data. The phase profiles were derived across the t4 region from the respective phase images shown in Fig. 44, having a spatial resolution of 5.4 nm and 15 nm, respectively. The profiles have been deliberately offset for clarity. 90

47 (a) SE SEM image of the GaAs-Pt specimen and (b) BF TEM image of the GaAs-W specimen prepared on MEMS support chips for *in situ* biasing experiments. The positions of the electrical bias ($\pm$V) and ground (GND) connectors are marked in red. The region of interest (ROI) for *in situ* biasing hologram acquisitions is highlighted in turquoise, and the GaAs p-n junction is indicated by the white dashed line. 93

48 Phase images of the p-n junction in a) the GaAs-W specimen and b) the GaAs-Pt specimen at selected reverse (-) and forward (+) bias voltages. Phase profiles for each specimen, shown in Figs. 49 and 55, are extracted from the indicated regions. 94

49 Phase profiles measured at different applied voltages across the p-n junction in the (a) GaAs-W specimen at $t_c = 450 \pm 17$ and (b) the GaAs-Pt specimen at $t_c = 370 \pm 10$. 95

50 The built-in potential across the GaAs p-n junction plotted as a function of the applied voltage. 95

51 Electric field distribution across the p-n junction in the (a) GaAs-W specimen at $t_C = 450 \pm 17$ and (b) the GaAs-Pt specimen at $t_C = 370 \pm 10$. The profiles were derived from the experimental potential profiles using the first differential equation (Eq. 51). 96

52 Width of the depletion region at the p-n junctions in the GaAs-W and GaAs-Pt specimen as a function of the applied voltage, measured by means of the electrical field profiles in Fig. 51. The expected values for the ideal junction (abrupt and complete ionization) under reverse bias, derived from the NEXTNANO simulation of the GaAs specimen, are shown for comparison. 97

53 Schematic *I-V* characteristics of Schottky (non-linear, rectifying) and ohmic (linear, non-rectifying) metal-semiconductor contacts. 100

54 Schematic energy band diagrams illustrating the four possible metal-semiconductor configurations, as summarized in Table 9. For Schottky contacts [(a) and (c)], a depletion region of width W_d forms on the semiconductor side, and majority carriers encounter a potential barrier of height V_{bi} at the interface. The barrier for electrons in the metal is the Schottky barrier, ϕ_{SB}. In contrast, for ohmic contacts [(b) and (d)], no depletion region forms, and majority carriers face no potential barrier at the interface. 101

55 Phase distribution starting from the metal/p-GaAs interface and extending across the GaAs p-n junction in (a) the GaAs-W specimen and (b) the GaAs-Pt specimen at different applied reverse biases. The *I-V* characteristics of the GaAs-W lamella are shown in the inset. 105

56 Schematic illustration of the generation mechanisms of the three primary signal contributions to EBIC in STEM. (a) Field-related EBIC generated by the separation of electron–hole pairs, induced by the electron beam, within the electric field (δE) at a semiconductor p–n junction. (b) Hole current arising from secondary electron (SE) emission, generated by the electron beam within the surface-near mean escape depth (MED). (c) Current of absorbed primary electrons, which are increasingly absorbed with greater specimen thickness. 112

57 SE SEM images of the two MEMS support chip configurations used in this study: a) the 2-track and b) the 4-track design. The number of contact points are indicated. The images are taken from blank chips without sample to illustrate the track design. 124

58 Electrical connection configuration of the TEM specimen to the MEMS chip: (a) GaAs-W on a 2-track chip, (b) GaAs-W-2 on a 2-track chip, and (c) GaAs-Pt on a 4-track chip. The indicated contact point numbers correspond to the assigned holder (Protochips Aduro 500) terminals, which can be controlled using the DISS 5 EBIC acquisition software (point electronics GmbH). 125

59 Schematic illustration of the possible connection configurations and their effects on the detected EBIC signal for a p-n junction specimen: (a) without and (b) with applied electrical bias (±). Note that only the influence on the presence and sign of the field-related EBIC signal is shown, as the presence and sign of the remaining signals – positive SEEBIC and negative EBAC – remain unaffected by the connection configuration. However, applying an electrical bias to the specimen can reduce or increase the SEEBIC and EBAC signals, in addition to affecting the field-related EBIC signal at the p-n junction. These effects will be discussed in detail by means of the experimental results in this chapter. 126

60 STEM-EBIC maps of the GaAs-W specimen for two electrical connection configurations: (a) the amplifier is connected to p-GaAs (terminal 1) with n-GaAs (terminal 4) grounded, and (b) the connections are reversed. Graphs (c) and (d) plot the EBIC signal intensity across the GaAs p-n structure for each specimen thickness region for the respective connection configurations. The direction of the profiles is exemplified by the dashed green line. 127

61 (a) STEM-HAADF image and (b) corresponding STEM-EBIC map of the GaAs-W specimen. (c) and (d) show the HAADF and EBIC signal intensity profiles across regions of varying thickness. The HAADF profile is measured within the n-GaAs layer, approximately 1 µm away from the junction, while the EBIC profiles are acquired both along the GaAs p-n junction and at the same position within the n-GaAs layer. The HAADF profile is integrated over 50 nm, whereas the EBIC profiles are not integrated to maintain spatial precision. 129

62 EBIC signal intensity measured in the different thickness regions of the GaAs-W specimen: at the GaAs p-n junction, in the n-GaAs layer 1 µm away from the junction, and the EBIC contrast of the junction, calculated as the difference between these two intensities. The specimen thickness is increasing from region #1 to #6. 130

63 (a) STEM-EBIC map acquired on a III–V p–n heterostructure specimen. The measurement location is indicated in the SE-SEM overview image shown in the inset. The vacuum region serves as the signal zero reference; negative and positive EBIC signals are represented by dark blue and yellow, respectively, as indicated by the colour scale bar. (b) EBIC profiles extracted from the map in (a) at the positions marked. The signals are normalised, as only relative variations with respect to the vacuum signal are considered. 133

64 STEM-EBIC maps of the GaAs-W-2 specimen recorded at various beam currents using (a) spot size 6 and (b) spot size 4. The EBIC intensity ranges (0–110 nA) are adjusted for comparison. 134

65 The effect of STEM-beam current on EBIC intensity compared for two different specimen thicknesses and spot sizes: (a) and (b) spot size 6 at 370 nm and $>$ 550 nm, respectively. (c) and (d) spot size 4 at 370 nm and $>$ 550 nm, respectively. The profiles are extracted across the GaAs-W-2 p-n structure (EBIC maps in Fig. 64) and integrated over 100 nm. The y-ranges are adjusted for comparison. Absolute EBIC pixel values are not specified, as the relative changes in EBIC intensity in relation to the relative changes in beam current were analysed. The absolute beam current values as measured on the fluorescent screen are not accurate. 135

66 The EBIC peak intensity measured at the GaAs p-n junction as a function of the STEM-beam current for different spot sizes (4 and 6) and specimen thicknesses (370 nm and $>$ 550 nm). The values are evaluated from the EBIC data in Fig. 64 and 65. 135

67 (a) STEM-EBIC maps (2048×1365 pixels) are acquired at various magnifications on the GaAs-W-2 specimen, with a 50 µs pixel dwell time. The data at 57kx and 80kx magnification is recorded on the thicker of the two sample regions. The EBIC intensity ranges (0–60 nA) are adjusted for comparison. The SEM-SE overview image shows the lamella connection configuration and measurement location as highlighted in a red box. STEM-HAADF images are included for comparison. (b) EBIC profiles extracted from the EBIC maps in (a) obtained with the respective magnifications. 137

68 The influence of pixel dwell time on the SNR of EBIC imaging. STEM-EBIC maps of 2048×1365 pixels are acquired with pixel dwell times of (a) 25 µs and (b) 50 µs, at 57kx magnification. EBIC intensity profiles (c) are extracted across the GaAs p-n junction from the maps obtained with the respective dwell times. . 138

69 (a)-(c) LM-STEM-EBIC maps of GaAs-W-2 acquired at 220× magnification under three different connection configurations of terminals 1 and 4 to the amplifier (A) and ground (GND). (d) Magnified region from map (a), indicated by the orange box, with adjusted EBIC signal range for enhanced contrast. (e) Correlated LM-STEM-HAADF image for structural reference. 139

70 EBIC profiles extracted from the vacuum regions of the LM-STEM-EBIC maps (Fig. 69). (a) Comparison of the profiles from all three maps reveals a significant shift in EBIC intensity in the vacuum region. (b) Highlights the inversion of the signal trend increasing towards the chip side connected to the amplifier when the connectors are reversed. (c) Demonstrates the increase in signal towards both chip sides when both are connected to the amplifier. 141

71 SEM-SE images illustrating the procedure for creating a conductive plug (VIA) connection from the MEMS chip substrate to the metal track. (a) Step 1: Cutting through the unconnected metal track 2 into the substrate using Ga-FIB milling. (b) Step 2: Filling the cuts with ion beam-deposited W. 144

72 LM-STEM-EBIC maps of GaAs-W-2 acquired at 1250× magnification under three different connection configurations of terminals 1 and 4 to the amplifier (A) and ground (GND). 144

73 LM-STEM-HAADF image of the GaAs-W-2 sample showing pronounced bending contours. 145

74 (a)–(c) LM-STEM-EBIC maps recorded using the three indicated connection configurations. (d)–(e) EBIC intensity profiles extracted from maps (a) and (b) at the specified positions. The profiles in (f) are derived from map (c). All profiles have been integrated over a width of 0.6 µm and corrected for the vacuum signal. 148

75 Dark *I-V* characteristics of the GaAs-W-2 sample, measured without electron beam illumination in the TEM over an applied voltage range of -3 to +3 V. . . . 148

76 LM-STEM-EBIC maps of GaAs-W-2 recorded under externally applied bias ranging from -3 to +3 V, using the connection configuration illustrated in the SE-SEM overview image. 150

77 (a) EBIC profiles extracted from LM-EBIC maps recorded under applied bias from -3 to +3 V along the [001] direction across a prominent bend contour in the 370 nm-thick region of the lamella. The profile location is indicated at the 0 V map. The red arrow marks the current drop at the bend contour, the green arrow the drop at the p-n junction. (b) EBIC contrast of the bend contour as a function of applied bias, derived from the profiles in (a) and referenced to the zero-adjusted vacuum signal. 152

78 (a) STEM-EBIC map recorded at 0 V, indicating the region from which the EBIC profiles in (b) and (c) are extracted. (b) EBIC profiles obtained from LM-EBIC maps recorded under applied bias voltages ranging from –3 V to +3 V (Fig. 76), along the [1$\bar{1}$0] direction across the 370 nm-thick n-GaAs region of the lamella. The profiles in (b) are corrected for the bias-induced dark current, measured in the vacuum region marked in the 0 V map in (a) and shown in (c). 154
79 STEM-EBIC maps and corresponding STEM-HAADF images of the GaAs-W-2 specimen acquired at the indicated STEM beam scan orientations (0°, 45°, −90°, and +90°). EBIC intensity profiles were extracted from the marked region across the 550 nm-thick specimen area along [001] to evaluate the influence of scan direction on EBIC signal distribution. 155
80 Electrical connection configuration of the GaAs-W-2 specimen for *in situ* biasing STEM-EBIC analysis at 20kx magnification. The p-GaAs top contact is connected to the bias input (±) via track 1, while the n-GaAs rear contact is connected to the current amplifier (A) via track 2. 156
81 STEM beam current measurement for the *in situ* biasing STEM-EBIC mapping at 20kx magnification: (a) 4k-Image of the 200 kV STEM beam recorded on the Gatan Oneview camera using spot size 6, a 50 µm C2 aperture, a camera length of 580 mm, and an exposure time of 0.04 s. (b) Corresponding averaged line profile across the beam image shown in (a). The total number of electrons detected on the CCD was $N_e = 6.84 \times 10^8$, yielding a beam current of 1.71×10^{10} electrons per second. This corresponds to 2.74 nA, calculated using the elementary charge of 1.6×10^{-19} C. 156
82 STEM-EBIC maps of GaAs-W-2 under externally applied biases from –3 to +3 V, using the contact configuration shown in Fig. 80. The 0 V reference map is acquired with both electrodes connected to the amplifier to suppress field-induced EBIC contributions. 157
83 (a) EBIC profiles extracted across the vacuum regions of the EBIC maps acquired under applied biases ranging from –3V to +3V along the [1$\bar{1}$0] direction. (b) Averaged vacuum current signal as a function of applied bias, showing the bias-induced shift in background signal. 158
84 (a) EBIC profiles extracted along the [001] direction across the 550 nm-thick region of the GaAs-W-2 specimen, based on the EBIC maps acquired under various applied biases (Fig. 82). The extraction path is exemplarily indicated in the 0 V map shown in the inset. All profiles are referenced to the vacuum signal. (b) EBIC contrast at the p–n junction, plotted relative to the vacuum signal, as a function of the applied bias. 160
85 EBIC profiles extracted along the [001] direction across the two thickness regions of the GaAs-W-2 specimen from EBIC maps recorded at 0 V using (a) the biasing connection configuration shown in Fig. 80 and (b) the reference configuration with both contacts connected to the amplifier. 160
86 Effect of the applied bias on the EBIC contrast between p- and n-GaAs, measured away from the junction in the >550nm-thick region of the GaAs-W-2 specimen. . 160

87 (a) Schematic J-V characteristics of an ideal TD, highlighting the three main current contributions. The peak current density J_{peak} defines the low voltage regime where low-resistivity band-to-band tunnelling dominates. For a given operating current density J_{op}, the voltage drop in the band-to-band tunnelling regime ($V_{op,BB}$) is significantly smaller than the voltage drop associated with thermal current ($V_{op,TH}$) (modified after Wheeldon et al.).[7] (b) Schematic illustration of direct band-to-band tunnelling in a degenerately doped p-n junction (adapted from Hermle et al.).[8] 166

88 Schematic representation of the III-V bulk specimen structures, including p-AlGaAs/n-GaInP tunnel diodes (TDs) in either an upright or inverted growth configuration. (a) Upright-grown III-V tandem cell structure (TAN) and (b) inverted-grown III-V tandem cell structure (INVTAN), each incorporating two p-AlGaAs/n-GaInP TDs. The TD positions within the epitaxial stack relative to the wafer surface are indicated. (c) Upright-grown and (d) inverted-grown TD test structures. The layer structure outside the TDs has been simplified, and the dimensions of the epitaxial layers are not to scale. Dopants and doping concentrations have been omitted for confidentiality reasons. 170

89 HAADF STEM images of the (a)-(c) as-grown and (d)-(f) annealed upright-grown TD test structures, imaged along the [1$\bar{1}$0] and [110] directions, respectively. Panels (c) and (f) show the corresponding atomic arrangements in III-V zincblende materials along [1$\bar{1}$0] (c) and [110] (f), with atomic models and magnified sections of the AlGaAs (left) and GaInP (right) layers, as seen in the HAADF images in panels (b) and (e). 172

90 HAADF STEM images of the upper p-AlGaAs/n-GaInP tunnel diode in upright-grown (TAN, (a) and (b)) and inverted-grown (INVTAN, (d) and (e)) configurations acquired along [110] direction. The green lines in (a) and (d) indicate the positions of EDX line profile scans yielding the elemental distribution across the upright grown (c) and inverted grown (f) heterojunction. 173

91 HAADF STEM images of the lower p-AlGaAs/n-GaInP tunnel diode in upright-grown (TAN, (a) and (b)) and inverted-grown (INVTAN, (c) and (d)) configuration acquired along [110] direction. 174

92 (a) Digital diffraction pattern obtained from the Fast Fourier Transform (FFT) of the HAADF STEM atomic resolution image of the upper TAN tunnel diode, imaged along the [110] direction. The atomic $CuPt_B$-type ordering of Ga and In on the group-III ⟨111⟩ sublattice planes in GaInP results in a doubled lattice periodicity, evident from additional superlattice reflections at half the distance between the ⟨111⟩ reflections, as indicated in red. (b) For comparison, a simulated diffraction pattern of the disordered F-43m zincblende crystal structure viewed along [110] is shown. 175

93 (a) Schematic orientation map for epitaxial growth on (001)B GaAs substrates in 6° off-tilt orientation towards [$\bar{1}$10] or [1$\bar{1}$0] (blue arrows). The orientation of the step edges in step flow growth and step bunching are indicated. Note that [$\bar{1}$10] is equivalent to [0$\bar{1}$1], [1$\bar{1}$0] is equivalent to [01$\bar{1}$], and [110] is equivalent to [011]. (b) Atomic force microscopy (AFM) image showing the surface topology of the INVTAN wafer (001)B surface. 177

94 STEM-EDX elemental maps of (a) the as-grown and (b) annealed upright-grown n-GaInP/p-AlGaAs tunnel diode test structures. Plots (c) and (d) show extracted profiles from the STEM-EDX maps in (a) and (b), respectively, illustrating the element distribution (left axis) and HAADF intensity distribution (right axis) across both heterostructures. 178

95 High-resolution HAADF images (a, c) showing the acquisition positions of STEM-EDX elemental profiles (b, d) across the p-AlGaAs rear interface of the upper tunnel diode (TD). Panels (a) and (b) correspond to the upright-grown (TAN) structure, while (c) and (d) correspond to the inverted-grown (INVTAN) structure. 179

96 EELS line profile of the P distribution recorded across the p-AlGaAs rear interface in the (a) upper and (b) lower n-GaInP/p-AlGaAs tunnel diode (TD) of the TAN III-V heterostructure, overlaid on STEM HAADF images in the background. The STEM-EELS data is acquired using an FEI Titan G2 ChemiSTEM at 200 kV with a 51 mm camera length, an EELS spectrometer energy dispersion of 0.1 eV/channel, and a drift tube voltage of 50 eV. 180

97 (a) Systematic analysis of the HAADF intensity change at the p-AlGaAs rear interface of the lower TAN tunnel diode using HAADF STEM images acquired using different STEM camera lengths (CL). (b) Normalized HAADF intensity profiles across the p-AlGaAs rear interface, extracted from the corresponding images in (a). 182

98 (a) Electron hologram stack acquired at 40kx magnification on the upper p-AlGaAs/n-GaInP heterojunction in the INVTAN structure. (b) STEM-CBED pattern showing the specimen tilt orientation off-zone axis during hologram acquisition. 186

99 Reconstructed electron phase images of the upper (a, b) and lower (d, e) p-AlGaAs/n-GaInP tunnel diodes (TDs) in the INVTAN structure, acquired at 21kx and 40kx magnification, respectively. Electrostatic potential distributions extracted from the phase images across the upper (c) and lower (f) junctions are compared to the simulated dopant potential and energy band structure. 187

100 Reconstructed electron phase images of the upper (a, b) and lower (d, e) p-AlGaAs/n-GaInP tunnel diodes (TDs) in the TAN structure, acquired at 21kx and 40kx magnifications, respectively. STEM-CBED patterns (c, f) illustrate the specimen tilt orientation during hologram acquisition at the upper and lower TDs. Electrostatic potential distributions extracted from the phase images across the lower (g) and upper (h) junctions are compared to the simulated dopant potential and energy band structure. 188

101 (a) STEM-HAADF overview image of the INVTAN TEM lamella, prepared with regions of varying thickness for measuring the tunnel junction (TJ) depletion width via EH as a function of lamella thickness determined by STEM-CBED, as shown in (b). Electron hologram stacks (30×8s) are acquired at 21kx magnification on the upper p-AlGaAs/n-GaInP TJ (pink dashed line) using a FEI Titan Ultimate operated at 200 kV with a standard diffraction lens excitation of 89%. A biprism voltage of 200 V provided a hologram fringe spacing of 2 nm. The STEM-CBED pattern (inset in (a)) shows the specimen tilt orientation off-zone axis during hologram acquisition. 193

102 EH analysis of the upright-grown p-AlGaAs/n-GaInP test structure. (a) STEM-HAADF overview image of the TEM lamella, showing regions of different crystalline thicknesses (indicated), where hologram stacks were acquired. (b) Example of a reconstructed electron phase image and (c) a STEM-CBED pattern, both recorded at the same thickness region (426 nm). (d) Extracted electrostatic potential distribution across the junction, as exemplarily indicated by the green line in (b), compared to the simulated dopant potential and the estimated MIP variation across the upright-grown TD III-V heterostructure. 196

103 EH analysis of the inverted-grown p-AlGaAs/n-GaInP test structure. (a) Overview image of the TEM lamella, showing regions of different crystalline thicknesses (indicated), where hologram stacks were acquired. (b) Example of a reconstructed electron phase image and (c) a STEM-CBED pattern, both recorded at the same thickness region (262 nm). (d) Extracted electrostatic potential distribution across the junction, as indicated by the green line in (b), compared to the simulated dopant potential and the estimated MIP variation across the upright-grown TD III-V heterostructure. 197

104 Experimentally measured depletion widths by EH of the p-AlGaAs/n-GaInP junctions in the upright- and inverted-grown TD test structures as a function of crystalline specimen thickness determined by STEM-CBED. For comparison, the simulated depletion width of 14.7 nm (NEXTNANO) is indicated by the dashed line. 198

105 Dark *J-V* characteristics of the as-grown and annealed p-AlGaAs/n-GaInP TD test structures: (a) upright (p-on-n) and (b) inverted (n-on-p). Measurements are performed on metallised bulk samples. Dashed and solid lines denote the current sweep direction. 199

106 Secondary electron SEM image of the annealed, upright-grown TD specimen prepared on a MEMS support chip for *in situ* biasing EH analysis using backside FIB milling to preserve the pre-deposited ohmic top contact. The TJ position is indicated by the purple dashed line, and the electrical connection configuration of the TJ in the biasing TEM holder is illustrated alongside. 203

107 Current–voltage (I-V) characteristics of the backside-milled *in situ* biasing TEM specimen from the annealed, upright-grown TD test structure. The bias-induced current is monitored during *in situ* biasing EH acquisition. 203

108 (a) Electron phase images of the p-AlGaAs/n-GaInP junction in the annealed, upright-grown TD specimen at selected forward (+) bias voltages. The connection configuration is schematically illustrated alongside. (b) Phase profiles extracted across the TJ at different forward voltages. (c) Depletion widths and phase steps across the p-AlGaAs/n-GaInP TJ, are derived from the experimentally measured phase distribution, as a function of the applied forward bias. 204

109 STEM-BF images of the annealed upright-grown TD *in situ*-biased TEM specimen after applying an electrical bias of up to 14.3 V during EH analysis. The formation of crystallographic defects, exhibiting dark BF contrast, as well as lamella deformation, is visible. The images are acquired using the FEI Titan Ultimate operated at 200 kV, with a camera length of 58 mm, a convergence angle of 5.19 mrad, and a C2 aperture size of 30 µm. 205

110 Optical microscope image of the wire-sawed wafer slice, attached and electrically contacted to the Si-half chip, recorded on a Leica 100 after curing. The connection geometry is illustrated by a schematic sketch of the slice (grey) on the chip, indicating the placement of the conductive epoxy (purple). 206

111 SE SEM images showing the PFIB pre-milling procedure, acquired at 10 kV and 0.40 nA. (a) Overview image of the wafer slice fixed on the Si-half chip prior to PFIB milling. (b-c) IBID deposition of a protective Pt-C layer using the GIS. (d-e) Widening of the chip trench via PFIB milling at 30 kV and 0.2 µA at 50° tilt. (f) Initial backside cut and (g-h) frontside cut. (i-j) Iterative backside and frontside milling. (k) Final frontside cleaning and (l) backside cleaning. Images (m-p) show the final result of the PFIB pre-milling. 208

112 TEM images of the annealed upright-grown TD specimen, prepared on a MEMS chip for *in situ* biasing TEM analysis using Approach 2. The low-magnification images provide an overview of the electron-transparent specimen regions of varying thickness, with the corresponding medium-magnification images – indicated by the coloured rectangles – offering higher-resolution details of the contact interface and the TJ ROI. 209

113 (a) Schematic of the GaInP/GaAs tandem solar cell featuring an upright-grown p-AlGaAs/n-GaInP tunnel diode (TD), positioned 1380 nm beneath the front metal contact on the top wafer surface. (b, c) Photographs of the fully processed 6-inch tandem solar cell wafer, with a hand included for scale reference. 211

114 (a) 2D map of the derived conversion efficiencies of the various series-connected tandem solar cells at different x- and y-positions on the tandem solar cell wafer. The cell with the highest efficiency (x3y4) is highlighted in red. (b) Example of the underlying light *I-V* measurement curve of the tandem solar cell, shown for the x3y4 cell. 212

115 Measured external quantum efficiency (EQE) of the x3y4 GaInP/GaAs tandem solar cell (blue curve) compared to that of a GaInP/GaAs/Si triple-junction (3-j) cell with 33.3% conversion efficiency (red curve). The photocurrent densities generated in each subcell, as determined by their spectral coverage corresponding to their bandgap energies, are shown in the respective colors. 212

116 (a) The peripheral region of the wafer containing isolated, i.e. not series-connected, tandem cells with uniformly applied front contact is cleaved for TEM specimen preparation, as shown in (b). The dumbbell-shaped metallised tandem cell, indicated in red in (b), is selected for *in situ* biasing TEM specimen preparation. The dark *J*-*V* measurement of this isolated tandem cell is shown in (c). 214

117 (a) Overview TEM image of the *in situ* biasing tandem solar cell TEM specimen. (b) STEM HAADF images providing detailed views of the two isolation cuts (IC1 and IC2) in the lamella. 215

118 STEM HAADF and BF images of the *in situ* biasing tandem solar cell TEM specimen, acquired at different magnifications, resolving the epitaxial layer structure. 216

119 Results of the STEM-CBED mapping of the crystalline specimen thicknesses. Exemplary CBED patterns, along with the corresponding measured thickness values, are shown for regions of uniform thickness, as indicated by the coloured markings in the TEM overview image. 217

120 Illustration of the electrical connections for the GaInP/GaAs tandem solar cell specimen for *in situ* biasing EH. The positions of the electrical bias ($\pm V$) and ground (GRD) connectors are indicated, with the forward and reverse biasing notation referring to the tandem cell p-n junctions. The p- and n-type sides of the device are labeled, and the ROI for *in situ* biasing hologram acquisitions is highlighted by the gray rectangle. 218

121 (a) Reconstructed electron phase image from a hologram stack recorded without applied bias on the GaInP/GaAs tandem solar cell specimen, featuring two tandem p-n junctions connected by the p-AlGaAs/n-GaInP tunnel junction (TJ). (b) Phase profile measured across the III-V device heterostructure in the indicated region of (a) at $t_c = 390 \pm 7$ nm. 219

122 Current-voltage (*I*-*V*) characteristics of the GaInP/GaAs tandem solar cell TEM specimen, measured in the dark (before electron beam exposure) and under electron beam illumination during the biasing EH experiment. Negative and positive bias voltages correspond to reverse and forward biasing of the tandem cells, respectively, and to forward and reverse biasing of the interconnecting TJ. 222

123 (a) Electron phase images reconstructed from electron hologram stacks recorded at selected applied voltages on the GaInP/GaAs tandem solar cell specimen, featuring two tandem p-n junctions connected by the p-AlGaAs/n-GaInP tunnel junction (TJ). (b-c) Phase profiles measured across the III-V device heterostructure under (b) reverse and (c) forward bias conditions. The locations of the tandem p-n junctions and the TJ are indicated in the plots by grey and purple arrows, respectively. 223

124 The measured step in phase across the p-AlGaAs/n-GaInP TJ plotted as a function of the voltage applied to the tandem solar cell specimen. 224

125 (a-b) Electric field distribution across the p-AlGaAs/n-GaInP TJ in the tandem solar cell specimen measured at different applied voltages in (a) reverse and (b) forward biasing direction. The profiles are derived from the experimental phase profiles using the first differential equation (Eq. 51). (c) Width of the depletion region at the p-AlGaAs/n-GaInP tunnel junction as a function of the applied voltage, measured by means of the electrical field profiles in (a) and (b). 225
126 Illustration of the electrical connection configuration of the tandem solar cell TEM specimen, mounted on the MEMS chip, to the EBIC detection system and electrical ground (GRD) for STEM-EBIC analysis. 227
127 (a) STEM-HAADF image and (b, c) STEM-EBIC maps of the tandem solar cell specimen, acquired using the acquisition parameters listed in Table 17 and a beam current of 400 pA, as measured on the fluorescence screen. The connection configurations for the EBIC maps are indicated in the insets. (d) EBIC profiles extracted from the marked regions in (b) and (c). 228
128 STEM-EBIC profiles across the tandem solar cell heterostructure, extracted from EBIC maps acquired at the indicated beam currents. The grey and purple arrows denote the locations of the tandem p-n junctions and the TJ, respectively. 228
129 a) STEM-HAADF image and (b) STEM-EBIC map of the isolation cut near the tandem solar cell specimen ROI used for electrical (S)TEM analysis. Data were acquired using the parameters listed in Table 17 and a beam current of 300 pA, as measured on the fluorescence screen. 229

List of Tables

1 Summary of reported MIP values for selected zincblende III-V binary compounds from calculations (Hartree-Fock, DFT) and experiments (electron holography). . 17

2 List of FIB-SEM devices employed in this work at the Ernst Ruska-Centre (ER-C) in Jülich and at the CEA LETI in Grenoble. LMIS and ICP refer to liquid metal ion source and inductively-coupled plasma source, respectively. 34

3 Parameters involved in the calculation of CBED thickness measurements for GaAs specimens using the K-A plot method. 71

4 List of TEM specimen prepared from the GaAs and the InP bulk specimen, shown in Fig. 35a and b respectively. IBID refers to the ion-beam-induced deposition of metal inside the FIB-SEM. 74

5 Simulated built-in potential and depletion width for a symmetrically 10^{18} cm^{-3} doped GaAs p-n junction under different applied reverse bias. 79

6 Properties of the GaAs p-n junction measured at different specimen thicknesses (ID) in the GaAs-AuPd and GaAs-W lamellae by means of EH. The crystalline thicknesses (t_c) were measured using STEM-CBED. The active thicknesses (t_a) were derived by subtracting the electrically inactive thicknesses, which are t_i(GaAs-W)= 151 ± 23 nm and t_i(GaAs-AuPd)= 165 ± 29 nm. 87

7 Comparison of phase shifts measured across the InP-1 p-n junction at different specimen thicknesses using standard and low-magnification (LM) EH. The crystalline thicknesses (t_c) were measured using STEM-CBED. The active thickness (t_a) is derived by subtracting the inactive layer (averaging 109 ± 18 nm in InP) from the crystalline thickness. The measured phase shifts are compared with predicted values simulated for the active thickness. 89

8 Acquisition settings for the *in situ* biasing electron hologram analysis of the GaAs-W and GaAs-Pt specimen. The spatial resolution in the phase image results from the mask size applied in the Fourier reconstruction. 93

9 Metal-semiconductor junction configurations and the assigned contact types based on the difference of the work function of the metal (ϕ_m) and the semiconductor (ϕ_s) (modified after Razeghi *et al.* (2019)[9]). 100

10 Metal-semiconductor configurations present in the GaAs-W and GaAs-Pt *in situ* biasing specimen, with their predicted contact types (ohmic or Schottky), determined by comparing the work functions of the metals (ϕ_m) and the p- or n-doped GaAs (ϕ_s). 103

11 Theoretically predicted properties of the Schottky contacts in the GaAs-W and GaAs-Pt specimens. 104

12 Calibrated pixel sizes for STEM-EBIC maps of 2048×2048 pixels per frame. . . 138

13 Acquisition settings for the EH analysis of the TAN and INVTAN specimen. The spatial resolution in the phase image results from the mask size applied in the Fourier reconstruction. 185

14 Properties of the p-AlGaAs/n-GaInP junctions in the upright-grown TAN and inverted-grown INVTAN structures (see Sect. 8.2). The experimentally measured depletion widths, derived from EH phase images, are compared with simulated values (NEXTNANO). The measurement uncertainty for depletion width is ±1 nm. The compositional interface widths were determined from amplitude images reconstructed from the same hologram stacks as the phase images, as well as from the HAADF intensity profiles obtained from STEM-HAADF images of the TAN and INVTAN specimens (Sect. 8.3.1, Fig. 90, and Fig. 91). 190
15 Acquisition settings for the *in situ* biasing electron holography analysis of the annealed upright-grown p-AlGaAs/n-GaInP TD specimen. The spatial resolution in the phase image results from the mask size applied in the Fourier reconstruction. 202
16 Acquisition settings for the *in situ* biasing analysis of the tandem solar cell specimen. The spatial resolution in the phase image results from the mask size applied in the Fourier reconstruction. 218
17 Acquisition settings for the STEM-EBIC analysis of the tandem solar cell specimen. 226

1 Introduction

1.1 Background and Motivation

Anthropogenic climate change is increasingly destabilising the Earth system [10], pushing it beyond critical tipping points and leading to a progressive deterioration of living conditions for both wildlife and human societies. This, in turn, exacerbates social inequalities and intensifies conflicts within society. [11] The urgent need to mitigate climate change, coupled with the growing global demand for energy, necessitates transitioning to a sustainable and diversified energy supply. Among the various renewable energy sources – such as hydropower, wind, and biomass – solar radiation stands out due to its abundance and global availability. [12] Photovoltaics (PV), which enable the direct conversion of sunlight into electricity, are therefore an indispensable component of the renewable energy supply for the clean energy society of the future. In 2024, renewable energies accounted for 62.9% of Germany's net public electricity generation, with solar photovoltaics contributing approximately 14.3%. [13] A wide range of solar cell technologies has emerged, each based on different light-absorbing materials such as crystalline silicon, perovskites, thin-film chalcogenides, and III-V compound semiconductors. These technologies vary in terms of cost, efficiency, and application scope. The current photovoltaic market is clearly dominated by silicon-based solar cells, as – despite the high energy demands associated with their production – they represent the best compromise between high efficiency, long-term stability, and cost-effectiveness, thus supporting their widespread adoption. However, multijunction solar cells (MJSCs) based on III-V compound semiconductor layers grown by metalorganic vapor-phase epitaxy (MOVPE) achieve the highest solar conversion efficiencies. [14] Due to their high energy output on small installation areas, they are leading in spezialised weight-constrained applications such as space technology (e.g., satellites) and concentrating photovoltaics (CPV). [15,16] In CPV, record efficiencies of 47% have been achieved under concentrated solar irradiation using a solar cell with 6 individual absorbers, stacked on top of each other. [17,18] At Fraunhofer ISE, a 4-junction GaInP/AlGaAs/InGaAsP/InGaAs solar cell has reached 46% record-efficiency. [19] Current research focuses on further enhancing performance by optimising materials, interfaces, and adding subcells to the MJSC stacks. State-of-the-art MJSCs can incorporate up to six subcells, so-called 6-junction cells, comprising tens of epitaxial layers and electrical junctions of varying ternary and quaternary III-V compounds, known as heterojunctions. Compared to homojunctions, heterojunctions provide higher flexibility in tailoring optoelectronic properties to device requirements. The key challenge in MJSC development is ensuring efficient transport of light-generated carriers across the multiple layers to the collecting contacts, requiring advanced band structure engineering and precise doping profile realisation during manufacturing. Heterojunction quality is crucial, as it directly influences minority carrier recombination and majority carrier transport resistance. MJSC design and fabrication often rely on iterative, trial-and-error-based optimisation, wherein growth parameters are adjusted and the performance of individual junctions can be evaluated only indirectly through bulk electrical characterisation. Consequently, a dedicated tool capable of directly probing specific interfaces within complex heterostructure devices is needed.

Transmission electron microscopy (TEM) techniques are unique in offering atomic-scale spatial resolution for the site-specific investigation of a material's crystallographic structure, chemi-

cal composition, and local electrical properties. The ability to combine multiple imaging and spectroscopic methods within a single microscope session on the same specimen makes TEM exceptionally well suited for the comprehensive nanoscale characterisation and quality assessment of complex semiconductor devices. High-angle annular dark field (HAADF) contrast imaging, also called atomic number contrast (Z-contrast) imaging, in aberration-corrected scanning TEM (STEM) combined with energy dispersive X-ray (EDX) spectroscopy and electron energy-loss spectroscopy (EELS) are now routinely used for atomic resolution structural characterisation as well as for chemical mapping of semiconductor interfaces.[20,21,22] The dopant concentration of the photovoltaic multilayers is below 0.01 at% and, hence, too low to detect diffusion of doping elements across the interface via EELS or EDX. Nevertheless, these methods can be applied to study the presence of defects and major element distribution at critical interfaces. For the epitaxial growth of semiconductor multilayers in MOVPE reactors, growth schemes for the respective interfaces are developed based on the reaction behavior of the precursor gases in the reactor. For instance, it is well known that large group-VI atoms used for doping tend to accumulate on the growth surface.[23,24] Thus, intermediate layers with a deviating composition can form when precursor gas sources are switched off. Such compositional variations can be detected by correlating EDX maps with Z-contrast changes in the HAADF image. Electro-optical characterisation of MJSCs is traditionally performed on bulk devices, where conclusions about individual junction quality are inferred from overall device performance. Structural and compositional (S)TEM studies provide complementary insights.
However, (S)TEM also enables to directly analyse electronic properties through techniques. The electrostatic potential distribution at specific p-n junctions can be directly measured inside the TEM with nm spatial resolution using off-axis electron holography (EH).[25,26] This technique provides the possibility to access the dopant potential distribution in real multijunction solar cells[1] and in all other working devices, where the large distance of the p-n junctions from the device surface hinders a reliable profiling of dopant concentrations by conventional secondary ion mass spectroscopy (SIMS) analysis. Furthermore, applying an electrical bias to the sample during the EH analysis inside the TEM allows to study the electrical response of the junctions under conditions which are similar to those of the solar cell under light illumination. Correlative to this *in situ* biasing EH technique, STEM electron beam induced current (EBIC) analysis can be used to map the generation and extraction of charge carriers at p-n junctions upon *in situ* contacting the specimen.[31,32,33,34] These complementary methods allow to detect the location of p-n junctions, and to reveal spatial non-uniformities of the electrical properties or the location of recombination centers.[33,35,36] Furthermore, they can be employed to visualize potential degradation and diffusion processes *in situ* during the biasing of the sample.[36,37]

However, the complexity of state-of-the-art III-V multijunction devices, given by the large variety of layers with different thickness, composition, doping and optoelectronic properties, poses major challenges on the reliable measurements of electric fields at interfaces and the related sample preparation to be overcome. Hetero-junctions in III-V MJSC often consist of extremely thin epitaxial layers in the range of a few tens of nanometers that require high spatial reso-

[1] Electric fields can also be quantitatively measured using STEM techniques such as differential phase contrast (DPC), 4D-STEM, or ptychography. However, these techniques were not employed in this work. For detailed comparisons of these methods, the reader is referred to the literature.[27,28,29,30]

lution analyses. Reliable investigations of the interface characteristics hence require dedicated aberration-corrected (S)TEM instrumentation, which allows to extract information from a very localized volume at highest spatial resolution. Furthermore, the investigation of electrostatic potentials is complicated by the presence of electronically inactive surface layers introduced during the TEM specimen preparation using focused ion beam (FIB) milling. The high-energy ion beam causes passivation of the surface layers due to surface band bending caused by implanted ions and/or introduced defects.[38,39] The thickness of the electronically inactive layer is dependent on the semiconductor material and on the ion beam energy used during FIB preparation. This surface layer causes a reduction of the built-in potential across p-n junctions and, hence, it is the reason for a common underestimation of electric fields measured in electron microscopy compared with the expected values from theoretical simulations.[40,41,42,43] Hence, analysing and considering the effects of the inactive layer is mandatory for reliable electronic investigations, in particular of hetero-junctions which include a material transition. The inactive thickness can be quantified by examining the change in the potential step measured across a p-n junction against the change in the specimen thickness, which should principally provide the electrostatic potential only in the active layer inside the specimen.[39,41,42,43] Apart from the preparation artefacts, the measurement techniques themselves have intrinsic limitations. While removing dynamical diffraction contrast is a necessity in off-axis electron holography, both, measuring the potential and the current distribution require limiting the effects of electron-beam charging. Specific to the *in situ* biasing experiments is further the need to apply suitable metal contacts ensuring ohmic connection of the electron transparent specimen to dedicated electrical biasing chips. The choice of contact metal for reliable ohmic contacting is specific to each semiconductor material.[44,45]

These preceding factors illustrate the fact that implementing and evaluating electrical investigations of real III-V multijunction solar cell devices using advanced *in situ* biasing electron microscopy techniques is non-trivial. However, (S)TEM is probably the only technique that provides all essential information on the decisive semiconducting properties. Correlating results from *in situ* biasing EH and STEM EBIC analyses helps distinguish measurement artifacts from intrinsic sample characteristics. Combining these complementary techniques with (S)TEM imaging and spectroscopy offers a direct, unambiguous correlation of structural, chemical, and electrical interface properties – essential for a comprehensive understanding of photovoltaic device junctions. The objective of this work is to advance this correlative methodology for *in situ* electrical device characterisation in TEM and make it applicable for analysing III-V heterojunctions in MJSCs and other III-V optoelectronic devices, including LEDs and transistors. To the best of our knowledge, this work presents the first combined application of TEM-EH and STEM-EBIC for the electrical characterisation of ternary compound III-V MJSCs. In a broader context, this research hence aims to contribute to the development and optimisation of next-generation semiconductor nanodevices through improved electrical detection technology.

2 High-Efficiency III-V Multi-Junction Solar Cells

The development of MJSCs is a highly complex research field, encompassing diverse cell concepts, semiconductor growth strategies, and band structure engineering. It requires a deep understanding of the underlying chemical and physical processes that govern crystal formation and their impact on the optoelectronic properties of the solar cell.

As a comprehensive discussion of these topics is beyond the scope of this work, this chapter provides an overview of the fundamental concepts of MJSCs, including their working principles and key properties of III-V materials. Particular focus is placed on the III-V systems studied in this thesis, with an emphasis on their relevance for solar cell applications.

For a more detailed introduction to the general physics and fundamental concepts of solar cells, the reader is referred to standard textbooks. [46,47,48]

2.1 Introduction to the Concept of III-V MJSCs

Solar cells are made of semiconductor materials, most prominently Si, perovskite and III-V compounds. Semiconductors are suitable for photovoltaic applications due to their material-specific energy bandgap (E_g), separating the valence band (E_V) from the conduction band (E_C), and giving them the quality to absorb light and convert a fraction of its energy into electrical current. Solar cells work by the following basic principle: Incident photons can excite electrons in the semiconductor from the E_V to the E_C, given that they have at least the energy $\hbar\upsilon = E_g$. [47] These light-generated carriers are then separated by the built-in electric field of the device and collected at selective contacts, where they are drawn into an external circuit.

Single-junction solar cells (SJSCs) consist of a single bandgap material (e.g., Si or perovskite), allowing light absorption of only a specific portion (colour) of the solar spectrum. Although state-of-the-art SJSCs can achieve power conversion efficiencies of 30%-32%, [49] their theoretical efficiency is intrinsically constrained by the Shockley-Queisser (S-Q) limit to approximately 32%-33% under AM 1.5G illumination. [50].

To surpass this limit, alternative cell architectures are required. One effective approach is the use of MJSCs, in which multiple subcells with different bandgaps are stacked to absorb different ranges (colours) of the solar spectrum, thus more efficiently using the solar light illumination. [14,1] The higher the number of subcells in an MJSC, the greater its achievable theoretical efficiency, as predicted by the S-Q limit. The multi-junction approach can be understood by means of a standard triple junction (3J) cell, as illustrated in Fig. 1, which consists of a GaInP top cell ($E_g = 1.8 - 1.9$ eV), a GaInAs middle cell ($E_g = 1.41$ eV), and a Ge bottom cell ($E_g = 0.67$ eV). A key principle in MJSC design is the sequential decrease in bandgap energy from the top to the bottom of the cell stack. Each subcell absorbs photons with energies equal to or greater than its bandgap, while lower-energy photons pass through to be absorbed by the underlying subcells. This approach mitigates two major loss mechanisms in SJSCs:

1. Thermalisation losses. In SJSCs, photons with energies significantly higher than $E_g (\hbar\upsilon >> E_g)$ lose excess energy as heat. In MJSCs, higher-energy photons are absorbed by the upper subcells, ensuring that each subcell primarily absorbs photons close to its own bandgap, thereby reducing thermalisation losses.

2. Transmission losses. Photons with energies below E_g ($\hbar\upsilon < E_g$) are not absorbed and are lost for current generation. In MJSCs, these losses are mitigated by selecting a bottom cell with a lower bandgap than common SJSCs, allowing absorption of longer-wavelength photons that would otherwise be lost in an SJSC.

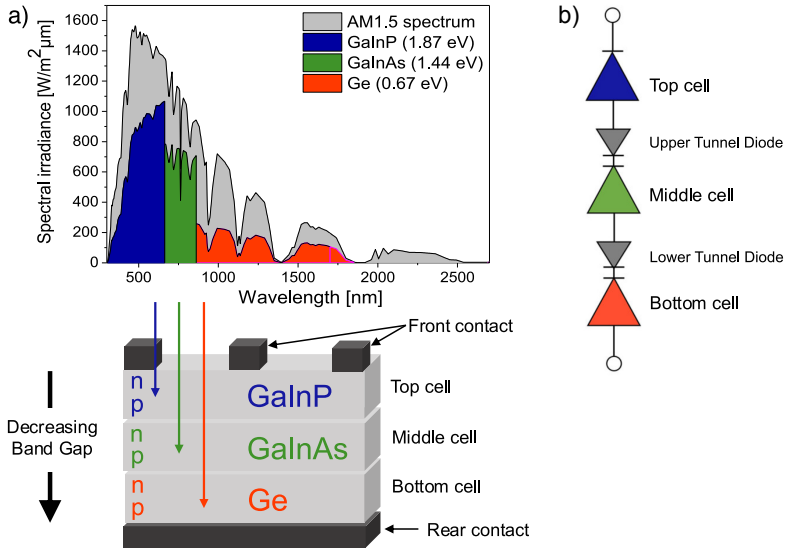

Figure 1: *(a) Schematic representation of the operating principle of a multi-junction solar cell, exemplified by a GaInP/GaInAs/Ge triple-junction (3-J) cell. Each bandgap material absorbs a specific wavelength range of the solar spectrum (modified after Philipps et al., 2018).*[1] *(b) Schematic representation of the electrical circuit of a 3-J solar cell.*

Due to the optimised spectral utilisation, MJSCs achieve the highest solar conversion efficiencies, significantly outperforming SJSCs. This is evident in Fig. 2, which presents the NREL efficiency chart, showing the highest confirmed efficiencies for various photovoltaic technologies from 1976 to the present.[2]

While some MJSC architectures rely on mechanical stacking or bonding of individual subcells, the monolithic approach remains the most commercially successful and is widely used in both space photovoltaics (PV) and terrestrial concentrator photovoltaics (CPV). In this design, all subcells within the MJ stack are grown as a single crystal and are electrically connected in series via Esaki tunnel diodes. Due to this series connection, the total current output of the MJSC is limited by the subcell generating the lowest current. Hence, an essential aspect of MJSC design, particularly in selecting bandgap combinations, is ensuring that the current output of each subcell is matched – a concept known as current matching. The monolithic concept further relies on efficient carrier transport across the different subcells, achieved through the interconnecting tunnel diodes (TDs), also known as tunnel junctions (TJs). Esaki TDs are p-n junctions composed of thin (~20 nm), highly doped p- and n-type III-V layers.[51] The high doping concentration causes the quasi-Fermi level (E_F) in the oppositely doped layers of the junction to shift into the E_V and E_C, respectively. The resulting band bending enables carriers to tunnel from the E_C of the n-type layer to the E_V of the p-type layer, thus providing a low-

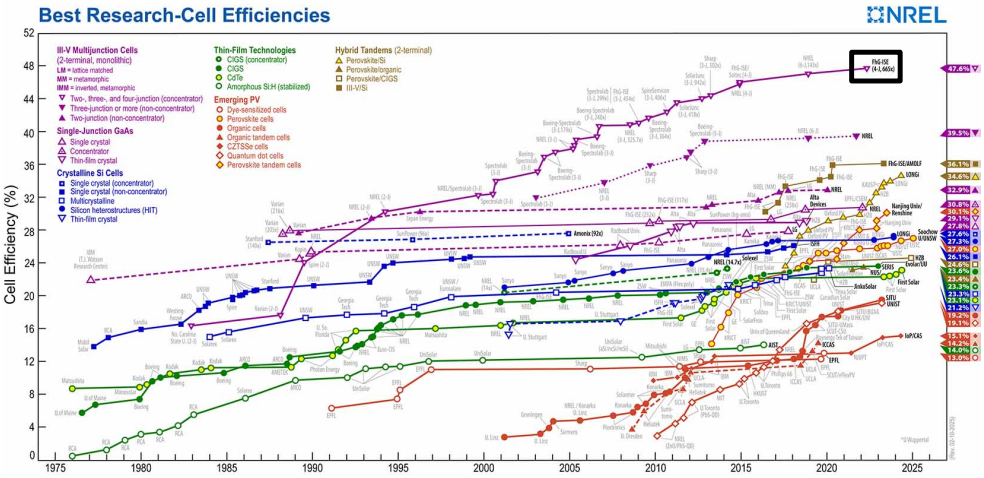

Figure 2: *Best research-cell efficiency chart (modified after NREL, 2025).*[2] *The black box highlights the current world record solar cell, a III-V 4-junction solar cell developed at Fraunhofer ISE, achieving an efficiency of 47.6% under concentrated light – the highest reported solar cell efficiency to date.*[3]

resistance electrical pathway for carrier transport. To minimise resistivity while maintaining high optical transparency to prevent absorption and associated losses in the underlying subcells, the III-V composition of the TJ, along with the dopant type and concentration, must be carefully optimised and tailored to the specific MJSC stack.

Here lies one of the key advantages of using III-V alloys (III-Vs) for MJSC: the wide range of possible III-V element combinations, providing high flexibility in tuning the bandgap (i.e., absorbance/transmittance) of the layers while maintaining nearly the same lattice constant, thereby enabling the growth of defect-free lattice-matched monolithic MJSCs. As shown in Fig. 3, III-Vs cover a broad range of bandgaps, suitable for solar light absorption from approximately 0.0 eV to around 2.4 eV, making them highly suitable for PV applications. It is also evident that, through careful stoichiometric combinations of binary compounds, the lattice constant can be maintained almost constant. Additionally, III-Vs can be both p- and n-doped over a wide range of doping concentrations, further contributing to their high flexibility in tuning electrical properties.

To better understand the advantages of using III-Vs for MJSCs, the following subsection will provide a more detailed description of the structural, elastic, and electronic properties of III-V semiconductors.

2.2 Fundamental Properties of Epitaxially-Grown III-V Heterostructures

III-V heterostructures, as used in MJSC applications, consist of stacked layers with the same crystal structure but varying III-V compositions. They can be grown as single crystals on single-crystal substrates such as GaAs, Ge, or InP using epitaxial growth techniques. Various epitaxy methods exist, including liquid phase epitaxy (LPE), hybrid vapor phase epitaxy (HVPE), and metal-organic vapor phase epitaxy (MOVPE). The III-V hetero-junction systems investigated

in this project were grown by MOVPE using an AIXTRON AIX2800 G4 reactor at Fraunhofer ISE, Freiburg. The III-V homo-junction GaAs and InP specimen were provided by Dr. David Cooper from CEA Grenoble.

In general, epitaxial crystal growth refers to the ordered deposition of a thin crystalline layer on a substrate, where the layer adopts the crystal structure of the substrate. The growth proceeds by the attachment of particles (atoms or molecules) to the growth surface, driven by the chemical potential.[52] MOVPE, in particular, is an epitaxial method where the particle deposition is realised by introducing metalorganic precursors and hydride sources into a heated reactor. The precursors decompose on the substrate surface, allowing for controlled layer-by-layer epitaxial growth with precise composition and doping. This technique is widely used to grow high-quality III-V semiconductors for fabricating optoelectronic devices due to its excellent uniformity and scalability. Semiconductor wafers of different sizes can be used as growth substrate depending on the intended application. In this work, III-V heterostructures were grown on either 4" or 6" GaAs substrates. Epitaxial layers are commonly grown on the (001) substrate surface, as are the structures investigated in this work. However, to facilitate epitaxial growth, the wafer substrates are cut with a slight misorientation from this high-symmetry crystallographic plane. This so-called off-tilt creates a vicinal surface, where epitaxial growth proceeds along atomic steps, thus avoiding nucleation growth. The presence of these steps promotes step-flow growth, as adatoms preferentially attach to them, enabling smoother and more uniform layer formation.[52] The primary goal in growing high-quality III-V heterostructures is to produce defect-free single crystals with a smooth surface.

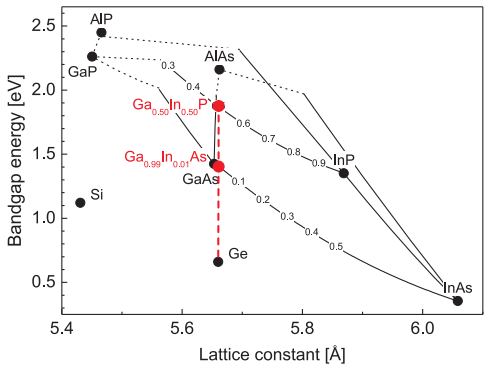

Figure 3: *Bandgap energy as a function of lattice constant for III-V semiconductor alloys. Direct- and indirect-bandgap semiconductors are represented by solid and dashed lines, respectively. Ternary compounds are represented by lines connecting the constituent binaries. The bandgap combination of a typical $Ga_{0.50}In_{0.50}P$/ $Ga_{0.99}In_{0.01}As$/Ge triple-junction solar cell is highlighted in red, with the red dashed line representing lattice-matched growth (modified after Philipps et al., 2018).*[1]

2.2.1 Structural Properties of III-V Semiconductors

The P- and As-based III-V semiconductors, such as GaAs and InP studied in this work, crystallize in a face-centered cubic (fcc) zincblende structure with the F-43m space group.[52] Fig. 4 illustrates the unit cell of a III-V fcc zincblende crystal, which, due to its cubic symmetry, can be de-

scribed by a single lattice parameter, a. The lattice vectors have equal lengths ($a_x = a_y = a_z = a$) and are mutually perpendicular (90°), so the unit cell is fully defined by a.

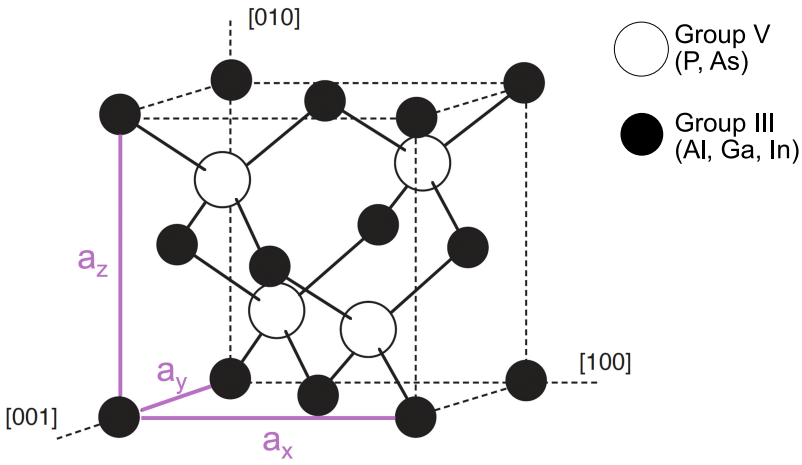

Figure 4: *Schematic unit cell of a zincblende III-V crystal structure.*

The lattice constant of III-V compounds can be estimated using Vegard's law, which uses linear interpolation between the lattice parameters of the constituent materials, provided they share the same crystal structure. For binary compounds AY, the relationship is given by:

$$a_{AY} = x a_A + (1-x) a_Y \tag{1}$$

For ternary compounds $\mathrm{A}_{1-x}\mathrm{B}_x\mathrm{Y}$, with a mixture of atoms A and B. on the III-site, Vegard's law interpolates between the lattice constants a_{AY} and a_{BY} of the binary compounds, AY and BY:

$$a_{\mathrm{A}_{1-x}\mathrm{B}_x\mathrm{Y}} = (1-x) a_{AY} + x a_{BY} \tag{2}$$

where x is the molar fraction of component B in the alloy. The concept can also be extended to quaternary III-V compounds $\mathrm{A}_{1-x}\mathrm{B}_x\mathrm{Y}_{1-y}\mathrm{Z}_y$ with a mixture of atoms Y and Z on the V-site. While Vegard's law provides a useful approximation for lattice constants in multinary compounds, actual values may differ from the predicted values due to factors such as atomic size differences, strain effects, or other interactions within the alloy.[53]

Since III-V compound semiconductors consist of different elements with varying electronegativity, the atomic bonds are at least partially ionic. The zincblende unit cell is composed of two fcc sublattices, one for the group III atoms and one for the group V atoms. Due to the absence of inversion symmetry, the zincblende crystal structure of III-V compound semiconductors is inherently polar. Consequently, the crystals contain both polar crystal planes (such as ⟨100⟩ and ⟨111⟩), which consist of only one type of atomic site, and non-polar planes (such as ⟨110⟩), which contain an equal number of both atomic sites, resulting in charge balance. The two types of planes have different properties, which have a particular impact on chemical processing or

epitaxial growth. For example, non-polar planes are well suited for wafer cleavage. Wafers with a (100) surface can be easily cleaved along parallel ⟨110⟩ planes, such as (011) and (01-1), as these planes preferentially form side surfaces that are both perpendicular to the wafer surface and mutually perpendicular. Additionally, these non-polar cleavage surfaces are thermodynamically more stable compared to polar planes. These factors are relevant for cross sectional TEM specimen preparation in this work and will be discussed in Chapter 4).
Conversely, polar planes, such as (001), are preferred surfaces for epitaxial growth because they contain only one type of atom.

2.2.2 Elastic Properties

III-V compounds exhibit different lattice constants due to variations in elemental composition, despite crystallising in the same zincblende structure. The lattice mismatch arises from differences in bond lengths, which depend on atomic properties such as electronegativity and Coulomb forces. Additionally, the thermal expansion coefficient of III-V compounds vary. [52,54]
In epitaxy, III-V layers are typically grown lattice-matched on a thick, unstrained single-crystal substrate with identical in-plane and out-of-plane lattice constants, denoted as $a_{\parallel,s} = a_{\perp,s} = a_s$. In the case of pseudomorphic heterolayers, the epitaxial layer adopts the in-plane lattice constant of the substrate ($a_{\parallel,s} = a_{\parallel,e}$), leading to a strain in the out-of-plane direction to preserve the bulk unit cell density. Consequently, the heterolayer lattice distorts such that $a_{\parallel,e} \neq a_{\perp,e} \neq a_{\perp,s}$, while the substrate remains unstrained due to its significantly greater thickness. In other words, the heterolayer lattice accommodates the stress induced through the in-plane lattice matching through a distortion perpendicular to the interface.
For epitaxial growth on the (001) plane of a cubic material, the induced strain is biaxial, resulting in a tetragonal distortion of the cubic unit cell, as illustrated in Fig. 5. The nature of the strain depends on the lattice constant mismatch:

- If $a_{\parallel,e} < a_{\parallel,s}$, the heterolayer experiences tensile strain, leading to $a_{\parallel,e} < a_{\perp,e}$.
- If $a_{\parallel,e} > a_{\parallel,s}$, compressive strain is exerted on the heterolayer, causing $a_{\parallel,e} > a_{\perp,e}$.

These elastically deformed pseudomorphic heterostructures remain stable only up to a critical thickness, t_c. Beyond this limit, which is the elastic regime, strain relaxation occurs that accompanies with the formation of misfit dislocations. The heterolayer remains pseudomorphic only as long as the lattice mismatch is below approximately 1%. [52]
For biaxially strained cubic epitaxial layers with thickness $t < t_c$, the strain can be described in the harmonic approximation using Hooke's law in the framework of continuum elasticity theory. Here, the relation between stress σ and strain ε is given by

$$\sigma_i = \sum C_{ij} \varepsilon_j \tag{3}$$

where C_{ij} is the elasticity stiffness (or compliance) tensor, composed of the elastic stiffness coefficients. Due to the high symmetry of cubic crystals, with the three principle axis being equivalent, the tensor simplifies to three independent elastic stiffness coefficients: C11, C12, and C44. Thus, the elasticity tensor for a cubic zincblende crystal is:

$$C_{ij} = \begin{pmatrix} C11 & C12 & C12 & 0 & 0 & 0 \\ C12 & C11 & C12 & 0 & 0 & 0 \\ C12 & C12 & C11 & 0 & 0 & 0 \\ 0 & 0 & 0 & C44 & 0 & 0 \\ 0 & 0 & 0 & 0 & C44 & 0 \\ 0 & 0 & 0 & 0 & 0 & C44 \end{pmatrix} \tag{4}$$

In epitaxial zincblende heterostructure grown on a (001) substrate, stress is applied equally in both in-plane directions, [110] and [1-10], such that $\sigma_{xx} = \sigma_{yy} = \sigma_{\parallel}$. Accordingly, the resulting strain can be described as $\varepsilon_{xx} = \varepsilon_{yy} = \varepsilon_{\parallel}$. For a free-standing epitaxial structure, no external stress is applied in the out-of-plane direction ($\sigma_{zz} = 0$) allowing ε_{zz} to adjust according to elastic constraints. Since the tetragonal distortion of the biaxially strained crystal involves neither in-plane shear strain nor rotation, the off-diagonal components of the stress and strain tensors remain zero. Thus, the stress tensor for a biaxially strained epitaxial heterostructure is

$$\sigma = \begin{bmatrix} \sigma_{\parallel} & 0 & 0 \\ 0 & \sigma_{\parallel} & 0 \\ 0 & 0 & 0 \end{bmatrix} \tag{5}$$

The corresponding strain tensor is

$$\varepsilon = \begin{bmatrix} \varepsilon_{\parallel} & 0 & 0 \\ 0 & \varepsilon_{\parallel} & 0 \\ 0 & 0 & \varepsilon_{zz} \end{bmatrix} \tag{6}$$

Substituting these stress and strain tensors along with the cubic elasticity tensor (Eq. 4) into Hooke's law, while omitting the shear modulus C_{44}, the stress-strain relation for a biaxially strained zincblende crystal is expressed as

$$\begin{pmatrix} \sigma_{\parallel} \\ \sigma_{\parallel} \\ 0 \end{pmatrix} = \begin{bmatrix} C11 & C12 & C12 \\ C12 & C11 & C12 \\ C12 & C12 & C11 \end{bmatrix} \begin{pmatrix} \varepsilon_{\parallel} \\ \varepsilon_{\parallel} \\ \varepsilon_{zz} \end{pmatrix} \tag{7}$$

From 7, the relation between the lateral strain $\varepsilon_{\parallel}$ and the resulting vertical strain ε_{zz} can be derived as:

$$\sigma_{zz} = 2\varepsilon_{\parallel} C_{12} + \varepsilon_{zz} C_{11} = 0 \tag{8}$$

Solving for ε_{zz} yields:

$$\varepsilon_{zz} = \frac{-2C_{12}\varepsilon_{\parallel}}{C_{11}} = \varepsilon_{\perp} \tag{9}$$

where $\varepsilon_{\perp}$ is the misfit-induced strain component perpendicular to $\varepsilon_{\parallel}$, acting along [001]. The ratio $\frac{2C_{12}}{C_{11}}$, known as the distortion factor D_{001}, describes the strain relationship between $\varepsilon_{\perp}$ and $\varepsilon_{\parallel}$ in (001)-oriented epitaxial heterostructures.

Assuming in-plane lattice matching of a pseudomorphic heterostructure ($a_{\parallel,s} = a_{\parallel,e}$), the change

in the out-of-plane lattice constant $a_{\perp,e}$ due to elastic unit cell deformation in [001] is given by

$$a_{\perp,e} = a_e(1 - D_{001}(a_{\parallel,e}/a_e) - 1) \tag{10}$$

where a_e is the unstrained lattice parameter of the epitaxial layer.[52]

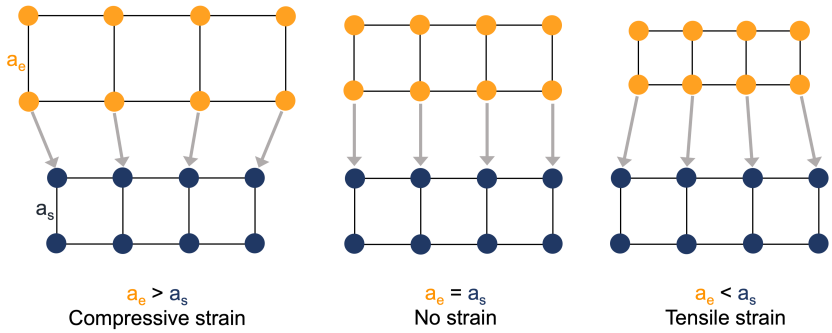

Figure 5: *Schematic illustration of different types of epitaxial heterostructures. The lattice mismatch between the epitaxial layer (a_e) and the substrate (a_s) determines the nature of the resulting elastic strain deformation.*

The discussion above applies to pseudomorphic heterostructures in the elastic regime, i.e., with layer thicknesses below the critical thickness and lattice mismatch within the tolerable range. If the lattice mismatch exceeds a critical threshold or the layer thickness surpasses t_c, elastic deformation can no longer fully accommodate the strain energy, leading to relaxation through crystallographic defect formation.

Defects are fatal for photovoltaic devices, as they serve as non-radiative recombination centers for free carriers. High non-radiative recombination rates must be avoided in solar cells to minimise dark currents and maximise open-circuit voltage.[55] Therefore, the development of multi-junction solar cells (MJSCs) requires careful control of lattice mismatch by adjusting the stoichiometric composition of III-V compounds (see Fig. 3) in order to reduce strain.

A key consideration in achieving lattice-matching is the difference in thermal expansion between various III-V materials. It is important to note that lattice matching is typically achieved at the growth temperature, which can reach up to 640°C at a pressure of around 50 mbar. However, while the lattice parameters may align at this temperature, they change at different rates upon cooling, leading to a mismatch at room temperature. Successful III-V heterostructure growth therefore requires ensuring that the room-temperature lattice mismatch remains within a range that allows for elastic strain relaxation in the out-of-plane direction, as described earlier.

Strain in III-V heterolayers significantly influences the electronic band structure, thereby affecting carrier transport and optical properties in solar cells. Therefore, strain effects must be carefully considered during device design. On the other hand, intentional strain engineering enables targeted tuning of optoelectronic properties. For instance, certain layers in MJSCs are intentionally grown strained to enhance optical transparency. In n-AlInP window layers and p-AlGaAs TD layers, increasing the Al content induces tensile strain at room temperature while raising the bandgap, thereby reducing absorption. Similarly, increasing the Ga content in n-GaInP TD layers increases the bandgap while introducing tensile strain. Nevertheless, strain engineering

must be carefully controlled to prevent defect formation, ensuring optimal performance of the device.

2.2.3 Electronic Properties

2.2.3.1 Bandgap Properties and Light Absorption

The bandgap properties of III-V semiconductors are central to MJSC performance, as they determine both light absorption efficiency and the spectral range of absorbed photons. The nature of the bandgap – whether direct or indirect – affects absorption efficiency, while the bandgap energy dictates which portions of the solar spectrum is absorbed. Understanding and engineering these properties is crucial for optimising MJSC performance.

Direct vs. Indirect Bandgaps

Direct bandgap materials, such as zincblende GaAs (1.424 eV) or InP (1.344 eV), allow electrons to transition between the valence and conduction bands without a change in momentum. The electronic band structure, described by the energy dispersion $E(k)$ as a function of the wavevector k in reciprocal space, is derived from the solutions of the Schrödinger equation for the periodic crystal potential. In direct bandgap materials, the conduction band minimum and valence band maximum occur at the same k-point, leading to strong optical absorption and efficient electron-hole pair generation. In direct-gap zincblende III-Vs, both extrema align at the Γ-point at the center of the first Brillouin zone ($k = 0$). This makes them ideal for MJSCs, where strong absorption over a broad spectral range is essential for maximizing power conversion efficiency. As shown in Fig. 3, III-V semiconductors exhibit a direct bandgap across a wide range of compositions, making them highly versatile for tailoring the optoelectronic properties of individual epitaxial layers.

In contrast, indirect bandgap materials, such as GaP or AlAs, have conduction band minima and valence band maxima at different k-points, meaning that electron transitions require momentum change through phonon interactions. This significantly weakens absorption, making indirect bandgap materials less suitable for solar cells, where efficient light absorption is critical.

Composition-Dependent Bandgap Engineering

The bandgap properties of III-V semiconductors are composition-dependent, making them highly tunable for MJSC applications. Both the bandgap type (direct vs. indirect) and the bandgap energy can be engineered by adjusting the stoichiometric composition of III-V alloys (see Fig. 3)

- Tuning the bandgap type: In certain III-V compounds, the bandgap transitions from indirect to direct with changing stoichiometry. For instance, this occurs as P content decreases in $GaAs_{1-x}P_x$ or as In content increases in $Ga_{1-x}In_xP$ (see Fig. 3), fundamentally altering the material's optical absorption efficiency.

- Tuning the bandgap energy: E_g can be precisely controlled through stoichiometric variation, allowing for precise control over the absorbed spectral ranges.

This tunability is particularly advantageous in MJSCs, where each subcell must be optimised for different spectral regions. By careful engineering of III-V semiconductor compositions, both absorption characteristics and overall device performance can be significantly enhanced.

Unlike the lattice constant, which follows a linear compositional dependence, E_g exhibits a nonlinear stoichiometric dependence due to atomic interactions and strain effects. It is better described by a quadratic relation incorporating a bowing parameter C, which accounts for these deviations from linearity. Accordingly, for ternary III-V compounds ($A_{1-x}B_xY$), the compositional dependence of E_g is given by:

$$E_g^{A_{1-x}B_xY} = (1-x)E_g^{AY} + xE_g^{BY} - x(1-x)C \tag{11}$$

Similarly, for quaternary III-V compounds, E_g can be determined as a weighted sum of the bandgaps of the constituent ternary alloys.

The extent of bowing varies across III-V material systems: some alloys, such as GaAsP ($C = 0.8$ eV) or InGaAs ($C = 0.477$ eV), exhibit strong nonlinearity with high C values, whereas others, like AlGaAs, follow an almost linear trend ($C = -0.127 + 1.310 \times x_{Al}$ eV).[56] As seen in AlGaAs, the bowing parameter is not always constant and may itself be composition-dependent to better account for the underlying physical interactions.

In the context of bandgap energy tailoring for MJSCs, it is important to note that E_g is temperature-dependent, typically decreasing with increasing temperature due to changes in electron-phonon interactions and interatomic bond distances[52]. This temperature dependence must be carefully considered when designing MJSCs for specific applications, such as space PV or terrestrial CPV, where operating temperatures differ significantly. The thermal behaviour of E_g for both direct and indirect bandgap semiconductors is commonly approximated by the Varshni formula:[57]

$$E_g(T) = E_g(T=0) = \frac{\alpha T^2}{T+\beta} \tag{12}$$

where α and β, known as the Varshni parameters, are material-specific coefficients determined through empirical fitting. Reported Varshni parameters for various III-V semiconductors can be found in literature.[56,58]

2.2.3.2 Minority Carrier Transport

Beyond their tunable bandgap properties, III-V compound semiconductor materials offer many advantageous electronic properties making them highly suitable for high-efficiency PVs, as well as other advanced optoelectronic devices, including lasers, photodetectors and transistors. Most prominently, III-V semiconductors exhibit high minority carrier mobilities μ, particularly electron mobilities μ_e, which are significantly higher than those of Si and Ge, along with relatively long minority carrier lifetimes, τ.[14,59] This results in relatively high minority carrier diffusion lengths, L_D, given by:

$$L_D = \mu\tau \tag{13}$$

For minority carrier devices, such as high-efficiency solar cells, optimizing minority carrier transport – achieving high L_D and minimizing (interface) recombination – is crucial. High L_D are particularly critical for MJSCs, where efficient charge collection and carrier extraction across the subcell stack are essential for high conversion efficiencies. If any subcell absorber has a low L_D, it causes considerable current limitation and degrades overall device performance. Therefore, a

key goal in MJSC development is to optimise L_D while minimizing recombination, especially non-radiative losses, by reducing dislocation densities. In bulk III-V semiconductors, L_D can be tuned by adjusting III-V stoichiometry, doping elements and concentrations. For example, Niemeyer *et al.* investigated L_D in ternary p-$Ga_{1-x}In_xAs$ and found that its dependence on In content varies with doping concentration.[59] In lower-doped (2.5E17 cm^{-3}) samples, L_D initially increases from p-GaAs (6.3 ± 0.2 µm) to $Ga_{0.79}In_{0.21}As$ (14 ± 2 µm), before decreasing at higher In contents (4.7 ± 0.2 µm for $Ga_{0.47}In_{0.53}As$). Conversely, in more heavily doped (2.5E18 cm^{-3}) samples, L_D remains relatively constant (~5.0 ± 0.7 µm), showing minimal dependence on In content. As a detailed review of minority carrier transport properties in various III-V multinary compounds relevant for MJSCs is beyond the scope of this work, theoretical discussions, including mathematical approaches to describe minority carrier transport, can be found in standard references.[60,52]

2.2.3.3 Electric Field Effects in III-V p-n Junctions

While the bandgap and minority carrier transport properties fundamentally determine the optoelectronic behavior of III-V materials – governing carrier generation and transport, respectively, within each epitaxial layer – the carrier transport across layers and subcells is driven by the electric field arising from a potential gradient.

$$\vec{E} = -\vec{\nabla} V \tag{14}$$

The fundamental physics of p-n junctions will be discussed in Ch. 6.2 in the context of measuring electrostatic potential distributions within the TEM. In this section, only the key factors that governs potential gradients, and thus electric fields, are introduced.
In zincblende III-V heterostructures, potential differences between epitaxial layers originate from two primary sources: doping and variations in mean inner potential (MIP).

Doping

Doping, the intentional introduction of impurity atoms with a different atomic number, modifies the charge carrier concentration in III-V semiconductors, thereby enhancing conductivity. Donor atoms, which contribute extra electrons, introduce n-type doping, whereas acceptor atoms, which have less valence electrons, create p-type doping. This process alters the electronic band structure by shifting the Fermi level (E_F) relative to its mid-bandgap position in an undoped material: n-doping moves E_F closer to the conduction band (E_C), while p-doping shifts it toward the valence band (E_V). Through precise doping design in III-V heterostructures, the resulting potential profile can be tailored to control carrier transport.
The effective number of ionized dopants – i.e., the fraction of introduced impurities that contribute free carriers – depends on their ionization energy. This energy, which determines how easily a dopant donates or accepts an electron, is lower for "shallow states" located near E_C (for donors) or E_V (for acceptors), facilitating efficient charge carrier generation. In contrast, "deep states" positioned near mid-bandgap act as trap states, capturing carriers and reducing conductivity. One advantage of III-V semiconductors over silicon is their generally lower ionization energies, which promote higher free carrier concentrations.
Achieving a targeted doping distribution requires selecting appropriate dopant species and con-

centrations suited to the specific III-V compound. Common dopants in zincblende III-V semiconductors include Zn or C for p-type doping and Si or Se for n-type doping. Typical doping concentrations in zincblende III-V materials, which have an atomic number density of 4.42×10^{22} cm^{-3},[61] range from 10^{15} to 10^{20} cm^{-3}.[52]

However, several factors can limit doping effectiveness during epitaxial growth. Dopant incorporation is constrained by solubility limits, while its behavior can vary depending on incorporation sites (III- or V-lattice sites) and lattice relaxation effects. Additionally, the ionization energy of the impurity, along with the native defect density, determines the fraction of electrically active dopants. Hydrogen incorporation during MOVPE growth can also lead to dopant passivation. Considering and optimising these parameters is crucial to realising the desired doping profile, and thus, the intended potential distribution and carrier transport in III-V devices.

A comprehensive discussion, including theoretical physical concepts and practical considerations for doping in epitaxial III-V semiconductors, can be found in the relevant literature.[62,52]

Mean Inner Potential

The MIP (V_0) is defined as the volume-averaged Coulomb potential within a crystalline material, referenced to a vacuum potential at infinite distance.[63,64] It is generally considered to be the predominant factor contributing to the specimen's electrostatic potential. It is influenced by the atomic structure and charge distribution across the crystal lattice, including charge redistribution in chemical bonds. Thus, the MIP depends on both the composition and atomic arrangement of a material.

In an epitaxial heterostructure, each III-V compound exhibits a distinct MIP, creating a potential gradient and, consequently, an electric field at the interface. Unlike the dopant-induced potential, which varies at low carrier frequencies, the MIP varies at high frequencies. As a result, MIP-induced electric fields are highly localized compared to the long-range fields generated by doping. MIP values can be obtained analytically via Hartree-Fock or density functional theory (DFT) calculations of the charge distribution within the crystal, or experimentally using off-axis electron holography (EH).[65,66,67,68] However, determining accurate values remains challenging, as theoretical and experimental results often show significant discrepancies. A summary of reported MIP values for zincblende III-V binary compounds is provided in Table 1. In contrast to binary III-Vs, MIP values for ternary and quaternary compounds are rarely reported and are typically estimated using Vegard's law as a linear interpolation between the constituent binaries.

$$V_0(\mathrm{A}_{1-x}\mathrm{B}_x\mathrm{Y}) = (1-x)V_0(AY) + xV_0(BY) \tag{15}$$

It is worth noting that in III-V materials crystallising in non-zincblende structures, such as wurtzite, spontaneous electric polarization in the absence of external fields or stress can contribute significantly to the specimen potential in addition to the MIP and doping. In contrast, spontaneous polarization effects do not occur in zincblende III-Vs.

However, in structures lacking inversion symmetry, including zincblende, piezoelectricity can be induced under strain. In zincblende crystals, piezoelectric effects arise only from strain along off-diagonal components of the strain tensor (see Eq. 6).[52] As a result, the biaxial strain introduced during lattice-matched pseudomorphic growth on (001) substrates does not induce piezoelectricity. Therefore, this contribution to the electric field can be ruled out in the specimens studied

in this work.

Table 1: Summary of reported MIP values for selected zincblende III-V binary compounds from calculations (Hartree-Fock, DFT) and experiments (electron holography).

III-V	**MIP [V]**		
Compound	DFT	Hartree-Fock	Electron Holography
GaAs	14.19 [67]	15.26 [67]	14.24 ± 0.08 [66], 14.00 ± 0.60 [69]
AlAs	12.34 [67]	–	12.10 ± 0.70 [69]
InAs	14.34 [67]	15.26 [67]	14.50 ± 0.08 [66]
GaP	13.63 [67]	14.88 [67]	14.38 ± 0.12 [66]
AlP	11.39 [67]	13.34 [67]	–
InP	13.90 [67]	15.06 [67]	14.53 ± 0.07 [66]

2.3 Motivation for TEM Analysis of MJSCs

To grow complex layer systems with multiple epitaxial layers, as thin as 10–20 nm, which are composed of alternating ternary and quaternary alloys with high quality, the switching of gas precursors in the reactor must follow pre-defined growth recipes. This requires advanced knowledge of the chemical interactions and deposition processes in MOVPE to precisely control layer growth and achieve atomically sharp material transitions.

With advancing technology, optoelectronic devices are becoming both smaller and more complex. Miniaturisation demands the growth of thinner layers, necessitating nanoscale control of the deposition process. At the same time, system complexity increases, as seen in the transition from 3-junction to 6-junction MJSCs, which requires a growing number of epitaxial layers to be fabricated as single crystals. Consequently, longer growth times at high temperatures lead to increasing thermal loads on the initially grown layers and allow for more elemental diffusion, which must be considered.

Chemical diffusion at III-V hetero-interfaces directly influences the electronic band structure (evident from Fig. 3), thereby controlling carrier transport and extraction and ultimately determining the optoelectronic properties of the device.

To ensure that the epitaxial structures provide the intended electric field distribution and carrier transport properties, a detailed understanding of the impact of various growth parameters is required. For example, thermal load and the specific growth direction of material transitions can significantly affect interface quality. This will be discussed in detail in Ch. 8, where the effects of growth direction and thermal load on the tunnelling characteristics of highly doped AlGaAs/GaInP interfaces are investigated.

To improve device growth, it is essential to analyse the electric fields of specific junctions at the nanometer scale and correlate them with structural and chemical deviations, which can be achieved using various TEM methods. Next chapters introduce these TEM methods that are implemented in this research project.

3 Transmission Electron Microscopy Measurements of III-V Semiconductors

This chapter provides an overview of the fundamental principles of TEM, starting with an introduction to electron-matter interactions responsible for signal generation and image formation. Then it presents the two primary operational modes: Transmission electron microscopy (TEM) and scanning TEM (S)TEM, followed by a discussion of the spatial resolution limit in (S)TEM. Finally, the (S)TEM techniques relevant to this work for the structural and chemical analysis of III-V semiconductor materials are introduced.

3.1 Fundamental Principles of Transmission Electron Microscopy

3.1.1 Electron-Matter Interaction

In TEM, highly accelerated electrons are directed at an electron-transparent specimen, leading to interactions between the electrons and the sample that generate different signals. By selectively detecting specific signals, different TEM techniques exploit various electron-matter interaction processes to analyse structural, compositional, or electrical properties of the sample. An overview of the numerous signals generated by electron-specimen interactions is presented in Fig. 6.

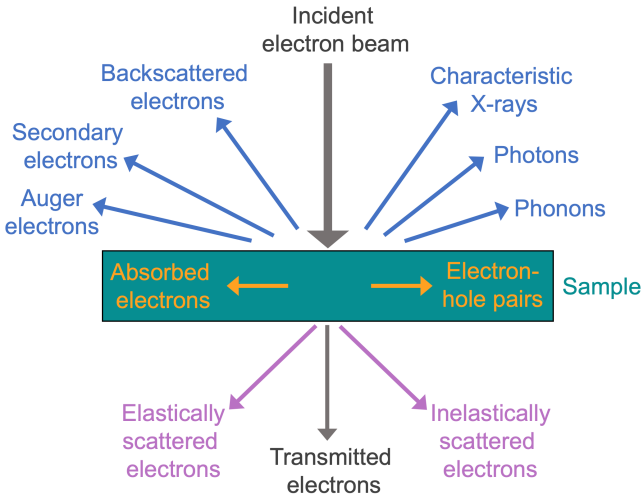

Figure 6: *Schematic illustration of the primary signals generated by the interaction of a high-energy electron beam with an electron-transparent semiconductor specimen (adapted from Williams & Carter (2008)).*[4]

To describe electron-specimen interactions, the electron beam can be treated either as a sequence of particles or through wave theory, reflecting the concept of wave-particle duality. The interactions are accordingly described as electron scattering or electron diffraction, respectively. Each approach provides useful insights into specific signal generation mechanisms in TEM. When applying the particle description, electron scattering within the specimen arises due to Coulomb interactions with the electrostatic potentials of the specimen's atoms and with long-range electric fields present in the material. In the case of electron scattering from atomic potentials, the

Coulomb interaction between the fast incident electrons and the electron cloud of the specimen atoms is weak, resulting in scattering at low angles. In contrast, the interaction with atomic nuclei is significantly stronger, leading to high-angle scattering. When analysing long-range electrostatic potentials, the scattering effects from the short-range atomic potentials can often be neglected.
Considering only those electrons that have transmitted through the specimen – thus contributing to image formation by detection below the sample – these electrons can be categorized according to the following scattering interaction mechanisms: unscattered ("direct") electrons, elastically scattered electrons, and inelastically scattered electrons. The direct beam consists of primary electrons that exit the specimen without undergoing any scattering, remaining aligned with the incident beam direction. Electrons that undergo elastic scattering experience a change in momentum without transferring energy to the scattering object. In contrast, inelastic scattering involves both momentum and energy transfer.
Elastic scattering is the primary mechanism responsible for image contrast in TEM. The strength of elastic interactions, which is characterised by the scattering angle, depends on factors such as the specimen thickness, the density and crystallographic structure of the sample material, and the atomic number (Z) of its constituent atoms. Furthermore, elastic scattering includes interactions between incident electrons and long-range electric fields, which are exploited in EH, as discussed in Ch. 5.
Inelastic scattering, which involves energy loss of the primary electrons and energy transfer to the specimen, can occur through various mechanisms, including:

- excitation of phonons, i.e., lattice vibrations
- excitation of plasmons, i.e., collective oscillations of the "free" outer shell electrons
- emission (or ionisation) of inner-shell electrons, which are replaced by outer-shell electrons, releasing excess energy in the form of characteristic X-rays or Auger electrons
- intra- or inter-band excitations, including the creation of electron-hole pairs in semiconductors
- emission of valence or conduction band electrons as secondary electrons (SEs)

Both the secondary signals resulting from inelastic scattering and the energy loss of the inelastically scattered primary electrons itself can be analysed using various TEM techniques, providing insights into the chemical composition and electronic structure of the specimen. However, it is important to note that inelastic scattering, due to its associated energy transfer, can lead to significant beam-induced damage to the specimen material.

3.1.2 Transmission Electron Microscopy Mode

The TEM column is schematically illustrated in Fig. 7. It consists of a series of electromagnetic lenses and apertures that govern the trajectory of the electron beam and focus it onto the specimen.
Electrons are initially emitted from an electron source, typically a field emission gun (FEG) in modern TEMs. Two primary types of FEGs are distinguished: Schottky FEG, which operates

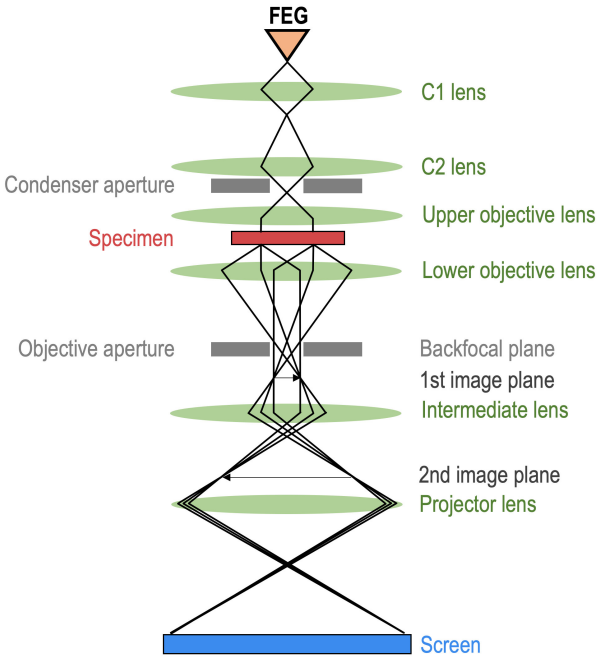

Figure 7: *Schematic illustration of the electron beam trajectory in TEM. Technical details omitted for clarity.*

at around 1700 K, and cold FEG, which operates at around 300 K. The cold FEG surpasses the Schottky FEG in terms of energy spread and crossover size. However, both types of FEGs, compared to thermionic emission sources, provide electron illumination with high brightness and coherence, which are particularly crucial for EH experiments.[70] A high voltage, typically ranging between 60 kV and 300 kV, is applied to accelerate the electrons from the source.

From the source, the electron beam passes through the condenser system, which typically comprises two or three condenser lenses. The first condenser lens (C1) induces a beam crossover that determines the spot size of the electron beam on the specimen, fundamentally controlling the beam current reaching the sample. By adjusting the excitation of C1, and thus the crossover position, a trade-off can be made between a smaller spot size (weaker C1 excitation), which results in lower beam current and higher spatial resolution at the expense of the signal-to-noise ratio (SNR), and a larger spot size (stronger C1 excitation), which increases the beam current and improves SNR but at the cost of spatial resolution.

The second condenser lens (C2) controls the beam convergence and the diameter of the illuminated area on the specimen. Weakening the C2 lens produces an underfocused image of the C1 crossover, leading to nearly parallel illumination.

Following the C2 lens, a condenser aperture restricts a portion of the beam. The fraction of the beam that is blocked depends on the spot size: larger spot sizes result in a greater beam spread, leading to a higher proportion of the beam being obstructed. Consequently, the C2 aperture regulates the number of electrons reaching the sample per unit time, i.e., the dose rate, depending on the selected spot size. Smaller spot sizes yield higher dose rates, and vice versa.

Reducing the electron current using the aperture enhances coherence at the expense of SNR and helps mitigate lens aberrations introduced by the condenser lenses. Furthermore, a smaller C2 aperture decreases the beam convergence angle, producing a more parallel beam.
The electron beam then passes through the electron-transparent specimen, which is mounted in a TEM holder. Depending on the holder system, the sample can be tilted in either one (single-tilt) or two (double-tilt) directions by adjusting the specimen stage. A wide range of commercially available TEM holder systems are now available, including various *in situ* holders that enable cooling, heating, control of the gas environment around the specimen, or electrical biasing of the sample, as employed in this work.
After passing through the specimen, the electrons are collected by the objective lens, which focuses them to form a diffraction pattern in the back focal plane and a first image in the image plane. The objective lens determines the magnification of the sample image.
In the back focal plane of the objective lens, an objective aperture selects the electrons contributing to the final image, which is then formed by the subsequent intermediate and projector lenses. The final image can be displayed either on a fluorescent screen or recorded using a digital detector, such as a charge-coupled device (CCD) camera, a complementary metal oxide semiconductor (CMOS) camera or a direct electron detector.

3.1.3 Scanning Transmission Electron Microscopy Mode

In STEM mode, a highly convergent electron probe is focused on the specimen using either the C2 lens or the upper objective lens. The beam convergence angle, α, determines the probe size on the specimen, which can reach sub-Ångström dimensions in aberration-corrected STEM. Probe aberration correction is achieved using multipole lenses positioned above the objective lens, ensuring aberrations are minimised before the beam interacts with the specimen. Deflection coils are used to scan the electron probe across the field of view (FOV) while the specimen is physically adjusted to the eucentric height via stage z-adjustment. At each probe position, different interaction mechanisms between the electron beam and the sample generate distinct signals. Detection of these signals using specific imaging and spectroscopy techniques enables comprehensive structural and chemical material analyses.
Unlike TEM imaging, where an objective aperture selects either direct or diffracted electrons, STEM imaging utilizes detectors positioned at specific collection angles to record transmitted electrons as a function of the scattering angle. Consequently, STEM imaging mode provides distinct material information, as it is associated with specific electron-specimen interactions (Sect. 3.1.1).
As in TEM, STEM imaging modes can be categorised into bright-field (BF) and dark-field (DF) imaging. The BF detector is located on the optical axis and primarily records unscattered, direct electrons and those scattered at very low angles, typically within a few milliradians (mrad).
In contrast, DF detectors, typically annular in shape, are positioned around the BF detector to collect electrons scattered to higher angles. Based on the angular collection range, DF imaging is further classified into annular dark-field (ADF) and high-angle annular dark-field (HAADF) imaging. ADF detectors typically collect electrons scattered at angles between 10 and 50 mrad, whereas HAADF detectors capture electrons scattered at angles exceeding 50 mrad.
In addition to STEM imaging of elastically scattered electrons, spectroscopy techniques based on

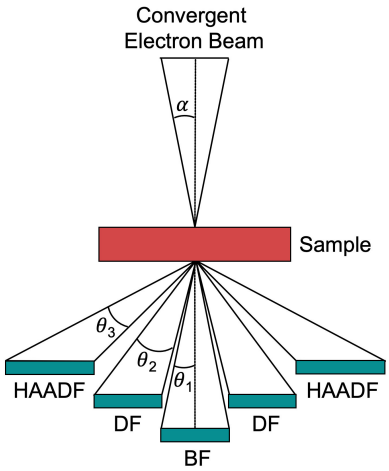

Figure 8: *Schematic representation of the STEM detector setup for BF, DF, and HAADF STEM imaging. Typical detector collection angles are $\theta_1 < 10$ mrad for BF, $\theta_2 \approx 10-50$ mrad for DF, and $\theta_3 > 50$ mrad for HAADF. The choice of convergence semi-angle (α) of the incident beam influences not only the probe size but also the contrast and resolution in different STEM imaging modes.*

inelastic electron scattering (Sect. 3.1.1) can be employed to analyse the chemical composition of a specimen. The most prominent methods include electron energy-loss spectroscopy (EELS) and energy-dispersive X-ray (EDX) spectroscopy.

In EELS, primary electrons undergo inelastic scattering, losing characteristic amounts of energy due to interactions with atomic excitations such as plasmons, phonons, and inner-shell ionization. By measuring the energy loss spectrum of the transmitted electrons using an energy filter, STEM-EELS provides high-resolution information on the elemental composition, electronic structure, and chemical bonding states of the sample.

In EDX, the high-energy electron beam excites inner-shell electrons of the specimen atoms, leading to the emission of characteristic X-rays unique to each element. Detecting and analyzing these X-ray signals enables the identification and quantification of elements within the sample, allowing for high-resolution elemental mapping.

3.1.4 Spatial Resolution

The unique advantage of using electrons instead of visible light for imaging is that their mass allows them to be be accelerated to high velocities, significantly reducing their wavelength. Since spatial resolution in electron microscopy is fundamentally governed by wavelength, this enables atomic-scale imaging. The wavelength limit of achievable spatial resolution in (S)TEM is given by the Rayleigh criterion, which describes the smallest resolvable distance between two points as:

$$\delta = \frac{0.61\lambda_e}{nsin(\alpha)} \tag{16}$$

where λ_e is the electron wavelength (2.51 pm for 200 kV electrons), and $n\sin(\alpha)$ represents

the numerical aperture, with n being the refractive index of the sample material and α the convergence semi-angle.[4] For simplicity, the numerical aperture can be approximated as unity, yielding:

$$\delta = 1.22\frac{\lambda_e}{\alpha} \tag{17}$$

However, in practice, this theoretical resolution is limited by multiple factors, most notably imperfections in electron optics. Aberrations introduced by apertures and electromagnetic lenses – particularly spherical (C_s) and chromatic aberration (C_c) – were constraining spatial resolution in TEM for many years. C_s occurs because electrons passing through the outer regions of a lens are focused more strongly than those passing through the center, preventing the beam from converging at a single focal point. C_c arises from energy spread in the electron beam, causing electrons with different energies to focus at different focal lengths. The first practical implementation of C_s-correction by Rose, Haider, and Urban marked a milestone in modern electron microscopy, enabling sub-Ångström resolution.[71,72,73] The first TEM with simultaneous C_s/C_c-correction was developed in 2010.[74] Aberration correction is achieved using multipole lens systems.

Beyond aberrations, several additional factors limit spatial resolution in (S)TEM experiments, including:[75]

- Detector limitations (collection efficiency, drift)
- Environmental influences (vibrations, magnetic fields, temperature and pressure fluctuations)
- Specimen effects (beam spreading due to elastic scattering, thickness variations, and inelastic scattering leading to Coulomb delocalisation and energy loss)

To estimate the spatial resolution of a STEM measurement, such as the STEM-EBIC experiments in Ch. 7 or the EDX and HAADF analyses of III-V tunnel junctions in MJSC in Ch. 8, the probe size must be determined. The probe size is commonly defined as the diameter of the central Airy disc (d_d), which can be approximated using the Rayleigh criterion (Eq. 17). In STEM, this is often rewritten as:

$$d_d = 1.22\frac{\lambda_e}{\alpha} \tag{18}$$

where d_d substitutes δ, since spatial resolution is directly linked to probe size, which is controlled by the convergence angle. This relation provides only a first approximation, as the central disc does not contain the full beam intensity. Aberrations reduce the peak intensity by about 20%, redistributing it into secondary rings that extend to larger distances.[76] Taking probe tail effects into account, the actual probe size is typically underestimated by a factor of ~ 3. The spatial resolution associated with a given probe size for a diffraction-limited system is the radius of the central Airy disc, i.e., $d_d/2$.[4]

3.2 (S)TEM Techniques for Structural and Chemical Analysis of III-V Semiconductors

As outlined above, various electron-specimen interactions generate signals that enable a comprehensive and correlative analysis of the structural, chemical, and electrical properties of a material

in (S)TEM, ideally within a single microscope session and using a single specimen. The primary focus of this work is–as outlined in the introduction–the investigation of electrical properties of III-V semiconductor junctions. The applied methods, namely TEM-based EH for measuring electrostatic potential distributions and STEM electron beam-induced current (EBIC) analysis for examining current distribution and extraction, are introduced and discussed in detail in dedicated chapters: EH in Chs. 5 and 6, and STEM-EBIC in Ch. 7. This chapter provides a brief introduction to the (S)TEM techniques employed in this work for correlative structural and compositional analysis, supporting the electrical characterisations.

3.2.1 High-Angle Annular Dark-Field Scanning Transmission Electron Microscopy

HAADF is a STEM imaging technique exploiting mass-thickness contrasts. As introduced in Sect. 3.1.3, HAADF detectors cover collection angles above 50 mrad. Electrons scattered to high angles due to Rutherford scattering – i.e., strong Coulomb interactions between the primary electrons and the atomic nuclei of the sample (see Sect. 3.1.1) – contribute to the HAADF image. On the other hand, contributions from Bragg-scattered electrons become surpassed at higher collection angles that result in a reduced diffraction contrast. The contribution of the lower-angle Bragg scattering information can be controlled by adjustments of the camera length, determining the inner collection angle. Shorter camera length yield larger inner collection angles. However, also the overall HAADF image intensity decreases at shorter camera length, as it is inversely related to the 4th power of the scattering angle.[77,78] For very high inner collection angles (>100 mrad), $I_{HAADF} \sim t \times Z^2$ applies.[79,78] As the scattered intensity in HAADF images is directly proportional to the atomic number, they are also referred to as Z-contrast images. More specifically, the differential cross-section $\frac{d\sigma}{d\Omega}$ is proportional to Z^2, meaning that as Z increases, the probability of high-angle scattering and, consequently, its contribution to the HAADF image also increases. Thus, HAADF imaging provides element-sensitive contrast, as atomic columns composed of heavier elements in the sample yield higher HAADF intensities and therefore appear brighter compared to those consisting of lighter elements. For atomic-resolution HAADF imaging, the incident electron beam should be aligned along a low-order zone axis to obtain well-defined atomic columns and enhance the HAADF signal through atomic focusing.[80,81] In this work, unless stated otherwise, high-resolution imaging was conducted along the [110] zone axis in the zincblende specimen.

In this work, medium- and high-resolution HAADF imaging was used as a qualitative method to study compositional variations of group III and V elements at the interfaces of epitaxial heterostructures with known stoichiometry, based on the approximation that HAADF intensity is proportional to Z^2. This approach allowed for a qualitative assessment of hetero-interface quality. An example is shown in Fig. 9, which depicts the interfaces between GaAs and AlGaInP, including elemental changes in both the group III and V lattice sites, as well as the interface between AlGaInP and GaInP, where only the group III element changes. Quantitative compositional analysis of experimental HAADF intensity patterns requires correlative image simulations and was not performed in this work.

Furthermore, in aberration-corrected STEM, the intensity distribution in HAADF images can often be directly interpreted in terms of the projected material structure, enabling the identification of atomic column positions.[82,83,84] By localizing atomic columns in the specimen,

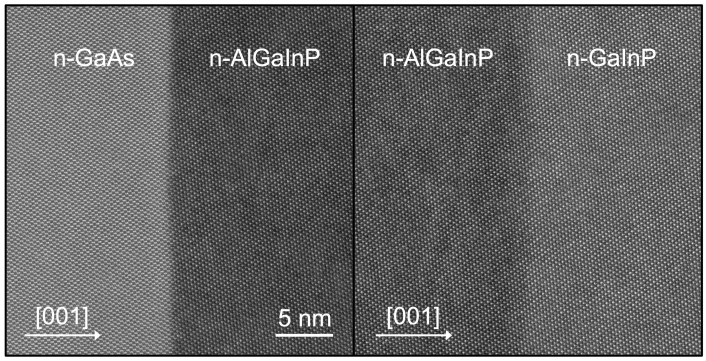

Figure 9: *High-resolution aberration-corrected STEM-HAADF images of III-V heterointerfaces.*

STEM-HAADF imaging can be used to analyse structural and crystallographic defects. This is demonstrated in Fig. 10, which shows the nucleation of a dislocation and twins in tensile-strained $GaAs_{1-x}P_x$ buffer structures on GaAs. The HAADF images clearly resolve the characteristic atomic dumbbells of the III-V material as well as the orientation of the atomic columns. In addition, the presence of an additional bright contrast around the defects indicate the formation of a strain field, which can be further analysed using TEM techniques (not discussed here).

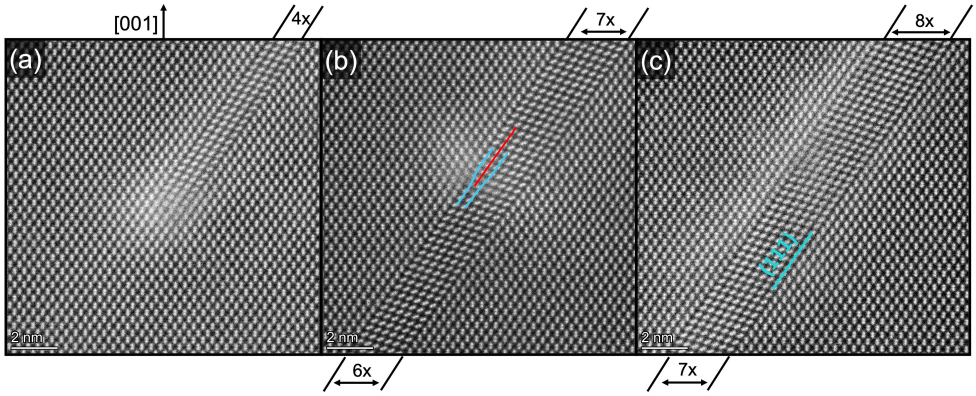

Figure 10: *High-resolution STEM-HAADF images of (a) the micro-core of a twinning dislocation formed under tensile strain in GaAsP buffer layers epitaxially grown on a GaAs substrate. The tensile strain arises from the reduced lattice spacing as the P content in* $GaAs_{1-x}P_x$ *increases. The width of the micro-twin, defined by the number of atomic columns, varies along the growth direction. (b) and (c) show STEM-HAADF images of the same twin, with the width increasing from 6 to 7 columns and from 7 to 8 columns, respectively, as the wafer surface is approached. Each dislocation step creates a strain field, visible through the bright contrast. The red line marks the additional plane bounded by the dislocation.*

However, care must be taken, as effects of specimen thickness and tilting can hinder an unambiguous structural interpretation by causing contrast reversal or apparent displacement of atomic positions in the HAADF image.[85] Nevertheless, STEM-HAADF imaging enables a straightforward interpretation of sample structures over a wide range of TEM sample thicknesses and defocus conditions.[83,84]

3.2.2 Energy-Dispersive X-ray Spectroscopy

As introduced earlier, the EDX technique exploits the inelastic interaction of the high-energy electron beam with the electron shells of atoms in a specimen to analyse its chemical composition.[86,87] The mechanism of signal generation in EDX is illustrated in Fig. 11.

When an inner-shell electron is knocked out by the incident electron beam, an electron from a higher energy level fills the resulting vacancy. This transition releases energy in the form of a photon, with an energy corresponding to the difference between the two levels. Since these energy differences are characteristic for each element, the emitted X-rays serve as unique elemental fingerprints.

The nomenclature of these transitions follows a standard convention: the shell where the electron was ejected gives the name (e.g., K, L, M), while the origin of the replenishing electron determines the Greek letter designation (e.g., α, β). For example, an electron transition from the L-shell to the lower K-shell is referred to as a Kα transition. The Kα, Kβ, and Lα transitions are presented in the schematic Fig. 11.

Thus, the chemical composition of the specimen can be mapped by detecting the emitted X-rays and assigning them to the corresponding elements. In STEM-EDX spectrum imaging, as applied in this work, the detection of emitted X-rays is synchronized with the STEM beam scanning position. After data collection, the elemental composition of the specimen is spatially resolved and analysed for each scanned point. Similar to high-resolution HAADF imaging, aligning the sample along a low-order zone axis enhances the X-ray yield from individual atomic columns.[88] Advancements in detector designs and implementation of aberration correction, that form Ångström-sized electron probes with high current densities, provide an opportunity to perform atomic-column resolution STEM-EDX mapping of the elements.

Absolute quantification of elemental concentrations using EDX is possible but non-trivial, as it requires careful consideration of distorting factors such as electron channeling, X-ray absorption, and, depending on the method, calibration with reference standards[89,88]. In complex specimens, such as the multinary compound semiconductors studied in this work, calibration can be time-consuming or even impossible if suitable reference standards with well-known compositions are unavailable.

A commonly used standard-free quantification approach is the Cliff-Lorimer method.[90] It relates the ratio of the characteristic X-ray intensities $\frac{I_A}{I_B}$ of two elements A and B to their atomic concentrations $\frac{C_A}{C_B}$ via the Cliff-Lorimer-factor, k_{AB}:

$$\frac{C_A}{C_B} = k_{AB}\frac{I_A}{I_B} \tag{19}$$

In simple words, the atomic fraction of the constituent elements can be derived by comparing the ratio of the intensity peaks in the recorded EDX spectrum. The k-factor accounts for the acceleration voltage, the detector efficiency, for differences in atomic weight, ionization cross section and fluorescent yield of the present elements, and for differences in the ratio of the Kα line to the total K lines of a substance. Since different elements have varying probabilities of emitting characteristic X-rays upon electron beam excitation, the k-factor corrects for these variations, enabling a more accurate quantification of elemental compositions. The k-factors are pre-determined by manufacturers through factory calibration and directly implemented in EDX

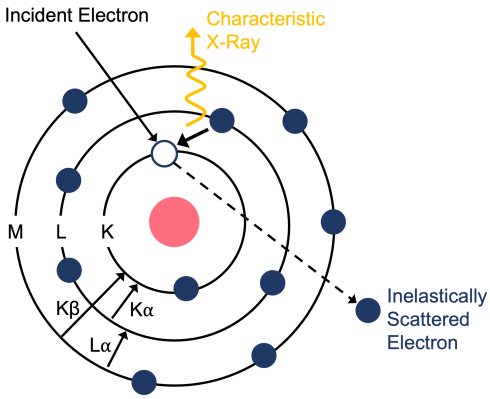

Figure 11: *Schematic illustration of EDX signal generation in (S)TEM. Inelastic interactions between the incident electron beam and atomic electron shells produce characteristic X-ray emission.*

data evaluation software. However, the accuracy of this method is low for sample materials composed of elements with greatly different atomic numbers, as the k-factor can not reliably correct for such differences. Additionally, this method assumes a thin specimen with negligible absorption. In practice, this assumption presents a dilemma, since thicker samples are usually preferred for EDX analyses, as they yield higher X-ray intensities.

The primary objective of EDX measurements in this study is to examine major element distributions at III-V heterointerfaces and to detect undesired elemental diffusion. Absolute quantification is not the focus; rather, the aim is to analyse qualitative spatial distributions and relative concentration variations. Nevertheless, the k-factor method was applied to estimate elemental concentrations in at.% – the percentage of a given element relative to the total number of atoms in the sampled volume. These values were compared with the stoichiometric expectations of the III-V compound to assess whether the MOVPE growth process achieved the intended composition. An example is shown in Fig. 12, presenting the STEM-EDX analysis of a GaInP/AlInP/GaAs heterostructure. Importantly, for quantifying EDX measurements of III-V materials, the III/V ratio in the solid (crystal) phase is always 1:1. As illustrated in Fig. 12, this means that the total atomic fraction of group III elements and group V elements must each sum to 50 at.%. The at.% values in this work were calculated using $N(GaAs) = 4.42 \times 10^{22}$ cm^{-3} as the reference value for the atomic density of zincblende GaAs.[61] This value also applies to related III-V compounds with the same crystal structure (e.g., AlGaAs).

For optimal STEM-EDX analysis, several experimental factors must be considered:

- Selection of X-ray lines: If possible, K-lines should be used for quantification, as they have higher yield, are less prone to peak overlaps, and suffer less absorption. However, practical limitations may require choosing alternative lines to ensure that all relevant elements are captured within a single spectrum without peak overlap.

- Energy range selection: The acquired EDX spectrum range should be as large as necessary to include all relevant element peaks but as small as possible to maximize the resolution per energy channel.

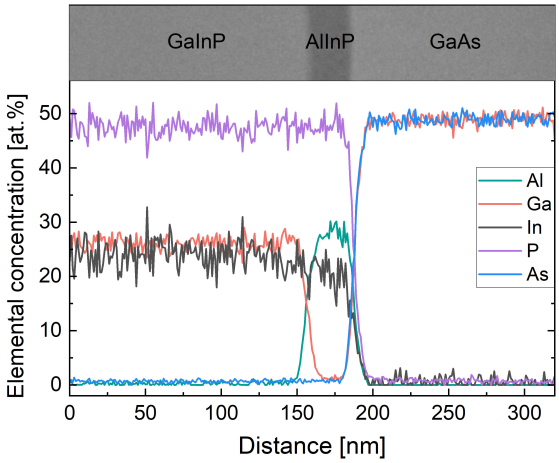

Figure 12: *Elemental distribution across a GaInP/AlInP/GaAs heterostructure, quantified from STEM-EDX maps using the k-factor method. The inset shows a STEM-HAADF overview image of the analysed sample region.*

- Acquisition time: The measurement should be long enough to achieve a sufficient signal-to-background ratio but short enough to minimise beam-induced sample damage and drift.

4 (S)TEM Sample Preparation

Every (S)TEM technique requires a specimen which is transparent to the incident electrons. In this work, all specimen were prepared using the well-established focused ion beam (FIB) lift-out method within a dual beam FIB/scanning electron microscope (FIB-SEM) system.[91,92] The III-V semiconductor structures are epitaxially grown on either 4-inch or 6-inch wafers, with diameters ranging from 100 to 150 mm. The FIB allows for site-specific extraction of electron-transparent slices from the bulk sample as well as the subsequent fixation to a specimen support, which can then be loaded to a dedicated (S)TEM holder to perform cross-sectional analyses.
Depending on the employed (S)TEM technique, specific requirements for the specimen arise, particularly concerning its thickness and geometry. This becomes evident when considering the various electron-matter interaction processes that the different analytical methods exploit (see Sect. 3.1.1). For example, high-resolution STEM imaging and EELS spectroscopy require very thin specimen, preferably below 50 nm, whereas EDX spectroscopy ideally requires thicker samples, ranging from 100 to 200 nm. FIB enables to adapt the cross-sectional sample geometry to suit the specific TEM method on a sub-micrometer scale.
In addition to conventional structural and compositional (S)TEM analysis, this work particularly aims to study the electrical properties of specific p-n junctions in III-V multi-junction devices inside the TEM, both with and without *in situ* biasing the semiconductor device. Here, the FIB-SEM is particularly advantageous for meeting the specific constraints on specimen geometry, thickness, and surface quality, providing flexible preparation beyond standard protocols. It enables precise shaping for circuit editing and can be additionally used to deposit conductive materials to create electrical connections between the extracted specimen and the dedicated specimen support for biasing within the TEM.
However, beside its advantages the FIB-SEM preparation has certain drawbacks, such as the ion milling introduces surface damage and modification. These effects are especially problematic for *in situ* biasing experiments, as they alter the electrical properties of the TEM specimen compared to the bulk device. As such, the impact of the ion-beam induced damage must be carefully evaluated and minimised to preserve the device properties and ensure reliable TEM electrical analysis.
This chapter firstly introduces the basic working principles of the FIB-SEM technique. Then the standard protocol for preparation of conventional TEM lamellae employed in this work is provided. Subsequently, the specific considerations for sample preparation required for electrical analyses within the (S)TEM is discussed. Finally, the preparation of samples for *in situ* biasing (S)TEM experiments is elaborated, with special attention given to the required sample geometry and the electrical contacting of the semiconductor samples on the TEM biasing support.

4.1 Basic Principles of Focused Ion Beam (FIB)-based Specimen Preparation

4.1.1 The FIB-SEM System

The FIB lift-out preparation method employs a dual-beam FIB-SEM system, which is schematically illustrated in Fig. 13a. The ion beam column is positioned at an angle of 52° relative to the SEM column in a vacuum chamber. The vacuum should typically be in the order of 1E-6 mbar for operation.[93] The bulk sample is placed on a stage at the eucentric height, which enables

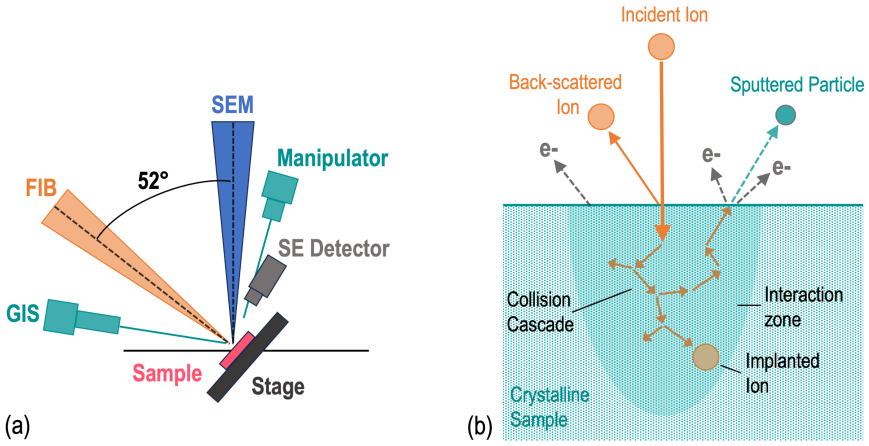

Figure 13: *a) Schematic representation of a FIB-SEM system. b) Simplified illustration of some ion-matter interaction mechanisms occuring during the FIB-milling of a crystalline specimen. The interaction zone refers to the depth in which ion-induced sample damage occurs, such as amorphisation, vacancies, interstitials and ion implantation.*

simultaneous sample imaging and ion beam processing. The stage allows sample navigation in x-, y- and z-direction, as well as rotation and tilt. A micromanipulator needle can be inserted to extract and precisely manipulate the prepared lamellae onto the TEM support. An electron detector is used to image the SEs resulting from the electron- or ion-irradiation of the sample. Hence, imaging can be performed in SEM mode or in FIB mode. A gas injection system (GIS) connected to various organo-metallic precursor gas sources can be inserted into the chamber for the purpose of electron-beam or ion-beam induced deposition (EBID, IBID) of materials, typically C, W or Pt. More details of the beam-induced deposition of materials are given in Sect. 4.4.2.

4.1.2 Ion-Matter Interaction

The incidence of the ion beam into the crystalline sample, similar to the electron-matter interactions described in Sect. 3.1.1, causes a range of elastic and inelastic scattering processes.[93,94] Fig. 13b provides an overview of the main mechanisms involved in ion-matter interaction. The FIB preparation method exploits some of these mechanisms, enabling imaging, milling, and material deposition. However, these interactions also come with undesired effects physically damaging or altering the composition of the specimen in the interaction zone.

As the ions strike the sample, they undergo a series of elastic and inelastic collisions within a near-surface interaction zone. SEs produced by the inelastic scattering of ions can, like those generated by electron irradiation, be detected for imaging and monitoring the FIB preparation process. During the collision cascade, momentum is transferred to the target atoms, leading to a temporary disorder of the crystalline structure in the collision zone. The affected atoms may then either return to equilibrium positions or be displaced into interstitial lattice sites, creating vacancies, leading to amorphisation, and potentially triggering defect formation. If the kinetic energy imparted by the ions is sufficient to overcome the surface binding energy, the target

atoms may be ejected from the bulk crystal. The cumulative effect of these sputtering events results in the milling of the sample surface.
The surface binding energy (SBE), typically in the range of a few eV, is material-specific.[94,95] Therefore, the nature of the sample largely determines the sputtering yield, which is otherwise influenced by the Ga-ion beam energy, current, and incidence angle.[95,96,97,98,99,100] A detailed review of the ion sputtering yields of GaAs and the relevant surface binding energies is provided elsewhere.[94,95,100]
Although most sputtered material is removed by the vacuum pumps, a significant portion may redeposit on the sample surface around the sputtering site, depending on the milling geometry and ion-beam incidence.[101,97,102]
During the collision cascade within the sample, the ions gradually lose their initial kinetic energy. If energy diminishes to the extent that they can not be back-scattered from the target, they eventually become implanted at a specific depth within the material, thus altering the composition in the interaction region.[99,93] In FIB-milled GaAs, Ga-ion implantation together with Ga-enrichment resulting from selective milling of As is known to lead to precipitation of Ga as liquid or amorphous particles.[103,98,97,104]
The depth of the interaction zone, where ion-beam milling and damage occurs, depends on the ion beam energy, current and incidence angle, as well as on the material properties, such as the composition and density.[105,93,106,96] The extent of the damage region can be reduced by using low ion beam energies (e.g. 5 kV or 2 kV) and low incidence angles, though this comes at the cost of lower sputtering yield and rate.[107,102,105,95,106,93] Minimizing damage is critical, as amorphisation and introduction of point defects, such as vacancies, interstitials and impurities, alter the specimen's crystallographic structure, composition, and eventually the electrical properties. These changes, along with topological effects such as redeposition and surface roughness, can compromise TEM analysis by skewing electrical measurements and introducing misleading features, such as artifacts in diffraction contrast.[101,105]

4.2 The FIB Preparation Methodology

4.2.1 FIB-SEM Devices

Different FIB-SEM systems listed in Table 2 were used depending on the aim of the preparation necessitating the availability of a specific ion source type or GIS precursor.
Commercial FIB-SEM systems are most commonly fitted with a liquid metal ion source (LMIS) for Ga^+ emission, as are the systems used herein. The only exception is the FEI Helios 5 Plasma-FIB (PFIB), which is fitted with an magnetically enhanced inductively-coupled plasma (ICP) ion source of Xe^+ ions instead. Xe^+ ICP systems are preferably used for applications, which require milling of a large volume and depth, as the higher achievable currents – up to 2.5 µA[108] for Xe^+ ICP compared to ≤ 65 nA[109] for Ga^+ LMIS – of the higher mass Xe^+ ions provide significantly increased milling rates.[110,111,107] Hence, they allow higher throughput, whereas for Ga^+ LMIS the sputtering yield is limited to depth ranges of tens of microns.[112] Since in this work the preparation at lower currents was favored to minimise ion-beam induced surface damage, the Ga^+ FIB was generally preferred, as it yields superior spatial resolution in the low-current regime. Xe^+ ICP sources are better-resolving in the high-current regime (above 60 nA).[110,112] Herein, the PFIB was only employed for an experiment elaborated in Ch. 8, which

required milling of more than 200 µm deep windows into a full wafer slice.
For the beam-induced deposition of materials, GIS precursors for C, W and Pt were available in this work. C was used as a protective deposition in standard (S)TEM lamellae preparation (Sect. 4.2.2), while W or Pt was used as a protecting and contacting material for the *in situ* biasing specimen preparation (Sect. 4.4). The selection of the material and the deposition method (EBID or IBID) was adjusted to meet the specific material properties needed for each preparation. More details on the properties of beam-induced metal depositions for *in situ* biasing specimen preparation are given in Sect. 4.4.2.

Table 2: List of FIB-SEM devices employed in this work at the Ernst Ruska-Centre (ER-C) in Jülich and at the CEA LETI in Grenoble. LMIS and ICP refer to liquid metal ion source and inductively-coupled plasma source, respectively.

Laboratory	Device Specification	Ion Source	Available GIS Precursors
ER-C	FEI Helios Nanolab 400S	LMIS (Ga^+)	C, W
ER-C	FEI Helios Nanolab 460F1	LMIS (Ga^+)	C, W, Pt, SiO_2
CEA LETI	FEI Strata 400S	LMIS (Ga^+)	C, W
CEA LETI	FEI Helios	LMIS (Ga^+)	C, Pt, SiO_2
CEA LETI	FEI Helios 5 PFIB CXe	ICP (Xe^+)	C, W, Pt, SiO_2

4.2.2 The Experimental Protocol

The FIB preparation of TEM lamellae in this work follows a standardised procedure, the individual steps of which can be seen in the SEM images in Fig. 14. The preliminary adjustments, such as locating the bulk sample region of interest and adjusting its z-height to the eucentric position of the FIB-SEM columns, are implemented in SEM mode using 5.0 kV and 0.34 nA.
Firstly, a protective layer (typically C) of a few hundred nanometer thickness is deposited via EBID (see Fig. 14a) before the first use of the ion beam to prevent ion induced damage of the wafer top surface. For standard preparation, usually C was used as a protective material, deposited with an electron beam current of 11 nA. But W and Pt could just as well be used for this purpose. Care should be taken to minimise drift during deposition in order to achieve a well-defined protective layer. When present, beam drift typically occurs within the first few seconds of deposition and is commonly attributed to specimen charging effects. To reduce blurring of the deposited layer, the bulk specimen wafer should be connected to the stub using conductive adhesive to minimise charging. Additionally, beam drift during the initial seconds of deposition can be corrected using the electron beam stigmators, guided by live SE imaging.
The following procedure used the FIB system. First, the FIB column must be oriented edge-on to the top edge of the sample by tilting the specimen stage to 52° (Fig. 13a). Next, a second and thicker C deposition of about 2 µm is deposited on top of the EBID-cover-layer using IBID at 30 kV and 0.28 nA (see Fig. 14b). Having deposited this main protective layer, the wafer surface should be efficiently protected throughout the subsequent FIB cut-out of the lamella. For this, trenches are firstly milled on each side of the protective deposit using 30 kV and 2.8 nA, as can be see in Fig. 14c. The depth of the trenches are adjusted to the intended size of the lamella, which usually ranges between 5 and 10 µm. Afterwards, the sidewalls are milled at an angle of ±2° off from 52° using the 'cleaning cross-section' pattern. The tilt provides a straighter cut, which facilitates cutting off the bottom of the lamella in the next step.

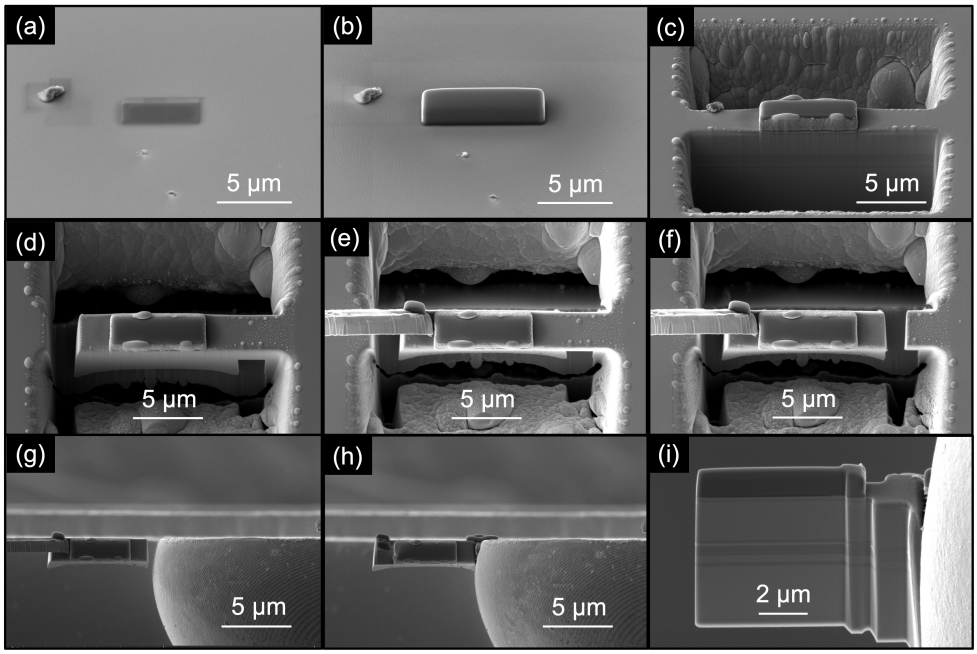

Figure 14: *Secondary electron SEM images showing the FIB preparation process for conventional TEM samples, acquired at 5 kV and 0.40 nA. (a) Electron-beam induced deposition (EBID) of a first C protective layer at 0°. (b) Ga-ion-beam induced deposition (IBID) of a second C protective layer at 52°. (c) FIB milling of trenches on each side of the protective layer, followed by a cleaning of the side-walls at lower ion-beam energy. (d) The lamella is cut free on one side and at the bottom using an L-cut at 7°. (e) The micro-manipulator is inserted and attached to the lamella with an IBID of C. (f) The last connection of the lamella to the bulk specimen is cut off, allowing the lift-out and (g) the transfer of the lamella to a TEM support grid. (h) The lamella is attached to the grid by a IBID of C and the manipulator is cut off and extracted. (i) Progressive thinning of the lamella to electron-transparent thickness is achieved through iterative milling of the front- and back sides at* $52° \pm 2°$*, respectively.*

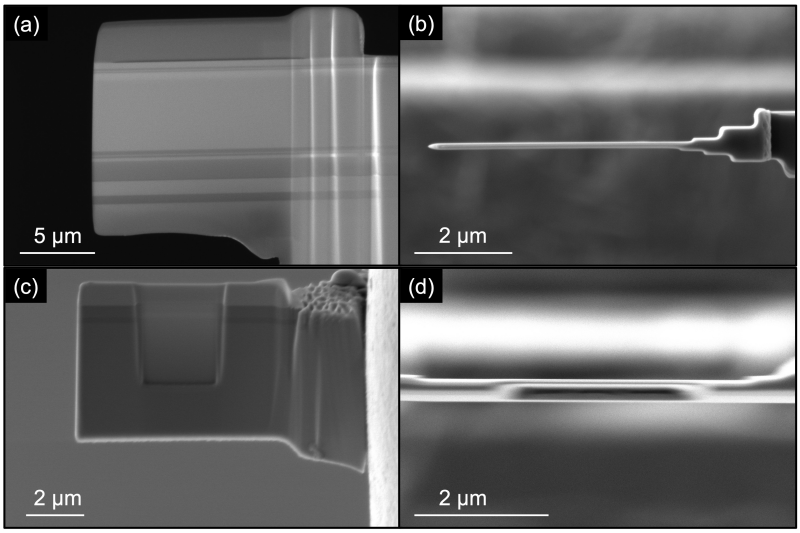

Figure 15: *Two (S)TEM sample cut geometries to avoid lamella bending. (a) Side-view and (b) top-view SE SEM images of a flat and short cut STEM-lamella. (c) Side-view and (b) top-view SE SEM images of a ~200 nm thick lamella with an U-shaped electron-transparent window of about 50 nm thickness.*

The undercut is milled at a tilt of 7° while simultaneously removing the left-side connection, which leaves a free-standing lamella attached only on the right side, as can be seen in Fig. 14d. For the lamella lift-out, the stage is tilted back to 0° and blocked to avoid unintentional movements, and hence, damage of the micro-manipulator, which is now inserted. Both, the SEM and the FIB images are used iteratively to navigate the needle to the left-end corner of the lamella, as shown in Fig. 14e. As in this configuration the FIB is not incident from the protected top, but normal to the side, the FIB current is significantly reduced to 28 pA and is used as sparingly as possible for the navigation.

The lamella is now attached to the tip of the needle with ion deposited C before the remaining connection to the bulk is cut (Fig. 14f). The specimen is then carefully lifted out and transferred to the TEM support grid, as shown in Fig. 14g. For all non-biasing experiments, Omniprobe lift-out copper grids are used. There it is attached in a flag-post position using again IBID of C at 30 kV and 0.28 nA, and the connection to the micro-manipulator is cut off. Fig. 14g and h show the lamella from top and side view.

Once fixed to the grid, the lamella can be thinned to an electron-transparent thickness of choice by iterative FIB milling of the front and back sides at tilt angles of $52° \pm 2°$, respectively. Milling from both sides and at low incidence angles is vital for minimizing surface roughness and damage, especially for specimens with regions composed of different material compounds.[106,96] During the thinning, the ion beam tails will preferentially mill the top surface. Here it becomes evident that the top sacrificial deposit must be sufficiently thick to prevent the beam from penetrating through it to the sample surface. With progressive thinning, the ion current is sequentially reduced to better control the milling and to minimise surface damage. Typically, the FIB is operated at 16 kV in a current range from 0.9 nA down to 40 pA. The z-depth of the milling pattern

must be optimised to achieve a parallel-sided lamella and avoid creating a trapezoidal shape by under- or over-milling the bottom of the lamella.
When the desired thickness is achieved, the final FIB preparation step is to polish the lamella surface using a low-energy ion beam, at 5 kV or ideally 2 kV and below. This step should help to minimise the amorphous surface layer induced by the higher-energy FIB milling to a large extent. It is particularly important for atomic-resolution imaging and for electrical characterisation by EH or STEM-EBIC mapping. After the thinning, the final step of the sample preparation is generally treating the TEM lamellae for 2–3 min in an Ar/O plasma cleaner using an argon/oxygen gas mixture in order to remove any carbonaceous contamination from the specimen surface.

It has to be noted that the applied beam currents applied during the preparation strongly depend on the physical properties of the material and the intended (S)TEM characterisation. The GaAs- and InP-based III-V multi-layer systems studied herein are rather soft and sensitive materials with high sputtering yields, which sputter very quickly, and hence, require for careful multi-step preparation in the low-current range.

The thickness and geometry of the lamella should be adapted to the intended analysis technique. For example, to prepare thin specimens (of <80 nm) for (S)TEM analysis, a particular care has to be taken to avoid bending of the lamella. Bending is a common problem in FIB preparation of rather soft semiconductor materials, such as the GaAs-based III-V compounds studied in this work. In this work, two approaches are applied to avoid bending of (S)TEM lamellae. Either the lamella is kept relatively short, with an electron-transparent region of about 5 µm, as shown in Fig. 15a and b; or the 'U-shape' milling approach is applied. Here, as shown in Fig. 15c and d, only a small, U-shaped window, located at the sample region of interest (ROI), is milled to electron-transparency, while the rest of the lamella remains thick and thereby provides a stabilising support frame. The procedure of the U-shape milling is illustrated in Fig. 16.

After conventional Ga-ion FIB-milling, usually an amorphous damaged layer that contains implanted Ga ions is present on the specimen surfaces of III-V alloys. Further, the specimen might still remain unfavorably thick for atomic-resolution imaging.
In this case, low-energy Ar-ion milling can be used as a post-FIB treatment to remove surface damage and gently thin the sample further.[113,114,98,106,95] Studies have shown that this approach can reduce the amorphous surface layer on ion-milled GaAs specimens to less than 1 nm.[98,95,115]
In this work, low-energy Ar-ion milling in a NanoMill (Fischione) system is performed for post-treating lamellae prepared for atomic-resolution STEM imaging. The FIB lamellae are milled from the top and bottom side at an incidence angle of $+10°$ and $-10°$, respectively, relative to a static beam orientation. A 2-step milling routine is employed, starting with an ion energy of 900 eV and finishing off by polishing at 500 eV. The duration of each milling step is adapted to the desired thickness reduction, ranging typically about milling for 5 min at 900 eV and 10 min at 500 eV. The Ar-beam is typically scanned over a 20 × 14 µm window. After the Ar-milling, the preparation is finished off as usual by plasma-cleaning.

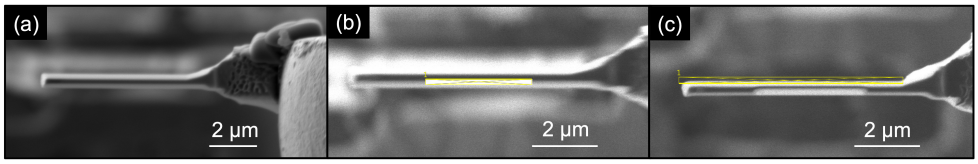

Figure 16: *To attain a U-shape cut, the sample lamella is (a) first milled down to a thickness of 400−500 nm by using the standard procedure described above. Then, (b) in an on-edge tilt position to the FIB, a rectangular cleaning-crosssection pattern is set on the desired window position. Milling parameters of 16 kV and 40 pA are used, and a very small z-depth of 0.1 µm, which can be adapted to the desired depth of the window. To achieve the target thickness, the front window can be iteratively milled with the entire back-side of the lamella, as shown in (c), using small off-tilts of ±0.8° from the edge-on 52°. Image (a) is a SE SEM image, whereas images (b) and (c) are FIB images.*

4.3 Sample Preparation Considerations for Electrical TEM Analysis of III-V Semiconductors

Since a key goal of this work is the electrical analysis of semiconductor devices and their *in-situ* biasing within the TEM, preserving the sample's electrical properties during FIB preparation of electron-transparent slices is critical. All changes induced by ion irradiation must be carefully assessed for their specific impact on electrical performance. The most important considerations for FIB sample preparation in relation to electrical (S)TEM analyses using EH and/or STEM-EBIC are as follows.

4.3.1 Electrical Surface Damage

As outlined in Sect. 4.1.2, various ion-matter interactions during FIB milling contribute to surface damage, which results in changes to the crystallinity and chemical composition, which in turn alter the electrical properties of the semiconductor sample. Even with effective protection of the top surface using EBID and IBID with thick protective metal layers, ion beam damage inevitably affects the side and bottom walls of the lamella.[101,97,105,116] The electrical damage of semiconductor FIB specimen generally manifests as increased resistivity. This higher resistivity is caused by the combined effect of various ion-matter interaction processes discussed in Sect. 4.1.2, which will be evaluated here in terms of their electrical effects.

Firstly, in the amorphised surface layer, the carrier mobility is significantly reduced, which causes a local rise in resistivity.[93,117] Secondly, the displacement of atoms during the atomic collision cascade leads to creation of point defects such as vacancy-interstitial pairs, which can form complexes with dopant atoms and act as recombination centers, hence, affecting the dopant activity and increasing the resistance.[118,119,93] Thirdly, atomic collisions can also displace substitutional dopants from their lattice sites, resulting in dopant deactivation and, consequently, increased resistivity.

As illustrated in Fig. 17a, the electrical surface damage on each lamella sidewall can be visualized as consisting of two layers: the fully amorphous, non-crystalline top layer, and an electrically damaged, yet still crystalline, sub-surface layer. This crystalline region, while retaining its structure, contains point defects (vacancies, interstitials, and impurities) negatively impacting the doping activity of the semiconductor, making this part of the lamella more electrically resistive.

In the literature, this crystalline sub-surface layer is often referred to as the "electrically inactive layer", as it is considered not to contribute to the absolute built-in potential across the junction, which is measured by EH.[42,120,121,38,117,119,42] However, this is a simplified assumption. Unlike the amorphous layer, which has completely lost its semiconductor properties, the electrically damaged crystalline region is not entirely electrically inactive. It rather acts as a depleted zone of varying extent, altering the original electrical properties of the semiconductor, such as the potential distribution. For example, it leads to a broadening of the space charge region (SCR) in the damaged layer relative to the undamaged region, due to the depletion of active carriers, as illustrated in Fig. 17.[122,123,119] This effect occurs in all three dimensions of the FIB lamella. However, for simplicity, and noting the simplification that this term entails, the electrically damaged crystalline sub-surface layer will be referred to as the electrically inactive thickness in the following.

The extent of the surface damage is generally defined by the depth of the ion-matter interaction zone (collision cascade), which is determined by the FIB milling parameters as well as the sample material. As mentioned earlier, it can be significantly reduced by using a low ion beam energy and current, along with a low-incidence angle of the Ga-ion beam. For instance, studies have shown that the ion-induced amorphous layer on the side walls of GaAs lamellae can be reduced from 22 nm to 11 nm, and on the bottom wall from 42 nm to 20 nm by using 10 kV instead of 30 kV.[116] The thickness of the amorphous damage in III-V materials is compound specific and depends beside others on the mass density difference of the atomic components leading to unequal recoiling. Hence, the damage layer from FIB milling at 10 kV is similar in InAs and GaAs (11 nm), but significantly larger in InP (15 nm), due to the greater atomic mass difference of In and P.[116]

The depth extent of the crystalline electrically damaged region is, however, not limited to the region of the collision cascade but can extend beyond it, as it is governed by the process of defect diffusion, which primarily depends on the doping concentration of the semiconductor.[123,124,120,39,119,117] At room temperature, the defects exhibit high diffusivity and create an exponentially decaying point defect profile as they readily diffuse into the crystal. The more active dopants are present in the sample to trap the defects (to form dopant-defect complexes), the shallower is the electrically damaged sub-surface region.[117] Or in other word, the more dopants available, the smaller the impact of a given number of recombination centers on the built-in electric field. Correspondingly, the depleted surface region is shallower in semiconductor materials with higher doping levels, as illustrated in Fig. 17b. This adds another level of complexity when studying III-V hetero-structure devices consisting of epitaxial layers of various III-V compounds, with different dopant types and concentrations.

In order to achieve an accurate electrical characterisation of the semiconductor sample, it is hence crucial to estimate the extent of this electrically damaged region. This is particularly important for EH, which measures the electrical potential distribution within a sample as a function of its thickness and compares it with simulations. Here it is crucial to subtract the damaged portion from the total crystalline thickness and account for it in both experiments and simulations.

The electrically damaged layer must also be carefully considered when choosing the final lamella thickness during FIB thinning to ensure sufficient electrical response from active dopants. In ge-

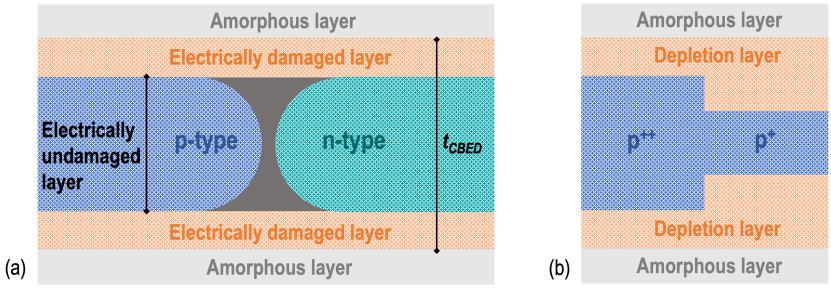

Figure 17: *a) Schematic cross-section of a TEM lamella prepared by FIB milling, including the ion-beam induced damaged surface layers and their influence on the depletion width (in dark grey) of the specimen p-n junction. t_{CBED} refers to the crystalline lamella thickness, which is measured by convergent beam electron diffraction. b) Schematic illustration of the dependency of the surface depletion (or electrically damaged) layer width on the doping concentration. Higher doping results in a smaller surface depletion layer.*

neral, the thicker the lamella, the smaller the influence of the passivated surface. Most reported specimen thicknesses of III-V materials for EH experiments range from 200 nm to 600 nm with crystalline electrically inactive surface layers in GaAs between 100 and 223 nm, depending on the doping level and applied FIB voltage.[42,125,40,119]

Due to its complex dependency, the inactive thickness should ideally be measured specifically for each lamella subjected to electrical TEM analysis. Unlike the amorphous surface layer, which can be readily quantified through STEM analysis, the transition from the crystalline inactive 'layer' to the crystalline electrically active lamella core is not abrupt and more difficult to determine.[123,39] However, it can be estimated by a method which involves studying the built-in potential across a p-n junction measured using EH or 4D-STEM as a function of the crystalline specimen thickness or measured using convergent beam electron diffraction (CBED).[125,30] The methods for the CBED specimen thickness measurement and the evaluation of the electrically inactive thickness are described in greater detail in Sects. 5.3.1 and 5.3.2, respectively.

4.3.2 Impurity Implantation

The FIB preparation process inevitably leads to ion implantation introducing various types of impurities into the sample. These include mainly the implantation of Ga-ions, originating from the ion source itself, and the self-implantation of recoil atoms. Apart from this, C impurities may be implanted, originating either from surface contamination of the sample or from the protective layers applied during FIB preparation. Even when materials like W or Pt are used for protection, their organometallic precursors contain C, resulting in the deposition of mixed compounds such as Pt-C and W-C rather than pure metals. Other impurities from the protective metal layers or surface contamination, such as Pt or W, may be implanted as well.

Ion implantation is the source of many mechanisms leading to surface damage discussed previously. As a result, Ga ion implantation indirectly contributes to the electrical damage by amorphising the top surface layer and by, along with the self-implanted recoil atoms, creating point defects that act as recombination centers for active dopants.

In addition to these indirect effects, the implanted impurities themselves have a direct impact on the electrical properties, which depends on the type of impurity and the target semiconductor material. Through this mutual dependency, the electrical effects of ion implantation cannot be generalized and must be considered for each specific case. For example, to most of the GaAs-based III-V compounds studied in this work, Ga is a native element and does not function as a dopant; instead, it leads to local variation of the III-V compound stoichiometry. Conversely, in Si, implanted Ga can act as a p-type dopant, although it requires activation through annealing to become electrically active.[117] Similarly, C is a commonly used p-type dopant in III-V materials. However, whether or not the implanted C dopants are active remains to be studied for the specific target materials.
As for metals from the protective layers, their electrical impact tends to be minor due to their high mass density, which results in shallow implantation and a higher likelihood of scattering or ejection rather than implantation.

The depth of ion implantation is influenced by key factors such as the incidence angle and energy of the ion beam. The greater the angle and energy of the FIB, the deeper the implantation (see previous Section) and the higher the concentration of implanted ions. For instance, Langford *et al.* (2001)[97] demonstrated that Si samples milled with a 5 keV ion beam contained 2.5 times less Ga than those milled with a 30 keV beam.
The second key factor is the mass density of the implanted impurities. Ions with lower mass density tend to penetrate deeper than those with higher mass density. This has been confirmed through simulations using stopping and range of ions in matter (SRIM) routines.[126,127] For example, Giannuzzi & Stevie (2005)[93] demonstrated that the stopping power of elements struck by 25 kV Ga ions correlates with their mass density, following a periodic trend across the groups of the periodic table. Rubanov *et al.* (2005)[116] studied this effect for the specific case of III-V compounds, by combining experimental data and SRIM simulations. Consistent with the previous results they showed that for Ga ions striking an InP specimen, the recoil P atoms (1.82 g/cm^3) penetrate deeper than both the recoil In atoms (7.31 g/cm^3) and the primary Ga ions (5.91 g/cm^3); a trend also seen in GaAs and InAs.[116]

4.3.3 Lamella Thickness Uniformity

The built-in potential across a p-n junction measured by EH is directly related to the specimen thickness, as will be elaborated in greater detail in Ch. 5. This dependency not only explains the need for relative thick TEM specimens to enhance potential variations, thereby improving the accuracy of the measurement. It also necessitates maintaining a parallel-sided lamella with uniform thickness across the ROI, as even small thickness variations can result in large phase changes and lead to misinterpretation of thickness-induced potential variations as intrinsic to the specimen. For GaAs and InP, which have a MIP of 14.2 V[66,67] and 14.5 V[66], respectively, a variation of 2 nm in the thickness of a 200-nm-thick specimen would cause a phase shift of 0.21 rad, when using 200 kV electrons.
By carefully adjusting the FIB incidence angle and milling depth (z), FIB lamellae can be cut with nearly parallel side walls, thus avoiding thickness gradients and the resulting potential variations. However, care must also be taken to avoid non-gradial thickness inhomogeneities

resulting from the differing milling rates of material compounds. The sputter rates of different III-V compounds slightly differ due to the different surface binding energy of each atomic species in the compounds. For example, the sputter rate in InP is approximately 1.5 times higher than in GaAs, while in InAs it is about 2.1 times higher.[116] Hence, the FIB milling can result in thickness corrugations across the epitaxial III-V layer structure. However, the variations of the milling rates among the III-V compounds are relatively small. Greater care must be taken when cutting III-V devices with metallization layers on their surfaces, as the significant difference in sputtering yield can lead to severe curtaining. To avoid this, specialized preparation procedures, such as back-side milling, can be employed.[128,93] Further details will be discussed in Sects. 8.5 and 8.6.2, focusing on the preparation of working MJSC devices.

4.3.4 Vacuum Reference Region (Sample Geometry)

The need for a vacuum reference region close to the specimen ROI within the recorded FOV is intrinsic to the EH technique, and is required as well for quantitative (S)TEM-EBIC measurements, as will be discussed in Ch. 5 and 7, respectively. For non-biasing EH, one can use the side edge of the specimen, as evident from Fig. 14(i). However, the side cut must be very straight and clean, to avoid artefacts in the measured electron phase distribution. Further, an undesired gradual thickness change from the edge towards the central part of the lamella is almost unavoidable, so that relatively large FOVs have to be acquired to probe the flat part. Hence, it is often preferable to have the vacuum reference at the top surface of the lamella. This allows also to study and compare regions of different thickness along the lamella. However, usually the top surface of the sample is covered with a 2-3 µm thick protective layer, as explained in Sect. 4.2.2. Hence, a special preparation is required to attain a free standing surface.
In order to achieve this, instead of performing the initial EBID metal deposition, an ink layer is applied with a marker on the wafer surface before introducing the sample into the FIB-SEM. Similar to the EBID layer, the ink protects the wafer surface from ion damage during the subsequent IBID process. Fig. 18a shows a lamella with a protective ink layer plus an overlying W deposition on the surface. The advantage of the ink layer is that it can be removed after the FIB lamella preparation using a 5-10 minute treatment in the plasma cleaner, leaving the sample surface exposed. The now free-standing IBID metal layer can then be pushed off using the micromanipulator in the FIB-SEM, as demonstrated in Fig. 18c-d. Afterwards the sample should be plasma-cleaned again to remove any potential ink remnants and provide a clean sample (see Fig. 18b).

4.4 TEM Specimen Preparation for *In Situ* Biasing Experiments

The preparation of TEM specimens for *in situ* biasing experiments can be performed similarly to standard lamella preparation using a FIB-SEM lift-out technique. However, some specific aspects must be considered. First, the geometry of the sample must be adjusted to ensure proper current flow through the device, with the applied voltage primarily dropped across the device p-n junction. In addition to this circuit editing, the sample must be electrically connected to the TEM support via FIB-induced metal deposition.
The following sections outline the specialized procedure for *in situ* biasing specimen preparation, review the properties of FIB-deposited metals for electrical contacts, and discuss considerations

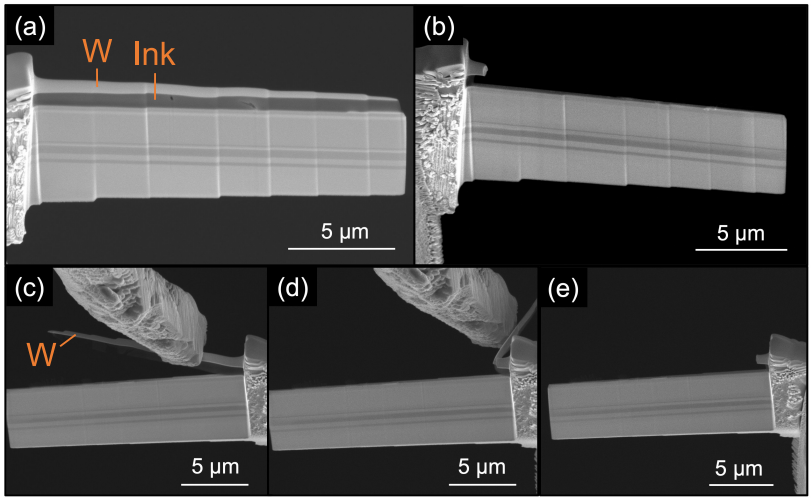

Figure 18: *A TEM lamella with steps of different thickness (a) before and (b) after the removal of the protective depositions (ink plus ion-beam induced W deposition) from the top surface. The sequence in (c)-(e) demonstrates the removal of the free-standing W-layer by using the micro-manipulator needle, after the ink-layer was removed by plasma-cleaning. All SE SEM images were acquired at 5 kV and 0.40 nA.*

that are unique to *in situ* biasing specimen preparation.

4.4.1 The Preparation Procedure

The procedure for the preparation of *in situ* biasing specimen can be comprehended by means of Fig. 19. The first step is, as for the standard lamella preparation, the deposition of a protective metal layer on the wafer surface (Fig. 19a). In this case however, the metal is not only serving as a protection to surface damage, but provides the electrical contact to the specimen required for biasing. In this work, either IBID of W or Pt were used. The properties of FIB-SEM deposited W and Pt are reviewed in Sect. 4.4.2. Since an initial protective EBID is omitted due to the highly resistive properties of EBID metals, the IBID deposition must be performed carefully, and extensive exposure of the wafer surface to the FIB prior to this first deposition should be avoided. As can be seen in Fig. 19a, the deposition consists of two parts: one layer of ~2 µm is deposited across the whole length of the lamella, and an additional deposit on the left side over approximately one-third of the total length and with a thickness of about 3−5 µm. This reinforcing deposition becomes critical in the later stages of the preparation.
The subsequent lamella lift-out procedure, including trench cuts, side- and under-cuts (Fig. 19b), welding of the micro-manipulator and lift-out (Fig. 19c), follow the same standard procedure as described in Sect. 4.2.2.
Afterwards, the lamella is transferred on a dedicated chip (Fig. 20a-b) which can be fitted and contacted in an electrical biasing TEM holder. In this work, Protochips Si-half chips were used in a Protochips Aduro 500 biasing TEM holder. The geometry of the MEMS chip is displayed in Fig. 21. It consists of a thick Si-frame with applied metal tracks for electrical contacting.
The lamella is positioned across the chip trench, onto the contacting metal tracks. The length of

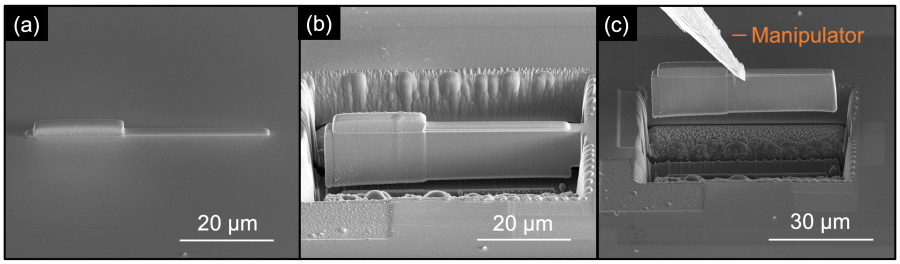

Figure 19: *SE SEM images of the first steps of the in situ biasing TEM specimen preparation, acquired at 5 kV and 0.40 nA. (a) Ion-beam induced metal (W or Pt) deposition (IBID) for protection and electrical contacting. (b) By milling side-trenches and performing an L-cut, a free-standing lamella is shaped. (c) The lamella is welded to a manipulator by IBID of W and the last side-connection is cut free to allow the lamella lift-out.*

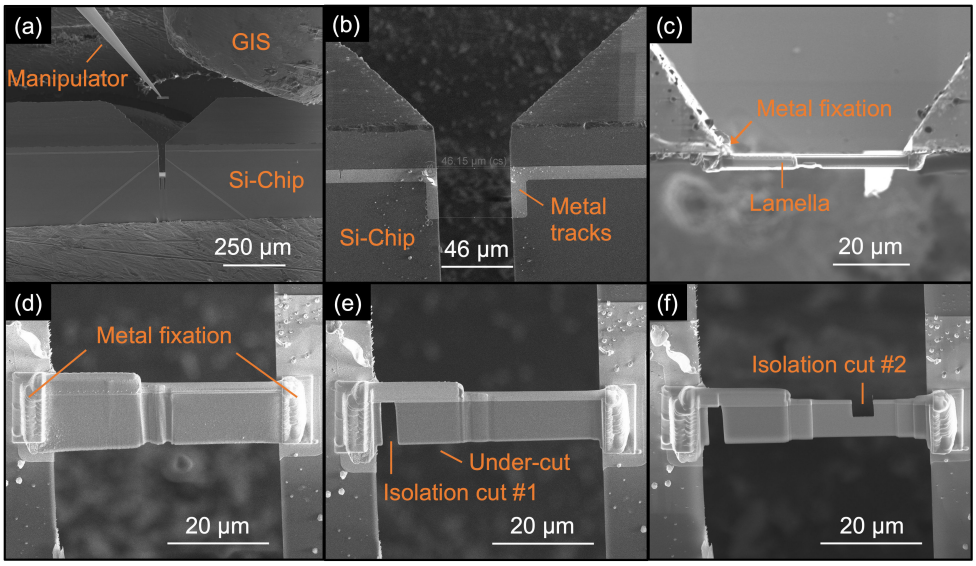

Figure 20: *Preparation of a TEM lamella on a chip for in situ biasing TEM analysis. (a) The lamella is transferred to the Si-half MEMS chip, where it will be positioned on the chip trench shown in (b). To allow the manipulator to be cut off, a preliminary metal fixation to the chip is deposited on the back of the lamella at 52° shown in (c). (d) Afterwards, each lamella side is electrically connected to the respective metal tracks by large ion-beam induced metal depositions at 0°. (e) The lamella side-walls are cleaned and damage at the bottom edge is removed by an undercut, and the first isolation is cut for circuit editing. (f) After shaping and thinning the lamella to the desired thickness, the second isolation cut is milled. The preparation is finished off by ion-polishing each side at 2 kV. All SE SEM images were acquired at 5 kV and 0.40 nA. The ion-beam generated image in (c) was taken at 30 kV and 0.46 nA.*

the lamella must be adapted to the width of the chip trench (usually 20−40 µm), which should be measured beforehand to allow for proper adjustment of the protective layer's size. The chip is tilted to 52° during the positioning, so that the FIB is incident on the top edge of the lamella. The W GIS is inserted to deposit a preliminary small fixation on the backside of the specimen, as shown in Fig. 20c. This allows the manipulator to be cut off and the chip to be tilted to 0° in order to properly secure the lamella on both sides of the trench with large-area IBID metal depositions (W or Pt), as shown in Fig. 20d, which also connect the lamella to the desired metal contact points of the chip.

Afterwards, to make the sample electrically functional, two special steps must be followed in addition to the standard protocol. The first is to perform an undercut bottom side of the lamella by performing an undercut at 16 kV and 1.4 nA. This should help to reduce the amorphous damage and re-deposition occuring during the lamella lift-out, thus reducing surface currents during biasing.

The second difference is that the current circuit in the specimen must be edited by introducing isolation cuts. Otherwise both the top and bottom of the lamella are connected to each side of the trench, hence creating a short circuit. To force the charge carriers to pass through the p-n junction of the specimen during biasing, each side of the junction must only be connected to a single side of the trench. Hence, two isolation cuts must be introduced. The cut geometry is evident from the sketch in Fig. 22a. The first, left isolation is cut from the bottom, through the semiconductor specimen into the top metal layer, while the second isolation is set on the right side milling through the top metal layer into the semiconductor substrate, thus isolating the p-n junction. Both isolations are ion milled using 16 kV and 1.4 nA, and a 0° tilt. The first is cut before and the second after the lamella is thinned down progressively to an electron-transparent thickness (see Fig. 20e-f). Care must be taken to cut with precision. Particularly when cutting the isolation on the left side of the sample, there is a high risk of cutting through the lamella top. Here it becomes evident why the reinforcing metal deposition on the left side, applied in the first preparation step, is necessary.

In the last preparation step, the surfaces of the lamella are polished as usual at 2 kV and 0.25 nA at 52° ± 7° to reduce amorphous surface damage (see Sect. 4.3).

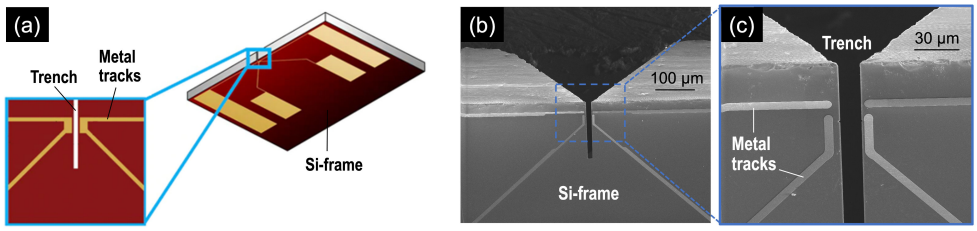

Figure 21: *a) Schematic of the Protochips MEMS Si-half chip for in situ electrical biasing experiments in a transmission electron microscope. The four large metallized pads are contacted electrically to wires in the sample holder using metal needles. Four metal tracks lead from the pads to a trench, where the specimen is attached for contacting. The dimensions are not on scale. (b)-(c) SE SEM images acquired at 10 kV and 0.54 nA, giving b) an overview of the front-side of a biasing chip and c) a close-up view on the chip trench.*

4.4.2 Electrical Properties of FIB Deposited Metals

For electrical TEM measurements, establishing a sufficient electrical connection between the sample and the metallized contact points of the TEM support chip is essential. A common approach for this is EBID or IBID of metal inside the FIB-SEM.[104] By scanning the focused ion or electron beam over a defined specimen region, the chosen precursor gas introduced by the GIS is decomposed into metal-rich components being deposited and volatile components being exhausted by the vacuum system. This method allows to accurately mount the specimen on the chip using the micro-manipulator, while using the IB or EB to precisely deposit the connecting and conducting material, as well as to further tailor the sample and contact geometry.

The most commonly available materials for deposition in FIB-SEMs are Pt[129,130,131], W[132,133,134], C[135], and SiO_2[136]. However, for electrical biasing, the deposited material must be metallic and, besides serving as a surface protection, provide a low-resistivity contact to the specimen. Therefore, only Pt and W are considered for *in situ* biasing specimen preparation. Both, Pt and W, are deposited using organo-metallic GIS precursor gases, namely methylcyclopentadienyl platinum trimethyl ($C_9H_{16}Pt$) and tungsten hexacarbonyl ($W(CO)_6$), respectively. The beam-induced application however, never yields a deposition of pure W or Pt. Instead, it is always a mixture of the metal with varying proportions of C, from the broke down precursor gas, and Ga, implanted from the source ion beam in the case of IBID. The microstructure of IBID-W was accordingly described to be disordered (amorphous), with a uniform distribution of W, C and Ga.[134,137] IBID-Pt was reported to consist of an extended network of Pt grains (2–8 nm in diameter)[138,139] embedded in a Ga-doped matrix of amorphous C.[138,139,140] In such a system, the electron transport is limited by both the diffusive transport within the nanoscale Pt grains and electron tunnelling between them.[139]

Due to the high amorphous C content in the deposition and the resulting microstructure, the resistivity of the FIB-deposited metals are usually much higher than the expected values for the respective pure bulk metal. The resistivity of IBID-Pt deposited on a flat sample surface, was reported to be 70−140 µΩ cm[130], and to be 10^3 to 10^5 times higher than that of bulk metallic Pt.[131] The resistivity of IBID-W layers was described to be around 200−250 µΩ cm[134,133], while bulk W has a resistivity of 5.5 µΩ cm[133].

Generally, for the purpose of electrical contacting of FIB lamellae, the metal is preferably deposited using IBID, as the resistivity of ion-beam deposited metal is much lower compared to the electron-deposited. For example, the resistivity of EBID-Pt is measured to be between 1−100 Ω cm[141], compared to the 70−140 µΩ cm[130] for IBID. Note the change in unit scale. The difference in resistivity is attributed to differences in nanostructure, chemical composition, and the presence of Ga. Ion-beam deposited metals have a higher metal content (Pt or W) and lower C content compared to EBID, which, as mentioned earlier, helps reduce resistivity. This variation in composition is attributed to the fact that the ion beam decomposes the organo-metallic GIS precursor gas more complete than the electron beam.[104] Langford *et al.* (2007)[138] reported the composition of 0.5 cm^3 sized Pt cubes deposited with a Ga-ion beam of 30 kV and 30 pA to be: Pt 40-50 at%, C 45-55 at%, and Ga 5-7 at%. Conversely, they measured a much higher C content of up to 70 at% in EBID-Pt. Sadki *et al.* (2004)[137] measured the composition of W, deposited using a ion beam energy of 30 kV and a beam current density of 33 pA/μm^2, to be: W 40 at%, C 40 at%, and Ga 20 at%. Similar high Ga contents were reported in previous analyses

of IBID-W.[132,133] Compared to Pt deposits, W deposits have lower C contents and are harder, hence are often preferred in terms of surface protection.[104]
Another reason for the lower resistivity of the ion-deposited metal is the presence of Ga-dopants, originating from the implantation of source ions. The Ga-impurities have been reported to be beneficial for the conductive properties of the deposition.[142,138,143]
Apart from using the ion beam for the metal deposition, the resistivity of the deposited material is highly dependent on the deposition parameters, with the ion beam current density being the most critical. It is important to consider that opting for IBID instead of EBID to achieve lower resistivities carries a greater risk of damaging the sample surface. IBID can be seen as a compromise between surface sputtering and material deposition. Consequently, higher ion beam currents shift this balance toward increased material ablation. The maximum ion beam current must be carefully adjusted to the chosen pattern size to prevent milling the specimen instead of depositing the precursor – if the beam current exceeds the optimal level for the pattern size, milling will start. However, utilizing the highest possible beam currents (up to the point of milling) is advantageous, as it increases the metal content (Pt or W) and the Ga doping relative to the C content in the deposited material.[104,143,142]
Optimised beam current densities for material deposition differ depending on the deposition geometry. The topography surrounding the chosen deposition area significantly influences how well adsorbed molecules can diffuse, which in turn affects the availability of the precursor gas for deposition and hence, the ratio of sputtering yield to ablation yield.[104] Therefore, it is essential to attentively track the deposition process and, if necessary, adjust the beam current or the pattern size to avoid damage of the specimen surface.

4.4.3 Specific Considerations

For *in situ* biasing electrical TEM analysis, the same fundamental considerations for specimen preparation apply as in non-biasing electrical TEM analysis discussed in Sect. 4.3. However, additional factors must be taken into account when designing the electrical circuit of the *in situ* biasing lamellae shown in Fig. 22b, particularly regarding the contact and surface resistances of the specimen.

4.4.3.1 Surface Damage and Short Circuits

For *in situ* biasing, as for electrical TEM analysis in general, it is critical to consider the surface damage caused by the FIB milling. The electrically damaged sub-surface depletion layer should be minimised, especially for *in situ* biasing experiments, as a significant electrical response from the p-n junction to the externally applied bias can only be achieved if a sufficient amount of active dopants remains in the specimen.
Additionally, the amorphous surface layers of the TEM lamella, caused by Ga-ion beam exposure, must be considered. In non-biasing experiments, this non-crystalline layer does not contribute to the measured built-in potential at the p-n junction, as it has lost its semiconductor properties. However, it severely impacts the measurements under *in situ* applied bias. This is because the amorphous surface is doped with Ga-ions implanted during the FIB exposure, and this Ga-doping has been reported to increase the conductivity of the amorphous material, hence providing low resistivity paths for active carriers during biasing, which can lead to short circuits. For successful

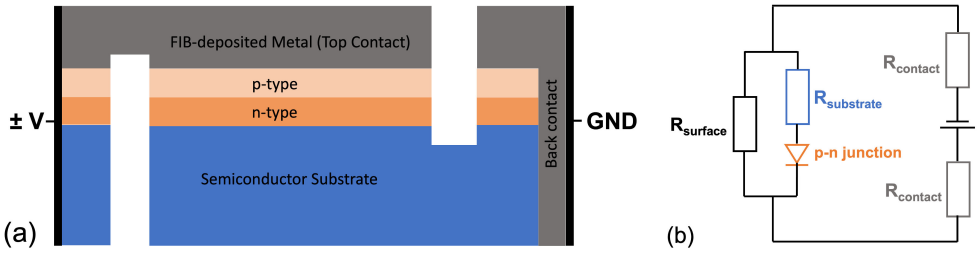

Figure 22: *a) Schematic illustration of the TEM lamella geometry designed for in-situ biasing experiments. b) Schematic representation of the electrical circuit within the TEM lamella.*

biasing experiments, it is therefore crucial to minimise the amorphous damage, particularly at the surfaces and edges of the lamella, through careful progressive FIB milling and polishing at low beam energies.

It should be noted that in some materials the Ga implantation as well as the local heating of the amorphous surface layer during the ongoing FIB milling can aid local re-crystallisation, which would be beneficial to restore the crystalline semiconductor properties in the surface layer.[104] This recrystallisation was for example reported for InAs, InP and Si.[144,116] However, in GaAs no recrystallisation was observed during FIB milling. This was firstly ascribed to Ga being native to the lattice, hence not aiding nucleation. And secondly, to the fact that the time scales, on which local heating occurs in the FIB, are too short to allow recrystallisation through annealing.[116]

4.4.3.2 Metal Contact Resistance

Ideally, the metal-semiconductor contact should be ohmic, meaning it has low resistance, to ensure that the applied bias during the experiment is primarily dropped across the specimen's p-n junction, minimizing parasitic losses at the contacts. Working semiconductor devices, such as the multi-junction III-V solar cells studied in Ch. 8, come with pre-deposited ohmic contacts. The preparation of these metallized wafers presents additional challenges, which will be discussed in the relevant chapter.

However, not all semiconductor specimens have pre-deposited ohmic contacts, as the pre-processing is both time-consuming and costly. In such cases, the FIB-deposited metal serves as the metal contact for the semiconductor specimen.

To achieve an ohmic contact, the applied metal must have an appropriate work function. The metals available as precursors in the FIB-SEM are typically W and Pt (see previous Sect. 4.4.2), and no alloys can be deposited to specifically tailor the work function to the semiconductor. As a result, these FIB deposits usually form Schottky contacts. Nevertheless, even if the contacts are not ohmic, by optimizing the FIB-induced deposition parameters as described in Sect. 4.4.2, the conductivity can be enhanced to achieve sufficiently low contact resistivities, enabling effective biasing of the p-n junction in the TEM.

5 Off-Axis Electron Holography for Electrostatic Potential Analysis of III-V Devices

TEM-based EH allows to measure the electrostatic potential distribution at p-n junctions. This chapter discusses an overview of the methodological principles of EH, covering the process from hologram acquisition to reconstruction, which is essential for extracting electrostatic potential information.

Subsequently, experimental considerations regarding the measurement setup and acquisition settings are discussed, with a particular emphasis on achieving an optimal balance between signal-to-noise ratio and spatial resolution, while maintaining a sufficiently large FOV. This balance is especially critical for *in situ* biasing experiments and the study of large epitaxial structures such as in III-V multijunction solar cells, which are central to this work.

In addition, the limitations and artefacts inherent to the technique, which can complicate quantitative EH analyses, are addressed. Finally, the determination of the TEM sample thickness is described, including the distinction between the crystalline thickness and the electrically active thickness, a crucial parameter for accurate quantitative EH measurements.

5.1 Introduction to Off-Axis Electron Holography

5.1.1 Fundamental Principles

EH is an electron wave phase imaging technique which is performed in the TEM. As originally described by Gabor (1949) electron holography is based on interfering a plane object wave with a reference wave to form an interference pattern.[145] Whereas in conventional TEM only the image intensity is recorded, both the amplitude and phase shift of the image wave are encoded in the interference fringes of the hologram and can be retrieved separately by simple Fourier reconstruction.[146,70] For non-magnetic materials, the phase shift measured at each sample position in the given FOV is directly proportional to the local electrostatic potential in the specimen projected along the electron beam direction z given by the relation[147]

$$\Phi(x,y) = \mathrm{C_E} \int_0^t V(x,y,z)\mathrm{d}z \tag{20}$$

where z is the direction of the electron beam propagation through the specimen of thickness t. $V(x,y,z)$ is the electrostatic potential within and around the specimen, and $\mathrm{C_E}$ is an interaction constant determined by the acceleration voltage of the electron beam. For 200 kV and 300 kV electrons $\mathrm{C_E}$ is $7.29 \times 10^6 \frac{\mathrm{rad}}{\mathrm{Vm}}$ and $6.53 \times 10^6 \frac{\mathrm{rad}}{\mathrm{Vm}}$, respectively.[148]

This direct relation of the phase shift to the potential given in Eq. 20 is based on the description of the specimen as a weak phase object. This so-called weak phase object approximation (WPOA) assumes that as the electron wave is traversing the specimen, solely its phase is shifted relative to an unchanged reference wave due to the acceleration of the electrons by the local electrostatic potential fields in the specimen. However, the amplitude of the object wave remains unchanged. This WPOA holds only for very thin, weakly scattering specimens. As the specimen thickness increases and exceeds the electron mean free path length, multiple electron scattering and inelastic scattering become significant. These processes introduce amplitude variations due to intensity redistribution and absorption, leading to a loss of phase contrast and

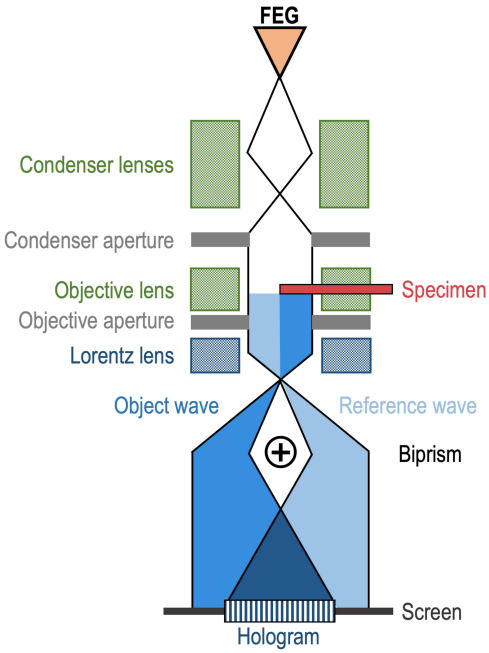

Figure 23: *Schematic representation of off-axis electron holography in TEM. The FEG provides coherent electron illumination on an electron-transparent specimen and an adjacent vacuum region. An electron biprism is used to interfer the object wave with the vacuum reference wave to form the hologram as an interference pattern on the screen.*

degradation of interpretable phase information. The thick semiconductor p–n specimens studied in this work are slowly varying, strong phase objects. Since the WPOA does not hold for these specimens, it is not possible to measure the absolute value of the specimen potential relative to vacuum. However, by tilting the specimen away from the zone axis to a low-diffraction condition, multiple scattering effects and the associated amplitude variations can be minimised. Under these conditions, the amplitude of the exit wave becomes approximately homogeneous across the field of view, which justifies measuring relative changes in potential between adjacent sample regions.[149,150,151,68]

5.1.2 The Experiment and Reconstruction

5.1.2.1 Hologram Acquisition

The operation principle of EH in TEM is represented in Fig. 23. A highly coherent FEG electron source is emitting a plane electron wave, which is illuminating the region of interest of an electron transparent specimen as well as a vacuum reference region. In passing through the specimen, the electron wave is modulated in both amplitude and phase, while it remains unchanged in vacuum. The object wave Ψ exiting the specimen is interfered with the reference wave Ψ_0 by using an electrostatic biprism.[152] The resulting interference pattern, the object hologram, is recorded by a detector. An example for a object hologram is shown in Fig. 24a.

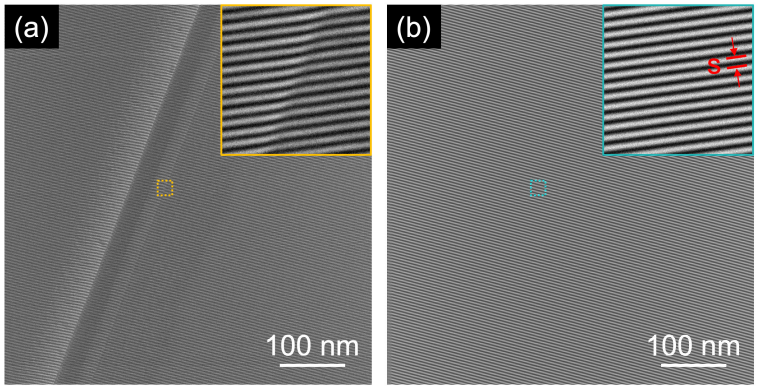

Figure 24: *Examples of (a) an object hologram recorded of a III-V multilayer structure and (b) the corresponding reference hologram acquired in vacuum. The zoomed inset in (a) highlights the fringe bending caused by the change in electrostatic potential at the p-n junction, whereas the zoomed inset in (b) shows that the fringes of the unperturbed reference wave exhibit no bending.*

The intensity distribution in a hologram can be described by the relation [5,70]

$$I_{hol}(\mathbf{r}) = \mid \Psi_0(\mathbf{r}) + \Psi(\mathbf{r}) \mid^2 = 1 + A^2(\mathbf{r}) + 2\mu A(\mathbf{r}) cos(2\pi \mathbf{q_c r} + \Phi(\mathbf{r})) \tag{21}$$

where the intensity contribution of the object wave is $A^2(\mathbf{r})$, while the reference wave has unity intensity, assuming it not being altered by interaction with the specimen. In Eq. 21, μ is the contrast of the interference fringes and q_c their carrier wave frequency, which is inversely related to the fringe spacing $s = 1/q_c$ and $\mathbf{r}$ is the position vector in the object exit plane.

As can be seen from Eq. 21, the hologram contains information on both the phase $\phi(\mathbf{r})$ and the amplitude $A(\mathbf{r})$ of the image wave: the change in amplitude induced by the specimen is encoded as contrast modulations and the phase shift as a bending of the interference fringes. As the electron phase is shifted due to changes in electrostatic potential in the specimen, local potential changes can for example be observed from the fringe bending across a p-n junction as can be see in the hologram presented in Fig. 24a. To retrieve the local modifications of the phase in the specimen, the position and shift of the interference fringes in the object hologram can be accurately determined relative to a vacuum reference hologram. Such a reference hologram, as presented in Fig. 24b, is formed by removing the specimen from the FOV so that the position of the fringes is not altered by the local electrostatic fields in the specimen as both interfered electron waves passed through vacuum. To precisely measure the fringe position, the fringes should be sampled by a sufficient number of detector pixels.

Further, an accurate detection of the fringe position requires a high contrast between the fringes, which determines the phase resolution in the object phase image. To attain a sufficient interference fringe contrast in the experiment, a high spatially coherent elliptical illumination is crucial, emphasizing the necessity of employing a highly coherent electron point source (e.g. a FEG), in addition to using a preferably small spot size and small condenser aperture. [70,153,148] While the phase resolution of the object phase image is given by the fringe contrast of the recorded hologram, the spatial resolution of the phase image is given by the spacing of the interference

fringes. The considerations for the adjustment of these parameters for EH experiments in this work are described in Sect. 5.2.

5.1.2.2 Hologram reconstruction

Phase images are commonly reconstructed from the hologram by employing Fourier processing.[154,70] First, the hologram is Fourier transformed to separate the intensity terms of the reference and object wave ($1+A^2(\mathbf{r})$) from the amplitude and phase information encoded in the cosinusoidal fringe pattern. The complex Fourier transform (FT) of the hologram $\mathrm{FT}(\mathrm{I_{hol}})$ is respectively composed of three parts, appearing as three peaks (or bands) in reciprocal space. An example for the FT of a hologram is presented in Fig. 25a. The three bands can be described by the three rows of the following equation:[70,148]

$$\begin{aligned} \mathrm{FT}(I_{hol}) = \quad & \delta(q) + \mathrm{FT}\left[1 + A^2(\mathbf{r})\right] \\ + \quad & \delta(q-q_c) \otimes \mu\mathrm{FT}\left[A(\mathbf{r})e^{-i\Phi_r(\mathbf{r})}\right] \\ + \quad & \delta(q+q_c) \otimes \mu\mathrm{FT}\left[A(\mathbf{r})e^{i\Phi_r(\mathbf{r})}\right] \end{aligned} \tag{22}$$

The centerband (CB) appears as a peak at the origin of the reciprocal space, that is at a carrier frequency $q_c = 0$. It carries the intensity information and hence corresponds to the FT of a conventional bright-field TEM image. The FT of the reference image results in a second peak at the origin. The two symmetric sidebands (SB) appear as peaks centered at $q = \pm q_c$. Hence, the distance of the SBs to the CB corresponds to the reciprocal interference fringe spacing. The SBs correspond to the FT of the image wave function and its complex conjugate. They both carry the phase and amplitude terms but with an opposite sign in phase.

To obtain the desired phase information, the SB yielding a positive sign in phase is selected by using a circular mask cutting out the intensity contributions from the CB. Additionally, a Gaussian line filter (Fig. 25) is applied to remove Fresnel fringes (see paragraph 5.2.6.2) from the hologram.

By adjusting the size of the mask selecting the SB, the frequency cut-off is chosen and consequently the spatial resolution of the resulting phase image. The cut-off should be chosen with care as an increased mask size yields a higher spatial resolution, but a smaller mask size might be beneficial to reduce high-frequency noise in the phase image. To ensure the exclusion of the intensity term, the mask radius should be maximal 1/2 or 1/3 of the carrier fringe frequency for strongly scattering objects.[25,155]

Regardless of the size, the edge of the selective mask should be smooth in order to reduce artefacts from abrupt information loss at the hologram edges.[146,156] In this work, a twelfth order low-pass Butterworth filter was used for masking.[157,158]

In the next reconstruction step, applying an inverse FT (FT^{-1}) to the selected sideband yields the complex image wave $\Psi_r(\mathbf{r})$ given by

$$\Psi_r(\mathbf{r}) = \mu A_r(\mathbf{r}) e^{i\Phi_r(\mathbf{r})} \tag{23}$$

From the reconstructed complex image, the amplitude image $A_r(\mathbf{r})$ and the phase image $\Phi_r(\mathbf{r})$

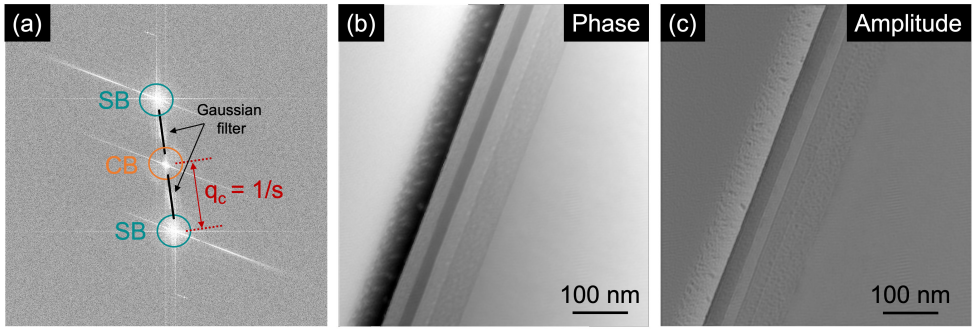

Figure 25: *a) Fourier transform of the object hologram shown in Fig. 24, displaying the centerband and sidebands that contain the phase and amplitude information. (b) Reconstructed phase image, and (c) reconstructed amplitude image of the III-V multilayer structure.*

can be separately extracted via

$$A_r(\mathbf{r}) = \sqrt{R(\Psi_r(\mathbf{r}))^2 + I(\Psi_r(\mathbf{r}))^2} \tag{24}$$

$$\Phi_r(\mathbf{r}) = tan^{-1}\left(\frac{I(\Psi_r(\mathbf{r})}{R(\Psi_r(\mathbf{r})}\right) \tag{25}$$

where R and I represent the real and the imaginary part of the respective image. Examples for a reconstructed phase and amplitude image are presented in Fig. 25b and 25c, respectively.
In this work, the entire hologram reconstruction was performed by using either the HoloView[159] or the HoloWorks version 5.1[158] softwares. Both are compatible as plug-ins with the DigitalMicrograph software suite provided by Gatan.

Because the phase shift is derived from complex numbers through an arctan-function, it is determined modulo 2π, i.e. the phase values are wrapped in a range of $-\pi$ to π. However, at positions where the specimen contains strong variations in electrostatic potential, the induced phase shifts may exceed 2π, resulting in ambiguous phase jumps in the reconstructed phase image. These artificial discontinuities can be removed by phase unwrapping algorithms, which add or subtract multiples of 2π to pixels where phase jumps occur.[160,161] This leaves the available phase information unchanged, but helps to achieve continuous values, and thus, allows unambiguous reconstruction of the electrostatic potential distribution in the specimen as the final step of the hologram evaluation.

The electrostatic potential distribution in the specimen can be directly derived from the phase shift by applying Eq. 20. It must be stressed again that to make this relation applicable, the sample must be tilted to low-diffraction conditions. If the specimen potential does not change along the beam direction z, Eq. 20 can be simplified to:

$$\Delta\Phi = \mathrm{C_E} V_{total} t \tag{26}$$

For a given electron beam acceleration voltage determining the interaction constant $\mathrm{C_E}$ and

a known specimen thickness t, the measured phase shift is sensitive to the total electrostatic potential in the specimen V_{total}. As introduced in Ch. 2.2.3.3, for zincblende materials, as the III-V compounds studied within this work, V_{total} is composed of two contributions: the mean inner potential (MIP) V_0 and the dopant-related potential V_{dop}.

$$V_{total} = V_0 + V_{dop} \tag{27}$$

The doping potential arises from the introduction of impurities (dopants) into the semiconductor. With the dopant atoms, additional charge carriers are introduced into the lattice, leading to local changes in the electrostatic potential, which is different from the MIP of the undoped material.[47] While the MIP is constant for a given semiconductor material, the doping potential can vary depending on the type and concentration of the active dopants.
It must be stressed that the total electrostatic potential obtained from the phase image with Eq. 26 is only entirely specimen related, if artificial phase shift contributions, e.g. from external fringing fields[162,163,122,164], electron beam induced charging[165,166,125] and dynamical diffraction[68,151] are negligible. The experimental limitations and artefacts arising from such specimen unrelated effects, and how they can be accounted for in the experiment and subsequent data treatment, are described in Sect. 5.2.6.

5.2 Experimental Setup and Considerations for Electron Holography

There are many practical aspects which need to be assessed for successful dopant potential measurements on real semiconductor specimens. The measurement settings as well as the sample preparation must to be adapted to the type of samples and the aim of the analysis. In this section, experimental EH is discussed in terms of the phase resolution − also referred to as the phase detection limit or phase sensitivity − and the spatial resolution which are related. Further, the limitations of the technique and the artifacts arising from various sources when analysing real specimens will be addressed. These aspects are discussed based on the experimental setup and settings adapted to the specimens used in this work.
All EH data in this work have been acquired using either the FEI Titan Ultimate microscope, located at the CEA-LETI, Grenoble, or the FEI Titan HOLO microscope located at the Ernst Ruska-Centre (ER-C), Jülich. Both microscopes are Cs aberration corrected and equipped for EH with rotatable electron biprisms mounted close to the image plane of the optical system.
The electron holograms are formed by operating the microscope in Lorentz mode, which uses the Lorentz lens (or the first corrector lens acting as a Lorentz lens) instead of the objective lens, which is switched off. Using the Lorentz mode is generally important for magnetic samples, as it provides field-free conditions around the specimen. Although the samples investigated in this work are non-magnetic, using the Lorentz mode is still beneficial for studying electrostatic potentials as it allows to maintain a large FOV during high sensitivity phase measurements with a high spatial resolution.

5.2.1 Phase Sensitivity

The phase sensitivity of a reconstructed phase image is defined as the smallest phase difference, which can be detected between neighboring pixels reconstructed from the hologram fringes. For

a given phase image, this phase resolution depends on the fringe contrast μ and the number of electrons counted per reconstructed pixel N_e given by the relation [167,168]

$$\delta\Phi = \frac{\sqrt{2}}{\mu\sqrt{N_e}} \tag{28}$$

Increasing the phase sensitivity is desirable to detect the smallest possible electrostatic potential variations in the specimen. As evident from Eq. 28, this can be achieved by increasing the product of $\mu\sqrt{N_e}$ through tuning the experimental settings.
To attain a sufficient interference fringe contrast in the experiment, a highly coherent illumination is crucial. This emphasizes the necessity of employing a highly temporally coherent electron point source (e.g. a FEG) in addition to using a preferably small condenser aperture and small spot size to enhance the spatial coherence. [70,153,148] In this work, commonly a spot size of 2 or 3 was employed in combination with a C2 aperture of 100 µm or 150 µm. Additionally, an elliptical illumination extended perpendicular to the biprism and narrowed parallel to it, is used to increase the coherent electron current density in compromise to using a small aperture. [153] Improved coherence enhances the fringe contrast at a cost of intensity, making it necessary to increase N_e to overall improve the phase sensitivity. Assuming the use of a highly bright electron source, there are two options to increase the number of detected electrons: either acquiring a single hologram with an increased exposure time (long time exposure) or recording a series of holograms with shorter exposure time and adding them together (stack acquisition).

Fig. 26a−d shows electron holograms recorded in vacuum at different indicated exposure times. As evident from the profiles taken across the hologram fringes (Fig. 26e), the number of electron counts N_e as well as the contrast increase with longer exposure. To assess the phase sensitivity in dependence of the acquisition time, the standard deviation was calculated from the centre of the reconstructed vacuum phase images. As visible in Fig. 26f, the standard deviation improves with increasing exposure times from 2−40 s, while the fringe contrast remains relatively constant above 50%. However, instrumental instabilities - such as drift of the specimen and/or biprism, variations in biprism voltage, and defocus drift - degrade the fringe contrast, and hence, limit the applicable exposure time. In this experiment, vacuum holograms could be acquired up to 48 s before instabilities lead to deterioration of the contrast. When imaging a specimen region, this time will be further constrained by sample drift. The higher the desired spatial resolution of the electrostatic potential measurements, the more critical small-scale drift processes become for measurement accuracy. [169]

Hence, it is generally advantageous to acquire a stack of holograms instead of a long single exposure, because specimen drift occuring in between exposures can be corrected by implementing an x-y alignment algorithm in the reconstruction procedure, while biprism drift can be addressed through phase offset correction. [170,159]
Fig. 27a and b compare a phase image reconstructed from a single hologram with one reconstructed and averaged from a stack of 30 holograms. Both images show the same section of a semiconductor layer structure. It is evident that the phase noise is significantly reduced in the stack acquisition, which is essential to ensure an accurate analysis of the phase distribution in the specimen. In contrast, the high noise level in Fig. 27a impairs the informational value of

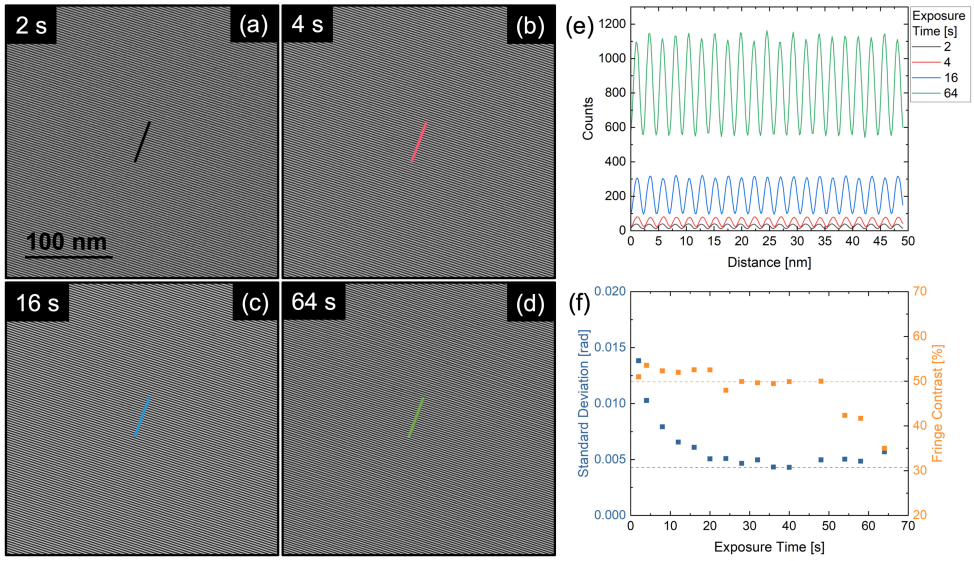

Figure 26: *(a)-(d) Electron holograms acquired using the indicated exposure times, with a Gatan K2 direct electron detection camera installed on a FEI Titan HOLO with a biprism voltage of 120 V and a fringe spacing of 2.3 nm. (e) Profiles extracted from the holograms in (a)-(d) perpendicular to the fringes displaying the dependence of the electron counts and the hologram contrast on the exposure time. (f) The phase noise (i.e. the standard deviation in the reconstructed vacuum phase image) and the hologram fringe contrast plotted as a function of the hologram acquisition time.*

the image. Fig. 27c and d show for two different microscope setups that the standard deviation as a measure for the phase noise and sensitivity clearly improves with an increasing number of averaged phase images. The data in Fig. 27c was acquired with a FEI Titan Ultimate microscope equipped with a Gatan OneView CCD camera, while the data in Fig. 27d was recorded with a FEI Titan HOLO microscope using a Gatan K2 direct electron detection camera. To ensure a reliable measurement of the phase sensitivity, it was avoided using a reference hologram for the reconstruction of the phase images in Fig. 27a and b to prevent introducing phase noise. Instead, the non-linear distortions in the single frame (Fig. 27a) and in each phase image of the stack (Fig. 27b) are corrected for by polynomial fitting. It must be emphasized that the improvement in SNR in phase images through averaging relies on the careful removal of artifacts such as distortions, Fresnel fringes and drift (see Sect. 5.2.6). After considering these corrections, the number of images per stack, which can be taken to improve the SNR is limited by the random streaks of the CCD camera.[170] As a result, in our experiment no further substantial improvement could be achieved with hologram series larger than 30. Additionally, varying the acquisition time between 4 s and 8 s does not noticeably affect the phase sensitivity (Fig. 27c). Consequently, typically stacks of 30 holograms are acquired in this work with frame exposure times of 4 or 8 s.

5.2.2 Spatial Resolution

The desired phase information is derived from the position of the interference fringes in the hologram. Consequently, the achievable spatial resolution of the measured phase distribution is limited by the spacing between these fringes.

In the experiment, this fringe spacing can be adjusted according to the required resolution by varying the voltage applied to the electron biprism. The effect of the biprism voltage on the formation of the interference pattern is illustrated in Fig. 28. As a function of the positive voltage applied to the biprism, the reference wave Ψ_0 and the object wave Ψ are deflected by an angle α. This deflection causes the two plane waves to appear as if they originate from two virtual sources, S_1 and S_2. A higher biprism voltage moves S_1 and S_2 further apart, resulting in a wider interference pattern with narrower fringe spacing (Fig. 28b).[5,70]

The fringe spacing can be described by

$$s = \lambda \left| \frac{(d_1 + d_2)}{2\alpha d_1} \right| \tag{29}$$

where λ is the electron wavelength (2.51 pm at 200 kV acceleration voltage; 1.96 pm at 300 kV), d_1 is the distance of the virtual source plane to the biprism plane, d_2 is the distance between the biprism plane and the screen (detector). An increasing distance of the virtual sources however strains the spatial coherence of the source, leading to a loss in fringe contrast at higher biprism voltages. Fig. 29 plots the relation of the biprism voltage to the fringe spacing and the fringe contrast for a fixed magnification of 24.5kx.

To maintain a sufficient phase sensitivity of the hologram, the fringe contrast should be minimum 20%. As an example, for the acquisitions at 24.5kx shown in Fig. 29a, this would correspond to a maximum applicable biprism voltage of 160 V, limiting the fringe spacing to 1.7 nm.

While the generally achievable spatial resolution of the phase measurement is limited by the

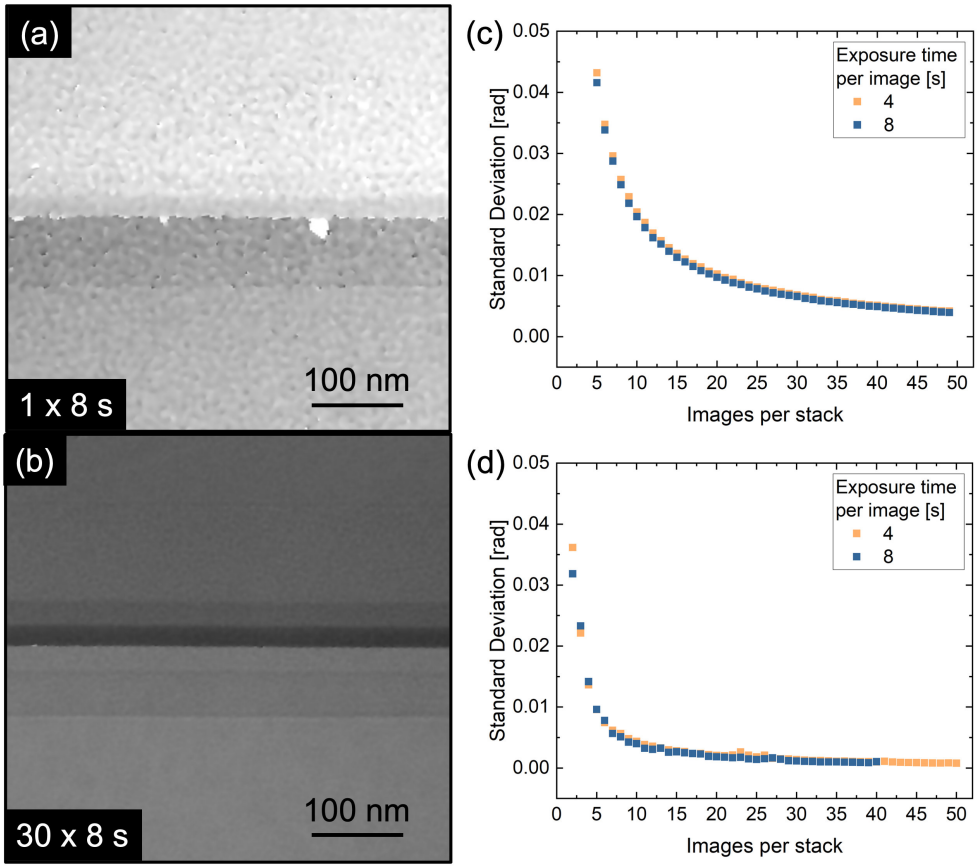

Figure 27: *Phase distribution in a semiconductor layer structure reconstructed (a) from a single hologram and (b) from a stack of 32 holograms. (c) and (d) The standard deviation of the phase measurement (i.e. the phase noise) improves with an increasing number of averaged phase images (holograms per stack). The standard deviation was measured in the central region of the phase images, reconstructed from hologram stacks acquired in vacuum with an exposure time of 4 s and 8 s per individual frame. The data in (a), (b), and (c) was recorded with a FEI Titan Ultimate using a biprism voltage of 125 V and an interference fringe spacing of 3 nm, while the data represented in (d) was taken with a FEI Titan HOLO using a biprism voltage of 120 V and a fringe spacing of 2.3 nm.*

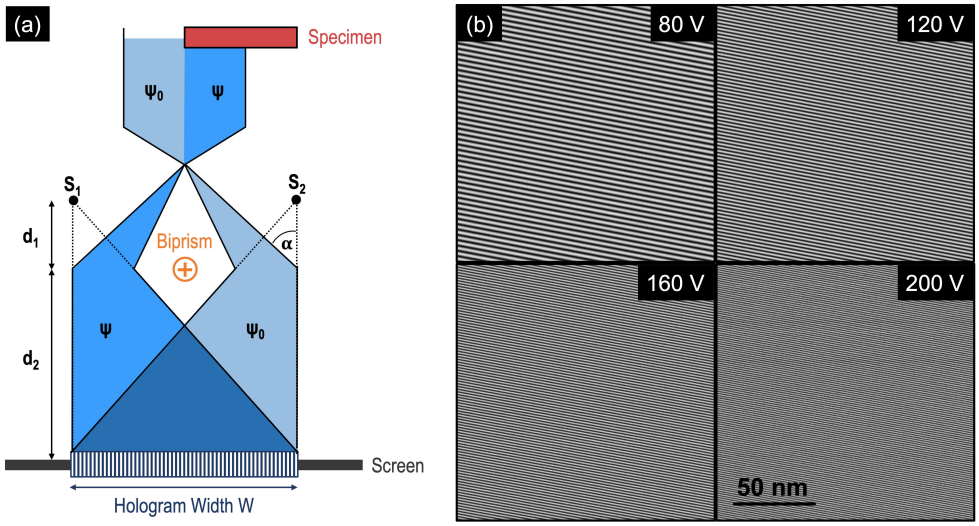

Figure 28: *(a) Schematic illustration of the electron hologram formation by means of an electron biprism. The voltage applied to the biprism controls the distance of the two virtual sources, S_1 and S_2, as well as the deflection angle α, thereby controlling the hologram width and the interference fringe spacing, respectively (modified after Midgley, 2001).*[5] *(b) The influence of the biprism voltage on the fringe spacing. The holograms were acquired in vacuum at a magnification of 24.5kx using a FEI Titan HOLO microscope equipped with a Gatan K2 camera.*

fringe spacing through controlling the biprism voltage, the actual spatial resolution in the reconstructed amplitude and phase images is given by the size of the mask applied to select the sideband in the FT of the hologram during the reconstruction procedure. As explained in Sect. 5.1.2.2, a larger mask size yields a higher spatial resolution, but it is common practice to adjust the mask radius to maximum 1/2 or 1/3 of the interband distance, corresponding to the reciprocal fringe spacing.[25,155] This results in a spatial resolution of the fringe spacing $\times 2$ or $\times 3$. As an example, if a hologram is acquired with a fringe spacing of 2 nm, the reconstructed phase image would have a spatial resolution of 4 nm or 6 nm.
Consequently, in the experiment, the biprism voltage should be selected such that the fringe spacing $\times 3$ achieves the desired spatial resolution. The minimum spatial resolution required to resolve the feature of interest in the potential distribution of a specimen, for example the depletion width of a p-n junction, should be calculated prior to the experiment based on simulations of the electrostatic potential in the sample.

5.2.3 Information Loss

In EH, the desired amplitude and phase informations are carried by the interference fringes. To prevent a loss of these informations, the fringes has to be sampled with a sufficient number of pixels, to allow precisely determining their position and avoiding the loss of contrast. Electron holograms are recorded using a CCD camera having a fixed size pixel array. Hence, for a given FOV recorded by the CCD there is only a finite number of pixels available to sample the fringes. A compromise must hence be made between spatial resolution and the recorded FOV, as a

larger FOV, with the fringe spacing remaining constant, results in fewer pixels being available for sampling the fringes. A common recommendation is to acquire holograms with 6 pixels per fringe, to allow to precisely determine their position and limit the loss of contrast. [155,38,28]

In this work, two different cameras are used to record the electron holograms. The first is a Gatan K2 direct electron detection camera with a array size of 3840×3712 and a physical pixel size of 5 µm, adding up to a total active sensor size of 19.2×18.6 mm. This camera provides a high detection sensitivity and spatial resolution enabling a larger sample area to be imaged at the same resolution. In other words, if data is recorded with a certain spatial resolution, using the K2 it can be acquired with a lower magnification compared to conventional CCDs.

The second detector used herein is a Gatan Oneview CCD camera with an array size of 4096×4096 pixels, where each pixel physically measures 15 µm, which equals a total array size of 61 mm^2.

Both cameras allow to maintain a large FOV while achieving a high spatial resolution with sufficient fringe sampling. This is particularly important for EH analysis of real devices, where it is often necessary to keep the vacuum reference region within the FOV, in addition to the sample region of interest.

For a dataset acquired with the Gatan K2 camera at the FEI Titan HOLO microscope, Fig. 29b shows how the pixels per fringe sampling changes with variations in the biprism voltage (i.e., the fringe spacing). With a constant magnification, the fringe sampling decreases as the biprism voltage increases and the fringe spacing becomes smaller. At the given magnification of 24.5kx, biprism voltages higher than 160 V, corresponding to fringe spacings smaller than 1.7 nm, result in undersampling of fringes (<6 pixels per fringe). As can be seen in comparison with Fig. 29a this corresponds to the resolution limit in terms of fringe contrast, as for this hologram data set acquired at 24.5kx, voltages above 160 V lead to fringe contrasts below 20%.

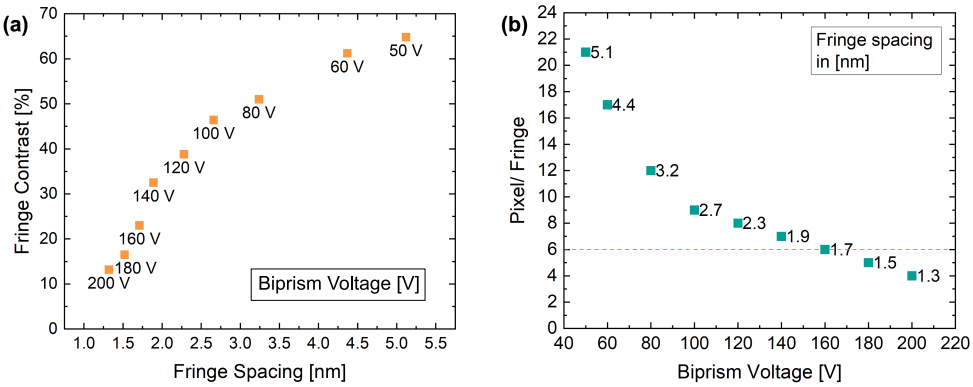

Figure 29: *The dependence of (a) fringe contrast and (b) pixels per fringe sampling on the fringe spacing, controlled by the biprism voltage. The hologram data set was acquired at a constant magnification of 24.5kx using a Gatan K2 camera on a FEI Titan HOLO microscope.*

5.2.4 Selecting the Field of View

For every EH experiment, the section of the hologram recorded with the detector, the FOV, has to be adjusted to the specimen ROI and the required spatial resolution of the phase mea-

surement. As evident from Fig. 28, the width W of the interference pattern is controlled by the biprism voltage. A high biprism voltage increases the interference width, while the fringe spacing decreases, yielding an improved spatial resolution at the cost of the fringe contrast. As elaborated in the preceding Sect. 5.2.3, the Lorentz magnification is used to adjust the size of the FOV on the detector, in order to achieve sufficient fringe sampling.

However, some experiments require a very large FOV. For example, if specimens have an extensive ROI, such as certain III-V multilayer structures, as will be elaborated in Ch. 8. Or, if the vacuum reference region is far from the ROI, as with TEM specimens prepared on *in situ* biasing chips, where metal deposits cover the top surface (see Sect. 4.4). Achieving a sufficient interference width for these analyses would necessitate using extremely high biprism voltages, and the correspondingly high magnification needed to maintain a sufficient fringe sampling would compromise the required FOV.
In these cases, the hologram width can be increased independent from the biprism voltage by adjusting the diffraction lens settings. The approach can be understood from Fig. 30, which shows holograms acquired in vacuum with the FEI Titan Ultimate using various diffraction lens excitations. Remaining in Lorentz mode, firstly a high magnification, in this work 40.0kx, is selected and kept constant while then the excitation of the diffraction lens is adjusted to widen the interference pattern. Common diffraction lens excitations used in this work for large FOV hologram acquisitions are 12%, 15% and 20%, which yield interference widths of 2.54 µm, 2.73 µm and 3.20 µm, respectively. These values are achieved operating the biprism at 80 V. Setting this into relation, even using a high biprism voltage of 200 V at standard diffraction lens settings, in this work 89%, only yields a hologram width of 1.1 µm.
As evident from Fig. 30, using diffraction lens excitations from 12%, 15% to 20%, the recorded FOV is increasing simultaneous with the interference width, even though the magnification is kept constant. It becomes clear that the FOV and the hologram width do not expand in the same proportion, but the hologram, although nominally increasing in width, becomes smaller in relation to the image section recorded on the detector. This leads to a decreasing fringe sampling with increasing interference width. Also the fringe contrast decreases due to the loss in beam coherence.
To still ensure a sufficient phase sensitivity when using these specialized settings for large FOV acquisitions, two factors must be addressed. Firstly, a sufficient fringe sampling must be maintained by adjusting the biprism voltage. It generally applies that larger interference widths necessitate the use of smaller biprism voltages. It must be kept in mind that the magnification has to be kept constant when adjusting the diffraction lens excitation. Hence, in the large-FOV acquisitions the magnification can not be used to control the FOV and hence the pixel per fringe sampling, as it is usually done when acquiring at standard diffraction lens settings.
Secondly, large stacks of holograms should be recorded to maintain a decent standard deviation, as described in Sect. 5.2.1. Fig. 31 shows that for hologram acquisitions at 20% diffraction lens excitation, although the fringe sampling is only 4 pixels, the standard deviation can still be minimised to below 0.02 rad for stacks recorded with 8 s per image, and to below 0.03 rad for stacks with 4 s per image. Due to the loss of coherence caused by the extreme broadening of the interference width, it is particularly critical in large FOV experiments to improve phase sensitivity through stack acquisition. This is evident from Fig. 31, as the standard deviation for

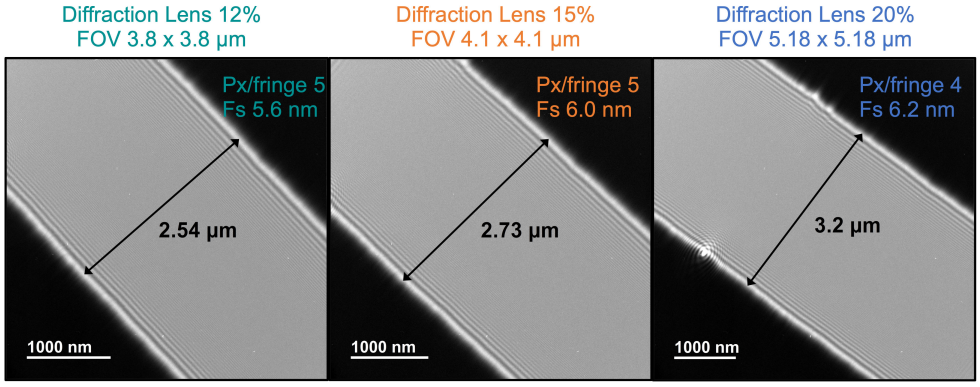

Figure 30: *The diffraction lens excitation can be adjusted to increase the hologram width for analysis requiring a large FOV. (a)–(c) show how the FOV, fringe spacing (fs), and pixels per fringe sampling change for holograms acquired at lens excitations of 12%, 15%, and 20%, which are the common large-FOV lens settings used in this work. The holograms were recorded with a Gatan OneView CCD camera at a FEI Titan Ultimate microscope operated at 200 kV.*

phase image stacks recorded with 20% excitation is significantly worse in the case of smaller hologram stacks and shorter acquisition times of 4 s (i.e., lower number of electrons N_e) compared to standard diffraction lens settings. As the stack size increases, the values tend to converge.
For this work, it was therefore concluded that for EH experiments requiring a large FOV, holograms acquired in stacks of more than 30 images with diffraction lens excitations of 12%, 15% and 20%, using a biprism voltage of 80 V, provide sufficient phase sensitivity.

5.2.5 The Influence of Electron Beam Illumination on the Phase Measurement

The electron beam illumination of the specimen can have a significant influence on the measured phase distribution. Considering the possible effects and optimising the beam settings accordingly is crucial to ensure reliable device characterisation with EH. Regarding the experimental beam parameters, the electron acceleration voltage and beam current are key factors to consider, as they directly influence the interaction between the electron beam and the specimen.
The selection of the optimal acceleration voltage cannot be directly made but must be determined by weighing the advantages and disadvantages of higher and lower beam energies, tailored to the specific specimen and the measurement objectives. High acceleration voltages of 200 kV or 300 kV are generally required for the thick semiconductor specimens, typically between 200–600 nm, chosen for EH measurements in this work to reduce the effect of preparation-induced surface damage on phase measurements, in order to minimise beam absorption and increase phase sensitivity. Therefore, the consideration was limited to the trade-off between these two values. The advantage of using high beam energies for examining thick specimens lies in the fact that, as the acceleration voltage increases, the beam extinction distance within the specimen also increases. This allows the specimen to exhibit more kinematic behavior, rather than dynamic, up to larger thicknesses.[171,172] Furthermore, at 300 kV, the angles required to tilt the specimen away from the zone axis to minimise dynamical diffraction are smaller compared to those at 200 kV.[6] This can be particularly advantageous for high-resolution analyses of junction potentials,

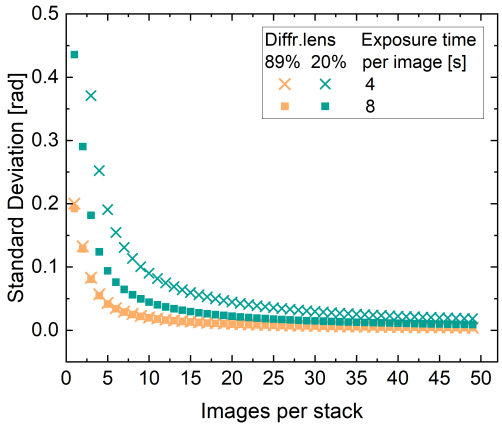

Figure 31: *The standard deviation of phase measurements as a function of the number of averaged phase images (images per stack). The hologram stacks were recorded with a magnification of 40.0kx operating a FEI Titan Ultimate at 200 kV. Holograms recorded with a diffraction lens excitation of 89% and a biprism voltage of 200 V correspond to the standard hologram acquisition setting used for higher spatial resolution in this work, yielding a 2.05 nm fringe spacing, with a 8 pixels/fringe sampling and a FOV of* 844×844 *nm. The lens excitation of 20% combined with a biprism voltage of 80 V is used to record holograms with a large FOV of* 5.18×5.18 *µm, a fringe spacing of 6.2 nm and a sampling of 4 pixels/ fringe. The standard deviation was measured in the central region of the phase images, reconstructed from hologram stacks acquired in vacuum with an exposure time of 4 s and 8 s per individual frame. The phase images were corrected for linear and polynomial distortions.*

where it is crucial to limit the loss of resolution in projection through the specimen. However, for the analysis of junction depletion widths, the specimens are exclusively tilted parallel to the studied interfaces to avoid blurring of the junction in projection (more details on the tilting strategy employed to reduce dynamical diffraction in this work are provided in Sect. 5.2.6.4). As a result, only the general loss of resolution due to specimen thickness needed to be considered during tilting.

Although 300 kV theoretically requires smaller off-tilts, in practice, it is easier to reduce dynamical diffraction contrast at 200 kV. At lower beam energy, the range of tilt orientations where the kinematic approximation applies is broader, because Kikuchi bands are wider and higher-order Kikuchi bands are less excited at 200 kV than at 300 kV.[6]

Additionally, selecting 200 kV over 300 kV helps to minimise knock-on damage caused by the electrons, which is important for the analysis of semiconductor specimens.[171,173] Another significant advantage of using the lower acceleration voltage is the increased phase shift resulting from the specimen's electrostatic potential.[171] This can be particularly beneficial when studying low-doped p-n junctions or in any analysis where increasing the phase shift gain is essential. In this work, EH analysis was primarily conducted at 200 kV for the reasons mentioned above. However, it is important to note that selecting 200 kV over 300 kV increases electron beam-induced secondary electron emission, which can exacerbate specimen charging.

The charging of the specimen during EH experiments analysis is an issue that can also be fundamentally controlled by adjusting the electron beam current. The higher the electron beam current, the greater the SE yield and the stronger the beam-induced generation of charge carri-

ers (electron-hole pairs) within the semiconductor specimen.
The emission of SEs generates a charged surface layer that, along with FIB-induced surface damage, causes surface band bending, which results in a reduction of the absolute potential step across the p-n junction in the TEM lamella compared to the bulk specimen. Consequently, the specimen surface charging diminishes the measurable phase contrast within the specimen. [164,125,174,166]
Furthermore, in the absence of a path to ground, the charges generated by the electron beam can accumulate due to separation in the built-in electric field of the semiconductor specimen. This accumulation can distort the measured potential distribution and may even lead to an inversion of the electric field. [165,148] The effect of specimen charging on the absolute potential step is most pronounced in specimens that are low-doped and/or very thin. [175,176,165,177]

Consequently, to mitigate the influence of electron-beam-induced charging on the measured electrostatic potential of the semiconductor specimen, using a low electron beam current is generally beneficial, as it reduces the generation of SE and electron-hole pairs (EHP). However, the most effective approach is to provide a conduction path to ground by applying electrical contacts to the TEM specimen. This facilitates charge dissipation, that helps to reduce any charge imbalances that may accumulate under electron beam illumination. [125,166,178] Cooper *et al.* demonstrated that, for a GaAs specimen systematically analysed in an *in situ* biasing holder, the measured phase profiles – importantly regarding the measured phase step and junction width – were independent of the beam currents used, except at very high beam intensities. [125] In this regard, the preparation of semiconductor specimens on *in situ* biasing chips (as described in Sect. 4.4.1) is preferable for EH potential analysis compared to the conventional preparation on Cu grids (described in Sect.4.2.2), even if no bias is applied.

5.2.6 Limitations and Artefacts

In addition to the total electrostatic potential in the specimen described by Eq. 27, several method-related and specimen-related factors can alter the phase of the imaged electron wave.

5.2.6.1 Geometric Distortions and Reference Holograms

Off-axis electron holograms are significantly affected by geometrical distortions artificially altering the phase of the imaged object wave. Accurate measurements of electrical fields in specimen hence require to correct for these distortion-induced phase modulations.
Distortions can arise from several different sources and cause linear or non-linear phase modulations in the low or high spatial frequency range. Linear distortions might arise from specimen or instrumental (e.g. biprism) drift causing a linear displacement of the hologram fringes. Non-linear artifacts are mainly ascribed to the low-frequency distortions of the projector lens system, as well as to the shear-distortions of the optic fibre system of the CCD camera, which are mainly in the high-frequency range. [179,180,159] Other non-linear contributions might stem from charging at apertures, or from inhomogeneities in the thickness and voltage of the biprism. [146,70,168]

The distortions have to be removed during the hologram reconstruction to avoid misinterpretation of the electrostatic potential distribution in the specimen. This is typically achieved using

a reference hologram.[70,168,148]

The reference hologram is recorded in a vacuum region undisturbed by the electric field of the specimen. This is particularly important when studying samples containing strong electric fields influencing the phase in the near vacuum. The reference should be acquired using the same optical parameters of the microscope and the same exposure time, and immediately after the object hologram to avoid any changes in the optical system. The complex reference image wave is reconstructed from the vacuum hologram using the same procedure described in Sect. 5.1.2.2 for the object image wave. The distortion-free object phase image is then obtained by dividing each complex object image of the stack by the complex reference image.[146,159,148]

Fig. 32 provides an example of an electron hologram acquired in vacuum (Fig. 32a), which was reconstructed using two different approaches: once without (Fig. 32b) and once with (Fig. 32c) the use of a reference hologram. It is clearly visible that including a reference hologram for the hologram reconstruction efficiently removes distortions from the retrieved phase image.

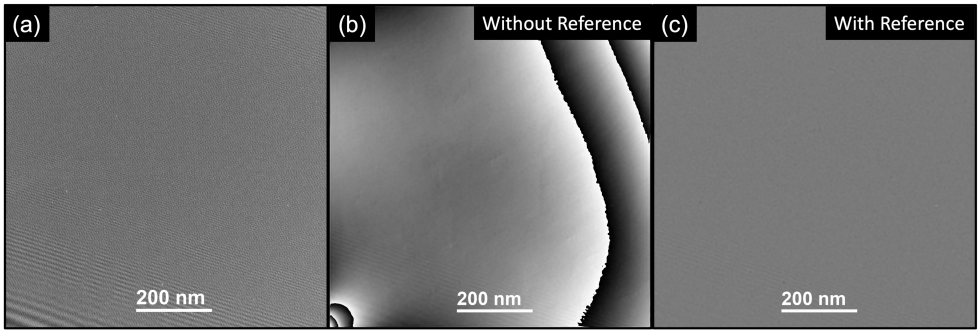

Figure 32: *(a) Off-axis electron hologram acquired at 200 kV using a FEI Titan Ultimate, a biprism voltage of 200 V and an interference fringe spacing of 2 nm. (b) and (c) show the corresponding phase image reconstructed without and with including a vacuum reference hologram, respectively.*

However, using a single vacuum hologram for the reference correction introduces errors into the reconstructed phase.[159] These phase errors can be mitigated by acquiring series of reference holograms. However, it is important to note that incorporating reference holograms – whether single or in stacks – still can introduce noise into the reconstructed phase.[180,159] To minimise this noise, an artificial reference image can be generated by fitting the reconstructed phase images, rather than recording a vacuum reference, to account for distortions caused by both the lenses and the CCD camera. Linear distortions can be corrected using linear fitting in the vacuum or undoped region, whereas non-linear phase modulations necessitate higher-order polynomial fitting. Additionally, including a camera ronchigram can help address high-frequency phase distortions introduced by the CCD.[180,159]

In this work, the traditional method of using reference hologram stacks to correct for distortions is employed. Phase errors from reference correction are mitigated by recording stacks of typically 4 reference holograms. Given that the primary interest is in studying the dopant potential, which varies at low carrier frequencies, the high-frequency phase noise was limited by selecting an appropriate cut-off frequency for masking the sidebands. This approach was chosen because the

specimen under investigation did not include an undoped layer for reliable fitting. Furthermore, fitting the vacuum region is avoided to prevent the introduction of artifacts from unknown contributions of charging and fields from the specimen.

5.2.6.2 Fesnel Diffraction

The diffraction of the electron beam at both edges of the biprism causes Fresnel fringes appearing as coarse modulations at the edges of the hologram, which are visible, for example, in Fig. 30 and 32a. These non-uniform fringes contribute to the interference pattern (fringe contrast and position) in addition to the uniform fine modulations resulting from the superposition of the reference and object wave. Consequently, Fresnel diffraction affects the reconstructed amplitude and phase shift, introducing artifacts in the derived electrostatic potential.[146,5,70]

The effects of Fresnel fringes can be most efficiently minimised during the hologram acquisition, by increasing the biprism voltage to widen the hologram, thereby moving its edges out of the FOV sampled by the CCD camera.[146,5,38] However, if the experiment does not allow for respectively high biprism voltages, positioning the sample region of interest in the centre of the hologram can help limiting the influence of the Fresnel fringes.[38]

In any case, to avoid remaining artifacts related to Fresnel fringes, they should be accounted during the hologram reconstruction procedure. Including a vacuum reference hologram in the reconstruction should eliminate Fresnel diffraction, as it modulates both the reference and object hologram equally.[148] However, instabilities of the biprism, and the resulting drift of the interference and Fresnel fringes during the acquisition of the object and reference hologram, may prevent the reference hologram from effectively removing the Fresnel fringes. Hence, applying a Gaussian line filter (see paragraph 5.1.2.2 on hologram reconstruction) should be included in the reconstruction procedure despite including a reference hologram. More advanced procedures to eliminate Fresnel fringes from holograms, by including multiple biprisms in the experiment[181,182] or by including simulations of the Fresnel diffraction in the data processing[183], exist.

5.2.6.3 Phase Wedge

To reconstruct the phase image, the selective mask must be centered on the selected sideband in the FT(I_{hol}). Precisely determining the center of the SB can be an issue, if the position of the SB frequency is not exactly matching a pixel in Fourier space. However, if accurate centering fails, the phase reconstruction will include an artificial tilt of the reconstructed wave, appearing as a phase wedge in the reconstructed phase image.[148,170]

Including a vacuum reference hologram in the reconstruction should help locating the sideband and thus eliminate the phase wedge. However, instrumental instabilities and related drift in the SB frequency necessitates the use of an additional least-square-root-based process to remove the phase wedge from the phase image.[184,170] In this work, this correction was performed by applying the corresponding "Phase Wedge" tool included in the HoloWorks V5.1 software.[158]

5.2.6.4 Dynamical Diffraction

Dynamical diffraction affects the electron phase measurement.[68,151,185] The assumption that the phase shift of the object wave is directly proportional to the total electrostatic potential

of the projected specimen thickness, described in Eq. 20, is only valid in the kinematical approximation. However, this approximation does not hold true for the thick specimen, which are used for EH analysis to minimise the impact of damaged surface layers and to enhance the thickness-dependent total potential step across the analysed p-n junction. As the lamella thickness increases (to being significantly larger than the material's extinction distance at the given electron beam acceleration voltage), the wave amplitude is progressively altered due to the rise in multiple scattering events.[186,185,187] Hence, at large thicknesses the specimen behaves dynamically rather than kinematically. Further, crystalline specimen may be affected by bending, or contain internal strain fields or crystallographic defects, all giving rise to diffraction contrast. The influence of dynamical diffraction on the electron phase can be minimised by tilting the specimen away from a low-index zone axis to a weakly diffracting, non-channelling orientation.[186,151,187,188,6] By doing this, and avoiding major Kikuchi bands crossing the transmitted beam reflection (000), a homogeneous, bright contrast can be achieved in the specimen ROI, indicating (quasi)kinematical conditions and justifying the quantification of the electron phase shift. In the experiment, the suppression of diffraction contrast should always be verified by examining the correlated amplitude image, which corresponds to an energy filtered BF-TEM image.

In this work, all examined III-V semiconductor structures are grown in [001] direction and the cross-sectional TEM lamella are cut for the (001) layer interfaces to be viewed along the [110] zone axis direction. The orientations are evident from Fig. 33. When tilting, the following points were considered: To move away from the [110] zone axis, the lamella should be tilted about the [001] axis rather than the [110] axis to prevent broadening of the measured phase distribution across a p-n junction in projection, which occurs if the interface is not aligned edge-on to the beam.[6]

Further, the tilt angle should not be extremely large, i.e. too far off the zone axis to limit the loss of resolution due to projection through the specimen. When analyzing semiconductor device potentials, the specimen can be tilted several degrees off the zone axis without the need for tilt correction, as the resolution in this case is still limited by the mask size chosen during phase reconstruction.[6]

The accurate tilt orientation of the specimen is particularly important when comparing the measured p-n junction potential across several semiconductor devices, as the potential drop at p-n junctions is known to vary with different sample orientations due to the changing influence of dynamical diffraction.[188,6,185] Generally, when the specimen is tilted, it assumes a uniform specimen thickness in the FOV; otherwise, the phase distribution will be distorted in projection.

5.3 Sample Thickness Assessment for Electron Holography

In EH, the phase shift across a p-n junction, caused by the built-in electrostatic potential, is measured as a function of the specimen thickness, as evident from Eq. 26. Consequently, reliable quantification of the electrostatic potential requires accurate measurement of the specimen thickness across the studied FOV.

However, as discussed in detail in Sect. 4, FIB preparation causes surface damage to the specimen, altering its crystallinity, chemical composition, and electrical properties compared to the bulk semiconductor. When measuring the lamella thickness, the amorphised top surface layer

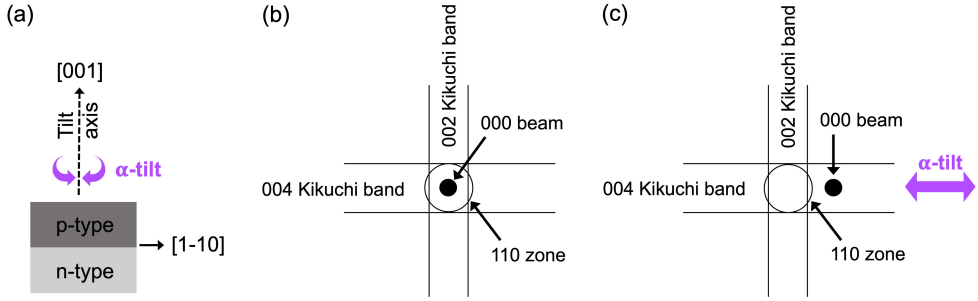

Figure 33: *Schematic illustration of the specimen orientation for EH analysis in this work. (a) The III-V structures are grown in [001] direction and cross-sectional lamellae are cut for viewing along the [110] zone axis. For EH, the specimen are tilted about the [001] axis away from the zone axis. (b) and (c) illustrate the specimen orientation in diffraction space when (b) viewed along the [110] zone axis and (c) tilted about the [001] growth-axis to weakly diffracting conditions for EH. The black dot indicates the changing position of the transmitted electron beam (000) when tilting along the 004 Kikuchi band, indicated by the α-tilt arrow. (b) and (c) are modified after Formanek et al. (2006).*[6]

must be excluded. This can be achieved using convergent beam electron diffraction (CBED) analysis, which is sensitive only to the crystalline thickness (t_c).[189,190]
Additionally, the thickness of the still crystalline, but electrically inactive surface layer – not contributing to the measured phase shift – must be quantified and subtracted from the total crystalline specimen thickness. This step is crucial for accurately retrieving the thickness of the electrically active core of the TEM lamella, which is the region probed by EH. Fig. 17 in Sect. 4.3 shows the schematic cross-section of a FIB-prepared lamella, illustrating the presence of the amorphous surface layer and the electrically inactive sub-surface layer, as well as their influence on the depletion width of the specimen p-n junction.

5.3.1 Crystalline Thickness Measurement Using Convergent Beam Electron Diffraction

5.3.1.1 Fundamental Principles

While rough estimations of lamella thickness can be directly obtained in the SEM, (S)TEM-CBED analysis offers a significantly more accurate yet highly localized measurement of the crystalline sample thickness. This is because CBED determines the thickness exclusively at the specific sample position illuminated by the electron beam, which is inherently small due to the limited probe size. To assess long-range variations in sample thickness, systematic CBED thickness mapping over a larger sample area is therefore required.

The CBED method is based on converging the electron beam onto the specimen to enhance dynamical diffraction and establish two-beam diffraction conditions. This configuration ensures that only the (000) reflection and one additional *hkl* reflection are strongly excited. Under ideal two-beam conditions, only two Bloch waves propagate through the specimen and undergo (ideally only) elastic scattering. The resulting dynamical diffraction effects produce Kossel-Möllenstedt (K-M) fringes, characterised by parallel alternating bright and dark contrast modulations within

the two non-overlapping diffraction discs.[191] An example of such a two-beam K-M pattern is shown in Fig. 34.

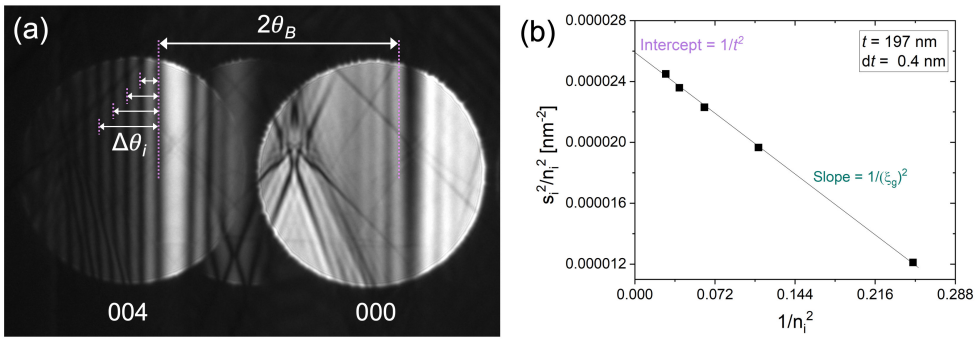

Figure 34: *(a) STEM-CBED pattern of GaAs under two-beam conditions, showing characteristic K-M fringe patterns in both diffraction discs. (b) K-A plot method, utilizing the linear relation* $y = -\frac{1}{\xi_g^2}x + \frac{1}{t^2}$ *to determine the crystalline sample thickness.*

More specifically, the number of fringes corresponds to the integer multiple of the extinction distance that equals the sample thickness. If the lamella is thinner than the extinction distance, no K-M fringes appear, as diffraction remains in the kinematical regime. As the thickness increases by one extinction distance, the number of K-M fringes increases by one. Consequently, thicker specimen exhibit more K-M fringes.

The crystalline sample thickness can be determined from the K-M fringe pattern by analyzing the spacing of the fringes in relation to the separation between the (000) and (hkl) diffraction discs. To understand how these relate to the thickness, the formation of fringe patterns must first be examined in more detail. Due to the beam convergence, electrons interact with the diffracting hkl planes at varying angles. The central bright fringe in the (000) disc, and correspondingly the central dark fringe in the (hkl) disc, originate from electrons that satisfy the exact Bragg diffraction condition at the Bragg angle θ_B, where the excitation error is $s = 0$. The distance between these two central fringes i.e., between the two diffraction discs in the CBED image, hence equals $2\theta_B$. The ith fringes adjacent to the central fringe correspond to electrons diffracting at angles deviating from the exact Bragg condition i.e., $s_i < 0$ or $s_i > 0$. The spacing between the central fringe and neighboring fringes is directly related to the variation in incidence angle on the (hkl) planes, denoted as $\Delta\theta_i$, or equivalently, to the difference in excitation error. The excitation error s_i for the ith fringe is given by

$$s_i = \lambda \frac{\Delta\theta_i}{2\theta_B d_{hkl}^2} \tag{30}$$

Where d_{hkl} is the interplanar spacing of the (hkl) planes. s_i relates to the lamella thickness via

$$\frac{1}{t^2} = \frac{s_i^2}{n^2} + \frac{1}{\xi_g^2 n^2} \tag{31}$$

where n is an integer. However, since ξ_g is often not precisely known for many materials, a graphical approach, the so-called K-A plot method, can be employed to determine the crystal-

line sample thickness. This method, based on the work of Kelly *et al.*[189] and Allen[190], is demonstrated using the example in Fig. 34b.
By plotting $\frac{s_i^2}{n^2}$ as a function of $\frac{1}{n^2}$, an appropriately chosen n yields a linear relationship, where the slope corresponds to $-\frac{1}{\xi_g^2}$ and the y-intercept gives $\frac{1}{t^2}$ i.e., the crystalline specimen thickness.

As this method relies on linear interpolation, a higher number of fringes in the diffraction discs improves measurement accuracy by increasing statistics. As the extinction distance depends on the electron beam energy, the kV used in CBED measurements can be adjusted to optimise the number of fringes. However, the choice of kV must always be adapted to the sample thickness. Thicker TEM specimens require higher acceleration voltages to mitigate absorption. However, even at high acceleration voltages, inelastic scattering in very thick specimens can lead to strong background intensities in the CBED patterns, masking the desired elastic scattering contrasts. Therefore, energy filtering (EF) is recommended to remove inelastic contributions, ensuring that only elastically scattered electrons contribute to the CBED pattern.[192] Thus, chromatic aberration effects induced by the specimen are eliminated, as all contributing electrons are focused at the same point in the BFP. Consequently, the contrast of the K-M fringe pattern is enhanced, facilitating more accurate thickness determination.

5.3.1.2 Experimental CBED Thickness Measurement of III-V TEM Specimens

In this work, CBED thickness measurements were performed using either a FEI Titan Ultimate or FEI Spectra microscope operated at 200 kV or 300 kV, adapted the thick TEM specimens, which were necessary to ensure a representative assessment of the specimen's electrical properties. Both microscopes are equipped with a Gatan image filter (GIF)-the FEI Titan Ultimate with a Gatan Tridium and the FEI Spectra with a Gatan Continuum 1066-fitted with a CCD camera for EF-CBED imaging. The energy slit width was set to 5 eV.
In general, CBED thickness evaluation can be performed in either TEM or STEM mode. In practice, STEM-CBED offers the advantage that the optimum diffraction pattern focus can be adjusted before setting up the two-beam conditions, for example by means of the ronchigram, whereas in TEM-CBED, focus adjustment is the final step and can be challenging to assess by eye. Even slight deviations from the optimal focus in TEM-CBED can cause significant errors in the derived thickness values. In this work, STEM-CBED has provided the most reliable thickness results and is therefore chosen as the standard method for thickness evaluation.
For the CBED thickness measurements of III-V materials viewed along [110], the two-beam condition is typically achieved by exciting the (004) diffracted g-vector. The C2 aperture, which controls the size of the diffraction discs, is chosen to prevent disc overlap, commonly set to 30 or 50 µm. Errors in the derived thickness values propagate from uncertainties in the y-intercept I of linear extrapolation as

$$\mathrm{d}t = \left(\frac{1}{2}\frac{1}{I^{3/2}}\right)\mathrm{d}I \tag{32}$$

The experimentally derived crystalline thickness values are further validated through the R^2 value of the linear fit in the K-A plot and by comparing ξ_g, obtained from the plot's slope, with reference values for the given material. The reference values for ξ_g corresponding to the respective electron beam energies (200 kV or 300 kV) are independently calculated using:[192]

$$\xi_g = \frac{\pi V cos(\theta_{B(hkl)})}{\lambda |F_g|} \tag{33}$$

where V is the unit cell volume and F_g is the structure factor $F(\theta_B)$ for the specific diffracted g-vector (hkl).
Eq. 33 illustrates that the extinction distance increases for higher electron beam energies in the TEM. θ_{hkl} is determined using Bragg's law:[193]

$$n\lambda = 2d_{hkl} sin(\theta_B) \tag{34}$$

with d_{hkl} for cubic structures being given by:

$$d_{hkl} = \frac{a}{\sqrt{h^2 + k^2 + l^2}} \tag{35}$$

The input parameters used for the calculation of t_c and ξ_g in this work are listed in Table 3. The calculated values for θ_B of (004) in GaAs are consistent with literature values.[194]

Table 3: Parameters involved in the calculation of CBED thickness measurements for GaAs specimens using the K-A plot method.

Input Parameters	
V_{GaAs}	190.13 Å
a_{GaAs}	5.75 Å
λ_{200kV}	0.0251 Å
λ_{300kV}	0.0196 Å
d_{004}	0.1413 nm
F_g	147.71 Å
Results	
θ_B (GaAs, 200 kV)	0.00888 rad
θ_B (GaAs, 300 kV)	0.00694 rad
ξ_g (GaAs, 200 kV)	161.1 Å
ξ_g (GaAs, 300 kV)	206.3 Å

5.3.2 Electrically Inactive Thickness Evaluation

The high-energy ion beam causes passivation of the surface layers due to surface band bending caused by implanted ions and/or introduced defects.[195,38] This surface layer causes a reduction of the built-in potential across p-n junctions and, hence, it is the main reason for a common underestimation of electric fields measured in electron microscopy compared with the expected values from theoretical simulations.[40,41,42] Hence, analysing the effects of the inactive layer is mandatory for reliable electric investigations, in particular for hetero-junctions which include a material transition. The inactive thickness can be quantified by examining the change in the potential step measured across a p-n junction against the change in the crystalline specimen thickness, which should principally provide the electrostatic potential only in the active layer inside the specimen.[42,43,41,195,40,119]

The procedure for evaluating the electrically inactive thickness can be understood by means of the analysis of the GaAs and InP p-n homo-junctions described in Sect. 6.4. It includes

the following steps: The first step is to prepare a TEM lamella from the bulk semiconductor with regions of different thickness. At each thickness region, the phase shift across the junction is measured using EH and STEM-CBED patterns are acquired to measure the crystalline thickness at the junction position.
As expected from Eq. 26, the measured step in phase increases with the specimen thickness. However, from the x-intercept it can be inferred that a minimum specimen thickness is required before any step in phase will be measured. This is given by the electrically damaged crystalline thickness. Assuming that this thickness is constant across the specimen, the measured phase across a p–n junction can now be expressed as

$$\Phi = \mathrm{C_E} V_{total} (t_{crystalline} - t_{inactive}) \tag{36}$$

6 Electrostatic Potential Analysis of Binary III-V p-n Junctions

EH is a well-established technique for investigating the electrostatic potential at p-n junctions in III-V semiconductor devices, particularly Si and GaAs.[124,119,40,26,38,28] However, as detailed in the previous chapter, accurate quantification of the phase shift is complicated by artefacts arising from sample preparation, dynamical diffraction, and electron-beam-induced charging. These artefacts are specific to every material and specimen under investigation and require adapting the experimental settings for the hologram acquisition.
This chapter aims to establish the methodology for subsequent electrostatic potential studies of p-n heterojunctions in multi-junction solar cell specimens under *in situ* applied bias, which will be the focus of Ch. 8. For the reference measurements presented here, binary III-V compounds such as GaAs and InP are utilized as calibration specimens, representing the basic constituents of the multinary compounds used in these devices.

The chapter begins with an introduction to the specimens and a brief theoretical overview of p-n junction properties, which are the basis for the numerical simulations of the expected electrostatic potential distributions. Subsequently, the electrostatic potential of the p-n junctions is measured using EH without applied bias. These initial measurements serve to evaluate the effects of sample thickness and specimen preparation-induced surface damage on the measured junction characteristics, including estimations of the electrically damaged layer thickness. Additionally, the influence of artefacts, such as electron-beam-induced charging and dynamical diffraction, on the interpretation of the measured phase distribution is assessed. Furthermore, hologram acquisition settings are optimised for large epitaxial III-V structures, balancing FOV, spatial resolution, accuracy, and precision for *in situ* biasing experiments.
The final section addresses the measurement of the electrostatic potential in GaAs p-n junctions under *in situ* applied bias. By analysing the response of junction properties (depletion width and built-in potential) to the applied bias, the impact of sample preparation was investigated, with a particular focus on challenges in circuit editing, including surface damage and the quality of metal-semiconductor contacts.

6.1 The Specimen

The experiments described in this chapter were employed on binary compound III-V materials. Two different bulk samples containing p-n homo-junctions were used. Schematic descriptions of the specimen structures are presented in Fig. 35. The first is a GaAs sample containing a p-n homo-junction with a symmetrical dopant concentration of 1×10^{18} cm^{-3}. The sample was grown by molecular beam epitaxy and comprises a 1 µm-thick Be-doped (p-type) layer grown on a 1 µm-thick Si-doped (n-type) layer on a n-doped GaAs (0 0 1) substrate.
The second is an InP specimen containing a p-n homo-junction, consisting of a 1200 nm-thick p-doped layer and a 200 nm-thick n-doped layer, with asymmetrical doping concentrations of 1×10^{17} cm^{-3} and 1×10^{18} cm^{-3}, respectively. The whole structure was grown on a p-doped InP (0 0 1) substrate.
Both, InP and GaAs are direct bandgap materials crystallizing in the cubic zinc blende structure. InP and GaAs are ideal reference systems for technique development and reference measurements

since they can be epitaxially grown as high-quality, defect-free single crystals. Moreover, both material systems have been extensively studied and discussed in the literature, and their properties are therefore well-documented and well-understood. Further, as p-n homo-junctions are used, only the doping changes across the junction, while the III-V element and stoichiometry remain constant. As a result, the lattice parameter remains unchanged, and no strain is introduced across the junction. Further, it allows us to relate the change in absolute electrostatic potential across the junction entirely to the change in dopant potential, as contributions from the MIP can be excluded.

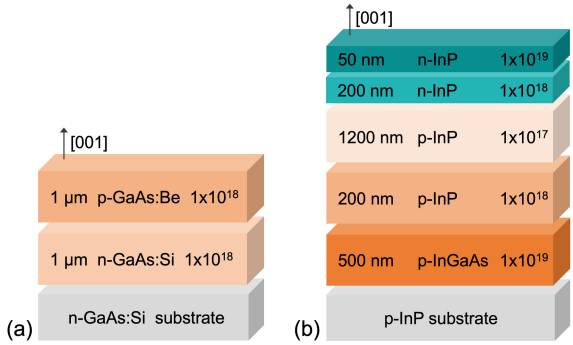

Figure 35: *Schematic illustration of the III-V semiconductor specimen structures, indicating each layer's thickness, III-V compound, as well as doping type and concentration. (a) GaAs p-n homo-junction specimen. (b) InP p-n homo-junction specimen. The dimensions of the epitaxial layers are not to scale.*

For the electrostatic potential analysis with and without *in situ* applied bias, parallel-sided TEM lamellae were prepared from the bulk GaAs and InP specimen. The *in situ* biasing TEM specimen were prepared on a MEMS chip using the FIB preparation procedure described in Sect. 4.4.1, while the conventional samples were prepared on an Omniprobe Cu-grid using the standard FIB preparation procedure described in Sect. 4.2.2. The lamellae were cut parallel to the crystallographic $1\bar{1}0$ direction, so that the TEM viewing direction is along the [110] zone axis. Table 4 provides a list of the TEM samples, indicating the sample ID, the employed FIB-SEM device, the type of preparation (biasing or non-biasing), as well as the type of contact material. For some preparations, the top surface of the bulk specimen wafer was coated by sputtering of gold/palladium (Au/Pd) prior to the FIB-SEM preparation.

Table 4: List of TEM specimen prepared from the GaAs and the InP bulk specimen, shown in Fig. 35a and b respectively. IBID refers to the ion-beam-induced deposition of metal inside the FIB-SEM.

Sample-ID	TEM support	Contacting metal	FIB-SEM Device
GaAs-AuPd	biasing-chip	AuPd + IBID-W (30 kV, 0.92 nA)	FEI Strata 400S
GaAs-W	biasing-chip	IBID-W (30 kV, 0.92 nA)	FEI Strata 400S
GaAs-Pt	biasing-chip	IBID-Pt (16 kV, 0.43 nA)	FEI Strata 400S, FEI Helios
InP-1	conventional Cu-grid	AuPd + IBID-W (30 kV, 0.92 nA)	FEI Strata 400S
InP-2	conventional Cu-grid	AuPd + IBID-W (30 kV, 0.92 nA)	FEI Strata 400S

6.2 The p-n Junction

Understanding the physics of p-n junctions is fundamental to the study of semiconductor devices. This section provides a brief summary of the key properties and principles underlying p-n junctions, which serve as the foundation for the electrical TEM characterisation of the semiconductor specimen presented in this work. A detailed exploration of the physical principles is beyond the scope of this study but can be found in standard reference works, such as [196,197,47]. For simplicity, an ideal, abrupt p-n junction is considered in the following, meaning that no dopant diffusion occurs between the p- and n-sides and partly depleted transition layers are not considered.

A p-n junction forms when a p-doped and a n-doped semiconductor layer are grown next to each other in an epitaxial structure. The introduction of impurity atoms (doping) changes the position of the Fermi level (E_F) compared to the mid-bandgap position in the undoped III-V material: n-doping shifts E_F towards the conduction band (E_C), while p-doping shifts it towards the valence band (E_V). When p-doped and n-doped layers are in contact, the Fermi levels align to reach equilibrium, leading to a bending of the energy bands, E_V and E_C, to accommodate this alignment. This creates a potential gradient that acts as a barrier for the carriers and induces an electric field across the junction, which can be measured using TEM techniques. In other words, the gradient in excess electron and hole concentrations between the adjacent p- and n-type regions leads to the diffusion of these excess majority carriers into the opposite region.; i.e. electrons diffuse from the n-type to p-type region and holes from the p-type to the n-type region, leaving positively/negatively charged donor/acceptor atoms behind. These net positively and negatively charged regions on either side of the junction induce an electric field and are depleted from excess carriers. Hence, this region in which the band bending occurs is called depletion region or space charge region (SCR).

Fig. 36 schematically shows the properties of a symmetrically doped p-n junction at equilibrium conditions, i.e. without externally applied bias, including the band edge diagram, the distributions of the electrostatic potential, the electric field and the charge. The SCR is confined between $-x_p$ and x_n with the junction positioned at $x = 0$. Following the abrupt junction approximation, and not considering possible partially depleted transition layers between the SCR and the not-depleted n- and p-type regions, the space charge region abruptly ends at these points in the p-side and n-side of the junction.

The following paragraph defines the key characteristics of the p-n junction relevant to this work: the built-in potential, the distribution of the electrostatic potential and the electric field, and the width of the depletion region. These properties are first described under equilibrium conditions (no external bias) before discussing the effects of applying a reverse voltage to the p-n junction.

6.2.0.1 Without Applied Bias

The **built-in potential**, V_{bi} (or ΔV_{p-n}), is defined as the potential difference between the n- and p-type layer and depends on the respective doping concentration which determines the positions of the intrinsic Fermi level in the p- and n-regions, and thus the resulting extent of the band bending, as evident from Fig. 36

$$V_{bi} = \frac{kT}{q} ln(\frac{N_A N_D}{n_i^2}) \tag{37}$$

with the Boltzmann constant k, the temperature T, the elementary charge q, the intrinsic carrier concentration n_i, and the acceptor (or p-type) and donor (or n-type) doping concentrations N_A and N_D, respectively.

The electrostatic potential and electric field distribution across the junction can be derived from **Poisson's equation**, which in the one-dimensional approximation is:

$$\frac{\mathrm{d}^2V}{\mathrm{d}x^2} = -\frac{\mathrm{d}E}{\mathrm{d}x} = -\frac{\rho}{\epsilon_s} \tag{38}$$

where V is the electrostatic potential, E is the electric field, ϵ_s is the permittivity and ρ is the charge density.

The charge densities in the p-side ($0 \geq x \geq -x_p$) and n-side ($0 \leq x \leq x_n$) of the depletion layer for a symmetrically doped p-n junction are shown in Fig. 36, can be expressed as:

$$\rho(x) = -qN_a \qquad 0 \geq x \geq -x_p \tag{39}$$

$$\rho(x) = qN_d \qquad 0 \leq x \leq x_n \tag{40}$$

Substituting Eqs. 39 and 40 into Eq. 38 and then integrating, one obtains the **electric field** distribution in the p-side ($0 \geq x \geq -x_p$)

$$E(x) = -\frac{qN_a}{\epsilon_s}x + C_1 = \frac{qN_a}{\epsilon_s}(x - x_p) \tag{41}$$

and in the n-side ($0 \leq x \leq x_n$)

$$E(x) = -\frac{qN_d}{\epsilon_s}(x - x_n) \tag{42}$$

The electric field is continuous, also at the junction $x = 0$. Based on this, equating Eq. 41 and Eq. 42 yields

$$N_a x_p = N_d x_n \tag{43}$$

which implies that the amount of positive charges in the n-side equals the amount of negative charges in the p-side per unit area.

Fig. 36 shows the electric field distribution across a symmetrically doped SCR. The gradient of the electric field is directly proportional to the net charge, as described by the Poisson equation. Consequently, the extremum of the electric field is located at the p-n junction, while in charge-free regions, i.e. the bulk p- and n-regions, the electric field is assumed to be zero. In a symmetrically doped p-n junction, the electric field is a linear function of the distance across the junction. Following the abrupt junction approximation hence yields a triangle shape of the electric field in the SCR.

The **electrostatic potential** in the p-side and the n-side is obtained by integrating the field.

$$V(x) = \frac{qN_a}{2\epsilon_s}(x - x_p)^2 \qquad 0 \geq x \geq -x_p \tag{44}$$

$$V(x) = -\frac{qN_a}{2\epsilon_s}(x - x_n)^2 \qquad 0 \leq x \leq x_n \tag{45}$$

The distance to which the SCR extends into the p-doped and n-doped side of the junction, can be determined by substituting Eq. 43 into Eq. 37, and solving for x_n and x_p, respectively.

$$x_n = \left\{ \frac{2\epsilon_s V_{bi}}{e} \left[\frac{N_a}{N_d} \right] \left[\frac{1}{N_a + N_d} \right] \right\}^{1/2} \tag{46}$$

$$x_p = \left\{ \frac{2\epsilon_s V_{bi}}{e} \left[\frac{N_d}{N_a} \right] \left[\frac{1}{N_a + N_d} \right] \right\}^{1/2} \tag{47}$$

Finally, the total **depletion width** W_d at zero applied voltage can be derived from Eq. 46 and Eq. 47 as

$$x_n - x_p = W_d = \sqrt{\frac{2\epsilon_s V_{bi}}{q} \left(\frac{1}{N_a} + \frac{1}{N_d} \right)} \tag{48}$$

6.2.0.2 With Reverse Applied Bias

If an electrical bias is applied to the p-n junction, the equilibrium conditions do not apply anymore, and the Fermi level is not constant across the junction. Instead, when applying a reverse bias, i.e. a positive voltage to the n-side and a negative voltage to the p-side, the Fermi level of the p-type material shifts upwards in energy, while it shifts downwards in the n-type. This enhances the band bending, leading to an increase of the total potential barrier, V_{n-p}, at the junction by the amount of applied reverse bias:

$$V_{n-p} = V_{bi} + V_R \tag{49}$$

where V_{bi} is the built-in junction potential at zero applied bias and V_R is the magnitude of the applied reverse voltage. As the barrier for majority charge carriers increases, the electric field strength and the width of the space charge region (SCR) both increase with increasing reverse bias. Consequently, the electric field in the n-side and p-side of the SCR under reverse bias can be calculated by substituting the total potential barrier, V_{n-p}, for the built-in potential in Eqs. 42 and 41. Equivalently, the total width of the SCR can be defined as a function of the applied reverse bias by reformulating Eq. 48 as

$$W_d = \left\{ \frac{2\epsilon_s (V_{bi} + V_R)}{q} \left[\frac{N_a + N_d}{N_a N_d} \right] \right\}^{1/2} \tag{50}$$

Applying a forward bias, i.e. a negative voltage to the n-side and a positive voltage to the p-side, leads to the opposite response of the junction characteristics, that is a decrease of the total potential barrier, the electric field strength as well as of the depletion width.

Although the term built-in potential applies more precisely under equilibrium conditions, the

term is also used interchangeably in the literature for the term total potential barrier, which applies under non-equilibrium conditions (with applied bias). To avoid confusion, the total potential barrier is hereafter referred to as built-in potential. The notation V_{bi} is kept for the built-in potential without applied bias, while the built-in potential with applied bias is denoted as V_{n-p}.

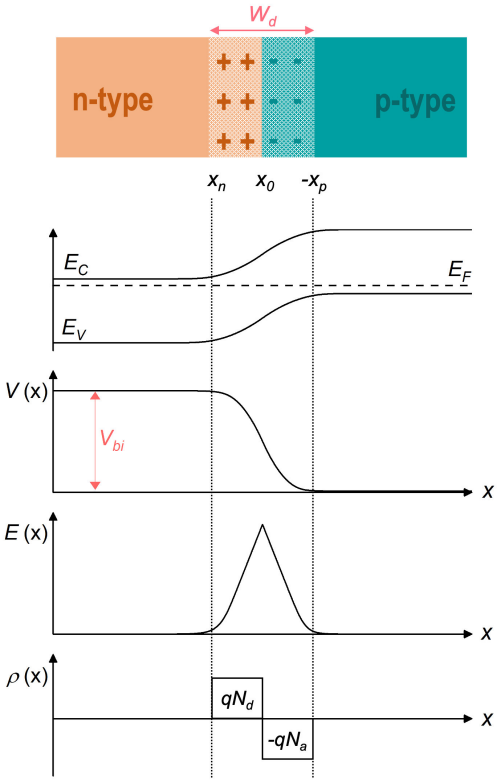

Figure 36: *Schematic illustration of a p-n junction and its key characteristics in equilibrium conditions (without applied bias). The energy band diagram displays the alignment of the Fermi level, E_F and the resulting bending of the conduction band, E_C, and the valence band, E_V. The built-in potential, V_{bi}, is given by the difference in electrostatic potential, $V(x)$, between the n-type and the p-type layer. The electric field distribution,$E(x)$, is non-zero in the depletion region, which is defined between $x_n - x_p$ with the depletion width W_d. The charge density distribution, $\rho(x)$, is defined as qN_d in the n-side of the SCR and as $-qN_a$ in the p-side.*

6.3 Simulation of the Electrostatic Potential

To provide a reference for the electrostatic potential measurements with EH, the expected dopant potential distribution for the III-V specimen structures was simulated using the commercial NEXTNANO software.[198,199] NEXTNANO serves to simulate the (opto-)electronic properties of semiconductor nanostructures, by calculating the band structure as a self-consistent solution to the Poisson-Schrödinger equation.

The epitaxial specimen structures were simulated in 1D in the [001] growth direction assuming full ionization of the impurities. This simplified approach yields the potential and electric field

distribution for the ideal, abrupt p-n junction, not accounting for incomplete dopant ionization or the effect of Fermi level pinning due to surface states in the FIB-prepared cross-sections.
The energy band structure at equilibrium state is shown in Fig. 37a alongside with the electrostatic potential distribution in Fig. 37b. The derived values for the built-in potential and the depletion width of the GaAs specimen at equilibrium conditions and at different applied reverse biases are listed in Table 5 and serve as a reference for the experimental values obtained by EH with and without applied bias.
Fig. 38 shows the simulated electric field distribution across the p-n junction of the GaAs specimen, which widens with increasing reverse bias. The peak of the triangular distribution is located at the p-n junction, with its height representing the total electric field strength. The width of the distribution corresponds to the total depletion width, W_d, which is the sum of the depletion width on the n-side and the p-side of the junction. Here, the edges of the triangle are symmetrical due to the symmetrical doping (10^{18} cm^{-3}) of the p-GaAs and n-GaAs layers, resulting in identical widths of the depletion region on either side of the junction, as they are inversely proportional to the dopant concentration. The field profiles in Fig. 38 illustrate that, as described in the previous section, with increasing reverse bias the SCR widens and the electric field strength increases.

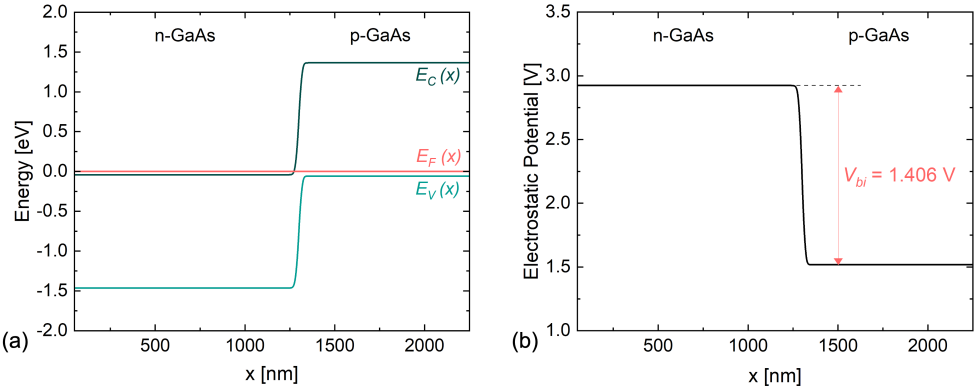

Figure 37: *Simulation of the a) energy band structure and b) electrostatic potential distribution across the symmetrically 1×10^{18} cm^{-3} doped GaAs p-n junction at equilibrium state (without applied bias).*

Table 5: Simulated built-in potential and depletion width for a symmetrically 10^{18} cm^{-3} doped GaAs p-n junction under different applied reverse bias.

Reverse Bias	Built-in potential	Depletion width
0 V	1.41 V	62 nm
- 1 V	2.41 V	98 nm
- 2 V	3.41 V	124 nm
- 3 V	4.41 V	146 nm

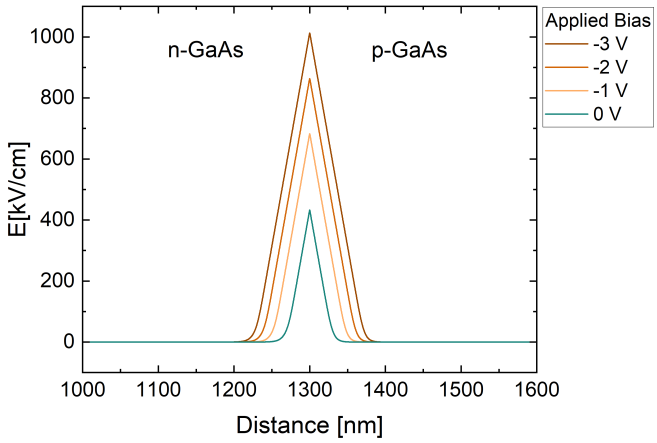

Figure 38: *Simulated electric field distribution across the symmetrically 10^{18} cm^{-3} doped GaAs p-n junction at different applied reverse biases.*

6.4 Electrostatic Potential Analysis of p-n Homo-Junctions of Binary III-V Compounds

6.4.1 GaAs

The electrostatic potential analysis without applied bias focused on the GaAs-AuPd and the GaAs-W samples, as they include areas of different thicknesses, which were milled to allow systematic studies of the effects of specimen thickness on the phase measurement. Electron holograms were recorded using the FEI Titan Ultimate microscope with the Gatan OneView CCD camera. The microscope was operated in Lorentz mode using 200 kV electrons to limit the electron-beam induced knock-on damage of the semiconductor specimen and to increase the gain of phase shift from electrostatic potentials.[171] As the specimen are prepared on a biasing chip, the vacuum reference region to be used is located above the specimen, as evident from the overview image in Fig. 39. This necessitates recording holograms with a large FOV. In the GaAs specimen, the p-n junction is located 1 µm below the wafer surface. Additionally, the lamella is covered with a protective metal layer of about 1 µm, with small variations depending on the thickness region. Consequently, the holograms were acquired with a diffraction lens excitation of 20% at a Lorentz magnification of 40.0kx using a biprism voltage of 80 V to provide an interference width of 3.2 µm (see Fig. 30). The FOV of 5.18×5.18 µm^2 acquired on 4096×4096 pixel array yielded a hologram pixel size of 1.27 nm. The interference fringe spacing of 6.2 nm leads to a spatial resolution of 18.6 nm in the reconstructed phase images. Due to the loss of beam coherence caused by the extreme broadening of the interference region and the relatively low sampling of 4 pixels per fringe, the measured fringe contrast is below 10%. This low contrast was compensated by recording stacks of 30–35 holograms with an individual exposure time of 8 s. The stacks were summed using the HoloWorks software[158], thus providing a phase resolution of 0.075 rad, which was measured in vacuum in the reconstructed phase images.

A key factor for EH experiments is to minimise the dynamical diffraction by tilting the speci-

men off the zone-axis to a weakly diffracting orientation, as described in Sect. 5.2.6.4. This is particularly difficult in thick specimen as they were used in this study to increase the signal from active dopants for the potential measurement. Additionally, during sample preparation for *in situ* biasing, the long lamella need to be attached on both sides of the chip trench. This can introduce strain, causing the lamella to bend, leading to bend contours and intensified dynamical diffraction in the holograms. Hence, it can be quite difficult to entirely remove the diffraction contrast from the FOV and the tilt orientation of the specimen has to be adjusted to each sample region analysed. Upon tilting, it must also be ensured that the (001) interfaces of the semiconductor layer structure are kept parallel to the beam to avoid information loss due to projection and broadening of the p-n junction, as explained in Sect. 5.2.6.4. The biasing TEM holder used in this study is a single-tilt holder, allowing only alpha tilt along one axis. As a result, beta tilt corrections along a second axis, like those possible with double-tilt TEM holders, are not feasible. This emphazises the importance of first, cutting the lamella precisely along the desired crystallographic orientation, and second, positioning the lamella as straight as possible across the chip trench. By accounting for these factors, the holder allows tilting parallel to the epitaxial layers. Here, the specimen was tilted parallel to the crystallographic $1\bar{1}0$ direction, that is around the [001] growth direction, so that the (000) reflection is kept centered in the 004 Kikuchi band. The orientation in diffraction space is evident from Fig. 33 in Sect. 5.2.6.4. Fig. 39 shows a series of BF-TEM images of the GaAs-AuPd lamella at different degrees off-tilt from the zone axis. Generally, the thicker the specimen region, the more it is affected by dynamical diffraction combined with absorption leading to a darker contrast in the BF-TEM image. The thinnest specimen region is more affected by strain induced bending, as visible from the bending contours. Obviously, when tilted to the zone axis, the strongest diffracting orientation, the dynamical diffraction is the most visible, as evident from the darkest contrast. At different degrees of off-tilts from zone axis, Kikuchi bands cut through the specimen at different positions leading to more or less darker contrasts. It was found that in this GaAs specimen a $+2.35°$ tilt from the zone axis yielded the lowest amount of dynamical diffraction and the most homogeneous contrast across the specimen region of interest, as evident from Fig. 39. For EH analysis of the junction in the thinnest specimen region, the lamella was tilted to $-4.26°$ to attempt minimising the effect of the bend contours on the phase shift.

Fig. 40(f)-(j) show the reconstructed phase images recorded at the different thickness regions of the GaAs-AuPd lamella. Fig. 40(a)-(e) show the correlated amplitude images, which are used to assess the influence of remaining dynamical diffraction contrast and possible undesired intensity contributions to the measured dopant potential. While neither the BF-TEM images nor the reconstructed amplitude images (indeed a reconstructed amplitude image corresponds to a filtered conventional bright-field image) [5] show significant contrast from the p-n junction, the differently doped regions of the GaAs specimen are clearly distinguishable in the phase images due to the opposing contrast caused by the phase difference of the object wave between the n-type and p-type regions. The n-doping induces a positive phase shift, appearing bright in the phase image, while the p-doping induces a negative phase shift, appearing dark.

When comparing the detected phase signal in the different specimen regions, the phase signal in the thickest area, shown in Fig. 40(f), exhibits more phase unwrapping errors and noise compared to the thinner regions. This can be explained by the fact that the thicker region is more affected

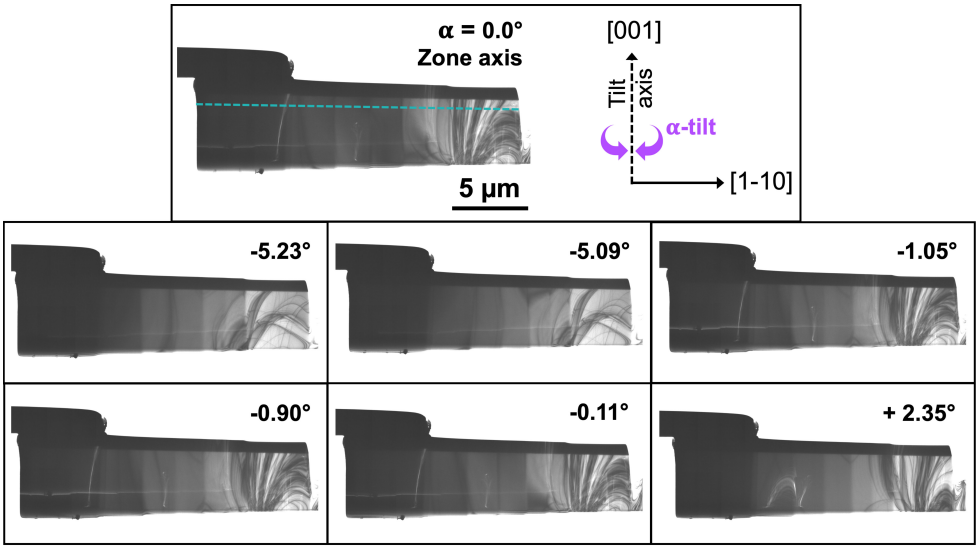

Figure 39: *BF-TEM images of the GaAs specimen α-tilted away from the [110] zone axis around the [001] growth direction. The presence of dark dynamical diffraction contrast varies depending on the tilt orientation. The indicated α-tilt angles are measured relative to the zone-axis orientation at 0°. The green line indicates the approximate position of the GaAs p-n junction.*

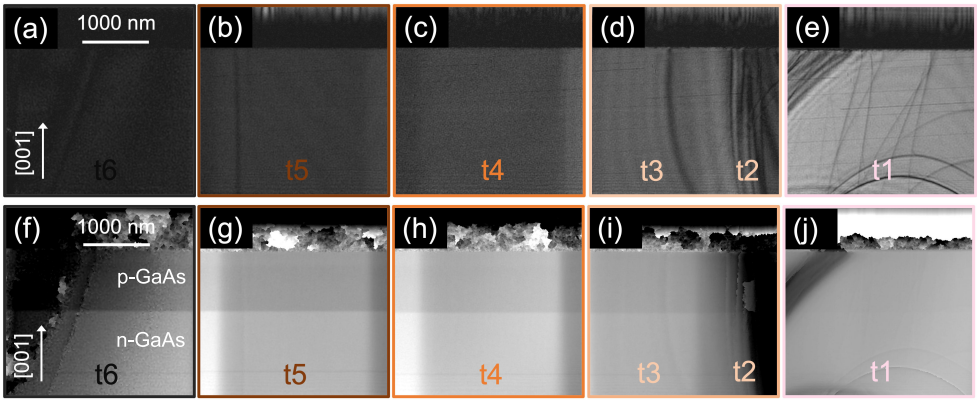

Figure 40: *(a)-(e) Amplitude images and (f)-(j) phase images reconstructed from electron hologram stacks recorded at the different thickness regions of the GaAs-AuPd specimen. The holograms yielding the images (a)-(d) and (f)-(i) were recorded at +2.35° off-tilt from the zone axis, while those yielding (e) and (j) were taken at −4.26°.*

by absorption contrast and dynamical diffraction contrast, both of which reduce the number of electrons N_e [159], leading to lower phase sensitivity and increased noise in the phase image, as evident from Eq. 28. This is confirmed by the amplitude image showing strong dynamical and thickness contrast, which however does not limit the phase resolution, as the phase contrast between the p- and n-layers is still clearly resolved. Unlike in the thinnest (t1 = 225 nm) and second thinnest (t2 = 385 nm) specimen regions, where the bending and diffraction contours, visible in the amplitude images in Fig. 40(e) and (d) respectively, lead to unwrapping errors in the reconstructed phase, thereby deteriorating the phase contrast in some areas. This highlights the importance of consulting amplitude images to select appropriate regions for deriving the phase distribution across the GaAs p-n junction. Acquiring holograms with a large FOV comes with the advantage of a larger lateral choice for retrieving interpretable phase profiles that are not distorted by diffraction contrast.

The phase profiles extracted from the phase images for each thickness region of the GaAs-AuPd and the GaAs-W specimen are shown in Fig. 41a and 42a, respectively. Each profile was integrated over a width of 200 nm. Due to the dominant diffraction contrast, the 361 nm-thick GaAs-AuPd specimen region was disregarded in this phase evaluation.
As expected from Eq. 26, the total step in phase measured across the p-n junction in both lamellae is increasing as a function of the specimen thickness. This is also evident from Figs. 41b and 42b, which plot the measured phase steps as a function of the crystalline thickness measured by STEM-CBED. However, when comparing the experimental values to the phase step predicted based on simulations of the electrostatic potential of the GaAs specimen, it is clear that the measured phase steps of 0.322 to 2.26 rad are significantly lower than the expected 2.31 to 5.92 rad for the given specimen thicknesses from 225 to 577 nm. This underestimation of the phase shift across the junction (or the built-in junction potential) is a common issue in electron microscopy analysis which can be mainly ascribed to the passivated specimen surfaces.

In Figs. 41b and 42b the deviation in the x-intercept of the linear approximation of the experimental data indicates the presence of these electrically damaged surface layers (as described in Sect. 4.3.1). In the present GaAs-AuPd and GaAs-W lamellae it is estimated to in total 165 ± 29 nm and 151 ± 23 nm, respectively, corresponding to about 82.5 nm and 75.5 nm on each lamella surface, which do not contribute to the total built-in junction potential. This value is close to the 172 ± 15 nm inactive thickness reported by Cooper *et al.* [125] for a GaAs p-n junction specimen with the same symmetrical doping concentration of 1×10^{18} cm^{-3}, prepared using the same FIB operating voltage of 16 kV. Sasaki *et al.* measure an inactive layer of about 120 nm for 1×10^{18} cm^{-3} doped GaAs. [119] Anada *et al.* reported a larger value of 202 ± 10 nm, although using a GaAs specimen with a higher doping concentration (1×10^{19} cm^{-3}). [40]
When the electrically damaged thickness of 151 nm is taken into account in the simulation of the expected phase shifts for the respective active thicknesses in the GaAs-W sample, the measured phase shifts are very close to the expected values. In fact, the phase shifts measured in the thicker areas are even slightly higher than expected for the active thicknesses, as are the resulting built-in potentials, listed in Table 6 and derived using Eq. 36. This illustrates the inaccuracy resulting from the simplified assumption in estimating the inactive thickness – that the inactive layer has a uniform thickness across the entire sample. In the real lamella, the density of surface defect states that pin the Fermi level in the electrically damaged surface region and lead to

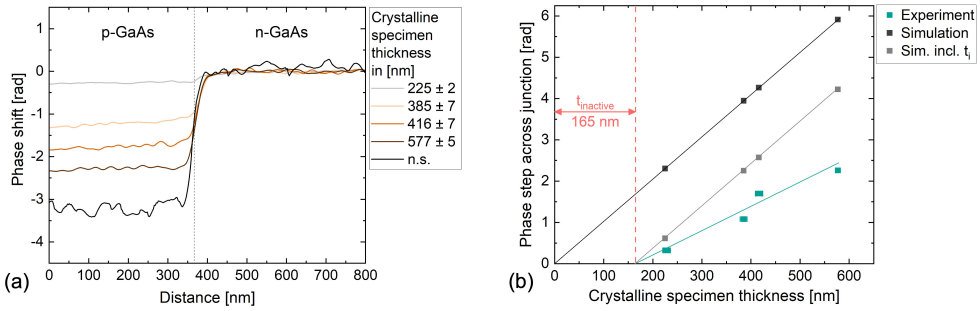

Figure 41: *(a) Phase profiles across the GaAs p-n junction extracted from regions of different crystalline thickness of the GaAs-AuPd lamella shown in Fig. 40. (b) Step in electron phase across the junction as a function of the total crystalline specimen thickness measured by STEM-CBED. The electrically damaged thickness ($t_{inactive}$) is derived from the x-intercept of the linear fit of the experimental phase values.*

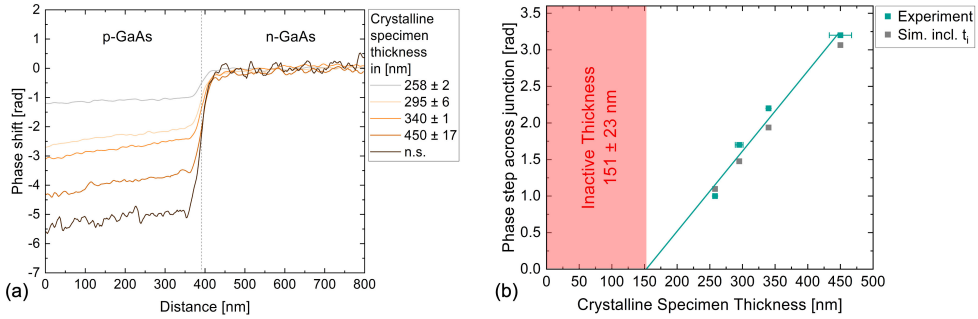

Figure 42: *(a) Phase profiles across the GaAs p-n junction extracted from regions of different crystalline thickness of the GaAs-W lamella. (b) Step in electron phase across the junction as a function of the total crystalline specimen thickness measured by STEM-CBED. The electrically damaged thickness (t_i) is derived from the x-intercept of the linear fit of the experimental phase values. Accounting for t_i in the simulation, the expected phase shifts for the remaining electrically active specimen thicknesses are shown for comparison.*

surface band bending is not constant.

The inaccuracies arising from this assumption are even more pronounced for the GaAs-AuPd sample. Even when accounting for the 165 nm electrically damaged thickness, the measured phase shifts, and the respectively calculated built-in potentials listed in Table 6, are still lower than expected. The values are approaching but the experimental data still underestimates the phase step by 52-66%, indicating that even less active dopants than expected remain in the specimen. The remaining underestimation of the phase shift can also be partly due to the 1D potential simulation assuming all donor and acceptor impurities are fully ionized, which is inaccurate at room temperature.

The examples presented here illustrate the difficulty of reproducibly quantifying the absolute built-in potential across a p-n junction, as surface damage inconsistently alters the electrical properties compared to those of the bulk specimen. Accurate quantification would require more advanced simulations of the electrostatic potential accounting for the material specific surface

band bending in all three dimensions of the lamella. However, these simulations are becoming very complicated for more complex material systems, particularly for the asymmetrically doped p-n hetero-junctions of multinary III-V compounds, which involve a change in both the dopant and the V element, as found in the multijunction solar cells discussed in Ch. 8. For this reason, these simulations are out of the scope of this work.
Experimental methods reported for minimising FIB-induced surface passivation and deriving more realistic built-in potentials include *in situ* annealing [41] and *in situ* electrical biasing [123,125,200]. These are independent of the strategies used to reduce damage during the preparation process, which are elaborated in detail in Ch. 4.3.1. *In situ* annealing is surmised to heal FIB induced defects and to reactivate passivated dopants in the damaged surface layers. [41] However, the measured phase steps across the junction were still reported to remain smaller than predicted by simulations. [125] On the other hand, applying a reverse bias to a p-n junction was reported to yield the expected, correct value of the built-in potential. [176,125,200] *In situ* biasing of the GaAs p-n junction specimen will be investigated in the next Sect. 6.5. However, for the investigation of the GaAs p-n junction the primary focus is not on accurately quantifying the total built-in potential, as previous studies have done, but rather on developing a reliable method for measuring the width of the depletion region at p-n junctions in view of the tunneljunction analysis in Ch. 8.

To derive the depletion width of the present GaAs p-n junction, the measured phase profiles in Fig. 41a were converted to electric field profiles using the first differential of Eq. 20:

$$E(x) = -\frac{dV(x)}{dx} \tag{51}$$

Fig. 43 exemplarily shows the electric field distribution across the junction in the GaAs-AuPd specimen at a thickness of 385 nm in comparison to the simulated electric field. The height of the peak indicates the relative strength of the electric field, while the width relates to the depletion width. The absolute field strength was not quantified, as the focus is on measuring the depletion region width, W_d. In this work, W_d is measured as the distance between the x-intercepts derived by extrapolating the linear fits of the electric field profile in the p- and n-type regions, respectively. [40] This approach is illustrated by means of the example in Fig. 43. It is based on the assumption that the electric field profile across an ideal abrupt p-n junction has a triangular shape, with the tilt of the edges indicating the depletion width on the n- and p-side, as described in Sect. 6.3 and as evident from the electric field profile derived from the NEXTNANO simulation of the present GaAs junction in Fig. 43. In the real specimen however, the junction is not perfectly abrupt but includes a zone which is partially depleted in free carriers in transition from the degenerated region to the SCR. This factor causes the experimentally derived electric field profile to deviate from the ideal triangular shape, by introducing extended tails to the linear edges.
Table 6 lists the depletion widths of the GaAs p-n junction in the GaAs-AuPd and GaAs-W samples, as derived from the electric field profiles at various specimen thicknesses. The error in measuring W_d was estimated to be 1 nm, based on the average uncertainty in the x-intercepts of the linear extrapolations. Generally, the experimental values are larger than the depletion width of 63 nm predicted by the simulation. This can be mainly ascribed to the aforementioned facts that firstly, the simulation does not account for the lower abruptness of the real p-n junction

and secondly, it assumes the full ionization of all p- and n-type dopants. The depletion width measured in the real specimen includes not only the entirely depleted SCR but also a part of the partially depleted transition region. Additionally, the intended doping concentrations were used as input for the simulations. Ideally, doping profiles derived from secondary ion mass spectroscopy (SIMS) would be used to simulate the electrostatic potential of the actual structure. However, as a comprehensive device characterisation was not the focus for this specimen, the simulations were not optimised in this regard.

Comparing the depletion widths measured at the different thickness regions within each specimen, the values are constant and small deviations from the average depletion width-83 ± 1 nm in GaAs-AuPd, and 81 ± 1 nm in GaAs-W-are within the error. The only major outlier of 71 nm was measured in the thinnest specimen region of GaAs-AuPd. This observation contradicts the common finding of a broadening of the depletion region in very thin specimen, which is explained by the dominant influence of Fermi level pinning and the resulting band bending in the passivated surface layers.[177,175,176] However, this explanation does not apply here, as the deviating value is smaller compared to the thicker specimen regions, and with a crystalline thickness of 225 nm, still an active thickness of approximately 60 nm remains after accounting for the damaged layers. Instead, it can be explained by the dominant diffraction contrast in this lamella region, evident in the respective amplitude and phase images in Figs. 40(e) and (j), which leads to high noise levels in the derived electric field profile. This emphazises once again that ensuring a homogeneous, weak diffraction contrast is key to obtain accurate information about p-n junctions from phase measurements. In considering additional factors influencing the junction width measurement, the potential effects of electron beam illumination must also be taken into account. As explained in Sect. 5.2.5, the electron beam generates electron-hole pairs – a process utilized in the STEM-EBIC method discussed in Ch. 7 – where higher beam currents increase the charge generation and, consequently, the electron-beam induced current across the specimen's p-n junction. However, by using reasonably low beam currents and grounding the specimen-for instance, and connecting it to a biasing chip, as in the present study-, charge accumulation is limited, which allows for accurate depletion width measurements.

Comparing the measured depletion widths of the two samples, GaAs-AuPd and GaAs-W, shows that the depletion width could be measured with a deviation of only 2 nm, despite the two specimen having different crystalline thicknesses in the range of about 250–600 nm, and using large FOV hologram acquisition settings yielding a spatial resolution of 18.6 nm. This illustrates that careful sample preparation following the standardized procedure described in Sect. 4.4.1 and 4.2.2 allows precise measurement of the depletion width and its comparison between different samples. The remaining difference of 2 nm could be explained by the fact that, although both samples were solely tilted about the [001] direction to avoid smearing of the junction, slightly different off-tilt angles from the [110] zone axis were used to suppress the individual dynamical diffraction contrast. Combined with possible small deviations from an exactly parallel orientation of the p-n layer interface along the alpha-tilt direction of the holder when positioning the lamella over the chip trench, this can explain small deviations in the junction width measured in projection. The two present datasets were acquired without the initial intention of direct comparison. However, when measuring the depletion width across multiple samples for comparative purposes, as it is the case of the tunneldiode study described in Ch. 8, the samples must be

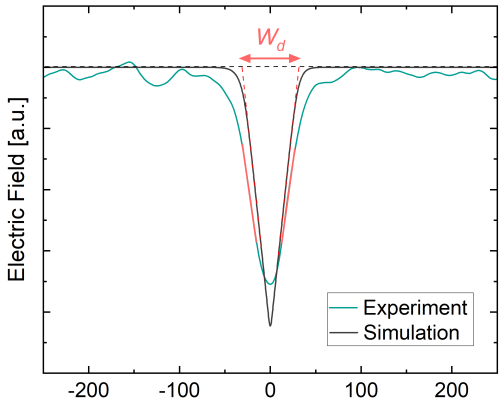

Figure 43: *Comparison of the electric field distribution across the GaAs p-n junction from experimental data and simulations, both at a specimen thickness of 385 nm. The experimental profile was obtained from the respective phase profile in Fig. 41a using the first differential equation 51. W_d indicates the width of the depletion region derived from the linear extrapolation of the peak flanks to the x-axis.*

oriented identically to ensure valid comparison.

Table 6: Properties of the GaAs p-n junction measured at different specimen thicknesses (ID) in the GaAs-AuPd and GaAs-W lamellae by means of EH. The crystalline thicknesses (t_c) were measured using STEM-CBED. The active thicknesses (t_a) were derived by subtracting the electrically inactive thicknesses, which are t_i(GaAs-W)= 151 ± 23 nm and t_i(GaAs-AuPd)= 165 ± 29 nm.

Specimen	ID	t_c [nm]	t_a [nm]	Step in phase [rad]	Built-in potential [V]	Depletion width ±1 nm
GaAs-AuPd	t1	225 ± 2	60	0.32	0.74	71
	t3	385 ± 7	220	1.08	0.67	82
	t4	416 ± 7	251	1.70	0.93	83
	t5	577 ± 5	412	2.26	0.75	83
	t6	-	-	3.14	-	83
GaAs-W	t1	258 ± 2	107	1.0	1.28	82
	t2	295 ± 6	144	1.7	1.62	81
	t3	340 ± 1	189	2.2	1.60	80
	t4	450 ± 17	299	3.2	1.47	81
	t6	-		4.97	-	80

6.4.2 InP

Electron holograms of the InP-1 specimen were recorded with the same microcope setup as for the GaAs specimen: using the Gatan OneView CCD 4k×4k camera on the FEI Titan Ultimate microscope operated at 200 kV. Two different data sets were acquired to compare standard with low-magnification (LM) EH. The LM data was taken using the same acquisition settings as for the GaAs specimen described before, that is a diffraction lens excitation of 20% at a Lorentz magnification of 40.0kx and a biprism voltage of 80 V, providing a hologram width of 3.2 µm and a total image FOV of 5.18×5.18 µm. The resulting fringe spacing of 6.2 nm provided a

spatial resolution of 18.6 nm in the reconstructed phase image.
The second data set was acquired at standard diffraction lens settings (89% excitation) with a Lorentz magnification of 32.0kx operating the biprism at 240 V, yielding a FOV of 1.43×1.43 µm. These settings produced interference fringes spaced at 1.8 nm and sampled with 6 pixels each, resulting in a spatial resolution of 5.4 nm in the reconstructed phase images.
In both data sets, stacks of 16 holograms were recorded with an acquisition time of 8 s per hologram to improve the phase sensitivity, particularly to compensate for the low contrast in the LM holograms.
The phase images reconstructed from both data sets are shown in Fig. 44. The corresponding LM amplitude images indicate that a weak and homogeneous diffraction contrast was achieved by tilting the specimen off-zone axis, thereby validating the phase analysis across the InP p-n junction.
Notably, the phase images reveal that the specimen surface appears relatively rough, despite using the same preparation procedure as for the GaAs specimen. This surface roughness seems to be a recurring issue with InP specimens, as similar inhomogeneities were observed in comparison lamellae. An example for another lamella (InP-2) prepared of the same bulk InP specimen is presented in Fig. 45 for comparison, with phase data acquired using standard EH settings. As mentioned in Sect. 4.3.1, InP is reported to be more susceptible to FIB-induced surface damage compared to GaAs, primarily due to the larger atomic mass difference between In and P.[116] However, this observation primarily concerns the extent of the amorphous surface damage. Interestingly, when the electrical damage in the present InP-1 specimen was evaluated, as shown in Fig. 46a, using the standard method of measuring the phase step across the junction as a function of crystalline specimen thickness (thus excluding the amorphous layer), t_i is quantified as 103 ± 18 nm. This value is significantly smaller than the electrical damage depth of 165 ± 29 nm observed in the GaAs specimen. This finding was confirmed in the analysis of another FIB lamella prepared from the same bulk InP specimen, which yielded an electrically damaged thickness of 115 ± 18 nm.
Based on these estimates of t_i in InP, the thinnest region of the current specimen, with a crystalline thickness of 126 nm, was excluded from subsequent phase evaluations. The phase contrast from the active dopants remaining in this region was too weak for accurate assessment, as evident in the phase image shown in Fig. 44t1.
The step in phase across the InP p-n junction measured in the two data sets with different spatial resolutions match well, as evident from Table 7.

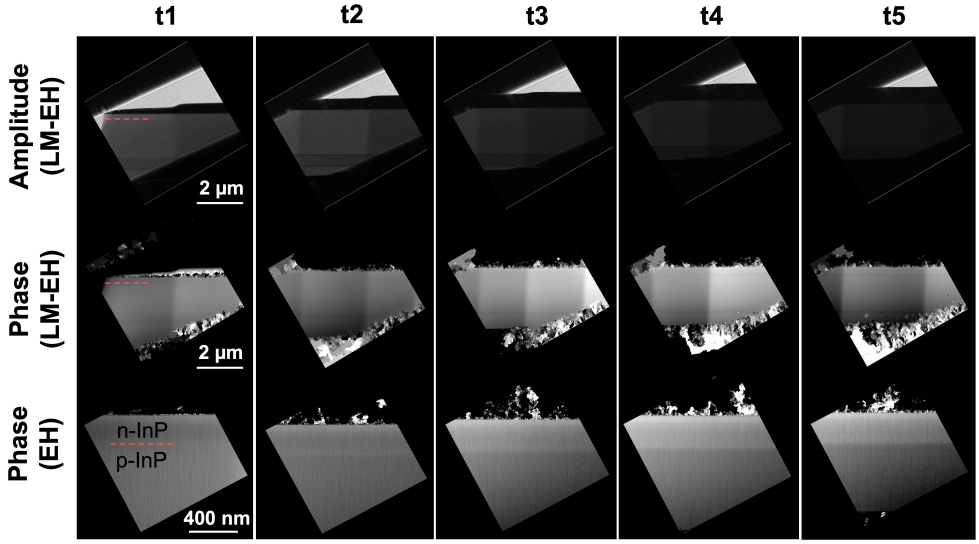

Figure 44: *Amplitude and phase images reconstructed from electron hologram stacks recorded at thickness regions t1–t5 of the InP specimen using low-magnification (LM) (top and middle rows) and standard (bottom row) EH settings.*

Table 7: Comparison of phase shifts measured across the InP-1 p-n junction at different specimen thicknesses using standard and low-magnification (LM) EH. The crystalline thicknesses (t_c) were measured using STEM-CBED. The active thickness (t_a) is derived by subtracting the inactive layer (averaging 109 ± 18 nm in InP) from the crystalline thickness. The measured phase shifts are compared with predicted values simulated for the active thickness.

Thickness [nm]		**Step in phase [rad]**			
		Simulation	**Experiment**		**Dev.**
t_c	t_a ± 18 nm		LM ± 0.08 rad	Standard ± 0.03 rad	
126 ± 1	17	0.15	–	–	–
170 ± 1	61	0.55	0.3	0.3	45%
256 ± 1	147	1.34	0.6	0.6	55%
273 ± 2	164	1.49	0.8	0.8	46%
381 ± 6	272	2.47	1.1	1.2	51%

Fig. 46b compares the phase distributions measured across the same specimen region (t4). Despite the differences in nominal spatial resolution between the standard (5.4 nm) and LM (15 nm) phase data, both data sets yield a consistent phase distribution. This highlights that the key factor in accurate phase detection is not solely spatial resolution, as the dopant potential changes with low frequency. Consequently, the width of the p-n junction is much broader compared to the compositional width of the interface. This justifies the use of LM EH for junction analysis in chip-prepared specimens for *in situ* biasing experiments, which require large FOV acquisitions. As long as the spatial resolution is smaller than the expected depletion width (sufficient to resolve it), and the measured phase shift contains a dominant contribution from the dopant

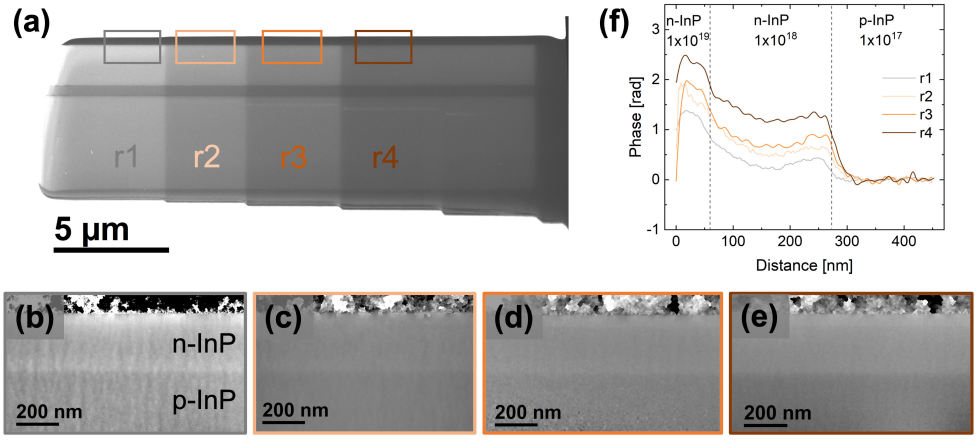

Figure 45: *Phase measurements of another InP lamella (InP-2), prepared of the same bulk specimen, are shown here for comparison. (a) Overview BF-TEM image of the specimen highlighting thickness regions labeled r1–r4. (b)–(e) Phase images reconstructed from holograms taken at the positions indicated in (a). (f) Phase distributions measured across the structure at each region. Each phase image was obtained from stacks of 30 holograms recorded with an 8 s acquisition time per hologram, using standard diffraction lens settings, a biprism voltage of 200 V, and a magnification of 28.5kx, resulting in a fringe spacing of 2.3 nm.*

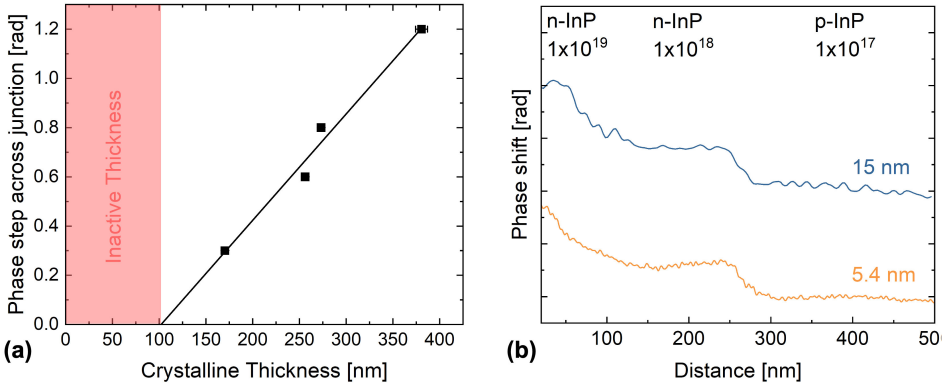

Figure 46: *(a) Evaluating the measured step in phase across the InP p-n junction as a function of the total crystalline specimen thickness yielded an inactive thickness of* 103 ± 18 *nm. (b) Comparison between standard and low-magnification (LM) phase data. The phase profiles were derived across the t4 region from the respective phase images shown in Fig. 44, having a spatial resolution of 5.4 nm and 15 nm, respectively. The profiles have been deliberately offset for clarity.*

potential, the limiting factor is providing adequate phase sensitivity to resolve changes in electrostatic potential across the specimen. This is particularly evident when studying low-doped p-n junctions, such as the present InP specimen, where the junction, p-doped at 1×10^{17} and n-doped at 1×10^{18}, yields a relatively weak phase contrast. The phase sensitivities of the standard and low magnification data sets were assessed as 0.03 rad and 0.08 rad, respectively, which are sufficient to resolve the junction. This is evident from Table 7, which shows the predicted phase shift across the InP p-n junction for each electrically active specimen thickness, with the inactive layer (averaging 109 ± 18 nm in InP) already subtracted. As previously mentioned, the thinnest region, with only approximately 17 nm of active thickness remaining, was excluded from the analysis. Although the expected phase step of 0.15 rad lies above the phase resolution threshold, additional noise from specimen roughness prevents clear resolution of the junction in this region. In t2, the thinnest region used in the phase analysis, the expected phase shift across the p-n junction is 0.55 rad, which is well above the phase resolution limit. Despite accounting for the inactive thickness in the simulations, the measured phase shifts underestimate the predicted values, as was previously observed for the GaAs specimen. This can again be attributed first to the simplicity of the 1D-potential simulations, which do not consider the surface band-bending effects induced by damage across all three dimensions of the specimen. Second, the estimation of inactive thickness relies on two assumptions, a clear boundary between the damaged and undamaged regions, without considering partially depleted transition zones, and a uniform thickness of t_i across the specimen. However, since the inactive layer and the Fermi level pinning induced surface band bending vary with dopant type and concentration, this assumption is particularly inaccurate for p-n junctions, especially when they are asymmetrically doped, as in the present InP specimen.

The difference between the 1×10^{18} and 1×10^{19}-doped n-type layers could be detected, but the expected phase shift of 0.19 nm for region t2 is close to the measurement limit. Thus, as specimen thickness increases, the accuracy of the measurement improves, which holds true for the analysis of the p-n junction as well. This is clearly illustrated in the phase images in Fig. 44, taken at standard settings, where the phase contrast between the differently doped layers becomes increasingly distinct with greater sample thickness.

While the phase sensitivity allowed resolving the step in phase at the p-n junction, the noise level resulting from the rough specimen surface in addition to the low doping was too high for reliable depletion width assessment from the correlated electric field profiles, as the differential process amplifies existing noise in the phase data. This underscores the importance of high specimen quality and, ideally, higher doping levels for precise characterisation of the space charge region.

In summary, for specimen preparation and EH analysis, the phase measurements of p-n homojunctions demonstrate the feasibility of using LM EH for accurate junction analysis on specimens prepared for *in situ* biasing experiments. The specialised diffraction lens settings provide a sufficiently large FOV to keep both, the junction of interest and the vacuum reference in the FOV, while maintaining a sufficient spatial resolution to accurately measure the junction's depletion width. Importantly, the measured phase distributions were consistent across standard and LM EH settings, as long as the spatial resolution and phase sensitivity were adequate to resolve the junction depletion width and potential differences across the semiconductor structure, respectively.

For GaAs specimens with high surface quality and suitable dopant concentration of 1×10^{18} cm^{-3}, the measured depletion width was independent of specimen thickness, as long as the thickness balances the trade-off between approximating kinematic conditions and yielding a sufficient contribution from active dopants in the phase shift. For the GaAs specimen, the applicable thickness range was about 250–600 nm. In this context, minimising surface damage during preparation proved essential for capturing a clear signal from dopants without requiring excessive sample thicknesses that might compromise phase accuracy. Additionally, evaluating the thickness of the electrically damaged surface layers helps in selecting suitable measurement regions, which were estimated here as 165 ± 29 nm for GaAs and between 103 ± 18 and 115 ± 18 nm for InP. These results also emphasise the importance of minimising dynamical diffraction effects, especially in long lamellae of III-V materials fixed on biasing chips, which are susceptible to bending. Additionally, amplitude images should be used to confirm the minimization of dynamical contributions, ensuring an appropriate ROI is selected for reliable potential distribution analysis across the junction.

6.5 Electrostatic Potential Analysis of *in situ* Electrically Biased III-V P-N Junctions

The study of semiconductor specimens under *in situ* applied bias inside the (S)TEM is crucial for comprehensive and meaningful device analysis. One example is the quality assessment of tunnel junctions in MJSCs, which will be discussed in detail in Ch. 8. By applying a bias, operational conditions such as light illumination can be simulated, allowing for the evaluation of tunnelling performance within the current regimes pertinent to intended applications, specifically regarding varying illumination intensities. To facilitate these experiments, it is essential to establish a methodology for preparing *in situ* specimens and to verify the biasing of the p-n junction using the *in situ* biasing TEM setup employed in this work. For these *in situ* biasing reference measurements, the GaAs p-n homo-junction introduced in Sect. 6.1 is utilized. Due to its well-known electrical properties, which have been extensively studied using EH, GaAs p-n junctions serve as an ideal reference sample.[40,200,201,125,121]

In this section, the electrical characteristics of the GaAs p-n junction, specifically the built-in potential and depletion width, under *in situ* applied bias are investigated using EH. Based on these measurements, preparation-induced artifacts and effects related to electron-beam illumination are discussed. To examine the influence of the FIB-deposited metal contacts on the semiconductor during *in situ* biasing, two different samples were prepared from the same GaAs bulk specimen: one with ion-beam-induced W deposition (GaAs-W) and the other with ion-beam-induced Pt deposition (GaAs-Pt). The impact of the FIB-deposited contact resistance on *in situ* biasing and EH analysis is evaluated by means of these two contact materials.

6.5.1 Experimental Description

The details of the GaAs-W and GaAs-Pt FIB preparation are listed in Table 4. The main considerations for specimen chip-preparation for *in situ* biasing experiments are given in Sect. 4.4 and a schematic illustration of the TEM lamella geometry designed for *in situ* biasing experiments as well as of the intended electrical circuit within the TEM lamella can be found in Fig. 22. Overview images of the GaAs-Pt and GaAs-W specimen, including indications of the electrical

connections to the biasing MEMS support chip, as well as of the hologram acquisition ROI, are shown in Fig. 47a and b. The crystalline thicknesses of the specimen ROI, measured by means of STEM-CBED analyses, are 450 ± 17 nm for GaAs-W and 370 ± 10 nm for GaAs-Pt. In the respective sample, Pt (or W) serve as electrical top and back contact of the GaAs lamella to the metal tracks of the chip. The specimen support chip is mounted in the Protochips Aduro 500 biasing TEM specimen holder, where the chip metals tracks can be contacted individually. *In situ* biasing of the samples was performed using a Keithley power supply connected to the TEM holder. The EH experiment is performed in the FEI Titan Ultimate at 200 kV. The electrical bias was applied to the top metal contact of the samples due to its proximity to the studied p-n junction. The back contact was connected to ground (GND). As the bias is thereby applied to the p-side of the GaAs junction, a positive voltage (+V) corresponds to forward biasing of the junction, while a negative voltage (-V) corresponds to reverse biasing.
Electron holograms were acquired at a range of different applied voltages - -6 V to +6 V for GaAs-W and -3.5 V to +3.5 V for GaAs-Pt - using the acquisition parameters listed in Table 8. To prevent the specimen from over-heating, the current flowing through the junction was limited to 100 µA by setting the compliance current in the Aduro Software. Using LM EH settings allowed both the specimen p–n junction and the vacuum reference region above it to fit within the image FOV.

Table 8: Acquisition settings for the *in situ* biasing electron hologram analysis of the GaAs-W and GaAs-Pt specimen. The spatial resolution in the phase image results from the mask size applied in the Fourier reconstruction.

Hologram acquisition parameter	GaAs-W	GaAs-Pt
C2 aperture	100 µm	100 µm
Diffraction lens excitation	20%	15%
Lorentz magnification	40.0kx	40.0kx
Biprism voltage	80 V	130 V
Pixels per fringe	4	3
Fringe spacing	6.2 nm	3 nm
Spatial resolution (phase image)	18.6 nm	15 nm

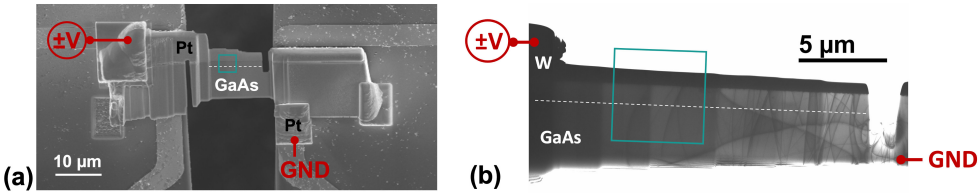

Figure 47: *(a) SE SEM image of the GaAs-Pt specimen and (b) BF TEM image of the GaAs-W specimen prepared on MEMS support chips for in situ biasing experiments. The positions of the electrical bias (±V) and ground (GND) connectors are marked in red. The region of interest (ROI) for in situ biasing hologram acquisitions is highlighted in turquoise, and the GaAs p-n junction is indicated by the white dashed line.*

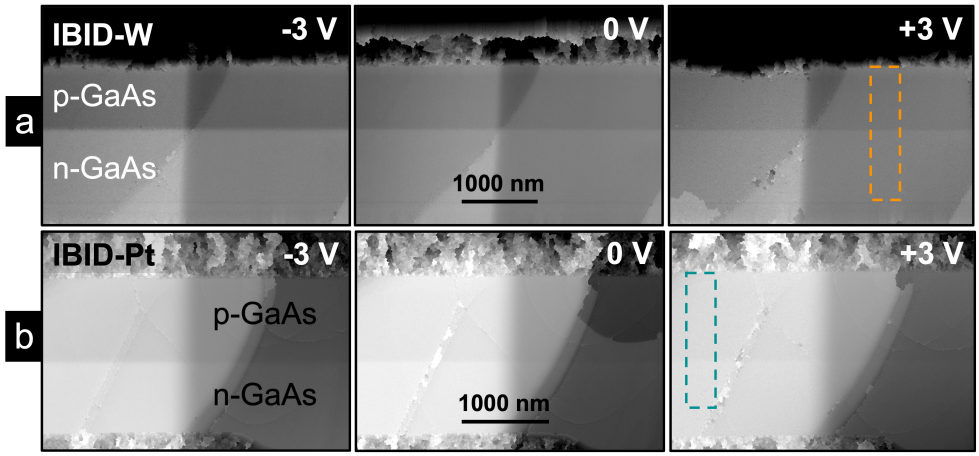

Figure 48: *Phase images of the p-n junction in a) the GaAs-W specimen and b) the GaAs-Pt specimen at selected reverse (-) and forward (+) bias voltages. Phase profiles for each specimen, shown in Figs. 49 and 55, are extracted from the indicated regions.*

6.5.2 The Built-In Potential of the GaAs p-n Junction Under Applied Bias

Fig. 48 shows the phase images reconstructed from the hologram stacks taken of the GaAs-W and GaAs-Pt at -3 V, 0 V and +3 V. The differently doped regions of the GaAs are distinguishable in all phase images due to the phase contrast variation. As described in Sect. 6.2, applying a reverse/forward bias to a p-n junction leads to an increase/decrease of the potential difference between the p-type and the n-type layer, as well as to an increase/decrease of the depletion width. The phase images clearly illustrate this expected effect of applying an electrical bias to the GaAs junction: the phase contrast, related to the difference in potential, between the differently doped GaAs layers increases under reverse bias and decreases under forward bias.

Electron phase profiles were retrieved across the p-n junction by averaging over a width of 200 nm. The results for reverse biasing are shown in Fig. 49a for GaAs-W and Fig. 49b for GaAs-Pt. These reveal more clearly that the height of the step in phase across the p-n junction is increasing with increasing applied voltage in reverse direction.
Assuming that the entire applied bias is dropped across the p-n junction, the built-in potential at the junction in equilibrium state (without applied bias) should be increasing by the magnitude of the applied reverse voltage, as described by Eq. 49. To verify the biasing of the specimen, the built-in potential ΔV_{n-p} at different applied voltages is quantified from the phase step $\Delta\Phi_{n-p}$ using Eq. 52, accounting for the estimated electrically inactive surface thickness (t_i).

$$\Delta\Phi_{n-p} = \mathrm{C_E}\Delta V_{n-p}(t_{crystalline} - t_{inactive}) \tag{52}$$

For GaAs-W, $t_i = 151 \pm 23$ nm is estimated from the non-biasing EH analysis of this specimen. As the GaAs-Pt lamella does not have a sufficient number of different thicknesses to derive the inactive thickness, the value of 165 ± 29 nm measured from the GaAs-Au sample was applied. Fig. 50 shows the built-in potential across the junction as a function of applied bias for both

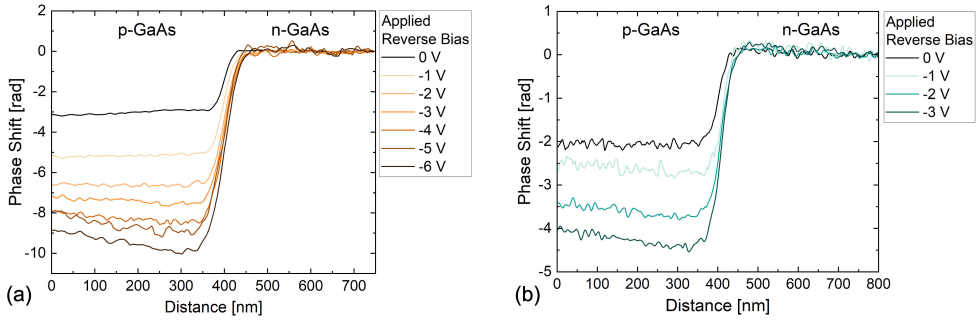

Figure 49: *Phase profiles measured at different applied voltages across the p-n junction in the (a) GaAs-W specimen at $t_c = 450 \pm 17$ and (b) the GaAs-Pt specimen at $t_c = 370 \pm 10$.*

specimen, GaAs-W and GaAs-Pt.

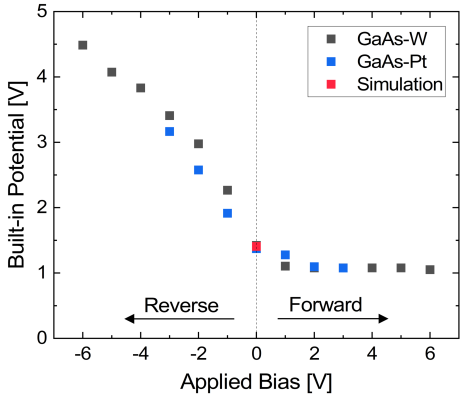

Figure 50: *The built-in potential across the GaAs p-n junction plotted as a function of the applied voltage.*

Firstly it is evident that, when accounting for t_i, at 0 V applied bias the measured built-in potential of the GaAs specimen p-n junction, 1.37 V in GaAs-Pt and 1.42 V in GaAs-W, is similar to the 1.41 V expected from the simulations (see Table 5). The slightly higher deviation for the GaAs-Pt sample can be explained by the fact that the assumed t_i was not specifically measured for this specimen. And although the same FIB-milling protocol was applied for all samples, t_i was observed to vary slightly from one sample to the next due to uncontrollable factors. Such might include minor deviations in the positioning of the sample on the chip relative to the ion beam or deviations of the actual ion beam currents from the values selected in the software, which occur with increasing use of the FIB due to the wear and expansion of the apertures.

With applied bias, the behaviour of the built-in potential seen in Fig. 50 is generally as expected, i.e. it is increasing with reverse bias, while it slightly decreases with forward bias. However, the absolute change in ΔV_{n-p} upon biasing is not equal to the amount of applied voltage as it is expected from theory. For example, at a reverse bias of -2 V, ΔV_{n-p} should be increasing from

1.41 V at 0 V to 3.41 V. However, the measured values are 2.58 V in GaAs-Pt and 2.98 V in GaAs-W. Hence, only 1.21 V and 1.56 V of the 2 V applied voltage are dropped across the p-n junction in the GaAs-Pt and GaAs-W respectively, indicating that some of the applied voltage is lost in the system, thus reducing the amount of voltage dropped across the junction. Another indication of this loss of voltage is evident from the measured built-in voltages at forward applied bias. When the applied forward voltage is larger than the built-in potential of the GaAs junction at equilibirum state ($V_{bi} = 1.41$ V), the potential barrier between the p- and n-type should disappear. However, the built-in potentials in GaAs-W and GaAs-Pt stagnate at about $\Delta V_{n-p} = 1$ V for forward voltages ≥ 2 V.

6.5.3 The Depletion Width of the GaAs p-n Junction Under Applied Bias

The depletion width, W_d, of the GaAs p-n junction in both specimen is derived from the electric field distribution, which is quantified as the first derivative of the electrostatic potential distribution using Eq. 51. Fig. 51a and b show the electric field profiles for the GaAs-W and GaAs-Pt at different applied reverse biases.

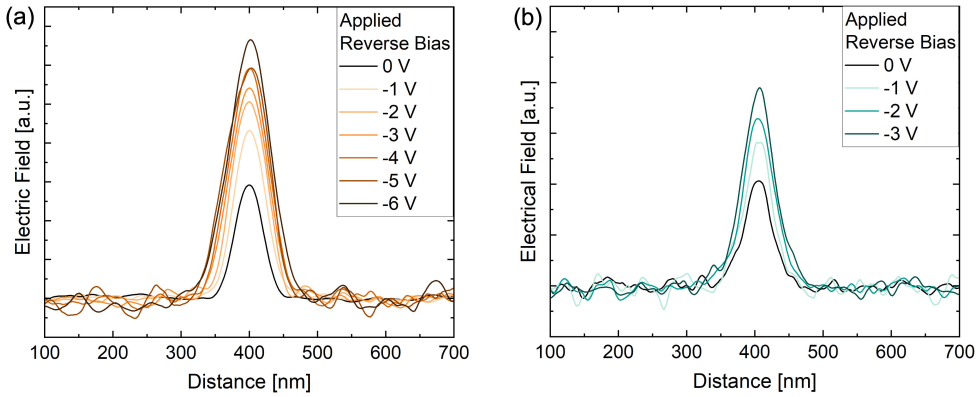

Figure 51: *Electric field distribution across the p-n junction in the (a) GaAs-W specimen at $t_C = 450 \pm 17$ and (b) the GaAs-Pt specimen at $t_C = 370 \pm 10$. The profiles were derived from the experimental potential profiles using the first differential equation (Eq. 51).*

It is already evident by eye that the peak in electric field strength at the p-n junction, corresponding to the depletion width W_d, is widening upon increasing reverse bias. Using the procedure outlined in Sect. 6.4.1, the depletion width is quantified from these profiles as the distance between the x-intercepts of the linear extrapolations of the peak edges to the x-axis. The results for both specimen are plotted in Fig. 52 as a function of the applied bias in comparison to the depletion width expected from simulations of the present GaAs structure (see Sect. 6.3).
Firstly, the depletion width of 82 ± 1 nm measured in the GaAs-Pt specimen without applied bias (at 0 V) is comparable to the values of 81 ± 1 nm in GaAs-W and 83 ± 1 nm in GaAs-AuPd, presented in the previous Sect. 6.4.1. This confirms that the junction depletion width can be reproducibly measured across different TEM lamellae, prepared from the same bulk specimen using a careful and consistent preparation scheme. As previously discussed, these experimental values at 0 V are higher than the depletion width of 62 nm expected from simulations. This was

primarily ascribed to the lower abruptness of the actual p-n junction, the incomplete ionization of p- and n-type dopants in the specimen, as well as the inclusion of partially depleted transition regions in the measured depletion width.
Secondly, the overall observed trend of the depletion width with applied voltage meets the expectations, as it significantly increases under reverse bias. The anticipated reduction of W_d with forward bias is more pronounced in the GaAs-Pt specimen, although it is also slightly noticeable in the GaAs-W sample. However, Fig. 52 shows that the relative increase of W_d with each reverse bias step is considerably smaller compared to the simulations.
Based on the properties of the simulated 'ideal' p-n junction (see Sect. 6.3), the anticipated increases in W_d are 36 nm for a voltage change from 0 V to -1 V, and 26 nm for a change from -1 V to -2 V. In the GaAs-W sample, the increase in W_d is 16 nm from 0 V to -1 V and 8 nm from -1 V to -2 V, corresponding to 44% and 31% of the theoretical increase, respectively. In GaAs-Pt, the increases are 9 nm and 7 nm, respectively, corresponding to 25% and 27% of the theoretical values. This deviation is another indication for the voltage loss, previously observed in the context of the measured built-in potential.

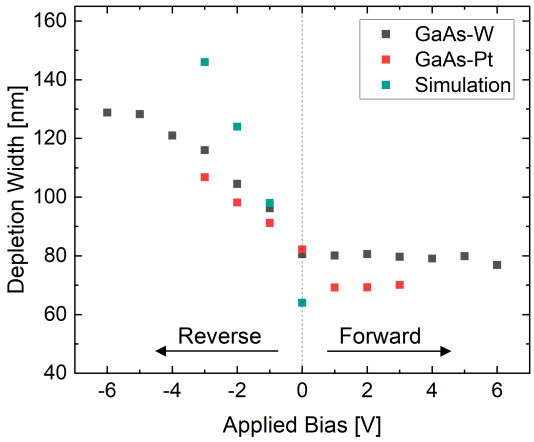

Figure 52: *Width of the depletion region at the p-n junctions in the GaAs-W and GaAs-Pt specimen as a function of the applied voltage, measured by means of the electrical field profiles in Fig. 51. The expected values for the ideal junction (abrupt and complete ionization) under reverse bias, derived from the* NEXTNANO *simulation of the GaAs specimen, are shown for comparison.*

6.5.4 The Electrical Circuit of the *In Situ* Biasing Specimen

To identify the source of the observed voltage loss, the electrical circuit of the sample must be analysed. This circuit, along with the cut geometry of the *in situ* biasing lamella, is illustrated in Fig. 22. The p-n diode is connected in series with the resistances of the substrate and the top and bottom metal contacts, while the surface resistance is connected in parallel.
The total resistance of the sample lamella can be estimated from its current-voltage (I-V) characteristics, which is shown in Fig. 55a for the GaAs-W specimen. At an applied voltage of 5 V the sample draws a current of 7.72 µA. Applying Ohm's law, this corresponds to a total sample resistance of 6.5×10^5 Ω. Analyzing the sample circuit reveals that the total resistance arises

from the combination of the series resistances of the p-n diode, the substrate, and the top and bottom metal contacts, along with the parallel-connected surface resistance.

6.5.4.1 Parallel Resistance

Firstly, the parallel resistance of the specimen surfaces is considered. This resistance is strongly influenced by the specimen preparation process, as FIB-induced surface damage reduces the surface resistance significantly. Although efforts are made to minimise this damage – primarily through careful FIB milling at low beam energies and small ion incidence angles (see Ch. 4.4) – a thin amorphous damage layer remains on both sides of the specimen and on its edges.

This amorphous layer is doped with Ga-ions implanted during the FIB process, which increases the conductivity of the layer, thereby creating a low-resistivity path for active carriers during *in situ* biasing. This can result in short circuits for the current during the *in situ* biasing experiment. To ensure the success of the biasing experiment, it is crucial to minimise this leakage current to prevent the specimen from excessively drawing current and overheating, which could damage or cause failure of the diode. However, the present potential measurements of the GaAs specimen show that the currents flowing through the residual damaged surfaces in parallel are not limiting. In fact, the parallel surface resistance decreases the overall resistance of the system, thus increasing the total current. However, it does not affect the amount of potential which is dropped across the p-n junction diode. This voltage loss in the system is solely attributed to the series resistances.

6.5.4.2 Series Resistances

The series resistances include both the substrate resistance and the contact resistances. In an ideal biasing setup, these series resistances should be minimised to prevent parasitic losses that would decrease the voltage dropped at the p-n junction. However, this is not always achievable in practical experiments. Hence, the individual series resistances were examined, starting with the substrate resistance. For a n-GaAs substrate with a doping concentration of 10^{15} cm^{-3}, a cross-section of 54 μm^2 and an average thickness of 400 nm, the substrate resistance was estimated to be approximately 10^3 Ω for the GaAs-W specimen. This value is significantly lower compared to the total resistivity of the specimen and thus plays only a minor role in contributing to the voltage loss.

Nevertheless, future samples could still be optimised in this regard, for example by reducing the cross-sectional area of the substrate, thus shortening the lamellae. However, the length of the lamella in our samples is constrained by the width of the chip trenches.

The primary contributor to the voltage loss, however, is the contact resistance at the top and bottom metal contacts, connecting the semiconductor specimen to the metal tracks of the biasing chip.

For electrical biasing experiments, generally a minimal contact resistance between the contact metal and the semiconductor specimen is desired to avoid parasitic voltage losses. Hence, ideally the specimen wafer comes with a pre-deposited ohmic contact. However, for the present unprocessed GaAs wafers, the metal (W or Pt) had to be deposited in the FIB via ion-beam-induced deposition (IBID), as described in Ch. 4.4. When regarding the resistivity of these FIB-deposited metal contacts, two factors have to be considered: first, the resistivity of the metal deposition

itself, which is significantly influenced by the FIB deposition procedure; and second, the metal-semiconductor contact resistance, which is governed by the work function of the metal deposit relative to the semiconductor work function.

As detailed in Sect. 4.4.2, the FIB-deposited metals (W or Pt) exhibit higher resistivities compared to pure, crystalline bulk metal due to changes in chemical composition (such as the incorporation of C and Ga impurities) and alterations in microstructure induced by the IBID process, which alter the conductive properties. However, the deposition procedure was optimised based on literature findings to maximize conductivity. The resistivities of the IBID-Pt and IBID-W contacts were estimated, based on comparable deposition conditions, to be 70−140 µΩ cm[130] and 200−250 µΩ cm[134,133], respectively.
However, the conductivity of the metal deposits and their optimization are fundamental for the construction of the circuit and the realization of the *in situ* biasing experiment, the resistive characteristics (ohmic or Schottky behavior) of the metal-semiconductor contact interface are primarily determined by the choice of metal in relation to the semiconductor material.

6.5.5 The GaAs-Pt and GaAs-W Semiconductor-Metal Contacts

In order to understand the characteristics of the metal-semiconductor interfaces in the GaAs-Pt and GaAs-W specimens, firstly the theoretical background of metal-semiconductor junctions is reviewed. Comprehensive physical explanations of metal-semiconductor interfaces can be found in standard references such as Neamen (2002) Ch. 9[196], Sze & Lee (2021) Ch. 3[197], which have been referenced in the following section. Here, only a brief summary of the key characteristics, relevant to the context of this work, is provided. This will be followed by predictions of the contact characteristics for GaAs-Pt and GaAs-W interfaces, derived from the theoretical concepts outlined earlier. These predictions will ultimately be compared to experimental results obtained through EH electrostatic potential analysis.

6.5.5.1 Theoretical Background: The Metal-Semiconductor Junction

Essentially, two types of metal-semiconductor junctions are distinguished based on the characteristics of the interface: Schottky contacts and ohmic contacts. The difference can be understood by means of the current-voltage (I-V) characteristics shown in Fig. 53. A Schottky contact exhibits non-linear I-V characteristics and thus rectifying (diode-like) behaviour, while ohmic contacts have a linear I-V characteristic and therefore a constant resistance. Hence, the ohmic contact is conductive regardless of the polarity of the applied external voltage. An ideal ohmic contact is referred to a low-resistance metal-semiconductor junction without a potential barrier or a depletion region forming at the junction. Consequently, the voltage drop across the contact is negligible compared to that across the bulk semiconductor.

Which type of contact applies to a given metal-semiconductor junction depends on the energy band structure and the Fermi level energy (E_F) of the constituent materials. For metal-semiconductor junctions commonly the work function is used as the reference value. The work function, ϕ, of a material is defined as the difference between the Fermi level and the vacuum level; or in other words, the work function is the amount of energy needed to remove a free electron

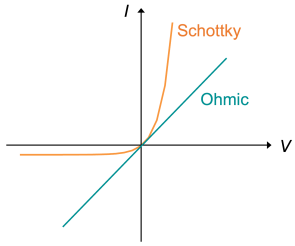

Figure 53: *Schematic I-V characteristics of Schottky (non-linear, rectifying) and ohmic (linear, non-rectifying) metal-semiconductor contacts.*

from the material to infinity. In thermal equilibrium, i.e. in the absence of an externally applied bias, the Fermi levels of the metal and the semiconductor in contact must align. To realize this alignment, electrons are extracted from the material with the lower ϕ to the material with the higher ϕ. This charge transfer results in the bending of the energy bands, just as it is the case for a semiconductor p-n junction. The direction of the electron transfer and the degree of the band bending, defining the characteristics of the contact (V_{bi} and W_d), depend on the difference of the work function of the metal (ϕ_m) and the semiconductor (ϕ_s). For $\phi_m > \phi_s$, electrons are extracted from the semiconductor to the metal, and vice versa for $\phi_m < \phi_s$. Whether this leads to formation of a depletion region or not, i.e. a Schottky or ohmic contact, depends on the doping type of the semiconductor, i.e. the nature of the majority carriers. Both, the doping type and doping concentration of the semiconductor are decisive for the contact properties, as they fundamentally governs its Fermi energy level and thus its work function. Consequently, four different metal-semiconductor junction configurations arise, which, based on the relative difference of ϕ_m and ϕ_s, can be classified as one of the two contact types: Schottky or ohmic. The assignments are shown in Table 9, while schematic energy band diagrams of all four configurations are presented in Fig. 54.

Table 9: Metal-semiconductor junction configurations and the assigned contact types based on the difference of the work function of the metal (ϕ_m) and the semiconductor (ϕ_s) (modified after Razeghi *et al.* (2019)[9]).

Junction Configuration	**Semiconductor**	**Contact Type**
$\phi_m > \phi_s$	n-type	Schottky
	p-type	ohmic
$\phi_m < \phi_s$	n-type	ohmic
	p-type	Schottky

For the case of a Schottky contact forming at the semiconductor-metal interface, the potential barrier which is forming controlls the conducting and rectifying behaviour of the contact. The key properties of a Schottky contact are the Schottky barrier height (ϕ_{SB}), and the built-in potential (V_{bi}) and the depletion width (W_d) on the semiconductor side of the contact interface. These parameters can be comprehended by means of the band structure schematics in Fig. 54. The Schottky barrier, ϕ_{SB}, is the potential barrier for the electrons in the metal at the interface to the semiconductor. In the ideal case, i.e. neglecting surface states, the height of a Schottky

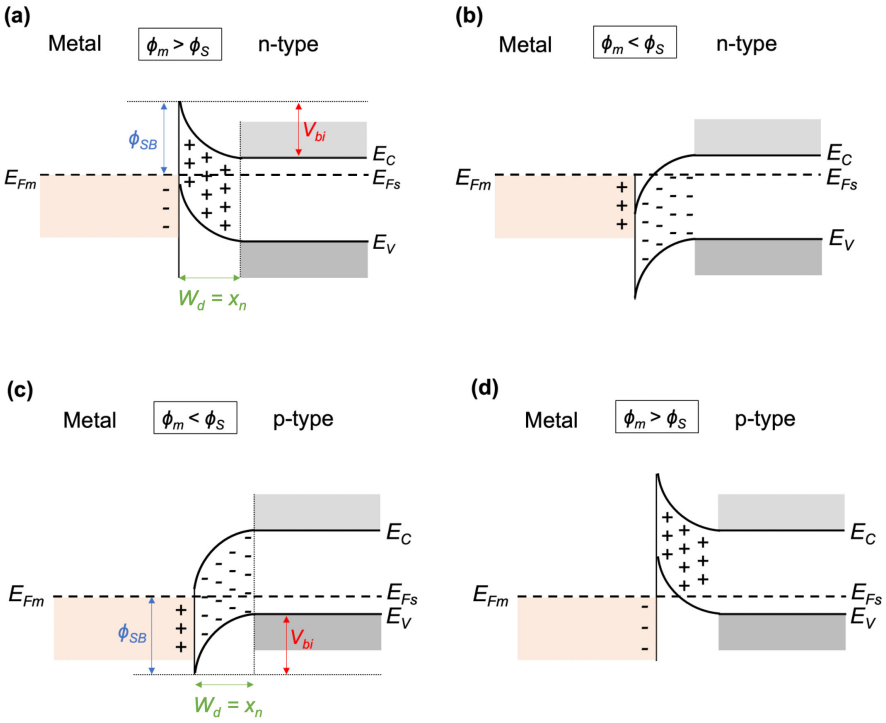

Figure 54: *Schematic energy band diagrams illustrating the four possible metal-semiconductor configurations, as summarized in Table 9. For Schottky contacts [(a) and (c)], a depletion region of width W_d forms on the semiconductor side, and majority carriers encounter a potential barrier of height V_{bi} at the interface. The barrier for electrons in the metal is the Schottky barrier, ϕ_{SB}. In contrast, for ohmic contacts [(b) and (d)], no depletion region forms, and majority carriers face no potential barrier at the interface.*

barrier for a n-semiconductor/ metal contact (ϕ_{SBn}) and a p-semiconductor/ metal contact (ϕ_{SBp}) is given by[196]

$$\phi_{SBn} = (\phi_m - \chi) \tag{53}$$
$$\phi_{SBp} = E_g - (\phi_m - \chi) \tag{54}$$

The built-in potential barrier on the semiconductor side of the contact is then given by

$$V_{bi}(\text{n-type}) = \phi_{SBn} - \phi_n \tag{55}$$
$$V_{bi}(\text{p-type}) = \phi_{SBp} - \phi_p \tag{56}$$

where ϕ_n is the energy difference between E_C and E_F in the n-type semiconductor, and ϕ_p is the energy difference between E_V and E_F in the p-type semiconductor, which are respectively defined as

$$\phi_n = \frac{\mathrm{k}T}{q}\ln\left(\frac{N_C(T)}{N_d}\right) \tag{57}$$
$$\phi_p = \frac{\mathrm{k}T}{q}\ln\left(\frac{N_V(T)}{N_a}\right) \tag{58}$$

where k is the Boltzmann constant, T is the temperature, $q = (1.6 \times 10^{-19})$ C is the elementary charge, and $N_C(T)$ and $N_V(T)$ are the effective conduction band density of states and the effective valence band density of states, respectively. N_d and N_a are the n-type (donor) and p-type (acceptor) doping concentrations, respectively.

The width of the depletion region, W_d, on the semiconductor side of the contact interface can be calculated similarly to that of a one-sided p-n junction. For an n-type semiconductor it is given by

$$W_d = x_n = \left[\frac{2\epsilon_s(V_{bi} + V_R)}{qN_d}\right]^{1/2} \tag{59}$$

and for a p-type semiconductor by

$$W_d = x_p = \left[\frac{2\epsilon_s(V_{bi} + V_R)}{qN_a}\right]^{1/2} \tag{60}$$

where V_R is the applied reverse bias. ϵ_s is the permittivity of the semiconductor material given by $\epsilon_s = \epsilon_0 \times \epsilon_r$, where $\epsilon_0 = 8.85 \times 10^{-14}$ Fcm is the vacuum permittivity.

6.5.5.2 Theoretical Predictions of the GaAs-Pt and GaAs-W Contact Characteristics

Based on the concepts introduced in the preceding paragraph, the junction characteristics of Pt and W contacts to n-GaAs and p-GaAs can be estimated by considering the work functions of these materials. For simplicity, a polycrystalline film of the pure metals was assumed. The work function of Pt is ϕ_m (Pt, poly) = 5.65 eV[202,196], and of W ϕ_m (W, poly) = 4.55 eV.[202,196]

Certainly, the properties of the FIB-deposited metals will differ from these values due to the ion-beam-induced introduction of C and Ga impurities, as well as due to the changes in microstructure, described in Sect. 4.4.2. However, the work functions of FIB-deposited Pt and W are not well-documented, so the values for the pure, crystalline metals were assumed in this approximation.
The work function of n-GaAs and p-GaAs can be derived by means of the following relations for p-type and n-type semiconductors:

$$\phi_s(\text{p-type}) = \chi + E_g - (E_F - E_{VB}) \quad (61)$$

$$\phi_s(\text{n-type}) = \chi + (E_{CB} - E_F) \quad (62)$$

GaAs has an energy bandgap of $E_g(300\ \text{K}) = 1.424$ eV and an electron affinity $\chi = 4.07$ eV.[61] The energy position of the valence band, E_{VB}, and the conduction band, E_{CB}, for the n-GaAs and p-GaAs specimen region are derived from the NEXTNANO band structure simulation of the 1×10^{18} cm^{-3} symmetrically-doped GaAs specimen, shown in Fig. 37a. Accordingly, Eq. 61 and Eq. 62 yield the work functions ϕ_s (p-GaAs) $= 5.43$ eV and ϕ_s (n-GaAs) $= 4.03$ eV. Based on the concepts outlined in Table 9 the different metal-semiconductor configurations for Pt and W, n-GaAs and p-GaAs are classified in Table 10. For the given doping concentration of 1×10^{18}cm^{-3}, W is expected to form a Schottky contact with both n-GaAs and p-GaAs, whereas Pt is anticipated to form a Schottky contact with n-GaAs but an ohmic contact with p-GaAs. Ohmic contacting of n-GaAs is generally more difficult due to its low work function compared to most standard metals.[202]

Table 10: Metal-semiconductor configurations present in the GaAs-W and GaAs-Pt *in situ* biasing specimen, with their predicted contact types (ohmic or Schottky), determined by comparing the work functions of the metals (ϕ_m) and the p- or n-doped GaAs (ϕ_s).

Metal/ Semiconductor	Junction Configuration	Contact Type
W/ p-GaAs	$\phi_m < \phi_s$ 4.55 eV < 5.43 eV	Schottky
Pt/ p-GaAs	$\phi_m > \phi_s$ 5.65 eV > 5.43 eV	ohmic
W/ n-GaAs	$\phi_m > \phi_s$ 4.55 eV > 4.03 eV	Schottky
Pt/ n-GaAs	$\phi_m > \phi_s$ 5.65 eV > 4.03 eV	Schottky

In order to assess the influence of the Schottky-type interfaces in the TEM lamellae on the resistive (or conductive) behaviour of the *in situ* biased specimen, the Schottky barrier height (ϕ_{SB}), as well as the built-in potential (V_{bi}) and the depletion width (W_d) on the semiconductor side of the contact interfaces were calculated based on the equations presented in the preceding section. Subsequently, the predicted values can be compared with the electrostatic potential measurements at the metal-semiconductor interface obtained via EH.

The following parameters are applied for the calculations:

$N_d(\text{n-GaAs}) = 1 \times 10^{18}\ \text{cm}^{-3}$
$N_a(\text{p-GaAs}) = 1 \times 10^{18}\ \text{cm}^{-3}$
$N_C(300\ \text{K, GaAs}) = 4.45 \times 10^{17}\ \text{cm}^{-3}$ [61]
$N_V(300\ \text{K, GaAs}) = 9.0 \times 10^{18}\ \text{cm}^{-3}$ [61]
$\epsilon_r(\text{GaAs}) = 12.9$ [61]
$\epsilon_s(\text{GaAs}) = 1.14 \times 10^{-12}\ \text{Fcm}$

The results are presented in Table 11. It can be assumed that these values underestimate the actual Schottky barrier in the samples, as the resistance of the FIB-deposited metal contacts is likely to be considerably higher compared to the pure, polycrystalline metal assumed in the calculations. The values can therefore be comprehended as minimum limit values.

Table 11: Theoretically predicted properties of the Schottky contacts in the GaAs-W and GaAs-Pt specimens.

Metal/ Semiconductor	Schottky Barrier Height	Built-in Potential	Depletion Width
W/ n-GaAs	$\phi_{SBn} = 0.48$ eV	$V_{bi,n} = 0.501$ eV	$W_d = x_n = 26.7$ nm
Pt/ n-GaAs	$\phi_{SBn} = 1.58$ eV	$V_{bi,n} = 1.601$ eV	$W_d = x_n = 47.8$ nm
W/ p-GaAs	$\phi_{SBp} = 0.94$ eV	$V_{bi,p} = 0.887$ eV	$W_d = x_p = 35.6$ nm

6.5.5.3 Experimental Analysis of the GaAs-Pt and GaAs-W Contact Characteristics

EH allows for qualitative and comparative analysis of the metal-semiconductor contact characteristics in the real specimen, as the phase distribution is sensitive to the built-in potential barrier and the depletion width on the semiconductor side of a Schottky contact, similar to the analysis of p-n junctions. To investigate the influence of the contact characteristics on the *in situ* biasing analysis of the GaAs p-n junction, the p-GaAs/Pt and p-GaAs/W interfaces in the GaAs-Pt and GaAs-W specimens were selected for comparative analysis for two main reasons: first, these top-surface contacts can be easily included in the hologram FOV alongside the GaAs p-n junction using LM-acquisitions. Second, the two interfaces are expected to exhibit distinct differences in potential distribution, as theoretical calculations predict ohmic behavior for the p-GaAs/Pt junction, while the p-GaAs/W contact is anticipated to display Schottky-like characteristics.

Fig. 55 shows the full phase distributions, derived from phase images recorded under varying applied reverse biases, starting from the metal/p-GaAs interface and extending across the p-n junction. At first glance, it is evident that the contact properties differ significantly.
For the Pt/p-GaAs interface, the phase shift is decreasing towards the contact, suggesting a decreasing potential towards the metal, which is characteristic of an ohmic contact to a p-type semiconductor. As the metal work function (ϕ_m) exceeds that of the semiconductor (ϕ_s), holes flow from the IBID-Pt into the p-GaAs until the Fermi levels align. This hole injection produces an accumulation on the semiconductor side of the interface (illustrated in Fig. 54), leading to a

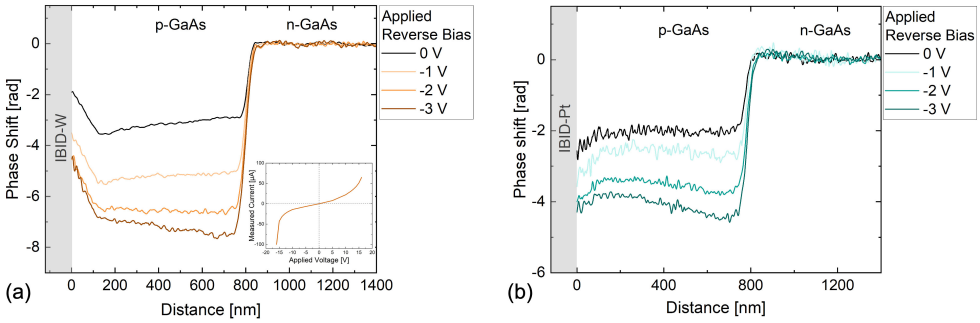

Figure 55: *Phase distribution starting from the metal/p-GaAs interface and extending across the GaAs p-n junction in (a) the GaAs-W specimen and (b) the GaAs-Pt specimen at different applied reverse biases. The I-V characteristics of the GaAs-W lamella are shown in the inset.*

slightly more negative phase contrast (i.e., a lower electrostatic potential) in the vicinity of the p-GaAs surface (Fig. 55b).

In contrast, the GaAs-W specimen exhibits a pronounced increase of the measured phase shift towards the metal, indicating the depletion region of the Schottky contact. This depletion region is also clearly visible in the phase images (Fig. 48a) as a bright phase contrast along the W/p-GaAs interface. As the metal work function (ϕ_m) is lower than that of the p-type semiconductor (ϕ_s), electrons flow from the IBID-W metal into the p-GaAs, forcing the semiconductor bands to bend upward until the Fermi levels of metal and semiconductor align. In this equilibrium state the p-GaAs region adjacent to the interface is depleted of holes, creating a potential barrier that impedes majority-hole transport to the contact, as illustrated in Fig. 54. The EH measurements therefore show an upward trend of the phase shift (i.e. the electrostatic potential) toward the W/p-GaAs interface (Fig. 55a).

The EH analysis thus confirms that the FIB-deposited Pt layer forms an ohmic contact to p-GaAs, whereas the FIB-deposited W layer forms a Schottky contact to the same p-GaAs. The IBID-W/n-GaAs bottom contact lies outside the FOV of the holography experiment; nevertheless, its Schottky character is evident from the I–V curve of the GaAs-W sample shown in Fig. 55a. The double Schottky contacts induce the characteristic symmetric I–V response. The interpretation of the I-V curve with respect to the potential drop at the p-n junction is not straightforward, as the metal contacts fundamentally control and influence the measured characteristics of the entire system. The cut-in voltage of the GaAs p-n junction should be close to the bandgap energy of 1.42 V.

The width of the Schottky depletion region at the contact interface, measured from the derivative of the phase profiles under zero applied bias, is with 133 ± 2 nm considerably broader compared to the 35.6 nm predicted for the ideal W/p-GaAs interface. However, these theoretical predictions are based on highly simplified and idealized models of metal-semiconductor contacts, which do not fully account for the complexities of the real specimen. Several factors contribute to these discrepancies, including the following:

- Firstly, as described in Ch. 4.4.2, the FIB-deposited metal layers are not pure in composition. They contain C and Ga impurities and exhibit microstructural deviations. For

instance, the Ga-doped W-C layers are typically amorphous[134,137], while the IBID-Pt forms micrometer-sized Pt grain networks embedded within a Ga-doped amorphous C matrix.[138,139,140]

- Secondly, the deposition of metal contacts on GaAs is inherently challenging due to several factors. GaAs surfaces are highly prone to As loss[203,204], and the high volatility of As often necessitates the use of a diffusion barrier layer (e.g., Ni)[205,206] prior to contact deposition to preserve the surface integrity. Furthermore, III-V semiconductors such as GaAs are particularly susceptible to Fermi level pinning caused by surface defect states. These defect states are introduced by the Ga-ion milling during FIB processing as well as by the metal deposition process itself. As a result, the induced surface Fermi level pinning can lead to the formation of Schottky barriers irrespective of the metal work function.[197,207,208]

- Thirdly, the quality of the metal contacts deposited via FIB is likely compromised by the less-than-ideal cleanliness of the deposition environment. Despite plasma cleaning of the semiconductor wafers prior to FIB processing, the transition from the plasma cleaner to the FIB chamber occurs under ambient air, which exposes the surface to potential contamination. Additionally, the FIB-SEM chamber itself is not a clean environment. Addressing this challenge will require the use of ultra-high vacuum (UHV) FIB-SEM systems and clean transfer mechanisms for bulk specimen loading, which would ensure better control over surface cleanliness during future contact deposition processes.

The factors outlined above contribute to the GaAs/metal contacts in the present specimens exhibiting generally higher resistance than theoretically expected. This supports the hypothesis stated before that the series resistance of the FIB-deposited contacts is the primary cause of the voltage loss during *in situ* biasing of the GaAs p-n junction, while the substrate resistance has a comparatively negligible influence, given by the relatively high conductivity of the n-doped GaAs substrate.
Ideally, ohmic contacts are required for reliable *in situ* biasing analysis of semiconductor p-n junctions, to ensure that the effects of the applied bias are solely attributed to the properties of the junction itself. Here, EH proved to be a valuable tool for investigating the nature and quality of contact characteristics in FIB-prepared specimens. This can aid in the selection of contacting metals for *in situ* biasing analysis, particularly for specimens that do not come with pre-deposited ohmic contacts. In the future, simulations of the metal-semiconductor interface that account for realistic effects, such as surface Fermi level pinning, could enable the quantitative analysis of contact potential barriers and resistance. However, these investigations were beyond the scope of this study. The primary focus here was to test and understand the influence of specimen preparation and the EH measurement conditions themselves on the observed electrical characteristics of the p-n junction under both biased and unbiased conditions.

Despite the observed voltage losses, the investigated p-n junctions exhibit the expected behavior under *in situ* applied bias, including the widening of the depletion width and the increase in the built-in potential of the junction. EH offers the significant advantage of measuring the electrostatic potential independently of the experimental circuit setup. The detected electron

phase shift is unaffected by the electrical connections within the *in situ* setup. Although, the behavior of the p-n junction still depends on the voltage that actually reaches the junction, which is influenced by losses in the circuit.
Since the phase shift measurement is independent of the circuit, this reduces the impact of preparation artifacts, such as contact resistance and short-circuit surface currents. This is particularly advantageous compared to methods like STEM-EBIC, discussed in the following chapter, where the induced current signal is detected through an amplifier connected to the circuit.

6.6 Summary

In this chapter, p-n junctions of simple binary III-V compounds, namely GaAs and InP, were employed to set up the EH methodology in preparation of characterising and measuring the electrostatic potential, particularly the depletion width, of p-n junctions in III-V multi-junction solar cells under *in situ* applied bias.
First, EH measurements without *in situ* biasing were conducted to optimise the experimental setup for the specific requirements of these specimens, focusing on achieving a sufficient hologram FOV, adequate phase accuracy, and spatial resolution to resolve junction depletion widths while minimising dynamical diffraction contrast.
The focus of this section was to investigate how specimen thickness affects the quantitative potential analysis of p-n junctions, emphasizing the critical importance of accurately determining the electrically active thickness for precise quantification of the built-in potential. For the specimens under study, the electrically damaged (inactive) thickness was approximately estimated at 151 ± 23 nm to 165 ± 29 nm for GaAs, and 103 ± 18 nm to 115 ± 18 nm for InP.
While the built-in potential was found to be highly sensitive to precise measurements of the active thickness, the depletion widths were reproducibly measured within a suitable thickness range of 250–600 nm. This range balances sufficient signal from active dopants (lower limit) and minimised dynamical diffraction effects (upper limit).
Using the optimised LM-EH experimental settings, the electrical characteristics – specifically the built-in potential and depletion width – of the GaAs p-n junction were analysed under *in situ* applied bias. The well-documented characteristics of the GaAs p-n junction allowed the focus on identifying preparation-induced artifacts and addressing challenges in designing an electrical circuit to ensure reliable biasing of the junction. The GaAs p-n junction exhibited typical behavior under applied bias, with the depletion width and built-in potential increasing under reverse bias, thus verifying the experiment. However, a comparison with theoretical predictions revealed discrepancies: the observed widening of the depletion region and the increase in the built-in potential barrier under reverse bias were smaller than anticipated. These deviations were attributed to a combination of factors mainly related to simulation assumptions and artifacts introduced by sample preparation. The numerical simulations of the electrical p-n junction characteristics rely on simplified and idealized assumptions, including a perfectly abrupt junction, neglecting the transition layer between the depletion region and the bulk semiconductor. Additionally, they are based on the intended doping concentrations, which ideally should be verified through SIMS profiling. However, even SIMS analysis cannot determine the number of electrically active dopant atoms. Here, the simulations assume full ionization for simplicity. Furthermore, the simulations do not account for the complex influence of the surface depletion layer, which varies depending

on the semiconductor material, doping type, and concentration. In addition to limitations in the simulations, artifacts introduced during sample preparation also had a significant impact. Examination of the electrical circuit revealed that the parallel resistance of the damaged surface regions – caused by FIB preparation – reduced the total specimen resistance by providing low-resistivity paths for active carriers. Nevertheless, these short-circuit paths were verified to not limit the biasing of the junction, as a dedicated FIB preparation scheme ensured minimization of the amorphous surface layer. The measurements of the built-in potential and depletion width under *in situ* applied bias also indicated that part of the applied bias was lost due to series resistance in the circuit, preventing the full voltage drop across the p-n junction. This voltage loss was primarily attributed to the potential barrier at the interface between the semiconductor specimen and the contacting metal. Ideally, the applied contacts should be ohmic to avoid parasitic voltage losses during *in situ* biasing. However, for non-contacted wafers, the simplest solution is depositing the metal directly onto the specimen during FIB preparation. Although applying metal via ion-beam-induced deposition does not create perfectly ohmic contacts and introduces some voltage losses, it was demonstrated that FIB-deposited metal can still serve as an effective contact, provided the contact resistance is not excessively high and does not prevent proper biasing. The observed junction response to applied bias confirmed the feasibility of this approach. Furthermore, it was shown that EH can be used to assess the quality and nature of the applied contact, effectively distinguishing between ohmic and Schottky behaviors. Hence, it proofed to be a valuable tool for optimising and adapting the conditions and nature of the metal deposition.

Having adapted and gained a better understanding of the method and sample preparation, the *in situ* biasing specimen preparation and EH analysis can now be applied to real III-V devices. While the method has limitations – primarily stemming from sample preparation – it remains effective, provided its drawbacks and associated influences are carefully considered.

7 STEM-Electron Beam Induced Current Analysis of *In-Situ* Biased III-V Semiconductor Junctions

Electron beam induced current (EBIC) analysis is an electron microscopy technique used to map the generation and extraction of charge carriers at p-n or Schottky junctions in semiconducting materials. It is widely applied in failure analysis of semiconductor devices, such as solar cells, enabling the study of charge carrier transport phenomena, including the minority carrier diffusion length [209,210,211], as well as the electrical activity of defects and grain boundaries. [212,213,214,215]

Traditionally, EBIC is conducted using scanning electron microscopy (SEM), but more recently, it has also been increasingly implemented in scanning transmission electron microscopy (STEM). [31,216,217,32] The broader adoption of STEM-EBIC has been limited by the demanding sample preparation requirements. For instance, building electrical connections to (S)TEM specimens is more challenging than with bulk samples in SEM. Furthermore, the FIB preparation alters the electrical properties of the lamella relative to the bulk material, as extensively discussed in the preceding chapters.

Nevertheless, STEM-EBIC offers significant advantages over SEM-EBIC. First, it enables current mapping at much higher spatial resolution, allowing for detailed analysis of nanoscale processes that influence the electrical performance of semiconductor devices. This enhanced resolution results from the thin specimen geometry and the high electron beam acceleration voltages, which minimise beam broadening and reduce the interaction volume. As a result, atomic-resolution STEM-EBIC mapping has been demonstrated. [32]

Second, STEM-EBIC can complement other (S)TEM methods, such as EH or 4D-STEM, for mapping electrical potential and fields in the same sample, providing a more comprehensive view of the specimen's electrical characteristics. Simultaneous acquisition of STEM-HAADF and EDX maps in aberration-corrected microscopes further enables direct correlation of electrical properties with structural and compositional features at high spatial resolutions.

This integrated approach is especially advantageous for advancing complex semiconductor devices, such as III-V MJSC, where precise understanding of material properties and charge transport mechanisms is crucial for optimising performance and efficiency.

Quantitative EBIC analysis is complicated due to the influence of specimen preparation and electron beam illumination, both of which can alter the specimen intrinsic electrical signals. Unlike EH, which relies on the phase change of transmitted electrons, EBIC signal detection requires direct electrical contact with the specimen, making it highly sensitive to the resistive properties of the metal contact as well as to preparation-induced artifacts. These include damaged surface layers, which provide low resistivity (short circuit) path for carriers, and FIB-induced defect states, which enhance carrier recombination and thereby limit the EBIC current extraction.

Beyond preparation-related artifacts, understanding the interaction processes during electron beam illumination is essential. These interactions generate a range of signals, which collectively contribute to the detected current. Contributions from transmitted electrons (TRE), absorbed electrons (ABE), backscattered electrons (BSE), and secondary electrons (SE) depend on specimen-related and beam-related parameters such as the specimen material, thickness and geometry, as well as the beam energy. The corresponding varying proportions of these quanti-

ties then determine the respective contributions to the associated current signals, such as the electron-hole pairs (EHPs) generated by the transmitted electrons, the electron beam absorbed current (EBAC), or the EBIC arising from SEs (SEEBIC).
While these effects complicate straightforward quantitative analysis, they also provide opportunities. Each signal provides specific insights into the electrical properties of the specimen, enabling a more nuanced analysis. For example, SE emission causes surface charging in TEM lamellae, modifying the surface potential and thus the electrical response of the specimen. However, when isolated, STEM-EBIC signal resulting from SE emission has been demonstrated to enable quantitative mapping of resistance contrast, electric potential, and work function.[31,216] Achieving accurate quantitative EBIC analysis of the electrical properties inherent to the device requires separating these signals and quantifying their relative contributions by comparing experimental data with simulations of electron scattering processes in the specimen. Thus, although illumination- and preparation-induced effects complicate straightforward interpretation of the EBIC signal, the sensitivity of the STEM-EBIC method to these influences can be exploited, as it enables a more comprehensive and specific electrical characterisation of devices. While on the other hand, it provides a better understanding of preparation-induced effects on the specimen's electrical response and aids in identifying issues related to circuit editing. Hence, these insights not only aid in improving preparation protocols, but they ensure that the electrical (S)TEM characterisation more accurately reflects the bulk semiconductor device properties.

For this reason, in this chapter, STEM-EBIC current mapping of the GaAs p-n junction is performed with and without *in situ* applied bias, complementary to the electrostatic potential analysis using EH described in the preceding Ch. 6. This serves as a preparatory step towards enabling a comprehensive and quantitative electrical (S)TEM characterisation of the current extraction and potential distribution at p-n junctions in III-V MJSCs.

While comprehensive explanations of the fundamental principles underlying the SEM-EBIC technique are well established in the literature, an equivalent in-depth review summarising the current understanding of STEM-EBIC – particularly regarding the origins of different signal contributions and the influence of experimental parameters on signal yield – remains currently unavailable. Therefore, this chapter begins with a comprehensive literature review of the fundamental principles essential for conducting and interpreting STEM-EBIC experiments, including a description of the different EBIC signal modes, their respective generation mechanisms, factors influencing signal yield, and the type of electrical information each mode provides. The second section offers a literature-based reflection on key experimental considerations, specifically the STEM-EBIC measurement geometry, the spatial resolution achievable with STEM-EBIC, and the influence of the electron beam acceleration voltage. The third section outlines the experimental STEM-EBIC methodology, detailing the employed setup. This includes the GaAs specimen geometries, the instrumentation used for EBIC signal detection, and how the electrical connection geometry of the specimen influences the observed EBIC signals. The fourth section focuses on the optimisation of STEM beam parameters and EBIC acquisition settings to enhance signal quality and improve data interpretation. The fifth section presents the *in situ* biasing STEM-EBIC analysis of GaAs p–n junctions. Initially, low-magnification (LM) STEM-EBIC is used to verify the electrical connectivity between the MEMS support chip, the sample lamella, and the

TEM biasing holder. LM STEM-EBIC is then performed on a GaAs p–n junction with and without externally applied bias, providing an overview of the current distribution across the entire specimen and the distinct contributions to the overall EBIC signal. This is followed by STEM-EBIC at standard magnification, which enables a higher-resolution investigation of the signal distribution across the GaAs p–n junction and its response to the applied bias. The chapter concludes with a summary of the current state of STEM-EBIC for semiconductor device analysis and outlines the remaining challenges on the path towards fully quantitative interpretation.

7.1 Fundamental Principles of EBIC Analysis

The basic working principle of STEM-EBIC analysis of p-n semiconductor devices is straightforward. A focused STEM probe is rastered across the ROI in the TEM lamella, generating EHPs, which are separated by the internal electric field of the device's p-n junction, thus inducing a current. This electron-beam-induced current is collected at the electrical contacts of the lamella, which are connected to an amplifier via the MEMS support chip in the biasing TEM holder. As the detection of the EBIC signal is synchronized with the electron beam scanning system, the measured current is associated with the probe position, yielding the EBIC-map. The recorded EBIC intensity is proportional to the strength of the local built-in electric field, for example at a p-n or Schottky junction, for a given beam excitation, and can be increased/decreased by applying a reverse/forward external voltage to the device p-n junction.

7.1.1 EBIC Signals

The term "EBIC" refers generally to the total current signal measured at each beam incidence position.[218] It comprises of different contributing signals resulting from the various inelastic interaction processes the incident primary electron beam undergoes when transmitting the specimen. To understand and interpret the contrast in the recorded EBIC map it is crucial to distinguish these different signal contributions.

When a thin TEM specimen is irradiated by high energy electrons (e.g. 200 kV) most of the incident primary electrons are transmitted, while only a minor part will be absorbed by the specimen, or even back-scattered. For electron-transparent TEM specimen the amount of back-scattered electrons is generally negligible, but should be taken into account when increasing the specimen thickness. The electrons transmitting the specimen undergo either no scattering at all, are elastically scattered (diffraction) or inelastically scattered, thereby loosing energy of up to a few thousand eV. The energy transfer from the primary electrons to the specimen during inelastic scattering gives rise to different phenomena, two of which are central to EBIC analysis. First, the inelastic electron scattering leads to the generation and emission of SE from both the top and bottom lamella surfaces. Second, electrons in the valence band of semiconductors are excited to the conduction band when absorbing sufficient energy (equal to or greater than the bandgap energy), generating EHPs as excess carriers. These either recombine radiatively (cathodoluminescence) and non-radiatively (phonon), or they get collected by the SCR and hence induce an excess carrier current.

Now, the detected EBIC signal comprises contributions from three current-generating processes, each governed by different inelastic electron-specimen interactions. These different signal contributions are schematically represented in Fig. 56. The first and most important contribution is

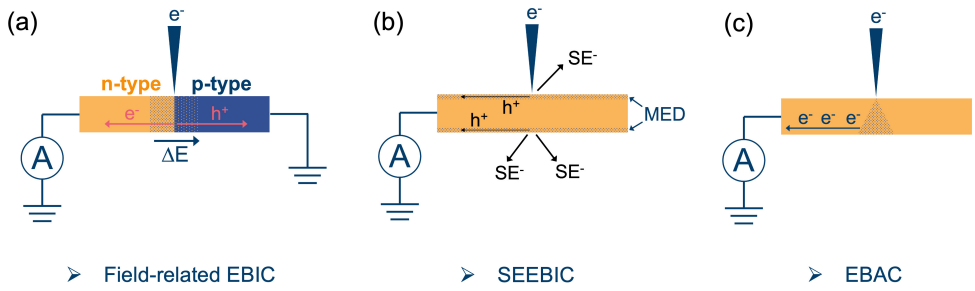

Figure 56: *Schematic illustration of the generation mechanisms of the three primary signal contributions to EBIC in STEM. (a) Field-related EBIC generated by the separation of electron–hole pairs, induced by the electron beam, within the electric field (δE) at a semiconductor p–n junction. (b) Hole current arising from secondary electron (SE) emission, generated by the electron beam within the surface-near mean escape depth (MED). (c) Current of absorbed primary electrons, which are increasingly absorbed with greater specimen thickness.*

the current generated by the field separation of the beam-generated EHPs, often referred to as "standard" EBIC[216,217,218], but referred to here as field-related EBIC for clarity. The second contribution to the EBIC signal is the positive hole current induced by the emission of SE, often referred to as SEEBIC.[31] The third is the negative current induced by the absorption of incident electrons (I_{EBAC}), which is named as the electron-beam absorbed current (EBAC). While the generation of the standard EBIC contrast requires the built-in electric field of a p-n junction, the EBAC and SEEBIC are generated independently of the internal field. The measured fractions of the different signals depend - aside from the sample's material properties - on the specimen geometry and the connection geometry, i.e. the electrical circuit design.

7.1.2 Signal Generation

To understand the fundamental differences in signal generation, a semiconductor sample with a p-n junction and both the n-side and p-side electrically contacted is considered, as schematically illustrated in Fig. 56. Each of these two contacts can either be floated, grounded, or connected to an amplifier on the path to ground for current detection.

7.1.2.1 Field-Related EBIC

For the field-related EBIC signal, the collection and separation of the EHPs by the p-n junction yields equal currents at both contacts, which are opposite in sign. To avoid charge built-up and allow both of the separated carriers to flow off, both contacts should be connected to ground. To enable the measurement of the field-related EBIC current, only one side of the device should be connected to the amplifier, as it is illustrated in Fig. 56a. This configuration prevents the recombination of the separated EHPs within the amplifier, as this would otherwise cancel out the net field-related current (which would occur if both contacts were connected to the amplifier).[217] Depending on whether the amplifier is connected to the p-doped or n-doped side of the device, it collects either electrons or holes. Consequently, the detected EBIC signal is either negative or positive in sign, respectively. In recorded EBIC maps, the field-related signal appears only at the location of the built-in electric field, i.e. the p-n junction. The intensity of this signal reflects the

strength of the built-in electric field at the p-n junction, and is further influenced by the charge carrier transport properties of the material, such as the minority carrier lifetime and diffusion length. These properties determine the fraction of beam-induced carriers that successfully reach the contacts and contribute to the measured field-related EBIC signal.

More specifically, the beam-generated EHPs are excess carriers, which recombine on a material-specific timescale known as the excess carrier lifetime, τ. During this lifetime, the carriers diffuse and may be collected by the SCR before recombination, thereby inducing an excess carrier current that can be extracted and detected in the circuit. In doped semiconductors, the EHP lifetime is determined by the minority carrier lifetime, as it is typically much shorter (hence limiting) due to the dominant availability of majority carriers for recombination.

The dependence of the detected EBIC signal on the minority carrier transport properties can thus be exploited to provide spatially resolved information on minority carrier diffusion lengths and recombination activity. This recombination activity may be locally enhanced by electrically active defects, ultimately affecting the charge collection and carrier extraction in a device. Charge collection is critical for the performance of many semiconductor photonic devices, particularly MJSC (as discussed in Ch. 2).

STEM-EBIC has been applied to study and map the induced current generation mechanisms [36] and the electrical activity of defects [33] in solar cells, and to map devices's photocurrent collection efficiency. [219]

7.1.2.2 SEEBIC

SEEBIC is, as described above, the current generated in the specimen as a result of SE emission, induced by the inelastically scattered incident electron beam. Upon emission of the SEs, the associated unpaired holes are left behind, which leads to charging if the specimen is electrically isolated. However, when an electrical connection to ground exists, the charges can flow off, generating a positive hole current, which is equivalent but opposite to the negative SE current emitted from the sample. This process is illustrated in Fig. 56b. In contrast to the field-related EBIC, the SEEBIC signal can be measured with one or both device contacts connected to the amplifier, since no opposing carriers are detected that would otherwise recombine. This means it can also be measured in specimens, which only have a single electrical connection, as a second path to ground is not required. For a p-n junction specimen with front and back contacts, two connection setups are possible, each providing different information in the EBIC map.

When only one side of the device is connected to the amplifier, while the other side is grounded, the SEEBIC contrast provides a spatially resolved map of the specimen's resistivity, i.e. a SEEBIC resistance contrast image (RCI). [216,220] This is due to the fact that the possibility of beam-generated excess holes to reach either the amplifier or the grounded contact is determined by the specimen's resistivity and is a function of the distance between the beam incidence (SE emission, charge generation) and the amplifier.

When both sides of the device are connected to the amplifier, the mapped SEEBIC contrast does not exhibit any spatially resolved resistance contrast, as the current reaching the amplifier from the two contacts are combined into a total SEEBIC signal. However, this configuration, as it suppresses the field-related EBIC contrast, enables the separation of the remaining SEEBIC and EBAC signals.

The application of STEM-SEEBIC as a distinct EBIC technique is relatively recent. It was primarily introduced by Hubbard *et al.* (2018)[31] and (2019)[216], who demonstrated its use in quantitatively mapping electronic properties, such as conductivity, electric field and work function.[31,216] Specifically, the potential of SEEBIC/RCI for resistance mapping has been exploited to study the electrical connectivity and conductivity in real devices.[216] Remarkably, STEM-SEEBIC mapping has been demonstrated at 2 Å resolution[32], which significantly surpasses the resolutions attainable with other EBIC modes.[221,217] The technique has further been applied for carrier transport mapping and device failure analysis in graphene nanodevices, where its high sensitivity and spatial resolution capabilities enabled the distinction of single graphene layers.[222,223]

More recently, the STEM-SEEBIC technique has emerged as an alternative approach to detect and map SEs by quantifying the current induced by SE emission, circumventing the inefficiencies of traditional external SE detection methods limited by detector geometry.[224,225,31] This approach has proven particularly effective for quantitative analysis of SE-related electronic properties, such as the work function[31], and for investigating charging mechanisms in TEM specimens.[225] The high surface sensitivity of the SEEBIC signal further makes it uniquely suited for correlating charge transport characteristics with morphological and topological changes, enabling its application in analysing the surface structure of nanomaterials.[224]

7.1.2.3 EBAC

The absorption of primary electrons generates a negative current of excess electrons, yielding a negative EBAC signal in the recorded EBIC map. While the sign of EBAC signal is opposite to that of SEEBIC, the connection setup required for its detection is the same.

Generally, EBAC contrast can be measured using only a single electrical connection to the specimen, as it is illustrated in Fig. 56c.[216,217] Upon connecting one side of a two-contact specimen to ground and the other to the amplifier, the excess electrons flow preferentially to one contact or the other depending on the resistance of the path. Thus, the position of the incident primary electron beam can be used to divide the resistance between these two contacts. And the portion of the absorbed current collected by each contact corresponds to the spatial resistance distribution. Thereby, EBAC/RCI in addition to SEEBIC/RCI provides a spatially resolved resistance map.[220,226]

Similarly, when both contacts are connected to the amplifier, the mapped EBAC contrast does not yield resistance contrast, as the combined EBAC signal collected at both contacts is detected by the amplifier.

In nano-device testing, EBAC mapping has been applied to trace electrical shorts and disconnects, and to map resistivities within circuits.[220,226] However, EBAC analysis is primarily conducted in SEM. In STEM, EBAC/RCI is limited by the low absorption probability in electron-transparent specimens and is inferior to SEEBIC/RCI in terms of spatial resolution.[217,223]

7.1.3 Approaches to the Qualitative Differentiation of EBIC Signals

Which of the three primary contrasting EBIC signals is detected depends fundamentally on the electrical connection setup. However, the individual generation, distribution and relative

intensity of the EBIC, SEEBIC and EBAC contrasts within the recorded STEM-EBIC map is then largely determined by a complexity of specimen- and beam-related factors. Considering a connection setup yielding contributions from all three signals in the EBIC map, a direct quantitative distinction of each signal – or of the signal of interest, e.g. the field-related EBIC – is impossible.

A first qualitative differentiation can be approached by considering the signal distribution in a STEM-EBIC map. As mentioned above, the field-related EBIC contrast is located exclusively at the SCR of a p-n junction or Schottky junction, with the intensity and distribution reflecting the strength of the built-in electric field and the width of the SCR, respectively. The generation of the SEEBIC and EBAC contrasts, on the other hand, is independent of the built-in field of the sample and is therefore present in the entire sample.

A second criterion for differentiation is the sign of the EBIC signal. While SEEBIC is positive (hole current) and EBAC negative (electron current), the sign of the EBIC depends on the electrical connection geometry relative to the built-in electric field, i.e. which side of the p-n junction is connected to the amplifier. This dependency provides a way of identifying the field-related EBIC signal, as the sign of the signal should be reversed by inverting the electrical connections, whereas the sign of SEEBIC and EBAC does not change.

The third way of distinguishing between the three EBIC signals is by the magnitude of the EBIC signal. The yield of each signal is given by $\delta = \frac{I_{EBIC}}{I_0}$, i.e. as the induced current relative to the incident primary beam current, I_0.[217] Although the absolute quantification of the signal yields is not trivial, a general relative ranking of the contributions can be made. Considering an electron-transparent semiconductor TEM specimen illuminated with a high-energy electron beam, the following order can be assumed: $I_{EHP} > I_{SEEBIC} > I_{EBAC}$
The I_{EHP} is generally expected to be the strongest signal due to the large gain of the EHP creation process.[217,36] As the energy required to produce an EHP is on the order of a few eV, a single 200 kV electron can produce up to 10^5 EHPs.[36] Due to this large production of EHPs, the I_{EHP} is by far the strongest, even though only a small fraction of the incident electrons are actually inelastically scattered in the depletion region of the p-n junction, where the collection probability is high. The second strongest STEM-EBIC signal is commonly the I_{SEEBIC}. Like the EHP creation process, the production of SEs is multiplicative, as many SEs can be emitted upon inelastic scattering of one incident high-energy electron. However, the yield of SEs per primary electron is generally lower than the yield of EHPs, since the SEs have exit energies of up to 50 eV, while the generation of EHP usually requires only a few eV.[150,36] Hence, the SEEBIC signal is typically smaller than the field-related EBIC.[32,31] I_{EBAC} can be assumed to be the weakest signal contribution in STEM-EBIC. For thin electron transparent samples, where $I_0 \simeq I_T$ is approached, I_{EBAC} is negligible. As the thickness of the TEM specimen increases, electron absorption certainly increases. However, for electron-transparent thicknesses, the contribution of I_{EBAC} will commonly remain the smallest in STEM-EBIC, in contrast to SEM-EBIC where it is usually the second strongest signal.[150,217,31]

Although this relative order of the EBIC signal contributions is valid in most cases, the individual

signal yields are highly dependent on the material, thickness and geometry of the sample, as well as on the parameters of the electron beam illumination. These parameters influencing the individual EBIC signal yields, are described in more detail in the following section.

7.1.4 Factors Influencing the Signal Generation and Yield

7.1.4.1 EBAC

The distribution and magnitude of the EBAC contrast primarily depend on the specimen thickness and the acceleration voltage of the electron beam. Due to the relatively high beam energies (e.g. 200 kV) and the electron-transparent specimens used in STEM-EBIC, the absorption probability of primary electrons – and consequently the EBAC yield – is generally lower compared to SEM-EBIC. However, as specimen thickness increases, the absorption probability must be considered when interpreting the EBIC signal.

While the STEM-EBAC signal is quite weak in general, the variation in EBAC contrast is governed by the specimen material, particularly by the atomic number (Z) of its constituent elements and the local variations thereof. Materials with high-Z elements, thus having a high mean Z, enhance electron absorption. If it is essential for an experiment to avoid EBAC contributing to the total EBIC signal, materials with low Z, or minimal variation thereof, are advantageous. However, for every given material, the EBAC contribution can be limited by reducing specimen thickness and increasing the primary electron energy.

7.1.4.2 SEEBIC

The intensity and distribution of the detected SEEBIC signal are governed by a complex interplay of factors controlling the SE emission process. SEs are ejected from the valence or conduction bands of atoms in the specimen through energy transfer (inelastic collisions) from primary electrons, provided the energy of these incident electrons is sufficient to overcome the material's work function.[221,227] The exit energy of these emitted SEs is relatively low, typically ≤ 50 eV. Consequently, they emerge from shallow exit depths, on the order of a few nanometers, just below the sample surface.[221,227] The total SE yield (SEY, δ) generally consists of SEs produced by primary electrons (SE1) and those generated by BSEs (SE2).[221,228] However, in TEM, the majority of SEs can be assumed to be directly produced by primary electrons, as the number of BSEs is negligible.[31] The actual BSE yield – and thus the SE2 yield – depends on the specimen, specifically the specimen thickness and Z.[228]

Now, the factors controlling the SEY and thus the SEEBIC signal intensity can be attributed to the three stages involved in SE emission: (1) the generation of SEs, (2) the probability of SEs reaching the sample surface, and (3) the escape probability of SEs leaving the sample.

Factors determining the SE generation rate include both material-related and electron beam-related parameters. The latter includes the primary electron energy, E_0, the beam current, I_0, and the incidence angle. The SEY is inversely proportional to the beam energy, although the proportion of high-energy SEs increases with higher primary electron energies.[229,230,32,31] The dependence of SE generation on specimen material is highly complex and a detailed explanation lies beyond the scope of this work. However, it can be noted that the SEY is proportional to the material's stopping power for electrons, which is a function of the differential cross-section $\frac{d\sigma}{dE}$.[231,232,233] The stopping power is itself proportional to the atomic number (Z) and depends,

among other factors, on the electron density distribution within the target atoms and their effective mean excitation energy.[231,228]

The second stage of SE emission – their movement towards the sample surface – is primarily determined by the mean free path (MFP) of SEs within the sample material and their generation depth, i.e., their distance from the surface.[31,233] The MFP depends on the energy of the SEs and the electron density of the material.[229,31] Due to the low energies of SEs, their MFP is generally very short. Materials with higher conductivity exhibit shorter SE MFPs. Consequently, metals have the shortest MFPs, while insulators have the largest. This short MFP in semiconductors and metals, combined with the small escape depths, explains the high surface sensitivity of the SEEBIC signal.[31]

Finally, the escape probability of SEs from the specimen surface depends on the material's work function (ϕ) and the surface potential (V_S).[31,233,231,228] However, there is no straightforward proportionality between the work function and the SEY, which could be formulated in an analytical expression.[231]

More detailed discussions on electron-induced SE emission, theoretical models, and their comparison with experimental data can be found elsewhere.[231,228] All these factors and dependencies highlight that interpreting the SEEBIC contrast and intensity distribution is far from straightforward. Simplified, the SEEBIC contrast provides the following information in the EBIC maps:

- The dependence of the SEY on the electron incidence angle produces topological contrast.
- The Z-dependence generates compositional contrast.
- The dependence on crystal orientation results in channelling contrast.
- Additionally, variations in the electrical (or magnetic) fields at the specimen surface can produce potential contrast.

7.1.4.3 Field-Related EBIC

The field-related EBIC signal yield is governed by two key processes: EHP (carrier) generation and carrier collection efficiency. Therefore, to identify the factors affecting this yield and facilitate EBIC signal quantification, a detailed examination of the EHP generation and collection processes is crucial.

In semiconductor materials under electron beam illumination, EHPs are generated when an inelastically scattered primary electron transfers energy to a valence band electron, promoting it to the conduction band and leaving a corresponding hole in the valence band. Hence, the energy required to generate an EHP is fundamentally determined by the bandgap energy (E_g) of the material. The efficiency of EHP generation – or the EHP yield – thus depends on the incident electron energy relative to E_g. However, the actual threshold for EHP creation exceeds E_g, as part of the transferred energy is lost to lattice phonon generation. Hence, the energy necessary to generate one EHP (E_{e-h}) is higher than E_g. For example, in GaAs $E_g = 1.42$ eV, but $E_{e-h} = 4.6$ eV.[234,201] Nevertheless, as the electron beam energies applied in (S)TEM are significantly higher (e.g. 200 kV) compared to the average E_{e-h} in semiconductors, a single high-energy electron can still generate multiple thousand EHPs along its trajectory through the specimen. The generation rate of EHPs G_{e-h} can be described by the following equation:[165]

$$G_{e-h} = \frac{1}{2} \frac{i_b \left| \frac{\mathrm{d}E_B}{\mathrm{d}z} \right|}{E_{e-h}} \tag{63}$$

where i_b is the the dose rate of the incident electron beam. $\left| \frac{\mathrm{d}E_B}{\mathrm{d}z} \right|$ is the energy loss of the incident electrons to the specimen per unit path length z, also known as the stopping power, which can be derived by implementing the Bethe theory.[235,236] The factor $1/2$ accounts for the assumed equipartition of the transferred energy for plasmon excitation and EHP generation in the specimen.[165,201]

It is important to note that the efficiency of EHP generation is strongly influenced by the type of bandgap (direct or indirect) in the material. In direct bandgap semiconductors, the conduction band minimum and valence band maximum align at the same momentum, facilitating efficient promotion of valence band electrons to the conduction band (EHP generation) under electron beam illumination. This is because electrons can transition directly between these bands without requiring a change in momentum. Conversely, in indirect bandgap semiconductors the conduction band minimum and valence band maximum are at different momenta. As a result, EHP generation in these materials requires not only energy transfer from the primary electron but also a phonon-assisted momentum change, making the process less efficient compared to direct bandgap materials. While the high efficiency of EHP generation in direct bandgap semiconductors makes them well-suited for EBIC analysis, it is important to note that the same efficiency applies for the recombination process. EHP recombination is significantly more efficient in direct bandgap materials than in indirect, where phonon assistance is again required. As a result, direct bandgap semiconductors exhibit shorter charge carrier lifetimes and diffusion lengths. These material-specific effects on the EHP generation must be considered when designing an EBIC experiment.

While EHP creation forms the basis for generating the field-related EBIC signal, the final signal yield depends on the number of EHPs separated by the built-in field and successfully collected by the contacts for detection by the amplifier. This collection efficiency describes the probability of an EHP generated at a specific location in the specimen to be collected. It is influenced by various specimen-related factors governing the carrier dynamics as a function of space. In other words, the dominant factors controlling the collection efficiency – and consequently the intensity distribution of the EBIC signal – vary depending on the position of the electron beam on the sample (i.e. the location of carrier generation).

Carriers generated within the device's depletion region (of a p-n junction or Schottky junction) have the highest probability to be collected, and thus exhibit the highest field-related EBIC intensity in the EBIC map. The strength and spatial distribution of the built-in electric field determine how efficiently EHPs are separated and collected by the junction.

In sample regions away from the depletion zone, the collection probability of generated EHP is exponentially decaying as a function of the distance from the edge of the SCR. In this region, the collection probability is determined by the material specific minority carrier lifetime and diffusion length. The longer the distance the carriers can travel before recombining, the more likely they reach the collection region (SCR). Hence, materials with longer minority carrier lifetimes and diffusion length generally exhibit higher collection probabilities. In addition to the

material inherent diffusive minority carrier dynamics, the detected EBIC profile is further influenced by the quality (defect density) of the semiconductor crystal. Defects act as recombination centers for active carriers, thus higher defect densities enhance carrier recombination. Hence, high-quality crystalline specimen with fewer defects are desirable to attain high EBIC signal. This relates both, to the defect density in the bulk material, which is determined during the semiconductor growth, as well as to the quality of the TEM specimen surface after preparation, which determines surface recombination. Even if the bulk sample is practically free of defects, charged defects at the TEM specimen surfaces induce surface band bending (SBB). As a result, carriers generated within this SBB region are highly likely to recombine before reaching the p-n junction and, therefore, do not contribute to the induced current. It should be noted, however, that SBB does not inherently lead to high surface recombination. In fact, surface trap states can act as either donor- or acceptor-like states. The corresponding trapped carriers induce a local electric field, resulting in SBB. Depending on the polarity of the trapped charges and the nature of the specimen material, this SBB can either enhance or suppress surface recombination activity, thereby decreasing or increasing the EBIC signal intensity. [237,238]
Another factor influencing the collection efficiency is the resistance of the specimen. Higher resistance reduces the carrier diffusion length, leading to decreased field-induced EBIC signals as excess EHPs recombine before being collected. [216] Related to the specimen resistance, the TEM specimen geometry also directly influences the collection efficiency. The location of the junction relative to the metal contacts determines how far the excess carriers must travel to be collected. Shorter distances enhance collection efficiency. Finally, the nature of the electrical contacts to the semiconductor is a key factor. The contact resistivity directly affects the ability to collect charge carriers without significant losses.
Understanding and optimising these influencing factors is essential for maximizing the desired EBIC signal(s) in STEM-EBIC studies.

7.1.5 Experimental Adjustment of the Signal Composition

It is impossible to directly and quantitatively separate the various contributions, such as primary beam absorption, SE emission and the electron beam, that induce current at the device p-n junction in the EBIC maps. The measured EBIC distribution always reflects a mixture of the dominant contributions. Based on understanding the respective generation mechanisms, they can to some extent be influenced to enhance the desired signal, which in this study is the signal of the device p-n junction, and reduce the others. The SE induced current can be reduced by ensuring that the lamella surfaces are as homogeneous as possible, to prevent any small scale variations related to morphology covering the EBIC signal from the device internal field. Using epitaxially grown single crystal specimens, which lack grain boundaries, enable FIB-preparing lamellae with uniform surfaces.
The EBAC signal can be reduced by minimising the specimen thickness. However, while thinner specimen are beneficial to minimise absorption and increasing the spatial resolution of the EBIC map, the influence of the damaged lamella surfaces becomes more dominant, while the signal from the dopant related field weakens. Therefore, as in EH, the choice of sample thickness is always a trade-off between these effects.
In general, the material of the sample of interest in device analysis is given and is not specifically

adapted to the experiment. It should be noted that a high atomic number of the elements present, or a strong variation thereof, is less desirable if EBAC-and also SE-contrast is to be avoided. In this regard, GaAs p-n homojunction specimen are suitable specimen to test and setup an EBIC experiment, because Z is not changing across the p-n junction. Studying MJSCs, in which the layer composition of the ternary to quaternary compounds change across the device structure and interfaces include changes in both the III and V elements, suppressing EBAC and SE contrasts is impossible. The EBIC analysis of such samples is therefore less straightforward.

7.2 Experimental Considerations

7.2.1 Measurement Geometry

In general, STEM-EBIC analysis can be performed in two different geometries, cross-sectional or plan view. Both geometries yield different information. In the plan-view specimen geometry the p-n junction is positioned perpendicular to the electron beam direction. Hence, it is more suitable to map the spatial homogeneity of the p-n junction's electrical activity, which cannot be spatially resolved in projection, i.e. when using the cross-sectional geometry, where the p-n junction is parallel to the incident beam. On the other hand, the cross-sectional setup is better suited to study the lateral current distribution within the built-in field, the investigation and correlation of which with the potential distribution measured using EH is the focus of the device analysis in this work. STEM-EBIC in the plane-view geometry has been successfully applied to the study of electrically active defects in semiconductors [239], such as organic/inorganic lead halide-based perovskite solar cells, which are inherently electron-transparent in thickness. [36] However, the epitaxial III-V semiconductor structures studied in this work are by far too thick to allow this geometry. The GaAs wafer substrates alone already measure at least 450 µm. This requires the preparation of electron-transparent cross-sectional lamellae, well knowing that this preparation introduces surface artefacts and is more difficult with regard to the electrical contacting of the sample. Therefore, in this work, all discussions of the STEM-EBIC method refer to the cross-sectional geometry.

7.2.2 Spatial Resolution

Using aberration-corrected STEM probes for the analysis of thin, electron-transparent specimens enables atomic-resolution STEM imaging (see Ch. 3.1.4). However, the spatial resolution of STEM-EBIC analysis does not correspond directly to the STEM probe diameter or the instrument resolution. To understand the factors that control spatial resolution in STEM-EBIC maps, it is essential to examine the processes underlying the generation of the various EBIC signals.

In general, SEEBIC achieves much higher spatial resolution compared to EBAC and field-related EBIC. [217,32] This is because the interaction volume for EBAC and field-related EBIC, which are associated with electron absorption and EHP generation, is significantly larger than the interaction volume for SE emission. [221,31] At least, this applies for SE1 emission caused by primary electrons, the dominant SE emission mechanism in thin, electron-transparent specimens. However, as the specimen thickness increases, SE2 emitted by BSE increasingly degrade the spatial resolution of SEEBIC. More details are provided in Sect. 7.4.2 below, which reviews the effects

of specimen thickness on the contributions of different signals.
Considering the interaction zone along the path of the transmitting primary electron beam through the specimen, SEEBIC is generated only within a few nanometers below the top and bottom surfaces of the specimen, within the material-specific mean escape depth (MED) of SEs. Due to the low energy of SEs (<50 eV), this escape depth is typically below 10 nm.[150] Because SEEBIC originates from this confined volume, it can lead to atomic resolution.[32] In contrast, EBAC is generated deep within the specimen, where primary electron absorption becomes significant. Field-related EBIC (EHPs) can be generated throughout the entire specimen thickness along the path of the transmitted electron beam.

While the spatial resolution of each EBIC signal is inherently determined by its specific generation region, the overall electron-specimen interaction volume – and thus the spatial resolution of a STEM-EBIC map – is fundamentally influenced by the interrelation between the TEM specimen thickness and the acceleration voltage. In general, STEM-EBIC analysis of electron-transparent specimens using high-energy electrons provides significantly improved spatial resolution compared to SEM-EBIC on thick, bulk specimens with low-energy electrons.[221,34,217,240] The reason for this is that the almost complete transmission of the primary electrons does not result in a large interaction volume typically present in bulk specimens.[221] Instead, carriers are generated more uniformly along the trajectory of the transmitting beam within the entire specimen.
Only slight broadening of the transmitted beam trajectory occurs, depending on the specimen thickness. Simulations of electron trajectories in electron-transparent specimens of varying thicknesses confirm this behavior.[34] Details of the physical mechanisms underlying beam broadening and its effects on spatial resolution in TEM have been reviewed, for instance, by Egerton & Watanabe (2022).[75]
To summarise the factors that control spatial resolution in STEM-EBIC, it can be stated that:

- Thinner specimens lead to more spatially confined and precise EBIC signal generation due to reduced lateral broadening of the electron beam.
- Thinner specimens also allow for more homogeneous EBIC signal generation across the entire specimen thickness, as electron absorption is minimised.
- The overall spatial resolution is determined by the interplay between the specimen thickness, the beam energy, and the specific EBIC signal mechanisms involved.

Therefore, adjusting specimen thickness and beam parameters is critical to achieving the desired spatial resolution in STEM-EBIC measurements.

7.2.3 Acceleration Voltage

In STEM-EBIC experiments, the choice of electron acceleration voltage arises from balancing two key factors: (1) the effect of beam energy on spatial resolution and the uniformity of EBIC generation within the specimen, and (2) its impact on the generation of the different EBIC signal contributions.
As described in the previous Sect. 7.2.2, the interplay between beam energy and specimen thickness determines the spatial resolution of the EBIC measurement, as it controls beam broadening

within the specimen, thereby defining the size of the interaction region where primary electrons generate carriers that induce EBIC.
Considering the second factor, the following effects of beam energy on EBIC signal generation can be observed: For a given electron-transparent specimen thickness, higher acceleration voltages reduce electron absorption, thereby decreasing the EBAC background signal.
Conversely, in STEM, the SE yield is inversely proportional to beam energy: higher primary electron energies result in a lower SEEBIC signal,[31,32] while the proportion of high-energy SEs within the total SE yield increases.[230] Consequently, for SEEBIC-specific experiments, using a lower STEM beam energy is advantageous for achieving better SEEBIC signal-to-noise ratios.
Similarly, the field-related EBIC signal also exhibits an inverse relationship with STEM beam energy. The STEM electron beam, due to its high energy – far exceeding the 4.6 eV required to generate a single EHP in GaAs[234] – is capable of generating a large number of EHPs. This is evident from Eq. 63, which illustrates the relationship between electron beam energy and the EHP generation rate. However, the EHP generation rate is not linearly proportional to the beam energy. As STEM beam energy increases, the inelastic interaction of primary electrons with the specimen decreases, leading to a reduction in EHP generation per primary electron. This effect explains why EHP generation is higher in SEM compared to STEM.[34] Conlan *et al.* report that the number of EHPs generated per beam electron decreases by an order of magnitude when the electron energy increases from 10 kV to 200 kV.[34] Therefore, the improved spatial resolution offered by high electron energies in STEM comes at the expense of the field-related EBIC signal intensity. However, a poor signal-to-noise ratio of STEM-EBIC can be mitigated by using higher electron beam currents, as the intensity of the detected total EBIC signal is directly proportional to the incident electron beam current.[31,32]
In conclusion, selecting the optimal STEM beam energy is a trade-off between low acceleration voltages, which enhance the signal-to-noise ratio for field-related EBIC and SEEBIC signals, and higher beam energies, which – in adjustment to the TEM lamella thickness – reduce beam absorption and improve the spatial resolution of EBIC measurements.

7.3 STEM-EBIC Methodology

7.3.1 The Specimen

The STEM-EBIC analyses presented in this chapter are conducted on the same GaAs p-n sample used for the EH studies described in Ch. 6. Details of the GaAs sample structure can be found in Sect. 6.1, with an illustration provided in Fig. 35a.
In addition to the primary purpose of providing correlative current mapping to complement the EH potential analysis of the same specimen, this structure is considered to be suitable for the STEM-EBIC study because GaAs is a well characterised III-V semiconductor material. Its direct bandgap enables efficient EHP generation under electron beam illumination.
Three TEM specimens of this bulk structure are employed for the study. Two of them, referred to as the GaAs-W and GaAs-Pt specimens, are previously used for the *in situ* biasing EH analysis described in Ch. 6.5. Overview images of these specimens, along with details of the FIB metal deposition, are provided in Fig. 47 and Table 4, respectively.
Additionally, a third *in situ* biasing TEM specimen, hereafter referred to as GaAs-W-2, is prepared using the FEI Strata 400S FIB-SEM. The preparation followed the FIB procedure outlined

in Ch. 4.4.1. For this specimen, IBID-W is deposited as the top and back metal contacts using 30 kV and 0.92 nA. The principles underlying FIB-induced metal deposition are discussed in Sect. 4.4.2. Like the GaAs-W and GaAs-Pt specimens, the GaAs-W-2 lamella is cut parallel to the crystallographic $[1\bar{1}0]$ direction, ensuring that the TEM viewing direction aligned with the [110] zone axis. Areas of different thicknesses are milled to allow systematic studies of the effects of specimen thickness on the EBIC signal. The crystalline thickness of the specimen regions of interest is measured using energy-filtered STEM-CBED patterns, following the method described in Sect. 5.3.1.

7.3.2 Experimental Setup and Instrumentation

The STEM-EBIC experiments are conducted using a point electronic GmbH EBIC system [241], which is compatible with the Protochips Aduro 500 biasing TEM specimen holder fitted with specialised Si half-chips featuring patterned electrical contacts for biasing. This configuration is integrated with the FEI Titan Ultimate double aberration-corrected (S)TEM microscope, which supports both parallel beam and convergent scanning beam modes enabling TEM-EH and STEM-EBIC characterisation, respectively. Notably, the EBIC system can be seamlessly incorporated into the same experimental setup that is used for the *in situ* biasing EH analysis described in Sect. 6. This integration facilitates a correlative analysis of potential and current distributions within a single microscope session.

The point electronic's EBIC system consists of two key components: (1) a STEM scan controller that enables integrated scan generation and high-speed image acquisition, and (2) an EBIC current amplifier designed for high signal-to-noise current detection. The system's factory-calibrated amplification allows for automatic quantification of the EBIC signal. [240]

The control of the electrical terminals and data acquisition is performed using the DISS 5 software package provided by point electronic GmbH. Similar to the TEM-EH experiments, the STEM-EBIC studies were conducted at an electron beam acceleration voltage of 200 kV. STEM-EBIC maps are acquired simultaneously with STEM-HAADF images. Subsequent data processing, including pixel quantification, was performed using the DIPS evaluation software, also supplied by point electronic GmbH.

7.3.3 Specimen Connection Geometries and Configurations

The Protochips Aduro 500 biasing TEM holder supports four electrical connections to the inserted sample support chip, which can be individually electrically controlled using the DISS 5 EBIC acquisition software. The software offers four options for connecting the individual metal tracks. They can either be (1) electrically grounded, (2) electrically floated, (3) connected to the amplifier for current detection, or (4) electrically biased. This set-up allows to control the detected EBIC signal and the current flow in the sample during the experiment. However, the connection geometry of the respective TEM specimen also depends on the chip design. In this work, chips with two distinct metal track geometries were utilised: 2-track and 4-track designs, featuring two or four individual metal tracks (or contact points), respectively. The two geometries are pictured in Fig. 57.

The chip supporting the GaAs-Pt sample features a 4-track geometry, whereas the GaAs-W and GaAs-W-2 sample chips have a 2-track design. Fig. 58 presents overview SEM images of the

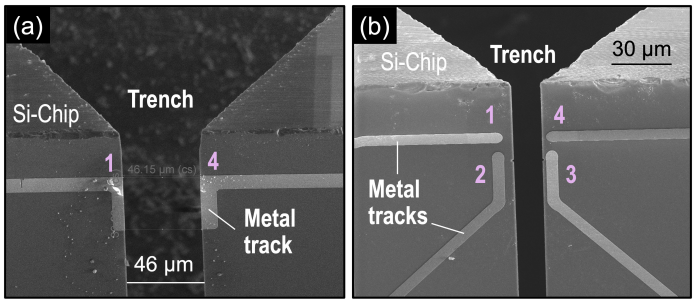

Figure 57: *SE SEM images of the two MEMS support chip configurations used in this study: a) the 2-track and b) the 4-track design. The number of contact points are indicated. The images are taken from blank chips without sample to illustrate the track design.*

three TEM specimens and their electrical chip connections.
In general, a 2-track design is preferred for optimal control of the EBIC signal. Additional tracks should be disconnected to prevent parasitic losses of induced currents or applied voltages. Based on a 2-track connection to the p-n junction specimen, three connection configurations can be implemented to control the detected EBIC signal without applying an electrical bias, which are illustrated in Fig. 59a-c. As described in Sect. 7.1.1, connecting the p-side to the amplifier and the n-side to ground, or vice versa, generates a positive or negative field-related EBIC signal, respectively, along with SEEBIC and EBAC signals. This occurs as either holes or electrons reach the amplifier, depending on the connection configuration. Alternatively, connecting both terminals to the amplifier suppresses the field-related EBIC signal, producing only SEEBIC and/or EBAC contrast in the recorded EBIC map. As described in Sect. 7.1.1, this SEEBIC and/or EBAC signal yields a spatially resolved resistance contrast.
In case of applying electrical bias to the specimen, only two connection configurations are possible, which are illustrated in Fig. 59b. One of the two terminals must be connected to the amplifier, while the bias is applied through the second terminal. In general, it is recommended to apply the bias at the front contact, close to the specimen p-n junction, to avoid losses.

7.4 Experimental STEM-EBIC: Parameter Adjustment and Signal Optimisation

7.4.1 EBIC Maps: Signal Contributions and Qualitative Distribution

To gain an overview of the signal distribution and assess the influence of sample thickness on the EBIC signal, measurements are performed on the GaAs-W specimen, which features six regions of varying thicknesses. The crystalline thickness, measured using STEM-CBED, is presented in Table 6, alongside the corresponding electrically active thickness estimated from EH.
EBIC maps of 1024×1024 pixels are recorded at a STEM-magnification of 5kx with a 300 pA beam current, as measured using the microscope's viewing screen. Figure 60 presents EBIC maps for two electrical connection configurations alongside the corresponding EBIC profiles, which are extracted across the GaAs p-n structure for each thickness region.
These maps show the distribution of the current signal extracted from the specimen and detected at the amplifier at each pixel position as the STEM beam is scanned across the FOV. As pre-

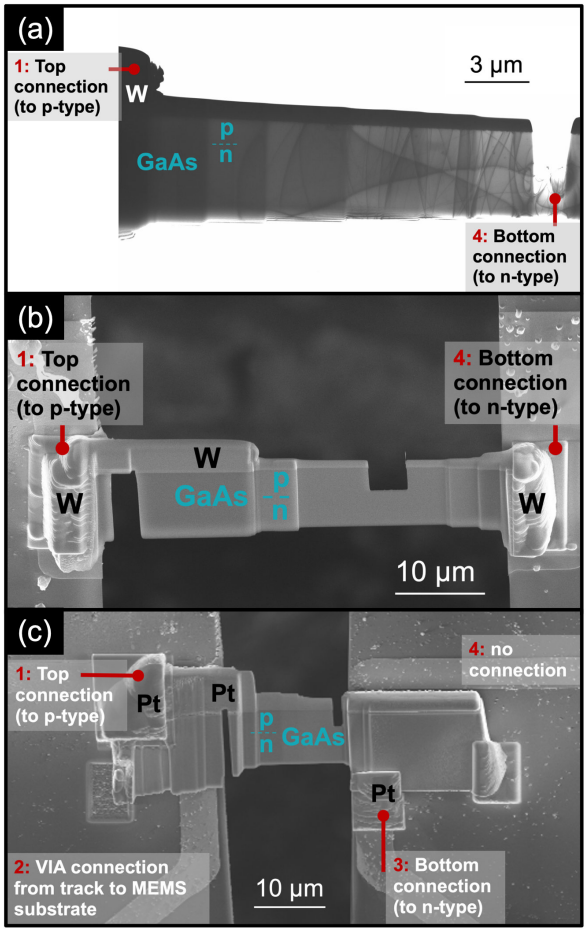

Figure 58: *Electrical connection configuration of the TEM specimen to the MEMS chip: (a) GaAs-W on a 2-track chip, (b) GaAs-W-2 on a 2-track chip, and (c) GaAs-Pt on a 4-track chip. The indicated contact point numbers correspond to the assigned holder (Protochips Aduro 500) terminals, which can be controlled using the DISS 5 EBIC acquisition software (point electronics GmbH).*

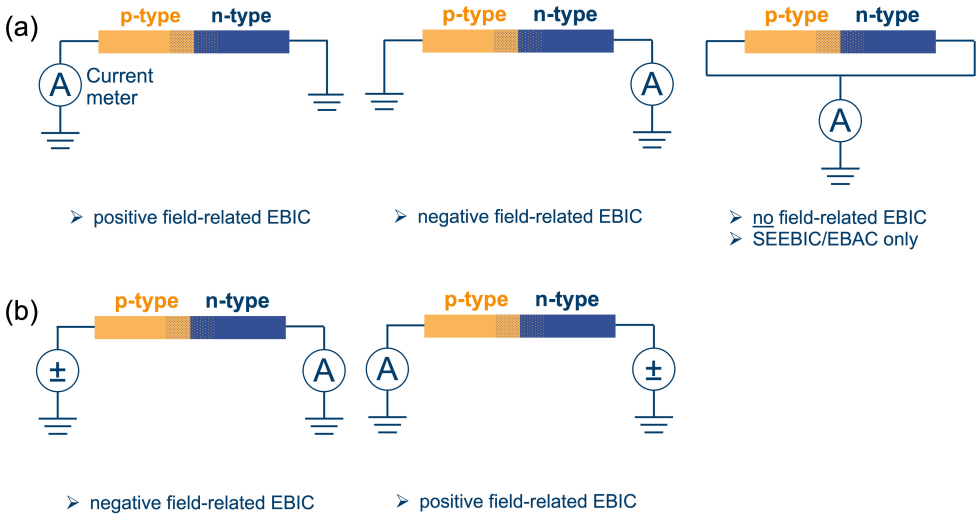

Figure 59: *Schematic illustration of the possible connection configurations and their effects on the detected EBIC signal for a p-n junction specimen: (a) without and (b) with applied electrical bias (±). Note that only the influence on the presence and sign of the field-related EBIC signal is shown, as the presence and sign of the remaining signals – positive SEEBIC and negative EBAC – remain unaffected by the connection configuration. However, applying an electrical bias to the specimen can reduce or increase the SEEBIC and EBAC signals, in addition to affecting the field-related EBIC signal at the p-n junction. These effects will be discussed in detail by means of the experimental results in this chapter.*

viously introduced, the EBIC maps reflect overlapping signal contributions, with the dominant components being field-related EBIC and SEEBIC, along with a minor contribution from EBAC, primarily dependent on the specimen thickness. Quantitatively separating these contributions is non-trivial and requires correlating experimental EBIC measurements with simulations of electron-specimen interactions. A qualitative distinction of the signal contributions, however, is possible based on criteria introduced in Sect. 7.1.3, including spatial signal distribution, signal sign, and relative signal yield.

As expected, a strong field-related EBIC signal, originating from electron-beam-generated and field-separated EHPs, is clearly visible along the GaAs p-n junction, appearing as bright contrast in Fig. 60a and as a prominent peak in the corresponding line profiles in Fig. 60c. The intensity and distribution of this signal correspond to the strength of the built-in electric field and the width of the SCR respectively. This field-related EBIC signal is exclusively localised at the SCR. In the remaining parts of the specimen, away from the junction, the signal originates from SEEBIC and EBAC, which are independent of the sample's built-in field. These contributions overlap with the field-related EBIC signal at the junction, hindering direct quantification of the field-induced current.

A clear identification and estimation of the field-related EBIC signal can be achieved by inverting the electrical connections. Depending on whether the amplifier is connected to the p-GaAs (Fig. 60a) or n-GaAs (Fig. 60b) side of the specimen, the amplifier collects either holes or electrons, resulting in a field-related EBIC signal of either positive or negative polarity, respectively. In contrast, SEEBIC and EBAC signals remain consistently positive and negative, regardless of

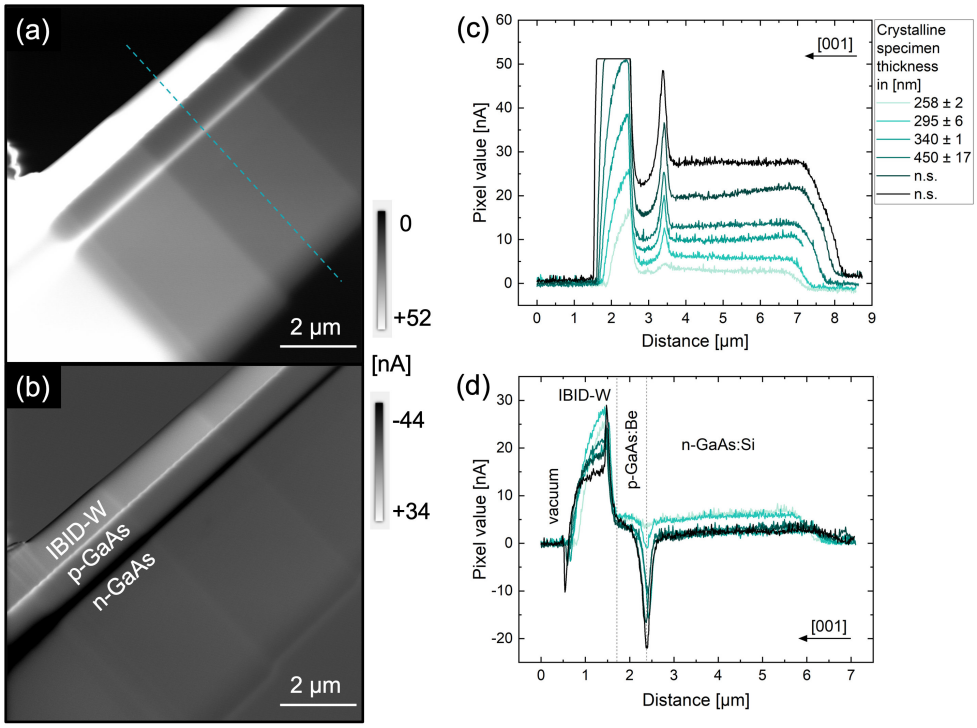

Figure 60: *STEM-EBIC maps of the GaAs-W specimen for two electrical connection configurations: (a) the amplifier is connected to p-GaAs (terminal 1) with n-GaAs (terminal 4) grounded, and (b) the connections are reversed. Graphs (c) and (d) plot the EBIC signal intensity across the GaAs p-n structure for each specimen thickness region for the respective connection configurations. The direction of the profiles is exemplified by the dashed green line.*

the connection configuration.
Comparing Figs. 60a and b demonstrates the expected sign inversion of the field-related EBIC signal at the p-n junction, while the remaining signal across the specimen remains unchanged (positive in this case). Furthermore, the EBIC signal intensity at the junction is lower when measuring a negative current with amplifier connected to n-GaAs. This highlights that the field-related EBIC signal at the junction overlaps with the underlying positive SEEBIC signal, which is present throughout the GaAs specimen. When the field-related signal is negative, the positive SEEBIC signal is subtracted, whereas the two contributions add when the field-related signal is positive.
In this particular specimen, the location of the GaAs p-n junction, approximately 1 µm below the wafer surface, is well known. However, this procedure is particularly useful in EBIC measurements where separating the field-induced EBIC signal from other contributions is less straightforward, such as in specimens where the junction location is unknown.
To assign the signal in the regions away from the junction to a dominant source (SEEBIC or EBAC), both the signal polarity and the typical relative yields of SEEBIC and EBAC in STEM-EBIC need to be considered. The EBIC signal in the p-GaAs and n-GaAs regions away from the junction, as well as in the top IBID-W layer in Fig. 60, is unambiguously positive, indicating a dominant SEEBIC contribution. Thus, for this specimen, the general expectation that SEEBIC contributions significantly outweigh EBAC in electron-transparent specimens is confirmed. This does not exclude the minor presence of EBAC, which due to its opposite (negative) polarity reduces the positive SEEBIC signal to varying degrees depending on the specimen material and thickness. Distinguishing the relative yields of SEEBIC and EBAC, i.e., determining the extent to which the positive signal is reduced by EBAC, requires an estimation of the absorbed primary electron fraction through electron scattering simulations.
The same applies to estimating the relative field-related EBIC yield. As theoretically predicted (see Sect. 7.1.3), the field-related EBIC signal is by far the strongest contribution in the GaAs specimen, as evident in Fig. 60, where the SEEBIC signal throughout the GaAs specimen is significantly weaker compared to the field-related EBIC signal at the junction.
The relatively strong SEEBIC signal observed in the IBID-W layer is attributed to the significantly higher SEY in the W metal layer compared to the GaAs semiconductor, resulting in a pronounced material contrast.
Further details regarding the composition and distribution of the signals in relation to the specimen material are discussed in Sect. 7.5.

7.4.2 The Effect of Sample Thickness and Surfaces

The influence of TEM specimen thickness on the EBIC signal is illustrated in the EBIC maps shown in Fig. 60a and b, along with the corresponding EBIC profiles taken from the different thickness regions across the GaAs structure. Generally, it is evident that the EBIC signal intensity increases with increasing TEM lamella thickness. This trend is observed in the IBID-metal layer, at the GaAs p-n junction, and in the p-GaAs and n-GaAs regions away from the junction. It is also evident in Fig. 61, where the STEM-HAADF image and the corresponding EBIC map of the thinner GaAs-W specimen regions are presented alongside with HAADF and EBIC profiles measured across different thickness steps in the $[1\bar{1}0]$ direction, perpendicular to the growth

direction. Two EBIC profiles are shown: one at the position of the p-n junction and another in the n-GaAs layer approximately 1 µm below the junction.
The HAADF signal shows a clear proportionality to thickness, as indicated by distinct intensity steps correlated with thickness. Similarly, the EBIC profiles exhibit the same general trend of decreasing signal with decreasing thickness, with intensity steps coinciding with those visible in the HAADF signal. However, the EBIC signal does not follow a simple linear relationship with thickness, suggesting a higher complexity in the signal generation and its dependence on specimen thickness.

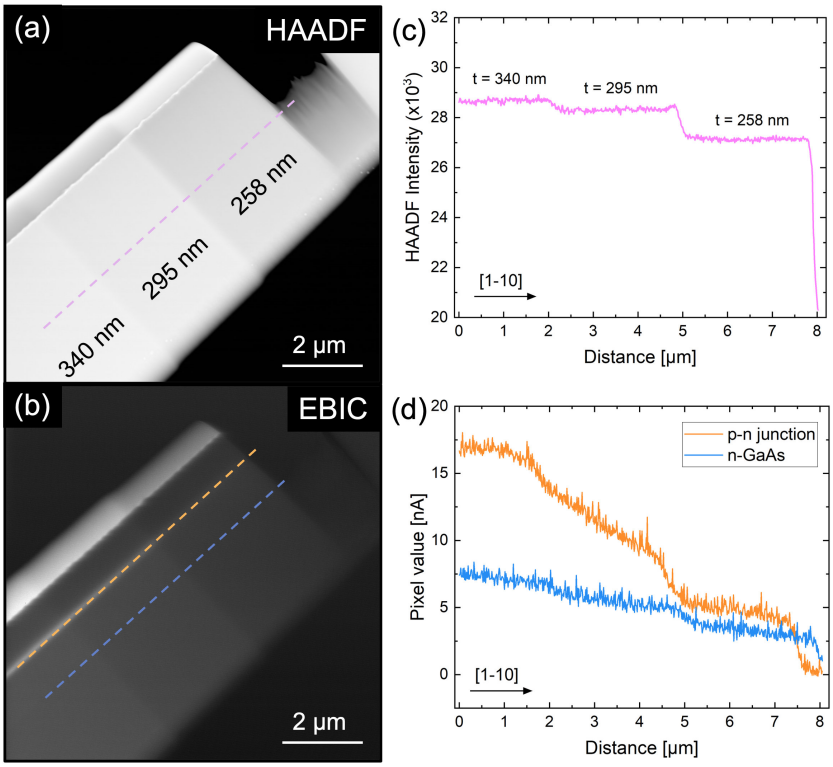

Figure 61: *(a) STEM-HAADF image and (b) corresponding STEM-EBIC map of the GaAs-W specimen. (c) and (d) show the HAADF and EBIC signal intensity profiles across regions of varying thickness. The HAADF profile is measured within the n-GaAs layer, approximately 1 µm away from the junction, while the EBIC profiles are acquired both along the GaAs p-n junction and at the same position within the n-GaAs layer. The HAADF profile is integrated over 50 nm, whereas the EBIC profiles are not integrated to maintain spatial precision.*

In the n-GaAs region away from the junction, where SEEBIC is prevalent, the signal reflects an overlap of thickness contrast and resistance contrast. The sharper intensity steps over shorter distances correspond to thickness changes, similar to the HAADF signal. Thickness contrast in EBIC maps is not linear. In thin areas of the sample, surface-related emission current dominates, while in thicker areas, additional absorption generates thickness- and density-related EBAC. The linear long-range decrease in SEEBIC intensity, visible in Fig. 61d, therefore likely represents resistance contrast, mapping the resistance between the two electrical connections on

either side of the lamella. Higher resistance generally produces a larger gradient.
At the p-n junction, the SEEBIC thickness and resistance contrast overlap with the field-induced EBIC signal, as visible in Fig. 61d. The field-related EBIC reveals a stronger dependence on specimen thickness, as the increase in EBIC contrast at the junction with thickness is more pronounced compared to the increase in SEEBIC signal within the n-GaAs layer. This relationship is illustrated in Fig. 62, which shows the EBIC signal at the junction, the n-GaAs layer, and their contrast as functions of the specimen thickness region.

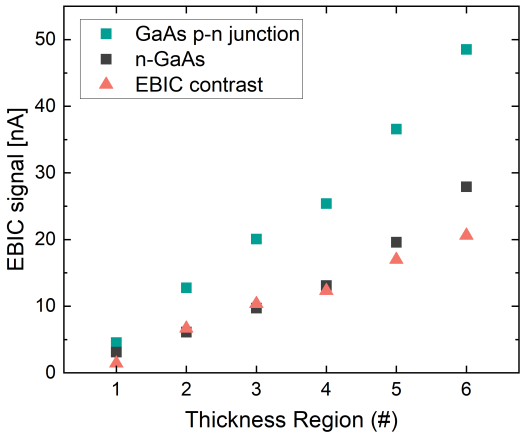

Figure 62: *EBIC signal intensity measured in the different thickness regions of the GaAs-W specimen: at the GaAs p-n junction, in the n-GaAs layer 1 µm away from the junction, and the EBIC contrast of the junction, calculated as the difference between these two intensities. The specimen thickness is increasing from region #1 to #6.*

The underlying processes governing the relationship between TEM specimen thickness and the EBIC signals are complex and less straightforward than in techniques like EH, where the measured electrostatic potential is directly proportional to the electrically active semiconductor thickness, which determines the number of available active dopants. This complexity arises because the different components of the EBIC signal have different dependencies on thickness.
EBAC has a relatively simple relationship with thickness: thicker specimens absorb more primary electrons, resulting in a stronger negative EBAC signal. However, as described earlier, the EBAC signal, and its proportionality to thickness, cannot be easily distinguished by eye or quantified in the EBIC data in Figs. 60 and 61 as the contribution is minor.
The proportionality of field-related EBIC to specimen thickness is evident in Figs. 60 and 61b and d. Thicker specimens exhibit higher EBIC at the SCR, which can be explained in a simplified approach, such as the greater the electrically active thickness available for electron-beam-induced EHP generation, the stronger the resulting current. Furthermore, in thicker specimens, EHP generation and field separation as well as subsequent carrier extraction, are less affected by recombination at the specimen surface, leading to stronger detected currents.
The specimen surfaces not only affect the strength of the field-induced currents – i.e., the EBIC peak height at the GaAs p-n junction – but also influence the confinement of the field-related EBIC signal within the SCR, i.e., the width of the peak. In the EBIC maps (Fig. 60 and 61b), the bright contrast observed at the GaAs p-n junction appears broader in the thicker regions

of the specimen. This broadening is primarily due to the impact of damaged specimen surfaces relative to the specimen thickness on the majority carrier diffusion length, L_D. The field-related EBIC signal outside the depletion width is constrained by L_D, leading to an exponential decay of the EBIC signal from the edge of the SCR into the bulk GaAs layer. As the specimen thickness decreases, carrier surface recombination is enhanced due to the proximity of the specimen surfaces. This reduces the fraction of minority carriers reaching the junction and being collected. Consequently, the diffusion length measured in STEM-EBIC is significantly shorter compared to the diffusion length in the bulk material.[34] This discrepancy hinders the quantification of the field-related EBIC, specifically the extraction of L_D and the depletion width representative of the bulk device.
The increasing confinement of the EBIC signal at the SCR with decreasing specimen thickness is not solely attributed to the reduced L_D. It can be additionally enhanced by the reduced beam broadening, i.e., the higher spatial confinement of the EHP generation volume, as the specimen thickness decreases. The effect of specimen thickness on spatial resolution is discussed in Sect. 7.2.2.

The SEEBIC signal, however, shows a more complex relationship with thickness. While there is a clear correlation – thicker specimens yield higher SEEBIC as shown in Figs. 60 and 61b and d – the exact origin of this trend is less evident. Considering the generation of SEEBIC signal, the SE yield depends on the primary electron energy and on various material properties, including atomic number, SE MFP, work function, and surface potential (introduced in Sect. 7.1.4). At high beam energies, such as the 200 kV used in this study, SEs can be generated relatively deeper within the specimen and with a higher proportion of high-energy SEs compared to lower beam energies. However, only SEs generated near the surface, within the material-specific MED, can leave the specimen and contribute to the SEEBIC signal. SEs generated deeper than this are scattered within the specimen, which prevents them from reaching the surface and being emitted. Therefore, it is not immediately clear why SEEBIC should increase with thickness as evident from the EBIC data in Fig. 60 and 61, given that SE emission is inherently limited to the MED, which does not vary with specimen thickness. One possible explanation could be the reduced relative influence of surface damage in thicker specimens, as fewer active surface defects trap the carrier flow induced by SE emission. However, this interpretation is also not straightforward. The estimated extent of surface damage caused by FIB preparation in GaAs exceeds 150 nm (see Ch. 6.4), which is significantly deeper than the SE escape depth in GaAs. This means SEEBIC carriers should always be significantly affected by surface trap states, as the extent of the surface damage is not changing with specimen thickness. Only the electrically unaffected thickness inside the lamella becomes relatively larger with increasing total thickness. The exact MEP of SEs in GaAs at STEM-relevant beam energies is not well established. Simulations of SE MEPs of metals and semiconductors in general have primarily focused on SEM-relevant energies up to 10 kV,[242,243,244] with the SE MFP in GaAs calculated as approximately 1.39 nm for this energy range.[242]

Although SEEBIC is the most surface-sensitive signal, all EBIC components are potentially influenced by surface-related effects in the TEM lamella, including surface band bending, Fermi level pinning, and surface charging. While a detailed investigation of these effects on individual

EBIC components is beyond the scope of this study, it can be assumed that a higher density of surface defects – introduced during FIB preparation – promotes recombination of electron-beam-induced carriers, thus reducing the total detected EBIC. In addition to this damage-induced reduction, the EBIC signal can further be altered by surface charging effects, which are caused by SE emission under electron beam irradiation. In specimens, such as that shown in Fig.63, surface-charging-induced effects have been observed at the specimen edge. Figure63 presents an EBIC map recorded on a III–V heterostructure comprising a GaAs p–n junction and a GaInP p–n junction grown on an n-GaAs substrate. While a detailed analysis of charge carrier extraction across these heterojunctions is beyond the scope of this work due to its complexity, this map serves as a clear example of how surface charging caused by SE emission can differently influence the EBIC signal in p- and n-doped materials.
Figure 63a shows the EBIC map and the profiles (Fig. 63b) extracted from vacuum into the semiconductor layers along the $[1\bar{1}0]$ direction – parallel to the epilayer interfaces. The EBIC signal measured at the specimen edge relative to vacuum is high (bright) in the p-doped regions and low (dark) in the n-doped regions. This observation is consistent with the findings of Conlan *et al.*, who similarly attributed such contrast to electron-beam-induced surface charging.[34] SE emission leads to the accumulation of positive surface charge, which elicits distinct responses in p- and n-type regions:

- p-type regions: The positive surface charge repels the majority holes, resulting in the formation of a surface SCR. This promotes carrier separation and leads to a strong EBIC signal at the specimen edge – similar to that observed at p–n junctions.

- n-type regions: In contrast, the positive surface charge attracts majority electrons towards the surface, enhancing surface recombination and thereby reducing the detected EBIC signal.

These distinct responses highlight how surface charging alters the EBIC signal in a manner that differs from preparation-induced surface damage. While surface damage typically reduces the EBIC signal through enhanced recombination across all regions, surface charging affects n- and p-doped materials differently.
In addition to these charging- and damage-related effects, other surface phenomena must also be considered, including surface contamination (e.g. C deposition), oxidation, FIB-induced counter-doping, and stoichiometric changes at the specimen surface (e.g. due to C or Ga implantation). These effects can influence the EBIC signal differently in p- and n-doped regions. For instance, Hubbard *et al.* demonstrated that surface contamination significantly affects work function measurements using SEEBIC.[31] Importantly, however, surface-related effects do not only impact the surface-sensitive SEEBIC. They are also expected to strongly affect the field-related EBIC signal, since it is fundamentally governed by the internal electric field of the specimen and thus highly sensitive to local variations in field strength, width, or even local field inversion. While a comprehensive investigation of the electrical impact of these surface effects lies beyond the scope of this study, a complex alteration of the EBIC signal due to the interplay of these various factors is always to be expected. This digression therefore serves as a reminder that the interpretation of STEM-EBIC maps in doped semiconductors should always be approached with the utmost care and caution.

Thick TEM specimens generally reduce the relative influence of surface-related effects on the overall signal. Future studies should focus on the effects of surface charging and band bending on field-related EBIC and SEEBIC to better distinguish surface effects from material-intrinsic properties.

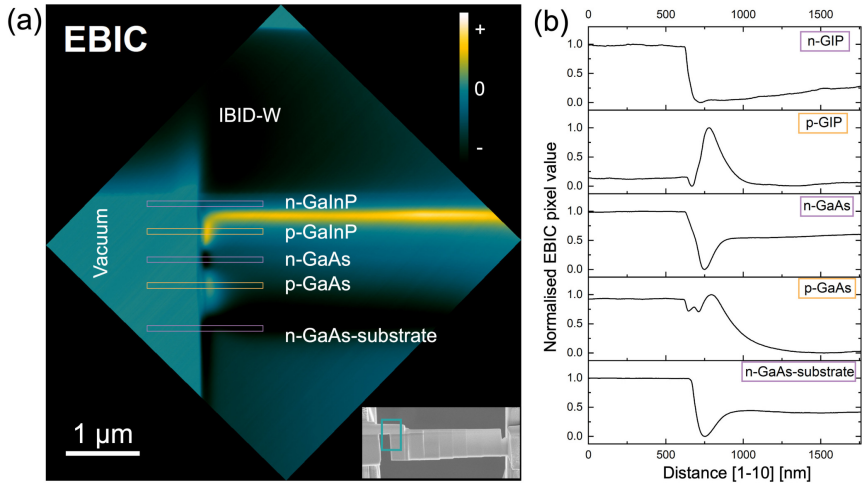

Figure 63: *(a) STEM-EBIC map acquired on a III–V p–n heterostructure specimen. The measurement location is indicated in the SE-SEM overview image shown in the inset. The vacuum region serves as the signal zero reference; negative and positive EBIC signals are represented by dark blue and yellow, respectively, as indicated by the colour scale bar. (b) EBIC profiles extracted from the map in (a) at the positions marked. The signals are normalised, as only relative variations with respect to the vacuum signal are considered.*

In addition to the effect of thickness and specimen surfaces on the individual signal contributions, the impact on the spatial resolution of the EBIC measurement must always be considered. As explained in Sect. 7.2.2, increasing specimen thickness promotes delocalisation of the EBIC intensity due to the larger carrier generation volume caused by beam broadening, as well as the increasing contribution of delocalised SE2 SEEBIC resulting from the higher production of BSE. To accurately quantify this delocalisation of the EBIC signal and the lateral spread of electron collisions within the GaAs specimen, simulations of electron scattering in GaAs must be conducted for the relevant specimen thicknesses.

From a practical perspective, it can be concluded that the choice of sample thickness for EBIC analysis of semiconductor p-n structures is a compromise between ensuring a sufficient electrically pristine thickness to reduce the influence of surface effects and enhance the field-related EBIC signal, and minimising the effects of electron absorption and STEM beam broadening by selecting an appropriate electron-transparent thickness.

7.4.3 The Effect of Beam Imaging Conditions: Beam Current and Spotsize

To optimise beam imaging conditions for STEM-EBIC analysis, the influence of beam current on EBIC measurements is investigated at 200 kV using the GaAs-W-2 specimen. EBIC maps of 2048×2048 pixels are acquired with a pixel dwell time of 50 µs. At a STEM magnification

of 10kx, the FOV was 9.5×9.5 µm, encompassing two specimen thickness regions: 370 nm and > 550 nm. EBIC maps are recorded using two STEM spot sizes, 4 and 6, with beam currents systematically varied between 200 pA and 1000 pA in 200 pA increments by adjusting the monochromator focus. Beam current values are measured using the microscope viewing screen, where absolute readings are known to be inaccurate, but relative changes are reliable. For instance, the difference between 400 pA and 600 pA is consistently 200 pA, allowing relative changes in EBIC signal to be correlated with relative beam current changes.

The resulting EBIC maps are shown in Fig. 64. Line profiles (Fig. 65) are extracted across the GaAs p-n junction as a function of beam current for both thickness regions and spot sizes. As only relative changes are analysed, absolute EBIC pixel values are not specified in the profiles. Figure 66 presents the evaluated EBIC peak current values at the GaAs p-n junction as a function of the beam current, comparing the two thickness regions and spot sizes.

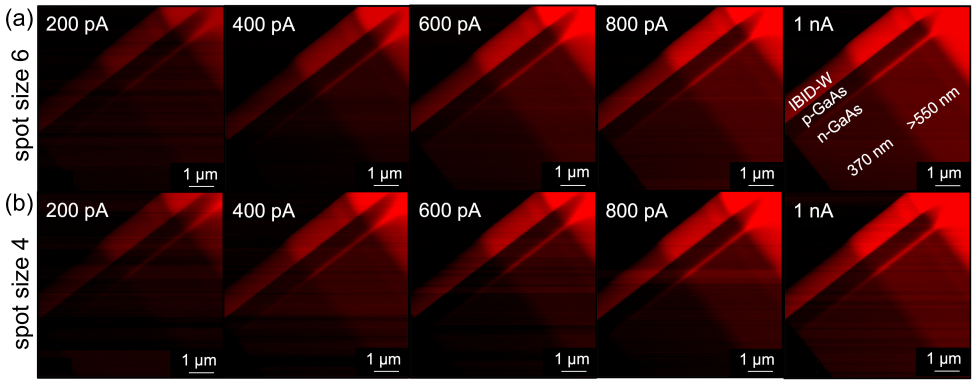

Figure 64: *STEM-EBIC maps of the GaAs-W-2 specimen recorded at various beam currents using (a) spot size 6 and (b) spot size 4. The EBIC intensity ranges (0–110 nA) are adjusted for comparison.*

The data clearly demonstrate the expected direct relationship between beam current and EBIC signal intensity. As beam current density increases, the number of free carriers generated through EHP generation and SE emission also increases. Consequently, the entire EBIC profile across the GaAs specimen, including the IBID-W layer, exhibits an upward shift in intensity with increasing beam current (Fig. 65). The linearity of this relationship, as seen in Fig. 66, is highest in the thicker sample region when using the larger spot size (6).

The beam current setting must be tailored to each STEM-EBIC experiment as a compromise between improving the EBIC SNR by increasing the beam current and minimising electron beam induced knock-on damage to the semiconductor specimen by limiting the beam current, taking into account the specimen thickness. This compromise must also take into account the impact of changes in spot size and monochromator focus on the STEM probe size, and consequently, on the spatial resolution of the EBIC measurement.

The choice of STEM spot size influences not only beam current but also probe size. Increasing the spot size to enhance beam current sacrifices spatial resolution due to the larger probe diameter.

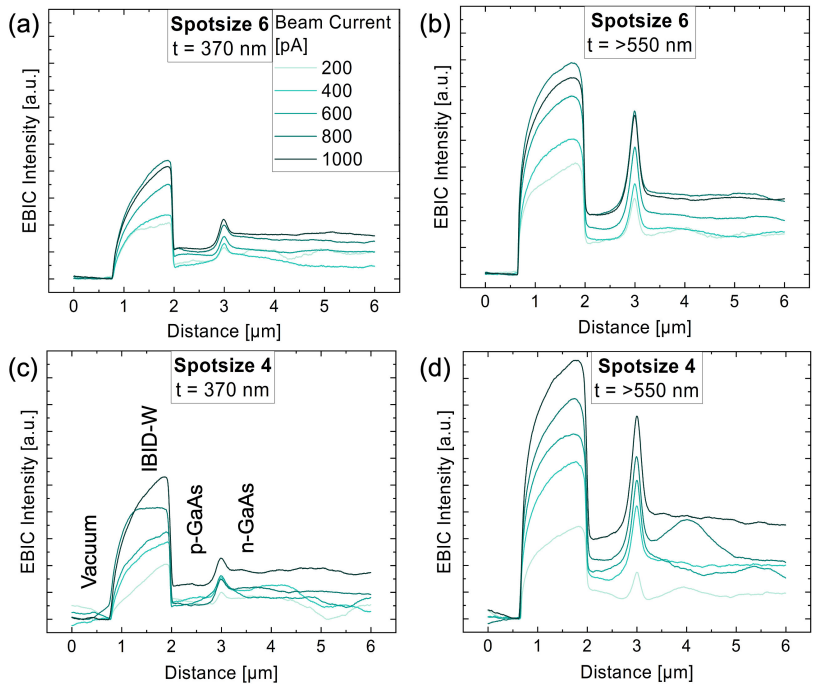

Figure 65: *The effect of STEM-beam current on EBIC intensity compared for two different specimen thicknesses and spot sizes: (a) and (b) spot size 6 at 370 nm and > 550 nm, respectively. (c) and (d) spot size 4 at 370 nm and > 550 nm, respectively. The profiles are extracted across the GaAs-W-2 p-n structure (EBIC maps in Fig. 64) and integrated over 100 nm. The y-ranges are adjusted for comparison. Absolute EBIC pixel values are not specified, as the relative changes in EBIC intensity in relation to the relative changes in beam current were analysed. The absolute beam current values as measured on the fluorescent screen are not accurate.*

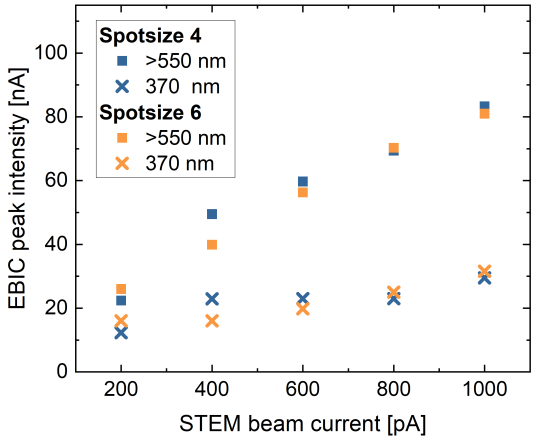

Figure 66: *The EBIC peak intensity measured at the GaAs p-n junction as a function of the STEM-beam current for different spot sizes (4 and 6) and specimen thicknesses (370 nm and > 550 nm). The values are evaluated from the EBIC data in Fig. 64 and 65.*

Therefore, in STEM-EBIC experiments, the spot size must balance spatial resolution and SNR. Comparison of EBIC maps for spot sizes 4 and 6 (Fig. 64) reveals that the data acquired with spot size 6 are less noisy for both thickness regions. Although the absolute EBIC peak current at the p-n junction is similar for both spot sizes at the same beam current, the higher noise in spot size 4 data causes irregular deviations. Therefore, using spot size 6 is preferable unless high spatial resolution is required, for example for SEEBIC-specific experiments.
Once the spot size is chosen, beam current can be adjusted by varying the monochromator focus. This approach is practical, especially when higher-order aberration correction has been performed for high-resolution acquisitions, as changing the spot size would necessitate re-optimisation. However, adjusting the monochromator focus alters the electron energy spread, which affects spatial resolution due to chromatic aberrations. Increasing the beam current by adjusting the monochromator focus increases the electron energy spread, which decreases spatial resolution as chromatic aberrations are enhanced. While this trade-off is relevant, it is acceptable in experiments that do not target spatial resolution that approach lattice distances.
At constant spot size (6), the optimal beam current depends on specimen thickness, balancing SNR and beam-induced damage. Analysis of line profiles in Fig. 65a and b (spot size 6) shows that higher beam currents are required in thinner regions (370 nm) to resolve the field-related EBIC peak at the GaAs p-n junction against a high-noise background. In thicker regions (> 550 nm), sufficient SNR is achieved at lower beam currents, such as 400 pA. This is due to the reduced influence of surface effects, such as enhanced surface carrier recombination, in thick specimens. In thin specimens, higher beam currents are needed to overcome surface-related signal losses and achieve adequate SNR. However, higher beam currents increase the risk of beam-induced damage, making thicker specimens preferable for EBIC analysis as they allow the use of lower beam currents while maintaining sufficient SNR.
In conclusion, recording EBIC data in thicker specimen regions using spot size 6 and medium beam currents (e.g., 600 pA) offers an optimal compromise between high SNR, limited beam damage, and acceptable spatial resolution. Quantification of beam damage has not been conducted in this study but should be included in future investigations in order to optimise beam current settings for STEM-EBIC analysis of semiconductors.

7.4.4 The Interrelated Effect of STEM Magnification, Pixel Frame Size and Pixel Dwell Time

The effect of STEM magnification on EBIC analysis is investigated using the GaAs-W-2 specimen. HAADF images and EBIC maps of 2048×1365 pixels are recorded at various magnifications ranging from 20kx to 80kx, while maintaining a constant pixel dwell time of 50 µs. The applied beam current is 600 pA as measured on the viewing screen. The pixel sizes corresponding to these STEM magnifications for the given frame size are listed in Table 12. The resulting images are shown in Fig. 67, along with a comparison of EBIC profiles extracted across the GaAs p-n junction for the different magnifications.

In EBIC experiments, the magnification and pixel frame size used to record an EBIC map must be selected to achieve the desired pixel size, i.e., the spatial resolution of the EBIC map. This selection depends on the specific specimen and experimental aims. For example, when analysing

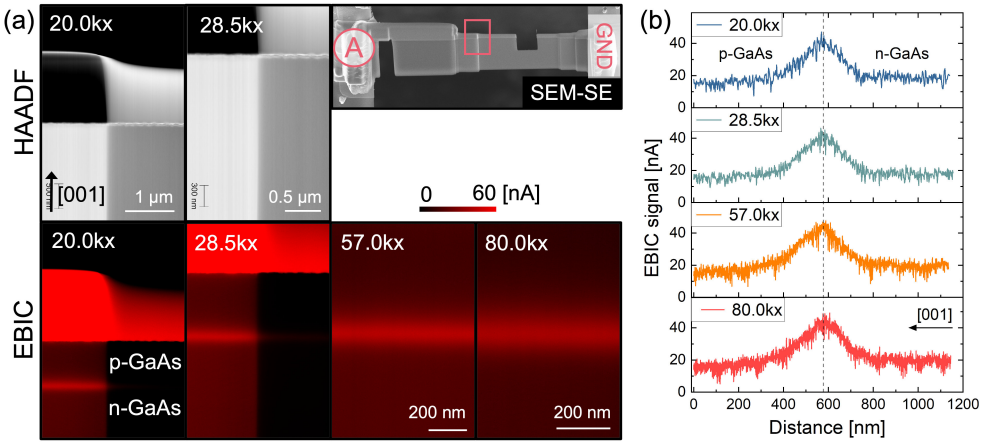

Figure 67: *(a) STEM-EBIC maps (2048 × 1365 pixels) are acquired at various magnifications on the GaAs-W-2 specimen, with a 50 µs pixel dwell time. The data at 57kx and 80kx magnification is recorded on the thicker of the two sample regions. The EBIC intensity ranges (0–60 nA) are adjusted for comparison. The SEM-SE overview image shows the lamella connection configuration and measurement location as highlighted in a red box. STEM-HAADF images are included for comparison. (b) EBIC profiles extracted from the EBIC maps in (a) obtained with the respective magnifications.*

semiconductor Schottky or p-n junctions, the pixel size must be small enough to resolve the depletion width of the junction. For the present GaAs p-n structure, which has a symmetrical doping concentration of 1×10^{18} cm^{-3}, an average depletion width of 82 nm was measured in multiple TEM lamellae using EH (Sect. 6.4.1). This provides a relatively broad range of applicable magnifications.

A comparison of the EBIC maps and corresponding profiles in Fig. 67 shows that the distribution of the EBIC signal across the GaAs p-n junction remains unchanged with varying STEM magnification. Thus, reducing the magnification from 80kx to 20kx does not alter the information content of the EBIC map for this specimen. This flexibility allows the magnification to be adjusted to accommodate the desired FOV. For instance, in the present specimen, the FOV can be set to include multiple thickness regions, the metal-semiconductor interface, and/or a vacuum region within a single image frame.

Unlike at EH, including a vacuum reference is not an intrinsic requirement for STEM-EBIC mapping. However, incorporating a vacuum region in the FOV can be advantageous as it provides an independent zero reference for pixel value calibration, supplementing the zero-adjustment tools available in the EBIC software.

The influence of pixel dwell time on EBIC measurements is investigated by comparing EBIC maps acquired at dwell times of 25 µs and 50 µs, under a fixed magnification of 57kx and a beam current of 600 pA (TEM viewing screen), as presented in Figure 68. For the specified frame size of 2048×1365 pixels, these dwell times correspond to total frame acquisition times of $1.1\bar{6}$ min and $2.\bar{3}$ min, respectively.

In general, longer dwell times improve the SNR in recorded EBIC maps. This is clearly demons-

trated in Fig. 68, where increasing the dwell time from 25 µs to 50 µs per pixel significantly enhances the SNR of the EBIC map. This improvement is particularly evident in the extracted profiles across the GaAs p-n junction. Adjusting the dwell time is therefore an essential way to compensate for low EBIC signal intensities, especially when investigating thin specimens and/or when experimental constraints require the use of relatively low STEM beam currents. However, the advantages of longer dwell times in improving the SNR must be carefully balanced against the risks of drift effects and beam damage. Longer dwell times can cause signal drift in vacuum regions, which may compromise previously established zero adjustments. Additionally, extended probe dwell times at individual pixel positions increase the potential for beam-induced damage to the specimen. For these reasons, shorter scan durations can be advantageous in minimising both drift and damage.

For this work, a dwell time of 50 µs/px is considered an optimal compromise to improve the EBIC SNR while still limiting drift effects and maintaining the total frame acquisition time within a practically acceptable range of $2.\bar{3}$ min for 2048×1365 frames and 3.5 min for 2048×2048 frames.

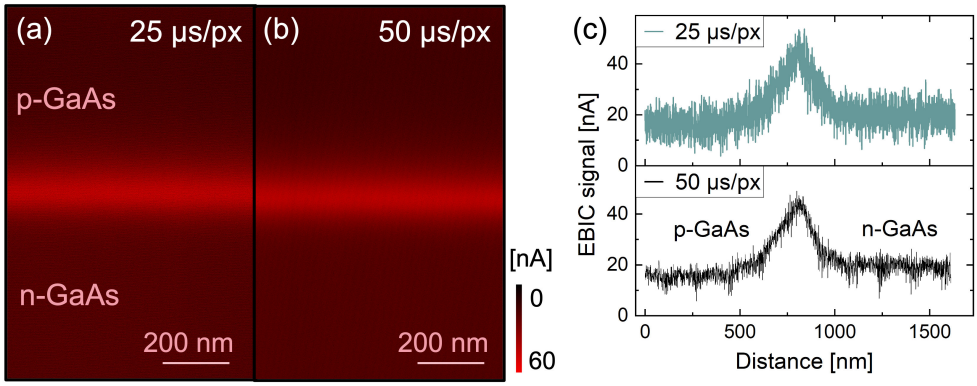

Figure 68: *The influence of pixel dwell time on the SNR of EBIC imaging. STEM-EBIC maps of 2048×1365 pixels are acquired with pixel dwell times of (a) 25 µs and (b) 50 µs, at 57kx magnification. EBIC intensity profiles (c) are extracted across the GaAs p-n junction from the maps obtained with the respective dwell times.*

Table 12: Calibrated pixel sizes for STEM-EBIC maps of 2048×2048 pixels per frame.

STEM-Magnification	Pixel Size [nm]
20.0kx	2.32
28.5kx	1.63
40.0kx	1.16
57.0kx	0.81
80.0kx	0.58

7.5 STEM-EBIC Analysis of GaAs p-n Junctions

The previously established STEM-EBIC method is employed to investigate the current distribution in a GaAs p-n junction device and its behavior under applied bias, serving as a complementary approach to electrical potential mapping via *in situ* biasing EH. The study focused on

the GaAs-W-2 specimen.
In the first part, LM STEM-EBIC is utilised to test the electrical connections of the MEMS chip and assess current extraction from the sample as well as its response to applied bias on a larger scale. LM-STEM-EBIC is particularly suited for mapping long-range variations, such as resistance contrasts or bending contrasts in EBIC signals.
Subsequently, higher magnification STEM-EBIC is conducted to analyse the GaAs p-n junction and its response to applied electrical bias in greater detail.

7.5.1 Low-Magnification STEM-EBIC Analysis

7.5.1.1 MEMS Chip Testing

To test the electrical connections of the MEMS chip to the specimen and to ground, the LM-STEM-EBIC maps shown in Fig. 69 are acquired without applied bias using the three different connection configurations illustrated in Fig. 58a. LM-STEM enables an extended FOV, allowing both the specimen and parts of the MEMS chip frame to be visualised simultaneously.

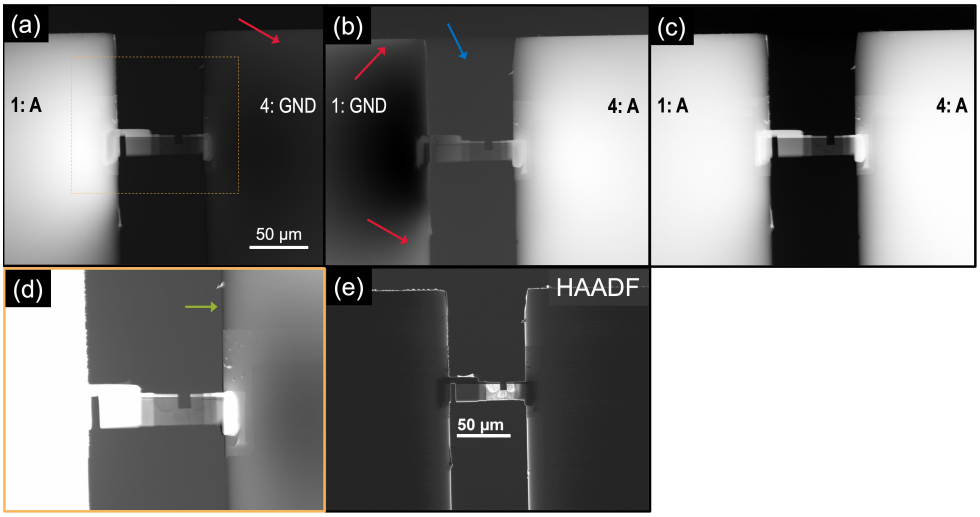

Figure 69: *(a)-(c) LM-STEM-EBIC maps of GaAs-W-2 acquired at 220× magnification under three different connection configurations of terminals 1 and 4 to the amplifier (A) and ground (GND). (d) Magnified region from map (a), indicated by the orange box, with adjusted EBIC signal range for enhanced contrast. (e) Correlated LM-STEM-HAADF image for structural reference.*

Examining the three different connection geometries in Fig. 69, the side of the MEMS chip including the metal track connected to the amplifier exhibit a strong bright EBIC contrast. This observation confirms that the current induced by the incident primary electrons flow directly to the detection electronics, thereby verifying the electrical connection of the metal tracks through the holder to the EBIC amplification system.
Conversely, the chip-side and metal track connected to electrical ground should appear dark in the EBIC map, if the chip is properly grounded, as in this case the carriers would preferentially follow the direct low-resistivity path to ground. While the contrast of the grounded chip-side

appears noticeably darker compared to the opposite chip side in Fig. 69a and b, several observations indicate that the MEMS chip frame is not properly grounded:

- Bright contrasts at the edges of the chip frame on the grounded chip side as indicated by the red arrows in Fig. 69a and b.
- Remaining bright contrast in the grounded metal tracks (Fig. 69a and b).
- Bright vacuum signal in the map with inversed connectors as indicated by the blue arrow in Fig. 69b.

To investigate the grounding of the MEMS chip, the EBIC map shown in Fig. 69a is magnified to focus on the regions of the chip closest to the TEM specimen, as displayed in Fig. 69d. By adjusting the EBIC signal range, the bright contrast of the grounded metal track becomes more pronounced. Additionally, a black contrast line can be observed along the rim of the right chip side (indicated by the green arrow), which opposes the intense bright contrast on the left side of the chip.
These observations strongly suggest the presence of a capacitor between the MEMS chip frame and the metal tracks. This phenomenon can occur if the back of the MEMS chip is electrically floating, i.e., not properly grounded. The MEMS chip frame consists of a thick Si wafer, and grounding is attempted by placing the chip in contact on grounded metal within the holder. However, achieving an ohmic connection through mere physical contact is challenging. On the contrary, it is likely that the contact between the chip frame and the holder yields a Schottky contact instead. The capacitive connection between chip frame and metal tracks can lead to inductive coupling.

While the bright contrast observed in the entire grounded metal track (Figs. 69a, b, and d) clearly indicates an issue with the chip grounding, an additional observation must be considered separately. A halo of bright contrast is visible on the grounded side of the chip near the specimen, which can be most prominently observed in Fig. 69a. This halo can be ascribed to the effect that a share of SEs emitted from the specimen are able to hit the chip or sample again, hence contributing themselves to EBIC signal generation. The SE scattering effect creates a bright halo around the specimen in the EBIC map, thereby also contributing to the bright contrast in the grounded metal track. However, the bright signal on the grounded chip side farther from the specimen and outside the halo region still indicates an inherent issue with the chip's ground connection, as it cannot be explained by SE scattering.

The hypothesis of inductive coupling between the chip frame and the metal tracks is supported by the analysis of the vacuum signal in the three LM-EBIC maps (Fig. 69). Fig. 70 shows EBIC profiles extracted from the vacuum region of these current maps.
Figure 70a shows that the vacuum signal levels are significantly offset depending on the connection setup. The configuration where both the n- and p-type sides are connected to the amplifier yields the highest pixel current values in the vacuum.
Under externally applied bias, shifts in the vacuum signal correspond directly to the bias-induced current within the specimen. However, since these maps are acquired without bias, the dark current is expected to remain constant across different acquisitions and uniform throughout the

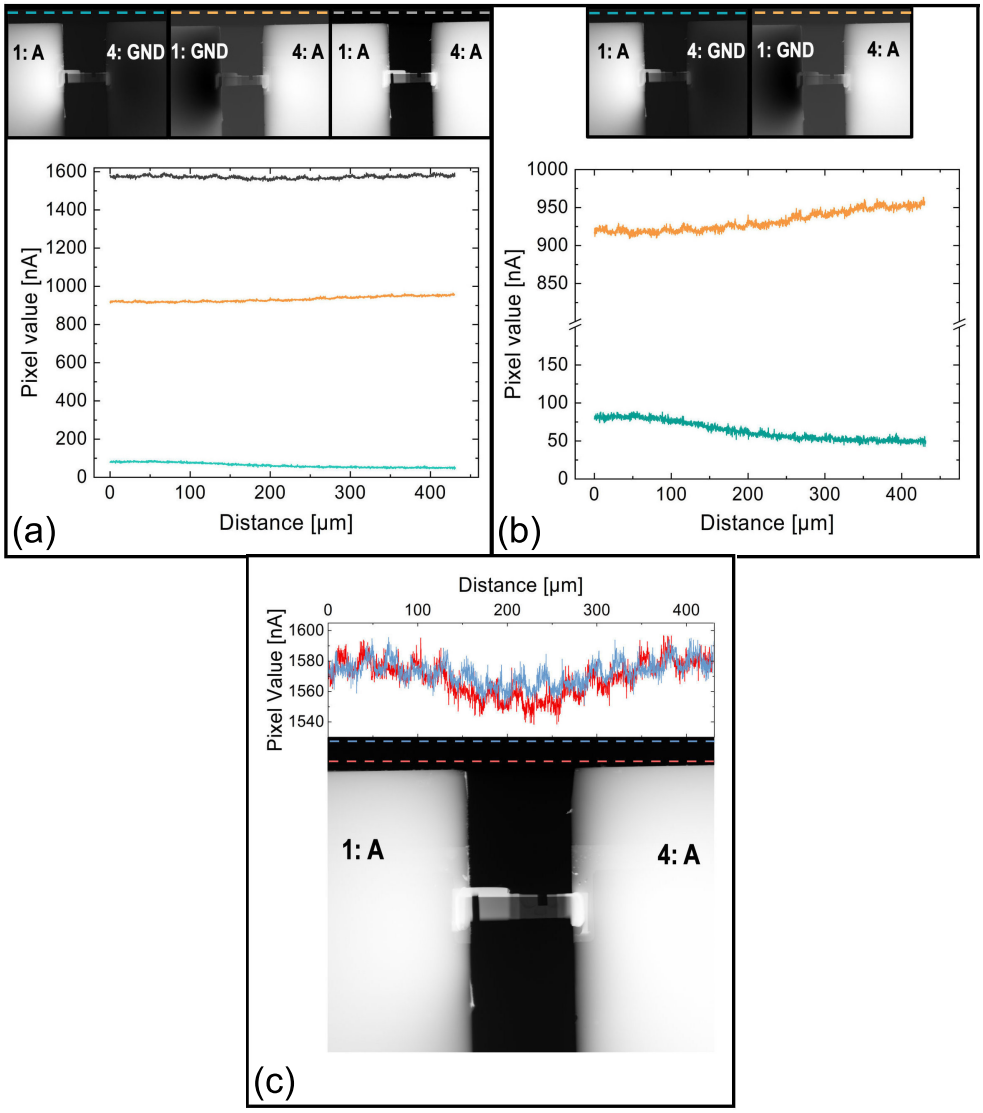

Figure 70: *EBIC profiles extracted from the vacuum regions of the LM-STEM-EBIC maps (Fig. 69). (a) Comparison of the profiles from all three maps reveals a significant shift in EBIC intensity in the vacuum region. (b) Highlights the inversion of the signal trend increasing towards the chip side connected to the amplifier when the connectors are reversed. (c) Demonstrates the increase in signal towards both chip sides when both are connected to the amplifier.*

vacuum region in each map. Contrary to this expectation, Fig. 70b and c reveal that the EBIC signal is not uniform throughout the vacuum but instead varies along the direction parallel to the lamella [$1\bar{1}0$]. The signal increases as the chip side connected to the amplifier is approached. Accordingly, the trend of the vacuum current profile reverses when the connectors are inverted (Fig. 70b), highlighting a systematic dependence on the connection configuration.
The observed inconsistencies in the dark current can be attributed to inductive coupling between the MEMS chip frame and the metal tracks, resulting from the improperly grounded Si-frame. The charging of the chip frame and subsequent discharging into the metal tracks cause time-dependent fluctuations in the current signal. As a consequence, the signal detection is not synchronised with the STEM beam position.
Minor additional contributions to the dark current variations may arise from the large beam size used in LM-STEM mode. Temperature drift in the electronics could also induced shifts in the dark current. While this effect is unavoidable, it is minor and hence cannot account for the observed magnitude of the shifts. Furthermore, the maps are acquired in succession within 15 minutes, minimising the impact of such drift. Variations in the vacuum current (or the fact that the vacuum signal is not flat within a single map but fluctuates) might also arise from stray electrons originating from apertures in the microscope column. However, such variations would be random, not systematic as observed in Fig. 70. The reversal of the trend with connector inversion thus rules out stray electrons as the cause.

Analysis of the dark current in the vacuum illustrates that insufficient grounding of the chip and the resulting inductive coupling could lead to unexpected effects in the EBIC signal, as the MEMS frame may charge and discharge into the metal tracks depending on the signal levels. However, the timescale of these charge-discharge processes is expected to exceed the duration of a frame acquisition. To mitigate these effects, it is hence advisable to include a vacuum region within the FOV of the recorded EBIC maps, enabling corrections of the induced noise.
In this work, these grounding issues are observed across multiple biasing chips. It is found that an improved ground connection could be achieved by using FIB milling to drill one of the metal tracks, which is not connected to the sample, down into the substrate. By subsequently refilling the cut with FIB-deposited metal, a conductive plug (VIA) connection can be created from the substrate to the track, as demonstrated in Fig. 71 by means of a different specimen.
However, this method is only applicable to chips with a 4-track geometry, where unconnected metal tracks are available for the VIA connection. In contrast, the present specimen is mounted on a 2-track chip, where both tracks are required for connecting the lamella, making this approach unsuitable.

7.5.1.2 EBIC Signal Contributions and Distribution

After testing the electrical connections and grounding of the MEMS chip, the focus is now on analysing the EBIC signal in the GaAs-W-2 p-n specimen. LM-STEM-EBIC maps, acquired at 1250× magnification using the three connection configurations (see Fig. 58a), are presented in Fig. 72.
The signal contributions in the GaAs-W-2 sample, as well as their spatial distribution and variation with thickness, closely resemble those observed in the GaAs-W sample described in

Sects. 7.4.1 and 7.4.2. The IBID-W metal protection layer exhibits a pronounced SEEBIC-dominated contrast that increases with thickness, as does the SEEBIC-dominated signal in the p-GaAs and n-GaAs regions away from the junction. Furthermore, the field-related EBIC contrast at the GaAs p-n junction increases and widens with thickness, as explained in Sect. 7.4.2. The expected sign inversion of the field-related EBIC upon inverting the connectors (Fig. 72a and b), as well as the suppression of the signal by connecting both connectors to the amplifier (Fig. 72c), is also clearly visible in the LM-EBIC maps. The large FOV in LM-mode further provides a clear visualisation of the electrical circuit design of the TEM lamella. The specimen is cut as a back-to-back diode. Consequently, the GaAs p-n junction exhibits opposite field-related EBIC contrast on either side of the top isolation cut, which inverts when the connector polarities are reversed (Fig. 72a and b). In general, it should be noted that the spatial resolution of LM-STEM-EBIC measurements is limited due to the extended probe size. The LM-EBIC maps are acquired using a 0.27 mrad convergence angle, yielding an estimated probe size of about 22.7 nm, given that the probe size is referred to as the diameter of the central Airy disc given by Eq. 18 and probe tail effects are neglected (see Sect 3.1.4). Hence, LM-EBIC contrasts at material transitions and sample regions close to the support chip should always be interpreted with caution due to the effects of the large probe. The current generation and extraction at the p-n junction should generally be studied under higher STEM resolutions, which are better suited to the depletion width of the examined junction. The LM mode, on the other hand, is particularly useful for investigating long-range variations in the EBIC signal, such as resistance contrast or EBIC contrast at bend contours, as discussed in the following paragraphs. Further, LM-EBIC remains valuable for qualitatively locating p-n junctions within the larger context of the lamella's electrical circuit. This is demonstrated by the LM-EBIC maps in Fig. 72a and b, where the position of the p-n junction in the GaAs-W-2 specimen is clearly identifiable. Therefore, in the following, LM-STEM-EBIC is employed to assess the specimen's response to *in situ* biasing, provide an overview of the induced current distribution, and detect short-circuit paths or recombination centers.

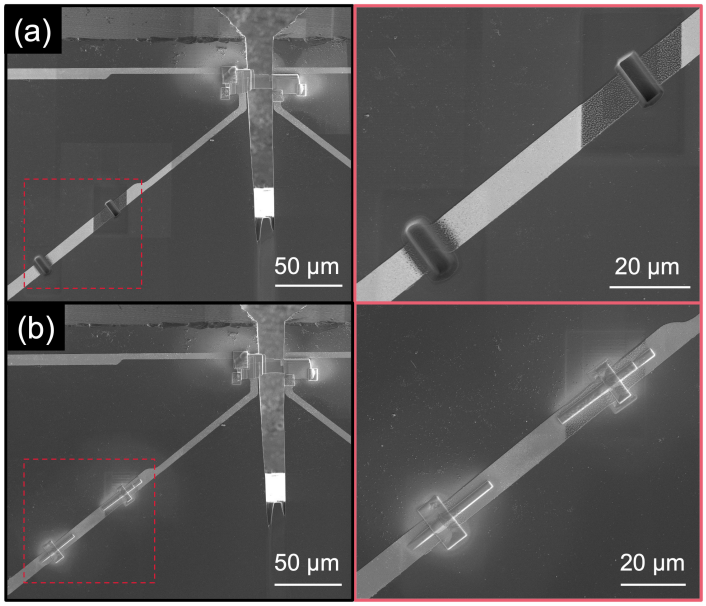

Figure 71: *SEM-SE images illustrating the procedure for creating a conductive plug (VIA) connection from the MEMS chip substrate to the metal track. (a) Step 1: Cutting through the unconnected metal track 2 into the substrate using Ga-FIB milling. (b) Step 2: Filling the cuts with ion beam-deposited W.*

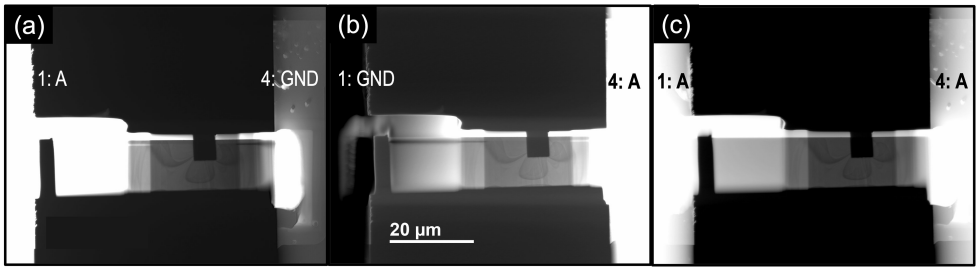

Figure 72: *LM-STEM-EBIC maps of GaAs-W-2 acquired at 1250× magnification under three different connection configurations of terminals 1 and 4 to the amplifier (A) and ground (GND).*

EBIC Contrast at Bend Contours

The LM-STEM-HAADF image, presented in Fig. 73, reveals pronounced bending contours in the GaAs-W-2 lamella. As previously described in the context of EH experiments (Sect. 6.4), such bending arises typically as the long and thin GaAs specimen are fixed on both sides of the biasing chip across the trench. Most interestingly, these bend contours also give rise to contrast in the EBIC maps (Fig. 72). This raises the question of the mechanism responsible for the contrast at the bend contours. Based on the following observations, it can be concluded that it is not a field-related EBIC signal:

- The contours are visible through the lamella, also far from the p-n junction.

- Upon inverting the electrical connectors, the contours still yield a dark contrast, thus no inversion of the contrast.
- When cancelling out the field-related EBIC contrast by connecting both connectors to the amplifier, the bend contour contrast remains.

Since the signal at the bend contours is negative (dark contrast), SEEBIC can be ruled out as the contrast-generating mechanism. Instead, the contrast may originate from EBAC, i.e., the current resulting from the absorption of primary electrons. To test this hypothesis, the signal at the bend contours must be analysed under an externally applied bias. Unlike SEs, primary electrons should not be affected by the bias. Therefore, while the SE current changes under applied bias, the EBAC signal should remain unchanged.
The mechanism responsible for the contrast at the bend contours, along with the corresponding investigation of EBIC contrast under applied bias, is further discussed in Sect. 7.5.1.3.

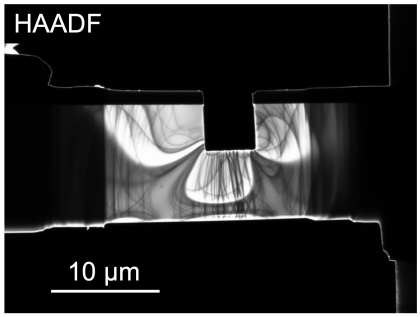

Figure 73: *LM-STEM-HAADF image of the GaAs-W-2 sample showing pronounced bending contours.*

Resistance Contrast

Apart from the field-induced EBIC signal generated at the p-n junction, STEM-EBIC maps also reveal resistance contrast through both SEEBIC (SEEBIC/RC) and EBAC (EBAC/RC) signals. As introduced in Sect. 7.1, observing resistance contrast requires two electrical connections to the specimen: one connected to the amplifier and the other to the ground. As the primary beam scans across the lamella, the resistance is divided between these contacts depending on the beam position, as the generated SEEBIC and EBAC carriers flow to the contact with the lower resistance along their respective paths.
STEM-EBIC maps, shown in Fig. 74a and b, are acquired at 2500× magnification for the two possible connection configurations. EBIC profiles (Fig. 74d) are extracted from both maps in the $[1\bar{1}0]$ direction at two distances, 6.6 µm and 9 µm as indicated by green and orange, away from the junction to exclude field-related EBIC contributions. The crystalline specimen thickness in this region is measured to be 370 ± 6 nm using STEM-CBED.
A gradual change in signal intensity from the left to the right side of the chip is observed. This long-range variation corresponds to resistance contrast, mapping the resistance between the two electrical contacts on either side of the lamella. The formation of SEEBIC/RC can be explained as follows: At the position where the beam illuminates the sample, SE leave the specimen. Considering the configuration with the amplifier connected to the left-side terminal 1 (Fig. 74a)

as an example, these electrons must be replenished either from the right contact (connected to ground) or the left contact (connected to the amplifier). Electrons are primarily supplied via the path with lower resistance. The closer the beam is to the amplifier, the lower the resistance for electron replenishment, leading to a higher detected current. As the beam moves further from the amplifier, the resistance increases, reducing the current drawn from that contact. Consequently, in this configuration, the recorded current is highest on the left side and decreases as the beam moves to the right. The map recorded with the reversed connection configuration (Fig. 74b) exhibits the opposite trend.

The formation of EBAC/RC follows a similar principle, with the difference that it maps the resistance encountered by the absorbed electrons as they travel toward the amplifier. However, in the 370 nm thick lamella region, SEEBIC is expected to be the dominant source of the resistance contrast, with only minor contributions from EBAC/RC. Since EBAC is magnitudes weaker than SEEBIC for a TEM specimen, separating EBAC/RC from SEEBIC/RC is challenging. While experimental data alone do not allow for a direct separation, simulations can provide estimates of the relative contributions of SEEBIC/RC and EBAC/RC. However, both SEEBIC and EBAC do not purely reflect resistance but show thickness and resistance contrast superimposed. Therefore, it must be verified whether the observed long-range signal trend (Fig. 74d) is exclusively due to resistance contrast.

STEM-CBED measurements confirm a uniform lamella thickness of 370 ± 6 nm in the analysed region, and thickness variations arising from FIB milling are typically limited to the vertical direction ([001] here). In this direction, the specimen may form a slight wedge depending on the milling angles. However, the standard FIB preparation procedure developed for EH experiments (see Ch. 4) ensures a near-parallel sided lamella. STEM-CBED measurements confirm a uniform thickness of 370 ± 6 nm over a 16 µm range from the GaAs (001) surface, with minor variations within the measurement error. Thus, thickness variations in this specimen can be ruled out as the cause of the observed systematic long-range trend in the EBIC signal along $[1\bar{1}0]$.

Further confirmation of resistance contrast is obtained by inverting the electrical connections (Fig. 74d), which reverses the signal trend. In each configuration, the current increases toward the chip side connected to the amplifier. This rules out thickness variations as the source of the long-range signal change and confirms resistance contrast as the underlying mechanism. EBIC intensity changes caused by thickness variations would not invert upon connector switching. This is confirmed by the EBIC profiles in Fig. 74e taken across different thickness regions in the n-GaAs layer (parallel to and 1 µm below the p-n junction). Here, the short-range EBIC intensity steps reflecting thickness changes remain independent of the electrical connection configuration.

Additional evidence ruling out thickness contrast as the cause of the long-range signal trend is the suppression of resistance contrast upon connecting both lamella contacts to the amplifier. While this configuration suppresses field-related EBIC at the junction (see Sect. 7.1 and 7.3.3), it also suppresses resistance contrast between the contacts. Indeed, the systematic trend in EBIC intensity is absent in the corresponding EBIC profiles in Fig. 74f. Instead, the overall signal remains constant, apart from non-systematic contrast variations due to bend contours. This provides definitive evidence that the long-range signal variation observed in the EBIC maps (Fig. 74a, b and c) is purely due to resistance contrast.

Neglecting the small-scale variations caused by bend contours, the overall gradient in EBIC in-

tensity is uniform, reflecting the uniform resistance distribution in the analysed lamella region of constant thickness. However, resistances are expected to vary depending on the lamella thickness and length. Previous studies demonstrated approaches for quantitative STEM-SEEBIC resistance contrast imaging (RCI).[216,217] Hubbard *et al.* calculated resistances, r, between a given pixel and the EBIC-detecting electrode as

$$r = R_{device}\left(1 - \frac{I_{pixel}}{I_{EBIC}}\right) \tag{64}$$

where I_{pixel} is the EBIC detected at a given pixel, I_{EBIC} is the total EBIC generated on the detecting electrode and R_{device} is the total resistance of the specimen between both electrodes.[216,217] In specimens that predominantly exhibit SEEBIC, applying this relation to derive an RCI from an EBIC map is relatively straightforward. However, an unambiguous evaluation of RCI is not possible for EBIC maps where SEEBIC is mixed with field-related EBIC contributions, as the latter's relationship to resistance differs from that of SEEBIC.[217]

In the present GaAs-W-2 specimen, there are sample regions, such as the n-GaAs substrate, that are located far enough from the p-n junction to avoid field-related EBIC contributions. However, absolute resistance measurements are not attempted, primarily because the interpretation of RC remains obscured by the significant influence of the damaged surface layers and their unresolved effect on SEEBIC/RCI.

In cases where quantifying resistance contrasts in STEM-EBIC is attempted, considering the difference between the resistance of the TEM lamella and that of the bulk GaAs p-n device is crucial. The overall resistance of the lamella is substantially reduced due to FIB-induced surface damage, which provides low-resistivity pathways for active carriers, although the FIB milling procedure has been optimised to minimise the damage as much as possible (see Ch. 4).

The persistent influence of short-circuit paths is evident in the dark I–V characteristics of the GaAs-W-2 lamella (Fig. 75), measured prior to the first electron beam exposure in the TEM using a Keithley power supply connected to the biasing holder. The pronounced shunt characteristics, likely originating from the damaged surface layers, presumably obscure the inherent properties of the p-n junction. As a result, the dark I-V behavior does not exhibit interpretable diode characteristics. Without electron beam illumination, the current induced by the externally applied voltage is predominantly flowing through the low resistivity surface paths along the applied bias field, resulting in a very low resistance of 4000Ω measured for the GaAs-W-2 specimen. Conversely, when the electron beam penetrates the sample during EBIC mapping, the current characteristics at the p-n junction are clearly visible in the EBIC map, as carriers are generated within the bulk, allowing EBIC to probe the entire volume of the lamella. Nevertheless, pronounced shunt resistances pose a challenge for the quantitative EBIC characterisation of semiconductor specimens, as they can obscure measurements of key parameters such as carrier diffusion lengths. Practical approaches to mitigate the influence of surface shunts include increasing the lamella thickness to enhance the ratio of the bulk signal to the shunt contribution from the damaged surface, and reducing the lamella length to minimise the surface area. However, both solutions are difficult to implement, as the lamella length is constrained by the trench width of the factory produced MEMS chips. Additionally, increasing the sample thickness must be carefully balanced against potential drawbacks, such as reduced spatial resolution

in the recorded EBIC maps and increased noise levels due to primary electron absorption and backscattering, as discussed in Sect. 7.4.2.

Regarding the spatial resolution of EBIC-RCI, although SEEBIC itself originates from a highly localised region at the sample surface, the resulting RC is influenced by all conductive paths to ground, similar to EBAC/RC. Consequently, the related resistance probes the entire volume of the imaged lamella.[217] Hence, the spatial resolution of EBIC-RCI is ultimately limited by the STEM probe size, which, as previously explained, is significantly extended in LM-STEM-EBIC.

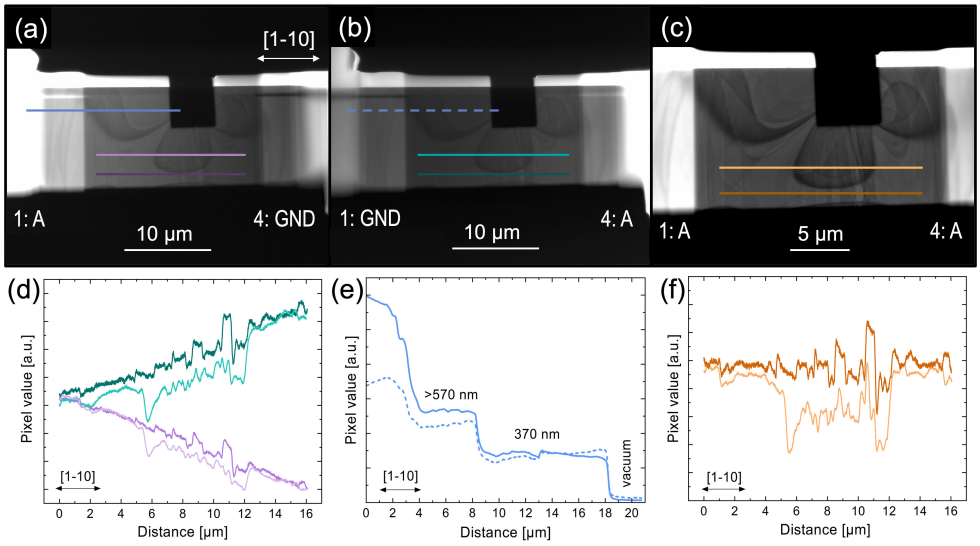

Figure 74: *(a)–(c) LM-STEM-EBIC maps recorded using the three indicated connection configurations. (d)–(e) EBIC intensity profiles extracted from maps (a) and (b) at the specified positions. The profiles in (f) are derived from map (c). All profiles have been integrated over a width of 0.6 µm and corrected for the vacuum signal.*

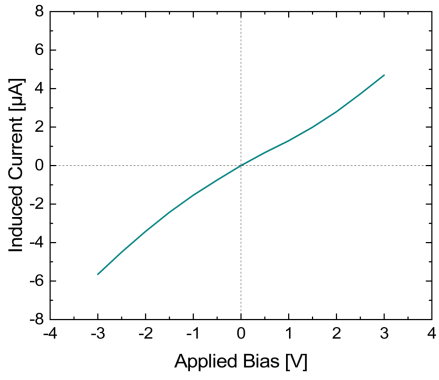

Figure 75: *Dark I-V characteristics of the GaAs-W-2 sample, measured without electron beam illumination in the TEM over an applied voltage range of -3 to +3 V.*

7.5.1.3 *In Situ*-Biasing LM-STEM-EBIC of a GaAs p-n Structure

After the LM-STEM-EBIC analysis without applied bias provided an overview of the induced current distribution in the GaAs-W-2 specimen, its response to externally applied bias is examined. The connection configuration used for biasing is shown in Fig. 76. The bias is applied to the top metal contact, as it is closer to the GaAs p-n junction, ensuring that the majority of the applied bias is dropped across the junction. Consequently, the amplifier is connected to the back contact (n-GaAs), resulting in a negative EBIC signal at the junction in the recorded EBIC maps, as the amplifier detects electrons extracted from n-GaAs. As previously mentioned, only the EBIC contrast in the region left of the isolation cut is considered. The complexity of the electrical circuit of the right-hand back-to-back diode prevents a straightforward interpretation of the contrasts at the junction.

Figure 76 presents the LM-STEM-EBIC maps recorded under externally applied bias ranging from -3 to +3 V. Since the bias is applied to p-GaAs, a positive applied voltage (+V) corresponds to forward biasing of the GaAs p-n junction, whereas a negative voltage (-V) corresponds to reverse biasing. The expected response of the GaAs p-n junction to the applied bias is clearly visible in the respective EBIC maps (Fig. 76). The EBIC contrast at the junction increases under reverse bias (-V) due to the widening depletion region (potential barrier) and decreases or vanishes under forward bias (+V) as the potential barrier is reduced. The *in situ* biasing LM-EBIC data thus confirms the effective biasing of the GaAs lamella.

Details of the electric field response at the junction to the external bias will be examined in the following section using EBIC maps recorded at higher magnifications. However, just as in the *in situ* biasing EH experiments, it must be considered that the applied bias is not entirely dropped across the specimen junction. The two primary reasons for this, as discussed in Ch. 6.5, are:

- The non-ideal metal-semiconductor interface between GaAs and IBID-W, leading to a Schottky barrier that causes a significant portion of the applied voltage to drop across this interface.
- The damaged lamella surfaces providing short-circuit paths for the induced current, preventing the device-intrinsic electric field at the junction from extending through the full projection of the specimen.

In addition to the response of the GaAs p-n junction to the external bias, changes in EBIC contrast are also observed in other regions of the specimen, namely in the top IBID-W protection layer and at the bend contours.

Protective Metal Layer

The EBIC maps in Fig. 76 show that with increasing reverse bias (–V), the contrast of the top-metal protection layer (IBID-W) in the thicker region inverts from bright at 0 V to dark at –3 V. In contrast, the thinner region shows no such inversion.

This behavior may be attributed to the higher probability of primary electron absorption in the thicker sample region (> 550 nm) compared to the thinner region (~370 nm). As such, the increasingly inverted (dark) contrast under reverse bias may be linked to a growing relative EBAC contribution, which is expected to have an opposite sign to that of the SEEBIC signal. Since the absorbed primary electrons are not expected to be influenced by the externally applied

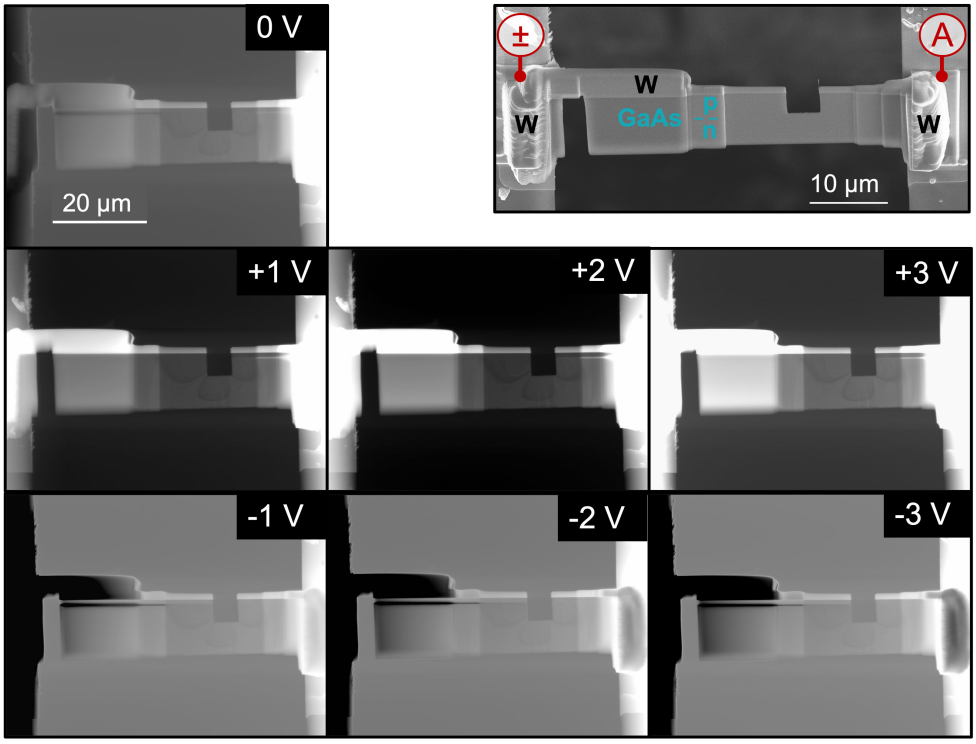

Figure 76: *LM-STEM-EBIC maps of GaAs-W-2 recorded under externally applied bias ranging from -3 to +3 V, using the connection configuration illustrated in the SE-SEM overview image.*

bias, it is unlikely that the EBAC signal itself is directly enhanced by the reverse bias. Instead, it is more plausible that the dominant SEEBIC signal reaching the amplifier is affected. According to literature[31], the SEEBIC signal from the metal layer is expected to vary with applied bias as follows:

- At +V: less SE are emitted from the sample (less SEEBIC).
- At -V: more SE are emitted (higher SEEBIC).

At first glance, it seems counterintuitive that under increasing reverse bias the EBAC contrast in the IBID-W metal layer should become more pronounced. One would expect that, under reverse bias, the negative EBAC signal (dark contrast) would be covered by the enhanced positive SEEBIC signal (bright contrast) in the metal layer. Instead, the EBAC signal would be more likely to emerge under forward bias conditions, where SEEBIC is reduced. However, it could be possible that under reverse bias, the increased SEEBIC carriers are attracted toward the negatively biased region and escape the specimen to ground via the nearby bias connection (track 1, Fig. 58b), rather than traversing the metal-GaAs interface and being collected at the rear p-GaAs contact (track 2).
Although the EBAC signal is typically several orders of magnitude weaker than field-related EBIC or SEEBIC – especially in thin samples or at high acceleration voltages – its detection is still possible. This is facilitated by the use of the *in situ* preamplifier from point electronic GmbH, which minimizes noise in EBAC/RCI measurements and enables detection even in low-impedance specimens, such as the GaAs-W-2 lamella studied here.
Nevertheless, the proposed explanations for the observed EBIC contrast changes in the IBID-W layer under electrical biasing remain a hypothesis. It will need to be validated in future studies through dedicated simulations of SE emission and primary electron absorption within the present specimen, as well as modeling of the resulting EBAC and SEEBIC carrier pathways and their extraction mechanisms.
Due to the complex surface modifications introduced by FIB preparation in the GaAs specimens, a clear and reliable interpretation of the SEEBIC signal generated by SE emission is not possible at this stage.
Furthermore, when interpreting SEEBIC signals in electrically biased semiconductor specimens, SE recapture effects must always be taken into account, as previously observed in *in situ* biasing STEM-SEEBIC experiments.[223,31] SE recapture is enhanced under positive bias applied to the metal, which can lead to a reduction in the detected SEEBIC current. However, these recapture effects have not yet been thoroughly investigated, and the quantitative impact of SE recapture on the measured EBIC signal remains difficult to assess.

Bend Contours

The EBIC contrast at the bend contours relative to the vacuum signal also varies with applied bias, as evident from Fig. 76. Building on the investigation of the mechanism responsible for EBIC contrast at bend contours from Sect. 7.5.1.2, these contrasts are analysed in greater detail as a function of applied bias to determine whether primary electron absorption is indeed the underlying mechanism for the negative current signal. For this purpose, Fig. 77a presents EBIC profiles extracted from LM-EBIC maps recorded under applied bias (-3 to +3 V) along the [001]

direction across a prominent bend contour in the 370 nm-thick region of the lamella. The profile location is shown in the map recorded at 0 V. The profiles reveal a current drop at the bend contour (red arrow), while the drop at the p-n junction (green arrow) remains barely resolved due to the low magnification. The contrast at the bend contour is evaluated as a function of applied bias relative to the zero-adjusted vacuum signal, which is corrected for the bias-induced current. As shown in Fig. 77b, the contrast increases with forward bias and decreases with reverse bias, demonstrating a clear dependence on the external bias. This excludes EBAC as the origin, as EBAC is assumed to be fundamentally unaffected by external bias.

The most plausible explanation for the EBIC contrast along bend contours is complex channelling and scattering effects induced by specimen bending. Ideally, simulations of channelling processes would be required to validate this hypothesis; however, their complexity exceeds the scope of this work. Experimentally, systematic tilting of the specimen and analysis of its effect on EBIC bend contrasts in future studies could provide further insights into the role of channelling.

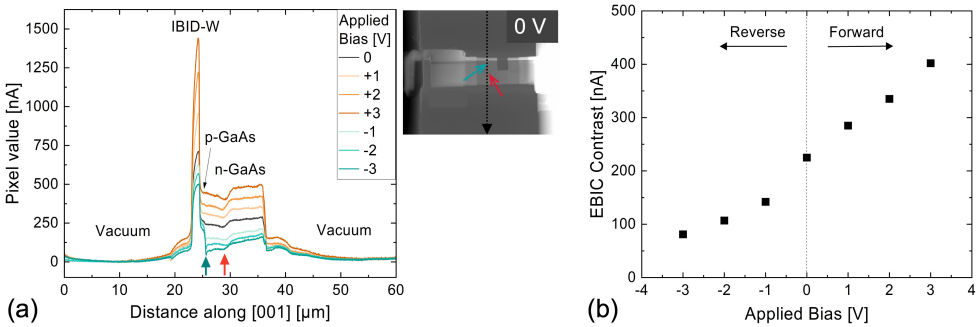

Figure 77: *(a) EBIC profiles extracted from LM-EBIC maps recorded under applied bias from -3 to +3 V along the [001] direction across a prominent bend contour in the 370 nm-thick region of the lamella. The profile location is indicated at the 0 V map. The red arrow marks the current drop at the bend contour, the green arrow the drop at the p-n junction. (b) EBIC contrast of the bend contour as a function of applied bias, derived from the profiles in (a) and referenced to the zero-adjusted vacuum signal.*

Resistance Contrast

To investigate the resistance contrast in the GaAs specimen under applied bias, EBIC profiles (Fig. 78b) are extracted from the LM-EBIC maps at various bias voltages (Fig. 76) in the $[1\bar{1}0]$ direction along the n-GaAs layer, at a distance of about 7.5 µm from the p–n junction. This distance is chosen to exclude contributions from field-related EBIC contributions. As described previously, the specimen exhibits a uniform crystalline thickness of 370 ± 6 nm across the analysed n-GaAs region.

The EBIC profiles are corrected for the dark current, which is measured in the vacuum region above the lamella (as indicated in Fig. 78a), to account for the bias-induced current. As shown in Fig. 78c, these dark current profiles extracted from the vacuum region generally exhibit the expected shift upon reverse and forward bias conditions applied to the GaAs p–n specimen. However, the values should not be interpreted as absolute bias-induced currents, as they may be additionally influenced by inductive coupling effects, as discussed in Sect. 7.5.1.1.

The observation that EBIC profiles extracted from the n-GaAs region (Fig. 78b) display a signal offset in the nA-range is suggesting bias-induced changes in the SEEBIC response away from the junction, despite dark current subtraction. Similar to the results of the RC study under zero bias (Sect. 7.5.1.2), the overall trend of increasing collected current as the STEM beam approaches the amplifier – indicative of resistance contrast – persists under both forward and reverse bias conditions.

The resistance contrast, represented by the slope of the linear trend in EBIC between the electrical contacts, increases slightly under reverse bias. Assuming the EBAC/RCI contribution is negligible in 370 nm thick GaAs, this increase may result from positively charged SEEBIC carriers being attracted towards the SCR under reverse bias. This could increase the resistance for these carriers to reach the amplifier connected to the n-side contact. Nevertheless, a detailed and quantitative interpretation of the observed resistance contrast and its variation with applied bias must be approached with caution. This is due to the complex origins of resistance contrast and its dependence on TEM sample characteristics, electron beam interactions, and their response to the applied bias.

While SEEBIC is assumed to be the dominant contribution to RCI in 370 nm GaAs, EBAC/RC contribution cannot be entirely ruled out. The relative contributions of SEEBIC and EBAC should be evaluated through electron scattering simulations for GaAs at the relevant thickness. It must also be considered that, although the SEEBIC signal originates at the specimen surface, the resulting resistance contrast in the EBIC map is determined by all conductive paths to ground. As such, the SEEBIC-based RCI effectively probes the entire specimen volume within the illuminated field of view.[217]

Although absorbed primary electrons are generally not expected to be significantly influenced by the applied bias, modulation of the SEEBIC is expected. Since SEEBIC is a surface-sensitive signal and the electrical surface properties of the FIB-prepared GaAs lamella are known to differ from those of the intrinsic semiconductor, it remains unclear to what extent the SEEBIC yield is controlled by the specimen-intrinsic field at the p–n junction. The necessary simulations, considering SE generation and the effects of surface-damage-induced Fermi level pinning in p–n GaAs are beyond the scope of this thesis but should be addressed in future studies aimed at understanding the EBIC signal in *in situ* biased semiconductor junctions.

It is, however, unequivocal that C contamination deposited by the STEM beam can alter surface resistivity over the course of the EBIC experiment, forming a low-resistivity conductive path parallel to the GaAs p–n junction, similar to the amorphous surface layers induced by FIB milling. Consequently, C contamination reduces the field-induced EBIC signal at the junction and simultaneously affects the SEEBIC signal due to its high surface sensitivity.[217] As C contamination accumulates on the GaAs lamella surface during repeated STEM-EBIC mapping, the contribution of the C film's resistance to the total SEEBIC/RC becomes increasingly dominant compared to that of the n-GaAs semiconductor. Nevertheless, both the C film and the n-GaAs region are expected to exhibit uniform resistivity across the area of homogeneous thickness, thereby producing a linear resistance contrast profile between the electrical contacts. To quantify the effect of C contamination on resistance contrast, the resistivities of both the C film and the underlying specimen would need to be known precisely. Quantifying this contribution should be the focus of future studies, as a step towards enabling quantitative resistance contrast mapping

of semiconductor devices via STEM-EBIC.

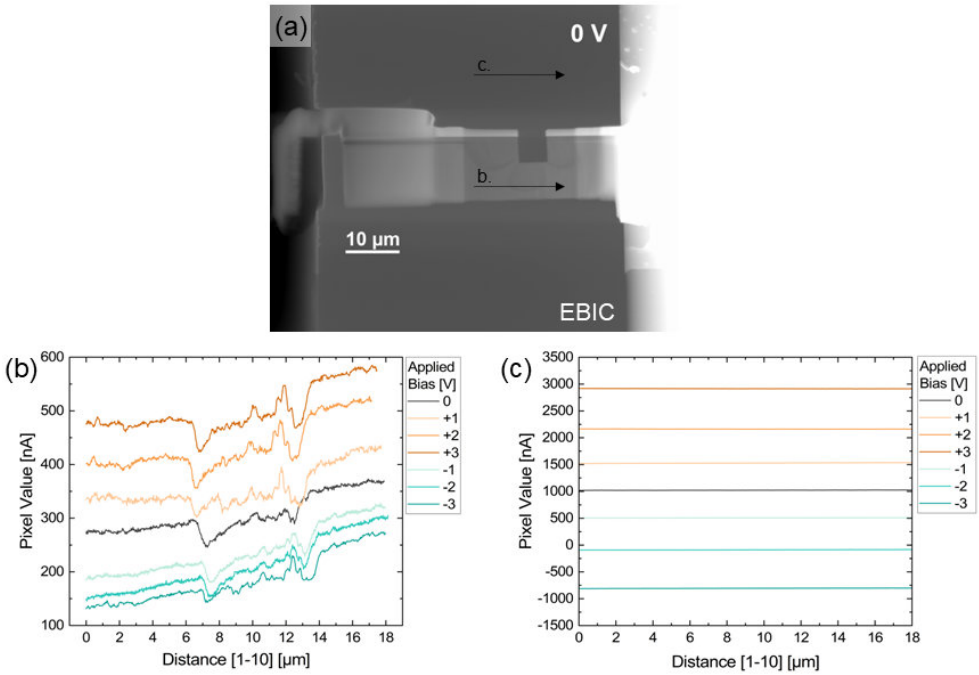

Figure 78: *(a) STEM-EBIC map recorded at 0 V, indicating the region from which the EBIC profiles in (b) and (c) are extracted. (b) EBIC profiles obtained from LM-EBIC maps recorded under applied bias voltages ranging from –3 V to +3 V (Fig. 76), along the [1$\bar{1}$0] direction across the 370 nm-thick n-GaAs region of the lamella. The profiles in (b) are corrected for the bias-induced dark current, measured in the vacuum region marked in the 0 V map in (a) and shown in (c).*

7.5.2 Standard-Magnification STEM-EBIC Analysis

This section presents a qualitative description of the STEM-EBIC signal obtained in the GaAs-W-2 p-n specimen at standard STEM magnification.

7.5.2.1 Testing the Effect of STEM Scan Direction

Prior to the *in situ* biasing STEM-EBIC analysis, EBIC signal is mapped without applied bias using different scan directions (0°, 45°, −90°, and +90°) to verify that scan orientation does not influence the recorded signal distribution.

Input 1 of the GaAs-W-2 MEMS chip (see Fig. 58b), the top contact to p-GaAs is connected to the detecting amplifier, while input track 2, the rear contact to n-GaAs, is connected to ground. This configuration yields a positive field-related EBIC signal at the GaAs p–n junction. EBIC maps of 2048×2048 pixels are acquired using a pixel dwell time of 50 µs at a STEM magnification of 20kx. The resulting FOV is 4.75×4.75 µm, covering both thickness regions of the GaAs-W-2 specimen: approximately 370 nm and >550 nm.

The resulting STEM-EBIC maps and simultaneously acquired STEM-HAADF images are shown

in Fig. 79, alongside with EBIC profiles extracted across the 550 nm-thick region in the [001] crystallographic direction from the maps acquired at each scan rotation. The results confirm that the direction of the STEM beam scan does not introduce artifacts or influence the mapped EBIC signal distribution. EBIC mapping using the +90° scan direction is selected for all subsequent measurements.

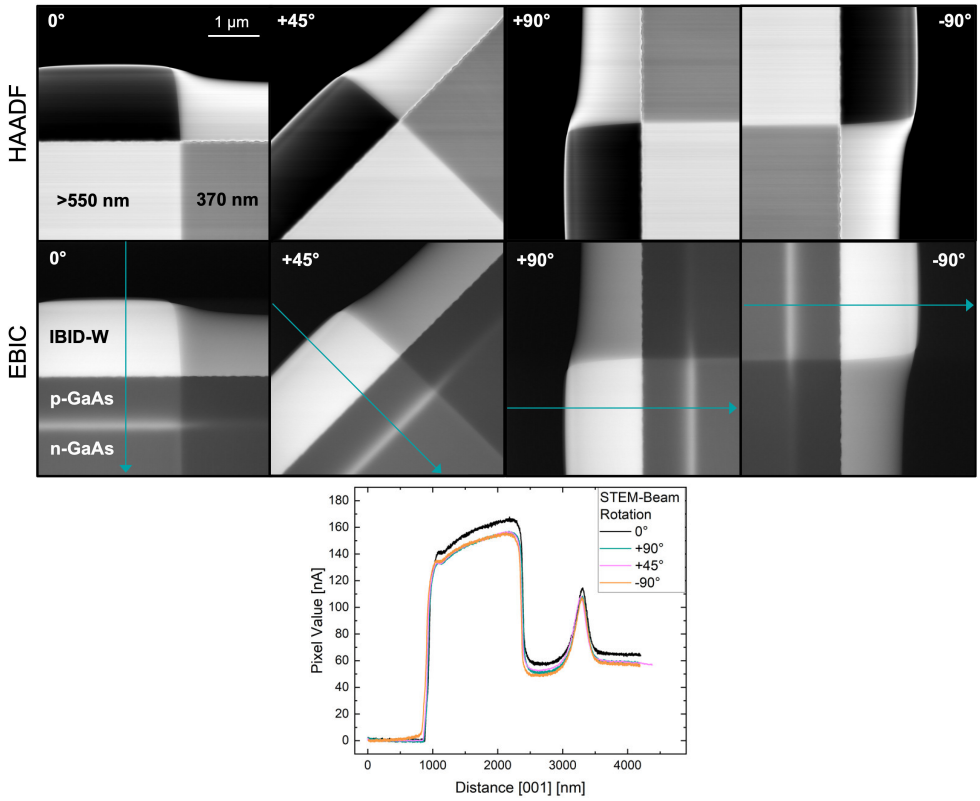

Figure 79: *STEM-EBIC maps and corresponding STEM-HAADF images of the GaAs-W-2 specimen acquired at the indicated STEM beam scan orientations (0°, 45°, −90°, and +90°). EBIC intensity profiles were extracted from the marked region across the 550 nm-thick specimen area along [001] to evaluate the influence of scan direction on EBIC signal distribution.*

7.5.2.2 *In Situ* Biasing STEM-EBIC Analysis

For the *in situ* biasing STEM-EBIC experiment, the electrical connection of the GaAs-W-2 specimen is configured as shown in Fig. 80, with track 1 connected to the bias input and track 2 connected to the amplifier. Bias is applied to the p-GaAs contact in the range of –3.0 V to +3.0 V in 0.5 V increments, where negative and positive voltages correspond to reverse and forward biasing of the GaAs p–n junction, respectively. For each applied bias, EBIC maps of 2048×1536 pixels are acquired using a pixel dwell time of 50 µs at a STEM magnification of 20kx. Compared to the previous experiment, the pixel array is reduced in the y-direction to shorten the total acquisition time, while still ensuring that both specimen thickness regions are included within the FOV, which measured to be 4.75×3.56 µm. The absolute STEM beam

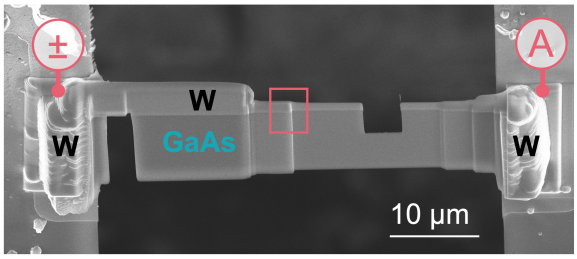

Figure 80: *Electrical connection configuration of the GaAs-W-2 specimen for in situ biasing STEM-EBIC analysis at 20kx magnification. The p-GaAs top contact is connected to the bias input (±) via track 1, while the n-GaAs rear contact is connected to the current amplifier (A) via track 2.*

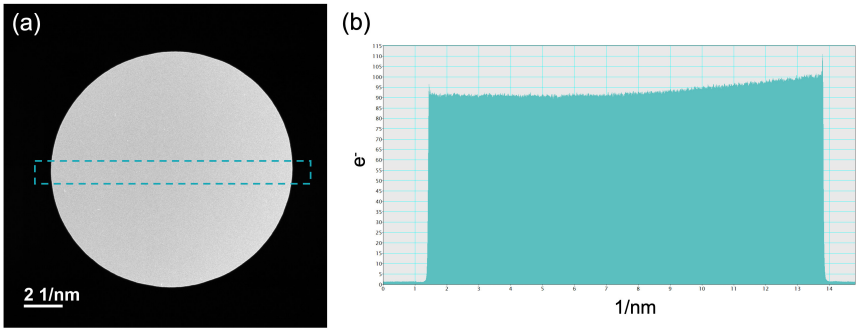

Figure 81: *STEM beam current measurement for the in situ biasing STEM-EBIC mapping at 20kx magnification: (a) 4k-Image of the 200 kV STEM beam recorded on the Gatan Oneview camera using spot size 6, a 50 µm C2 aperture, a camera length of 580 mm, and an exposure time of 0.04 s. (b) Corresponding averaged line profile across the beam image shown in (a). The total number of electrons detected on the CCD was $N_e = 6.84 \times 10^8$, yielding a beam current of 1.71×10^{10} electrons per second. This corresponds to 2.74 nA, calculated using the elementary charge of 1.6×10^{-19} C.*

current used for EBIC mapping was 2.74 nA, measured on the Gatan OneView CCD camera as shown in Fig 81.

Figure 82 presents the recorded STEM-EBIC maps at selected applied voltages. The chosen connection configuration resulted in a negative field-related EBIC signal at the GaAs p–n junction, which appears as dark contrast. To unambiguously attribute this dark contrast to the field-driven EBIC component originating from the SCR, a reference EBIC map is acquired at 0 V with both contacts connected to the current amplifier. As expected, this configuration eliminates the field-related EBIC contribution at the junction, while SEEBIC and EBAC signals remain unaffected.

Dark Current Analysis

Before further examining the EBIC signal within the GaAs specimen, the current signal detected in the vacuum regions of the EBIC maps is analysed. To this end, line profiles are extracted across the vacuum areas at various applied biases (Fig. 83a). The measured current signal in

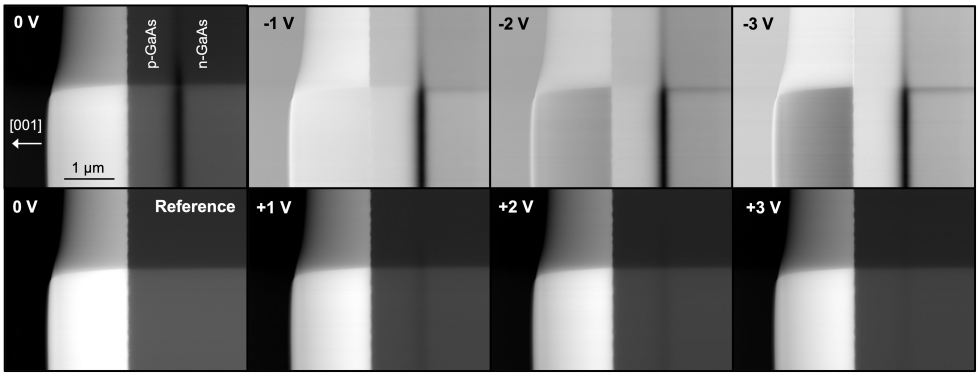

Figure 82: *STEM-EBIC maps of GaAs-W-2 under externally applied biases from –3 to +3 V, using the contact configuration shown in Fig. 80. The 0 V reference map is acquired with both electrodes connected to the amplifier to suppress field-induced EBIC contributions.*

vacuum consists of two primary contributions:

1. Dark current, which remains constant regardless of the applied voltage.

2. Bias-induced current, which varies linearly with the applied voltage.

Contrary to expectations for an ideally zero-adjusted dark current and no bias-induced signal at 0 V, a current of approximately 600–700 nA is detected in vacuum. In principle, the dark current should be adjusted to zero at 0 V; however, performing and maintaining dark current compensation is challenging during the course of the biasing EBIC experiment and is therefore omitted. As a result, all EBIC maps contain a constant current offset on the measured pixel values due to this dark current background. In addition to this offset, a bias-dependent shift in the vacuum current is observed: for positive voltages, the signal increases, while for negative voltages, it decreases. This shift shows an approximately linear dependence on the applied bias (Fig. 83b), consistent with a bias-induced current contribution. However, if the shift is solely due to this bias-induced current contribution, a perfectly linear trend with applied bias would be expected. The minor deviations from linearity may arise from:

- Changes in sample impedance under electron beam exposure (see Sect. 7.5.1.1), which could influence the dark current background underlying the bias-induced current contribution.

- Small fluctuations in dark current due to thermal drift of the electronics over time. The full *in situ* EBIC data set is acquired over a duration of approximately one hour.)

Furthermore, the vacuum signal within a single EBIC map is not perfectly uniform but shows slight variations across the vacuum region (Fig. 83a). Unlike in EH experiments, these fluctuations cannot be attributed to electrostatic stray fields extending into the vacuum. Instead, this spatial variation in the vacuum current signal provides further evidence for inductive coupling between the MEMS chip frame and the electrical connection tracks. This coupling results in time-dependent fluctuations in the detected current that are independent of the STEM beam

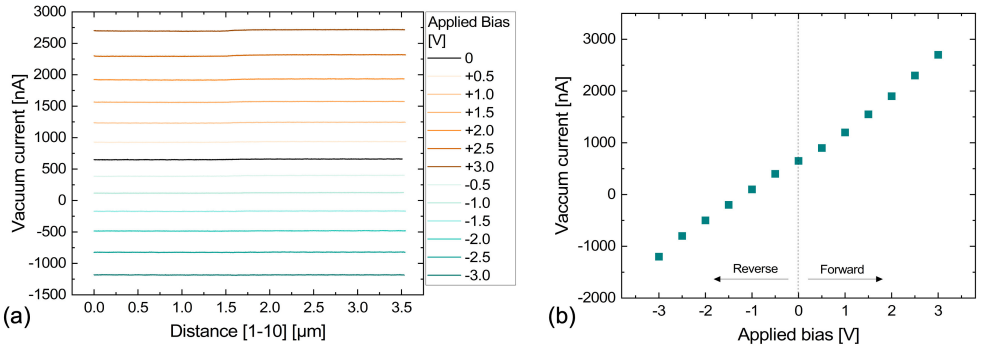

Figure 83: *(a) EBIC profiles extracted across the vacuum regions of the EBIC maps acquired under applied biases ranging from –3V to +3V along the [1$\bar{1}$0] direction. (b) Averaged vacuum current signal as a function of applied bias, showing the bias-induced shift in background signal.*

position. Thermal drift of the electronics, which would show as a gradual and continuous change over a longer time span, can be ruled out as the primary cause of these short-term fluctuations. To definitively confirm inductive coupling, additional data sets should be recorded using different pixel dwell times. While the EBIC signal itself remains constant, inductive artifacts are expected to vary with acquisition time due to their time-dependent nature.

Analysis of the GaAs p-n Junction

To investigate the EBIC signal across the GaAs p–n junction under applied bias, EBIC profiles are extracted from the recorded maps along the [001] direction across the 550 nm-thick specimen region (Fig. 84). These profiles are corrected for the dark current background using the vacuum region as a reference. As also evident from the EBIC maps (Fig. 82), the extracted profiles clearly demonstrate the expected response of the field-related EBIC (appearing as dark contrast) at the GaAs p–n junction under bias:

- The signal increases under reverse bias, consistent with the widening of the depletion region.
- The signal decreases and nearly vanishes under forward bias, due to the narrowing of the depletion region.

Figure 84b shows the EBIC contrast at the p–n junction as a function of the applied bias, which is calculated relative to the vacuum level to account for dark current offset. The vacuum region is chosen as a reference over the n-GaAs substrate, which is influenced by additional signal contributions such as SEEBIC and related RC.

Interestingly, both at 0 V and under bias, the measured EBIC signal differs between the p-GaAs and n-GaAs regions away from the junction. Figure 85a compares EBIC profiles acquired at 0 V across both specimen thickness regions: >550 nm and 370 nm. As expected, due to the variation in thickness, the absolute current levels differ between the two profiles. The thinner region (370 nm) exhibits a lower field-related EBIC contrast at the junction and a reduced positive SEEBIC signal in both the GaAs layers and the metallic top contact. While negative EBAC is

expected to suppress SEEBIC more strongly in the thicker region, the overall signal (dominated by SEEBIC) remains higher there due to the increased material thickness. As previously emphasised, the experimental results must be complemented by simulations of electron scattering processes within the specimen to estimate the relative contributions of SEEBIC and EBAC in the respective specimen thickness regions.
Notably, irrespective of the specimen thickness, the EBIC signal in the p-GaAs region is consistently higher than in the n-GaAs region, even at positions well away from the junction. It would appear as a plausible initial hypothesis that this difference originates from variations in SE emission caused by the differing work functions of p- and n-doped GaAs. It has been frequently shown that SEY changes across the p-n junction of semiconductor devices in SEM SE imaging, where the p-doped region emits more SE compared to the n-doped region. [245,246,244,247] However, if the contrast difference between p- and n-GaAs in the present specimen would indeed be doping contrast related to work function differences, the contrast should persist even when both contacts of the specimen are connected to the amplifier and the field-related EBIC signal is suppressed. To test this, EBIC profiles are extracted from maps recorded at 0 V with both inputs of the MEMS chip connected to the current amplifier, eliminating the field-related EBIC contribution (Fig. 85b). The resulting profiles show that the signal difference between the p- and n-GaAs regions disappears entirely, ruling out work function differences as the cause.
An alternative and more plausible explanation is that the EBIC signal difference reflects the resistance contrast between the p- and n-type GaAs. This hypothesis is supported by two key observations:

1. Like the field-related EBIC signal, RC is suppressed when both inputs are connected to the amplifier, matching the observation that the signal difference between p- and n-GaAs is absent in this configuration.

2. The bias-induced change in signal difference between the p-GaAs and n-GaAs layers resembles the behavior of a diode resistance.

This is evident in Fig. 86, which plots the EBIC contrast between the p- and n-GaAs layers (away from the junction) in the >550nm-thick region as a function of applied bias. A clear trend emerges: the contrast increases under reverse bias and decreases under forward bias. Under reverse bias, the depletion width increases, leading to a higher barrier and hence higher junction resistance, which approaches constant values at higher reverse bias exceeding -1.5 V. In the reverse bias regime, the junction acts as a resistive divider for the generated current. Under forward bias, the depletion width is reduced, lowering the junction resistance and reducing the resistance contrast between p- and n-GaAs.

7.6 Summary

The STEM-EBIC results presented in this section clearly demonstrate that, through optimisation of specimen preparation and experimental settings, the SNR can be sufficiently improved to reliably resolve the EBIC signal from GaAs p–n junctions and its response to externally applied bias.
This study has highlighted the potential of STEM-EBIC for electrical characterisation of semiconductors, enabled by the various signal contributions that comprise the total EBIC signal, each

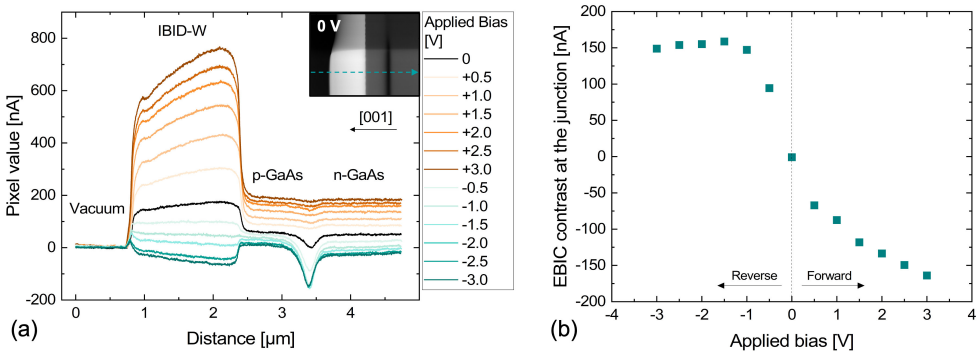

Figure 84: *(a) EBIC profiles extracted along the [001] direction across the 550 nm-thick region of the GaAs-W-2 specimen, based on the EBIC maps acquired under various applied biases (Fig. 82). The extraction path is exemplarily indicated in the 0 V map shown in the inset. All profiles are referenced to the vacuum signal. (b) EBIC contrast at the p–n junction, plotted relative to the vacuum signal, as a function of the applied bias.*

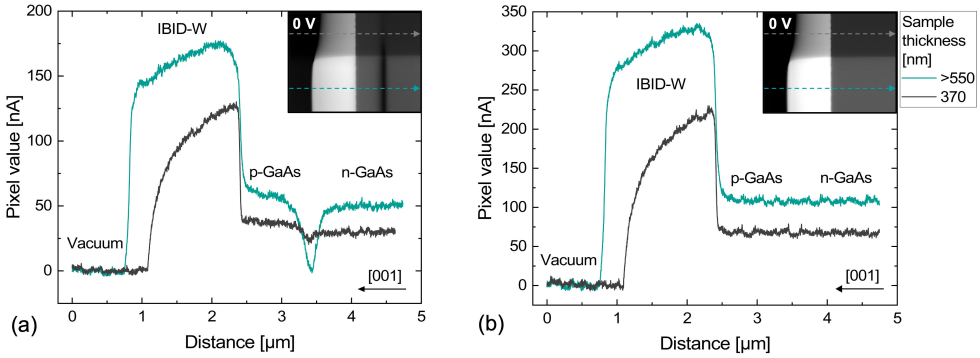

Figure 85: *EBIC profiles extracted along the [001] direction across the two thickness regions of the GaAs-W-2 specimen from EBIC maps recorded at 0 V using (a) the biasing connection configuration shown in Fig. 80 and (b) the reference configuration with both contacts connected to the amplifier.*

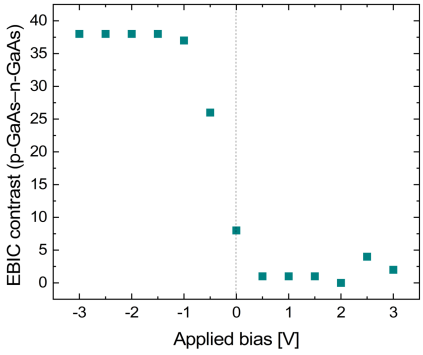

Figure 86: *Effect of the applied bias on the EBIC contrast between p- and n-GaAs, measured away from the junction in the >550nm-thick region of the GaAs-W-2 specimen.*

sensitive to distinct electrical properties of the specimen. These include, for example, resistance measurements, the visualisation of electric fields at p–n junctions, and work function mapping. At the same time, the challenges posed by the superposition of different signal contributions and their distinct generation mechanisms have been discussed in detail. Even when used qualitatively, the STEM-EBIC measurements presented here offer valuable insight into the complex interaction mechanisms occurring in the specimen under electron beam illumination. They also provide information about the electrical behaviour of the *in situ* biased TEM specimen, which can complement the interpretation of correlative TEM-EH potential analyses.
However, STEM-EBIC has not yet been employed successfully for quantitative measurements of the current distribution across p–n junctions in correlation with EH potential measurements. To enable such quantitative interpretation, future experiments should be complemented by Monte Carlo simulations. These would help quantify inelastic scattering contributions, such as the SE yield, and estimate the relative contributions of BSE, ABE, and TRE for the given specimen geometry.
Integrating experimental EBIC results with such simulations would advance the understanding of EBIC signal generation, facilitating the differentiation between measurement artefacts (e.g., surface charging) and the intrinsic electrical properties of the sample. Based on this integrated approach, STEM-EBIC holds strong potential for quantitative semiconductor device analysis, particularly for the measurement of resistances, work function variations, and the extraction of minority carrier properties across p–n junctions.
The following outlook summarises the current status and outlines the remaining challenges on the path towards quantitative STEM-EBIC interpretation.

7.7 Towards Quantitative STEM-EBIC: Opportunities and Challenges

7.7.1 Work Function Measurements in Electronic Devices

In addition to RC measurements (see Sect. 7.5.1.2, 7.5.1.3 and 7.5.2.2), STEM-SEEBIC mapping has shown promising potential for mapping local work function variations in electronic devices.[31,217,223] This technique relies on the sensitivity of the SEEBIC signal to the local work function of (semi)conducting materials. As described in Sect. 7.1, the work function – together with the surface potential – fundamentally influences the escape probability of SEs, which in turn affects the SEY and the resulting SEEBIC signal intensity.
However, absolute quantification of SEEBIC contrast related to doping remains challenging. The full process, from SE generation and emission to the collection of the corresponding positive hole current, is influenced by a multitude of parameters, which complicates quantitative interpretation.
In the p- and n-GaAs layers located away from the junction, the measured EBIC signal comprises a minor EBAC contribution in addition to the SEEBIC component. For regions with uniform specimen thickness across both doping types, this underlying EBAC contribution is expected to remain constant, thereby allowing for relative measurements of the doping-induced SEEBIC contrast. To achieve absolute values, however, a simulation of the EBAC contribution is essential. Moreover, the SEEBIC contrast results from multiple mechanisms and cannot be attributed solely to the work function difference between n-GaAs and p-GaAs. For instance, the SEEBIC/RC contribution, which originates from resistive effects at the biased GaAs p–n

junction, as observed in this study (see Sect. 7.5.2.2), also contributes to the measured signal. This convolution of effects currently prevents a clean separation of SEEBIC contributions into individual physical origins.

Despite its promise, the process of SE emission from semiconductor specimens under electron beam illumination is still not understood well enough to allow absolute work function quantification via SEEBIC. Critical questions include: What is the energy distribution and MED of SEs generated in GaAs by a 200 kV, 2.74 nA STEM beam? What fraction of these SEs is reabsorbed as a function of specimen thickness?

Comprehensive simulations are essential for better interpretation of SEEBIC signal distributions. Hussain *et al.*, for example, provided theoretical estimates of the MED of SEs from compound semiconductors like GaAs based on Monte Carlo simulations.[242] However, these are limited to 0.1–10 kV, suitable for SEM, and must be extended to the higher STEM energy regime (60–200 kV).

In addition, the effects of FIB-induced surface modifications must be carefully considered in the electrical characterisation of III–V semiconductors via SEEBIC. Since the SE escape depth is only a few nanometers (Sect. 7.1), the condition of the surface and near-surface region (e.g. oxidation, carbon contamination, FIB-induced damage) critically affects the SEEBIC signal. In GaAs specimens prepared by FIB, such modifications can significantly alter the surface potential and band structure. To enable meaningful interpretation, surface effects, such as band bending and charging, must be incorporated into electron scattering and electrostatic simulations. While a detailed investigation of SE generation and emission is beyond the scope of this work, acknowledging their impact is essential for advancing quantitative SEEBIC analysis.

In parallel to SEEBIC, which represents a relatively new approach for work function and doping contrast measurements in STEM, conventional SE imaging in low-energy SEM has been extensively studied and widely applied.[245,246,244,247] Like SEEBIC, it exploits the dependence of SE yield on the local work function, which is affected by doping. Numerous studies have investigated this effect through both experiments and simulations.

For example, Guo *et al.* modelled SE and BSE yields in doped GaAs for 0.05–50 kV and compared them to SE imaging results supported by AFM. Their study emphasised the importance of surface cleanliness and topography, calling for standardised preparation procedures and calibrated test structures for reliable quantification.

By contrast, SEEBIC avoids dependence on external SE detection and instead measures the resulting hole current directly inside the electrically contacted specimen. This enables integration into STEM-based characterisation but places stringent demands on sample integrity, especially regarding electrical damage and contact quality.

While both methods are highly surface-sensitive, they differ in key challenges: SE imaging in SEM depends on vacuum conditions, detector geometry and emission behavior, while SEEBIC relies on efficient internal charge extraction and minimal resistive loss. These distinct mechanisms make SEEBIC a complementary and promising alternative, particularly for *in situ* studies within TEM environment.

7.7.2 Quantitative Field-Related EBIC Measurements at III–V p–n Junctions and the Extraction of Minority Carrier Characteristics

As demonstrated in this chapter, STEM-EBIC already serves as a powerful qualitative tool for locating p–n junctions, visualising spatial current distributions, and identifying recombination-active defects. However, the overarching objective of EBIC analysis in semiconductor devices is often the quantitative extraction of physical parameters, such as the minority carrier diffusion length and lifetime.

Achieving such quantification is far from trivial. It requires a detailed understanding of the EBIC signal formation mechanisms, the effects of high-energy electron beam excitation, and particularly the interactions at and near the specimen surface.

Quantitative STEM-EBIC measurements of minority carrier properties, such as diffusion length, can only be meaningfully interpreted when supported by simulations of EHP generation in the SCR, taking into account specimen-specific parameters including doping profiles, lamella thickness, and STEM beam characteristics. These simulations are currently under development and are not included in the present work. Accordingly, no attempt is made to extract quantitative carrier properties from the presented STEM-EBIC data.

As with SEEBIC, field-related EBIC signals at GaAs p–n junctions are fundamentally affected by surface damage introduced during sample preparation. FIB-induced surface defects can result in Fermi level pinning, which in turn leads to surface band bending and alters the intrinsic electrostatic field at the junction. Since STEM-EBIC is a projection technique, the measured signal across the SCR is integrated over the entire specimen thickness, encompassing both pristine and damaged regions. Consequently, the detected signal reflects not only the intrinsic junction properties but also contributions from surface-affected layers.

In addition to modifying the SCR field, damaged specimen surfaces may act as low-resistance pathways, enabling current flow in parallel to the junction. These surface shunts can hinder charge separation in the intrinsic electric field and thereby reduce the effective field-related EBIC signal. This effect is strongly dependent on specimen thickness, as discussed throughout the prior experimental sections.

Both of these surface-related artefacts, like the field modification at the p–n junction and the creation of parasitic current paths, can significantly distort field-related EBIC signal interpretation, especially when aiming to extract parameters such as minority carrier diffusion lengths. As Zhou *et al.* pointed out, high EBIC signals at a junction may not unambiguously indicate long diffusion lengths or low surface recombination.[237] They could instead arise from surface charging or local field passivation effects induced by electron beam exposure.

Therefore, artefacts such as surface band bending, charging, and their impact on minority carrier dynamics (e.g. recombination behaviour and collection efficiency) must be included in physical models that describe the STEM-EBIC experiment. Zhou *et al.*, for instance, developed a 2D numerical model to study EBIC profiles of p–n junctions in a cross-sectional geometry, contributing valuable insights into EBIC behaviour in crystalline silicon solar cells.[237] However, as is often the case, their model is developed for SEM-EBIC conditions and does not account for the bidirectional surface effects present in electron-transparent cross-sectional lamellae used in STEM-EBIC.

Nevertheless, as shown in this chapter, the surface-related artefacts – particularly surface shun-

ting, did not prevent qualitative STEM-EBIC mapping of the GaAs p–n junction. Through optimisation of specimen preparation (Ch. 4.4), control of lamella thickness, and careful tuning of STEM beam parameters and acquisition settings (Sect. 7.4), the intrinsic electric field at the junction and its variation under *in situ* biasing could be reliably resolved.

Despite this progress, these preparation-induced artefacts continue to limit the quantitative extraction of minority carrier properties using cross-sectional STEM-EBIC. Still, the method retains unique potential for probing lateral current distributions within built-in fields and correlating them with electrostatic potential profiles obtained through EH.

8 Investigation of n-GaInP/p-AlGaAs Tunnel Diodes for Multi-Junction Solar Cells

8.1 Introduction

8.1.1 Tunnel Diodes for Multi-Junction Solar Cells

Tunnel diodes (TDs), as introduced in Ch. 2, are key components of MJSCs, providing the series interconnection between adjacent subcells. Specifically, they connect the p-side of one subcell to the n-side of the adjacent subcell. To ensure optimal MJSC performance, TDs must:

- Provide a high peak tunnelling current density (J_{peak}), significantly exceeding the photogenerated current in the solar cell, to prevent the TD from limiting the overall device current and performance.
- Exhibit low equivalent electrical resistivity for free carriers to minimise voltage drop and associated current loss.
- Allow high optical transmittance to minimise photon absorption and subsequent losses in the underlying subcells.

For this purpose, Esaki interband TDs – thin, degenerately doped p-n junctions – are the standard in MJSCs.[51] Their working principle is illustrated in Fig. 87, which schematically presents the band structure and the ideal J-V characteristics of a TD. Due to the high (degenerate) doping concentrations – typically above 10^{19} cm^{-3} – in both the n- and p-type layers, the E_F shifts into the E_C in the n-type layer and into the E_V in the p-type layer. This induces band bending, enabling electrons to tunnel through the thin depletion region from the E_C of the n-type layer into the E_V of the p-type layer.
This interband (band-to-band) tunnelling process is desirable for MJSC applications as it provides the lowest-resistivity current path. It dominates TD operation at small positive voltages (blue region in Fig. 87a), where the TD ideally exhibits ohmic J-V behavior. In this regime, empty E_V states in the p-type layer align with full E_C states in the n-type layer, facilitating tunnelling. However, at higher voltages, the energy states on both sides of the junction become misaligned, suppressing interband tunnelling and allowing higher-resistivity mechanisms, such as excess current and thermal current.[7] A comprehensive discussion of tunnelling mechanisms in degenerately doped p-n junctions can be found in the relevant literature.[248,8] In this work, however, emphasis is placed on direct band-to-band tunnelling, which is crucial for low-resistivity current transport in MJSCs.
TDs for MJSCs must therefore be designed such that the interband tunnelling regime matches with the solar cell's operating current, which varies depending on the application. For instance, commercial CPV operate at 500× concentration, corresponding to operating currents of approximately 7 A/cm^2.[7] Higher light concentrations require higher J_{peak} to maintain interband tunnelling as the dominant transport mechanism and prevent the TDs from limiting the overall device current.
The material design of TDs for MJSCs thus requires a trade-off between achieving high J_{peak} and ensuring high optical transparency. These properties impose conflicting bandgap requirements: low bandgap materials enhance tunnelling, whereas high bandgap materials improve

optical transparency. Balancing these factors is crucial for optimising TD performance in MJSC applications.

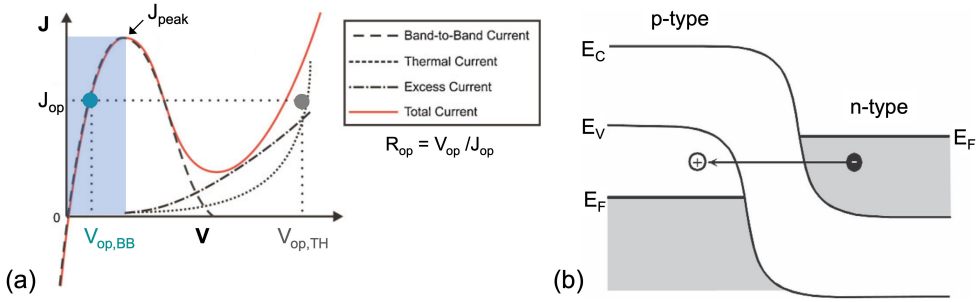

Figure 87: *(a) Schematic J-V characteristics of an ideal TD, highlighting the three main current contributions. The peak current density J_{peak} defines the low voltage regime where low-resistivity band-to-band tunnelling dominates. For a given operating current density J_{op}, the voltage drop in the band-to-band tunnelling regime ($V_{op,BB}$) is significantly smaller than the voltage drop associated with thermal current ($V_{op,TH}$) (modified after Wheeldon et al.).*[7] *(b) Schematic illustration of direct band-to-band tunnelling in a degenerately doped p-n junction (adapted from Hermle et al.).*[8]

8.1.2 High-bandgap p-AlGaAs/n-GaInP Tunnel Diodes for MJSCs

A typical TD for MJSC applications is the p-AlGaAs/n-GaInP junction.[249,7,23,250,251] This TD, consisting of high-bandgap ternary alloys, offers both high optical transparency and high current capability, making it well-suited for the very high current densities encountered in CPV. Among wide-bandgap TDs, the p-AlGaAs/n-GaInP system demonstrates the highest performance[252,250,23,251] and is thus the present standard in MJSCs for space PV.[23]

While high-bandgap TDs reduce parasitic absorption and increase transparency, they also introduce a higher energy barrier for tunnelling.[252] The wide bandgap of the p-AlGaAs/n-GaInP system thus necessitates very high doping concentrations to create steep energy band slopes (high band offsets between n-GaInP and p-AlGaAs), to achieve a narrow depletion width and enhance tunnelling probability. Notably, high n-doping concentrations are achievable in GaInP, enabling the required band offsets in p-AlGaAs/n-GaInP TDs.[23] Consequently, the peak tunnelling currents achievable in p-AlGaAs/n-GaInP TDs are comparable to those in conventional, smaller-bandgap GaAs TD systems, such as p-GaAs/n-GaAs or p-AlGaAs/n-GaAs.[23]

However, the p-AlGaAs/n-GaInP TD exhibits particularly high sensitivity to crystallographic growth conditions, making reliable production challenging.[252,23] This is primarily due to the difficulty of achieving high-concentration doping with precise spatial confinement, which is necessary to attain the small depletion width required for interband tunnelling. Despite the feasibility of high doping in the p-AlGaAs/n-GaInP system, the actual achievable doping concentrations depend on the choice of dopant elements. Dopant interdiffusion at the junction or segregation during growth can significantly degrade TD performance by widening the depletion region and reducing the tunnelling probability. To mitigate junction degradation during subsequent epitaxial growth, fast-diffusing dopants such as Zn are commonly avoided. However, dopant segregation during growth can still occur, particularly due to surface accumulation, so-called memory effects,

which are frequently observed for group VI dopants such as Te and Se.[253,24]

Beyond doping-related issues, thermal annealing during subsequent growth steps can influence TD performance, a phenomenon known as the thermal load effect. This refers to the degradation of TD performance caused by the thermal load during the epitaxial growth of subsequent subcells, a problem that becomes more critical with an increasing number of subcells in MJSCs. As the MJSC stack increases, so does the duration of the epitaxial growth process, leading to greater exposure to high temperatures (up to around 640°C). While this effect has been widely observed, and (depending on the doping type) may be linked to dopant diffusion[251], it can neither be definitively identified nor exclusively attributed to doping-related mechanisms. Various studies have reported temperature-dependent performance changes in different TD systems, yet the specific mechanisms influencing p-AlGaAs/n-GaInP TDs remain unclear in the literature.[23] Some studies suggest that thermal annealing degrades the overall performance of the MJSC and indirectly associate this effect with the deterioration of the p-AlGaAs/n-GaInP TD.[252] Others report only a minor increase in voltage drop[251] and negligible changes in peak current densities[249] between as-grown and annealed p-AlGaAs/n-GaInP systems, doped with Se and C[251] or Te and C[249], respectively, suggesting no significant impact on device performance. Barrigon *et al.* for example report that despite minor reductions in J_{peak}, the *J-V* characteristics after thermal annealing verify that TD performance remains largely unaffected and does not impose electrical limitations on MJSCs in practical CPV applications.[249] However, these studies were performed by post-growth thermal annealing of TDs in a 2-J[251] (tandem) and a 3-J[249] solar cell. To the best of the current knowledge, few studies have investigated the thermal load effect on p-AlGaAs/n-GaInP TDs in larger-scale 4-J to 6-J systems. Furthermore, the exact mechanisms that may contribute to the thermal degradation of TD performance during growth remain to be clearly identified.

Besides possible thermal-load-related effects influencing TD performance during epitaxial growth, the *I-V* characteristics have also been found to be sensitive to the growth direction. As a result, it appears that growing the junction upright (p-on-n) or inverted (n-on-p) significantly affects the tunnelling characteristics.
Fraunhofer ISE[254] and Sharp[255] have successfully implemented inverted-grown p-AlGaAs/n-GaInP TDs in metamorphic solar cell concepts, achieving record efficiencies. This demonstrates that high-performance TDs can be reliably fabricated using the inverted approach. However, p-AlGaAs/n-GaInP TDs grown in the upright configuration exhibit significantly lower peak tunnelling currents compared to their structurally equivalent inverted counterparts. While both configurations perform similarly under 1-sun illumination (without light concentration), the difference becomes pronounced at the high current densities relevant for CPV applications. According to the defined standard for solar irradiance based on Air Mass (AM1.5) G173 Global Tilt, 1-sun corresponds to 1000 W/m^2.[256] The underlying cause of this discrepancy remains unclear. Therefore, detailed analyses of the structure, the dopant distribution, the electric field and the current distribution at the interface are required to improve the understanding of this junction and, thus, the device production.

8.1.3 Research Motivation

The influence of epitaxial growth conditions, such as growth direction and thermal load, on the performance of high-bandgap TDs is often inferred indirectly through comparative electrical analysis of bulk solar cells. However, such bulk analyses make it difficult to draw definitive conclusions about the tunnelling characteristics of specific TDs within the stack. While the role of TDs as current limiters can be inferred, it remains impossible to identify which specific TD is limiting or to determine the underlying cause. As a result, much of the optimisation process for TD design and growth relies on iterative trial-and-error approaches, where growth parameters are adjusted, and the quality of specific TDs is indirectly assessed through bulk electrical characterisation.

To assess the tunnelling performance of specific TDs in MJSC stacks, measuring their depletion width serves as a key quality indicator. The performance of TDs fundamentally depends on a narrow depletion region in degenerately doped, atomically sharp junctions, as the probability of interband tunnelling decreases exponentially with increasing depletion region width. [257,250] Therefore, a tool is needed to analyse the dopant potential distribution across TDs and compare it between different TDs within the structure.

SIMS analysis is the most commonly used tool for dopant profiling. However, it is not suitable for quality assessment of TDs in operating MJSCs, as the junctions of interest in these large epitaxial stacks are located too far from the wafer surface to derive reliable dopant profiles. The roughening of the wafer surface during the SIMS sputtering process impairs high-resolution measurements of deep interfaces within the structure. Furthermore, SIMS measures the total doping concentration but provides no measure of dopant activity, i.e., the proportion of active dopants that ultimately governs the band bending, facilitating carrier tunnelling. (S)TEM analysis allows for atomic-resolution structural imaging and element mapping via EDX or EELS (see Ch. 3.2). However, despite the comparably high doping levels in the TD layers (above 10^{19} cm^{-3}), the sensitivity of these methods is insufficient to detect small deviations in dopant distributions. Additionally, these methods would only provide an indirect measure, as electrical behavior would have to be inferred from structural and compositional features. In contrast, EH allows for direct, spatially resolved measurements of the electrostatic potential distribution at the nanometer scale. Thus, it enables direct assessment and comparison of TD quality in MJSCs by measuring the depletion width.

Hence, in this study, the procedure for measuring the electrostatic potential distribution via EH and deriving the depletion width, which was tested and verified on binary GaAs and InP p-n junctions in Ch. 6, is applied to the analysis of p-AlGaAs/n-GaInP TDs in MJSCs. The primary aim was to investigate the effect of:

1. Epitaxial growth direction

2. Thermal load

on the p-AlGaAs/n-GaInP junction depletion width and draw conclusions on the carrier tunnelling efficiency. The device-related goal was to contribute to understanding the mechanisms governing the observed differences in tunnelling performance between upright and inverted p-AlGaAs/n-GaInP TDs and to assess the relevance of thermal load effects in this.

For this, EH was used as the central method to analyse p-AlGaAs/n-GaInP junctions grown in upright (p-on-n) and inverted (n-on-p) configurations, comparing junctions grown with different thermal loads in both configurations. Since the difference in TD performance between upright and inverted TDs is observed only at higher current densities, the final aim of this investigation is to perform EH potential mapping while applying an *in situ* electrical bias to the TD specimen to simulate the current regimes relevant under solar cell operation, particularly the break-in current regime of the TDs. Applying STEM-EBIC to measure minority carrier diffusion length and quantify carrier extraction in MJSCs would be a future goal. However, due to the challenges in performing quantitative STEM-EBIC experiments, as discussed in Ch. 7, STEM-EBIC is used in this study solely as a correlative tool to understand the current distribution and electrical behavior of the *in situ* biasing TEM specimen.

The first section of this chapter presents the epitaxial layer structures of the bulk specimens used for this investigation. The second section briefly covers STEM-HAADF atomic-resolution imaging and compositional EDX mapping, which were used as a first approximation to exclude the presence of defects and unintended major element segregation at the TDs. The third section elaborates on the EH electrostatic potential analysis. The fourth section describes the *in situ* biasing electrical TEM studies, with a special focus on the preparation of *in situ* biasing specimens, including the various preparation approaches and geometries tested. In the fifth section, the attempt to apply the *in situ* biasing EH methodology for analysing the p-AlGaAs/n-GaInP TD in a working tandem solar cell device is presented.

While this chapter is driven by a device-related research question – specifically, uncovering the reasons behind the differing tunnelling performance in upright and inverted grown p-AlGaAs/n-GaInP TJs – the primary focus is on evaluating and advancing the methodological feasibility of electrical TEM characterisation for real III-V semiconductor specimens. This includes electrostatic potential mapping using EH without biasing, as well as *in situ* biasing approaches. The chapter examines the successful aspects and potential of the method while also addressing the challenges and complexities of *in situ* biasing EH characterisation and the associated sample preparation, using p-AlGaAs/n-GaInP in MJSCs as a case study.

8.2 Bulk Specimen Structures

The III-V heterojunction systems examined in this study were grown by MOVPE in an AIXTRON AIX2800 G4 reactor at Fraunhofer ISE, Freiburg.[2] The fundamental principles of MOVPE growth for pseudomorphic III-V heterostructures are introduced in Sect. 2.2.

Two sets of bulk samples containing p-AlGaAs/n-GaInP TJs were investigated. Schematic representations of the heterolayer structures are provided in Figs. 88.

The first set of samples (Fig. 88a-b) consists of two tandem solar cell III-V heterolayer stacks: one with p-AlGaAs/n-GaInP TJs grown in an upright (p-on-n) configuration, referred to as TAN, and the other with p-AlGaAs/n-GaInP TJs in an inverted (n-on-p) configuration, referred to as INVTAN. Both tandem cell stacks contain two interconnecting p-AlGaAs/n-GaInP tunnel junctions.

The second set of bulk samples (Fig. 88c-d) comprises two TD test structures: one with a p-

[2]The reader is informed that detailed information on the MOVPE growth schemes and the nature of the doping elements are omitted throughout this chapter for confidentiality.

AlGaAs/n-GaInP junction grown in an upright (p-on-n) configuration and the other with a p-AlGaAs/n-GaInP junction grown in an inverted (n-on-p) configuration. However, in contrast to the first sample set, the p-AlGaAs/n-GaInP TDs in this set, including the adjacent barrier layers, are grown in isolation on doped GaAs substrates. As a result, these TDs are not embedded within the complete III-V solar cell epilayer stack.

For both the upright- and inverted-grown TD test structures, two structurally and compositionally identical wafers are produced. These wafers differ only in the growth duration of the GaAs cap layer. A slower cap-layer growth is employed in one sample to simulate the increased thermal load experienced by TDs grown early in a large MJSC stack, such as the bottom TD in a tandem solar cell structure. This sample is referred to as "annealed", whereas the other, grown under standard cap-layer conditions, is termed "as-grown".

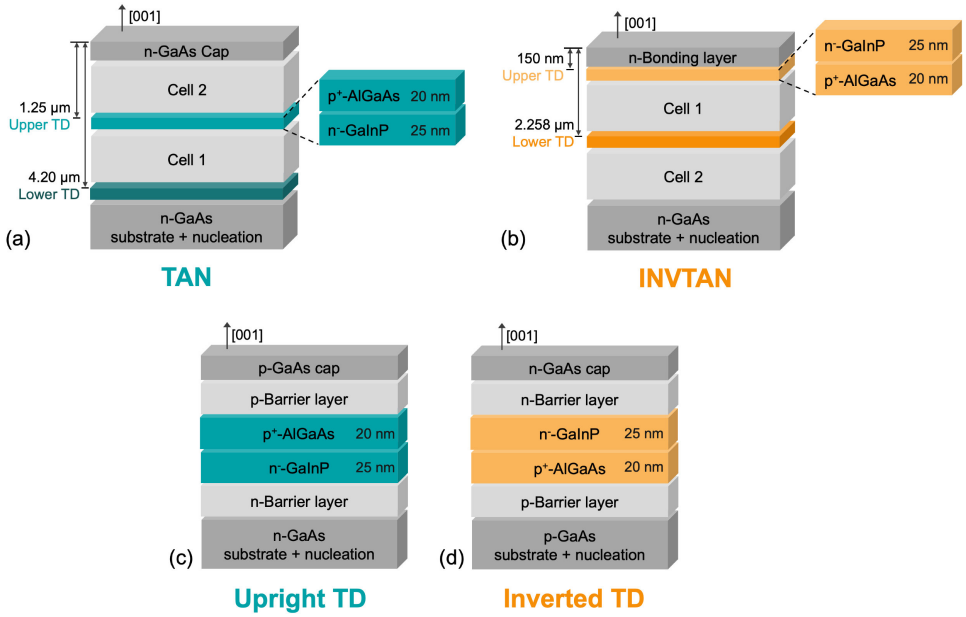

Figure 88: *Schematic representation of the III-V bulk specimen structures, including p-AlGaAs/n-GaInP tunnel diodes (TDs) in either an upright or inverted growth configuration. (a) Upright-grown III-V tandem cell structure (TAN) and (b) inverted-grown III-V tandem cell structure (INVTAN), each incorporating two p-AlGaAs/n-GaInP TDs. The TD positions within the epitaxial stack relative to the wafer surface are indicated. (c) Upright-grown and (d) inverted-grown TD test structures. The layer structure outside the TDs has been simplified, and the dimensions of the epitaxial layers are not to scale. Dopants and doping concentrations have been omitted for confidentiality reasons.*

8.3 Structural and Compositional STEM Analysis of p-AlGaAs/n-GaInP Interfaces

To analyse the interfaces of inverted and upright n-GaInP/p-AlGaAs junctions for structural defects and elemental segregation, electron diffraction and aberration-corrected STEM-HAADF imaging are combined with STEM-EDX spectrum imaging. For this comparative structural and

compositional study, electron-transparent cross-sections are prepared from TAN and INVTAN bulk specimens, as well as from annealed and as-grown upright test structures.
Sample preparation has followed the standard protocol outlined in Ch. 4.2.2 and performed using an FEI Helios Nanolab 400S FIB-SEM (see Tab. 2). Non-polar (110) and ($1\bar{1}0$) cross-sectional planes are selected to enhance thermodynamic stability (see Ch. 2.2.1). Accordingly, the TEM viewing direction (zone axis) is set to [110] (or [$\bar{1}\bar{1}0$]). Only the as-grown upright TD test structure is prepared for viewing along [$1\bar{1}0$]. Final surface polishing is performed at 900 V using a Fischione 1040 NanoMill to reduce Ga-ion-beam-induced amorphous layers. Surface amorphisation reduces diffraction contrast and should therefore be minimised for STEM-HAADF analysis.[105] The annealed and as-grown upright test structures are examined using a FEI Spectra 300 operated at 300 kV, while the INVTAN and TAN samples are analysed using a FEI Titan G2 ChemiSTEM or Hitachi HF5000 operated at 200 kV. All three microscopes are C_s-corrected to enable atomic-resolution analysis.

8.3.1 STEM-HAADF Atomic Structure and Z-Contrast Analysis

Figures 89 and 90 present a selection of high-resolution STEM-HAADF images of the annealed and as-grown upright TD samples, as well as the TAN and INVTAN samples. The images at different magnifications provide both an overview of the n-GaInP/p-AlGaAs TDs embedded in the epitaxial layer stacks and a detailed resolution of the atomic structure of the n-GaInP/p-AlGaAs layers and interfaces. The Z-contrast variations observed in the STEM-HAADF images directly reflect compositional differences across the III-V heterolayers in the epitaxial structure (see Ch. 3.2.1). As the samples are viewed along the [110] (or [$1\bar{1}0$]) direction, a clear distinction between the III-arsenide and III-phosphide compound layers is observed. Zincblende structures imaged along these zone axes typically exhibit a characteristic dumbbell structure, where each atomic column consists exclusively of either III- or V-site atoms. This effect arises because, in the [110] projection, each atomic column contains only one atomic species. The corresponding schematic crystal projections in Fig. 89c and f illustrate this geometry. Depending on the TEM viewing direction – either along [110] or [$1\bar{1}0$] – the V-atoms appear positioned either above or below the III-atoms, respectively.
These III-V dumbbells are clearly visible in the presented HAADF images shown in Figs. 89 and 90. However, their visibility varies between III-arsenide epitaxial layers (e.g., AlGaAs) and III-phosphide layers (e.g., GaInP). In GaInP, the significant Z-difference between the III-site atoms ($Z_{Ga} = 31$, $Z_{In} = 49$) and the V-site atoms ($Z_P = 15$) results in a dominant contrast from the high-Z III-site atoms in HAADF images. In contrast, the III-arsenide layers exhibit more comparable Z values for the III- and V-atoms, leading to similar contrast intensities at both atomic sites, making the dumbbell structure more distinct. For instance, in GaAs ($Z_{Ga} = 31$, $Z_{As} = 33$), the contrast within the dumbbells is nearly balanced, while in AlGaAs, the lower Z of Al ($Z_{Al} = 13$) results in a more pronounced asymmetry in contrast. The observed contrast distribution in the dumbbells also provides a means to confirm the exact zone axis orientation of the TEM samples.[258] In the HAADF images shown in Figs. 89a-c, the III-atoms appear above the V-atoms in the dumbbells, confirming a viewing direction along [$1\bar{1}0$]. Conversely, in Figs. 89d-f, the V-atoms are positioned above the III-atoms, verifying the [110] zone axis. The same interpretation applies to the TAN and INVTAN sample lamellae shown in Fig. 90, which

were prepared along the [110] zone axis.

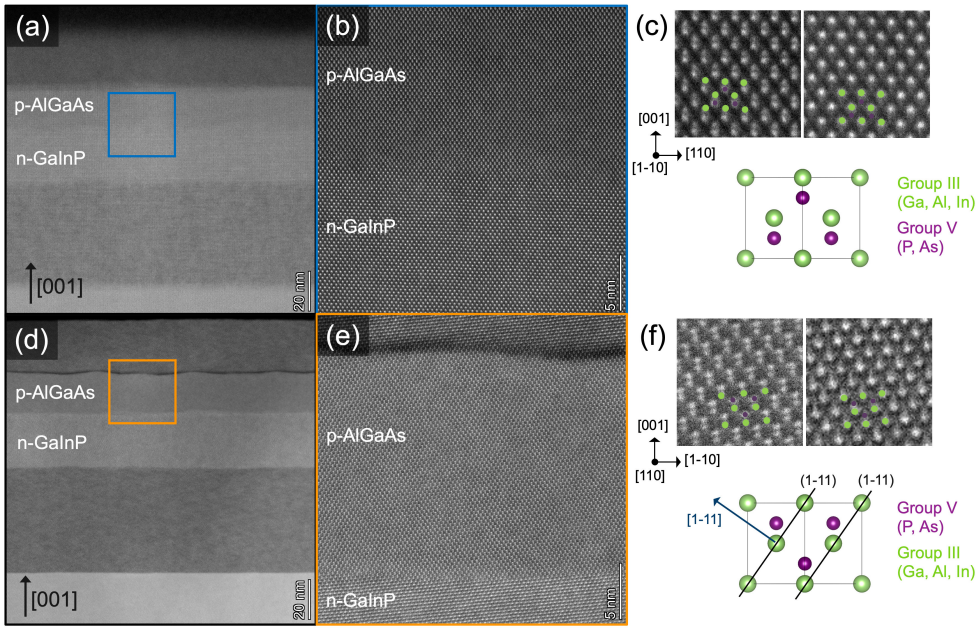

Figure 89: *HAADF STEM images of the (a)-(c) as-grown and (d)-(f) annealed upright-grown TD test structures, imaged along the [1$\bar{1}$0] and [110] directions, respectively. Panels (c) and (f) show the corresponding atomic arrangements in III-V zincblende materials along [1$\bar{1}$0] (c) and [110] (f), with atomic models and magnified sections of the AlGaAs (left) and GaInP (right) layers, as seen in the HAADF images in panels (b) and (e).*

8.3.1.1 CuPt-type Atomic Ordering

A structural feature visible only in the [110] projection of HAADF images – but not in [1$\bar{1}$0] – is $CuPt_B$-type ordering (hereafter referred to as CuPt ordering) in GaInP.[259,258] The ordered GaInP structure, characterised by alternating In- and Ga-enriched ⟨111⟩ planes, is evident in the HAADF images of the TAN and INVTAN samples (Fig. 90), as well as in the annealed upright TD sample (Fig. 89d–e), where the ⟨111⟩ planes exhibit alternating bright and dark contrast. In contrast, this ordering is not observed in the as-grown upright TD sample imaged along the [1$\bar{1}$0] direction (Fig. 89a–b).

Usually in III-V compounds, the group-III and group-V atoms are randomly distributed on their respective sublattice sites. However, in epitaxial $Ga_xIn_{1-x}P$ grown lattice-matched to GaAs ($x = 0.51$), as in the present TD samples, a tendency for CuPt ordering arises on the group-III sublattice.[52,258,259,260,261] In this ordering, alternating ⟨111⟩ planes are occupied by Ga and In atoms, forming monolayer superlattices along the [$\bar{1}$11] or [1$\bar{1}$1] directions. This periodic arrangement is only visible in TEM when the crystal is viewed along the [110] zone axis, as shown schematically in Fig. 89f. Since the TAN and INVTAN specimens are also prepared for TEM analysis along [110], CuPt ordering has been observed in the HAADF images of both the upper (Fig. 90) and lower (Fig. 91) GaInP TD layers.

The presence of CuPt ordering introduces a doubled periodicity in the crystal lattice compared

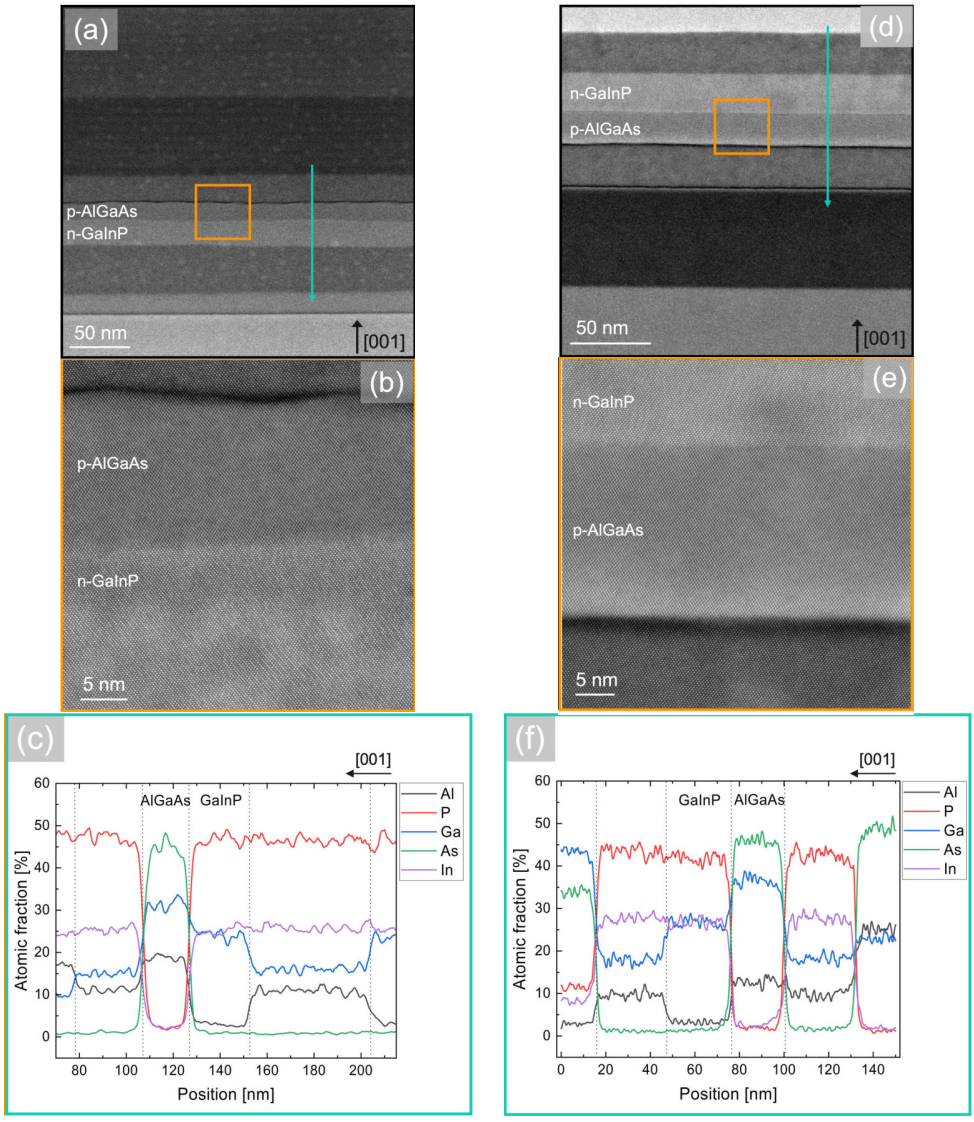

Figure 90: *HAADF STEM images of the upper p-AlGaAs/n-GaInP tunnel diode in upright-grown (TAN, (a) and (b)) and inverted-grown (INVTAN, (d) and (e)) configurations acquired along [110] direction. The green lines in (a) and (d) indicate the positions of EDX line profile scans yielding the elemental distribution across the upright grown (c) and inverted grown (f) heterojunction.*

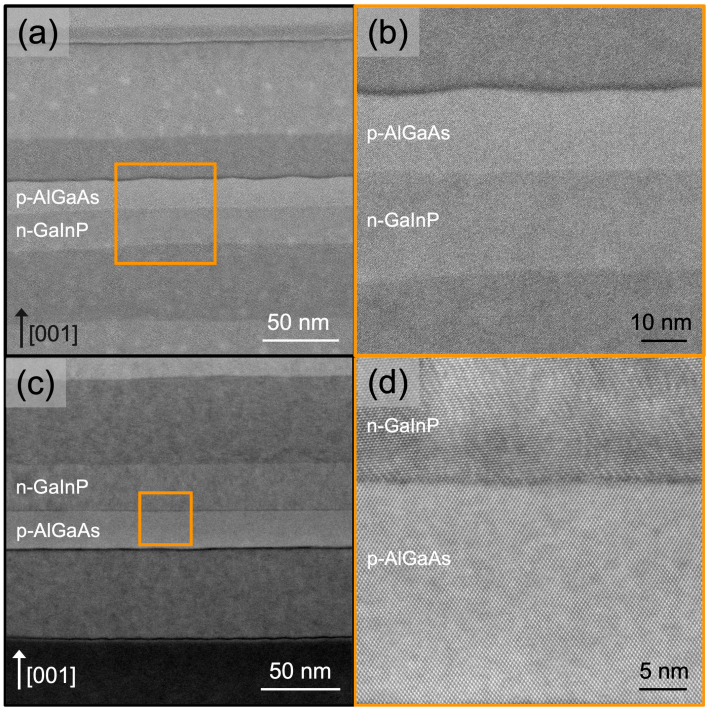

Figure 91: *HAADF STEM images of the lower p-AlGaAs/n-GaInP tunnel diode in upright-grown (TAN, (a) and (b)) and inverted-grown (INVTAN, (c) and (d)) configuration acquired along [110] direction.*

to the fundamental unit cell. In TEM diffraction patterns, such as the fast FT (FFT) of the upper TAN TD STEM-HAADF image shown in Fig. 92, this is evidenced by additional superlattice reflections, which appear at half the distance to the ⟨111⟩ reflections in reciprocal (k) space.
CuPt ordering in GaInP significantly affects its electronic properties, particularly the bandgap. In a fully disordered $Ga_{0.51}In_{0.49}P$ alloy, the bandgap at room temperature is approximately 1.92 eV. However, when CuPt ordering is present, the bandgap is reduced to about 1.85 eV. [259,262,258] In practice, GaInP epitaxial layers do not exhibit complete ordering, and the degree of ordering varies within the layer, leading to spatial fluctuations in the bandgap.
Since precise bandgap engineering is critical for MJSCs, CuPt ordering in GaInP absorbers, such as used for 3-J top cells, is undesirable. Variations in E_g can introduce parasitic absorption and reduce the efficiency of the underlying subcells. To mitigate this issue, the ordering is commonly suppressed during MOVPE by introducing Sb as a surface-active reactant (a surfactant). [263] Although Sb is not incorporated into the crystal, it forms a monolayer on the growth surface, disrupting the formation of P dimers, which are the primary driving force for CuPt ordering in pseudomorphic GaInP epilayers, induced by the present biaxial tensile strain. [264,263,258]
For TDs, a high bandgap in the GaInP layers is also generally desirable to enhance optical transmittance (see Sect.8.1). Nevertheless, no Sb surfactant was used during the growth of the n-GaInP TD layers in this study. While CuPt ordering is expected to reduce transmittance, it cannot be the cause of the observed differences in tunnelling performance between the inverted and upright TD configurations, as ordering occurs in the GaInP layers of both structures (see Fig. 90).

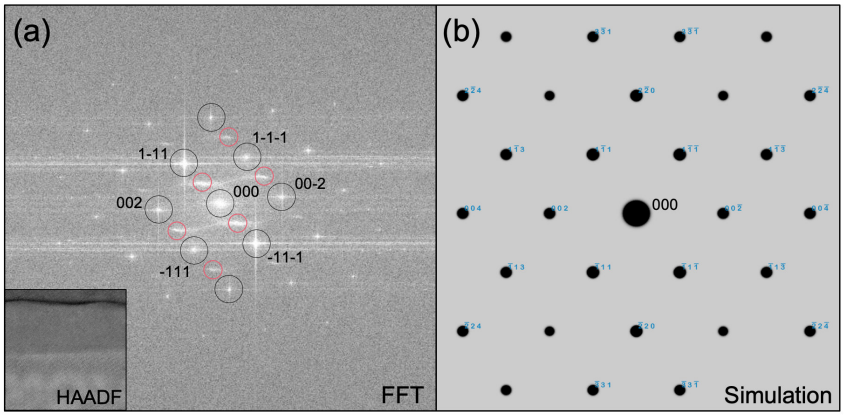

Figure 92: *(a) Digital diffraction pattern obtained from the Fast Fourier Transform (FFT) of the HAADF STEM atomic resolution image of the upper TAN tunnel diode, imaged along the [110] direction. The atomic $CuPt_B$-type ordering of Ga and In on the group-III ⟨111⟩ sublattice planes in GaInP results in a doubled lattice periodicity, evident from additional superlattice reflections at half the distance between the ⟨111⟩ reflections, as indicated in red. (b) For comparison, a simulated diffraction pattern of the disordered F-43m zincblende crystal structure viewed along [110] is shown.*

Apart from the atomic ordering in the n-GaInP layer, the p-AlGaAs/n-GaInP tunnelling interface and adjacent layers exhibit a well-defined dumbbell structure and show no crystallographic defects in any of the samples (Fig. 89, Fig. 90 and Fig. 91). To ensure statistical validation,

multiple positions along the interface are analysed in TEM, mitigating the intrinsically limited sampling of TEM projection analysis. The high-resolution HAADF images thus exclude crystallographic defects as a potential cause of impaired electrical performance in both the inverted and upright TD configurations, as well as in the as-grown and annealed upright TDs.

8.3.1.2 The p-AlGaAs Rear Interface

Despite the absence of crystallographic defects, the HAADF images of the TAN and INVTAN samples (Figs. 90 and 91) reveal a clear Z-contrast deviation at the interface between p-AlGaAs and the adjacent epilayer. This deviation appears in both the upper and lower TDs of each structure, suggesting a possible compositional variation at the interface. Notably, this interface exhibits a dark HAADF contrast and is corrugated compared to the straight heterointerfaces elsewhere in the structure. A similar dark contrast and corrugation are observed at the p-AlGaAs interface in the annealed upright TD test structure (Fig. 89d-e).

In the as-grown upright TD, which is imaged along the perpendicular $[1\bar{1}0]$ direction, the interface corrugation is less visible. Instead, it manifests as a broader transition zone in the HAADF image (Fig. 89a-b). Interestingly, the dark HAADF contrast observed at the interface in [110] projection is not visible in $[1\bar{1}0]$ projection.

8.3.1.3 Step Bunching as the Cause of Interface Corrugation

The observed corrugation at the p-AlGaAs interface can be attributed to step bunching. As discussed in Ch. 2.2, MOVPE-grown III-V heterostructures are typically deposited on substrates with a 6° offcut to promote step-flow growth on terraced surfaces. However, depending on the growth parameters, such as deposition rate, terrace width and surface ion diffusion kinetics controlled by the III/V ratio and growth temperature, a transition from step-flow to step-bunching growth can occur.[52,265,266] Step bunching is particularly likely if intermediate heating steps are introduced during MOVPE growth.

The heterostructures studied here are grown on B-type GaAs(001) substrates, which are off-tilted toward either the $(1\bar{1}1)$ or the $(11\bar{1})$ plane – that is, in the $[01\bar{1}]$ or $[0\bar{1}1]$ direction, respectively. Consequently, step edges during growth align orthogonally to the primary wafer flat (OF), as illustrated in Fig. 93a. The presence of step bunching at the p-AlGaAs rear interface is confirmed by correlating the STEM images with surface morphology analysis by means of atomic force microscopy (AFM) performed by colleagues at Fraunhofer ISE. The AFM map of the INVTAN wafer (Fig. 93b) reveals surface undulations with crests orthogonal to the OF, confirming step bunching. Furthermore, the periodicity of these undulations in AFM closely matches the observed corrugation periodicity at the p-AlGaAs rear-interface in the STEM images (Fig. 90 and Fig. 91).

If the corrugated interface observed in STEM results from step bunching, the undulations should be visible only in projection along the wafer crests (i.e., in [110]) but not perpendicular to them. This expectation is confirmed by the experimental observations: in STEM images viewed along [110] (Fig. 89d-f), the interface appears corrugated, whereas in $[1\bar{1}0]$ projection (Fig. 89a-b), a broad transition zone is observed instead. The height of this transition zone matches the undulation amplitude seen in both [110] STEM projections and AFM, further supporting step bunching – most likely triggered by a heating step during growth – as the underlying cause.

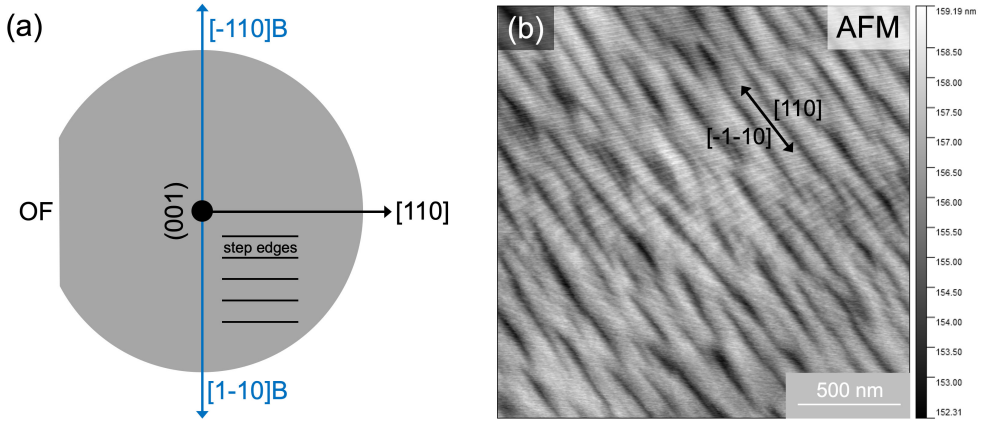

Figure 93: *(a) Schematic orientation map for epitaxial growth on (001)B GaAs substrates in 6° off-tilt orientation towards [$\bar{1}$10] or [1$\bar{1}$0] (blue arrows). The orientation of the step edges in step flow growth and step bunching are indicated. Note that [$\bar{1}$10] is equivalent to [0$\bar{1}$1], [1$\bar{1}$0] is equivalent to [01$\bar{1}$], and [110] is equivalent to [011]. (b) Atomic force microscopy (AFM) image showing the surface topology of the INVTAN wafer (001)B surface.*

8.3.2 STEM-EDX Analysis of Major Element Distribution

To investigate whether the difference in tunnelling behavior between upright and inverted TDs is caused by compositional segregation – and to further examine the origin of the dark HAADF contrast – correlative compositional STEM-EDX analyses are performed. Strong *Z*-contrast variations in the HAADF images suggest a potential compositional segregation at this interface, which warrants further investigation. STEM-EDX elemental maps and extracted compositional profiles across the n-GaInP/p-AlGaAs interface are acquired for the TAN and INVTAN specimens, as well as for the as-grown and annealed upright TD test structures. The results are presented in Fig. 90c and f, and in Fig. 94. The doping concentrations in the investigated p-AlGaAs/n-GaInP layers range between 0.001 and 0.1 at%, corresponding to approximately 10–1000 atomic ppm. This is below the detection limit of both STEM-EDX and STEM-EELS, meaning that these techniques cannot resolve such low doping concentrations in the present TD specimens. Therefore, STEM-EDX is solely used to analyse the distribution of major elements and to exclude possible agglomerations.

The STEM-EDX analysis reveals a clear chemical differentiation of the epitaxial layers in all specimens, without any indications of major element segregation. Neither at the tunnelling junction between p-AlGaAs and p-GaInP nor at the interfaces between these TD layers and their adjacent epilayers is any pronounced elemental separation detected.

However, none of the major element distributions correlate with the HAADF contrast deviation at the p-AlGaAs interface. Although the dark *Z*-contrast suggests the local accumulation of a lighter major element, no clear evidence of such segregation is visible in the EDX results. To further investigate this interface and detect potential minor elemental segregations, additional high-magnification STEM-EDX measurements are performed at the p-AlGaAs rear-interface in the upper TDs of the TAN and INVTAN specimens (Fig. 95). The only possible correlation is observed in the P distribution, where a slightly premature increase in P content – compared to

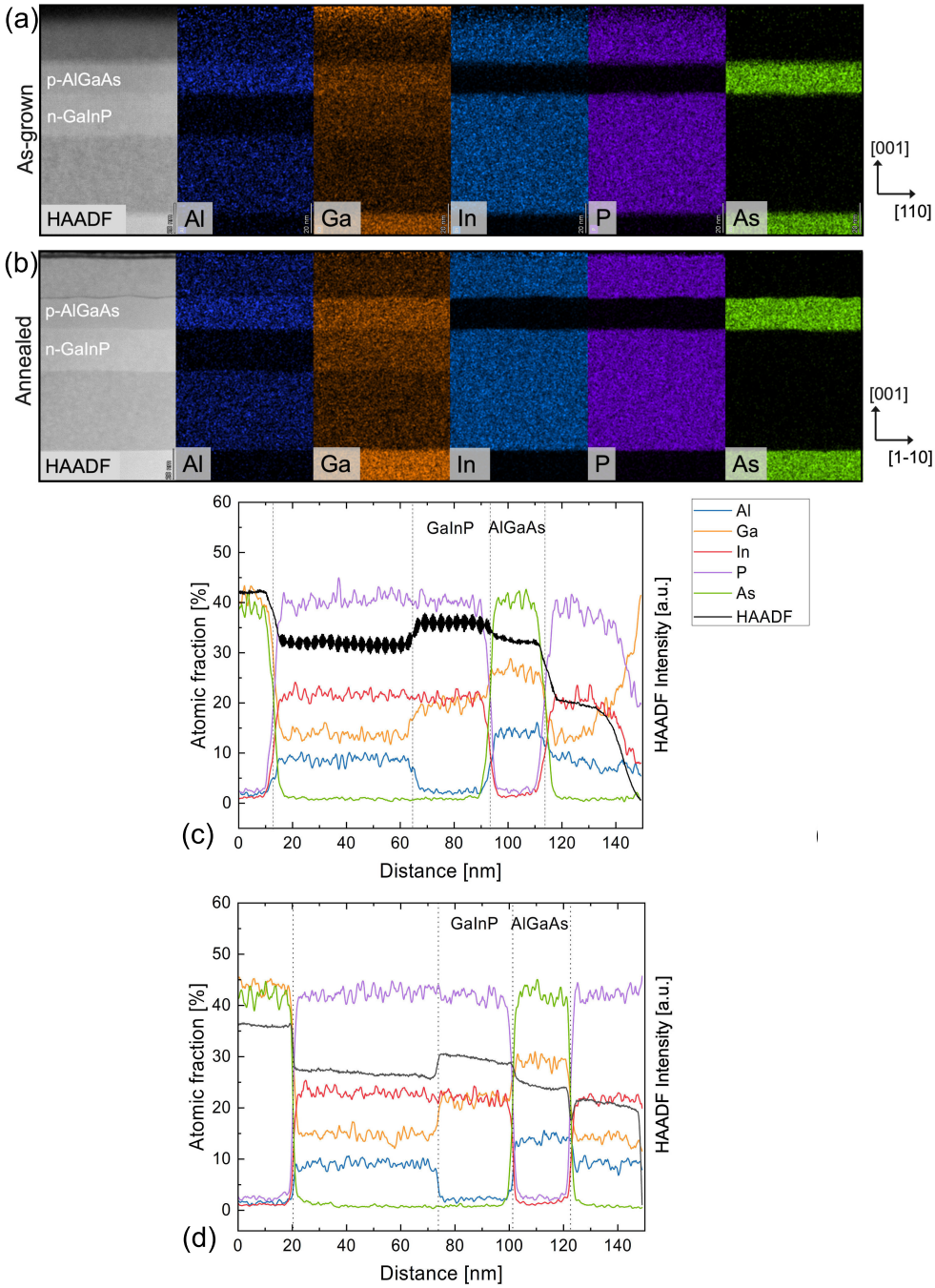

Figure 94: *STEM-EDX elemental maps of (a) the as-grown and (b) annealed upright-grown n-GaInP/p-AlGaAs tunnel diode test structures. Plots (c) and (d) show extracted profiles from the STEM-EDX maps in (a) and (b), respectively, illustrating the element distribution (left axis) and HAADF intensity distribution (right axis) across both heterostructures.*

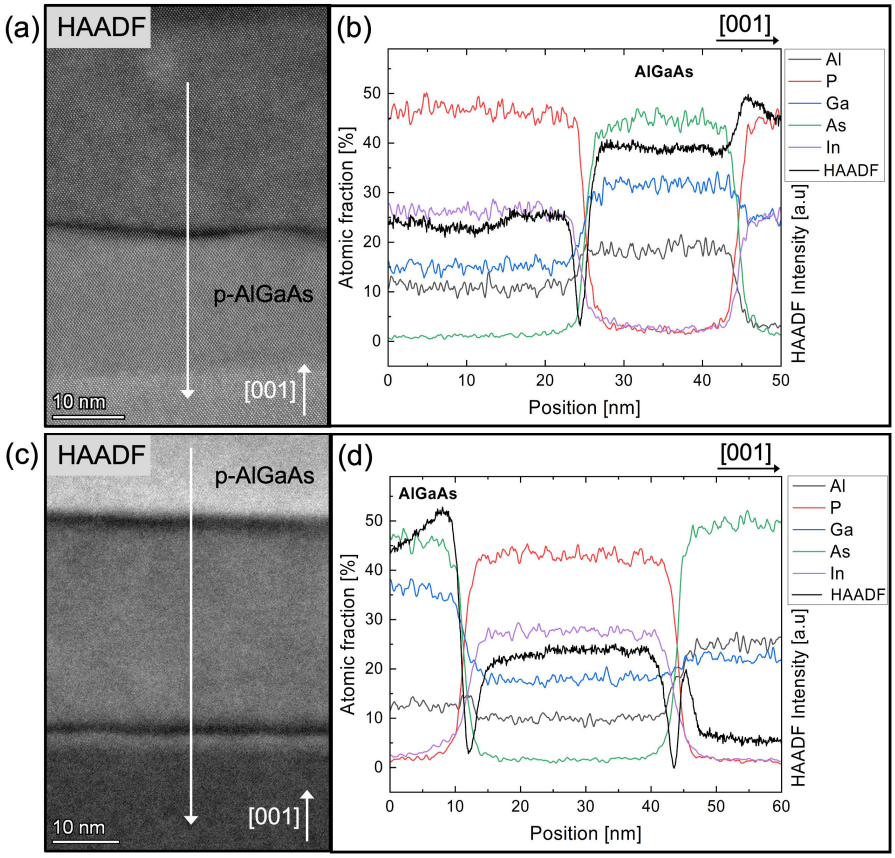

Figure 95: *High-resolution HAADF images (a, c) showing the acquisition positions of STEM-EDX elemental profiles (b, d) across the p-AlGaAs rear interface of the upper tunnel diode (TD). Panels (a) and (b) correspond to the upright-grown (TAN) structure, while (c) and (d) correspond to the inverted-grown (INVTAN) structure.*

the transition of other elements at this interface – may indicate a slight P incorporation into AlGaAs near the boundary. However, this observation is not clearly reflected in the compositional profiles and may be misleading in the presented view. In any case, the extent of an interfacial transfer would be minor.
Since this observation occurs in both the upright and inverted configurations but is not reproducible in the measurements of other upright-grown TD test structures (Fig. 94), it is unlikely that this minor P incorporation is responsible for the dark HAADF contrast or the differences in tunnelling performance between the inverted and upright structures.

8.3.3 STEM-EELS Verification of P Distribution

In order to verify the presence of an unintended P distribution, as it was not clearly discernible in the EDX profiles, STEM-EELS profiling of the P content at the p-AlGaAs rear-interface is performed for both the upper and lower TDs in the TAN sample. The results, shown in Fig. 96, confirm that there are no unintended P accumulations at the p-AlGaAs rear-interfaces in the TAN TDs. Futhermore, no correlation was observed between the P profile and the minimum HAADF intensity.

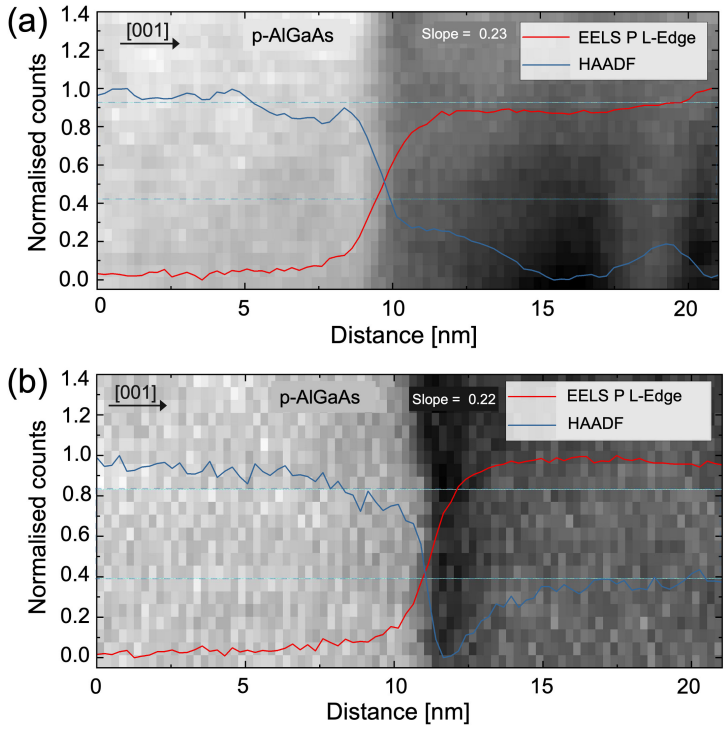

Figure 96: *EELS line profile of the P distribution recorded across the p-AlGaAs rear interface in the (a) upper and (b) lower n-GaInP/p-AlGaAs tunnel diode (TD) of the TAN III-V heterostructure, overlaid on STEM HAADF images in the background. The STEM-EELS data is acquired using an FEI Titan G2 ChemiSTEM at 200 kV with a 51 mm camera length, an EELS spectrometer energy dispersion of 0.1 eV/channel, and a drift tube voltage of 50 eV.*

8.3.4 Measuring HAADF Contrast as a Function of Camera Length

Previous measurement suggest that compositional distribution of major elements can be excluded as the origin of the observed dark HAADF contrast in Fig. 95. Although this might have seemed likely, since at higher collection angles Bragg scattering becomes negligible and the scattered intensity in HAADF images becomes proportional to Z (see Sec. 3.2.1), Bragg scattering contributions can only be excluded for very large inner collection angles (>100 mrad). Therefore, $I_{HAADF} \sim t \times Z^2$ applies for angles greater than 100 mrad.

To verify whether the contrast in HAADF images is governed by Rutherford scattering (composition-related) or Bragg scattering (strain-related), one can systematically study the HAADF image contrast as a function of the inner collection angle, controlled by the STEM camera length (CL). When used quantitatively, this method can even be applied to determine the chemical composition from HAADF images, as demonstrated by Walther *et al.* for InGaAs/GaAs heterostructures.[78] In this work, the method is applied qualitatively to investigate whether the observed drop in HAADF intensity at the p-AlGaAs rear-interface changes with the camera length, and thus to determine whether the contrast is related to strain or to compositional variations at the p-AlGaAs rear-interface.

If the drop in HAADF contrast is strain-related, a broadening of the HAADF intensity drop with increasing CL would be expected, as strain contributions to the HAADF intensity increase with larger CL. At very short CL, the HAADF collection angle is largest, meaning only Z-contrast should contribute to the image intensity. With increasing CL, the diffraction (i.e., strain) contribution to the image intensity increases. Therefore, if the observed intensity drop is strain-related, the interface drop should broaden with increasing CL. Conversely, if the intensity drop remains constant at short CL and does not broaden with increasing CL, it must be related to compositional variations.

The HAADF intensity distribution across the p-AlGaAs rear-interface in the lower TAN TD is systematically profiled as a function of STEM camera length, between 51 and 210 mm. The experiment is conducted on the C_s-corrected FEI Titan G2 ChemiSTEM operating at 200 kV. The resulting HAADF images are presented in Fig. 97, along with the extracted HAADF intensity profiles across the interface.

The HAADF intensity drop across the p-AlGaAs/p-AlGaInP interface (dark contrast) is consistently observed at all used CLs, with the width and depth of the drop remaining unchanged as the CL increased from 51 mm to 210 mm. Therefore, as originally assumed, the contrast drop is most likely compositional rather than strain related. However, the fact that none of the main element distributions (EDX, EELS) correlates clearly with the HAADF intensity drop suggests that this feature might be related to the dopant distribution.

8.3.5 Summary of Structural and Compositional Analyses

Through the correlative structural and compositional STEM-HAADF and -EDX analysis, both crystallographic defects and major element segregation can be excluded as causes for the difference in tunnelling performance between upright and inverted p-AlGaAs/n-GaInP TDs. The only noticeable feature is the dark HAADF contrast at the interface, which could not be linked to major element distribution, nor does it appear to be directly governed by strain. Thus, the origin of this dark HAADF contrast remains unclear, and it is uncertain whether the underly-

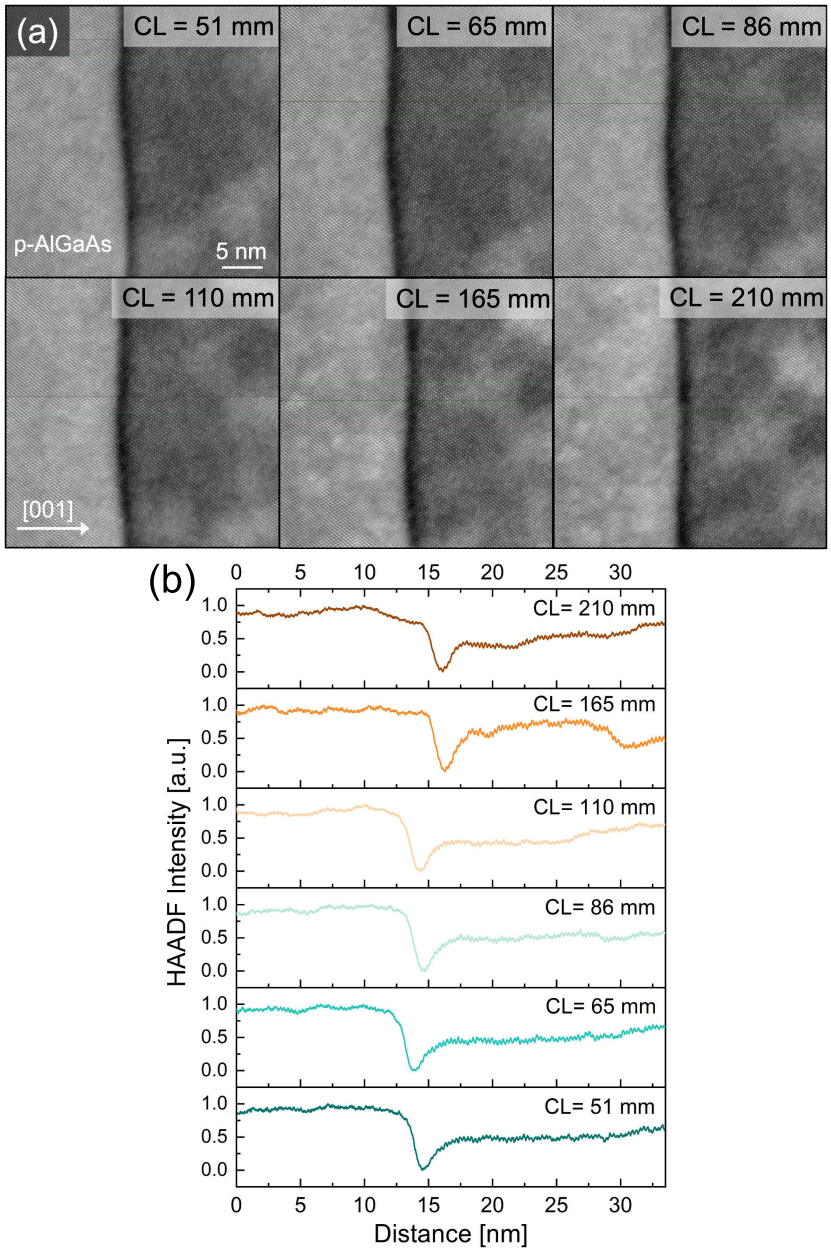

Figure 97: *(a) Systematic analysis of the HAADF intensity change at the p-AlGaAs rear interface of the lower TAN tunnel diode using HAADF STEM images acquired using different STEM camera lengths (CL). (b) Normalized HAADF intensity profiles across the p-AlGaAs rear interface, extracted from the corresponding images in (a).*

ing cause is related to the difference in tunnelling performance between upright and inverted p-AlGaAs/n-GaInP TDs. So far, the results suggest that both the HAADF contrast deviation and the difference in tunnelling characteristics are likely to be related to dopant segregation. However, it cannot be ruled out that strain-induced alterations of the band structure may influence the tunnelling behavior.

Therefore, in the next step, EH is applied to directly measure the potential distribution across the p-AlGaAs/n-GaInP interfaces. This method is sensitive to the active dopant potential distribution and, as such, allows the depletion width to be derived and, thereby, provides a means to assess and compare the tunnelling probabilities. Unlike the structural and compositional investigations, EH directly provides insights into the electrical properties and differences at the TDs grown in different configurations and with varying thermal loads.

Although the observed image contrast is not directly governed by strain, the general presence of strain in the p-AlGaAs/n-GaInP tunnelling diode layers is indisputable. Even though these layers are grown lattice-matched to the GaAs substrate, yielding a pseudomorphic structure with a matching in-plane lattice constant, the difference in unstrained lattice constants results in biaxial strain, which leads to deformation in the out-of-plane direction. In the thin, cross-sectional TEM samples, the thermodynamic equilibrium of the bulk structure no longer holds, so in-plane relaxation could also occur. Therefore, the strain distribution in these samples should also be investigated.

Strain measurements of the p-AlGaAs/n-GaInP and adjacent layers were performed on the upper and lower TAN TDs using 4D-STEM nanobeam electron diffraction (NBED) and TEM-based dark-field electron holography (DFEH) methods. However, both measurements were complicated by method- and specimen-related factors, which prevented a clear interpretation of the results concerning the in-plane and out-of-plane lattice constants (via NBED) as well as the strain distribution relative to the unstrained GaAs substrate (via DFEH) in the p-AlGaAs/n-GaInP heterostructures. In particular, neither method allowed for reliable quantitative strain measurements at the layer interfaces. Therefore, the data is not presented in this thesis, as it was not conducive to addressing the device-related research question.

The 4D-STEM data is evaluated using LiberTEM-blobfinder, a package for correlation-based peak finding and strain mapping.[267] However, the cross-correlation procedure used to determine the diffraction disc positions – and hence the lattice parameters – is affected by the Cu-Pt ordering in the GaInP layers, leading to significant variations in the measured d-spacings. Additionally, achieving an optimal sample thickness for NBED strain measurements is challenging. In thicker samples, dynamical diffraction hinders accurate cross-correlation, while thin TEM lamellae (<50 nm) are difficult to fabricate, as III-V materials tend to bend (due to internal strain), which in turn compromises the interpretability of strain measurements. Furthermore, in-plane relaxation can occur in thin cross-sections, further affecting accuracy.

In DFEH, strain values at III-V heterointerfaces are considered unreliable because the MIP contributions to the measured phase shift are significant when the composition changes at the interface. This MIP contribution produces peaks in the phase gradient at the hetero-interfaces. In theory, tilting to two-beam conditions should suppress this effect (as the MIP signal is contained in the direct 000 beam), but in practice, residual contributions are still present.

8.4 Electrostatic Potential Analysis of p-AlGaAs/n-GaInP Tunnel Junctions

This section presents the electrostatic potential analysis of p-AlGaAs/n-GaInP TDs measured using EH without *in situ* applied bias.
The first part examines the upper and lower p-AlGaAs/n-GaInP TDs in the TAN and INVTAN specimens to assess the impact of growth direction and thermal load – both relevant factors in the actual tandem solar cell growth process – on the dopant potential distribution across the TJ. Specifically, it focuses on the depletion width (W_d), which is crucial for tunnelling efficiency. The second part investigates the potential distribution across the p-AlGaAs/n-GaInP junction in the as-grown and annealed upright TD test structures, as well as in the as-grown inverted TD. This allows for the specific study of thermal annealing and growth direction effects, independent of the complex multi-layer heterostructure of the actual solar cell.
The high doping concentration of the p-AlGaAs/n-GaInP tunnel junctions makes them well-suited for TEM-based potential analysis for two main reasons: First, the electrically damaged surface layer caused by FIB milling is thinner in highly doped specimens. As a result, the electrically damaged thickness is expected to be smaller than in the lower-doped GaAs (165 ± 29 nm) and InP (103 ± 18 to 115 ± 18 nm) p-n junctions studied in Ch. 6.4. Second, the large dopant potential difference at the junction generally enhances the electron phase contrast, leading to a stronger phase shift contribution from active dopants. This, in turn, enables more accurate dopant potential measurements via EH.

8.4.1 Analysis in Upright and Inverted III-V Tandem Solar Cell Heterostructures

For the non-biasing EH electrostatic potential analysis of the p-AlGaAs/n-GaInP junctions in the TAN and INVTAN samples, TEM lamellae were prepared on standard Omniprobe Cu grids for viewing along the [110] zone axis following the protocol in Ch. 4.2.2, with specific considerations for electrical TEM characterisation detailed in Ch. 4.3. The crystalline thicknesses of the TAN and INVTAN TEM lamellae are determined via STEM-CBED analysis, as described in Sect. 5.3.1. At the positions of the upper and lower TDs, the TAN lamella was measured to be 111 ± 1 nm and 146 ± 2 nm thick, respectively. In contrast, the INVTAN lamella had a uniform thickness of 374 ± 2 nm at both TD positions. The thickness variation in the TAN specimen can be attributed to the greater vertical separation between the TDs, which are spaced 2.950 µm apart in TAN compared to 2.108 µm in INVTAN. Additionally, in the TAN structure, the TDs are positioned deeper below the wafer surface (1.25 µm and 4.20 µm) than in INVTAN (0.150 µm and 2.258 µm). As discussed in Ch. 4.3.3, maintaining a parallel-sided lamella during FIB milling becomes increasingly challenging with depth, particularly in heterostructures composed of materials with different milling rates.
Since even small thickness variations can induce significant phase changes (see Ch. 4.3.3 and Ch. 5.1.2.2), it is essential to measure the thickness at the exact location where the potential measurement is performed in these specimens.
EH analyses are conducted using an FEI Titan Ultimate microscope operated at 200 kV in Lorentz mode. The specimens are tilted away from the [001] growth axis to weakly diffracting conditions, as illustrated in Fig. 33, ensuring that the heterointerfaces remain edge-on to the beam. This alignment minimised broadening of the measured phase distribution across the p-n junction in projection (see Sect. 5.2.6.4).

Holograms of the upper and lower TDs in both TAN and INVTAN specimens are recorded using a Gatan OneView CCD camera at two different magnifications, employing the acquisition parameters listed in Table 13. To enhance phase sensitivity, 32 holograms are acquired per stack with an 8 s exposure per image (see Sect. 5.2.1).

Table 13: Acquisition settings for the EH analysis of the TAN and INVTAN specimen. The spatial resolution in the phase image results from the mask size applied in the Fourier reconstruction.

Specimen	**Biprism Voltage**	**Lorentz magnification**	**Pixel size** [nm]	**Pixels per fringe** [nm]	**Fringe spacing**	**Spatial resolution** [nm]
TAN	200 V	26kx	0.319	6	2.0 ± 0.2	6.0 ± 0.6
	200 V	40kx	0.206	8	2.0 ± 0.2	6.0 ± 0.6
INVTAN	200 V	21kx	0.394	4	2.0 ± 0.2	6.0 ± 0.6
	200 V	40kx	0.206	8	2.0 ± 0.2	6.0 ± 0.6

The measurement geometry is illustrated by the hologram acquired at the upper p-AlGaAs/n-GaInP junction in the INVTAN sample, shown in Fig. 98. Alongside the hologram, a CBED pattern is presented, which confirms the off-zone axis tilt orientation of the lamella during hologram acquisition. Fig. 99a-b and d-e display the reconstructed phase images of the upper and lower TJs at different magnifications. The total electrostatic potential (V_{total}) distribution is extracted from the measured phase distribution across the junctions using Eq. 26. As discussed in Ch. 5.1.2.2, in zincblende III-V semiconductors, V_{total} consists of both the dopant potential and the MIP (see Eq. 27). The experimental V_{total} profiles across the upper and lower INVTAN TDs (Fig. 99c, f) are compared with the expected dopant potential distribution and the simulated energy band structure obtained using NEXTNANO (see Ch. 6.3 for details on NEXTNANO simulations).

Although EH does not directly measure the band offsets illustrated in the band structure diagram, they are shown here as they are influenced by various material properties, including the dopant potential, MIP, and strain in the pseudomorphic structure. This supports the understanding of TJ properties, which are governed by the degenerate band bending evident in the band diagram, and aids in interpreting the measured potential distribution.

Fig. 100 presents the corresponding data set for the upper and lower TDs in the TAN specimen. The effects of the experimental settings, along with their adaptations to the specimen and experimental objectives, are discussed in detail in Chs. 5 and 6. Therefore, a full review is omitted here. Instead, the discussion at this point is limited to the key considerations for W_d measurements of the p-AlGaAs/n-GaInP TDs in the TAN and INVTAN structures.

As shown in Fig. 88, which illustrates the TAN and INVTAN MJ structures, the TDs – particularly the lower TDs – are located deep below the wafer surface: 1.25 µm and 4.20 µm in TAN, and 0.15 µm and 2.258 µm in INVTAN. Therefore, in these non-biasing EH experiments, the measurement geometry is configured with the vacuum reference region positioned on the cut-side beside the specimen rather than above the wafer surface. This setup allowed a smaller FOV by applying a standard diffraction lens excitation of 89%, resulting in a hologram width of 1.1 µm for the 200 V biprism voltage thus enabling to achieve higher spatial resolutions in the phase shift images.

Chapter 6.4 showed that, despite compromises in spatial resolution, LM EH acquisitions – which

provide large FOVs of up to 5.1 µm (see Sect. 5.2.4) – allow for reliable depletion width (W_d) measurements at p-n junctions even far from the vacuum reference region (e.g., below surface metal contacts in *in situ* biased specimens), given that high phase resolution is maintained. However, in the TAN and INVTAN samples, the p-AlGaAs and n-GaInP TD epilayers are very thin and embedded within a complex multilayer epistructure. Hence, to facilitate orientation and navigation within the intricate multi-layer structure – which is especially challenging in Lorentz mode – the standard diffraction lens settings (89%) are used for this non-biasing analysis.

As described in Ch. 6, the key to reliable W_d measurements in EH is ensuring that both spatial resolution and phase resolution are sufficient to resolve the potential variation across the p-n junction under study. Thus, the fringe spacing and pixels per fringe must be chosen according to the expected W_d, which for the p-AlGaAs/n-GaInP TJ in the TAN and INVTAN structures are 20 nm and 18 nm, respectively. These values are derived from the simulated dopant potential distributions of the INVTAN (Fig. 99c and f) and TAN (Fig. 100g and h) structures. The EH settings used in this experiment (Tab. 13) yield a spatial resolution of 6 nm, which is significantly smaller than the expected W_d. Although this resolution does not allow for atomic-scale resolution of the interface, it is more than sufficient to accurately measure W_d from the dopant potential distribution in these specimens.

Additionally, the biprism orientation is adjusted relative to the specimen lamella so that the hologram fringes are aligned approximately parallel to [001], i.e., perpendicular to the p-AlGaAs/n-GaInP junction. This ensures that the spatial resolution in the [001] direction is not limited by the fringe spacing, preventing information loss. As a result, the measured V_{total} distribution across the p-AlGaAs/n-GaInP junctions remains consistent across different magnifications (26kx and 40kx for TAN, and 21kx and 40kx for INVTAN), despite the variation in pixel count (see Tab. 13). This consistency is evident in the extracted potential profiles presented in Fig. 99c and f and Fig. 100g and h for the different magnifications.

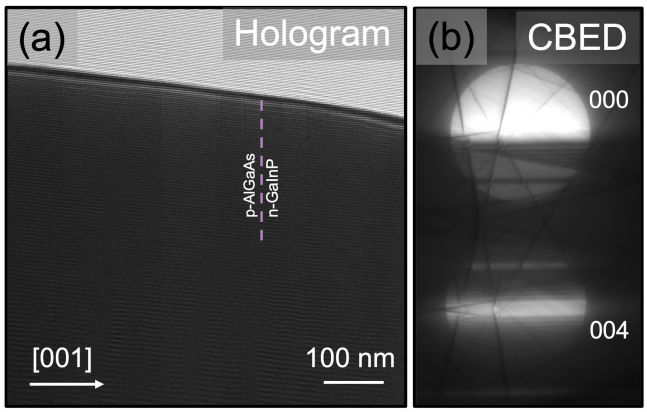

Figure 98: *(a) Electron hologram stack acquired at 40kx magnification on the upper p-AlGaAs/n-GaInP heterojunction in the INVTAN structure. (b) STEM-CBED pattern showing the specimen tilt orientation off-zone axis during hologram acquisition.*

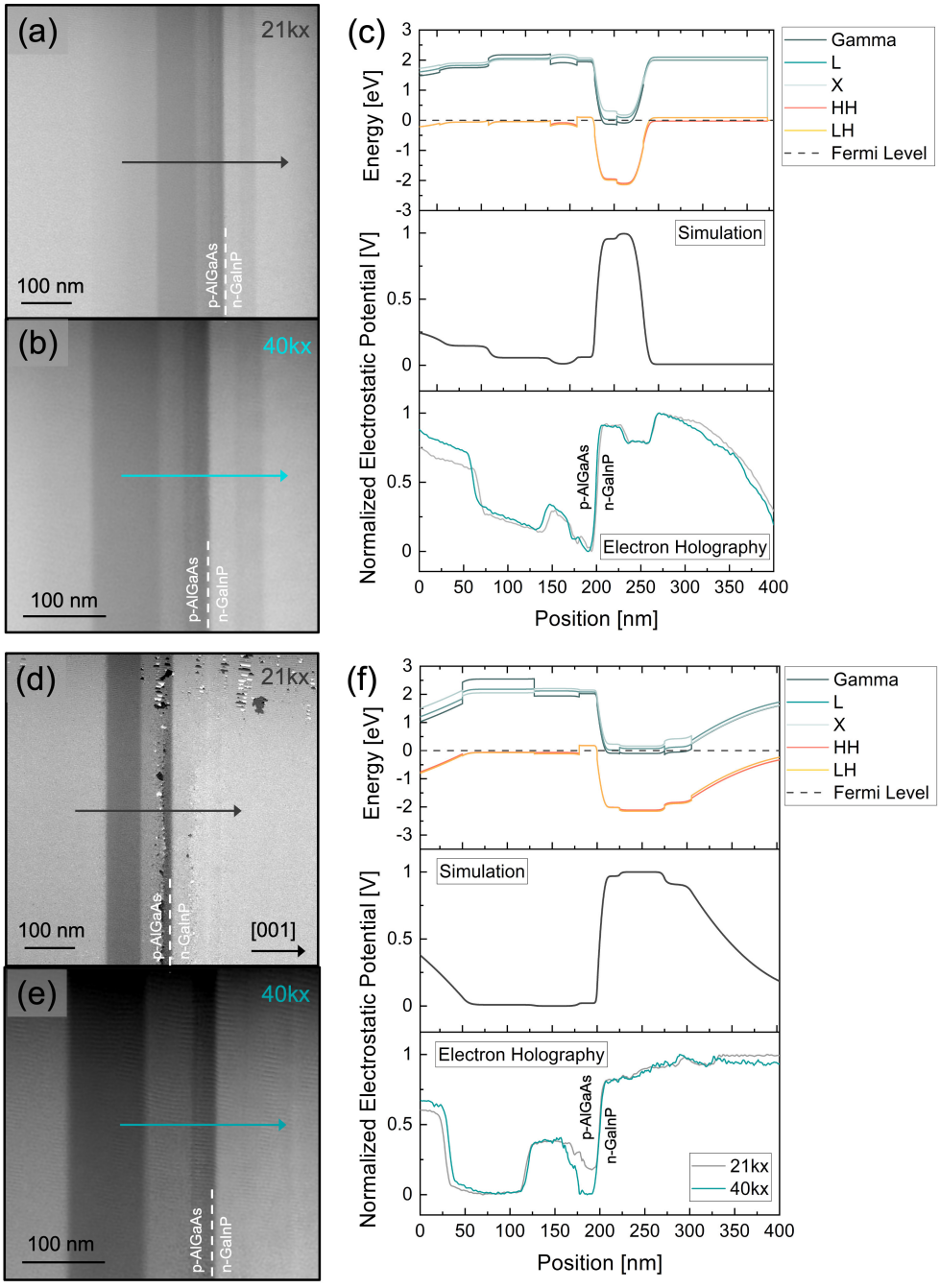

Figure 99: *Reconstructed electron phase images of the upper (a, b) and lower (d, e) p-AlGaAs/n-GaInP tunnel diodes (TDs) in the INVTAN structure, acquired at 21kx and 40kx magnification, respectively. Electrostatic potential distributions extracted from the phase images across the upper (c) and lower (f) junctions are compared to the simulated dopant potential and energy band structure.*

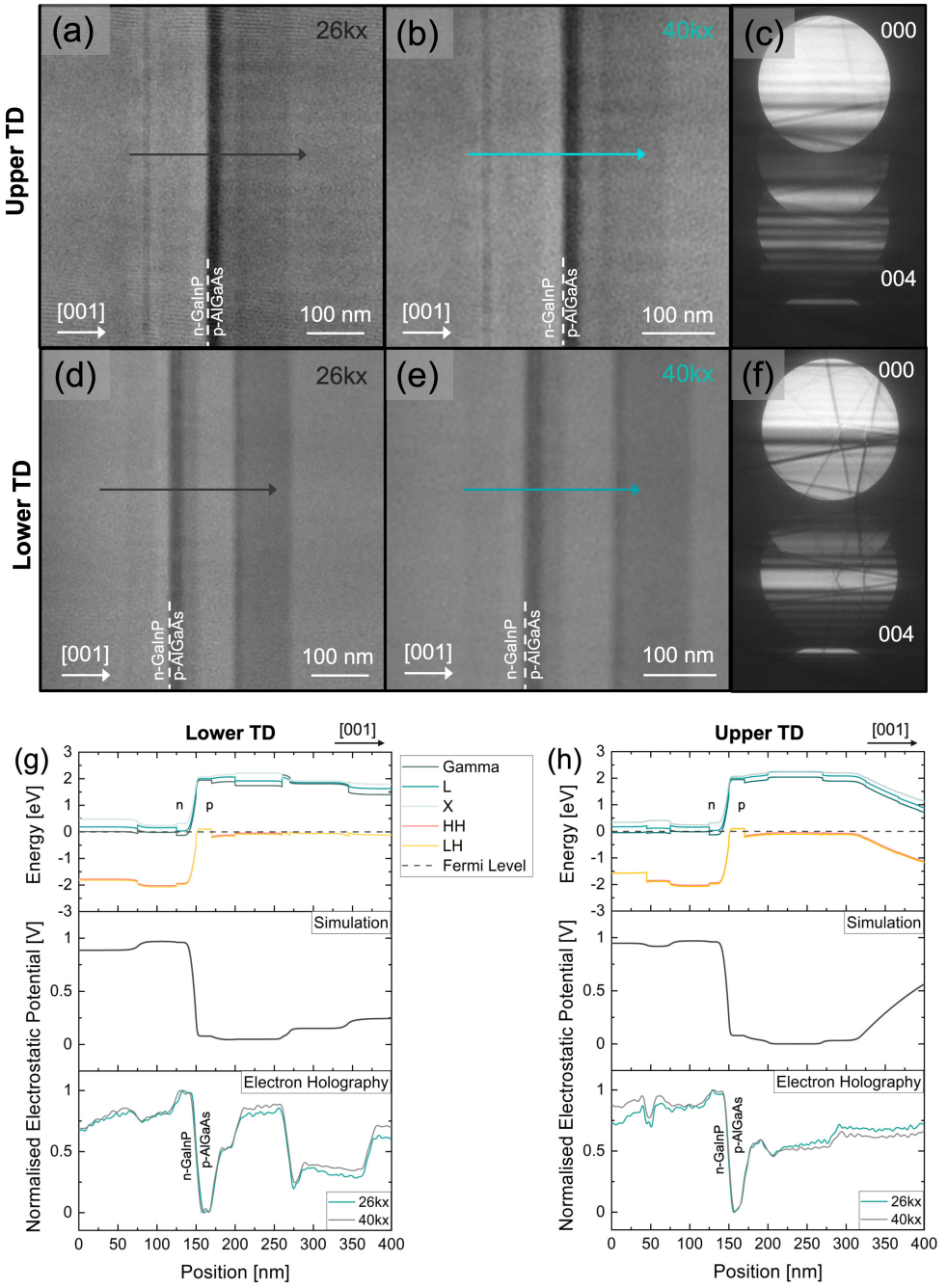

Figure 100: *Reconstructed electron phase images of the upper (a, b) and lower (d, e) p-AlGaAs/n-GaInP tunnel diodes (TDs) in the TAN structure, acquired at 21kx and 40kx magnifications, respectively. STEM-CBED patterns (c, f) illustrate the specimen tilt orientation during hologram acquisition at the upper and lower TDs. Electrostatic potential distributions extracted from the phase images across the lower (g) and upper (h) junctions are compared to the simulated dopant potential and energy band structure.*

8.4.1.1 The Challenges in Quantifying the p-n Junction Built-In Potential Across Hetero-Junctions

As expected, the dopant level in the present III-V TD structures is sufficiently high to generate a strong electric field at the junction, resulting in a distinct step in the electrostatic potential that is clearly detectable by EH, as shown in Figs. 99 and 100. However, the absolute potential distribution, i.e., V_{total} across the TDs measured by EH, is challenging to interpret, and a quantitative evaluation of the potential step at the junction is hindered by two primary factors: First, the MIP contributing to V_{total} varies across the p-AlGaAs/n-GaInP heterojunction due to changes in both group-III and group-V elements. The deviation of the potential distribution measured by EH from the simulated dopant-induced potential distribution hence arises from the fact that the potential contribution from active dopants in the TEM specimen is superimposed by the MIP contribution. To precisely compare the potential step across different TJs, the MIP contribution must be accurately removed. This requires precise knowledge of the MIP values for the p-AlGaAs and n-GaInP compounds.

However, as elaborated in Sect. 2.2.3.3, the MIP is a complex intrinsic material property that depends on composition, crystal structure, bonding, and strain state. Exact MIP values are difficult to obtain and can be determined either analytically using DFT calculations or experimentally using EH. The experimental approach is limited by the challenge of measuring absolute phase shifts of the electron wave in real materials, where the WPOA does not hold.[268,269] The analytical approach, on the other hand, becomes computationally demanding as the complexity of the multinary III-V system increases. Consequently, most reported MIP values in the literature pertain to binary III-V compounds.

A compilation of experimentally and computationally derived MIP values for the binary constituents of the ternary AlGaAs and GaInP compounds used in this study is presented in Table 1 in Sect. 2.2.3.3. The MIP of AlGaAs and GaInP can be estimated by linear interpolation between the MIP values of the binary constituents using Vegard's law. Based on DFT-derived MIP values (Table 1) and the compositional stoichiometries defined in the MOVPE growth recipe, this approach yields to 13.64 eV for AlGaAs and 13.76 eV for GaInP. However, this method does not provide highly accurate values due to the fact that the actual bonding and strain state in these ternary compounds differs from that of the binary constituents and is not accounted for in this simple interpolation. The TD heterolayers are grown in-plane lattice-matched to the GaAs substrate at high growth temperatures, leading to biaxial strain deformation in the out-of-plane direction at room temperature (further details can be found in Sect. 2.2.2). Moreover, deviations from the bulk thermodynamic equilibrium state in cross-sectional TEM specimens may alter the strain state in the heterolayers due to relaxation effects.

Beyond neglecting variations in bonding and strain states state in the ternary III-V compounds in the TEM specimen, the linear interpolation approach also requires precise determination of the actual stoichiometric composition of the III-V heterolayers, which may deviate from the intended values due to various factors, such as MOVPE growth-related effects or foreign ion implantation during FIB preparation.

Previous studies have demonstrated successful subtraction of MIP contributions from EH-measured potential distributions across III-V heterojunctions, such as InGaN/GaN tunnel diodes.[173] However, these junctions involve a change in only the group-III element, allowing for

relative quantification of the In-content via STEM-EDX. This approach is not applicable to the present p-AlGaAs/n-GaInP TDs, where both group-III and group-V elements change. Absolute compositional measurements via STEM-EDX are challenging (see Sect. 3.2.2) and further complicated by large interaction volumes, which hinder precise quantification at interfaces and in thin epilayers. As a result, accurately determining the MIP values of the p-AlGaAs/n-GaInP TD layers in the present specimens – and thereby reliably removing the MIP contribution from the measured potential distribution – remains a significant challenge.
Second, in different III-V materials, surface Fermi-level pinning varies and is not directly comparable between different compound layers. The present p-AlGaAs/n-GaInP heterojunction layers contain different dopant elements and doping concentrations, resulting in differing surface band bending thicknesses in the n- and p-type layers. This makes quantification of the potential distribution across these tunnelling heterojunctions using EH particularly difficult. Accurate quantification of EH measurements on ternary III-V compound heterojunctions would therefore require comprehensive 3D potential simulations that account for variations in Fermi-level pinning.

Given these challenges, this TD investigation avoids direct quantification of the dopant potential distribution from the measured V_{total}. Instead, relative measurements are performed, and V_{total} is presented on a normalised y-scale. The primary focus of this EH TD study is not the absolute built-in potential but rather the measurement and comparison of TD depletion widths.

Table 14: Properties of the p-AlGaAs/n-GaInP junctions in the upright-grown TAN and inverted-grown INVTAN structures (see Sect. 8.2). The experimentally measured depletion widths, derived from EH phase images, are compared with simulated values (NEXTNANO). The measurement uncertainty for depletion width is ±1 nm. The compositional interface widths were determined from amplitude images reconstructed from the same hologram stacks as the phase images, as well as from the HAADF intensity profiles obtained from STEM-HAADF images of the TAN and INVTAN specimens (Sect. 8.3.1, Fig. 90, and Fig. 91).

Specimen	**TD**	**Junction Width [nm]**			**Compositional Width [nm]**		
		Phase Image		**Simulation**	**Amplitude Image**		**STEM-HAADF**
		21kx/26kx	40kx		21kx/26kx	40kx	
INVTAN	upper	16	17	18	5.5	5.8	3.5
	lower	16	17	18	6.1	6.2	3.6
TAN	upper	16.5	16.5	20	7.0	5.0	3.5
	lower	19	20	20	6.5	7.0	4.1

8.4.1.2 Depletion Width Analysis in p-AlGaAs/n-GaInP Tunnel Junctions

Despite the difficulties in quantifying the built-in potential across the p-AlGaAs/n-GaInP TJ in the present TAN and INVTAN samples, comparing the measured depletion width of the p-n junction to simulations of the expected dopant potential distribution nevertheless allows for indirect assessment of the dopant confinement to the epitaxial junction layers. Reliable quantification of the depletion width of the p-AlGaAs/n-GaInP heterojunctions does not necessitate the subtraction of MIP contributions, because, as explained in Ch. 5 and 6, the dopant potential changes at much lower carrier frequencies and hence the depletion width is generally not affected

by the short range potential variation induced by the MIP changing across the heterojunction. Accurate quantification and comparison of the TD depletion width is therefore possible, despite varying Fermi level pinning, given that the specimens have a minimum threshold thickness and the measured potential distribution contains a dominant contribution from active dopants.
The depletion widths of each p-AlGaAs/n-GaInP junction in the TAN and INVTAN sample are measured by means of the electric field profiles derived as the 1st differential of the electrostatic potential (Eq. 51) using the procedure described in Sect. 6.4.1. The error in measuring W_d is estimated to be 1 nm, based on the average uncertainty in the x-intercepts of the linear extrapolations. The results are presented in Table 14.

Verification of Depletion Width Measurements
To ensure reliable depletion width measurements, it is essential to verify the accuracy and comparability of the measured W_d across different TDs – both within a single TEM specimen and between multiple specimens – before interpreting the results. This requires confirming that the following experimental factors do not introduce artifacts in the dopant potential distribution, thereby ensuring the validity of the measurements.

1. **Sample Tilt Orientation**
   When tilting the TEM lamellae off-zone axis, it must be ensured that the tilt occurs parallel to the epilayers so that the heterojunction remains perfectly on-edge during potential profiling. This prevents artificial broadening of W_d in projection. Additionally, to enable direct comparison of W_d between different specimens, a consistent specimen tilt orientation must be maintained across all measurements.
   In this study, the uniform tilt orientation of the TAN and INVTAN specimens about the [001] axis is confirmed by CBED patterns (Fig. 98 and Fig. 100), which are recorded immediately after the hologram acquisitions for each TD.

2. **Effect of TEM Lamella Thickness on W_d Measurements**
   The CBED-derived crystalline thicknesses of the TAN (146 ± 2 nm at the lower TD, 111 ± 1 nm at the upper TD) and INVTAN (374 ± 2 nm) specimens vary significantly. To verify comparison of TJ widths across specimen, it must be verified that the difference in TEM lamella thickness does not affect the depletion width measurements. As discussed in Ch. 6, W_d should remain independent of TEM specimen thickness, provided that the thickness exceeds a critical threshold. Below this threshold, damaged surface layers dominate the junction characteristics, and the specimen intrinsic W_d cannot be measured reliably.
   To assess whether TEM lamella thickness affects W_d at the p-AlGaAs/n-GaInP junctions, a TEM lamella of the INVTAN bulk specimen is specifically prepared to include regions of varying thicknesses, ranging from 165 nm to 353 nm, as measured by STEM-CBED. Fig. 101a presents a STEM-HAADF overview image of the lamella. The depletion width is measured using EH at each thickness region. An exemplary CBED pattern confirms that the sample tilt orientation during hologram acquisition matches that of the previous EH TAN and INVTAN analyses. The extracted W_d values are plotted as a function of specimen thickness in Fig. 101b. No significant variation or trend in W_d is observed with changing thickness. Despite an overall thickness variation of 188 nm, W_d remained constant

at 16 nm, with only minor deviations within the error range of ±1 nm.
Consequently, it can be concluded that the differences in TEM lamella thickness between the TAN and INVTAN specimens do not affect the comparability of W_d, thus justifying the direct comparison between the different specimens.
The specimen thickness at the upper TAN TD position is 111 ± 1 nm, which is slightly below the tested thickness range. However, since the same W_d values are measured for this TD as for the upper TD in the 374 ± 2 nm thick INVTAN specimen (see Table 14), this indicates that the thickness remains above the critical minimum threshold required for reliable depletion width measurement. Since the p-AlGaAs/n-GaInP TD is a heterointerface, the electrically inactive thickness cannot be reliably estimated using the method demonstrated in Ch. 6.4, which involves measuring the electron phase step across the junction as a function of lamella thickness and extrapolating to determine the thickness corresponding to zero phase step, the electrically inactive thickness.
However, due to the high doping concentrations ($> 10^{19}$ cm^{-3}) in both p-AlGaAs and n-GaInP TD layers, the electrically damaged surface layer induced by FIB milling is expected to be relatively small compared to lower-doped materials such as GaAs (165 ± 29 nm) and InP (103 ± 18 to 115 ± 18 nm) (see Ch. 6.4). Thus, the TD W_d can still be reliably measured up to low specimen thicknesses, including the 111 ± 1 nm thick region at the upper TD position.

3. **Verification of Active Dopant Contribution to the Measured Phase Shift**

   For reliable depletion width measurements that accurately represent the intrinsic TJ characteristics in the bulk specimen, the measured phase shift must contain a significant contribution from the electrostatic potential of active dopants. This can be validated by comparing the depletion widths derived from the EH phase images with the compositional width of the p-AlGaAs/n-GaInP interface, measured from the intensity distribution in both the reconstructed EH amplitude images and STEM-HAADF Z-contrast images, as presented in Table 14. If the measured phase shift across the p-AlGaAs/n-GaInP junction is indeed dominated by the long-range field from active dopants, the junction widths observed in the phase images should be significantly broader than those measured in the amplitude images, which are governed by the short-range contrast from the compositional and density variations (i.e. MIP). The comparison in Table 14 confirms this expectation: the TJ width measured in the electron phase images is substantially larger than the compositional interface width derived from both the reconstructed amplitude images and STEM-HAADF images. This verifies that the electrostatic potential distribution V_{total} across the TDs includes a significant contribution from active dopants, thus confirming the validity of the depletion width measurements.
   It should be noted that, despite tilting the TD specimen to low-diffraction conditions to minimise multiple scattering effects, residual weak amplitude variations across the III-V heterostructure cannot be entirely eliminated. These can be caused by dynamical diffraction due to local strain or bending of the lamella.

The preceding verification of TD depletion width measurements justifies the interpretation of the results for the inverted- and upright-grown TDs presented in the following section.

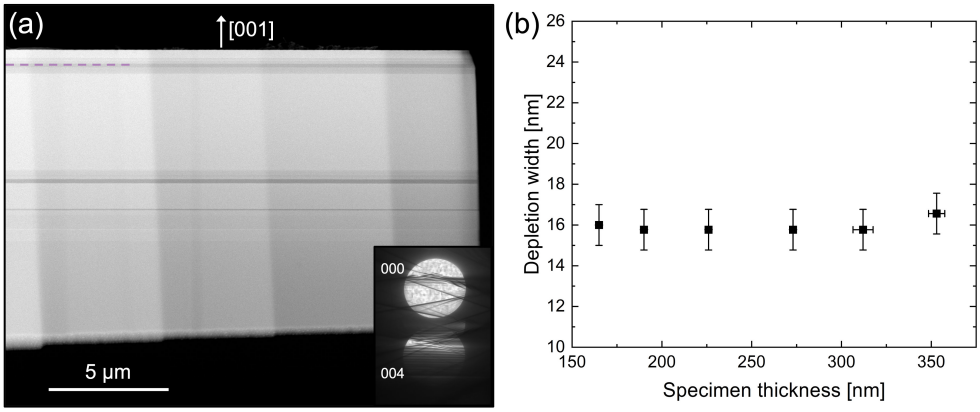

Figure 101: *(a) STEM-HAADF overview image of the INVTAN TEM lamella, prepared with regions of varying thickness for measuring the tunnel junction (TJ) depletion width via EH as a function of lamella thickness determined by STEM-CBED, as shown in (b). Electron hologram stacks (30 × 8s) are acquired at 21kx magnification on the upper p-AlGaAs/n-GaInP TJ (pink dashed line) using a FEI Titan Ultimate operated at 200 kV with a standard diffraction lens excitation of 89%. A biprism voltage of 200 V provided a hologram fringe spacing of 2 nm. The STEM-CBED pattern (inset in (a)) shows the specimen tilt orientation off-zone axis during hologram acquisition.*

Discussion

Overall, the measured TJ widths are similar to the expected W_d, being either equal to or slightly smaller than the simulated values. At this point, however, it is important to reiterate the point made in Ch. 6.3, namely that the potential simulations do not reflect the actual state of the cross-sectional TEM lamella, as they (1) are based on the intended rather than the actual dopant concentration distribution, which cannot be reliably measured using SIMS in such large III-V heterostructures, and (2) do not account for damage-induced surface Fermi level pinning. Thus, they merely serve as an approximate reference for interpreting the measured depletion widths and adjusting the EH acquisition settings. The focus is on the relative comparison of the measured depletion widths between the samples.

In the inverted-grown INVTAN structure, the upper and lower p-AlGaAs/n-GaInP TJs exhibit identical depletion widths, with measurements differing by only 1 nm between data recorded at 21kx and 40kx magnifications. While this variation is within the experimental error, it could be attributed to the lower number of pixels per fringe in the lower magnification holograms. Consequently, the data that is recorded at high magnification is considered to be more reliable. Here, the measured depletion width of 17 nm for both the upper and lower TDs agrees with the expected width of 18 nm within the error margin.

In the upright-grown TAN structure, using the same magnification, the measured W_d of the upper TJ is slightly smaller – by 2.5 and 3.5 nm – compared to the lower TJ. However, the lower TJ's values match the expected W_d of 20 nm within the error. A comparison of measurements at different magnifications (26kx and 40kx) shows consistency within the error for each junction. The slightly smaller depletion width of 16.5 nm at the upper TJ, located 1.25 µm below the wafer surface, is comparable to the 16–17 nm widths measured at the TDs of the inverted-grown

INVTAN structure, positioned at 0.15 and 2.258 µm below the surface.
The fact that the lower upright TD is located significantly deeper in the TAN structure (at 4.20 µm) and was thus subjected to a higher thermal load compared to the upper TD – and to both TDs in the INVTAN structure – suggests that the observed difference in W_d may be related to thermally induced changes during annealing.
However, since all measured W_d values are equal to or smaller than the expected 20 nm, it is difficult to definitively determine the cause of the differing tunnelling performance between the upright- and inverted-grown TDs from EH measurements alone. Based on the observation that the tunnelling current break-in, measured in bulk tandem solar cell devices, occurs at lower current densities in the TAN devices, a significant widening of the depletion width compared to the simulated 20 nm would be expected in the upright-grown TDs. This is because an expansion of the SCR at the p-AlGaAs/n-GaInP junction would lead to a substantial reduction in carrier tunnelling probability, which has been reported to decrease exponentially with increasing W_d.[257,250] However, no such broadening is observed in the present specimens. Thus, the premature drop in tunnelling currents at lower operating current densities in TAN devices, compared to INVTAN devices, cannot be explained by the non-biasing EH analysis.
Bulk device performance studies have shown that TAN and INVTAN devices operate similarly under 1-sun illumination. The difference becomes apparent only under concentrated light, where the TAN structure exhibits a break-in of tunnelling currents at lower current densities, whereas the INVTAN TDs maintain high tunnelling performance at higher current densities. This suggests that the mechanism responsible for the premature TD breakdown in TAN devices might only emerge at higher current densities. Consequently, the underlying cause may not be detectable under non-operational conditions, such as the non-biased state in TEM measurements.
To address this limitation, EH depletion width measurements must be conducted while electrically biasing the TD specimen *in situ* in the TEM. This approach would simulate the current regimes experienced under concentrated light and could potentially trigger the mechanisms impairing tunnelling.
Beyond the absence of operational conditions in the present EH analysis, isolating the cause of the difference in tunnelling performance is further complicated by the complex multilayer structure of the TAN and INVTAN devices. Various interdependent processes occurring during the growth of different epilayers may influence the band structure and, consequently, the depletion width at the TD. Therefore, before conducting *in situ* biasing experiments, EH W_d measurements are first performed on TD test structures (presented in Sect. 8.2). In these specimens, the p-AlGaAs/n-GaInP TDs are isolated, allowing for the investigation of influencing factors in a simplified system. Specifically, comparative EH measurements are conducted on the annealed upright-grown and inverted-grown TD test structures in order to analyse the impact of growth direction on junction properties.

8.4.2 Analysis in Upright- and Inverted-Grown Test Structures

For the non-biasing EH electrostatic potential analysis of the p-AlGaAs/n-GaInP junctions in the upright- and inverted-grown TD test structures, presented in Sect. 8.2, TEM lamellae with varying thickness regions are prepared on standard Omniprobe Cu grids for viewing along the [110] zone axis, as shown in Figs. 102a and 103a. The crystalline thicknesses of these regions are

determined via STEM-CBED analysis (see Sect. 5.3.1).
EH analyses are performed using the FEI Titan Ultimate microscope operated at 200 kV in Lorentz mode, following the methodology of prior TAN and INVTAN EH studies. The specimens are tilted to weakly diffracting conditions, ensuring edge-on imaging of the p-AlGaAs/n-GaInP junction. Electron holograms are acquired using a 2k×2k CCD camera fitted to the GIF rather than the 4k×4k Gatan OneView CCD camera due to technical issues. Despite the GIF camera's smaller FOV, comparable EH acquisition conditions are maintained using a biprism voltage of 125 V and a magnification of 1950×, yielding to a hologram interference width of 730 nm, a fringe spacing of 2.9 nm, and a sampling of 4 pixels per fringe.
Electron holograms of the p-AlGaAs/n-GaInP junction are recorded for the various thickness regions in both specimens, allowing phase distribution analysis across the junction. Figs. 102b and 103b present exemplary reconstructed phase images for the upright- and inverted-grown junctions, respectively. The corresponding CBED patterns in Figs. 102c and 103c confirm matching sample tilt orientations, validating the comparative potential distribution measurements. Figs. 102d and 103d show the normalised electrostatic potential distribution extracted from the phase images, compared to the simulated dopant potential and the approximate MIP variation across the heterolayers. The MIP values for the III-V compounds in the present heterostructures were estimated via linear interpolation between the MIP values of their binary constituents (see Tab. 1), following Vegard's law (Sect. 8.4.1.1). A comparison of the experimentally derived potential distribution with the estimated MIP variation indicates that discrepancies between the measured relative potential differences across the heterolayers and the simulated dopant potential distribution can be attributed to the MIP contribution to the total measured potential V_{total}.

The depletion width of both the upright- and inverted-grown p-AlGaAs/n-GaInP junctions is extracted from the electrostatic potential distribution at each thickness step. The results, plotted in Fig. 104, are compared to the depletion width derived from the simulated dopant potential, which has been determined to be 14.7 nm for both TD test structures. Within the measurement uncertainty of ±1 nm, the experimentally measured W_d remains consistently around 14 nm across different crystalline thicknesses in both upright- and inverted-grown specimens. This indicates that sample thickness does not influence the measured depletion width.
Regarding the investigation of the different tunnelling performance between the upright- and inverted-grown TD structures, the present non-biasing EH analyses – as well as those carried out for the TAN and INVTAN structures – do not reveal any underlying mechanisms or causes, since both configurations exhibit the same depletion width. Consequently, the next step involves *in situ* biasing analysis of the electrostatic potential distribution to examine the p-AlGaAs/n-GaInP junction under conditions closer to real operation.

8.5 *In Situ* Biasing (S)TEM Analysis of Upright-Grown n-GaInP/p-AlGaAs Tunnel Junctions

In view of the *in situ* biasing TEM TD analysis, parts of the test structure wafers – comprising the as-grown and annealed upright-grown TDs as well as the as-grown and annealed inverted-grown TDs (see Sect. 8.2) – are metallised with Au-based alloys on both the top and rear wafer sides at Fraunhofer ISE. Specifically, a Pd/Au/Ge/Ti/Pd/Ag alloy is deposited as the contact

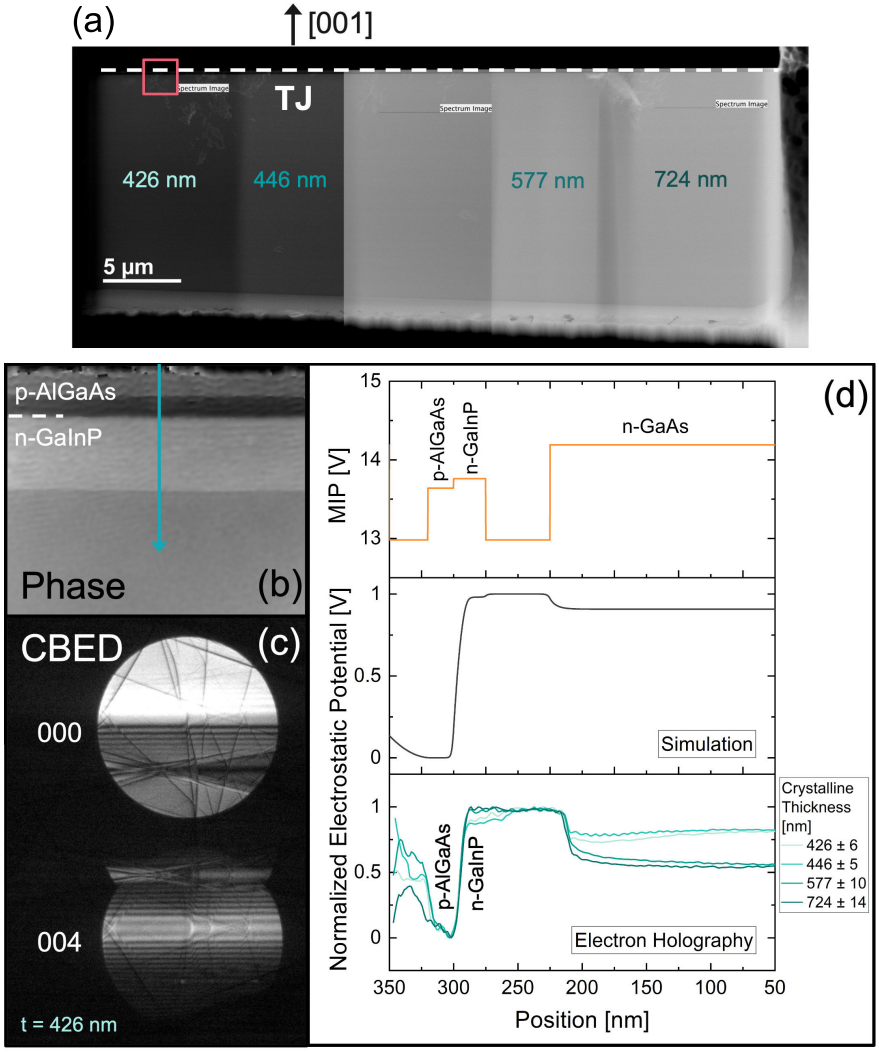

Figure 102: *EH analysis of the upright-grown p-AlGaAs/n-GaInP test structure. (a) STEM-HAADF overview image of the TEM lamella, showing regions of different crystalline thicknesses (indicated), where hologram stacks were acquired. (b) Example of a reconstructed electron phase image and (c) a STEM-CBED pattern, both recorded at the same thickness region (426 nm). (d) Extracted electrostatic potential distribution across the junction, as exemplarily indicated by the green line in (b), compared to the simulated dopant potential and the estimated MIP variation across the upright-grown TD III-V heterostructure.*

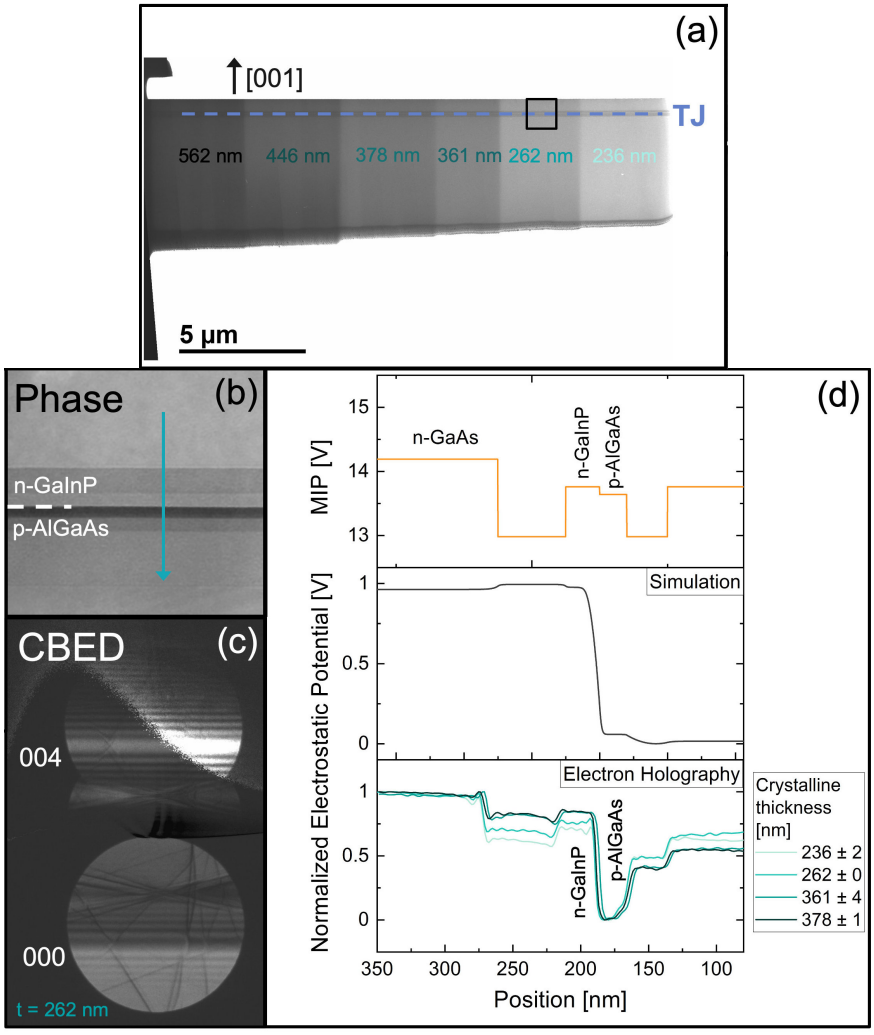

Figure 103: *EH analysis of the inverted-grown p-AlGaAs/n-GaInP test structure. (a) Overview image of the TEM lamella, showing regions of different crystalline thicknesses (indicated), where hologram stacks were acquired. (b) Example of a reconstructed electron phase image and (c) a STEM-CBED pattern, both recorded at the same thickness region (262 nm). (d) Extracted electrostatic potential distribution across the junction, as indicated by the green line in (b), compared to the simulated dopant potential and the estimated MIP variation across the upright-grown TD III-V heterostructure.*

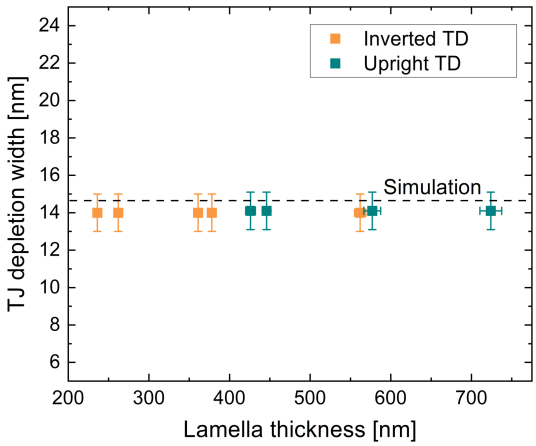

Figure 104: *Experimentally measured depletion widths by EH of the p-AlGaAs/n-GaInP junctions in the upright- and inverted-grown TD test structures as a function of crystalline specimen thickness determined by STEM-CBED. For comparison, the simulated depletion width of 14.7 nm (NEXTNANO) is indicated by the dashed line.*

for p-GaAs, while a Pd/Zn/Pd/Au alloy was used for n-GaAs. These metal alloys are standard and specifically optimised to ensure reliable low-resistance contacts to the III-V epistructure, i.e., ohmic characteristics of the metal-GaAs interfaces (see Ch. 6.5). Accordingly, the metallised wafers are selected as the starting material for the *in situ* biasing experiments. As discussed in Ch. 6.5.5, achieving reliable ohmic contacts using FIB-induced metal deposition (e.g., W or Pt) is particularly challenging for semiconductor specimens, especially for n-GaAs. Establishing a low-resistance ohmic contact is critical, as contact resistance contributes to the overall series resistance of the TEM lamella (see Ch. 6.5.4). Excessive series resistance in the *in situ* biasing TEM specimen can obscure the p-n junction characteristics of the semiconductor device – here, the TD characteristics – since a significant portion of the applied voltage may drop across the metal-semiconductor interface rather than the device p-n junction.
The isolated TD test structures allow to specifically analyse the TD break-in by means of *J-V* measurements. This is challenging in a complete MJSC, as will be discussed in greater detail on the example of the full tandem solar cell studied in Sect. 8.6.

Fig. 105 presents the dark *J-V* characteristics of the TD test structures, measured on the metallised bulk wafers by colleagues at Fraunhofer ISE using a Keithley SourceMeter. While TD break-in is clearly observed in the upright-grown TDs, no break-in is detected in the inverted-grown TD within the applied *J*-sweep measurement range. The measurements thus confirm the general observation that upright-grown p-AlGaAs/n-GaInP TJs break in at lower current densities than their inverted-grown counterparts. A comparison of the *J-V* characteristics of the as-grown and annealed upright TDs (Fig. 105a) reveals that the annealed TD exhibits break-in at a slightly lower J than the as-grown TD.
Compared to the *J-V* characteristics of an ideal TD (see Fig. 87), the tunnel current break-in does not appear as the characteristic drop in *J* in the experimental curves, but is observed as a plateau instead. This is due to measurement constraints, as the used Keithley SourceMeter only

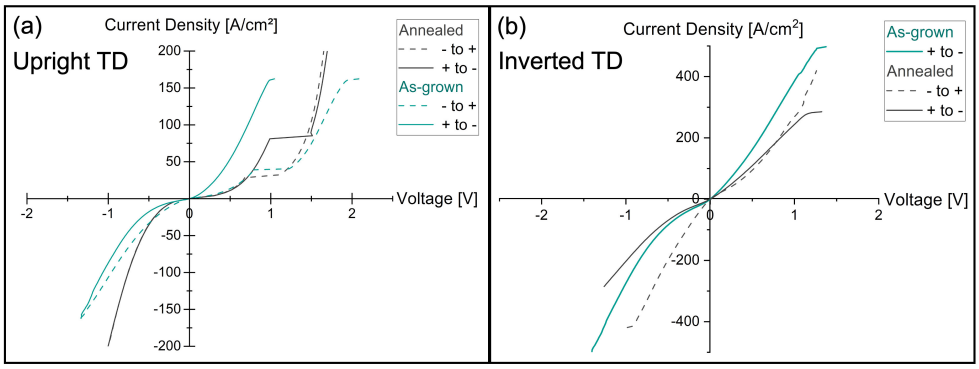

Figure 105: *Dark J-V characteristics of the as-grown and annealed p-AlGaAs/n-GaInP TD test structures: (a) upright (p-on-n) and (b) inverted (n-on-p). Measurements are performed on metallised bulk samples. Dashed and solid lines denote the current sweep direction.*

allows for current sweeping, making it impossible to resolve the dip. Ideally, voltage sweeping would be performed to obtain the necessary measurement points to resolve the dip.
Furthermore, *J-V* curves measured in the opposite sweep direction on the same sample should ideally overlap, as observed for the annealed upright TD (grey curves in Fig. 105a). However, the slight misalignment of the *J-V* curves for the other samples is a measurement artifact resulting from difficulties in accurately determining the contact area.
Another measurement artifact could be that, unlike the ideal TD *J-V* (Fig. 87), the measured *J-V* curves do not exhibit the expected ohmic (linear) behavior in the zero-bias range. In general, the *J-V* profile measured on an isolated TD test structure does not purely represent the TJ characteristics but also includes contributions from resistances, parasitic inductance, and capacitance inherent to the contact structure and measurement setup – factors that are not present in a full solar cell device. The observed non-ohmic behavior in the present TD *J-V* measurements likely arises from the combined effects of several factors:

- Majority carrier barriers at the adjacent GaAs layers (GaAs cap and GaAs substrate)
- Cable resistance: only a two-point measurement was feasible for the present specimen. Ideally, the specimen wafers would be mesa-etched to enable four-point measurements, allowing to subtract cable resistances
- Series resistance, e.g., due to the GaAs substrate (~450–550 µm) and GaAs nucleation layer (400 nm)
- Contact resistance

Since a well-established metal alloy composition is used for contacting, Schottky behavior at the metal-GaAs interfaces is considered an unlikely cause of the nonlinear *J-V* characteristics in the zero-bias range.
However, despite these measurement challenges, the *J-V* curves still provide the desired information – namely, they identify the break-in current density of the upright-grown TD. This

allows determining the light concentration at which the tunnel currents break in. For the annealed upright TJ, break-in occurs at approximately 80 A/cm^2. For a 4-J cell, which generates a current density of 14 mA/cm^2 under 1-sun illumination, this corresponds to a break-in at approximately 5700 suns. For a 2-J cell, which generates 20 mA/cm^2 under 1-sun illumination, this corresponds to approximately 4000 suns. These values match the typical current density range in which break-in is observed for upright-grown TDs.

As the annealed upright-grown TD sample is representative of the investigated problem, it was selected for *in situ* biasing TEM characterisation. The metallised wafer was used as a bulk specimen to ensure reliable ohmic contact. However, while pre-deposited metal contacts can provide more reliable ohmic behavior compared to FIB-induced metal deposition, the TEM sample preparation of these metallised wafers introduces additional challenges. The two most prominent challenges are:

1. Due to the density variation between the contact metal layer and the III-V epistructure, curtaining effects (a.k.a. thickness corrugations) can occur on the area of interest during FIB milling. 2. Due to the large thickness of the specimen wafer, slicing the entire wafer to preserve both the bottom and top metal contact is challenging.

To address these challenges, two different approaches are used for preparing the metallised wafer of the upright-grown TD test structure for *in situ* biasing TEM analysis on Si half-chips. The following subsections present these two approaches alongside the *in situ* biasing analysis of the resulting specimen in the TEM, followed by an evaluation of each respective preparation approach.

8.5.1 Approach 1

8.5.1.1 Backside FIB Milling Preparation of Metallised Wafers

In the first approach to preparing an *in situ* biasing TEM lamella from an annealed upright TD specimen wafer with pre-deposited top and bottom ohmic metal contacts, backside FIB milling was employed. Backside milling is a common approach to mitigate curtaining effects in the region of interest caused by metallised surfaces (contacting metal layers) in semiconductor devices.[270,128,271,26].

The backside milling preparation is conducted using the FEI Strata 400S FIB-SEM.

The overall preparation procedure follows the standard *in situ* biasing lamella preparation described in Sect. 4.4.1, with specific adaptations. The initial steps, including lamella lift-out from the bulk specimen, deposition of a protective metal layer, trench cuts, side and under-cuts, micromanipulator welding, and lift-out, follow the standard procedure. However, during transfer to the MEMS support chip, the lamella is rotated by 180° and consequently fixed upside-down, with the top metal layer facing downward across the chip trench.

This inversion is essential to mitigate curtaining effects during FIB milling while preserving the ohmic front contact. Since the protective top metal layer ends up on the downward-facing edge, an additional protective metal layer must be deposited on the upward-facing bottom edge of the lamella before Ga-ion thinning from the substrate side. This layer simultaneously substitutes the original bottom wafer contact of the device (here, the contact to n-GaAs), which could not be preserved during the FIB lift-out process. To enhance the electrical contact quality of this metal layer – specifically to minimise contact resistivity – any amorphous surface damage on

the undercut edge of the lamella must be removed as thoroughly as possible. For this purpose, the edge is precision-cut using FIB milling at 2.8 nA with a 90° tilt. The lamella is then rotated another 90° to complete the full 180° inversion, followed by the deposition of the metal layer on the cleaned edge. As per standard *in situ* biasing specimen preparation, ion-beam-induced metal deposition (IBID) is employed to reduce the electrical resistivity of the deposited contact metal (see Sect. 4.4.2 for further details). Due to the limited availability of metal precursors in the FEI Strata 400S FIB-SEM system, IBID-W is applied as the contact to n-GaAs.
The lamella is then transferred to the MEMS chip and fixed in its 180° inverted configuration, with the pre-deposited top metal layer facing downward across the chip trench. The remaining preparation steps, including thinning the lamella to an electron-transparent thickness for EH analysis and performing the final low-energy ion polishing, follow standard procedures.
The resulting backside-milled *in situ* biasing TEM lamella of the annealed upright TD specimen is shown in Fig. 106.

8.5.1.2 *In Situ* Biasing Electron Holography Analysis

In situ biasing EH analysis is conducted to investigate the electrostatic potential distribution across the annealed upright-grown p-AlGaAs/n-GaInP TJ, specifically the depletion width, as a function of the applied bias. The aim is to study the behaviour of the TJ under operation, ideally at the break-in current regime. The experiment is performed using the FEI Titan Ultimate operated at 200 kV, using the same experimental setup as described in Ch. 6.5.1. The specimen support chip is mounted in the Protochips Aduro 500 biasing TEM holder, with the electrical connection configuration illustrated in Fig. 106. Under illumination in MJSCs, TJs operate in forward bias, where the photocurrent flows from the n-type emitter into the p-side of the TD. To replicate this operating condition and specifically analyse the TJ break-in, a forward bias is applied to the TEM lamella in the holder. This is achieved by applying a positive bias voltage to the p-side of the TJ, i.e., the pre-deposited ohmic contact, using a Keithley power supply connected to the TEM holder, while the n-side contact is grounded. Electron hologram stacks (30×8s) are acquired at different applied forward voltages, ranging from 0 V to +14.3 V in 0.1 V increments, using the acquisition parameters listed in Table 15. The induced current drawn by the specimen is tracked throughout the experiment. To prevent overheating, the compliance current is limited to 1000 µA in the Aduro software.
The recorded *I-V* curve is presented in Fig. 107. Fig. 108a displays exemplary phase images reconstructed from hologram stacks acquired at selected forward bias voltages. Electron phase profiles, shown in Fig. 108b, are extracted across the TJ by averaging over a width of 200 nm. The measured phase step across the p-AlGaAs/n-GaInP junction, along with the depletion width derived from the phase distribution, is presented in Fig. 108c.
The difference in electrostatic potential between the p-AlGaAs and n-GaInP layers, as well as the adjacent layers, is clearly distinguishable in all phase images due to phase contrast variations. The extracted phase profiles distinctly reveal the position of the TJ. Apart from short-range phase contrast variations caused by electrostatic potential differences in the differently doped III-V heterolayers, the phase profiles exhibit a pronounced overall linear trend (slope) between the metal contacts of the semiconductor device.
While neither the phase step across the TJ, nor the depletion width decreases with increasing

forward bias – as would be expected for a forward-biased p-n junction (see Ch. 6.5) – the overall slope in phase shift between the contacts increases with increasing applied positive voltage. This suggests that the TEM specimen behaves as a capacitor. Such behavior can occur in *in situ*-biased TEM specimens if one or both metal contacts form a high-resistance Schottky contact to the semiconductor, preventing the applied bias from being effectively dropped across the p-n junction.

Under electron beam illumination, charge carriers are generated and separated within the electric field of the semiconductor p-n junction. However, if one or both metal contacts form a high-resistance Schottky barrier, a low-resistance path to ground is absent, leading to charge accumulation. This distorts the measured potential distribution, manifesting as the overall linear trend in the phase images, and may even counteract the built-in electric field of the p-n junction. Such a counteracting field could explain why the p-n junction does not exhibit a clear response to the applied bias in the recorded phase images.

As the forward bias applied to the front contact increases, charge accumulation is enhanced, resulting in an increasing electric field between the contacts. This effect is evident from the growing phase shift difference with increasing forward bias. Since the pre-deposited front contact is unlikely to introduce such a high resistance, it is probable that the IBID-W contact to n-GaAs, which is expected to form a Schottky barrier (see Ch. 6.5.5), induces the capacitive behavior of the specimen and prevents proper grounding, thereby impeding charge dissipation.

At a high forward bias of +14.3 V, the overall linear slope in the phase profiles abruptly disappears, leaving only phase shift variations corresponding to the potential distribution in the epilayer structure. Simultaneously, the current drawn by the specimen sharply increases, reaching the compliance limit of 1000 µA, as shown in the *I-V* characteristics (Fig. 107). Both observations indicate the formation of a short-circuit path, which allows charges to dissipate, thereby eliminating charge accumulation and collapsing the built-up field between the contacts. The high short-circuit currents led to specimen overheating and defect formation, evident in Fig. 109. This resulted in deformation and bending, which introduced dynamic diffraction contrast in the phase images recorded at +14.3 V.

The contacting issues in the present *in situ*-biased TEM specimen prevented the study of the p-AlGaAs/n-GaInP TJ characteristics, specifically the TJ breakdown. Therefore, a more detailed discussion of the recorded electron phase data and *I-V* characteristics is not considered productive and is therefore omitted.

Table 15: Acquisition settings for the *in situ* biasing electron holography analysis of the annealed upright-grown p-AlGaAs/n-GaInP TD specimen. The spatial resolution in the phase image results from the mask size applied in the Fourier reconstruction.

Hologram acquisition parameter	
C2 aperture	150 µm
Diffraction lens excitation	89%
Lorentz magnification	40.0kx
Biprism voltage	220 V
FOV	844×844 nm
Pixels per fringe	7
Fringe spacing	2 nm
Spatial resolution (phase image)	4 nm

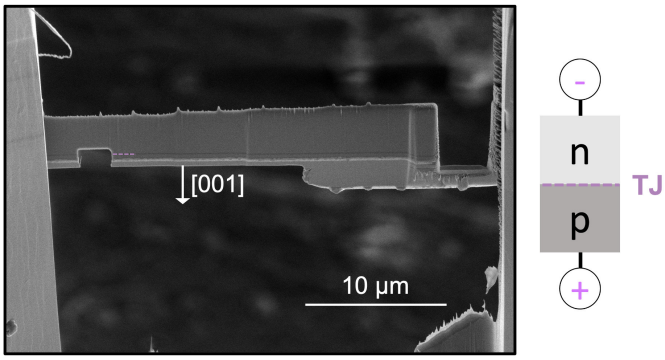

Figure 106: *Secondary electron SEM image of the annealed, upright-grown TD specimen prepared on a MEMS support chip for in situ biasing EH analysis using backside FIB milling to preserve the pre-deposited ohmic top contact. The TJ position is indicated by the purple dashed line, and the electrical connection configuration of the TJ in the biasing TEM holder is illustrated alongside.*

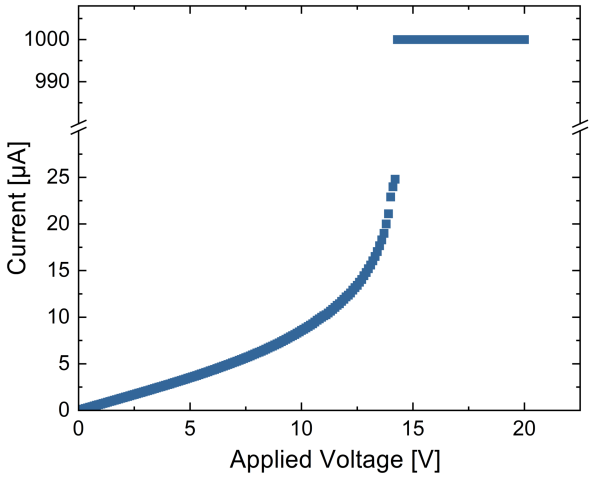

Figure 107: *Current–voltage (I-V) characteristics of the backside-milled in situ biasing TEM specimen from the annealed, upright-grown TD test structure. The bias-induced current is monitored during in situ biasing EH acquisition.*

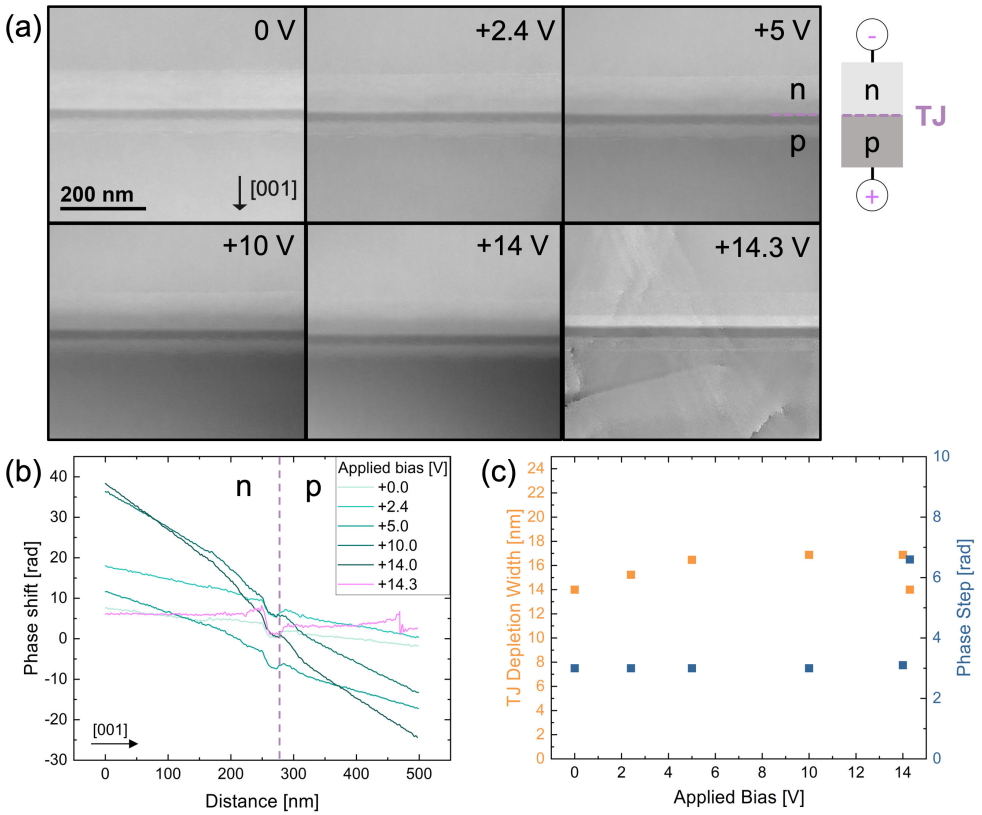

Figure 108: *(a) Electron phase images of the p-AlGaAs/n-GaInP junction in the annealed, upright-grown TD specimen at selected forward (+) bias voltages. The connection configuration is schematically illustrated alongside. (b) Phase profiles extracted across the TJ at different forward voltages. (c) Depletion widths and phase steps across the p-AlGaAs/n-GaInP TJ, are derived from the experimentally measured phase distribution, as a function of the applied forward bias.*

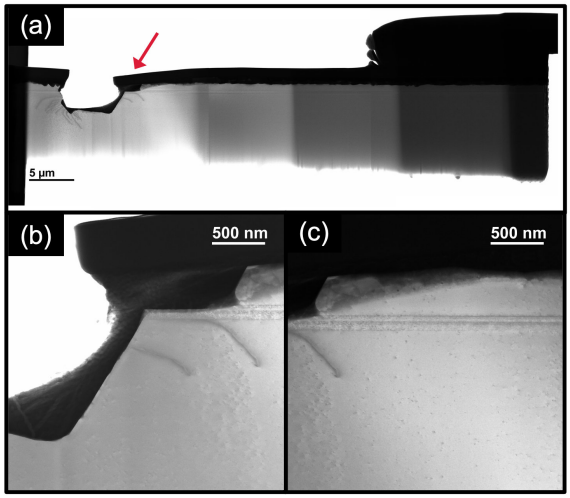

Figure 109: *STEM-BF images of the annealed upright-grown TD in situ-biased TEM specimen after applying an electrical bias of up to 14.3 V during EH analysis. The formation of crystallographic defects, exhibiting dark BF contrast, as well as lamella deformation, is visible. The images are acquired using the FEI Titan Ultimate operated at 200 kV, with a camera length of 58 mm, a convergence angle of 5.19 mrad, and a C2 aperture size of 30 µm.*

8.5.2 Approach 2

Since a single pre-deposited ohmic contact proved insufficient for revealing and studying the p-AlGaAs/n-GaInP TJ characteristics, an alternative preparation method to backside milling is tested, aiming to preserve both the top and bottom metal contacts of the entire III-V epistructure. This approach combines mechanical slicing with plasma-FIB (PFIB) and Ga-ion-FIB milling.

The methodology significantly deviates from the standard Ga-ion FIB-SEM preparation for *in situ* biasing specimens. The procedure is divided into multiple steps, involving numerous transfers between different devices, making the approach prone to errors. Successfully completing individual steps often required several test runs, particularly for the PFIB milling. PFIB devices have only recently become more widely available in research labs, resulting in limited experience with their specific application for preparing III-V semiconductor devices for *in situ* biasing TEM analysis. Therefore, the following approach is preceded by numerous test runs, during which the PFIB milling parameters for the existing III-V wafer specimens are tested and optimised.

8.5.2.1 Full Wafer Slicing Biasing TEM Sample Preparation

In the first step, the annealed upright TD specimen wafer, including its top and bottom metal layers, is mechanically sliced into ~200 µm thick slabs using a wire saw.

In the second step, the specimen slice is affixed to the Si-half chip (Protochips) using the non-conductive MBOND 610 Adhesive (Micro Measurements). The adhesive is applied over the entire contact cross-section of the slice, which interfaces with the biasing chip. This served two primary purposes: (i) to prevent unintended current paths between the sample and the chip, and (ii) to avoid short circuits caused by uncontrolled spreading of the conductive adhesive,

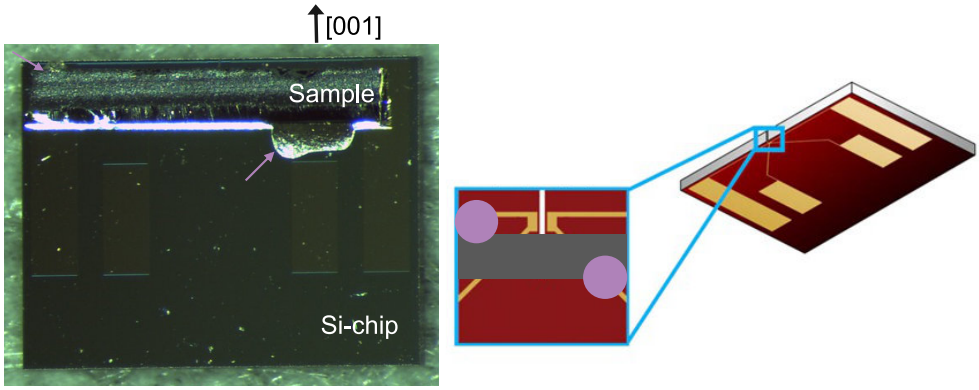

Figure 110: *Optical microscope image of the wire-sawed wafer slice, attached and electrically contacted to the Si-half chip, recorded on a Leica 100 after curing. The connection geometry is illustrated by a schematic sketch of the slice (grey) on the chip, indicating the placement of the conductive epoxy (purple).*

which is subsequently applied in the third step to establish the electrical connection between the specimen slice and the MEMS chip.

To achieve the desired viscosity of the conductive adhesive, a 1:1 mixture of two silver conductive epoxy adhesives (MG Chemicals) is prepared. The components included (i) a silver-containing tetraglycidyl ether/methylene-p-dianiline adduct and (ii) a silver-containing formulation comprising nonylphenol, N-aminoethylpiperazine, diethylenetriamine, and bisphenol A. Drops of this conductive epoxy are used to connect the top and bottom metal contacts of the wafer to the metal tracks of connection inputs 1 and 3 of the Si-half chip, respectively. Both the MBOND adhesive and the conductive epoxy are left to cure for three days, followed by a heat treatment at 60°C for 1 h to ensure complete curing.

The specimen geometry is illustrated in Fig. 110, which presents a light optical microscope image of the wafer slice affixed to the chip after the annealing step.

After slicing, fixation, and electrical contacting of the specimen, the next preparation steps involve ion beam sputtering the sample. Before Ga-ion FIB milling could be employed to create an electron-transparent window, pre-thinning is performed using PFIB milling to reduce the thickness of the slice. This step is carried out using the FEI Helios 5 PFIB CXe. As introduced in Ch. 4.2.1, the Xe^+ ICP system is preferred for applications requiring the removal of large volumes or deep milling, as in this preparation, due to its higher achievable currents, which enable increased throughput. Therefore, it is well suited for the pre-thinning step in this preparation procedure, which involves: (i) milling a deep window to ensure a sufficient range for specimen tilting during subsequent TEM analysis, and (ii) reducing the ~200 nm thick slice to a thickness suitable for final thinning with Ga-ion FIB, allowing milling of an electron-transparent region within a reasonable time frame.

The steps involved in the PFIB preparation are illustrated in Fig. 111. First, a protective Pt-C layer is deposited on top of the pre-deposited metal on the wafer's top surface using IBID at 12 kV and 2.5 nA. The layer dimensions are x = 60 µm, y = 20 µm and z = 3 µm. Next, the chip trench is cut at 30 kV and 0.2 µA under a 50° tilt to allow milling of the wafer slice's

backside. For the preceding thinning steps, the specimen is tilted to 52°. Initial deep cuts on the backside and frontside are milled at 30 kV using 0.2 µA and 0.5 µA, respectively. The beam dwell time is set to 100 µs, with an overlap of 80%. These settings are maintained throughout the subsequent milling steps. Milling on both the frontside and backside is iterated at 30 kV and 0.2 µA to carefully approach the protective metal layer. Once this layer is reached, final cleaning is performed using lower currents: 30 kV and 15 nA for the front-window, achieving a depth of 135 µm, and 30 kV and 60 nA for the back-window, achieving a depth of 161 µm.

After the PFIB pre-milling, Ga-ion FIB milling is employed to cut an electron-transparent window for TEM analysis. The preparation is carried out using the FEI Strata 400A FIB-SEM. Progressive thinning of the lamella to electron-transparent thickness is achieved through iterative milling of the front and backside at $52° \pm 2°$. The Ga-ion beam intensity is gradually reduced from 30 kV at 21 nA, to 30 kV at 2.8 nA, and finally to 16 kV at 0.47 nA. In the final thinning step, regions of different thickness are milled from the frontside using 16 kV at 0.24 nA. Final polishing of both lamella surfaces is conducted using 2 kV at 0.25 nA and $52° \pm 5°$ tilt. The final thicknesses of the different sample regions are estimated by SEM measurements to be 340 nm, 225 nm, 200 nm, and 170 nm.

8.5.2.2 Specimen Assessment

Fig. 112 presents TEM images of electron-transparent specimen regions of varying thickness, recorded using the FEI Titan Ultimate operated at 200 kV. Already in the SEM images (Fig. 111), it is evident that strong beam tail effects lead to difficult-to-control damage of the metallised wafer surface beyond the FIB-deposited protective layer. This issue is mitigated as much as possible through careful, iterative PFIB milling at a significant distance from the ROI protected by the IBID-Pt layer.

In projection, the LM overview images clearly reveal that, despite this highly time-consuming and meticulous approach, beam tail effects resulted in local removal of the pre-deposited ohmic contact layer on both sides of the protective IBID-Pt layer (indicated by the red arrow in Fig. 112). This disruption prevents direct electrical contact with the electron-transparent ROI, thereby hindering reliable EH characterisation of the TJ under *in situ* applied bias in this region.

The higher-resolution Lorentz-TEM images of the various thickness regions further highlight that milling from the metallised wafer top side led to pronounced curtaining effects in the III-V ROI beneath the metal contact.

Although the TEM images already indicate significant issues with the electrical contact of the specimen, the sample is electrically connected to the Keithley power supply via the biasing TEM holder for *I-V* characterisation. As per standard procedure, voltage is applied through the top contact (connector 1) to minimise losses due to substrate resistance, while the bottom contact (connector 3) is connected to electrical ground. The compliance current is limited to 100 µA.

Upon applying an increasing forward voltage, the induced current rose from 0 µA at 0 V, to 50 µA at +0.01 V, and reached the compliance current of 100 µA at +0.02 V. This rapid current breakthrough, along with the low equivalent resistance of 197 Ω, strongly indicates the dominant presence of short current paths within the specimen, preventing accurate measurement of the TJ characteristics in response to the applied bias.

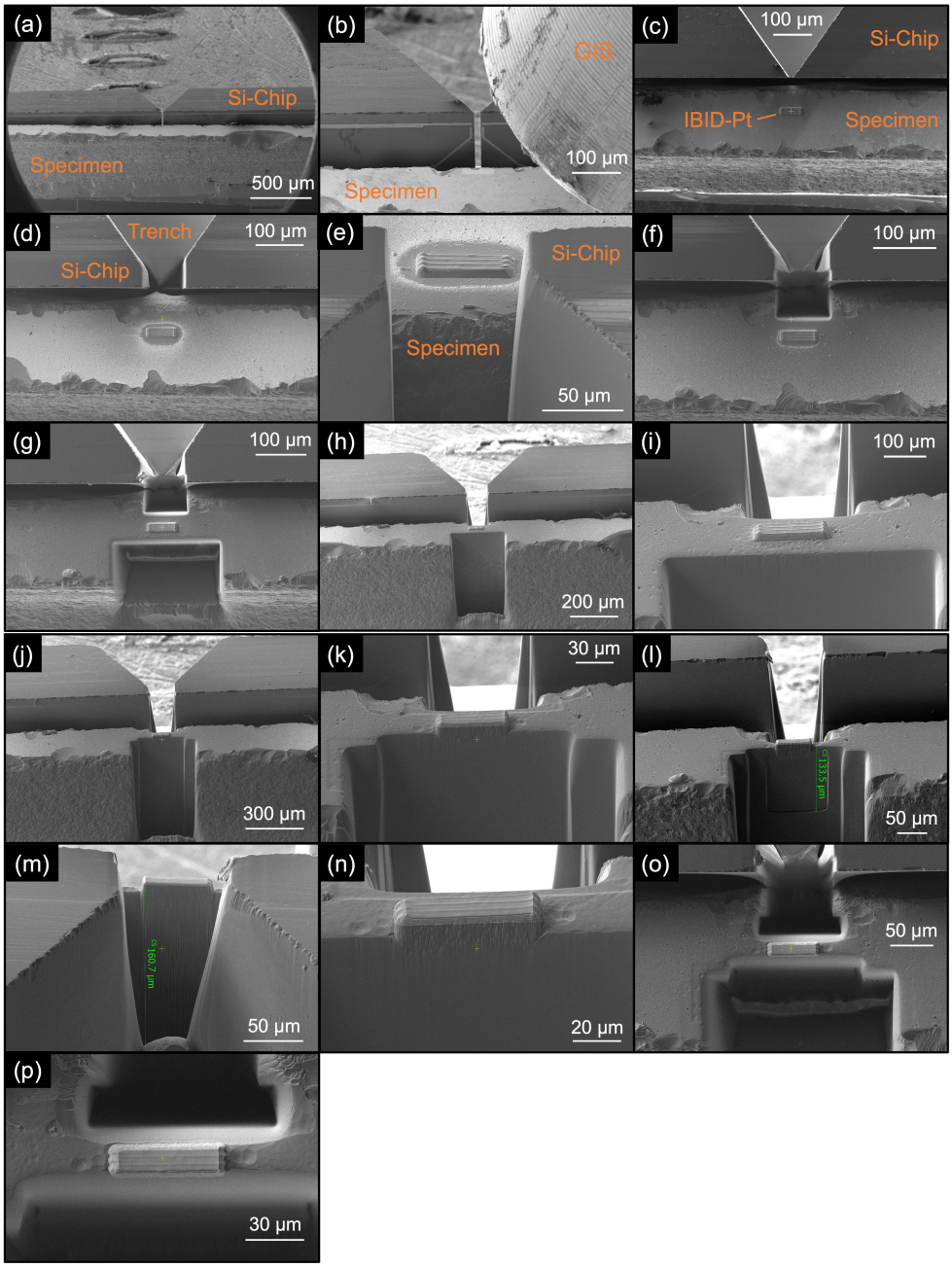

Figure 111: *SE SEM images showing the PFIB pre-milling procedure, acquired at 10 kV and 0.40 nA. (a) Overview image of the wafer slice fixed on the Si-half chip prior to PFIB milling. (b-c) IBID deposition of a protective Pt-C layer using the GIS. (d-e) Widening of the chip trench via PFIB milling at 30 kV and 0.2 µA at 50° tilt. (f) Initial backside cut and (g-h) frontside cut. (i-j) Iterative backside and frontside milling. (k) Final frontside cleaning and (l) backside cleaning. Images (m-p) show the final result of the PFIB pre-milling.*

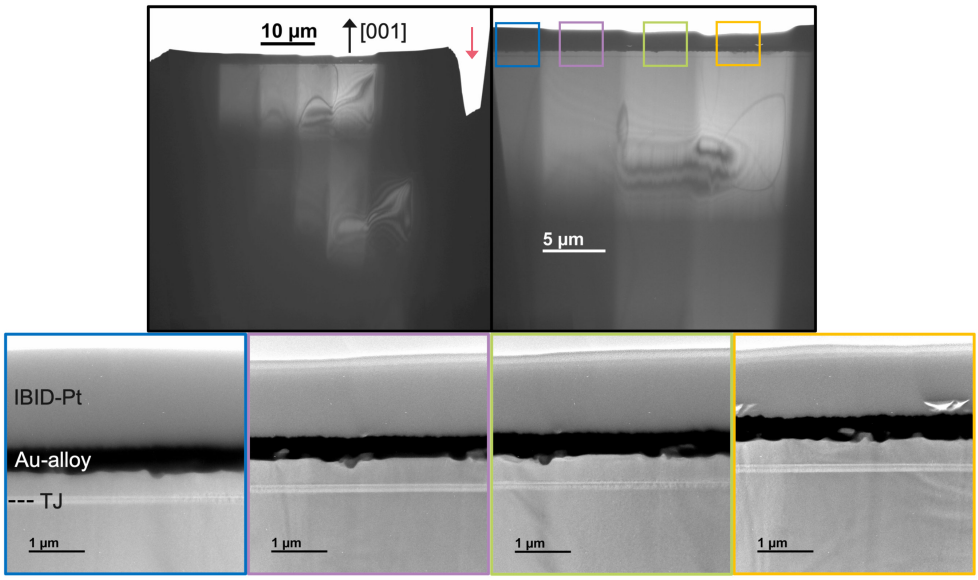

Figure 112: *TEM images of the annealed upright-grown TD specimen, prepared on a MEMS chip for in situ biasing TEM analysis using Approach 2. The low-magnification images provide an overview of the electron-transparent specimen regions of varying thickness, with the corresponding medium-magnification images – indicated by the coloured rectangles – offering higher-resolution details of the contact interface and the TJ ROI.*

Given the numerous preparation steps involved, many of which deviate from standard protocols, it is challenging to pinpoint the exact cause of the short circuit paths. The most likely explanation is the incomplete coverage of the sample slice's rear side with non-conductive epoxy, leading either to unintended contact between the semiconductor sample and the metal tracks of the MEMS chip running along the back, or to the unintended spread of conductive glue. Thus, optimising the electrical isolation of the sample's back side from the underlying chip would be crucial to make this preparation approach applicable.

Beyond the potential short circuit paths, the issue of top-metal contact degradation, caused by the PFIB top-milling, remains to be addressed. Despite careful optimisation of PFIB energy and current densities to balance milling efficiency and precision with minimal surface damage, PFIB proved to be an extremely powerful milling tool for III-V semiconductor specimens. Its high milling throughput comes at the cost of difficult-to-control beam tail effects, which damage the specimen surface. Possible strategies to mitigate this top contact damage include depositing a larger protective metal layer before milling and stopping PFIB milling at greater thicknesses of the cross-sectional window. However, this would significantly prolong the subsequent Ga-ion FIB milling step, as milling through larger thicknesses down to electron-transparent dimensions is highly time-intensive due to the relatively low throughput of Ga-ion FIB. Consequently, this approach is considered to be impractical.

For applications requiring the preparation of III-V semiconductor samples for electrical TEM characterisation, where maximum precision in circuit editing and surface/contact integrity is essential, PFIB is found to be unsuitable. This conclusion holds despite the theoretical advantage

of Xe^+ plasma over Ga-ion FIB, as it avoids Ga-ion implantation into the III-V specimen, which can alter stoichiometry, thus energy band structure, and cause surface amorphisation (see Ch. 4.1.2 for further details). PFIB appears most applicable for preparing samples intended for non-biasing TEM analysis or for harder materials requiring high-throughput milling tools for time-efficient preparation – tasks that are not feasible with Ga-ion FIBs.
While alternative preparation methods for maintaining both pre-deposited metal contacts should be explored, the backside milling approach is hence considered as the more reliable method, despite the IBID back-contact issues discussed. This approach is therefore chosen for the preparation of the working III-V tandem solar cell sample presented in the following section. Aside from reducing the risk of top-surface contact damage and curtaining effects, the smaller sample dimensions also minimise the likelihood of preparation-induced electrical shorts. Additionally, the reduced substrate resistance lowers parasitic losses and allows for a more direct and reliable biasing of the junction of interest.

8.6 Investigation of a n-GaInP/ p-AlGaAs Tunnelling Junction in a Working GaInP/GaAs Tandem Solar Cell

While the previous section discussed the challenges and complexities of *in situ* biasing EH characterisation and the associated sample preparation of p-AlGaAs/n-GaInP tunnel junctions in test structures, this chapter extends the methodological discussion by applying the *in situ* biasing methodology to a fully operational III-V tandem solar cell device.
First, the device structure is introduced, followed by bulk electrical analysis to characterise the working device and illustrate the specific potential of electrical TEM characterisation. Subsequently, the *in situ* biasing TEM sample preparation of the working tandem cell is described. Finally, the results of the *in situ* biasing EH and STEM-EBIC analyses are used to discuss the prevailing challenges and limitations of *in situ* biasing sample preparation, specifically for working III-V heterostructure devices.

8.6.1 The Tandem Solar Cell Structure and Bulk Electrical Characteristics

The device under investigation is a GaInP/GaAs tandem solar cell. The epitaxial layer structure is schematically illustrated in Fig. 113a. A p-AlGaAs/n-GaInP tunnel junction is incorporated between the GaAs bottom subcell and the GaInP top cell to facilitate current conduction between the tandem p-n junctions.
The III-V heterostructure is grown on a 6-inch p-GaAs wafer substrate by MOVPE using an AIXTRON AIX2800 G4 reactor at Fraunhofer ISE, Freiburg. The solar cell is fully processed as a functional device, including the deposition of front and back metal contacts and the application of an anti-reflective coating to the non-metallised regions of the front wafer surface. The front metal contact layer consists of a Pd/Zn/Pd/Au alloy with an approximate thickness of 270 nm. Fig. 113b-c presents photographs of the fully processed tandem solar cell wafer, where the individual series-connected cells are visible.
The light *I-V* characteristics of the bulk solar cell are analysed using uncalibrated laboratory measurements with a Halogen Lamp at Fraunhofer ISE. Unlike dark *I-V* measurements, where current is injected externally into the cell, a solar cell under illumination generates current "on its own" through light absorption. Consequently, light illumination is equivalent to applying

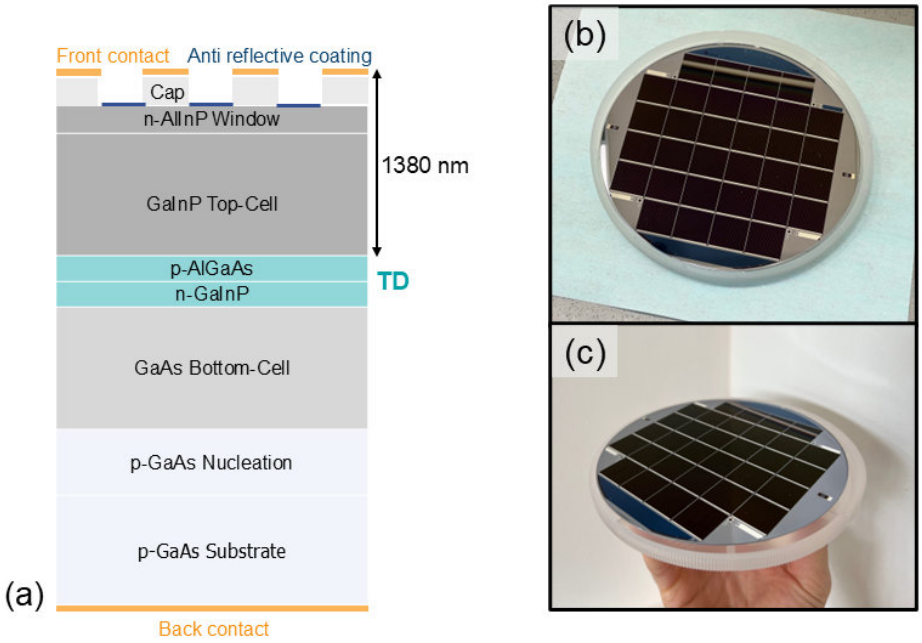

Figure 113: *(a) Schematic of the GaInP/GaAs tandem solar cell featuring an upright-grown p-AlGaAs/n-GaInP tunnel diode (TD), positioned 1380 nm beneath the front metal contact on the top wafer surface. (b, c) Photographs of the fully processed 6-inch tandem solar cell wafer, with a hand included for scale reference.*

a forward external bias, leading to a narrowing of the depletion region as majority carriers are drawn towards the SCR of the p-n junctions. This reduces the built-in potential across the junction by an amount equal to the open-circuit voltage (V_{oc}), which results from the Fermi-level splitting induced by illumination. In contrast, under dark conditions, no Fermi-level splitting occurs. A more detailed explanation of these underlying physical principles can be found in standard textbooks.[47,272,273]

Fig. 114 presents a 2D map of the derived conversion efficiencies of the various series-connected cells on the wafer. The highest efficiency is measured at wafer position x3y4, reaching 28.53%. The corresponding light *I-V* curve, measured in forward direction for cell p-n junctions, is shown in Fig. 114b. The curve results from the superposition of the *I-V* characteristics of the two subcells, which can be additionally influenced by the tunnelling characteristics of the TD. The expected cut-in voltage for the GaInP top cell ($E_G = 1.9$ eV) is approximately 1.5 V, while for the GaAs bottom cell ($E_G = 1.42$ eV), it is around 1 V. Thus, the expected cut-in voltage for the overall tandem cell is about 2.5 V. The measured *I-V* curve exhibits a V_{oc} of approximately 2.55 V, confirming these expectations. Fig. 115 presents the external quantum efficiency (EQE) of the GaInP and GaAs subcells as a function of incident light wavelength for the x3y4 cell. For comparison, the EQE of a GaInP/GaAs/Si triple-junction solar cell with a conversion efficiency of 33% is also shown. The photocurrent output of each subcell is indicated to assess current matching within the tandem cell, a crucial factor in MJSC engineering when selecting bandgap combinations (see Ch.2.1). In the x3y4 cell, the GaInP top cell ($E_G(Ga_{0.51}In_{0.49}P) =$

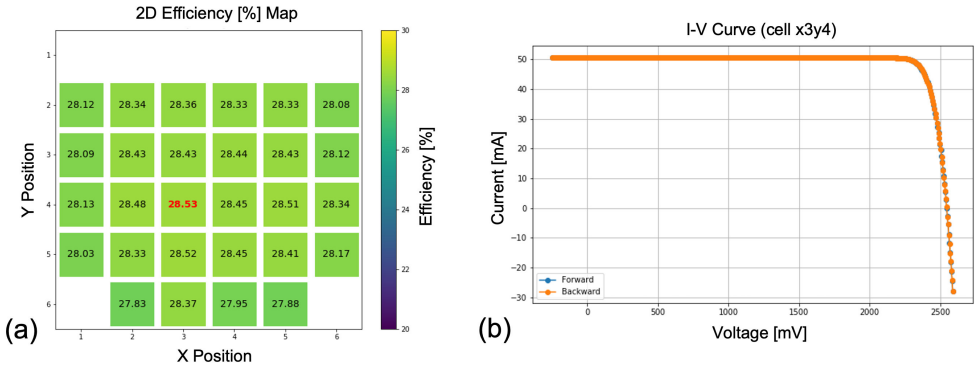

Figure 114: *(a) 2D map of the derived conversion efficiencies of the various series-connected tandem solar cells at different x- and y-positions on the tandem solar cell wafer. The cell with the highest efficiency (x3y4) is highlighted in red. (b) Example of the underlying light I-V measurement curve of the tandem solar cell, shown for the x3y4 cell.*

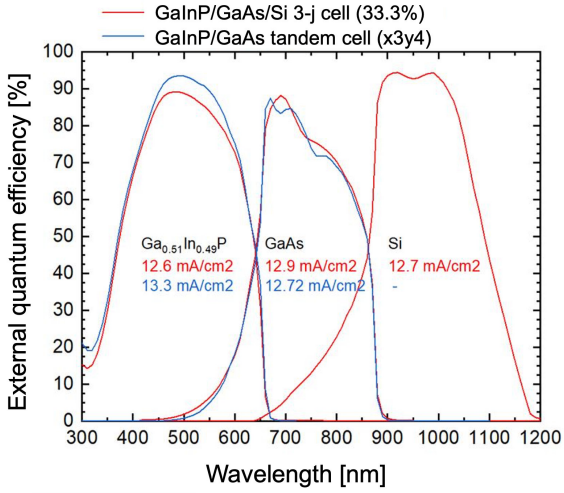

Figure 115: *Measured external quantum efficiency (EQE) of the x3y4 GaInP/GaAs tandem solar cell (blue curve) compared to that of a GaInP/GaAs/Si triple-junction (3-j) cell with 33.3% conversion efficiency (red curve). The photocurrent densities generated in each subcell, as determined by their spectral coverage corresponding to their bandgap energies, are shown in the respective colors.*

1.9 eV) generates a photocurrent density of 13.3 mA/cm^2, while the GaAs bottom cell produces 12.72 mA/cm^2. Compared to the subcells of the presented 3-J cell, the series-connected tandem subcells are not perfectly current-matched but they are reasonably close. Therefore, the limitation of the total current output by the subcell generating the lowest current (the GaAs subcell in this tandem cell) and the associated losses remain within an acceptable range.

As mentioned in the chapter introduction (Sect. 8.1), bulk solar cell electrical characterisation does not directly resolve TJ characteristics. Consequently, the presented light *I-V* curves do not provide information on the tunnel current break-in behavior. This is because the measurements probe the wrong quadrant. The light *I-V* curves are recorded in the forward-bias direction of the solar cell p-n junctions (n-on-p), which corresponds to the reverse direction of the upright-grown p-AlGaAs/n-GaInP (p-on-n) TJ. However, TJ breakdown can only be observed when measuring in the forward direction of the TJ, which corresponds to the negative voltage range of the light *I-V* curve. Measuring the reverse voltage range of the cell under dark conditions is not feasible, as the cells exhibit excessive reverse blocking, leading to potential breakdown at higher applied reverse biases. Under illumination, however, the cells become conductive in both directions. Thus, to measure the TJ breakdown, the cells would need to be tested in reverse under illumination. This would only be possible on a separately processed, non-series-connected individual cell, but on the available sample wafer, all cells are series-connected.
In series-connected cells, the current density is not high enough to induce TD breakdown, as the series resistance limits the maximum current density achievable through illumination with a maximum equivalent illumination intensity of about 60 suns. Consequently, TJ breakdown cannot be measured on this wafer. Nevertheless, since the incorporated upright-grown p-AlGaAs/n-GaInP TJ is grown identically to previously analysed test structures, it can be assumed that its break-in behavior is equivalent to those structures, as observed in the *J-V* curves presented in Fig. 105. This reinforces the previously discussed limitation that bulk solar cell characterisation is not conclusive for analysing the quality of tunnel junctions in MJSCs (see elaborations in Sect. 8.1). Alternative methods are required to specifically measure the TJ characteristics and assess their tunnelling performance.

Therefore, the aim of this study, analogous to the investigations on the TJ test structures, is to perform EH measurements on the tandem solar cell under *in situ* applied bias. This approach promises the derivation of the TJ depletion width in response to the applied bias, serving as a key quality indicator for TJs and providing insights into the relatively early tunnel current breakdown observed in upright-grown p-AlGaAs/n-GaInP TDs compared to their inverted-grown equivalent.

To prepare a TEM specimen for *in situ* biasing EH analysis, the 6-inch wafer is cleaved, separating a peripheral region of the wafer, as shown in Fig. 116a, which contains small processed structures with larger-area metal contacts. These structures are electrically isolated from the series-connected cells. For FIB preparation, a small dumbbell-shaped structure with a uniformly applied metal contact is selected, as this larger-area metallisation allowed for easier sample preparation relative to cutting along the narrow metal fingers of the regular cells.
Prior to FIB preparation, dark *J-V* curves are measured on this isolated structure, as its full-area metallisation precludes light *I-V* measurements. The results are shown in Fig. 116c. Compared to the previously presented light *I-V* curve of the x3y4 cell, the onset of the current density

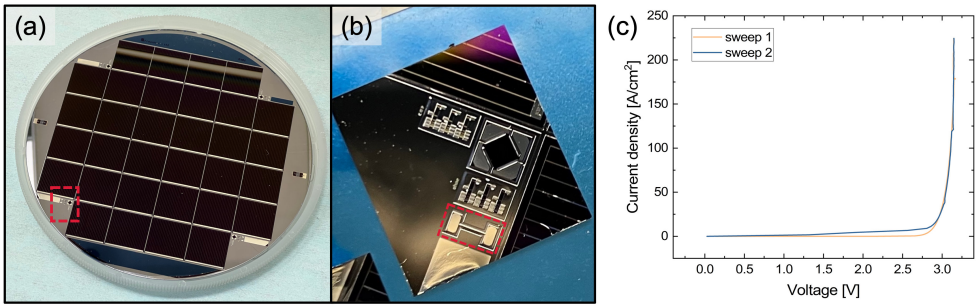

Figure 116: *(a) The peripheral region of the wafer containing isolated, i.e. not series-connected, tandem cells with uniformly applied front contact is cleaved for TEM specimen preparation, as shown in (b). The dumbbell-shaped metallised tandem cell, indicated in red in (b), is selected for in situ biasing TEM specimen preparation. The dark J-V measurement of this isolated tandem cell is shown in (c).*

increase in the dark *J-V* curve occurs at 3 V. This is expected, as the cell can generate a maximum V_{oc} of 2.55 V due to the Fermi-level splitting induced by light illumination. However, under dark conditions, the bias at the junction is externally controlled and not limited by the internal V_{oc}.

8.6.2 Specimen Preparation For *In Situ* Biasing TEM Analysis

For the chip preparation of the *in situ* biasing TEM specimen of the tandem solar cell device, backside Ga-ion FIB milling was performed according to the procedure described in Sect. 8.5.1.1 using the FEI Strata 400S FIB-SEM. The rationale for selecting this preparation approach is discussed in Sect. 8.5. While this approach preserves the front metal contact of the tandem solar cell, the device's rear contact is replaced with IBID-W. Ideally, IBID-Pt would be preferred, as the substrate of this specimen is p-GaAs, which, in theory, would allow for a relatively low contact resistance, at least within the possibilities of FIB-induced metal depositions (see Ch. 6.5.5 for more details). However, only the W precursor was available in the accessible FEI Strata 400S FIB-SEM system.

Attention is taken to ensure that the cleaning of the undercut edge prior to metal layer deposition and the isolation cuts for circuit editing are carried out with the utmost precision and care.

Fig. 117 presents an overview TEM image of the backside-milled *in situ* biasing TEM lamella of the tandem solar cell device, alongside with medium-resolution STEM images providing detailed views of the two isolation cuts. The epitaxial solar cell heterolayer structure is evident from the STEM HAADF and BF images presented in Fig. 118. All images are recorded using the FEI Titan Ultimate at 200 kV. The STEM images are recorded using a 145 mm camera length, a 3.28 mrad beam convergence angle, and a 30 µm C2 aperture.

The crystalline specimen thickness was mapped across different regions of the *in situ* biasing lamella using STEM-CBED. The results presented in Fig. 119 show that the specimen thickness is highly uniform across the entire electron-transparent lamella region, ranging between 400 ± 12 and 440 ± 13 nm in the horizontal direction parallel to the epilayer interfaces. In the region of the specimen used for EH and STEM-EBIC analyses, the measured thickness remains nearly

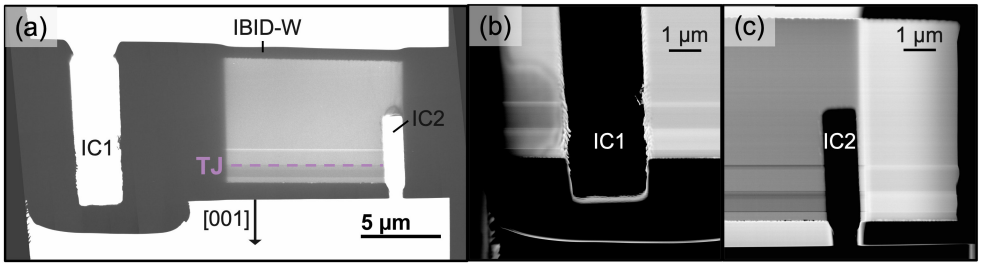

Figure 117: *(a) Overview TEM image of the in situ biasing tandem solar cell TEM specimen. (b) STEM HAADF images providing detailed views of the two isolation cuts (IC1 and IC2) in the lamella.*

uniform, as the variations in the recorded thickness values – 390 ± 7 nm and 400 ± 12 nm – fall within the measurement error. Consequently, the sample is well-suited for EH, exhibiting nearly parallel sidewalls and minimising strong thickness gradients and the associated potential variations. The measurements are performed after the electrical (S)TEM investigations to prevent any STEM beam-induced damage to the semiconductor material, which could otherwise distort the results.

8.6.3 *In Situ* Biasing Electrostatic Potential Analysis Using Off-Axis Electron Holography

For the *in situ* biasing EH analysis, the specimen support chip is mounted in the Protochips Aduro 500 biasing TEM holder and electrically connected to a Keithley power supply. The connection setup is illustrated in Fig. 120. The p-contact of the tandem solar cell is connected to the bias supply, while the n-contact is grounded.

The EH experiment is conducted using the FEI Titan Ultimate at 200 kV. The specimen is tilted away from the zone axis to minimise diffraction contrast, as described in Ch. 5.2.6.4. Electron hologram stacks (30 frames, 8 s per frame) are first acquired at 0 V (short-circuit, I_{sc}, conditions) and subsequently at different applied forward and reverse voltages, ranging from -2 V to +2 V in 0.2 V increments, using the LM acquisition parameters listed in Table 16.

As detailed in Ch. 5.2.4 and 6.4, the *in situ* biasing TEM specimens require large hologram FOV to include a vacuum reference region and maintain sufficient distance from the isolation cut edge. This precaution minimises the impact of surface damage effects, which can be particularly pronounced at the isolation cut edge due to the difficulty of controlling damage in the milling geometry of the chip preparation compared to conventional Cu-grid lamella preparation.

Studies on p-n homojunction specimens (Ch. 5.2.4) have confirmed that reliable depletion width measurements can be achieved using LM EH, despite the lower spatial resolution imposed by the increased fringe spacing in LM EH compared to standard EH. This remains valid as long as the spatial resolution of the measured phase shift is smaller than the expected depletion width and the phase sensitivity is sufficiently high to resolve the expected phase shift across the junction. 1D simulations of the dopant potential distribution in the tandem solar cell specimen predict a depletion width of 15 nm. However, these simulations serve as an approximate reference due to their simplified assumptions (Ch. 6.3), as they do not account for factors such as incomplete

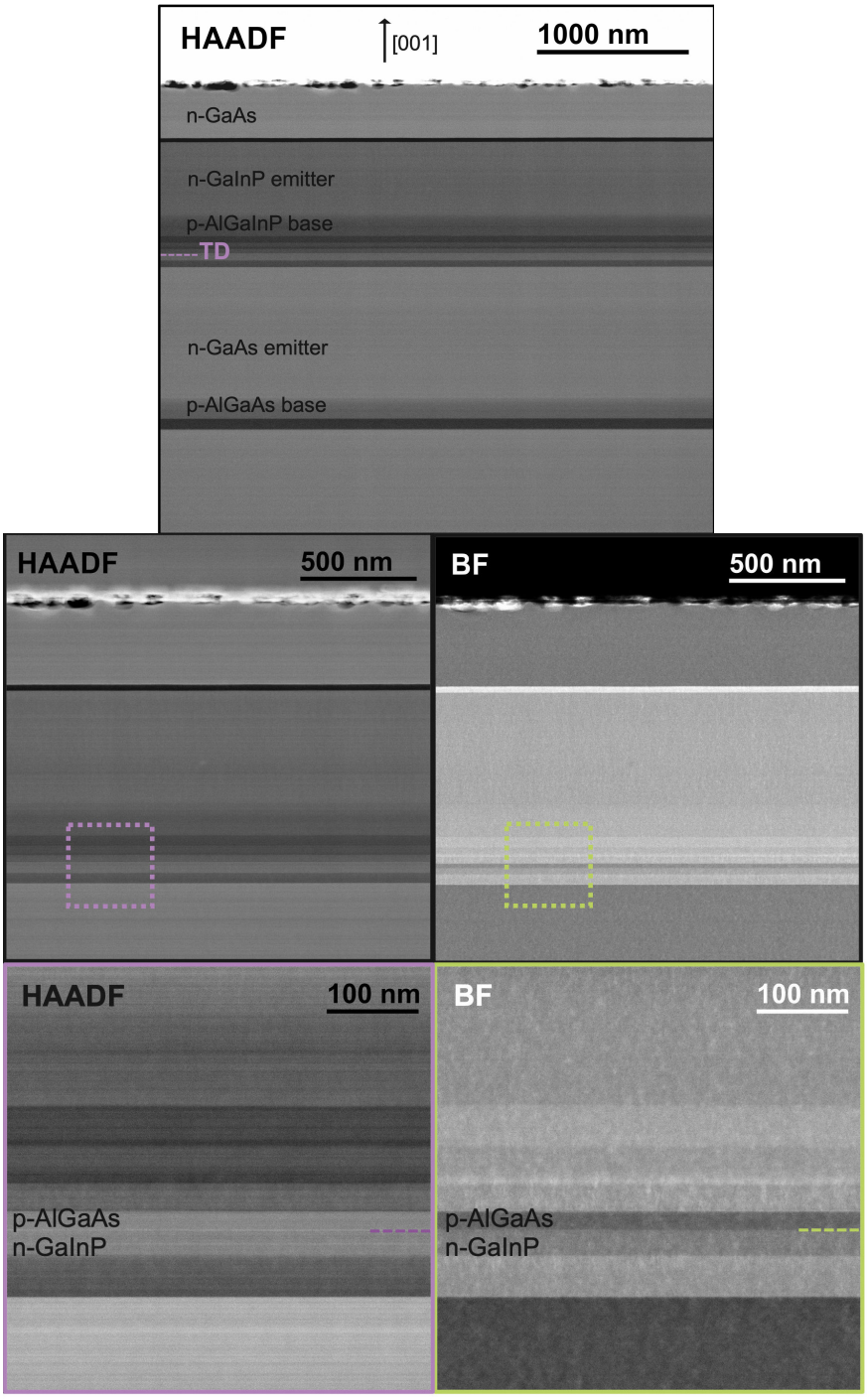

Figure 118: *STEM HAADF and BF images of the in situ biasing tandem solar cell TEM specimen, acquired at different magnifications, resolving the epitaxial layer structure.*

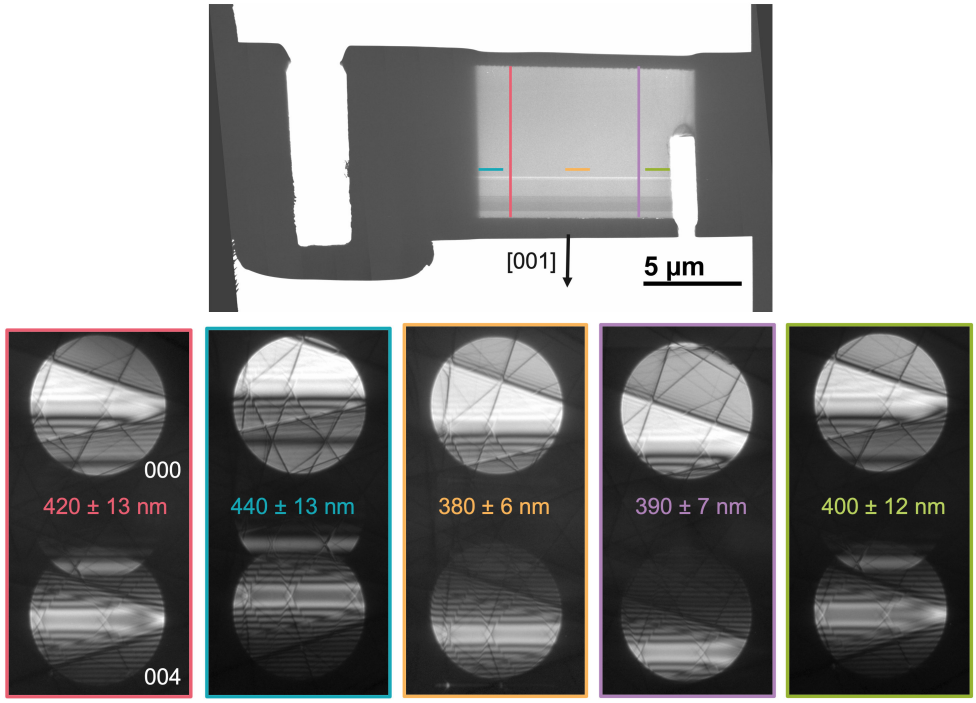

Figure 119: *Results of the STEM-CBED mapping of the crystalline specimen thicknesses. Exemplary CBED patterns, along with the corresponding measured thickness values, are shown for regions of uniform thickness, as indicated by the coloured markings in the TEM overview image.*

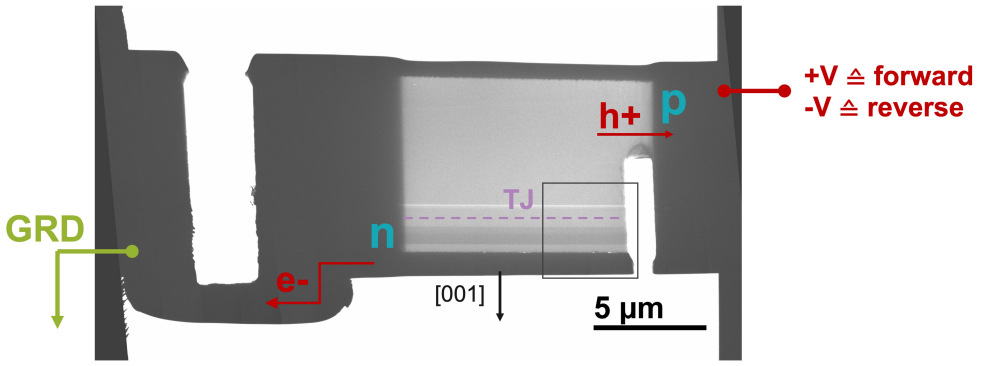

Figure 120: *Illustration of the electrical connections for the GaInP/GaAs tandem solar cell specimen for in situ biasing EH. The positions of the electrical bias (±V) and ground (GRD) connectors are indicated, with the forward and reverse biasing notation referring to the tandem cell p-n junctions. The p- and n-type sides of the device are labeled, and the ROI for in situ biasing hologram acquisitions is highlighted by the gray rectangle.*

dopant ionisation or Fermi level pinning at surface states in FIB-prepared cross-sections. Nevertheless, by comparing the measured depletion width with the expected value, it is evident that the fringe spacing of 4.4 nm in the applied LM-EH settings, providing a spatial resolution of 8.8 nm in the reconstructed phase image, is sufficient to resolve the depletion width. By acquiring stacks of 30 holograms with 8 s per image, the standard deviation of the phase measurement is reduced to below 0.02 rad, despite the fringe sampling being only 4 pixels. This ensured high phase sensitivity, which is more than sufficient given the expected strong phase contrast of the highly doped TJ.

Table 16: Acquisition settings for the *in situ* biasing analysis of the tandem solar cell specimen. The spatial resolution in the phase image results from the mask size applied in the Fourier reconstruction.

Hologram acquisition parameter	
C2 aperture	100 µm
Diffraction lens excitation	15%
Lorentz magnification	40.0kx
Biprism voltage	100 V
FOV	4.1×4.1 µm
Hologram width	3.55 µm
Pixels per fringe	4
Fringe spacing	4.4 nm
Spatial resolution (phase image)	8.8 nm

Figure 121 presents the electron phase image reconstructed from the hologram stack acquired at 0 V, alongside the extracted phase profile across the III-V heterolayer stack, measured at a 2 µm distance from the isolation cut edge and averaged over a width of 200 nm. Both the phase image and extracted profile clearly indicate the TJ due to the strong phase contrast between the highly doped p-AlGaAs and n-GaInP TD layers. The measured relative phase shift across the TJ at 0 V is 4.25 rad.

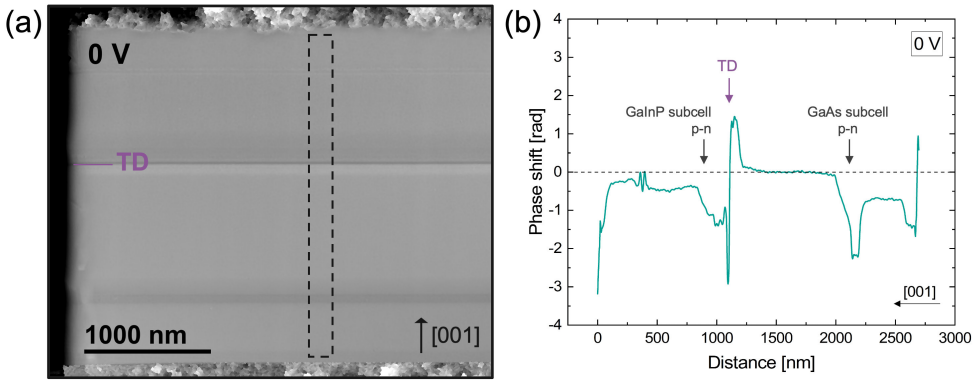

Figure 121: *(a) Reconstructed electron phase image from a hologram stack recorded without applied bias on the GaInP/GaAs tandem solar cell specimen, featuring two tandem p-n junctions connected by the p-AlGaAs/n-GaInP tunnel junction (TJ). (b) Phase profile measured across the III-V device heterostructure in the indicated region of (a) at* $t_c = 390 \pm 7$ *nm.*

The p-n junctions of the tandem subcells (GaAs bottom cell and GaInP top cell) are also well resolved, confirming the sufficient sensitivity of the phase measurement. The depletion width derived from the phase measurement at 0 V is 13 nm, only slightly smaller than the simulated reference value of 15 nm. Although this comparison cannot be considered absolute due to the simplified simulation assumptions (more reliable comparisons involve relative measurements between different specimens, as in Sect. 8.4), the results demonstrate that through careful optimisation of the EH measurement methodology for highly doped III-V semiconductor junctions, precise W_d measurements of the TJ can be achieved even when embedded within a full III-V heterostructure with varying MIP contributions.

Key methodological improvements include:

- Optimised EH measurement geometry and acquisition settings.
- Careful Ga-ion FIB milling to minimise electrically damaged surface layers, ensuring the measured potential distribution is predominantly governed by active dopants.
- Selection of an appropriate specimen thickness based on prior measurements of the inactive layer thickness in GaAs and InP homojunctions (Ch. 6.4), balancing the largest possible proportion of electrically active thickness while avoiding diffraction contrast effects.

Building on these developments, to enable device-related interpretation of TJ width measurements from a single specimen, without requiring comparative measurements across multiple samples, a major challenge remains: the complex impact of surface-related effects (Fermi level pinning), which varies across the III-V heterostructure. Addressing this challenge requires:

- Further reduction of preparation-induced surface damage, either by developing alternative methods to Ga-ion FIB milling or further refining milling geometries. At this stage, despite its outlined drawbacks, FIB milling represented the best compromise between the introduction of damage/artefacts and precision/circuit editing.

- Development of realistic 3D simulations of the electrostatic potential distribution and energy band structure, incorporating surface Fermi level pinning and damage-induced effects. Current limitations include the lack of precise MIP values for most ternary and quaternary III-V compounds present in the device, as well as insufficient data on Ga-ion beam-induced damage effects across different doping levels in these compounds. Additionally, strain effects and cross-sectional approximation deviations from bulk equilibrium must be systematically investigated. These cross-sectional effects can vary depending on the bulk strain state, the specific III-V compound layer, and the heterointerface.

These factors are non-trivial to quantify and require extensive systematic measurements on standard specimen systems before reliable EH analysis of complex III-V heterostructure devices such as MJSCs can be performed.
Nevertheless, the EH analysis of the tandem solar cell specimen under *in situ* applied bias was conducted to gain methodological insights into *in situ* biasing EH measurements and specimen preparation. A further aim is to determine whether relative changes in the TJ depletion width occur under bias, while avoiding direct device-related interpretations due to the aforementioned limitations.
To assess the electrical response of the specimen, the *I-V* characteristics of the TEM specimen are first measured in the dark (before electron beam exposure) and subsequently monitored throughout the biasing EH experiment under electron beam illumination. The resulting *I-V* curves (Fig. 122) differ significantly from those of the bulk device (Fig. 114, 116) due to modifications in the electrical circuit within the cross-sectional lamella (compare Ch. 4.4 and Ch. 6.5.4).
FIB-induced surface damage lowers the parallel surface resistance, increasing leakage currents and reducing overall device resistance, thereby increasing the total current. While efforts are made to minimise this damage, it remains unavoidable in the current Ga-ion FIB-based *in situ* biasing chip preparation approach. In particular, controlling damage at the isolation cut edges remains challenging. However, the reduced parallel surface resistance does not affect the amount of potential dropped across the specimen p-n junction during biasing. Nevertheless, it still influences the measured *I-V* characteristics of the tandem cell TEM specimen (Fig. 122), as indicated by the slight bending of the curves.
The voltage loss in the *in situ* biasing TEM p-n specimen is primarily due to increased series resistance, with the main contributor being the contact resistance at the metal interface connecting the semiconductor specimen to the metal tracks of the biasing chip. While the backside milling preparation of the present tandem cell specimen preserved at least one pre-deposited ohmic contact, the FIB-deposited back contact still forms a Schottky barrier. This potential barrier at the interface between the IBID-W contact and the p-GaAs substrate significantly affects the overall *I-V* behavior and specifically limits the voltage drop across the device's p-n junctions. These modifications to the circuit within the TEM lamella, compared to the bulk device, result in a phase distribution measured across the tandem cell device that does not exhibit the expected response. Selected reconstructed phase images at different applied forward and reverse biases are presented in Fig. 123, alongside the extracted phase shift profiles across the device stack. The positions and dimensions of these profiles match those extracted from the 0 V phase image. In an ideal sample with two low-resistivity ohmic contacts, applying a reverse bias to the cell would be expected to increase the phase step across both subcell p-n junctions, as carrier tun-

nelling through the interconnecting p-AlGaAs/n-GaInP junction facilitates carrier transport. An ohmic back contact would provide a reliable low-resistivity connection to ground, preventing specimen charging, distortion, or counteraction of the specimen's electric field, as observed in the *in situ* biasing phase measurements of the TD test structures in Sect. 8.5.1.2.
Such distortions in the potential distribution due to specimen charging and the build-up of counteracting fields are also evident in the measured phase profiles of the tandem device under bias. While the phase step across the p-n junction of the GaAs bottom subcell does not clearly respond to the applied bias in either direction, the p-n junction of the GaInP top subcell exhibits a slight response. However, contrary to expectations, the phase step decreases under reverse biasing and increases under forward biasing.

The variation in the phase step across the TJ with applied bias is difficult to assess directly in the LM phase data and is therefore separately illustrated in Fig. 124. The notation of the applied bias in this figure corresponds to the TJ, where -V indicates reverse biasing of the TJ (forward biasing of the tandem cell), and +V denotes forward biasing of the TJ (reverse biasing of the tandem cell).

A slight overall evolution of approximately 0.5 rad in the applied bias range is observed in the step potential across the p-AlGaAs/n-GaInP TJ. While this trend generally follows the expected pattern of an increasing phase step under reverse bias and a decreasing phase step under forward bias, the measured trend is highly inconsistent and far from linear, as demonstrated by Anada *et al.* in their *in situ* biasing EH analysis of GaAs p-n tunnel junctions.[40]

Absolute measurements of the built-in potential at p-n junctions using *in situ* biasing EH are challenging due to voltage losses caused by circuit-related issues in the TEM lamella, as previously shown for the GaAs p-n homojunction in Ch. 6.5.2. While the simple GaAs p-n sample showed at least the expected trend in the step potential change at the junction with bias, in the tandem device with its complex energy band structure, the circuit modifications in the TEM lamella compared to the bulk device have an equally complex effect on the electrical characteristics of the device. As a result, potential distributions across the heterostructure and their changes with applied bias are difficult to interpret, even qualitatively.

Absolute quantification of built-in potentials at the tandem cell p-n junctions and the TJ, as well as their changes with applied bias, are omitted in this study of p-AlGaAs/n-GaInP. However, EH analysis of TD p-n junctions without applied bias, presented in Sect. 8.4, demonstrated that accurate and reproducible depletion width measurements of highly doped p-AlGaAs/n-GaInP junctions can be routinely performed, both in isolated TD test structures and in TDs incorporated into III-V multilayer heterostructures (TAN and INVTAN).
Nevertheless, electrical analysis of the TJ in operational MJSC devices under *in situ* applied bias remains a significant challenge.

Non-biasing EH analysis offers the advantage of measuring the electrostatic potential independently of the experimental circuit setup. The detected electron phase shift is unaffected by the electrical connections within the *in situ* holder. While this also applies to phase measurements in *in situ* biasing EH experiments, the p-n junction's response still depends on the actual voltage reaching the junction, which is influenced by circuit losses. The *in situ* biasing EH technique remains advantageous in that the signal detection itself does not occur within the external circuit,

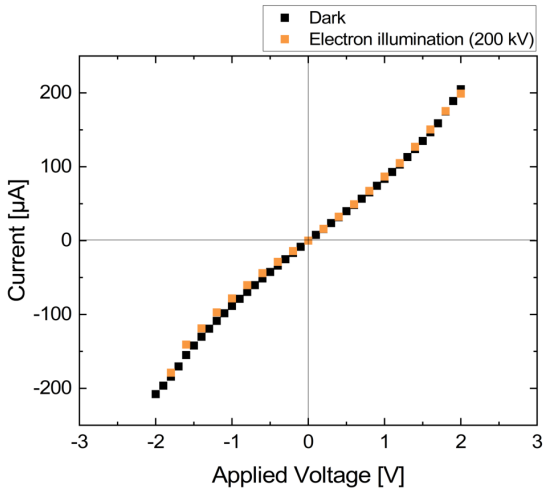

Figure 122: *Current-voltage (I-V) characteristics of the GaInP/GaAs tandem solar cell TEM specimen, measured in the dark (before electron beam exposure) and under electron beam illumination during the biasing EH experiment. Negative and positive bias voltages correspond to reverse and forward biasing of the tandem cells, respectively, and to forward and reverse biasing of the interconnecting TJ.*

unlike STEM-EBIC, where the induced current signal is detected through an amplifier connected to the circuit. However, when studying the bias-induced response of the electric field at p-n junctions, the *in situ* biasing EH method still fundamentally relies – albeit indirectly compared to STEM-EBIC – on an intact electrical circuit in the TEM specimen.

Thus, *in situ* biasing EH experiments are equally affected by circuit-related voltage losses when measuring both the response of the p-n junction depletion width to applied bias and the bias-induced changes in absolute built-in potential.

The qualitative electric field distribution across the p-AlGaAs/n-GaInP TJ, derived from the measured phase distribution of the tandem cell under *in situ* applied bias, is presented in Fig. 125, along with the corresponding depletion width measurements for different applied forward and reverse biases in the range of -2 V to +2 V. The results show no clear bias-induced change in the depletion width of the p-AlGaAs/n-GaInP TJ. Regardless of the applied bias, a depletion width of 13 nm ±1 nm, which is consistent with the unbiased specimen.

This result confirms that *in situ* biasing depletion width measurements are also impaired by the contacting issue in the tandem solar cell TEM specimen, due to the high-resistivity contact interface between the p-GaAs substrate and the IBID-W back contact:

1. The applied voltage does not sufficiently drop across the p-n junction to induce the expected depletion width response, namely an increase under reverse bias.

2. Charge carriers are not efficiently extracted from the semiconductor specimen, leading to the build-up of counteracting fields that affect the electric field and, consequently, the measured depletion width at the specimen p-n junctions.

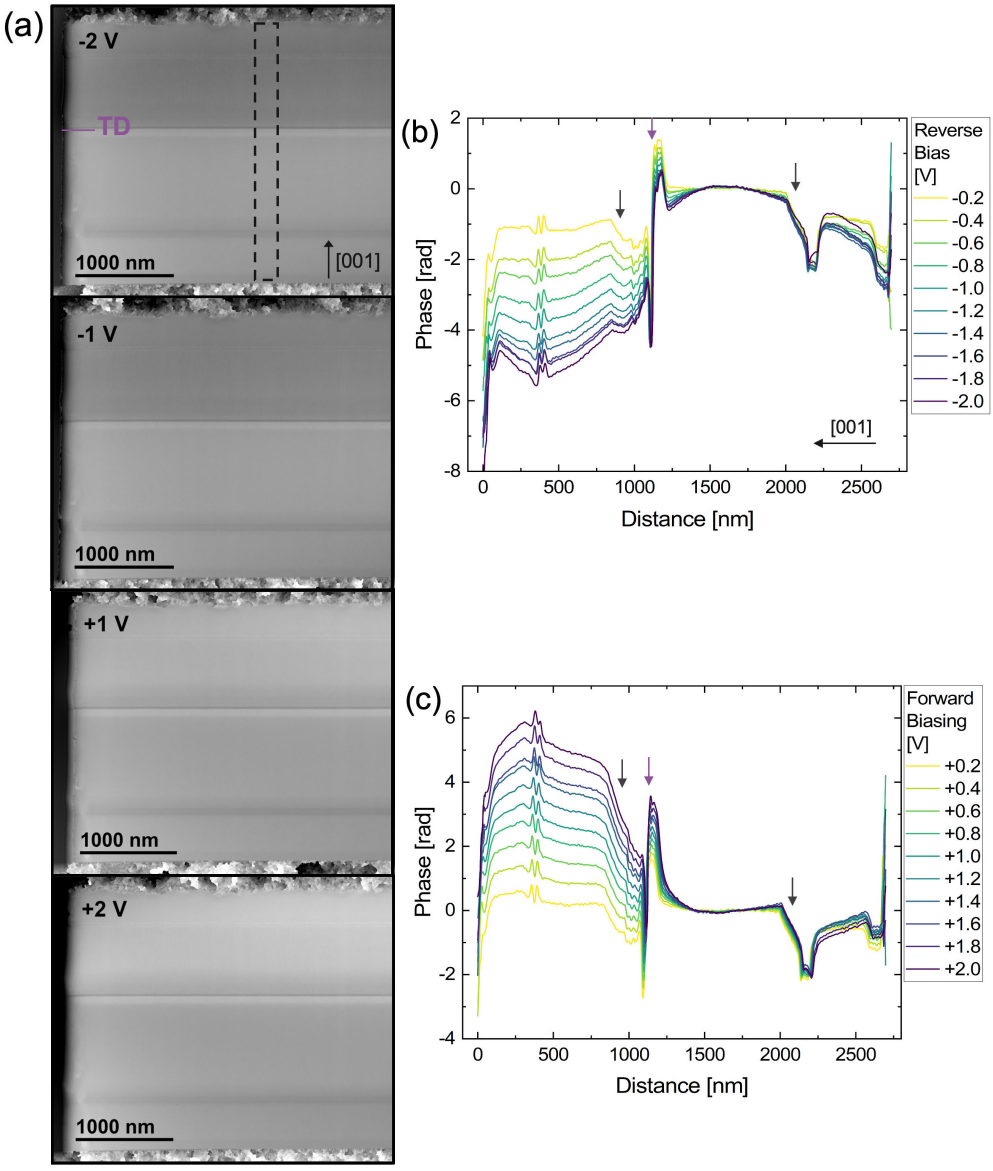

Figure 123: *(a) Electron phase images reconstructed from electron hologram stacks recorded at selected applied voltages on the GaInP/GaAs tandem solar cell specimen, featuring two tandem p-n junctions connected by the p-AlGaAs/n-GaInP tunnel junction (TJ). (b-c) Phase profiles measured across the III-V device heterostructure under (b) reverse and (c) forward bias conditions. The locations of the tandem p-n junctions and the TJ are indicated in the plots by grey and purple arrows, respectively.*

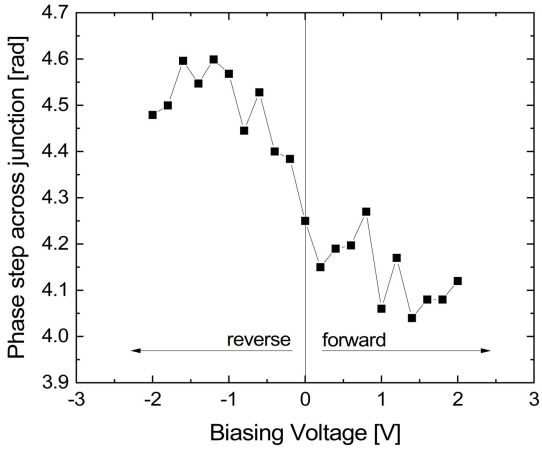

Figure 124: *The measured step in phase across the p-AlGaAs/n-GaInP TJ plotted as a function of the voltage applied to the tandem solar cell specimen.*

8.6.4 STEM-EBIC Current Mapping

STEM-EBIC mapping of the tandem solar cell specimen is performed without an externally applied bias in order to:

- Test the electrical connections to the specimen. Here, the "disadvantage" of the STEM-EBIC technique is exploited, wherein the current signal can only be detected if the electrical connection of the specimen lamella to the MEMS chip, and ultimately to the externally connected current amplifier, is intact.
- Investigate the current pathways in the specimen lamella, specifically to determine whether recombination centres and/or short-circuit paths, are present/limiting the electrical (S)TEM characterisation.

The STEM-EBIC experiment is conducted using the FEI Titan Ultimate operated at 200 kV, in conjunction with the point electronic GmbH EBIC system described in Ch. 7.3.2. As this EBIC system is compatible with the Protochips holder, and the FEI Titan Ultimate (S)TEM microscope supports both parallel beam and convergent scanning beam modes, the STEM-EBIC analysis of the tandem solar cell could seamlessly follow the *in situ* biasing EH experiment. This is a significant advantage, as any transfer of the MEMS chip between holders or even between microscopes can be detrimental to the fragile *in situ* biasing sample.
The chip supporting the tandem solar cell sample has a 2-track geometry, which is preferable for optimal control of the EBIC signal. EBIC maps are recorded using two connection configurations, illustrated in Fig. 126, to regulate the detected field-related EBIC signal. As elaborated in Ch. 7, connecting the p-side of the tandem solar cell to the amplifier and the n-side to the ground, or vice versa, generates a positive or negative field-related EBIC signal, respectively. The STEM-EBIC maps are recorded using the acquisition settings listed in Table 17, at beam currents of 200 pA, 300 pA, and 400 pA, adjusted using the monochromator focus. Beam current values are measured on the TEM phosphor screen, where absolute readings are imprecise, but relative

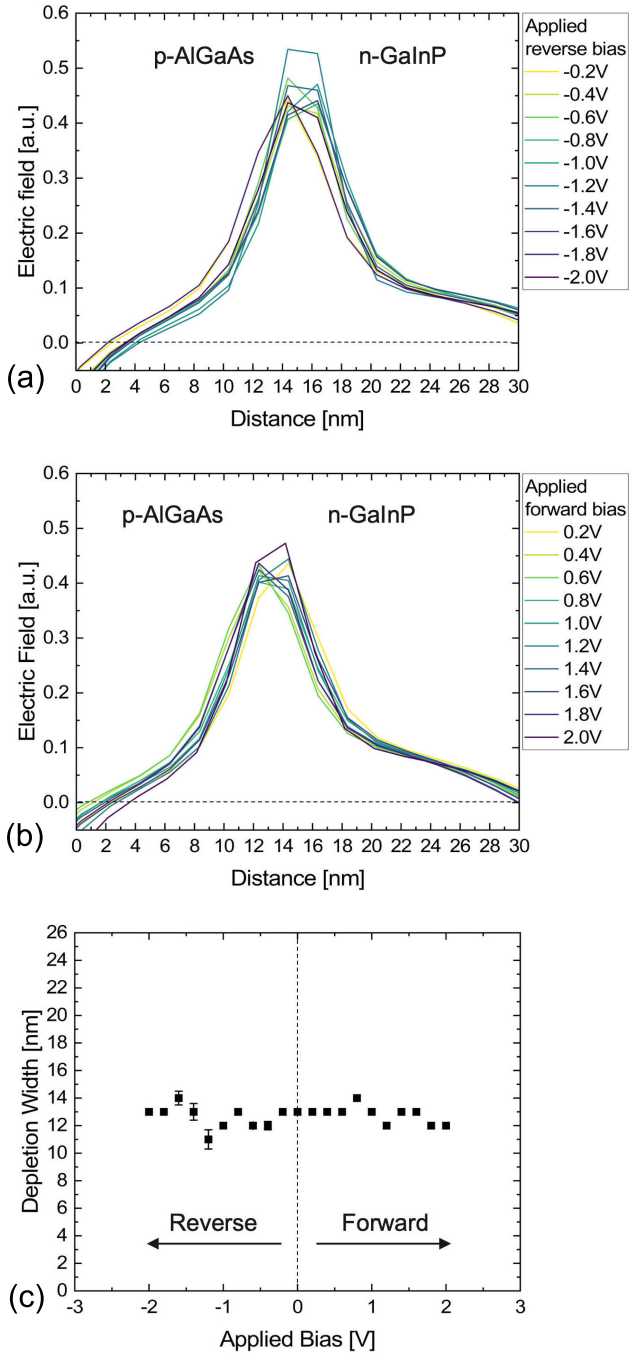

Figure 125: *(a-b) Electric field distribution across the p-AlGaAs/n-GaInP TJ in the tandem solar cell specimen measured at different applied voltages in (a) reverse and (b) forward biasing direction. The profiles are derived from the experimental phase profiles using the first differential equation (Eq. 51). (c) Width of the depletion region at the p-AlGaAs/n-GaInP tunnel junction as a function of the applied voltage, measured by means of the electrical field profiles in (a) and (b).*

changes remain reliable. Considerations and optimisation of the experimental settings for STEM-EBIC experiments are described in detail in Ch. 7.4.

Table 17: Acquisition settings for the STEM-EBIC analysis of the tandem solar cell specimen.

STEM-EBIC acquisition parameter	
C2 aperture	70 µm
Spot size	6
STEM magnification	5000x
Pixel array size	1024×1024
Pixel size	18.6 nm
Pixel dwell time	500 µs/px
Frame acquisition time	8.74 min/frame

STEM-EBIC maps recorded at 400 pA in both connection configurations (Fig. 126) are presented in Fig. 127 alongside a simultaneously acquired STEM-HAADF image and profiles extracted from the EBIC maps across the tandem solar cell heterostructure. The STEM-EBIC map ROI on the tandem cell specimen corresponds to the one used for the *in situ* biasing EH imaging.

As extensively detailed in Ch. 7, the EBIC maps reflect overlapping signal contributions, with the dominant components being field-related EBIC and SEEBIC. While SEEBIC is present throughout, and particularly strong in the contact metal layer (as seen in Fig. 127), the field-related EBIC signal, originating from electron-beam-generated and field-separated EHPs, is exclusively localised at the SCRs. The p-n junctions in the tandem solar cell specimen can be clearly identified using this field-related EBIC signal, appearing as bright/dark contrast in the EBIC maps in Fig. 127b/c and as a pronounced peak in the corresponding line profiles in Fig. 127d. The highly doped p-AlGaAs/n-GaInP TJ exhibits the strongest field-related EBIC signal. Upon inverting the electrical connections, the polarity of the signal detected at the three p-n junctions – i.e. the two tandem p-n junctions and the TJ – inverts from positive to negative, confirming the identification of the field-related EBIC (see Ch. 7.4.1 for further explanation). Additional confirmation of the field-related EBIC assignment can be derived from Fig. 128, which presents EBIC profiles obtained from maps recorded at different beam currents (200 pA, 300 pA, and 400 pA). As the beam current increases, the field-related EBIC signal intensifies as expected (compare Ch. 7.4.3).

These observations demonstrate that even though *in situ* biasing of the specimen was not successful, a response from active carriers separated by the electric field in the specimen is still obtained, and charge carriers are successfully extracted from the specimen and detected in the external circuit. This confirms that the electrical (S)TEM characterisation is not limited by recombination centres or low-resistivity short-circuit paths, such as those potentially present at the cross-sectional surfaces or isolation cuts of the *in situ* biasing lamella. No indications of such short circuit paths are observed in the EBIC maps, as the field-related EBIC contrast at the junctions extends to the specimen edge at the isolation cut. This is confirmed by the STEM-EBIC map shown in Fig. 129, which captures the entire isolation cut. The EBIC signal in the specimen region to the left of the isolation cut exceeds the signal range due to the significantly greater lamella thickness in this region near the contact.

Furthermore, defects acting as recombination centres for carriers, which would appear as pro-

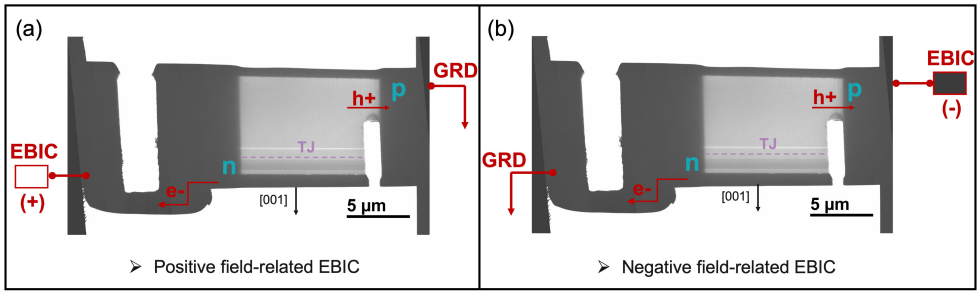

Figure 126: *Illustration of the electrical connection configuration of the tandem solar cell TEM specimen, mounted on the MEMS chip, to the EBIC detection system and electrical ground (GRD) for STEM-EBIC analysis.*

nounced bright/dark EBIC signals, are absent in the examined ROI of the tandem solar cell specimen. As inferred from the *in situ* biasing EH results, the STEM-EBIC findings further suggest that the reason for the unsuccessful biasing (i.e. the specimen did not exhibit the expected bias-induced response of the built-in electric field and depletion width at the tandem cell p-n junctions and TJ) is the high-resistivity Schottky barrier between the IBID-W contact and the p-GaAs substrate of the tandem cell.

8.7 Summary

The device-related research question driving the investigation in this chapter is to determine the cause of the differing tunnelling performance in upright- and inverted-grown p-AlGaAs/n-GaInP TDs in III-V multi-junction solar cells (MJSCs). Routine structural and compositional STEM analysis using HAADF imaging and EDX characterisation excluded structural defects and major elemental segregation as the underlying cause. However, these methods did not provide insights into the electrical mechanisms governing the different tunnelling behaviors. To directly probe the electrical characteristics of the tunnel junctions, governed by active dopants in the III-V heterostructures, the study focused on measuring the depletion width of the TDs using EH, as this serves as a direct indicator of tunnelling performance. The investigation highlighted the prevailing limitations in quantifying the absolute built-in potential in p-n heterojunctions of multinary III-V compounds using EH. However, the methodological feasibility of using EH to quantify the depletion width of highly doped p-AlGaAs/n-GaInP tunnel junctions is verified by:

- Demonstrating that sufficient spatial and phase resolution can be achieved through optimised EH acquisition settings;
- Confirming that the measured phase shift across the tunnel junctions is predominantly influenced by active dopants.

The depletion widths measured using EH without applied bias in different p-AlGaAs/n-GaInP TD specimens are all comparable, and either matched or only slightly smaller than the values predicted by idealised electrostatic potential simulations. The relative comparison of the measured TD depletion widths across different specimens is deemed more meaningful, given the simplified assumptions used in the simulations. Both the upright- and inverted-grown p-AlGaAs/n-GaInP

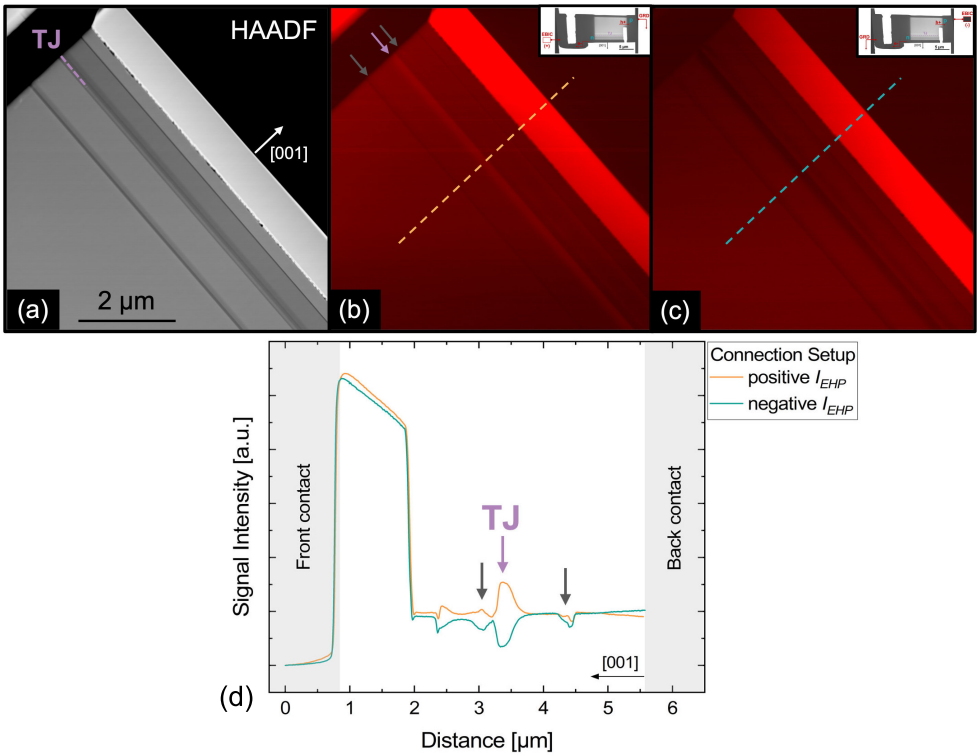

Figure 127: *(a) STEM-HAADF image and (b, c) STEM-EBIC maps of the tandem solar cell specimen, acquired using the acquisition parameters listed in Table 17 and a beam current of 400 pA, as measured on the fluorescence screen. The connection configurations for the EBIC maps are indicated in the insets. (d) EBIC profiles extracted from the marked regions in (b) and (c).*

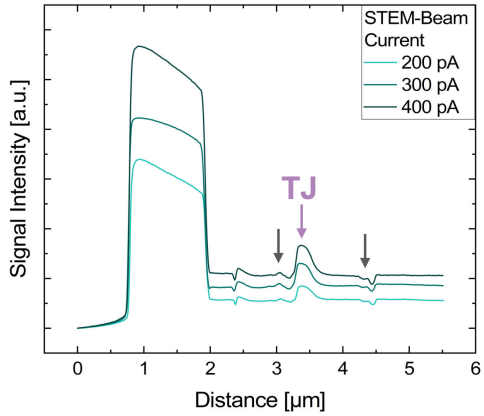

Figure 128: *STEM-EBIC profiles across the tandem solar cell heterostructure, extracted from EBIC maps acquired at the indicated beam currents. The grey and purple arrows denote the locations of the tandem p-n junctions and the TJ, respectively.*

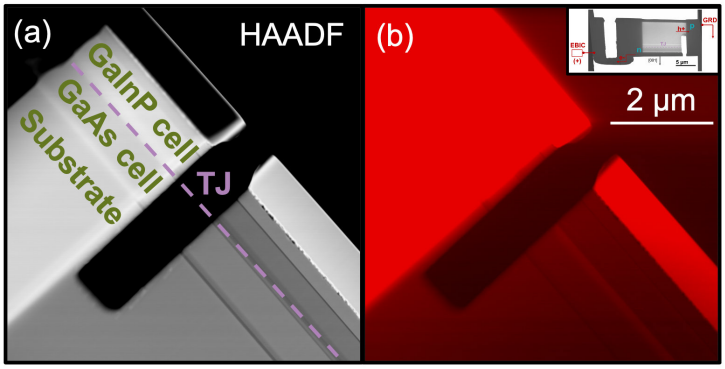

Figure 129: *a) STEM-HAADF image and (b) STEM-EBIC map of the isolation cut near the tandem solar cell specimen ROI used for electrical (S)TEM analysis. Data were acquired using the parameters listed in Table 17 and a beam current of 300 pA, as measured on the fluorescence screen.*

TJ test structures exhibited a depletion width of 14 ± 1 nm, which is consistent with the simulated value of 14.3 nm within the error margin. For the INVTAN heterostructure, the depletion widths of both the upper and lower TDs are identical between 16 and 17 ± 1 nm, compared to the simulated 18 nm. Only in the TAN structure did the depletion width of the upper TJ deviate, measuring 16.5 ± 1 nm, while the lower TJ exhibited a depletion width of 19 to 20 ± 1 nm, compared to the expected 20 nm. As this deviation in the depletion width of the upper TJ is towards smaller values, it is ruled out as the cause of the difference in tunnelling performance between the upright- and inverted-grown TDs. Thus, the non-biasing EH analysis do not provide a conclusive answer to the research question, highlighting the necessity of *in situ* biasing characterisation for meaningful electrical analysis of p-n junctions in working semiconductor devices.

Two approaches for preparing *in situ* biasing TEM specimens from metallised semiconductor wafers are presented, and the prevailing preparation-induced artifacts and their impact on the electrical TEM characterisation of TDs using EH are extensively discussed using the annealed upright-grown p-AlGaAs/n-GaInP test structure as a case study. This methodological discussion is then extended to the preparation and *in situ* biasing EH and STEM-EBIC analysis of a working GaInP/GaAs tandem solar cell. A device-related discussion of the *in situ* biasing phase measurements across the III-V heterostructure of the solar cell is omitted due to preparation-induced artifacts impairing reliable biasing of the specimen junctions. The investigation demonstrated that while depletion width measurements of tunnel junctions can be routinely quantified using standard EH, *in situ* biasing methodology remains hindered by preparation-related artifacts. The central challenge identified is the difficulty in establishing and maintaining two low-resistivity ohmic connections at the front and back of the III-V MJSC specimen to the MEMS support chip. While low parallel resistance is a challenging and often unavoidable issue in *in situ* biasing TEM specimen preparation using Ga-ion FIB, it is shown not to limit the present *in situ* biasing study, as confirmed by the correlative STEM-EBIC analysis of the tandem solar cell specimen.

9 Summary and Outlook

This thesis has investigated the current challenges associated with applying *in situ* biasing TEM techniques – namely EH and STEM-EBIC – for the electrical characterisation of III-V semiconductor p-n junctions in the context of solar cell applications. By tailoring *in situ* biasing EH and STEM-EBIC methodologies to the specific demands of III-V p-n junction analysis, this work has identified and addressed key methodological limitations on the path towards a comprehensive and quantitative *in situ* biasing electrical (S)TEM analysis of operating MJSCs. A central aim of this thesis was the quantification of depletion widths for assessing the tunnelling performance of p-AlGaAs/n-GaInP hetero-compound tunnel junctions, to aid the development of functional MJSC devices using *in situ* biasing EH.

In view to this, EH measurements of the electrostatic potential distribution were first validated as a viable technique for quantifying the depletion width of GaAs and InP p–n homo-junctions. Essential calibration experiments were carried out to optimise the hologram acquisition geometry and parameters specifically for studying individual junctions in large epitaxial III-V structures and *in situ* biasing specimens mounted on chips, thus ensuring that the sample quality and experimental EH conditions-namely spatial resolution and phase sensitivity-were sufficient for accurate depletion width measurements. Surface damage (defects and related surface Fermi level pinning) introduced by FIB milling is known to reduce the concentration of electrically active dopants near the surface. By combining EH measurements of the phase shift across the GaAs and InP p-n junctions with STEM-CBED measurements of the crystalline specimen thickness, this electrically damaged (inactive) surface thickness was determined to be 151 ± 23 nm to 165 ± 29 nm for GaAs, and 103 ± 18 nm to 115 ± 18 nm for InP. For reliable measurements of the intrinsic depletion widths of the devices, this surface damage must be taken into account, and appropriate specimen thicknesses must be selected accordingly. Independent EH measurements on two TEM lamellae with regions of differing thickness demonstrated that, in the GaAs p–n junction, a depletion width of 82 ± 1 nm could be successfully and reproducibly measured across a crystalline thickness range of 250–600 nm. In thinner samples (below 250 nm), surface damage was found to obscure the ability to probe a dominant phase shift contribution from active dopants, whereas in thicker samples (above approximately 600 nm), dynamical diffraction effects became limiting. This reveals 250–600 nm as the optimal thickness range for successful depletion width quantification in GaAs-based III–V semiconductors.

In the next step, electrostatic potential measurements were performed on GaAs p-n junctions under *in situ* applied bias. The results demonstrated successful biasing of the p–n junctions, as both the measured depletion width and electric field strength clearly increased with applied reverse bias. Furthermore, the EH measurements distinctly revealed the expected differences in contact characteristics at the W/p-GaAs and Pt/p-GaAs interfaces, with FIB-deposited W forming a higher Schottky barrier to p-GaAs compared to FIB-deposited Pt. Despite the presence of these Schottky barriers, the clearly observable electrical response of the GaAs p–n junctions to the applied bias confirmed that the contact series resistance at the metal/GaAs interfaces was sufficiently low in both specimens. Additionally, FIB-induced amorphisation and related surface shunting paths were effectively minimised. These findings therefore validate the established *in situ* biasing specimen preparation procedure. Achieving precise circuit editing, avoiding surface shunts, and forming reliable ohmic contacts to enable *in situ* biasing EH experiments is not trivial

and remains one of the greatest current challenges in TEM specimen preparation and device characterisation. Thus, the unambiguous biasing of the GaAs p–n junctions demonstrated here represents a significant milestone on the path towards reproducible *in situ* biasing EH analysis.

The adapted EH methodology for depletion width analysis was subsequently applied to investigate p-AlGaAs/n-GaInP tunnel junctions in III–V MJSCs. Bulk electrical characterisation of operating MJSC devices has revealed that the tunnelling performance of this high-band gap TJ is sensitive to the epitaxial growth direction. The upright-grown (p-on-n) configuration exhibits tunnel current break-ins at significantly lower voltage regimes compared to the inverted-grown (n-on-p) configuration, which hinders its application in solar cells operating under concentrated sunlight. In such devices, the upright-grown p-AlGaAs/n-GaInP TJ currently limits efficient carrier transport and extraction across the MJSC subcells. The motivation for conducting *in situ* biasing EH measurements of the TJ depletion widths – used here as a proxy for tunnelling performance – was to identify the origin of the differing behaviour under operational conditions and support targeted device optimisation. Prior to these measurements, high-resolution structural and compositional STEM pre-characterisation was conducted, which ruled out crystallographic defects and major elemental segregation as the cause of the observed differences in tunnelling behaviour between upright- and inverted-grown TJs, arising in operation under high current densities in concentrator PV. EH depletion width analysis performed without applied bias revealed no significant differences in tunnel junction width between the two configurations, suggesting that the performance discrepancies arise only under bias conditions relevant to operation under concentrated illumination.

In accordance with theoretical predictions based on simulations of the electrostatic potential distribution, accurate depletion widths of 14 nm were reproducibly measured in both inverted- and upright-grown p-AlGaAs/n-GaInP TJs, with an uncertainty of only 1 nm across a broad range of crystalline thicknesses (approximately 240–720 nm). To enable *in situ* biasing EH investigations of the upright-grown p-AlGaAs/n-GaInP TJ in functioning solar cell devices, different specimen preparation workflows were evaluated, with the objective of establishing reliable, low-resistance electrical contacts at both device terminals to mitigate voltage losses. One approach aimed to preserve both pre-deposited metal contacts by combining mechanical slicing and Xe^+ PFIB thinning with Ga-FIB milling. The alternative approach preserved the pre-deposited front ohmic contact while replacing the rear contact with a FIB-deposited W contact.

Electrical testing of these *in situ* biasing specimen revealed that the latter approach was successful in achieving low-resistivity front contacting. It also provided improved control over circuit editing and reduced the extent of surface damage, compared to the more invasive slicing and Xe^+ PFIB-based method. Therefore, this workflow was employed to prepare a working III–V tandem solar cell incorporating the upright-grown p-AlGaAs/n-GaInP TJ for *in situ* biasing TEM analysis. Within the applied bias range, the *in situ* biasing EH measurements did not show any obvious change in the TJ depletion width that could be linked to a tunnel current break-in. Correlated *in situ* biasing STEM-EBIC analysis was successfully conducted to test the electrical integrity of the FIB-prepared specimen, confirming functional biasing of the device p-n junctions in selected specimen regions.

The TJ study successfully demonstrated the methodological feasibility of using EH to accurately quantify depletion widths in highly doped p-AlGaAs/n-GaInP TJs. Specifically, it was

shown that the necessary spatial and phase resolution could be achieved through optimised EH acquisition settings, and that the measured phase shift across the junction was predominantly governed by active dopants. This validates the use of EH for determining depletion widths in III–V hetero-junctions without requiring the subtraction of the compositional MIP, which contributes to the absolute potential but does not impact the depletion width – as long as diffraction-related contributions to the phase shift are carefully minimised.

The STEM-EBIC current mapping of GaAs p-n junctions was applied correlative to *in situ* biasing EH. The results demonstrated the unique potential of this technique for investigating the electrical integrity of p–n junction specimen under applied bias, as well as for fundamental studies of electron–specimen interactions at the nanoscale. This potential results from the complex nature of the EBIC signal, arising from the sensitivity of the overlapping contributions from SEEBIC, EBAC and field-related EBIC to numerous specimen–electron interaction mechanisms.

Differences in SE-induced surface charging effects on electrical properties in n- and p-doped GaAs could be visualised. Moreover, the STEM-EBIC analysis confirmed that parasitic short-circuit current paths along the lamella surfaces were not as dominant as to hinder effective biasing of the junction or the extraction of field-related EBIC, thereby supporting the findings obtained from *in situ* biasing EH. The expected EBIC response of the GaAs p-n junction under reverse bias was clearly observed: an increase in field-related EBIC intensity at the junction, corresponding to the enhanced electric field strength. Additionally, increased contrast between the doped layers under reverse bias revealed enhanced resistance of the p-n junction. Further, the study demonstrated that long-range resistance variations in electrical devices can be effectively mapped using low-magnification STEM-EBIC.

Building on the achievements presented in this thesis, dedicated Monte Carlo simulations of electron scattering processes in GaAs p–n junctions are currently underway to complement the experimental STEM-EBIC measurements. These simulations aim to deepen the understanding of EBIC signal generation mechanisms and to enable the separation of SEEBIC, EBAC, and field-driven EBIC contributions. Such insight is essential for advancing towards a quantitative STEM-EBIC analysis of current extraction in heterostructure devices, particularly for the determination of minority carrier properties. In the context of quantitative STEM-SEEBIC mapping of local work function variations, further simulations focusing on inelastic scattering processes are expected to improve the understanding of SE generation and emission under high-voltage electron beam illumination in STEM. In this regard, the influence of surface conditions – specifically surface Fermi level pinning, band bending, and surface shunting – on SE yields in p- and n-doped semiconductors should also be systematically investigated.

Pushing the concept of correlative current and potential mapping in (S)TEM further, future experiments should explore the combination of STEM-EBIC with 4D-STEM-based electric field measurements. This approach would circumvent the need to alternate between STEM and TEM illumination settings, as is currently required when correlating EBIC with EH analysis. A fully integrated methodology enabling simultaneous EBIC and 4D-STEM mapping could offer the following advantages: It could enhance the comparability of the effects of electron beam illumination on the measured electrical specimen characteristics, by allowing direct correlation between the extracted current and the local electric field distribution. It could reduce overall beam exposure and thereby minimise beam-induced surface modifications such as surface damage and

carbon contamination. However, for this approach to be viable, successful electric field mapping via 4D-STEM at III–V p–n junctions would require the integration of beam precession to mitigate the effects of dynamical diffraction. These effects can impair the accurate detection of diffraction disc shifts in 4D-STEM datasets and thus compromise the quantitative reconstruction of local electric fields. In this work, 4D-STEM-based electric field mapping was not pursued. Instead, EH was favoured, as it benefits from the use of parallel illumination, which enables efficient suppression of dynamical diffraction contributions through specimen tilting away from zone axis to weakly diffracting orientations. This approach remained effective even for relatively thick specimens – in the range of 250–600 nm – which are essential to reducing the influence of electrically altered surface layers on TEM-based electrical characterisation. To provide a truly equivalent alternative to EH for electrostatic potential measurements, reliable suppression of dynamical diffraction effects via precession-assisted 4D-STEM would need to be demonstrated in specimens exceeding ~250 nm in thickness.

Regarding specimen preparation, Ga-FIB remains, despite its well-known drawbacks, the most suitable approach at present for *in situ* biasing TEM sample preparation, owing to its capacity for site-specific milling at low current regimes – something PFIB technology, in its current state, cannot yet match. Nevertheless, continuous development of alternative preparation methods is essential. These should aim to minimise or eliminate Ga-ion beam-induced damage, improve the quality of metal contacts, and ideally enable the preservation of pre-fabricated ohmic contacts. If future PFIB systems can offer comparable milling precision at low beam currents, they may present a superior alternative due to the absence of Ga implantation – a significant concern in III–V semiconductors, where Ga implantation alters the compound stoichiometry. However, the effects of different PFIB plasma species on the electrical surface properties of III–V materials must be systematically explored before PFIB can be routinely applied for *in situ* biasing TEM preparation.

Despite the prevailing challenges in quantitative electrical characterisation of III-V semiconductor devices using *in situ* biasing techniques, (S)TEM remains uniquely capable of resolving local active dopant characteristics at p-n junctions and hetero-interfaces with high spatial precision. This is especially relevant in large, complex heterostructure devices such as MJSCs, where bulk electrical measurements can only provide indirect information on the properties of specific junctions. Moreover, the large physical dimensions of such devices hinder the application of techniques such as SIMS, which in any case can only quantify total dopant concentration without resolving dopant activity.

Therefore, continued work to advance *in situ* biasing (S)TEM methodologies is essential to fully unlock their exceptional potential for comprehensive and quantitative correlative electrical characterisation of current extraction and potential distribution at p–n junctions in operational III-V MJSCs.

10 References

[1] S. P. Philipps, F. Dimroth, and A. W. Bett, 'Chapter I-4-B - High-Efficiency III–V Multijunction Solar Cells', in S. A. Kalogirou, ed., 'McEvoy's Handbook of Photovoltaics (Third Edition)', pp. 439–472, Academic Press, third edit edn., ISBN 978-0-12-809921-6, 2018, doi:10.1016/B978-0-12-809921-6.00012-4.

[2] NREL, 'Best Research-Cell Efficiency Chart', Available at `https://www.nrel.gov/pv/cell-efficiency.html`.

[3] P. Schygulla, P. Beutel, S. Heckelmann, O. Höhn, M. Klitzke, J. Schön, E. Oliva, F. Predan, M. Schachtner, G. Siefer, and Others, 'Quadruple Junction Solar Cell with 47.6% Conversion Efficiency under Concentration', 2022.

[4] D. B. Williams and C. B. Carter, *The Transmission Electron Microscope*, chap. 1, pp. 3–22, Springer US, Boston, MA, ISBN 978-0-387-76501-3, 2009, doi:10.1007/978-0-387-76501-3_1.

[5] P. A. Midgley, 'An introduction to off-axis electron holography', *Micron*, 2001, **32**, 167–184.

[6] P. Formanek and E. Bugiel, 'On specimen tilt for electron holography of semiconductor devices', *Ultramicroscopy*, 2006, **106**(4-5), 292–300, ISSN 03043991, doi:10.1016/j.ultramic.2005.09.003.

[7] J. F. Wheeldon, C. E. Valdivia, A. W. Walker, G. Kolhatkar, A. Jaouad, A. Turala, B. Riel, D. Masson, N. Puetz, S. Fafard, R. Arès, V. Aimez, T. J. Hall, and K. Hinzer, 'Performance comparison of AlGaAs, GaAs and InGaP tunnel junctions for concentrated multijunction solar cells', *Progress in Photovoltaics: Research and Applications*, 2011, **19**(4), 442–452, doi:10.1002/pip.1056.

[8] M. Hermle, G. Létay, S. P. Philipps, and A. W. Bett, 'Numerical simulation of tunnel diodes for multi-junction solar cells', *Progress in Photovoltaics: Research and Applications*, 2008, **16**(5), 409–418, doi:10.1002/pip.824.

[9] Manijeh Razeghi, *Fundamentals of Solid State Engineering*, Springer Cham, 4 edn., 2019, doi:10.1007/978-3-319-75708-7.

[10] G. V. Wolfe, 'Earth System Science: From Biogeochemical Cycles to Global Change', in G. H. Jacobson, Michael C.; Charlson, Robert J.; Rodhe, Henning and Orians, ed., 'International Geophysics', vol. 72, pp. 498–507, ISBN 9780123793706, 2000, doi:10.1016/S0074-6142(00)80125-4.

[11] IPCC, 2022, *Climate Change 2022: Impacts, Adaptation and Vulnerability. Contribution of Working Group II to the Sixth Assessment Report of the Intergovernmental Panel on Climate Change*, Cambridge University Press, Cambridge, UK and New York, NY, USA, 2022, doi:10.1017/9781009325844.

[12] L. Clarke, Y.-M. Wei, A. D. L. V. Navarro, A. Garg, A. Hahmann, S. Khennas, I. Azevedo, A. Löschel, A. Singh, L. Steg, G. Strbac, and K. Wada, 'IPCC 2022: Energy Systems', in P. Shukla, J. Skea, R. Slade, A. A. Khourdajie, R. van Diemen, D. McCollum, M. Pathak, S. Some, R. F. , P. Vyas, M. Belkacemi, A. Hasija, G. Lisboa, S. Luz, and J. Malley, eds., 'Climate Change 2022: Mitigation of Climate Change. Contribution of Working Group III to the Sixth Assessment Report of the Intergovernmental Panel on Climate Change', Cambridge University Press, Cambridge, UK and New York, NY, USA, 2022, doi:10.1017/9781009157926.008.

[13] Fraunhofer Institute for Solar Energy Systems ISE, 'Energy Charts', Available at `https://www.energy-charts.info/index.html?l=en{&}c=DE`.

[14] M. Yamaguchi, F. Dimroth, J. F. Geisz, and N. J. Ekins-Daukes, 'Multi-junction solar cells paving the way for super high-efficiency', *Journal of Applied Physics*, 2021, **129**(24), ISSN 10897550, doi:10.1063/5.0048653.

[15] J. Li, A. Aierken, Y. Liu, Y. Zhuang, X. Yang, J. H. Mo, R. K. Fan, Q. Y. Chen, S. Y. Zhang, Y. M. Huang, and Q. Zhang, 'A Brief Review of High Efficiency III-V Solar Cells for Space Application', *Frontiers in Physics*, 2021, **8**(February), 1–15, ISSN 2296424X, doi:10.3389/fphy.2020.631925.

[16] H. Cotal, C. Fetzer, J. Boisvert, G. Kinsey, R. King, P. Hebert, H. Yoon, and N. H. Karam, 'III-V Multijunction Solar Cells for Concentrating Photovoltaics', *Energy & Environmental Science - ENERGY ENVIRON SCI*, 2009, **2**, doi:10.1039/b809257e.

[17] J. F. Geisz, R. M. France, K. L. Schulte, M. A. Steiner, A. G. Norman, H. L. Guthrey, M. R. Young, T. Song, and T. Moriarty, 'Six-junction III–V solar cells with 47.1% conversion efficiency under 143 Suns concentration', *Nature Energy*, 2020, **5**(4), 326–335, ISSN 20587546, doi:10.1038/s41560-020-0598-5.

[18] J. F. Geisz, M. A. Steiner, K. L. Schulte, M. Young, R. M. France, and D. J. Friedman, 'Six-junction concentrator solar cells', *AIP Conference Proceedings*, 2018, **2012**(September), ISSN 15517616, doi:10.1063/1.5053512.

[19] F. Dimroth, T. N. Tibbits, M. Niemeyer, F. Predan, P. Beutel, C. Karcher, E. Oliva, G. Siefer, D. Lackner, P. Fus-Kailuweit, A. W. Bett, R. Krause, C. Drazek, E. Guiot, J. Wasselin, A. Tauzin, and T. Signamarcheix, 'Four-junction wafer-bonded concentrator solar cells', *IEEE Journal of Photovoltaics*, 2016, **6**(1), 343–349, ISSN 21563381, doi:10.1109/JPHOTOV.2015.2501729.

[20] F. Predan, A. Kovács, J. Ohlmann, D. Lackner, R. E. Dunin-Borkowski, F. Dimroth, and W. Jäger, 'Effects of thermal annealing on structural and electrical properties of surface-activated n-GaSb/n-GaInP direct wafer bonds', *Journal of Applied Physics*, 2017, **122**(13), ISSN 10897550, doi:10.1063/1.5002080.

[21] S. V. Kalinin, C. Ophus, P. M. Voyles, R. Erni, V. Grillo, A. R. Lupini, M. P. Oxley, E. Schwenker, J. Etheridge, and M. K. Y. Chan, 'Machine learning in scanning transmission electron microscopy', doi:10.1038/s43586-022-00095-w.

[22] H. Lakner, C. Mendorf, B. Bollig, W. Prost, and F. J. Tegude, 'Determination of interface composition in III-V heterojunction devices (HBT and RTD) with atomic resolution using STEM techniques', *Materials Science and Engineering B*, 1997, **44**(1-3), 52–56, ISSN 09215107, doi:10.1016/S0921-5107(96)01800-4.

[23] P. Colter, B. Hagar, and S. Bedair, 'Tunnel junctions for III-V multijunction solar cells review', *Crystals*, 2018, **8**(12), ISSN 20734352, doi:10.3390/cryst8120445.

[24] I. García, I. Rey-Stolle, B. Galiana, and C. Algora, 'Analysis of tellurium as n-type dopant in GaInP: Doping, diffusion, memory effect and surfactant properties', *Journal of Crystal Growth*, 2007, **298**(SPEC. ISS), 794–799, ISSN 00220248, doi:10.1016/j.jcrysgro.2006.10.099.

[25] H. Lichte, P. Formanek, A. Lenk, M. Linck, C. Matzeck, M. Lehmann, and P. Simon, 'Electron Holography: Applications to Materials Questions', *Annual Review of Materials Research*, 2007, **37**(1), 539–588, doi:10.1146/annurev.matsci.37.052506.084232.

[26] M. R. McCartney, R. E. Dunin-Borkowski, and D. J. Smith, 'Quantitative measurement of nanoscale electrostatic potentials and charges using off-axis electron holography: Developments and opportunities', *Ultramicroscopy*, 2019, **203**, 105–118, ISSN 18792723, doi:10.1016/j.ultramic.2019.01.008.

[27] C. Ophus, 'Four-Dimensional Scanning Transmission Electron Microscopy (4D-STEM): From Scanning Nanodiffraction to Ptychography and Beyond.', *Microscopy and microanalysis : the official journal of Microscopy Society of America, Microbeam Analysis Society, Microscopical Society of Canada*, 2019, **25**(3), 563–582, ISSN 1435-8115 (Electronic), doi:10.1017/S1431927619000497.

[28] B. Haas, J. L. Rouvière, V. Boureau, R. Berthier, and D. Cooper, 'Direct comparison of off-axis holography and differential phase contrast for the mapping of electric fields in semiconductors by transmission electron microscopy.', *Ultramicroscopy*, 2019, **198**(November 2018), 58–72, ISSN 18792723, doi:10.1016/j.ultramic.2018.12.003.

[29] L. Bruas, V. Boureau, A. P. Conlan, S. Martinie, J.-L. Rouvière, and D. Cooper, 'Improved measurement of electric fields by nanobeam precession electron diffraction', *Journal of Applied Physics*, 2020, **127**(20), 205703, ISSN 0021-8979, doi:10.1063/5.0006969.

[30] A. Beyer, M. S. Munde, S. Firoozabadi, D. Heimes, T. Grieb, A. Rosenauer, K. Müller-Caspary, and K. Volz, 'Quantitative Characterization of Nanometer-Scale Electric Fields via Momentum-Resolved STEM', *Nano Letters*, 2021, **21**(5), 2018–2025, ISSN 15306992, doi:10.1021/acs.nanolett.0c04544.

[31] W. A. Hubbard, M. Mecklenburg, H. L. Chan, and B. C. Regan, 'STEM Imaging with Beam-Induced Hole and Secondary Electron Currents', *Physical Review Applied*, 2018, **10**(4), 1, ISSN 23317019, doi:10.1103/PhysRevApplied.10.044066.

[32] M. Mecklenburg, W. A. Hubbard, J. J. Lodico, and B. C. Regan, 'Electron beam-induced current imaging with two-angstrom resolution', *Ultramicroscopy*, 2019, **207**, 112852, ISSN 18792723, doi:10.1016/j.ultramic.2019.112852.

[33] T. Meyer, B. Kressdorf, J. Lindner, P. Peretzki, V. Roddatis, C. Jooss, and M. Seibt, 'High-resolution Scanning Transmission EBIC Analysis of Misfit Dislocations at Perovskite pn-Heterojunctions', *Journal of Physics: Conference Series*, 2019, **1190**(1), ISSN 17426596, doi:10.1088/1742-6596/1190/1/012009.

[34] A. P. Conlan, G. Moldovan, L. Bruas, E. Monroy, and D. Cooper, 'Electron beam induced current microscopy of silicon p-n junctions in a scanning transmission electron microscope', *Journal of Applied Physics*, 2021, **129**(13), ISSN 10897550, doi:10.1063/5.0040243.

[35] A. P. Conlan, M. A. Luong, P. Gentile, G. Moldovan, M. I. Den Hertog, E. Monroy, and D. Cooper, 'Thermally propagated Al contacts on SiGe nanowires characterized by electron beam induced current in a scanning transmission electron microscope', *Nanotechnology*, 2022, **33**(3), 35712, ISSN 13616528, doi:10.1088/1361-6528/ac2e73.

[36] M. Duchamp, H. Hu, Y. M. Lam, R. E. Dunin-Borkowski, and C. B. Boothroyd, 'STEM electron beam-induced current measurements of organic-inorganic perovskite solar cells', *Ultramicroscopy*, 2020, **217**, ISSN 18792723, doi:10.1016/j.ultramic.2020.113047.

[37] G. Moldovan, P. Kazemian, P. R. Edwards, V. K. Ong, O. Kurniawan, and C. J. Humphreys, 'Low-voltage cross-sectional EBIC for characterisation of GaN-based light emitting devices', *Ultramicroscopy*, 2007, **107**(4-5), 382–389, ISSN 03043991, doi:10.1016/j.ultramic.2006.10.002.

[38] D. Cooper, 'Off-axis electron holography for the measurement of active dopants in silicon semiconductor devices', *Journal of Physics D: Applied Physics*, 2016, **49**(47), ISSN 13616463, doi:10.1088/0022-3727/49/47/474001.

[39] D. Cooper, C. Ailliot, J. P. Barnes, J. M. Hartmann, P. Salles, G. Benassayag, and R. E. Dunin-Borkowski, 'Dopant profiling of focused ion beam milled semiconductors using off-axis electron holography; reducing artifacts, extending detection limits and reducing the effects of gallium implantation', *Ultramicroscopy*, 2010, **110**(5), 383–389, ISSN 03043991, doi:10.1016/j.ultramic.2010.02.001.

[40] S. Anada, K. Yamamoto, H. Sasaki, N. Shibata, Y. Hori, K. Kinugawa, A. Imamura, and T. Hirayama, 'Precise measurement of electric potential, field, and charge density profiles across a biased GaAs p-n tunnel junction by in situ phase-shifting electron holography', *Journal of Applied Physics*, 2017, **122**(22), ISSN 10897550, doi:10.1063/1.5006837.

[41] D. Cooper, A. C. Twitchett, P. K. Somodi, P. A. Midgley, R. E. Dunin-Borkowski, I. Farrer, and D. A. Ritchie, 'Improvement in electron holographic phase images of focused-ion-beam-milled GaAs and Si p-n junctions by in situ annealing', *Applied Physics Letters*, 2006, **88**(6), 1–4, ISSN 00036951, doi:10.1063/1.2172068.

[42] W. D. Rau, P. Schwander, F. H. Baumann, W. Höppner, and A. Ourmazd, 'Two-Dimensional Mapping of the Electrostatic Potential in Transistors by Electron Holography', *Phys. Rev. Lett.*, 1999, **82**(12), 2614–2617, doi:10.1103/PhysRevLett.82.2614.

[43] Z. Wang, T. Hirayama, K. Sasaki, H. Saka, and N. Kato, 'Electron holographic characterization of electrostatic potential distributions in a transistor sample fabricated by focused ion beam', *Applied Physics Letters*, 2002, **80**(2), 246–248, doi:10.1063/1.1432746.

[44] G. Y. Robinson, 'Schottky Diodes and Ohmic Contacts for the III-V Semiconductors BT - Physics and Chemistry of III-V Compound Semiconductor Interfaces', pp. 73–163, Springer US, Boston, MA, ISBN 978-1-4684-4835-1, 1985, doi:10.1007/978-1-4684-4835-1_2.

[45] V. L. Rideout, 'A review of the theory and technology for ohmic contacts to group III-V compound semiconductors', *Solid State Electronics*, 1975, **18**(6), 541–550, ISSN 00381101, doi:10.1016/0038-1101(75)90031-3.

[46] M. A. Green, *Solar Cells: Operating Principles, Technology, and System Applications*, Prentice-Hall Contemporary Comparative Politics Series, Prentice-Hall, 1982, ISBN 9780138222703.

[47] P. Würfel and U. Würfel, *Physics of solar cells: From basic principles to advanced concepts*, Wiley-VCH Verlag GmbH & Co. KGaA, Weinheim, Germany, third edit edn., 2016.

[48] Soteris A. Kalogirou, ed., *McEvoy's Handbook of Photovoltaics*, Elsevier, 3 edn., 2017, doi:https://doi.org/10.1016/C2015-0-01840-8.

[49] M. Yamaguchi, 'Fundamentals and R&D status of III-V compound solar cells and materials', *Physica Status Solidi (C) Current Topics in Solid State Physics*, 2015, **12**(6), 489–499, ISSN 16101642, doi:10.1002/pssc.201400216.

[50] W. Shockley and H. J. Queisser, 'Detailed balance limit of efficiency of p-n junction solar cells', *Journal of Applied Physics*, 1961, **32**(3), 510–519, ISSN 00218979, doi:10.1063/1.1736034.

[51] L. Esaki, 'New phenomenon in narrow germanium p-n junctions', *Physical Review*, 1958, **109**(2), 603 – 604, doi:10.1103/PhysRev.109.603.

[52] U. W. Pohl, *Epitaxy of Semiconductors: Physics and Fabrication of Heterostructures*, Springer Cham, 2 edn., 2020, doi:https://doi.org/10.1007/978-3-030-43869-2.

[53] S. T. Murphy, A. Chroneos, C. Jiang, U. Schwingenschlögl, and R. W. Grimes, 'Deviations from Vegard's law in ternary III-V alloys', *Phys. Rev. B*, 2010, **82**(7), 73201, doi:10.1103/PhysRevB.82.073201.

[54] U. Pietsch, V. Holý, and T. Baumbach, *Lattice Parameters and Strains in Epitaxial Layers and Multilayers*, pp. 179–203, Springer New York, New York, NY, ISBN 978-1-4757-4050-9, 2004, doi:10.1007/978-1-4757-4050-9_9.

[55] H. Kawanami, 'Heteroepitaxial technologies of III–V on Si', *Solar Energy Materials and Solar Cells*, 2001, **66**(1), 479–486, ISSN 0927-0248, doi:10.1016/S0927-0248(00)00209-9.

[56] I. Vurgaftman, J. R. Meyer, and L. R. Ram-Mohan, 'Band parameters for III-V compound semiconductors and their alloys', *Journal of Applied Physics*, 2001, **89**(11 I), 5815–5875, ISSN 00218979, doi:10.1063/1.1368156.

[57] Y. P. Varshni, 'Temperature dependence of the energy gap in semiconductors', *Physica*, 1967, **34**(1), 149–154, ISSN 0031-8914, doi:10.1016/0031-8914(67)90062-6.

[58] R. Pässler, 'Dispersion-related description of temperature dependencies of band gaps in semiconductors', *Phys. Rev. B*, 2002, **66**(8), 85201, doi:10.1103/PhysRevB.66.085201.

[59] M. Niemeyer, J. Ohlmann, A. W. Walker, P. Kleinschmidt, R. Lang, T. Hannappel, F. Dimroth, and D. Lackner, 'Minority carrier diffusion length, lifetime and mobility in p-type GaAs and GaInAs', *Journal of Applied Physics*, 2017, **122**(11), ISSN 10897550, doi:10.1063/1.5002630.

[60] R. K. Ahrenkiel, 'Chapter 2 Minority-Carrier Lifetime in III–V Semiconductors', in R. K. Ahrenkiel and M. S. Lundstrom, eds., 'Minority Carriers In III-V Semiconductors: Physics and Applications', vol. 39 of *Semiconductors and Semimetals*, pp. 39–150, Elsevier, 1993, doi:10.1016/S0080-8784(08)62594-6.

[61] Ioffe Institute, 'Electronic archive: New Semiconductor Materials. Characteristics and Properties—Physical Properties of Semiconductors', 2024. Available at `https://www.ioffe.ru/SVA/NSM/Semicond/index.html`.

[62] E. F. Schubert, *Doping in III-V Semiconductors*, Cambridge Studies in Semiconductor Physics and Microelectronic Engineering, Cambridge University Press, 1993.

[63] M. O'Keeffe and J. C. H. Spence, 'On the average Coulomb potential and constraints on the electron density in crystals', *Acta Cryst.*, 1994, **50**, 33–45, doi:10.1107/S010876739300474X.

[64] D. K. Saldin and J. C. H. Spence, 'On the mean inner potential in high- and low-energy electron diffraction', *Ultramicroscopy*, 1994, **55**(4), 397–406, ISSN 0304-3991, doi:10.1016/0304-3991(94)90175-9.

[65] M. Y. Kim, J. M. Zuo, and J. Spence, 'Ab-initio LDA Calculations of the Mean Coulomb Potential V0 in Slabs of Crystalline Si, Ge and MgO', *Physica Status Solidi (a)*, 1998, **166**(1), 445–451.

[66] P. Kruse, A. Rosenauer, and D. Gerthsen, 'Determination of the mean inner potential in III-V semiconductors by electron holography', *Microscopy of Semiconducting Materials 2003*, 2003, **96**, 45–48, doi:10.1201/9781351074636.

[67] P. Kruse, M. Schowalter, D. Lamoen, A. Rosenauer, and D. Gerthsen, 'Determination of the mean inner potential in III-V semiconductors, Si and Ge by density functional theory and electron holography', *Ultramicroscopy*, 2006, **106**(2), 105–113, ISSN 03043991, doi:10.1016/j.ultramic.2005.06.057.

[68] A. Lubk, D. Wolf, and H. Lichte, 'The effect of dynamical scattering in off-axis holographic mean inner potential and inelastic mean free path measurements', *Ultramicroscopy*, 2010, **110**(5), 438–446, ISSN 03043991, doi:10.1016/j.ultramic.2009.09.009.

[69] S. Chung, D. J. Smith, and M. R. McCartney, 'Determination of the inelastic mean-free-path and mean inner potential for AlAs and GaAs using off-axis electron holography and convergent beam electron diffraction', *Microscopy and Microanalysis*, 2007, **13**(5), 329–335, ISSN 14319276, doi:10.1017/S1431927607070687.

[70] M. Lehmann and H. Lichte, 'Tutorial on off-axis electron holography', *Microscopy and Microanalysis*, 2002, **8**(6), 447–466, ISSN 14319276, doi:10.1017/S1431927602029938.

[71] H. Rose, 'Outline of a spherically corrected semiaplanatic medium-voltage transmission electron microscope', *Optik*, 1990, **85**, 19–24.

[72] M. Haider, S. Uhlemann, E. Schwan, G. Rose, B. Kabius, and K. Urban, 'Electron microscopy image enhanced [7]', *Nature*, 1998, **392**(6678), 768–769, ISSN 00280836, doi:10.1038/33823.

[73] M. Haider, H. Rose, S. Uhlemann, E. Schwan, B. Kabius, and K. Urban, 'A spherical-aberration-corrected 200 kV transmission electron microscope', *Ultramicroscopy*, 1998, **75**(1), 53–60, ISSN 03043991, doi:10.1016/S0304-3991(98)00048-5.

[74] M. Haider, P. Hartel, H. Mller, S. Uhlemann, and J. Zach, 'Information transfer in a TEM corrected for spherical and chromatic aberration', *Microscopy and Microanalysis*, 2010, **16**(4), 393–408, ISSN 14319276, doi:10.1017/S1431927610013498.

[75] R. F. Egerton and M. Watanabe, 'Spatial resolution in transmission electron microscopy', *Micron*, 2022, **160**(March), 103304, ISSN 09684328, doi:10.1016/j.micron.2022.103304.

[76] C. B. Carter and D. B. Williams, eds., *Transmission Electron Microscopy: Diffraction, Imaging, and Spectrometry*, Springer Cham, 1 edn., 2016, doi:https://doi.org/10.1007/978-3-319-26651-0.

[77] E. Rutherford, 'LXXIX. The scattering of α and β particles by matter and the structure of the atom', *The London, Edinburgh, and Dublin Philosophical Magazine and Journal of Science*, 1911, **21**(125), 669–688, doi:10.1080/14786440508637080.

[78] T. Walther, Y. Qiu, and A. G. Cullis, 'Measuring the contrast in annular dark field STEM images as a function of camera length', *Journal of Physics: Conference Series*, 2010, **241**(July 2017), ISSN 17426596, doi:10.1088/1742-6596/241/1/012068.

[79] A. H. M. M. J. Treacy and C. J. Wilson, 'Z contrast of platinum and palladium catalysts', *Philosophical Magazine A*, 1978, **38**(5), 569–585, doi:10.1080/01418617808239255.

[80] J. M. Cowley, J. C. H. Spence, and V. V. Smirnov, 'The enhancement of electron microscope resolution by use of atomic focusers', *Ultramicroscopy*, 1997, **68**(2), 135–148, ISSN 0304-3991, doi:10.1016/S0304-3991(97)00022-3.

[81] K. H. W. van den Bos, A. De Backer, G. T. Martinez, N. Winckelmans, S. Bals, P. D. Nellist, and S. Van Aert, 'Unscrambling Mixed Elements using High Angle Annular Dark Field Scanning Transmission Electron Microscopy', *Phys. Rev. Lett.*, 2016, **116**(24), 246101, doi:10.1103/PhysRevLett.116.246101.

[82] S. J. Pennycook and D. E. Jesson, 'High-resolution Z-contrast imaging of crystals', *Ultramicroscopy*, 1991, **37**(1), 14–38, ISSN 0304-3991, doi:10.1016/0304-3991(91)90004-P.

[83] M. Varela, A. R. Lupini, K. Van Benthem, A. Y. Borisevich, M. F. Chisholm, N. Shibata, E. Abe, and S. J. Pennycook, 'Materials characterization in the aberration-corrected scanning transmission electron microscope', *Annual Review of Materials Research*, 2005, **35**, 539–569, ISSN 15317331, doi:10.1146/annurev.matsci.35.102103.090513.

[84] S. J. Pennycook and P. D. Nellist, eds., *Scanning Transmission Electron Microscopy*, Springer-Verlag New York, 2011, ISBN 9781441971999, doi:10.1007/978-1-4419-7200-2.

[85] J. Cui, Y. Yao, Y. G. Wang, X. Shen, and R. C. Yu, 'Origin of atomic displacement in HAADF image of the tilted specimen', *Ultramicroscopy*, 2017, **182**, 156–162, ISSN 0304-3991, doi:10.1016/j.ultramic.2017.07.007.

[86] D. Shindo and O. Tetsuo, *Analytical Electron Microscopy for Materials Science*, Springer Tokyo, 1 edn., 2002, doi:10.1007/978-4-431-66988-3.

[87] D. B. Williams and C. B. Carter, *Transmission Electron Microscopy*, Springer New York, 2 edn., 2009, doi:10.1007/978-0-387-76501-3.

[88] K. E. MacArthur, A. B. Yankovich, A. Béché, M. Luysberg, H. G. Brown, S. D. Findlay, M. Heggen, and L. J. Allen, 'Optimizing Experimental Conditions for Accurate Quantitative Energy-Dispersive X-ray Analysis of Interfaces at the Atomic Scale', *Microscopy and Microanalysis*, 2021, **27**(3), 528–542, ISSN 14358115, doi:10.1017/S1431927621000246.

[89] K. E. MacArthur, H. G. Brown, S. D. Findlay, and L. J. Allen, 'Probing the effect of electron channelling on atomic resolution energy dispersive X-ray quantification.', *Ultramicroscopy*, 2017, **182**, 264–275, ISSN 1879-2723 (Electronic), doi:10.1016/j.ultramic.2017.07.020.

[90] G. Cliff and G. W. Lorimer, 'The quantitative analysis of thin specimens', *Journal of Microscopy*, 1975, **103**(2), 203–207, doi:10.1111/j.1365-2818.1975.tb03895.x.

[91] L. A. Giannuzzi, J. L. Drown, S. R. Brown, R. B. Irwin, and F. A. Stevie, 'Focused Ion Beam Milling and Micromanipulation Lift-Out for Site Specific Cross-Section Tem Specimen Preparation', *MRS Online Proceedings Library*, 1997, **480**(1), 19–27, ISSN 1946-4274, doi:10.1557/PROC-480-19.

[92] M. H. F. Overwijk, F. C. van den Heuvel, and C. W. T. Bulle-Lieuwma, 'Novel scheme for the preparation of transmission electron microscopy specimens with a focused ion beam', *Journal of Vacuum Science & Technology B: Microelectronics and Nanometer Structures Processing, Measurement, and Phenomena*, 1993, **11**(6), 2021–2024, ISSN 1071-1023, doi:10.1116/1.586537.

[93] L. A. Giannuzzi and F. A. Stevie, *Introduction to Focused Ion Beams*, Springer New York, NY, 1 edn., 2005, doi:https://doi.org/10.1007/b101190.

[94] J. B. Malherbe, 'Sputtering of Compound Semiconductor Surfaces. I. Ion-Solid Interactions and Sputtering Yields', *Critical Reviews in Solid State and Materials Sciences*, 1994, **19**(2), 55–127, ISSN 15476561, doi:10.1080/10408439408244588.

[95] A. Barna, B. Pécz, and M. Menyhard, 'Amorphisation and surface morphology development at low-energy ion milling', *Ultramicroscopy*, 1998, **70**(3), 161–171, ISSN 03043991, doi:10.1016/S0304-3991(97)00120-4.

[96] A. Strecker, J. Mayer, B. Baretzky, U. Eigenthaler, T. Gemming, R. Schweinfest, and M. Rühle, 'Optimization of TEM specimen preparation by double-sided ion beam thinning under low angles', *Journal of Electron Microscopy*, 1999, **48**(3), 235–244, ISSN 00220744, doi:10.1093/oxfordjournals.jmicro.a023673.

[97] R. M. Langford and A. K. Petford-Long, 'Preparation of transmission electron microscopy cross-section specimens using focused ion beam milling', *Journal of Vacuum Science & Technology A: Vacuum, Surfaces, and Films*, 2001, **19**(5), 2186–2193, ISSN 0734-2101, doi:10.1116/1.1378072.

[98] T. Matsutani, K. Iwamoto, T. Nagatomi, Y. Kimura, and Y. Takai, 'Flattening of surface by sputter-etching with low-energy ions', *Japanese Journal of Applied Physics, Part 2: Letters*, 2001, **40**(5 A), 481–483, ISSN 00214922, doi:10.1143/jjap.40.l481.

[99] T. Ishitani, H. Koike, T. Yaguchi, and T. Kamino, 'Implanted gallium-ion concentrations of focused-ion-beam prepared cross sections', *Journal of Vacuum Science & Technology B: Microelectronics and Nanometer Structures Processing, Measurement, and Phenomena*, 1998, **16**(4), 1907–1913, ISSN 1071-1023, doi:10.1116/1.590106.

[100] J. G. Pellerin, D. P. Griffis, and P. E. Russell, 'Focused ion beam machining of Si, GaAs, and InP', *Journal of Vacuum Science & Technology B: Microelectronics Processing and Phenomena*, 1990, **8**(6), 1945–1950, ISSN 0734-211X, doi:10.1116/1.584880.

[101] J. Belz, A. Beyer, T. Torunski, W. Stolz, and K. Volz, 'Direct investigation of (sub-) surface preparation artifacts in GaAs based materials by FIB sectioning', *Ultramicroscopy*, 2016, **163**, 19–30, ISSN 18792723, doi:10.1016/j.ultramic.2016.01.001.

[102] J. P. McCaffrey, M. W. Phaneuf, and L. D. Madsen, 'Surface damage formation during ion-beam thinning of samples for transmission electron microscopy', *Ultramicroscopy*, 2001, **87**(3), 97–104, ISSN 03043991, doi:10.1016/S0304-3991(00)00096-6.

[103] M. Tanaka, K. Furuya, and T. Saito, 'In-situ observation of focused ion beam micropatterns on semiconductors and insulators', *Japanese Journal of Applied Physics, Part 1: Regular Papers and Short Notes and Review Papers*, 1998, **37**(12 B), 7010–7014, ISSN 00214922, doi:10.1143/jjap.37.7010.

[104] I. Utke, P. Hoffmann, and J. Melngailis, 'Gas-assisted focused electron beam and ion beam processing and fabrication', *Journal of Vacuum Science & Technology B: Microelectronics and Nanometer Structures Processing, Measurement, and Phenomena*, 2008, **26**(4), 1197–1276, ISSN 1071-1023, doi:10.1116/1.2955728.

[105] N. I. Kato, 'Reducing focused ion beam damage to transmission electron microscopy samples', *Journal of Electron Microscopy*, 2004, **53**(5), 451–458, ISSN 00220744, doi: 10.1093/jmicro/dfh080.

[106] Á. Barna, B. Pécz, and M. Menyhard, 'TEM sample preparation by ion milling/amorphization', *Micron*, 1999, **30**(3), 267–276, ISSN 09684328, doi:10.1016/S0968-4328(99)00011-6.

[107] N. Bassim, K. Scott, and L. A. Giannuzzi, 'Recent advances in focused ion beam technology and applications', *MRS Bulletin*, 2014, **39**(4), 317–325, ISSN 08837694, doi:10.1557/mrs.2014.52.

[108] Thermo Fisher Scientific Inc., 'Datasheet - Helios G4 PFIB CXe DualBeam', 2018.

[109] D. Meertens, M. Kruth, and K. Tillmann, 'FEI Helios NanoLab 400S FIB-SEM', *Journal of large-scale research facilities JLSRF*, 2016, **2**, A60, doi:10.17815/jlsrf-2-106.

[110] N. S. Smith, W. P. Skoczylas, S. M. Kellogg, D. E. Kinion, P. P. Tesch, O. Sutherland, A. Aanesland, and R. W. Boswell, 'High brightness inductively coupled plasma source for high current focused ion beam applications', *Journal of Vacuum Science & Technology B: Microelectronics and Nanometer Structures Processing, Measurement, and Phenomena*, 2006, **24**(6), 2902–2906, ISSN 1071-1023, doi:10.1116/1.2366617.

[111] L. Giannuzzi and N. Smith, 'TEM Specimen Preparation with Plasma FIB Xe + Ions', *Microscopy and Microanalysis*, 2011, **17**(S2), 646–647, ISSN 1431-9276, doi:10.1017/s1431927611004107.

[112] T. L. Burnett, R. Kelley, B. Winiarski, L. Contreras, M. Daly, A. Gholinia, M. G. Burke, and P. J. Withers, 'Large volume serial section tomography by Xe Plasma FIB dual beam microscopy', *Ultramicroscopy*, 2016, **161**, 119–129, ISSN 18792723, doi:10.1016/j.ultramic.2015.11.001.

[113] R. R. Cerchiara, P. E. Fischione, J. Liu, J. M. Matesa, A. C. Robins, H. L. Fraser, and A. Genc, 'Raising the Standard of Specimen Preparation for Aberration-Corrected TEM and STEM', *Microscopy Today*, 2011, **19**(1), 16–19, ISSN 1551-9295, doi:10.1017/s1551929510001197.

[114] A. Lotnyk, D. Poppitz, U. Ross, J. W. Gerlach, F. Frost, S. Bernütz, E. Thelander, and B. Rauschenbach, 'Focused high- and low-energy ion milling for TEM specimen preparation', *Microelectronics Reliability*, 2015, **55**(9-10), 2119–2125, ISSN 00262714, doi:10.1016/j.microrel.2015.07.005.

[115] Á. Barna, 'Low angle and low energy ion beam etching for TEM sample preparation', *Journal of Computer-Assisted Microscopy*, 1997, **9**, 101–104.

[116] S. Rubanov and P. R. Munroe, 'Damage in III-V compounds during focused ion beam milling', *Microscopy and Microanalysis*, 2005, **11**(5), 446–455, ISSN 14319276, doi:10.1017/S1431927605050294.

[117] K. Pandey, K. Paredis, T. Hantschel, C. Drijbooms, and W. Vandervorst, 'The impact of focused ion beam induced damage on scanning spreading resistance microscopy measurements', *Scientific Reports*, 2020, **10**(1), 1–15, ISSN 20452322, doi:10.1038/s41598-020-71826-w.

[118] M. A. Berding, A. Sher, M. van Schilfgaarde, P. M. Rousseau, and W. E. Spicer, 'Deactivation in heavily arsenic-doped silicon', *Applied Physics Letters*, 1998, **72**(12), 1492–1494, ISSN 0003-6951, doi:10.1063/1.121036.

[119] H. Sasaki, S. Otomo, R. Minato, K. Yamamoto, and T. Hirayama, 'Direct observation of dopant distribution in GaAs compound semiconductors using phase-shifting electron holography and Lorentz microscopy', *Microscopy*, 2014, **63**(3), 235–241, ISSN 20505701, doi:10.1093/jmicro/dfu008.

[120] D. Cooper, C. Ailliot, R. Truche, J. P. Barnes, J. M. Hartmann, and F. Bertin, 'Experimental off-axis electron holography of focused ion beam-prepared Si p-n junctions with different dopant concentrations', *Journal of Applied Physics*, 2008, **104**(6), ISSN 00218979, doi:10.1063/1.2982415.

[121] D. Cooper, R. Truche, and J. L. Rouvière, 'Reduction of electrical damage in specimens prepared using focused ion beam milling for dopant profiling using off-axis electron holography', *Ultramicroscopy*, 2008, **108**(5), 488–493, ISSN 03043991, doi:10.1016/j.ultramic.2007.08.006.

[122] A. C. Twitchett, R. E. Dunin-Borkowski, R. F. Broom, and P. A. Midgley, 'Quantitative electron holography of biased semiconductor devices', *Journal of Physics Condensed Matter*, 2004, **16**(2), ISSN 09538984, doi:10.1088/0953-8984/16/2/021.

[123] A. C. Twitchett-Harrison, T. J. Yates, S. B. Newcomb, R. E. Dunin-Borkowski, and P. A. Midgley, 'High-resolution three-dimensional mapping of semiconductor dopant potentials', *Nano Letters*, 2007, **7**(7), 2020–2023, ISSN 15306984, doi:10.1021/nl070858n.

[124] A. C. Twitchett-Harrison, R. E. Dunin-Borkowski, and P. A. Midgley, 'Mapping the electrical properties of semiconductor junctions - The electron holographic approach', *Scanning*, 2008, **30**(4), 299–309, ISSN 01610457, doi:10.1002/sca.20125.

[125] D. Cooper, R. Truche, A. C. Twitchett-Harrison, R. E. Dunin-Borkowski, and P. A. Midgley, 'Quantitative off-axis electron holography of GaAs p-n junctions prepared by focused ion beam milling', *Journal of Microscopy*, 2009, **233**(1), 102–113, ISSN 13652818, doi:10.1111/j.1365-2818.2008.03101.x.

[126] J. F. Ziegler and J. P. Biersack, *The Stopping and Range of Ions in Matter*, pp. 93–129, Springer US, Boston, MA, ISBN 978-1-4615-8103-1, 1985, doi:10.1007/978-1-4615-8103-1_3.

[127] J. F. Ziegler, 'Interactions of Ions With Matter', Available at `http://www.srim.org/`.

[128] R. E. Dunin-Borkowski, S. B. Newcomb, T. Kasama, M. R. McCartney, M. Weyland, and P. A. Midgley, 'Conventional and back-side focused ion beam milling for off-axis electron

holography of electrostatic potentials in transistors', *Ultramicroscopy*, 2005, **103**(1), 67–81, ISSN 03043991, doi:10.1016/j.ultramic.2004.11.018.

[129] J. Puretz and L. W. Swanson, 'Focused ion beam deposition of Pt containing films', *Journal of Vacuum Science & Technology B: Microelectronics and Nanometer Structures Processing, Measurement, and Phenomena*, 1992, **10**(6), 2695–2698, ISSN 1071-1023, doi:10.1116/1.586028.

[130] T. Tao, J. Ro, J. Melngailis, Z. Xue, and H. D. Kaesz, 'Focused ion beam induced deposition of platinum', *Journal of Vacuum Science & Technology B: Microelectronics Processing and Phenomena*, 1990, **8**(6), 1826–1829, ISSN 0734-211X, doi:10.1116/1.585167.

[131] S. B. Simonsen, Z. Ma, E. Mariegaard, S. De Angelis, W. L. Dacayan, K. S. Mølhave, and C. Chatzichristodoulou, 'Ion-beam deposited platinum as electrical contacting material in operando electron microscopy experiments at elevated temperatures', *Microscopy Research and Technique*, 2023, **86**(8), 1003–1011, ISSN 10970029, doi:10.1002/jemt.24373.

[132] D. W. Jenkins, G. C. Allen, P. D. Prewett, and P. J. Heard, 'Focused ion-beam assisted deposition of tungsten and carbon', *Journal of Physics: Condensed Matter*, 1991, **3**(S), ISSN 09538984, doi:10.1088/0953-8984/3/S/032.

[133] H. Langfischer, B. Basnar, H. Hutter, and E. Bertagnolli, 'Evolution of tungsten film deposition induced by focused ion beam', *Journal of Vacuum Science & Technology A: Vacuum, Surfaces, and Films*, 2002, **20**(4), 1408–1415, ISSN 0734-2101, doi:10.1116/1.1486230.

[134] I. J. Luxmoore, I. M. Ross, A. G. Cullis, P. W. Fry, J. Orr, P. D. Buckle, and J. H. Jefferson, 'Low temperature electrical characterisation of tungsten nano-wires fabricated by electron and ion beam induced chemical vapour deposition', *Thin Solid Films*, 2007, **515**(17), 6791–6797, ISSN 00406090, doi:10.1016/j.tsf.2007.02.029.

[135] B. Van Leer, L. A. Giannuzzi, and Y. C. Wang, 'Protective carbon deposition for superior FIB prepared (S)TEM specimens', *Microscopy and Microanalysis*, 2009, **15**(SUPPL. 2), 336–337, ISSN 14319276, doi:10.1017/S1431927609093428.

[136] R. J. Young and J. Puretz, 'Focused ion beam insulator deposition', *Journal of Vacuum Science & Technology B: Microelectronics and Nanometer Structures Processing, Measurement, and Phenomena*, 1995, **13**(6), 2576–2579, ISSN 1071-1023, doi:10.1116/1.588026.

[137] E. S. Sadki, S. Ooi, and K. Hirata, 'Focused-ion-beam-induced deposition of superconducting nanowires', *Applied Physics Letters*, 2004, **85**(25), 6206–6208, ISSN 00036951, doi:10.1063/1.1842367.

[138] R. M. Langford, T. X. Wang, and D. Ozkaya, 'Reducing the resistivity of electron and ion beam assisted deposited Pt', *Microelectronic Engineering*, 2007, **84**(5-8), 784–788, ISSN 01679317, doi:10.1016/j.mee.2007.01.055.

[139] Z. M. Liao, J. Xu, X. Z. Zhang, and D. P. Yu, 'The relationship between quantum transport and microstructure evolution in carbon-sheathed Pt granular metal nanowires', *Nanotechnology*, 2008, **19**(30), ISSN 09574484, doi:10.1088/0957-4484/19/30/305402.

[140] C. Zhong, R. Qi, Y. Zheng, Y. Cheng, W. Song, and R. Huang, 'The relationships of microscopic evolution to resistivity variation of a FIB-deposited platinum interconnector', *Micromachines*, 2020, **11**(6), ISSN 2072666X, doi:10.3390/MI11060588.

[141] H. W. P. Koops, A. Kaya, and M. Weber, 'Fabrication and characterization of platinum nanocrystalline material grown by electron-beam induced deposition', *Journal of Vacuum Science & Technology B: Microelectronics and Nanometer Structures Processing, Measurement, and Phenomena*, 1995, **13**(6), 2400–2403, ISSN 1071-1023, doi:10.1116/1.588008.

[142] K. A. Telari, B. R. Rogers, H. Fang, L. Shen, R. A. Weller, and D. N. Braski, 'Characterization of platinum films deposited by focused ion beam-assisted chemical vapor deposition', *Journal of Vacuum Science & Technology B: Microelectronics and Nanometer Structures Processing, Measurement, and Phenomena*, 2002, **20**(2), 590–595, ISSN 1071-1023, doi:10.1116/1.1458958.

[143] J. Wiedemair, N. Menegazzo, J. Pikarsky, K. S. Booksh, B. Mizaikoff, and C. Kranz, 'Novel electrode materials based on ion beam induced deposition of platinum carbon composites', *Electrochimica Acta*, 2010, **55**(20), 5725–5732, ISSN 00134686, doi:10.1016/j.electacta.2010.05.008.

[144] S. Rubanov and P. R. Munroe, 'The Effect of Implanted Gallium on the Recrystallization of Amorphous Layers formed during FIB Milling of Silicon', *Microscopy and Microanalysis*, 2001, **7**(S2), 958–959, ISSN 1431-9276, doi:10.1017/S1431927600030865.

[145] D. Gabor and W. L. Bragg, 'Microscopy by reconstructed wave-fronts', *Proceedings of the Royal Society of London. Series A. Mathematical and Physical Sciences*, 1949, **197**(1051), 454–487, doi:10.1098/rspa.1949.0075.

[146] E. Völkl, L. F. Allard, and D. C. Joy, *Introduction to Electron Holography*, Springer New York, NY, 1 edn., 1999.

[147] H. Lichte and M. Lehmann, 'Electron holography - Basics and applications', *Reports on Progress in Physics*, 2008, **71**(1), ISSN 00344885, doi:10.1088/0034-4885/71/1/016102.

[148] R. E. Dunin-Borkowski, A. Kovács, T. Kasama, M. R. McCartney, and D. J. Smith, *Electron Holography*, pp. 767–818, Springer International Publishing, Cham, ISBN 978-3-030-00069-1, 2019, doi:10.1007/978-3-030-00069-1_16.

[149] D. B. Williams and C. B. Carter, *High-Resolution TEM*, chap. 28, pp. 483–509, Springer US, Boston, MA, ISBN 978-0-387-76501-3, 2009, doi:10.1007/978-0-387-76501-3_28.

[150] H. Kohl and L. Reimer, *Electron-Specimen Interactions*, chap. 5, pp. 139–192, Springer New York, New York, NY, ISBN 978-0-387-34758-5, 2008, doi:10.1007/978-0-387-40093-8_5.

[151] M. Gajdardziska-Josifovska, M. R. McCartney, W. J. de Ruijter, D. J. Smith, J. K. Weiss, and J. M. Zuo, 'Accurate measurements of mean inner potential of crystal wedges using digital electron holograms', *Ultramicroscopy*, 1993, **50**(3), 285–299, ISSN 03043991, doi:10.1016/0304-3991(93)90197-6.

[152] G. Möllenstedt and H. Düker, 'Beobachtungen und Messungen an Biprisma-Interferenzen mit Elektronenwellen', *Zeitschrift für Physik*, 1956, **145**, 377–397.

[153] M. Lehmann, 'Influence of the elliptical illumination on acquisition and correction of coherent aberrations in high-resolution electron holography', *Ultramicroscopy*, 2004, **100**(1-2), 9–23, ISSN 03043991, doi:10.1016/j.ultramic.2004.01.005.

[154] E. N. Leith and J. Upatnieks, 'Reconstructed Wavefronts and Communication Theory', *J. Opt. Soc. Am.*, 1962, **52**(10), 1123–1130, doi:10.1364/JOSA.52.001123.

[155] M. R. McCartney and D. J. Smith, 'Electron Holography: Phase Imaging with Nanometer Resolution', *Annual Review of Materials Research*, 2007, **37**(1), 729–767, doi:10.1146/annurev.matsci.37.052506.084219.

[156] J. Russ and F. Neal, *The Image Processing Handbook*, CRC Press, 7 edn., 2016, doi:https://doi.org/10.1201/b18983.

[157] S. Butterworth, 'On the Theory of Filter Amplifiers', *Experimental Wireless and the Wireless Engineer*, 1930, **7**, 536–541.

[158] E. Völkl, L. F. Allard, and B. Frost, 'A software package for the processing and reconstruction of electron holograms', *Journal of Microscopy*, 1995, **180**(1), 39–50, doi:https://doi.org/10.1111/j.1365-2818.1995.tb03655.x.

[159] V. Boureau, R. McLeod, B. Mayall, and D. Cooper, 'Off-axis electron holography combining summation of hologram series with double-exposure phase-shifting: Theory and application', *Ultramicroscopy*, 2018, **193**(March), 52–63, ISSN 18792723, doi:10.1016/j.ultramic.2018.06.004.

[160] M. A. Schofield and Y. Zhu, 'Fast phase unwrapping algorithm for interferometric applications', *Opt. Lett.*, 2003, **28**(14), 1194–1196, doi:10.1364/OL.28.001194.

[161] D. C. Ghiglia and M. D. Pritt, *Two-Dimensional Phase Unwrapping: Theory, Algorithms, and Software*, Wiley, 1998, ISBN 9780471249351.

[162] R. E. Dunin-Borkowski and W. O. Saxton, 'The Electrostatic Contribution to the Forward-Scattering Potential at a Space Charge Layer in High-Energy Electron Diffraction. II. Fringing Fields', *Acta Crystallographica Section A: Foundations of Crystallography*, 1997, **53**(2), 242 – 250, doi:10.1107/S0108767396015243.

[163] R. E. Dunin-Borkowski, 'The development of Fresnel contrast analysis, and the interpretation of mean inner potential profiles at interfaces', *Ultramicroscopy*, 2000, **83**(3), 193–216, ISSN 0304-3991, doi:https://doi.org/10.1016/S0304-3991(00)00015-2.

[164] M. Beleggia, P. F. Fazzini, G. Pozzi, and P. G. Merli, 'Influence of charged oxide layers on TEM imaging of reverse-biased p-n junctions', *Physical Review B - Condensed Matter and Materials Physics*, 2003, **67**(4), 2–5, ISSN 1550235X, doi:10.1103/PhysRevB.67.045328.

[165] L. Houben, M. Luysberg, and T. Brammer, 'Illumination effects in holographic imaging of the electrostatic potential of defects and pn junctions in transmission electron microscopy', *Physical Review B - Condensed Matter and Materials Physics*, 2004, **70**(16), 1–8, ISSN 01631829, doi:10.1103/PhysRevB.70.165313.

[166] D. Cooper, A. C. Twitchett-Harrison, P. A. Midgley, and R. E. Dunin-Borkowski, 'The influence of electron irradiation on electron holography of focused ion beam milled GaAs p-n junctions', *Journal of Applied Physics*, 2007, **101**(9), 1–5, ISSN 00218979, doi:10.1063/1.2730557.

[167] A. Harscher and H. Lichte, 'Experimental study of amplitude and phase detection limits in electron holography', *Ultramicroscopy*, 1996, **64**(1), 57–66, ISSN 0304-3991, doi:10.1016/0304-3991(96)00019-8.

[168] H. Lichte, 'Performance limits of electron holography', *Ultramicroscopy*, 2008, **108**(3), 256–262, ISSN 03043991, doi:10.1016/j.ultramic.2007.06.006.

[169] T. Niermann and M. Lehmann, 'Averaging scheme for atomic resolution off-axis electron holograms', *Micron*, 2014, **63**, 28–34, ISSN 0968-4328, doi:https://doi.org/10.1016/j.micron.2014.01.008.

[170] E. Voelkl, 'Noise in off-axis type holograms including reconstruction and CCD camera parameters', *Ultramicroscopy*, 2010, **110**(3), 199–210, ISSN 03043991, doi:10.1016/j.ultramic.2009.11.010.

[171] H. Lichte, F. Börrnert, A. Lenk, A. Lubk, F. Röder, J. Sickmann, S. Sturm, K. Vogel, and D. Wolf, 'Electron holography for fields in solids: Problems and progress', *Ultramicroscopy*, 2013, **134**, 126–134, ISSN 03043991, doi:10.1016/j.ultramic.2013.05.014.

[172] F. Winkler, A. H. Tavabi, J. Barthel, M. Duchamp, E. Yucelen, S. Borghardt, B. E. Kardynal, and R. E. Dunin-Borkowski, 'Quantitative measurement of mean inner potential and specimen thickness from high-resolution off-axis electron holograms of ultra-thin layered WSe2', *Ultramicroscopy*, 2017, **178**, 38–47, ISSN 18792723, doi:10.1016/j.ultramic.2016.07.016.

[173] D. Cooper, V. Fan Arcara, B. Damilano, L. Amichi, A. Mavel, N. Rochat, G. Feuillet, A. Courville, S. Vézian, and J. Duboz, 'Mapping of the electrostatic potentials in MOCVD and hybrid GaN tunnel junctions for InGaN/GaN blue emitting light emitting diodes by off-axis electron holography correlated with structural, chemical and optoelectronic characterization', *Journal of Applied Physics of A*, 2021.

[174] D. Cooper, R. Truche, P. Rivallin, J. M. Hartmann, F. Laugier, F. Bertin, A. Chabli, and J. L. Rouvière, 'Medium resolution off-axis electron holography with millivolt sensitivity', *Applied Physics Letters*, 2007, **91**(14), 1–4, ISSN 00036951, doi:10.1063/1.2794006.

[175] P. K. Somodi, A. C. Twitchett-Harrison, P. A. Midgley, B. E. Kardynał, C. H. Barnes, and R. E. Dunin-Borkowski, 'Finite element simulations of electrostatic dopant potentials in thin semiconductor specimens for electron holography', *Ultramicroscopy*, 2013, **134**, 160–166, ISSN 03043991, doi:10.1016/j.ultramic.2013.06.023.

[176] A. C. Twitchett, R. E. Dunin-Borkowski, and P. A. Midgley, 'Quantitative Electron Holography of Biased Semiconductor Devices', *Physical Review Letters*, 2002, **88**(23), 4, ISSN 10797114, doi:10.1103/PhysRevLett.88.238302.

[177] D. Cooper, L. Bruas, M. Bryan, and V. Boureau, 'Measuring electrical properties in semiconductor devices by pixelated STEM and off-axis electron holography (or convergent beams vs. plane waves).', *Micron*, 2024, **179**(January), 103594, ISSN 09684328, doi:10.1016/j.micron.2024.103594.

[178] D. Cooper, J. M. Hartmann, B. Aventurier, F. Templier, and A. Chabli, 'Quantitative dopant profiling of laser annealed focused ion beam-prepared silicon p-n junctions with nanometer-scale resolution', *Applied Physics Letters*, 2008, **93**(18), 1–4, ISSN 00036951, doi:10.1063/1.3013834.

[179] F. Hüe, C. L. Johnson, S. Lartigue-Korinek, G. Wang, P. R. Buseck, and M. J. Hÿtch, 'Calibration of projector lens distortions', *Journal of Electron Microscopy*, 2005, **54**(3), 181–190, ISSN 0022-0744, doi:10.1093/jmicro/dfi042.

[180] T. Denneulin, C. Gatel, F. Houdellier, and M. J. Hÿtch, 'Projector lens and CCD camera distortions in a Hitachi HF-3300 TEM Projector lens and CCD camera distortions in a Hitachi HF-3300 TEM', in '18th International Microscopy Conference Proceedings', September 2015, Prague, 2014 .

[181] K. Yamamoto, T. Hirayama, and T. Tanji, 'Off-axis electron holography without Fresnel fringes', *Ultramicroscopy*, 2004, **101**(2-4), 265–269, ISSN 03043991, doi:10.1016/j.ultramic.2004.07.001.

[182] K. Harada, T. Matsuda, A. Tonomura, T. Akashi, and Y. Togawa, 'Triple-biprism electron interferometry', *Journal of Applied Physics*, 2006, **99**(11), 113502, ISSN 0021-8979, doi:10.1063/1.2198987.

[183] T. Fujita and M. R. McCartney, 'Phase recovery for electron holography using Gerchberg–Papoulis iterative algorithm', *Ultramicroscopy*, 2005, **102**(4), 279–286, ISSN 0304-3991, doi:https://doi.org/10.1016/j.ultramic.2004.10.009.

[184] J. F. Walkup and J. W. Goodman, 'Limitations of fringe-parameter estimation at low light levels', *J. Opt. Soc. Am.*, 1973, **63**(4), 399–407, doi:10.1364/JOSA.63.000399.

[185] Z. Gan, M. DiNezza, Y. H. Zhang, D. J. Smith, and M. R. McCartney, 'Determination of Mean Inner Potential and Inelastic Mean Free Path of ZnTe Using Off-Axis Electron Holography and Dynamical Effects Affecting Phase Determination', *Microscopy and Microanalysis*, 2015, **21**(6), 1406–1412, ISSN 14358115, doi:10.1017/S1431927615015378.

[186] M. Gajdardziska-Josifovska and A. H. Carim, 'Applications of Electron Holography', in E. Völkl, L. F. Allard, and D. C. Joy, eds., 'Introduction to Electron Holography', chap. 12, pp. 267–293, Springer New York, NY, 1 edn., 1999.

[187] Z. Akase and D. Shindo, 'Effects of dynamical electron diffraction on phase shift detected by electron holography', *Materials Transactions*, 2019, **60**(10), 2120–2124, ISSN 13459678, doi:10.2320/matertrans.MT-MI2019007.

[188] J. Li, M. R. McCartney, R. E. Dunin-Borkowski, and D. J. Smith, 'Determination of mean inner potential of germanium using off-axis electron holography', *Acta Crystallographica Section A: Foundations of Crystallography*, 1999, **55**(4), 652–658, ISSN 01087673, doi: 10.1107/S010876739801719X.

[189] P. M. Kelly, A. Jostsons, R. G. Blake, and J. G. Napier, 'The determination of foil thickness by scanning transmission electron microscopy', *physica status solidi (a)*, 1975, **31**(2), 771–780, doi:https://doi.org/10.1002/pssa.2210310251.

[190] S. M. Allen, 'Foil thickness measurements from convergent-beam diffraction patterns', *Philosophical Magazine A*, 1981, **43**(2), 325–335, doi:10.1080/01418618108239412.

[191] W. Kossel and G. Möllenstedt, 'Elektroneninterferenzen in konvergentem Bündel', *Naturwissenschaften*, 1938, **26**(40), 660–661, ISSN 1432-1904, doi:10.1007/BF01590351.

[192] D. Delille, R. Pantel, and E. Van Cappellen, 'Crystal thickness and extinction distance determination using energy filtered CBED pattern intensity measurement and dynamical diffraction theory fitting', *Ultramicroscopy*, 2001, **87**(1-2), 5–18, ISSN 03043991, doi:10.1016/S0304-3991(00)00067-X.

[193] W. H. Bragg and W. L. Bragg, 'The reflection of X-rays by crystals', *Proceedings of the Royal Society of London. Series A, Containing Papers of a Mathematical and Physical Character*, 1913, **88**(605), 428–438, doi:10.1098/rspa.1913.0040.

[194] H. Fitouri, M. M. Habchi, and A. Rebey, 'High-Resolution X-Ray Diffraction of III–V Semiconductor Thin Films', in A. E. Ares, ed., 'X-ray Scattering', chap. 7, IntechOpen, Rijeka, 2017, doi:10.5772/65404.

[195] D. Cooper, A. Bch, J. M. Hartmann, V. Carron, and J. L. Rouvìre, 'Strain evolution during the silicidation of nanometer-scale SiGe semiconductor devices studied by dark field electron holography', *Applied Physics Letters*, 2010, **96**(11), 2010–2013, ISSN 00036951, doi:10.1063/1.3358149.

[196] D. Neamen, *Semiconductor Physics And Devices*, McGraw-Hill, Inc., USA, 3 edn., 2002, ISBN 0072321075.

[197] S. M. Sze and M.-K. Lee, *Semiconductor Devices: Physics and Technology*, Wiley & Sons Ltd, 3rd editio edn., 2012.

[198] 'nextnano - Software for semiconductor nanodevices', Available at `https://www.nextnano.com/`.

[199] S. Birner, T. Zibold, T. Andlauer, T. Kubis, M. Sabathil, A. Trellakis, and P. Vogl, 'nextnano : General Purpose 3-D Simulations', *IEEE Transactions on Electron Devices*, 2007, **54**(9), 2137–2142, doi:10.1109/TED.2007.902871.

[200] S. Anada, K. Yamamoto, H. Sasaki, N. Shibata, M. Matsumoto, Y. Hori, K. Kinugawa, A. Imamura, and T. Hirayama, 'Accurate measurement of electric potentials in biased GaAs compound semiconductors by phase-shifting electron holography', *Microscopy*, 2019, **68**(2), 159–166, ISSN 20505701, doi:10.1093/jmicro/dfy131.

[201] S. Anada, T. Hirayama, H. Sasaki, and K. Yamamoto, 'Direct visualization of the photovoltaic effect in a single-junction GaAs cell via in situ electron holography', *Journal of Applied Physics*, 2020, **128**(24), ISSN 10897550, doi:10.1063/5.0030728.

[202] J. Hölzl and F. K. Schulte, *Work function of metals*, pp. 1–150, Springer Berlin Heidelberg, Berlin, Heidelberg, ISBN 978-3-540-35253-2, 1979, doi:10.1007/BFb0048919.

[203] L. Miroshnik, B. D. Rummel, A. B. Li, G. Balakrishnan, T. Sinno, and S. M. Han, 'Maintaining atomically smooth GaAs surfaces after high-temperature processing for precise interdiffusion analysis and materials engineering', *Journal of Vacuum Science & Technology B*, 2021, **39**(6), 62212, ISSN 2166-2746, doi:10.1116/6.0001399.

[204] J. R. Arthur, 'Surface stoichiometry and structure of GaAs', *Surface Science*, 1974, **43**(2), 449–461, ISSN 0039-6028, doi:https://doi.org/10.1016/0039-6028(74)90269-6.

[205] R. H. van Leest, P. Mulder, G. J. Bauhuis, H. Cheun, H. Lee, W. Yoon, R. van der Heijden, E. Bongers, E. Vlieg, and J. J. Schermer, 'Metal diffusion barriers for GaAs solar cells', *Phys. Chem. Chem. Phys.*, 2017, **19**(11), 7607–7616, doi:10.1039/C6CP08755H.

[206] P. Vitanov, N. Tyutyundzhiev, P. Stefchev, and B. Karamfilov, 'Low cost multilayer metallization system for silicon solar cells', *Solar Energy Materials and Solar Cells*, 1996, **44**(4), 471–484, ISSN 0927-0248, doi:https://doi.org/10.1016/S0927-0248(95)00170-0.

[207] W. E. Spicer, P. W. Chye, C. M. Garner, I. Lindau, and P. Pianetta, 'The surface electronic structure of 3–5 compounds and the mechanism of Fermi level pinning by oxygen (passivation) and metals (Schottky barriers)', *Surface Science*, 1979, **86**, 763–788, ISSN 0039-6028, doi:https://doi.org/10.1016/0039-6028(79)90458-8.

[208] W. E. Spicer, I. Lindau, P. Skeath, C. Y. Su, and P. Chye, 'Unified Mechanism for Schottky-Barrier Formation and III-V Oxide Interface States', *Phys. Rev. Lett.*, 1980, **44**(6), 420–423, doi:10.1103/PhysRevLett.44.420.

[209] E. B. Yakimov, 'What is the real value of diffusion length in GaN?', *Journal of Alloys and Compounds*, 2015, **627**, 344–351, ISSN 0925-8388, doi:https://doi.org/10.1016/j.jallcom.2014.11.229.

[210] O. Marcelot and P. Magnan, 'From EBIC images to qualitative minority carrier diffusion length maps', *Ultramicroscopy*, 2019, **197**, 23–27, ISSN 18792723, doi:10.1016/j.ultramic.2018.11.005.

[211] Z. Taghipour, S. Lee, S. A. Myers, E. H. Steenbergen, C. P. Morath, V. M. Cowan, S. Mathews, G. Balakrishnan, and S. Krishna, 'Temperature-Dependent Minority-Carrier Mobility in p-Type InAs/GaSb Type-II-Superlattice Photodetectors', *Phys. Rev. Appl.*, 2019, **11**(2), 24047, doi:10.1103/PhysRevApplied.11.024047.

[212] S. I. Maximenko, M. P. Lumb, R. Hoheisel, M. Gonzalez, D. A. Scheiman, S. R. Messenger, T. N. Tibbits, M. Imaizumi, T. Ohshima, S. I. Sato, P. P. Jenkins, and R. J. Walters, 'Radiation response of multi-quantum well solar cells: Electron-beam-induced

current analysis', *Journal of Applied Physics*, 2015, **118**(24), 0–6, ISSN 10897550, doi: 10.1063/1.4939067.

[213] M. Vaisman, K. N. Yaung, Y. Sun, and M. L. Lee, 'GaAsP/Si solar cells and tunnel junctions for III-V/Si tandem devices', *Conference Record of the IEEE Photovoltaic Specialists Conference*, 2016, **2016-Novem**, 2043–2047, ISSN 01608371, doi:10.1109/PVSC.2016.7749988.

[214] J. I. Hanoka and R. O. Bell, 'Electron-Beam-Induced Currents in Semiconductors', *Annual Review of Materials Science*, 1981, **11**(1), 353–380, ISSN 0084-6600, doi:10.1146/annurev.ms.11.080181.002033.

[215] J.-M. Bonard and J.-D. Ganie, 'Quantitative analysis of electron-beam-induced current profiles across', 1996, **79**(May), 6987–6994.

[216] W. A. Hubbard, Z. Lingley, J. Theiss, S. Sitzman, T. Ayvazian, M. Brodie, and B. Foran, 'Scanning transmission electron microscope mapping of electronic transport in polycrystalline BaTiO3 ceramic capacitors', *Applied Physics Letters*, 2019, **115**(13), ISSN 00036951, doi:10.1063/1.5117055.

[217] W. A. Hubbard, Z. Lingley, J. Theiss, M. Brodie, and B. Foran, 'STEM EBIC for High-Resolution Electronic Characterization', *IEEE International Reliability Physics Symposium Proceedings*, 2020, **2020-April**, 1–5, ISSN 15417026, doi:10.1109/IRPS45951.2020.9129618.

[218] H. J. Leamy, 'Charge collection scanning electron microscopy', *Journal of Applied Physics*, 1982, **53**(6), R51–R80, doi:10.1063/1.331667.

[219] E. R. White, A. Kerelsky, W. A. Hubbard, R. Dhall, S. B. Cronin, M. Mecklenburg, and B. C. Regan, 'Imaging interfacial electrical transport in graphene-MoS2 heterostructures with electron-beam-induced-currents', *Applied Physics Letters*, 2015, **107**(22), 1–5, ISSN 00036951, doi:10.1063/1.4936763.

[220] C. A. Smith, C. R. Bagnell, E. I. Cole, F. A. Dibianca, D. G. Johnson, W. V. Oxford, and R. H. Propst, 'Resistive Contrast Imaging: A New SEM Mode for Failure Analysis', *IEEE Transactions on Electron Devices*, 1986, **33**(2), 282–285, ISSN 15579646, doi:10.1109/T-ED.1986.22479.

[221] H. Kohl and L. Reimer, *Transmission Electron Microscopy: Physics of Image Formation*, Springer New York, NY, 5 edn., 2008, doi:https://doi.org/10.1007/978-0-387-40093-8.

[222] O. Dyck, J. L. Swett, A. R. Lupini, J. A. Mol, and S. Jesse, 'Imaging Secondary Electron Emission from a Single Atomic Layer.', *Small methods*, 2021, **5**(4), e2000950, ISSN 2366-9608 (Electronic), doi:10.1002/smtd.202000950.

[223] O. Dyck, J. L. Swett, C. Evangeli, A. R. Lupini, J. Mol, and S. Jesse, 'Contrast Mechanisms in Secondary Electron e-Beam-Induced Current (SEEBIC) Imaging', *Microscopy and Microanalysis*, 2022, **28**(5), 1567–1583, ISSN 14358115, doi:10.1017/S1431927622000824.

[224] E. Vlasov, A. Skorikov, A. Sánchez-Iglesias, L. M. Liz-Marzán, J. Verbeeck, and S. Bals, 'Secondary electron induced current in scanning transmission electron microscopy: an alternative way to visualize the morphology of nanoparticles', *ACS Materials Letters*, 2023, **5**(7), 1916–1921, ISSN 26394979, doi:10.1021/acsmaterialslett.3c00323.

[225] W. Feng, J. Schultz, D. Wolf, S. Pylypenko, T. Gemming, K. Weinel, L. Agudo Jacome, B. Büchner, and A. Lubk, 'Secondary electron emission from gold microparticles in the transmission electron microscope: comparison of Monte Carlo simulations with experimental results', *Journal of Physics D: Applied Physics*, 2024.

[226] J. D. Russell and C. Leach, 'Problems associated with imaging resistive barriers in BaTiO3 PTC ceramics using the SEM conductive mode', *Journal of the European Ceramic Society*, 1995, **15**(7), 617–622, ISSN 0955-2219, doi:https://doi.org/10.1016/0955-2219(95)00023-N.

[227] D. B. Williams and C. B. Carter, *Inelastic Scattering and Beam Damage*, chap. 4, pp. 53–71, Springer US, Boston, MA, ISBN 978-0-387-76501-3, 2009, doi:10.1007/978-0-387-76501-3_4.

[228] J. Schou, 'Secondary electron emission from solids by electron and proton bombardment', *Scanning Microscopy*, 1988, **2**(2), 607–631.

[229] M. S. Chung and T. E. Everhart, 'Simple calculation of energy distribution of low-energy secondary electrons emitted from metals under electron bombardment', *Journal of Applied Physics*, 1974, **45**(2), 707–709, ISSN 00218979, doi:10.1063/1.1663306.

[230] J. G. Trump and R. J. de Graaff, 'The Secondary Emission of Electrons by High Energy Electrons', *Phys. Rev.*, 1949, **75**(1), 44–45, doi:10.1103/PhysRev.75.44.

[231] A. K. Haque, M. M. Haque, M. A. R. Patoary, M. A. Uddin, M. I. Hossain, M. S. Mahbub, A. K. Basak, M. Maaza, and B. C. Saha, 'Electron impact secondary electron emissions from elemental and compound solids', *Vacuum*, 2017, **141**, 192–209, ISSN 0042207X, doi:10.1016/j.vacuum.2017.04.004.

[232] D. M. Suszcynsky and J. E. Borovsky, 'Modified Sternglass theory for the emission of secondary electrons by fast-electron impact', *Physical Review A*, 1992, **45**(9), 6424 – 6428, doi:10.1103/PhysRevA.45.6424.

[233] H. Inada, D. Su, R. F. Egerton, M. Konno, L. Wu, J. Ciston, J. Wall, and Y. Zhu, 'Atomic imaging using secondary electrons in a scanning transmission electron microscope: Experimental observations and possible mechanisms', *Ultramicroscopy*, 2011, **111**(7), 865–876, ISSN 03043991, doi:10.1016/j.ultramic.2010.10.002.

[234] A. Nouiri, S. Chaguetmi, and N. Belabed, 'Monte Carlo model of the temperature rise at a GaAs surface under an electron beam', *Surface and Interface Analysis*, 2006, **38**(7), 1153–1157, doi:https://doi.org/10.1002/sia.2372.

[235] H. Bethe, 'Zur Theorie des Durchgangs schneller Korpuskularstrahlen durch Materie', *Annalen der Physik*, 1930, **397**(3), 325–400, doi:https://doi.org/10.1002/andp.19303970303.

[236] H. Bethe, 'Bremsformel für Elektronen relativistischer Geschwindigkeit', *Zeitschrift für Physik*, 1932, **76**(5), 293–299, ISSN 0044-3328, doi:10.1007/BF01342532.

[237] R. Zhou, M. Yu, D. Tweddle, P. Hamer, D. Chen, B. Hallam, A. Ciesla, P. P. Altermatt, P. R. Wilshaw, and R. S. Bonilla, 'Understanding and optimizing EBIC pn-junction characterization from modeling insights', *Journal of Applied Physics*, 2020, **127**(2), ISSN 10897550, doi:10.1063/1.5139894.

[238] S. W. Glunz, D. Biro, S. Rein, and W. Warta, 'Field-effect passivation of the SiO2Si interface', *Journal of Applied Physics*, 1999, **86**(1), 683–691, ISSN 0021-8979, doi:10.1063/1.370784.

[239] D. Fathy, T. G. Sparrow, and U. Valdrè, 'Observation of dislocations and microplasma sites in semiconductors by direct correlations of STEBIC, STEM and ELS', *Journal of Microscopy*, 1980, **118**(3), 263–273, doi:https://doi.org/10.1111/j.1365-2818.1980.tb00273.x.

[240] G. Moldovan, A. P. Conlan, and D. Cooper, 'In-Situ EBIC STEM: Automated Quantification', *Microscopy and Microanalysis*, 2022, **28**(S1), 1718–1719, ISSN 1431-9276, doi:10.1017/s143192762200681x.

[241] 'Point Electronic GmbH', Available at `https://www.pointelectronic.de/`.

[242] A. Hussain, L. H. Yang, Y. B. Zou, S. F. Mao, B. Da, H. M. Li, and Z. J. Ding, 'Theoretical calculations of the mean escape depth of secondary electron emission from compound semiconductor materials', *Journal of Applied Physics*, 2020, **127**(12), ISSN 10897550, doi:10.1063/1.5144721.

[243] Y. B. Zou, S. F. Mao, B. Da, and Z. J. Ding, 'Surface sensitivity of secondary electrons emitted from amorphous solids: Calculation of mean escape depth by a Monte Carlo method', *Journal of Applied Physics*, 2016, **120**(23), ISSN 10897550, doi:10.1063/1.4972196.

[244] A. K. Chee, R. F. Broom, C. J. Humphreys, and E. G. Bosch, 'A quantitative model for doping contrast in the scanning electron microscope using calculated potential distributions and Monte Carlo simulations', *Journal of Applied Physics*, 2011, **109**(1), ISSN 00218979, doi:10.1063/1.3524186.

[245] R. Guo and T. Walther, 'Towards quantification of doping in gallium arsenide nanostructures by low-energy scanning electron microscopy and conductive atomic force microscopy', *Journal of Microscopy*, 2024, **293**(3), 160–168, ISSN 13652818, doi:10.1111/jmi.13263.

[246] L. Frank, M. Hovorka, M. M. El-Gomati, I. Müllerová, F. Mika, and E. Mikmeková, 'Acquisition of the dopant contrast in semiconductors with slow electrons', *Journal of Electron Spectroscopy and Related Phenomena*, 2020, **241**(July 2018), 146836, ISSN 03682048, doi:10.1016/j.elspec.2019.03.004.

[247] M. Dapor, *Applications*, pp. 139–149, Springer International Publishing, Cham, ISBN 978-3-030-43264-5, 2020, doi:10.1007/978-3-030-43264-5_11.

[248] K. Jandieri, S. D. Baranovskii, O. Rubel, W. Stolz, F. Gebhard, W. Guter, M. Hermle, and A. W. Bett, 'Resonant electron tunneling through defects in GaAs tunnel diodes', *Journal of Applied Physics*, 2008, **104**(9), ISSN 00218979, doi:10.1063/1.3013886.

[249] E. Barrigón, I. García, L. Barrutia, I. Rey-Stolle, and C. Algora, 'Highly conductive p-AlGaAs/n-GaInP tunnel junctions for ultra-high concentrator solar cells', *Progress in Photovoltaics: Research and Applications*, 2014, **22**(4), 399–404, doi:10.1002/pip.2476.

[250] R. R. King, C. M. Fetzer, P. C. Colter, K. M. Edmondson, J. H. Ermer, H. L. Cotal, H. Yoon, A. P. Stavrides, G. Kinsey, D. D. Krut, and N. H. Karam, 'High-efficiency space and terrestrial multijunction solar cells through bandgap control in cell structures', *Conference Record of the IEEE Photovoltaic Specialists Conference*, 2002, pp. 776–781, ISSN 01608371, doi:10.1109/pvsc.2002.1190685.

[251] D. Jung, C. A. Parker, J. Ramdani, and S. M. Bedair, 'AlGaAs/GaInP heterojunction tunnel diode for cascade solar cell application', *Journal of Applied Physics*, 1993, **74**(3), 2090–2093, ISSN 00218979, doi:10.1063/1.354753.

[252] N. H. Karam, R. R. King, M. Haddad, J. H. Ermer, H. Yoon, H. L. Cotal, R. Sudharsanan, J. W. Eldredge, K. Edmondson, D. E. Joslin, D. D. Krut, M. Takahashi, W. Nishikawa, M. Gillanders, J. Granata, P. Hebert, B. T. Cavicchi, and D. R. Lillington, 'Recent developments in high-efficiency Ga0.5In0.5P/GaAs/Ge dual- and triple-junction solar cells: Steps to next-generation PV cells', *Solar Energy Materials and Solar Cells*, 2001, **66**(1-4), 453–466, ISSN 09270248, doi:10.1016/S0927-0248(00)00207-5.

[253] C. Ebert, Z. Pulwin, D. Byrnes, A. Paranjpe, and W. Zhang, 'Tellurium doping of InGaP for tunnel junction applications in triple junction solar cells', *Journal of Crystal Growth*, 2011, **315**(1), 61–63, ISSN 00220248, doi:10.1016/j.jcrysgro.2010.09.050.

[254] J. F. Geisz, D. J. Friedman, J. S. Ward, A. Duda, W. J. Olavarria, T. E. Moriarty, J. T. Kiehl, M. J. Romero, A. G. Norman, and K. M. Jones, '40.8% Efficient Inverted Triple-Junction Solar Cell With Two Independently Metamorphic Junctions', *Applied Physics Letters*, 2008, **93**(12), 1–4, ISSN 00036951, doi:10.1063/1.2988497.

[255] K. Sasaki, T. Agui, K. Nakaido, N. Takahashi, R. Onitsuka, and T. Takamoto, 'Development Of InGaP/GaAs/InGaAs inverted triple junction concentrator solar cells', *AIP Conference Proceedings*, 2013, **1556**, 22–25, ISSN 15517616, doi:10.1063/1.4822190.

[256] 'ASTM G173-23 Standard Tables for Reference Solar Spectral Irradiances: Direct Normal and Hemispherical on 37° Tilted Surface', doi:10.1520/G0173-23. Available at `https://store.astm.org/g0173-23.html`.

[257] Y. Zhang, S. Krishnamoorthy, F. Akyol, S. Bajaj, A. A. Allerman, M. W. Moseley, A. M. Armstrong, and S. Rajan, 'Tunnel-injected sub-260 nm ultraviolet light emitting diodes', *Applied Physics Letters*, 2017, **110**(20), ISSN 00036951, doi:10.1063/1.4983352.

[258] P. Y. Su, H. Liu, R. M. Kawabata, E. C. Weiner, R. Jakomin, M. P. Pires, R. R. King, P. L. Souza, and F. A. Ponce, 'Effect of InAs quantum dots capped with GaAs on atomic-

scale ordering in Ga 0.5 In 0.5 P', *Journal of Applied Physics*, 2019, **125**(5), 0–9, ISSN 10897550, doi:10.1063/1.5063941.

[259] T. Suzuki, A. Gomyo, S. Iijima, K. Kobayashi, S. Kawata, I. Hino, and T. Yuasa, 'Band-Gap Energy Anomaly and Sublattice Ordering in GaInP and AlGaInP Grown by Metal-organic Vapor Phase Epitaxy', *Japanese Journal of Applied Physics*, 1988, **27**(11R), 2098, doi:10.1143/JJAP.27.2098.

[260] L. C. Su, I. H. Ho, and G. B. Stringfellow, 'Effects of substrate misorientation and growth rate on ordering in GaInP', *Journal of Applied Physics*, 1994, **75**(10), 5135–5141, ISSN 00218979, doi:10.1063/1.355759.

[261] M. Zorn, P. Kurpas, A. I. Shkrebtii, B. Junno, A. Bhattacharya, K. Knorr, M. Weyers, L. Samuelson, J. T. Zettler, and W. Richter, 'Correlation of InGaP(001) surface structure during growth and bulk ordering', *Physical Review B - Condensed Matter and Materials Physics*, 1999, **60**(11), 8185–8190, ISSN 1550235X, doi:10.1103/PhysRevB.60.8185.

[262] B. T. McDermott, K. G. Reid, N. A. El-Masry, S. M. Bedair, W. M. Duncan, X. Yin, and F. H. Pollak, 'Atomic layer epitaxy of GaInP ordered alloy', *Applied Physics Letters*, 1990, **56**(12), 1172–1174, ISSN 0003-6951, doi:10.1063/1.102553.

[263] G. B. Stringfellow, J. K. Shurtleff, R. T. Lee, C. M. Fetzer, and S. W. Jun, 'Surface processes in OMVPE - the frontiers', *Journal of Crystal Growth*, 2000, **221**(1-4), 1–11, ISSN 00220248, doi:10.1016/S0022-0248(00)00640-0.

[264] H. Murata, T. C. Hsu, I. H. Ho, L. C. Su, Y. Hosokawa, and G. B. Stringfellow, 'Surface photoabsorption study of the effect of V/III ratio on ordering in GaInP', *Applied Physics Letters*, 1996, **68**(13), 1796–1798, ISSN 00036951, doi:10.1063/1.116016.

[265] A. L. Chua, E. Pelucchi, A. Rudra, B. Dwir, E. Kapon, A. Zangwill, and D. D. Vvedensky, 'Theory and experiment of step bunching on misoriented GaAs(001) during metalorganic vapor-phase epitaxy', *Applied Physics Letters*, 2008, **92**(1), 2006–2009, ISSN 00036951, doi:10.1063/1.2832370.

[266] K. Bellmann, U. W. Pohl, C. Kuhn, T. Wernicke, and M. Kneissl, 'Controlling the morphology transition between step-flow growth and step-bunching growth', *Journal of Crystal Growth*, 2017, **478**, 187–192, ISSN 00220248, doi:10.1016/j.jcrysgro.2017.09.007.

[267] 'LiberTEM-blobfinder', Available at `https://libertem.github.io/LiberTEM-blobfinder/index.html`.

[268] R. S. Pennington, C. B. Boothroyd, and R. E. Dunin-Borkowski, 'Surface effects on mean inner potentials studied using density functional theory', *Ultramicroscopy*, 2015, **159**(P1), 34–45, ISSN 18792723, doi:10.1016/j.ultramic.2015.07.011.

[269] D. Cooper, C. Licitra, Y. Boussadi, B. Ben-Bakir, and B. Masenelli, 'Mapping of the Electrostatic Potentials in a Fully Processed Led Device with nm-Scale Resolution by In Situ off-Axis Electron Holography', *Small Methods*, 2023, **7**(9), 1–9, ISSN 23669608, doi:10.1002/smtd.202300537.

[270] S. M. Schwarz, B. W. Kempshall, L. A. Giannuzzi1, and M. R. McCartney, 'Avoiding the Curtaining Effect: Backside Milling by FIB INLO', *Microscopy and Microanalysis*, 2003, **9**(S02), 116–117, ISSN 1431-9276, doi:10.1017/S1431927603441044.

[271] D. Cooper, T. Denneulin, N. Bernier, A. Béché, and J. L. Rouvière, 'Strain mapping of semiconductor specimens with nm-scale resolution in a transmission electron microscope', *Micron*, 2016, **80**, 145–165, ISSN 09684328, doi:10.1016/j.micron.2015.09.001.

[272] M. A. Green, 'Photovoltaic principles', *Physica E: Low-Dimensional Systems and Nanostructures*, 2002, **14**(1-2), 11–17, ISSN 13869477, doi:10.1016/S1386-9477(02)00354-5.

[273] A. Luque and S. Hegedu, *Handbook of Photovoltaic Science and Engineering - Wiley Online Library*, John Wiley & Sons, Ltd, Chichester, 2005.

List of Publications

Conference Talks

1. Mergner, V., Klitzke, M., Schygulla, P., Lackner, D., Kovács, A., Jäger, W., Dimroth, F., Dunin-Borkowski, R.E., Cooper, D., Off-Axis Electron Holography of *In-Situ*-Biased Highly-Doped p-AlGaAs/n-GaInP Junctions for Solar Cell Applications. European Microscopy Congress 2024, 25.–30.08.2024

2. Mergner, V., Kovács, A., Schygulla, P., Lackner, D., Jaeger, W., Dimroth, F., Dunin-Borkowski, R.E., Cooper, D., *In situ* Off-Axis Electron Holography and Electron Beam Induced Current Measurements of III-V Junctions for Solar Cell Applications. FEMS EUROMAT 2023, 03.–07.09.2023

3. Mergner, V., Schygulla, P., Kovács, A., Lackner, D., Jaeger, W., Dimroth, F., Dunin-Borkowski, R.E., Cooper, D., *In situ* Off-Axis Electron Holography and Electron Beam Induced Current Microscopy for the Electrical Investigation of GaAs, InP and GaInP p-n Junctions. Microscopy of Semi-Conducting Materials (MSM), 03.–06.04.2023

Conference Posters

1. Mergner, V., Schygulla, P., Lackner, D., Ebert, P., Kovács, A., Dimroth, F., Dunin-Borkowski, R.E., The effect of epitaxial growth direction on the properties of highly doped p-AlGaAs/n-GaInP interfaces. PICO 2022, Frontiers of Aberration Corrected Electron Microscopy, 08.–12.05.2022

Band / Volume 292
Tolerance engineering of Pseudomonas for the efficient conversion and production of aldehydes
T. Lechtenberg (2025), XVI, 185 pp
ISBN: 978-3-95806-817-9

Band / Volume 293
Exploring the process window for production of itaconic, 2-hydroxyparaconic, and itatartaric acid with engineered *Ustilago* strains
P. Ernst (2025), x, 145 pp
ISBN: 978-3-95806-825-4

Band / Volume 294
Surface Plasmon Resonance Microscopy for the Characterization of Cell-Substrate Distances
J. Bednar (2025), xxiii, 187 pp
ISBN: 978-3-95806-830-8

Band / Volume 295
Microfluidic-MEA hybrid systems for electrophysiological recordings of neuronal co-cultures
J. Stevanović (2025), ix, 186 pp
ISBN: 978-3-95806-831-5

Band / Volume 296
Structural and Magnetic Properties of Biocompatible Iron Oxide Nanoparticles for Medical Applications
A. Nasser (2025), xii, 140 pp
ISBN: 978-3-95806-837-7

Band / Volume 297
Metabolic engineering of *Pseudomonas taiwanensis* for the improved production of styrene
J. Rönitz (2025), XII, 147 pp
ISBN: 978-3-95806-841-4

Band / Volume 298
Elucidation of anti-viral strategies in *Streptomyces*
B. U. Rackow (2025), xii, 148 pp
ISBN: 978-3-95806-842-1

Band / Volume 299
Ab initio investigations of spin-orbit functionalized graphene
D. Mazhjoo (2025), 163 pp
ISBN: 978-3-95806-847-6

Band / Volume 300
3D neural implants for* in vivo *applications
M. Jung (2025), xvi, 215 pp
ISBN: 978-3-95806-852-0

Band / Volume 301
Phonons in Magnetic Systems by means of Density-Functional Perturbation Theory
A. Neukirchen (2025), xviii, 195 pp
ISBN: 978-3-95806-853-7

Band / Volume 302
Optimal control and machine learning of quantum device dynamics
F. Preti (2025), iv, 211 pp
ISBN: 978-3-95806-856-8

Band / Volume 303
Development of a New, Miniaturized and Flexible Temperature Sensor
S. Hamacher (2025), XXII, 153 pp
ISBN: 978-3-95806-863-6

Band / Volume 304
Investigation of spin current generated THz transients in materials with high spin-orbit coupling
S. Heidtfeld (2026), viii, 112, v pp
ISBN: 978-3-95806-893-3

Band / Volume 305
Structural and Electronic Characterization of MBE-grown Topological Insulator Thin Films
X. Hou (2026), iv, 168 pp
ISBN: 978-3-95806-918-3 (Print)
ISBN: 978-3-95806-919-0 (E-Book)

Band / Volume 306
***In Situ* Biasing Off-Axis Electron Holography and Electron Beam Induced Current Microscopy for the Electrical Investigation of p-n Junctions in High-Efficiency III-V Multi-Junction Solar Cells**
V. Mergner (2026), XXXII, 259 pp
ISBN: 978-3-95806-924-4 (Print)
ISBN: 978-3-95806-925-1 (E-Book)

Weitere ***Schriften des Verlags im Forschungszentrum Jülich*** unter
http://wwwzb1.fz-juelich.de/verlagextern1/index.asp

Schlüsseltechnologien / Key Technologies
Band / Volume 306
ISBN 978-3-95806-925-1

Mitglied der Helmholtz-Gemeinschaft

JÜLICH
Forschungszentrum